

RAIL STEELS- Developments, Processing, and Use

Stone/Knupp, editors



STP 644



American Society for Testing and Materials

RAIL STEELS— DEVELOPMENTS, PROCESSING, AND USE

A symposium
sponsored by ASTM
Committee A-1 on Steel,
Stainless Steel, and Related Alloys
AMERICAN SOCIETY FOR
TESTING AND MATERIALS
Denver, Colo., 17-18 Nov. 1976

ASTM SPECIAL TECHNICAL PUBLICATION 644
D. H. Stone, Association of American Railroads
G. G. Knupp, Bethlehem Steel Corporation
editors

List price \$45.00
04-644000-01



AMERICAN SOCIETY FOR TESTING AND MATERIALS
1916 Race Street, Philadelphia, Pa. 19103

Copyright © by AMERICAN SOCIETY FOR TESTING AND MATERIALS 1978
Library of Congress Catalog Card Number: 77-087213

NOTE

**The Society is not responsible, as a body,
for the statements and opinions
advanced in this publication.**

**Printed in Tallahassee, Fla.
May 1978**

Foreword

The symposium on Rail Steels—Developments, Processing, and Use was presented at a meeting held in Denver, Colo., 17–18 Nov. 1976. The symposium was sponsored by the American Society for Testing and Materials through its Committee A-1 on Steel, Stainless Steel, and Related Alloys. D. H. Stone, Association of American Railroads, and G. G. Knupp, Bethlehem Steel Corporation, presided as symposium chairmen and editors of this publication.

Related ASTM Publications

Second Edition Unified Numbering System for Metals and Alloys, DS 56A
(1977), \$49.00 (04-056001-01)

Inclusions in Steel—E 45 Adjunct, \$6.00 (12-500450-01)

Temper Embrittlement of Alloy Steels, STP 499 (1972), \$10.00
(04-499000-02)

A Note of Appreciation to Reviewers

This publication is made possible by the authors and, also, the unheralded efforts of the reviewers. This body of technical experts whose dedication, sacrifice of time and effort, and collective wisdom in reviewing the papers must be acknowledged. The quality level of ASTM publications is a direct function of their respected opinions. On behalf of ASTM we acknowledge with appreciation their contribution.

ASTM Committee on Publications

Editorial Staff

Jane B. Wheeler, *Managing Editor*

Helen M. Hoersch, *Associate Editor*

Ellen J. McGlinchey, *Senior Assistant Editor*

Sheila G. Pulver, *Assistant Editor*

Contents

Introduction	1
AN INTRODUCTION TO RAIL STEELS	
A Review of the Manufacture, Processing, and Use of Rail Steels in North America—A Report of AISI Technical Subcommittee on Rails and Accessories—G. G. KNUPP, W. H. CHIDLEY, J. L. GIOVE, H. H. HARTMAN, G. F. MORRIS, AND C. W. TAYLOR	7
The Effect of Mechanical Properties Upon the Performance of Railroad Rails—D. H. STONE AND R. K. STEELE	21
Discussion	48
Rail Wear Under Heavy Traffic Conditions—J. KALOUSEK AND A. E. BETHUNE	63
The Assessment of Rail Steels—K. MORTON, D. F. CANNON, P. CLAYTON, AND E. G. JONES	80
A Metallurgical Examination of Control-Cooled, Carbon-Steel Rails with Service-Developed Defects—D. E. SONON, J. V. PELLEGRINO, AND J. M. WANDRISCO	99
Welding of Railroad Rails—A Literature and Industry Survey—DANIEL HAUSER	118
EFFECTS OF ALLOY ADDITIONS AND SPECIAL PROCESSING ON RAIL STEELS	
Role of Alloying and Microstructure on the Strength and Toughness of Experimental Rail Steels—G. K. BOUSE, I. M. BERNSTEIN, AND D. H. STONE	145
Discussion	162
Development of High-Strength Alloyed Rail Steels Suitable for Heavy Duty Applications—S. MARICH AND P. CURCIO	167
Discussion	198

Alloy Steels for High-Strength, As-Rolled Rails—Y. E. SMITH AND F. B. FLECTCHER	212
Some Features and Metallurgical Considerations of Surface Defects in Rail Due to Contact Fatigue—H. MASUMOTO, K. SUGINO, S. NISIDA, R. KURIHARA, AND S. MATSUYAMA	233
United Kingdom Development of Rails Rolled from Continuously Cast Blooms—J. D. YOUNG	256

STRENGTH AND FRACTURE OF RAIL STEELS

Mechanism of Cleavage Fracture in Fully Pearlitic 1080 Rail Steel— YONG-JIN PARK AND I. M. BERNSTEIN	287
Fracture Mechanics Analysis of Rails with Shell-Initiated Transverse Cracks—P. M. BESUNER	303
Stresses Around Transverse Fissure Flaws in Rails Due to Service Loads—S. G. SAMPATH, T. G. JOHNS, P. M. MC GUIRE, AND K. B. DAVIES	330
Prediction of Rail Steel Strength Requirements—A Reliability Ap- proach—R. I. MAIR AND R. GROENHOUT	342

FATIGUE IN RAIL STEELS

The Effect of Grain Boundary Ferrite on Fatigue Crack Propagation in Pearlitic Rail Steels—G. J. FOWLER AND A. S. TETELMAN	363
Discussion	383
Fatigue and Fracture Behavior of Carbon-Steel Rails—J. M. BARSOM AND E. J. IMHOF, JR.	387
Discussion	410
Fatigue Crack Propagation in Rail Steels—C. E. FEDDERSEN AND DAVID BROEK	414
An Evaluation of the Fatigue Performance of Conventional British Rail Steels—B. J. DABELL, S. J. HILL, AND P. WATSON	430
Cyclic Inelastic Deformation and Fatigue Resistance Characteristics of a Rail Steel—B. N. LEIS	449

SUMMARY

Summary	471
Index	475

Introduction

The technical literature is lacking in the specific area of rail steel, the steel rail, and the why and how of service developments currently experienced in this most basic component of our great railroad industry. ASTM Subcommittee A01.01 on Steel Rails and Accessories recognized in 1975 the need for a forum through which state-of-the-art technical papers on rail steel, its development, processing, and use could be presented. A symposium on rail steel, the first conference of its kind ever in the United States, was held during Committee Week, 17–18 Nov. 1976, in Denver, Colo., under the direction of the editors.

An international response to the call resulted in the acceptance of more than 20 papers in the general categories of “An Introduction to Rail Steels,” “Effects of Alloy Additions and Special Processing on Rail Steels,” “Strength and Fracture of Rail Steels,” and “Fatigue in Rail Steels.” The papers were presented and discussed, and are published herein along with several pertinent postmeeting written discussions. The international attendance and participation throughout the symposium is greatly appreciated. These contributions have made possible this initial publication in a field that invites increased activity.

Rails in today's heavy-duty service lines in North America are, relatively speaking, in a state of accelerating deterioration. This is the state, not by design but rather by the lack of it. The increased wear, deformation, and failure rate occurring in rails is, in the opinion of many, the direct result of the unfavorable economic atmosphere under which the railroads have had to operate for several decades, and the regrettable development of oversize rolling stock designed to cope with the situation. While the growth of railroading, the railroad rail, and the rail problem are covered in detail in the introductory symposium paper, the resumé in the next few paragraphs will give those not familiar with railroading sufficient background to put the technical papers into the proper context.

The concept of free interchange of freight traffic among American railroads in the early 1860s made possible the development of one of the world's great transportation systems. Mandatory interchange rules by the Master Car Builders Association and its successor, The Mechanical Division of the Association of American Railroads, guided rolling stock development from the early 30-ton capacity freight cars, through the 40, 50, 70, and 90-ton types, to the 100-ton and heavier capacity units which now make up the bulk

2 RAIL STEELS—DEVELOPMENTS, PROCESSING, AND USE

of new car acquisitions. Similarly, motive power was developed from the early 35-ton American-type steam locomotive, through the massive 400 to 500-ton articulated steam types, and on to the more versatile electric and diesel-electric power units that are standard today. These latter units provide greater flexibility in tractive effort and permit operation at higher train speeds.

The configuration of locomotives and cars in trains changed dramatically. The amount of motive power, the number of cars, and the lading have been increased until, in recent years, commonplace unit trains are in excess of 10 000 tons.

Reductions in main line trackage through centralized traffic control, mergers, and abandonments in the last two decades have increased the traffic density on existing tracks until some heavy haul lines carry up to 70 million gross tons annually.

Marketing interests in the railroad industry promoted this upward spiral in car size and loading, train size and speed, to recapture fading business in a highly competitive transport market. The Mechanical Division of the Association of American Railroads supported the trend, and the operations departments of the railroads moved the heavier trains.

The Engineering Division of the Association of American Railroads, responsible for the track structure and its maintenance, recognized early that the rails, accessories, and roadbed were showing the adverse effect of the more destructive forces being transmitted through the wheel/rail interface. However, lacking authority to force a change, its recommendations went unheeded until great numbers of 90 and 100-ton cars had entered the interchange fleet, and the early destruction of the rails, etc., was underway. The concept that commercial benefits would justify the higher maintenance costs incurred proved erroneous.

Although the acceptance in interchange of 125-ton cars has been stalled, maintenance problems escalate as the ratio of heavy to lighter cars increases, and the accompanying heavier wheel loads are at that point where the high contact stresses between the wheel and the railhead greatly exceed the elastic limit of the steel. Service-induced plastic deformation, abrasion, and fatigue-developed detailed fractures in rails therefore are considered to be the direct result of the unfavorable in-track stress environment.

The depressed economic atmosphere under which the heavy rail loading developed manifested itself in other ways. For example, the general state of track maintenance deteriorated; research and test work by individual railroads, the Association of American Railroads, and the American Railway Engineering Association was virtually halted; and the fluctuating rail market curtailed major capital investments by rail producers in new manufacturing facilities. In the latter case, the general rail needs of the railroads have been met, and, where possible, new technologies have been applied in the production of rails.

The historical approach of increasing the size of the rail became ineffective years ago, and, although higher strength steel in rails, through heat treatment or alloying, has proved effective in delaying development, it is a treatment but not a cure for the ills from service abuse.

What has happened to the rails placed into heavy-duty service since the late 1940s is self evident. With little hope that currently accepted wheel loadings could be materially reduced, it has become necessary for the industry to search for a better understanding of the mechanisms involved in rail failures. In the early 1970s, revitalization of the Association of American Railroads Technical Center in Chicago got underway, and rail problem studies and Track-Train-Dynamics programs were initiated as money and manpower were made available through the railroads, related industries, and government agencies. Certain of the papers published herein evolved from such programs.

The papers presented in the "Introduction to Rail Steels" section of this volume document the aforesaid for the most part. Surface and internal fatigue failures, and wear are described, and the influence of metallurgical composition, structure, and properties on service life is discussed. A study of the metallurgical characteristics and fractographic analysis of selected rails from service in a search for correlation between material characteristics and failure is presented.

Evaluations of laboratory and actual performance are given in the second grouping of papers, "Effects of Alloy Additions and Special Processing on Rail Steels." Service-developed defects are further defined, and possible ways to enhance the resistance of the steel to these developments are explored. The production of rails from continuously cast steel blooms from one mill is described and the product evaluated.

The probability of being able to predict the rail steel strength required to control damaging plastic deformation and resulting failures in a given service is explored in the "Strength and Fracture of Rail Steels" section. Attention is directed also to the mechanism of fracture, fracture mechanics analysis, and stress intensity considerations for cracks that have developed in rail steel while in service.

The "Fatigue in Rail Steels" section offers papers with differing views on fatigue crack growth rate, cyclic inelastic deformation behavior, and the effect of metallurgical notches and load environment.

We believe that, in general, the papers in this volume present initial work in diverse areas on rail steel and rails to technically analyze and assess possible modes of initiation and progression of service failures. The need for correlated in-track stress environment studies on rails in heavy service, particularly in failure-prone track locations, is recognized.

Metallurgical and strength-of-material considerations may dictate the need for railroads to upgrade their requirements for rails. It can be similarly projected that the seemingly obvious overstressing of rails in service will

4 RAIL STEELS—DEVELOPMENTS, PROCESSING, AND USE

need to be controlled by the railroads to attain a balanced and economically sound rail maintenance posture. Thus, directions for future research efforts in several areas are indicated.

G. G. Knupp

Senior Metallurgical Engineer,
Bethlehem Steel Corporation,
Bethlehem, Pa. 18016; coeditor.

An Introduction to Rail Steels

G. G. Knupp,¹ W. H. Chidley,² J. L. Giove,³ H. H. Hartman,⁴
G. F. Morris,⁵ and C. W. Taylor⁶

A Review of the Manufacture, Processing, and Use of Rail Steels in North America—A Report of AISI Technical Subcommittee on Rails and Accessories

REFERENCES: Knupp, G. G., Chidley, W. H., Giove, J. L., Hartman, H. H., Morris, G. F., and Taylor, C. W., "A Review of the Manufacture, Processing, and Use of Rail Steels in North America—A Report of AISI Technical Subcommittee on Rails and Accessories," *Rail Steels—Developments, Processing, and Use, ASTM STP 644*, D. H. Stone and G. G. Knupp, Eds., American Society for Testing and Materials, 1978, pp. 7–20.

ABSTRACT: The intent of this, the initial paper of this publication, is generally to set the stage for the more specific and detailed state-of-the-art papers to follow. The evolution of the North American tee rail in its struggle to "keep its head" under progressively heavier and faster-moving motive power and rolling stock is traced briefly. Technological developments in rail steel and rail production designed to improve quality and enhance resistance to service developments are reviewed. This includes adaptation of various steelmaking processes and grades of steel to the production of rails, and the handling of the steel through the forming, cooling, finishing, and in some cases further treatment of the rails.

KEY WORDS: steels, railroad tracks, abrasion, plastic deformation, cracks, flakes, rolling stock, shear, crushing, butt welds, fillets, vacuum degassing, hot topping, cooling, thermit welding

It is not the intention in this, the introductory paper of the symposium, to explore in detail the historical evolution of the railroad rail and railroading.⁷ However, it is essential that we review sufficient railroad history and rail

¹Metallurgical engineer, Bethlehem Steel Corporation, Bethlehem, Pa.

²Consulting engineer, Technical Subcommittee on Rails and Accessories, American Iron and Steel Institute, Chicago, Ill.

³Manager, Railroad Products Metallurgy, United States Steel Corporation, Pittsburgh, Pa.

⁴Superintendent, Product Development and Research, CF&I Steel Corporation, Pueblo, Colo.

⁵Manager, Quality Control, Primary Rolling and Structural Mills, Algoma Steel Corporation, Ltd., Sault Ste. Marie, Ont., Canada.

⁶Manager, Metallurgical Services, Sydney Steel Corporation, Sydney, N.S., Canada.

⁷This being a historical paper, measurements are given in the original English units.

production and use through more than a century to document, in part, developments contributing to the rail problems currently facing North American railroads and the producers of rails.

Those students who wish to review rail history in depth will find a wealth of references on the subject. Historical background on rails is offered in the Association of American Railroad Research and Test Department Report No. R-120, entitled "Rail Research-Problem Definition" [1],⁸ and in the paper "Evolution of Rail Steel and Rail Sections and What is Being Done Relative to This Material Today" by K. W. Schoeneberg, as published in the American Railway Engineering Association Bulletin 653 [2]. A reasonable measure of rail history is contained in the American Iron and Steel Institute steel products manual "Railway Track Materials" [3], last revised in October 1975.

Growth of Railroad, the Railroad Rail, and Rail Problems

Standardization

For the purpose of this paper, railroad developments predating the Civil War can be considered academic. The Civil War forced American railroads into the concept of free interchange, which in turn fostered much of the later standardization, and together made possible the development of one of the world's great transportation systems.

The interchange of freight cars between railroads and indeed countries and the resulting need for standardization promoted the birth of various organizations created to handle evolving problems. The Master Car Builders Association, which is a direct ancestor of the present Mechanical Division of the Association of American Railroads (AAR), was organized in 1867, and was responsible for issuing the first interchange rules adopted in 1872, consisting of two printed pages containing nine rules. The American Railway Engineering Association (AREA), chartered prior to the turn of the century, has since served as the Engineering Division of the AAR. However, unlike the Mechanical Division, it has never possessed rule-making powers and its actions, even today, are only "recommendatory."

Rail Designs

At this point in history, the tee rail, as we know it today, had been developed. Future changes in rail design were to involve, principally, increases in section dimensions, and therefore weights, to provide greater bending strength; more wear metal in the railhead; a wider base for better lateral stability; and more generous fillets to reduce local stresses to better cope with increasing service demands. This should not be construed to imply that section design, following acceptance of the tee type, became stagnant.

⁸The italic numbers in brackets refer to the list of references appended to this paper.

Indeed, design changes proliferated to an extent that would be difficult to justify based upon engineering data. The railroads of the day no doubt exercised pride of authorship in developing individual section designs and perpetuating their use, even though many such designs were as essentially alike as peas in a pod. In recent years, AREA has encouraged restraint in this area, and today lists only seven recommended sections to cover all service conditions [4].

Service Conditions

There existed in 1874, 69 mills in the United States engaged in rolling railroad rails [3], primarily from Bessemer process steel in section weights less than 100 lb/yd.

The equipment which operated on these rails consisted, in the main, of freight cars of 30-ton capacity or less on two 4-wheel trucks equipped with 33-in.-diameter, cast-iron wheels. The capacity of freight cars was very limited prior to 1870, when ten tons per car was considered heavy loading [5].

The steam locomotives of the day, such as the well-known, American-type passenger locomotive, having a wheel configuration of 4-4-0, weighed in the neighborhood of 35 tons [5], and wheel loads were approximately 400 lb/in. of wheel diameter. It is interesting to note that some of this early equipment was capable of quite high speeds even by today's standards. The famous speed record of 112.5 mph was set by Locomotive No. 999, hauling the Empire State Express on the New York Central's Syracuse Division, prior to the turn of the century [6]. However, average freight train speeds, due to servicing requirements and other operating conditions, were generally quite low.

Given these service requirement parameters, it appeared reasonable to assume that rail problems would be minor. In fact, overall performance was good enough to make viable a railroad system which was largely responsible for the industrial development of the nation.

Service demands on the rails did not remain stationary. Freight cars of 40 and 50-ton capacity appeared in numbers, followed by cars of 70 and 100-ton capacity. Steam locomotives reached a size which required enlarged engine houses and shop facilities to handle their necessary servicing and repair, and weighed up to 350 tons and more. At the peak of their development, steam locomotives in working order weighed up to 500 tons, these being of the articulated types [7]. With deference to the development and use of the electric locomotive in certain geographic locations, the era of the diesel-electric locomotive was at hand. Improved economics, adaptability to multiple unit operation providing flexibility in tractive effort and speed requirements, and numerous additional advantages were to bring about a complete transition from steam to diesel power in a relatively short time.

The rails in service had been dealt additional blows! Evidence of the effect of higher contact and shear stresses, increased lateral loading, and wheel

flange abrasion readily manifested itself in the railhead metal. Under the heavier stressing, the transverse fissure type rail failure became more and more of a problem. Service developed transverse failures of this type most often initiated at "shatter cracks or flakes" in the steel caused by entrapped dissolved gases, primarily hydrogen, which did not evolve from the steel during air cooling of the rolled rail. Since 1937, however, shatter cracks have been effectively eliminated by controlled cooling, a development by the rail producers which, along with other effective means of hydrogen control, is covered in more detail later in this presentation. It is interesting to note that considerable quantities of rail rolled prior to the general adoption of controlled cooling can still be found in service.

Heavier sections were periodically designed to provide rails better able to cope with service developments. The 100 lb/yd section was developed in 1900, the 130-lb section in 1916, the 140-lb section in 1946, and finally, the heaviest, the 155 lb/yd section, in 1947 [3,7]. But, at the end of 1933, the average weight for rails in the main line tracks of Class 1 railroads of the United States was only 92 lb/yd, and 66 percent of all main line track on a mileage basis was laid with rail of a weight less than 100 lb/yd [8]. In fact, some of the rails which were rolled and laid when 50-ton equipment was the heaviest rolling stock in use remain in service today.

Growth in the scope and severity of service requirements also produced other equipment technology. In the case of rolling stock, the use of fail-safe air brakes and automatic couplers had been made mandatory by federal regulation. Sophisticated high-capacity draft gears and sliding sill cushioning devices were developed; and finally, the cast-iron freight car wheel was eliminated in 1959 [9] in favor of wrought and cast-steel wheels. Freight car wheel sizes, other than 33 in., were not made standard until later, with the introduction of the 100-ton car. Journal roller bearings rapidly started to replace plain bearings in freight equipment. Nevertheless, it appeared to be a reasonable assumption at this point that heavier section rails could meet the service demands associated with the operation of heavier equipment.

In the 1940s, a type of service development in rails which actually had made its appearance under 50 and 70-ton equipment, namely, plastic deformation or flow of the railhead metal, came into focus. "Shelling," a condition where the rail steel, stressed beyond its elastic limit, deforms and fails in subsurface shear, was to be found predominantly in the high side rails in curves on many railroad properties, and crushing or mashing of the head metal in low side rails in curves was observed.

More serious service experiences evolved, especially after 100-ton capacity freight cars entered the rolling stock fleet in significant numbers during the early 1960s. Cars weighing 263 000 lb when loaded to capacity, on two 4-wheel trucks equipped with 36-in.-diameter wheels, which are loaded to over 900 lb/in. of diameter, have demonstrated in service considerable damage to the rails and the track structure generally and have also indi-

cated accelerated maintenance requirements for many freight car components. Modern powerful six-axle diesel locomotives have also contributed measurably to the excessive shear stresses imposed upon the rails.

Today, shelling and crushing occur quite frequently, even in tangent track locations. An ever-increasing number of wheel loads are at that point where the high contact stresses between the wheel and the railhead greatly exceed the elastic limit of the steel. The historic approach, that of beefing up the section design, is no longer the answer, and it may be fair to state that the true extent of the impact on maintenance costs involving both track and equipment is still not fully realized.

An early appraisal of this condition was made by Chief Engineer C. J. Code, of the Pennsylvania Railroad. Code's work was published in the 1960 AREA proceedings [10] and contained recommendations for maximum loads on wheels of various sizes. He recommended maximum wheel loads of between 800 lb/in. of diameter for 33-in. wheels, and 830 lb/in. for 42-in. wheels. These proposed limitations on wheel loads were referred to the Mechanical Division of the AAR, with recommendations that they be made mandatory. This curious circumstance, where the Engineering Division attempted to ensure protection for the track structure, which was the immediate concern and responsibility of its members, by suggesting that rules limiting wheel loadings be progressed and adopted by another division, was of course due to the fact that then, as now, the Engineering Division had no rule-making procedures. The interchange rules under the jurisdiction of the AAR Mechanical Division provided the only vehicle available through which compliance might have been gained.

Although the proposed limits on wheel loading were never approved and placed in the rules by the Mechanical Division, it was not due to any basic disagreement with Code's conclusions. The fact is that high-capacity cars had become so important, with respect to marketing and rate-making practices, that any limits on car capacity to prevent projected rail deterioration had become unacceptable to railroad management. The popular reaction was that, even though the rail might require premature replacement due to the damage being inflicted, sufficient business was being generated through the use of such large equipment that money would be available to make replacement when necessary. Experience has shown that, in many cases, such optimism was excessive.

This story does not end with 100-ton equipment which today comprises the bulk of new car construction. The 125-ton car was introduced about 1964. The only reason this car did not achieve free interchange status was due to the fact that the bridges and structures on many railroads could not handle it. As a result, it has remained subject to special routing requirements. Even so, the truck components for 125-ton cars, 38-in.-diameter wheels, which are loaded to over 1000 lb/in. of diameter, side frames, bolsters, etc., have been made AAR standard designs [11].

It might be regretted that some other marketing philosophy, possibly the

use of some simple form of articulation, was not successfully substituted to meet the demand for oversize cars. The fact is that only the physical clearances involved and the ability to handle such cars to destination limited their construction and their acceptance.

After it had been clearly demonstrated that the inherent restrictive parameters on load capacity and length were being exceeded, rules were adopted limiting the overall load on two 4-wheel trucks to 263 000 lb and the overall length of cars to 89 ft, 4 in. over the end sills for use in interchange service [12].

At present, the railroads stand in a situation reminiscent of that which existed prior to the introduction of controlled cooling. The industry needs a solution for the present rail service experience which appears to be in a pattern of accelerating deterioration. Since it probably is unrealistic to believe that present wheel loadings will be reduced, it would seem that the possible choices involve the acceptance of substantially higher maintenance costs, certainly not a palatable solution to the railroads, or the expanded use and further development of premium rail steels which might better handle the contact loads involved without excessive plastic deformation and wear. Some aspects of carbon and alloy higher strength steel rails and how they have been and are being used in heavy service locations are offered under the steelmaking and treating review presented later.

Rail Joints

Through the years, problems with rail joints somewhat paralleled those associated with wear and plastic deformation. Head-web separations starting primarily at the ends of the rails, cracks emanating from the bolt-holes, particularly end holes, and end batter or local flow of the head metal on each side of the joint took their toll on the rails in service. New rail designs included more generous fillets to reduce stress and corrosion oriented cracks; the first bolt-hole was drilled further from the end in new rails; and end hardening at the mill, a localized heat treatment of the metal at the top of the railhead as developed by the rail manufacturers, provided more uniform wear across bolted joints.

The prospect of elimination of the bolted joint came with the joining of rails by butt welding, which was initiated in the mid-1930s. The practice has progressed to a point where some railroads install only continuously welded rails (CWR) [13].

Generally, quarter-mile strings are produced in a weld plant by joining individual rails of nominal 39 ft length by electric flash (resistance) or gas pressure butt welding. These strings, after installation in track, may be bolted together conventionally or joined by in-track thermite type welding [14].

The actual butt welding has not been without problems. In an effort to minimize costs, rails ordered and produced to bolted rail standards are still

adapted by the railroads to the welding operation. Problems associated with straightness, and the inherent internal characteristics of the open-top type of steel employed, particularly at the ends of the rails, complicate weld plant operations, and appear to contribute in some degree to unsatisfactory in-track experiences. However, neither the end straightness nor normal internal steel conditions posed service problems in bolted track applications down through the years. A brief discussion of open-top ingot steel characteristics and a comparison with other modes of rail steel casting is presented herein, and rail straightness is treated toward the end of the paper.

Economics

It would not be proper to leave this portion of the paper without mention of the depressed railroad economic atmosphere under which current damaging rail service problems developed. Obviously, rails and rail joints need to be supported properly on a well-maintained roadbed if a reasonable service life is to be expected under the stresses applied by modern motive power and rolling stock. Frankly, deferred roadbed maintenance programs, such as those which have been a way of life for some time on many North American railroads, have resulted in less-than-desired rail support in many cases. Consequently, much of the rail population operates in a highly detrimental stress environment induced by overloading and enhanced by lack of proper support. Rail life shortened by abnormal wear, deformation, bending, and fatigue type failures is to be expected. In cases where curtailed rail renewal programs have necessitated keeping worn rails in service longer than normal, the chances of rail failure in fatigue and derailments are greatly enhanced.

For decades, the rail manufacturers have been faced with a widely fluctuating but generally depressed rail market, which certainly is not conducive to capital investments in new production facilities. With no inference that a valid comparison exists, it is interesting to note that, in contrast to the earlier mentioned number of 69 mills in the United States engaged in the production of rails in 1874, there are in North America today only seven mills producing rails, and historically they have not enjoyed year-round, rail-producing schedules.

The rail-manufacturing industry has generally met the needs of the railroads. It has produced rails to changing section designs, from steels produced by the latest processes; developed controlled cooling and end hardening at the mills, to respectively eliminate transverse fissure from shatter crack type failures, and resist end batter; provided heat-treated and alloy rails to resist service developments; and, where equipment was available or could economically be installed, provided from certain plants, rails from vacuum degassed steel, continuously cast steel, and rails that have been rotary straightened. Rails produced utilizing these and perhaps other technological improvements can be expected if and when new facilities become economically feasible at the rail-producing mills.

Rail Steelmaking, Heat Treatment, and Finishing*Steelmaking*

At the turn of the 20th century, the acid-Bessemer process was the principal method of melting steel for rails. Molten blast furnace pig iron was converted to liquid steel by blowing cold air through the bottom of the Bessemer converter. Sufficient heat was generated in the vessel by the chemical oxidation of silicon, manganese, and carbon. In 1907, over 3.5 million ingot tons of steel rails were produced in the United States, practically all by the Bessemer process [15]. The acid-Bessemer produced satisfactory steel from pig iron that was low in phosphorous and high in manganese and silicon. Despite the high-grade ore available in the United States from the Mesabi Range, the acid-Bessemer process declined and has been abandoned since 1967 as a source of raw steel production [15].

The basic open hearth process rapidly supplanted the Bessemer steel-making process. In 1910, almost half of the 3.5 million ingot tons of rail steel was produced in open hearths [15]. The increased yield of finished steel from pig iron, economical use of more scrap and iron of phosphorous contents higher than the Bessemer could utilize were important factors that made the basic open hearth the leading steelmaking process in this country. At its peak in 1955, almost 105 million tons of ingots were produced in the United States by this method [16].

Until recently, electric arc furnaces were utilized chiefly for the production of alloy steels. Electric furnace production of carbon steels has increased because of the relatively low investment cost and the ability to produce quality steels without a source of hot metal. One U.S. rail producer is using this steelmaking practice to produce ingots for rolling into rails.

During the past quarter century, the outstanding development in steel-making technology has been the increasing use of manufactured oxygen. Oxygen of high purity is now used as an integral tool in basic open hearth and basic electric steelmaking processes and as the foundation for the bottom blown open hearth and basic oxygen furnace steelmaking processes. In the United States and in one Canadian plant producing rails, the basic oxygen process is carried out in a tapered basic lined vessel. The oxygen jet equipment for top blowing consists of a tubular water-cooled retractable lance kept in a vertical position above the bath. For bottom blowing in the vessel, or in open hearths as exists in one rail-producing Canadian plant, the multiple oxygen jet tuyeres are each designed with two concentric pipes; the outer carries the hydrocarbon and the inner the high-purity oxygen. Impinging on the surface of the liquid bath or rising as bubbles through the bath, the oxygen immediately starts reactions leading to the formation of iron oxide, part of which disperses rapidly through the bath. Carbon monoxide is evolved which gives rise to a vigorous stirring action and accelerates the refining process. A major advantage of the basic oxygen process is its flexibility in handling raw materials which cover a wide range

of types and compositions. The production of heats at regular, comparatively short intervals is an advantage of the basic oxygen process when it is used to supply molten steel for the continuous casting process. The basic oxygen process does not possess the flexibility of the open hearth or electric furnace processes with regard to the amount of scrap that can be charged and melted. However, steel which has been made by the basic oxygen process is quite similar, chemically and metallurgically, to basic open hearth steel of the same grade. The greater portion of present day rail production in North America is from basic oxygen steel.

All rail steel produced in the United States today is cast into big-end-down, open-top molds, whereas, in Canada, a large proportion of continuously cast bloom steel is employed in rail production.

Ingot molds are usually tapered from the top to the bottom of the mold to facilitate stripping of the ingot. The taper gives rise to the two principal types of molds: big end down and big end up. As the mold is being filled with molten steel, the metal next to the mold walls and mold stool is chilled by contact with the cooler surfaces. The liquid steel solidifies at the walls and bottom of the mold and shrinks as it solidifies, leaving a shrinkage cavity, or pipe, located in the upper portion of the ingot. In open-top, big-end-down killed steel ingots poured without a hot top, the practice commonly used in making ingot rail steel in North America, primary pipe is ordinarily discarded. Under some conditions, another shrinkage cavity, known as secondary pipe, may form in the ingot below, but not connected with, the primary pipe. Due to its nature, secondary pipe normally welds in rolling.

The phenomenon of selective freezing associated with the solidification of steel causes segregation, with resultant chemical composition and mechanical property nonuniformity. Segregation of varying degrees is found in all types of steel ingots. The manner in which these conditions weld together during reduction by rolling, along with the amount of segregation involved, determines the degree of segregation pattern, porosity, or pipe in the finished product after discards are removed. The potential for these internal problems is greatest in the top cut or "A" rails of open-top ingots.

Hot topping provides a reservoir of molten steel over and above the normally cast ingot body, in a position to feed the ingot as the cooling and shrinkage takes place. The remaining porous hot-top portion is discarded, leaving a more sound ingot body.

Changing from open-top to hot-topped ingots for rails would require capital expenditure for major changes in mill facilities to handle the variety of hot top settings and the increased time of heating in the ingot soaking pits. In some cases, the soaking pits used in heating rail ingots do not have the necessary height to accommodate taller hot-topped ingots.

Among the more significant changes in steelmaking technology stands the introduction of the continuous casting process. This process comprises the direct solidification of liquid steel into a solid bloom which is continuously extracted from the casting machine and cut into required lengths. Con-

tinuous casting eliminates from the conventional production sequence the following steps: the pouring of the liquid steel into molds, the stripping of the molds off the solidified ingot, the reheating of the ingots in soaking pits, the rolling of the ingots to bloom form, and the cutting of the blooms to the required length.

The continuous casting process has been applied successfully to bloom production for carbon steel rails, and is now considered a standard production method throughout most of the world. The faster and more uniform bloom cooling rates which occur during solidification with this process, as compared to ingot production, greatly reduce the occurrence of macrosegregation, and minimize the occurrence of pipe. Consequently, these benefits are seen at the rail welding plants, where the problems which have been associated traditionally with "A" rails are not encountered.

Currently, changes in rail specifications to accommodate continuously cast steel are under consideration. These would include adjustments in the areas of chemistry, testing, and rail identification requirements.

Rail Steel Composition

The chemical composition of rail steel has been revised repeatedly over the years. Advancing wheel loads and speeds have dictated the need for a more abrasion- and flow-resistant rail steel. Since increasing the carbon content is the most economical method of increasing the strength of the rail steel to resist these particular service developments, the current AREA specification requires that the chemical composition shall be within the limits shown in Table 1. However, specified carbon contents higher than the 0.82 percent shown for heavy rails in both the AREA and ASTM A 1 specifications could result in undesirable metallurgical and mechanical properties in the rail steel.

Since the previously discussed service problems of railhead abrasion, plastic deformation, shelling, crushing, and corrugation have resulted in high rail maintenance and replacement costs to the railroads, the rail producers have responded to counter them in a variety of ways. The broad

TABLE 1—*Chemical composition—tee rails.^a*

Constituents, %	Nominal Weight, lb/yd			
	70/80	81/90	91/120	121 and Over
Carbon	0.55 to 0.68	0.64 to 0.77	0.67 to 0.80	0.69 to 0.82
Manganese	0.60 to 0.90	0.60 to 0.90	0.70 to 1.00	0.70 to 1.00
Phosphorus, max	0.04	0.04	0.04	0.04
Sulphur, max	0.05	0.05	0.05	0.05
Silicon	0.10 to 0.25	0.10 to 0.25	0.10 to 0.25	0.10 to 0.25

^aCourtesy of the American Railway Engineering Association.

approach has been to increase the level of hardness and the yield and tensile strengths of the rail steels available, while retaining a fine pearlitic structure. This has been accomplished through alloying of the rail steel, and heat treating the entire rail or only the head of conventional carbon steel rails.

As early as 1949, trial chemistries based on alloying the normal AREA composition primarily with chromium were introduced and installed in track [17]. In these early trials, various problems were encountered, and it was not until the last decade that volume production and installation of alloyed rails was successfully achieved.

At the present time, premium rails are being produced from four alloyed rail steel compositions in North America. These are high silicon, intermediate manganese, manganese-vanadium, and chromium steel rails. Generally speaking, these steels exhibit improvements in yield and tensile strengths in the range of 15 to 35 percent over standard carbon rail steel.

It is of interest to note that the development of alloy rail steels in Europe has reached the same general level, with the approaches there being based on chromium and manganese as the main alloying elements. Subsidiary additions of molybdenum, vanadium, or silicon are used by some rail producers.

There is a high level of interest in alloy rail development at this time. However, it appears that further development of properties using this route might well be limited by metallurgical phenomena, such as microsegregation, which are inherent in ingot steel. In this context, it is probable that research will be directed toward trials using continuously cast steel.

Heat-Treated Rails

Heat treating of conventional carbon steel rails offers another metallurgical route to improved rail steel mechanical properties. Two major products have been developed: a rail with the head hardened using induction heating and air quenching, and a fully heat-treated, oil-quenched, and tempered rail. Both products have been established for a significant number of years and have realized definite improvements in track performance [17] which have also justified the higher costs involved. The heat-treated rails have offered a major advantage over alloyed rails, that of ease of welding, both in butt-welding at weld plants and repair welding in the field. In addition, improvements to yield and ultimate strengths over standard carbon rail steel are in the range 40 to 55 percent.

It may be said that significant improvements in resistance to wear and to crushing, plastic flow, and shelling have been achieved using both heat-treated and alloy rails. Indeed, a number of railroads now use these higher strength rails as standard practice on curves meeting particular radius and annual traffic density criteria.

Hydrogen Control

Earlier in this presentation, one successful solution to the problem of transverse fissures from shatter cracks or flakes was briefly noted. Addi-

tional coverage appears warranted since processes other than that of controlled cooling of the rails, which is defined in the AREA and ASTM A 1 rail specifications [18], can be applied successfully to cope with the hydrogen-induced flakes in rails.

One of several theories on the formation of flakes in steel holds that hydrogen atoms diffuse out of solution in the steel toward nuclei, such as inclusions, where they combine to form the molecular gas, the pressure of which subsequently causes a small rupture called a flake or shatter crack. Controlled or retarded cooling of the rolled rails allows the elemental hydrogen to diffuse out of the steel before it collects to form the gas. The amount of gas retained that could possibly produce flaking is dependent upon the section size of the rail, the chemistry, and the rate of cooling. Adding certain alloying elements to the steel increases the susceptibility to flaking for a given hydrogen content and must be compensated for by modifying the cooling cycle.

Proper cooling of rail steel blooms prior to reheating for rolling into rails may be practiced, particularly where the blooming and rail rolling operations are discontinuous, or continuously cast blooms are adapted for latter processing into rails as is done to some extent in Canada.

Another approach to reducing the susceptibility of steel to shatter cracking is to lower the hydrogen content of the liquid steel to a harmless level, generally considered to be three parts per million or less, by exposing the steel to a low-pressure atmosphere created by vacuum treatment. Vacuum treatment of rail steel is also advantageous from a chemical analysis viewpoint. Greater uniformity of chemistry from the front to the back of the heat of steel appears to result from the mixing action that takes place during vacuum treatment. However, only one rail mill in North America is equipped to vacuum degas rail steel on a production basis.

Rail Straightness

Straightness is the last rail production feature to be discussed in this review. While roller straightening of rails has been practiced for more than 50 years in Europe and for a similar or lesser time in other parts of the world, it is only in North America that gagging is still the primary method of straightening heavy section rails. One of the seven rail mills has been rotary straightening for several years; another is in the process of total conversion; and a third is utilizing the method to a major degree.

The quality of new rail straightness demanded by the railroads, especially for continuously welded track applications, has made this aspect of the product as essential as correct profile, chemical composition, and mechanical strength. Decreasing tolerances on straightness and the increasing weight and strength of rail sections has made it more and more difficult to produce rails with acceptable line, surface, and end straightness characteristics by the gag straightening method. Consequently, the practice of sight

lining and incrementally pressing into alignment any distorted areas in either plane of the as-rolled rail is, where economically feasible, being replaced by roller machine straightening.

The roller straightener is a machine with two banks of rolls, one above the other and offset by a half pitch. One bank, which may be three, four, or five rolls in the case of rail straighteners, is driven continuously, and the piece to be straightened passes through the machine between the banks of rolls. Rail roller straightener installations in recent years have consisted of two machines, usually in tandem, the first working the rail in the major axis, and the second, or lighter machine, working the minor axis. This provides an excellent method for removing handling and cooling distortions common in both planes of the as-rolled rails.

In some instances, it is necessary to gag or press straighten localized misalignments not totally removed by the rotary processing. Generally speaking, roller or rotary straightening as it is often called offers smooth, uniform-finished rail alignment beyond that normally attainable with gag straightening.

Summary

The story of these developments has been one of cooperation between producer and user, with change and experimentation coming as a result of definition and analysis of field problems. The need for further progress on rail development is well recognized, and this area will be one of considerable interest in the coming years.

The struggle of the North American tee rail to survive in an unfavorable stress environment, even with the help of technological production and use improvements, has been traced through growth and troublesome periods in railroading in this historical and descriptive account. Some of the problems facing the rail-producing industry have also been noted.

How we got where we are appears to be quite evident. Hopefully, the technical papers to follow will establish exactly where we are and indicate where we should be going in the effort to find economic aid for the railroad rail.

References

- [1] Schoeneberg, K. W., "Rail Research—Problem Definition," AAR Report R-120, Association of American Railroads Research and Test Department, Chicago, Ill., March 1973.
- [2] Schoeneberg, K. W., "Evolution of Rail Steel and Rail Sections and What is Being Done Relative to this Material Today," *Proceedings of the American Railway Engineering Association*, Chicago, Ill., Vol. 76, Bulletin 653, June-July 1975.
- [3] *Railway Track Materials*, steel products manual, American Iron and Steel Institute, Washington, D.C., Oct. 1975.
- [4] *AREA Manual*, American Railway Engineering Association, Chicago, Ill., Chapter 4, Part 1, pp. 4-1-1, 4-1-6.1.

20 RAIL STEELS—DEVELOPMENTS, PROCESSING, AND USE

- [5] Sinclair, A., *Development of the Locomotive Engine*, Angus Sinclair Publishing Co., New York, 1907.
- [6] Jensen, O., *History of Railroads in America*, American Heritage Publishing Co., Inc., New York, 1975.
- [7] *Car and Locomotive Encyclopedia*, Simmons-Boardman, New York, 1950.
- [8] Johnson, R. P., *The Steam Locomotive*, Simmons-Boardman, New York, 1942.
- [9] "Report of the Committee on Wheel and Axles," *AAR Mechanical Division Proceedings*, Association of American Railroads, Chicago, Ill., 1960.
- [10] Code, C. J., "Action of Joint Committee on Relation Between Track and Equipment," *Proceedings of the American Railway Engineering Association*, Chicago, Ill., Vol. 61, 1960, pp. 1223-1227.
- [11] *Manual of Standards and Recommended Practices*, Association of American Railroads, Chicago, Ill., Section D, p. 8A.
- [12] *Field Manual of Interchange Rules*, Mechanical Division, Association of American Railroads, Chicago, Ill.
- [13] *AREA Manual*, American Railway Engineering Association, Chicago, Ill., Glossary, p. 7.
- [14] *AREA Manual*, American Railway Engineering Association, Chicago, Ill., Chapter 4, pp. 4-2-6.7, 4-2-6.9.
- [15] Sellew, W. H., *Steel Rails*, D. Van Nostrand Co., London, 1913.
- [16] "Annual Statistical Report," American Iron and Steel Institute, Washington, D.C., 1955.
- [17] "Report of Committee 4—Rail," *AREA Proceedings*, American Railway Engineering Association, Chicago, Ill., Vol. 51, 1950; Vol. 52, 1951; succeeding annual volumes.
- [18] *AREA Manual*, American Railway Engineering Association, Chicago, Ill., Chapter 4, Part 2, pp. 4-2-2, 4-2-1.

The Effect of Mechanical Properties Upon the Performance of Railroad Rails*

REFERENCE: Stone, D. H. and Steele, R. K., "The Effect of Mechanical Properties Upon the Performance of Railroad Rails," *Rail Steels—Developments, Processing, and Use*, ASTM STP 644, D. H. Stone and G. G. Knupp, Eds., American Society for Testing and Materials, 1978, pp. 21-62.

ABSTRACT: The behavior of rails in service is reviewed on the basis of past rail steel research. The formation of rail defects and rail wear are discussed. The mechanical properties of rail steels and their dependence on chemical composition and microstructure are presented.

KEY WORDS: steels, railroad tracks, fatigue (materials), wear, pearlite, tensile strength, fractures (materials)

Annual gains in the carrying capacity of railroad freight cars, an unbroken upward trend for the past fifty years, have been especially pronounced in recent years. In 1975, the average capacity of new freight cars was 89 tons, compared with a 62 ton average for cars retired [1].³ This increase in loads combined with increasing train speeds, and in some cases changing maintenance practices, have placed new and severe demands on the existing rail steels.

Railroad rail is called upon to support and guide rapidly moving vehicles in such a fashion that the cargo, be it merchandise or people, is not inordinately distressed in transit. Thus, the serviceability of rail is a reflection of how well rail meets these needs by resisting structural failure and excessive wear. In order for the service offered to be economically viable, the rail must retain an adequately high level of serviceability for a long enough period of time to return the original investment costs.

*Original experimental data were measured in U. S. customary units.

¹Director—Metallurgy, Association of American Railroads, Technical Center, Chicago, Ill.

²Metallurgist, Department of Transportation, Transportation System Center, Cambridge, Mass. 02142.

³The italic numbers in brackets refer to the list of references appended to this paper.

Serviceability Requirements and Performance

The ultimate limit on serviceability is structural integrity. Although most rail removed from service in the United States is removed because of excessive wear, those very wear limits have been selected and imposed to avoid the increasing risk of fracture, loss of gage control, or excessive dynamic loads (as caused by corrugations) likely to result from further wear. Indeed, because the macroscopic crack growth rate in most metals responds to approximately the fourth power of stress, relatively small decreases in section modulus can result in very large increases in crack growth rate. On the other hand, modest wear may be something of an advantage, since rails with moderate wear have been reported to exhibit a lower defect⁴ occurrence rate [2,3].

The ability of the rail to resist both wear and fracture depends upon its mechanical properties, and it has become the lot of the metallurgist to attempt to provide a steel of satisfactory strength and toughness at a price which the user is willing to pay and the producer finds compensatory. Because of the sometimes conflicting demands for fracture resistance versus wear resistance, the first problem can be to define what mechanical properties or characteristics shall be considered in the effort to optimize serviceability. However, before entering into a discussion of how mechanical properties and characteristics can influence serviceability, the environment in which the rail must function should be described briefly.

Through the years, freight train speeds and train tonnage have increased, with the average train length remaining at approximately 70 cars since 1969. Although both speed and length influence the forces imposed upon the rail, perhaps the factor which has given engineers the most concern is the increase in wheel loads without a corresponding increase in wheel diameter. These trends reflected as average loaded car capacity are illustrated in Fig. 1.

Early studies by Thomas and Hoersch [4] and subsequent work by Code [5] and Frocht [6] revealed that, as wheel loads exceed 700 lb/in. of diameter, one may expect increasing plastic flow of the rail running surface with an ensuing increased likelihood of shelling type failures. A second way in which increased wheel loads can damage rail is through the progressive deterioration of the rail support structure (that is, ties, ballast, and subgrade) with ensuing increases in flexure stresses induced into rail. Although wheel loads have increased, Way [7] has pointed out effectively that the predictions of dire consequences have not yet completely come to pass.

An examination of rail failure statistics over the last ten years will reveal several interesting trends. The detail fracture⁵ has been selected for consideration because it is most likely to be influenced by increases in the

⁴The term "defect," most often used in conjunction with a descriptive adjective such as transverse, etc., historically has been used in the railroad industry to categorize service-induced fatigue separations of the metal in rails and should not be construed to mean inherent imperfections in the steel.

⁵A transverse fatigue crack progressing from the corner of the railhead.

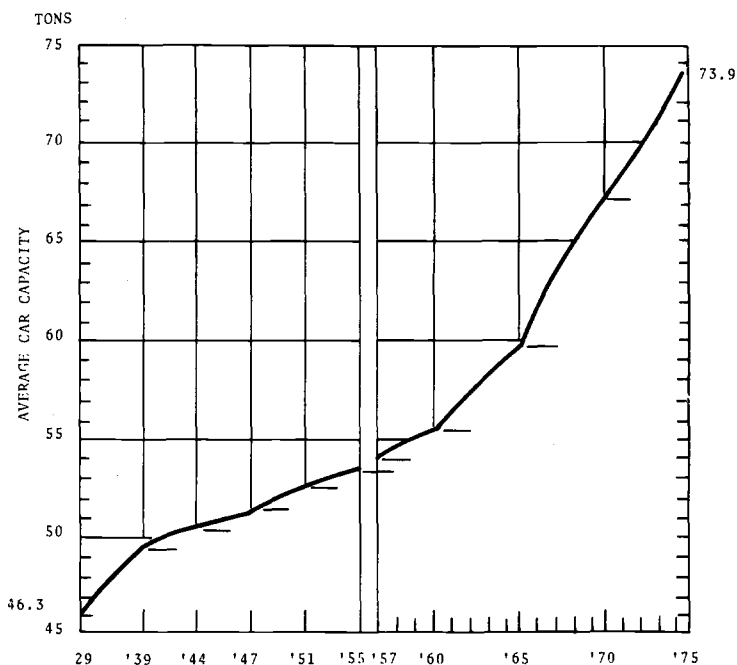


FIG. 1—Increase in freight car capacity from 1929 to 1975 [1].

wheel/rail contact stresses and also represents one of the most potentially dangerous defects. Using figures compiled by the Sperry Rail Service for the years 1965 through 1975, Curve (a) in Fig. 2 illustrates that the total number of detail fractures rose up to 1969 after which the number of defects remained essentially constant through 1975. From 1965 through 1969, the number of track miles tested remained constant within 2000 miles, after which the miles inspected has been rising fairly steadily. Figure 2 Curve (b) shows the number of detail fractures normalized for ton miles of traffic and average car capacity. Sperry [8] attributes the increase in the 1960s to both "increasing effectiveness of test systems (primarily in the rail end region) and increasing incidence of defects resulting primarily from heavier tonnage and axle loading." The overall decrease (for all defects) following 1970 is attributed to "more frequent inspection of certain main line areas rather than any significant improvement of rail conditions in North America." Interestingly, when the data are normalized for ton miles and car capacity, that is, more heavier cars, the trend of defect occurrence prior to 1970 is still upward, suggesting a nonlinear relationship between damage and wheel load or the progressive accumulation of roadbed damage which in turn contributes to rail damage, although detail fractures should perhaps be less influenced by rail support conditions during their initiation than other types of defects. If the reduction in detail fracture defect rate which has occurred

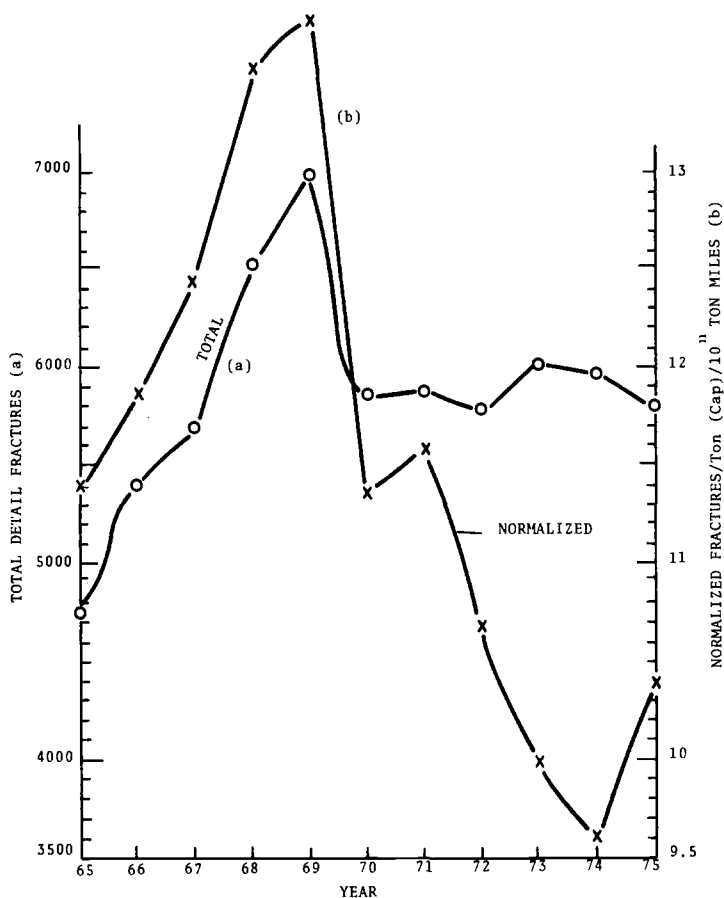


FIG. 2—Occurrence of detail fractures between 1965 and 1975.

after 1970 is indeed caused by more frequent inspection of main line areas, then perhaps it might be assumed that a substantial number of detail fractures might have been expected on branch lines.

A somewhat different view of the consequence of the rail failure problem can be gained by an examination of reported accident statistics attributed to broken rails. Figure 3 Curve (a) shows the ratio of reported main line accidents per 10^{11} ton miles which occurred between 1967 and 1974, adjusted for inflation using the Federal Railroad Administration (FRA) inflation index. Although somewhat irregular between 1969 and 1974, the overall trend is upward. If the number of reported accidents is adjusted for system utilization (ton miles) and wheel load (car capacity), the basic trend upward still persists as shown in Fig. 3 Curve (b). Unfortunately, it is not possible to distinguish the influence of those transverse defects caused primarily by wheel/rail contact stresses on train accidents because, until 1975, causes due

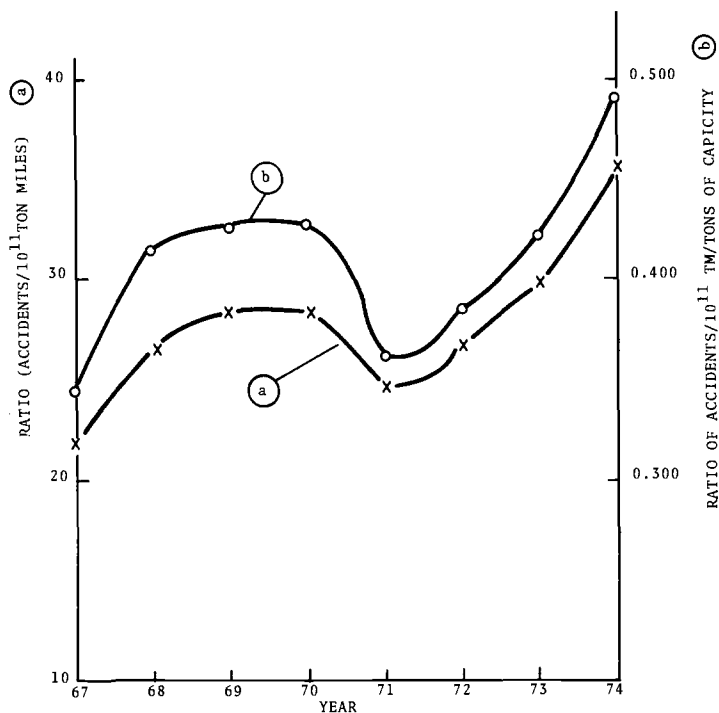


FIG. 3—Ratios of reported main line accidents (corrected for inflation) attributed to broken rails/traffic carried.

to transverse defects, under which detail type fractures would fall, were lumped into the “other causes” category. Nevertheless, the data do suggest that a rail failure problem does still exist although its exact causal relationship with wheel loads remains subject to the need for better definition.

At this point, it will be fruitful to see how the mechanical properties of rail steel influence the failure behavior of rail. The shelling-type defect which can turn transversely into the detail fracture is perhaps the best-studied illustration. The contact-induced shear stresses which develop within the railhead cause plastic deformation which, under the influence of many wheel passages, leads to work hardening of the upper portion of the railhead such that eventually the stress reversals become essentially elastic, and further plastic flow becomes minimal.

The shelling-type flaw develops well below the region of maximum shear stress and maximum hardness as is illustrated in Fig. 4 [10]. This region has been shown to be characterized by stresses which have been caused by the cold working of the railhead [9]. These residual stresses probably also contribute to the generation of other head defects such as horizontal and vertical split heads.

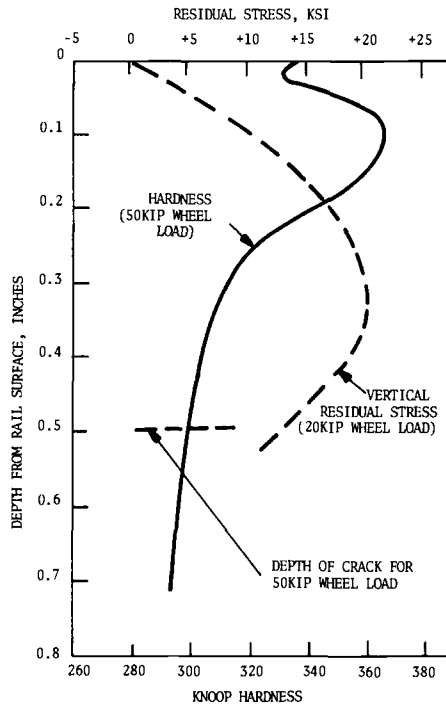


FIG. 4—Variation of hardness [10] and residual stress [9] with depth below running surface of rail in rolling load type tests.

The rate of fatigue damage accumulation would be reduced in the region of maximum shear stress (~ 2.5 to 5 mm (~ 0.1 to 0.2 in.) beneath the running surface) if work hardening is allowed to progress and concomitantly the region at that depth sees compressive residual stress at least in the longitudinal and transverse directions (Fig. 4). Consider that the normal tensile fatigue endurance strength of rail steel is near 410 MPa (60 ksi) [11], implying a shear fatigue endurance strength near 205 MPa (30 ksi). Presuming that the endurance strength increases due to cold work in about the same proportion as the increase in ultimate tensile [12], the shear endurance strength at ~ 2.5 to 5 mm (~ 0.1 to 0.2 in.) depth of the rail shown in Fig. 4 would rise to ~ 275 MPa (240 ksi). By reference to Fig. 5 showing the octahedral shear stress as a function of wheel load, wheel loads as low as 45 kN ($10\,000$ lb) would cause some damage within the region of maximum shear stress [13]. But if the residual stresses, predominantly compressive at 2.5 to 5 mm (0.1 to 0.2 in.) depth, are factored into the calculation of octahedral shear stress (see Appendix I), the value of octahedral shear at ~ 90 N ($\sim 20\,000$ lb) wheel load would be found to drop to ~ 160 kN ($\sim 36\,000$ lb)—under the endurance limit; indeed, wheel loads as high as 25 tons ($50\,000$ lb) (33 -in.-diameter wheel) would be expected to cause little fatigue damage in the region of maximum shear.

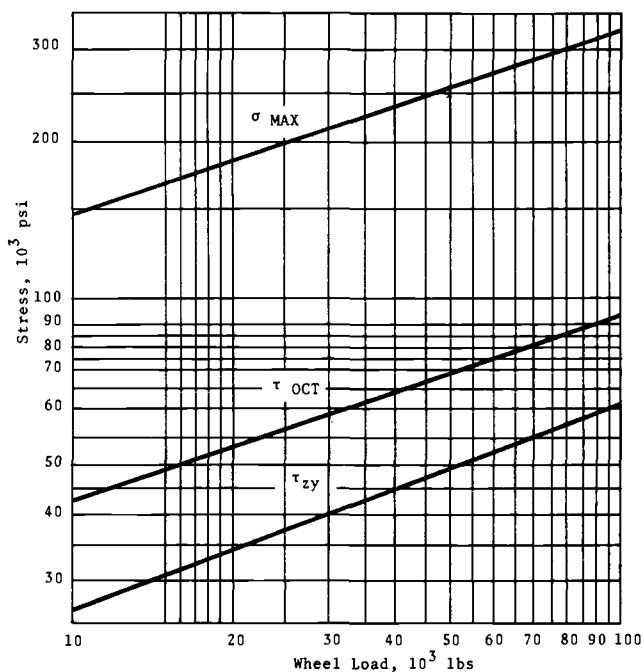


FIG. 5—Maximum compressive, octahedral shear, and alternating traverse shear stress in a rail for new 33-in.-diameter wheel and rail having 10-in. crown radius [12].

However, the region beneath the cold-worked layer can see a substantial vertical tensile stress of perhaps as high as 40 percent of the tensile fatigue endurance strength [9]. Considering that endurance strength is actually a statistical distribution as shown in the modified Goodman diagram of Fig. 6, the tensile residual stresses can increase the likelihood of fatigue crack initiation. Indeed the benefit of using stronger rail can be seen by the upward and rightward displacement of the endurance life line. A second advantage of harder rail is that its use will reduce the cyclic plastic flow as reflected in the depths of the peak hardnesses (compare Figs. 4 and 7), thereby delaying the occurrence of adverse residual stresses beneath the cold-worked region. Modest vertical wear of the rail will permit the residual stress pattern to move downward gradually so that a volume of metal originally in the residual tensile stress field will come under the influence of compressive stresses, and the rate of accumulation of fatigue damage will diminish.

At this point, it would be well to consider the distribution of loads that occur today in U.S. freight service. Figure 8 illustrates the distribution of wheel/rail vertical loads observed experimentally on a main line trans-continental railroad for Class I track. Note that, even with today's train consists (including six axle locomotives), the 50 percent exceedance level occurred at only 45 kN (10 000 lb) wheel loads, and 133 kN (30 000 lb) wheel loads constituted only approximately 10 percent of the exceedances.

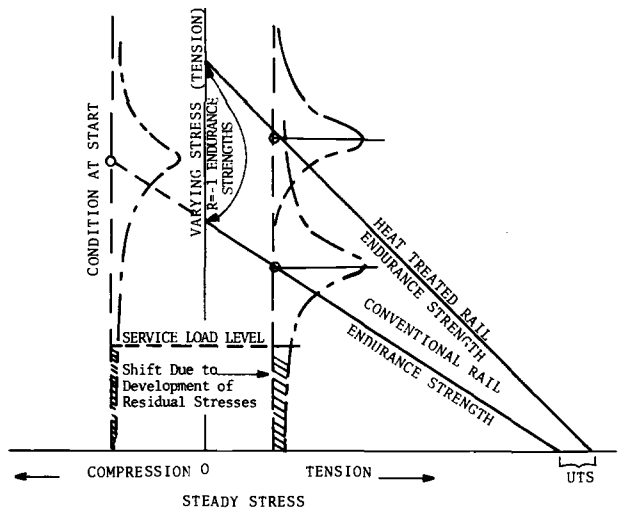


FIG. 6—Modified Goodman diagram showing effect of residual stress and distribution of fatigue strength on rail fatigue behavior.

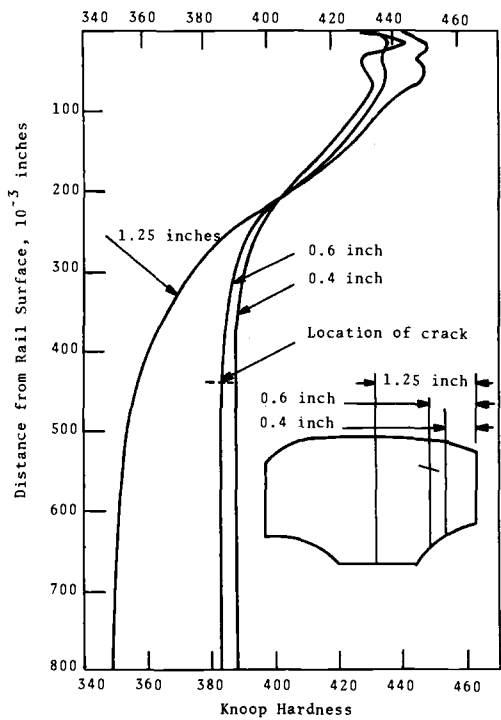


FIG. 7—Hardness profile of heat-treated standard rail under rolling load test [10].

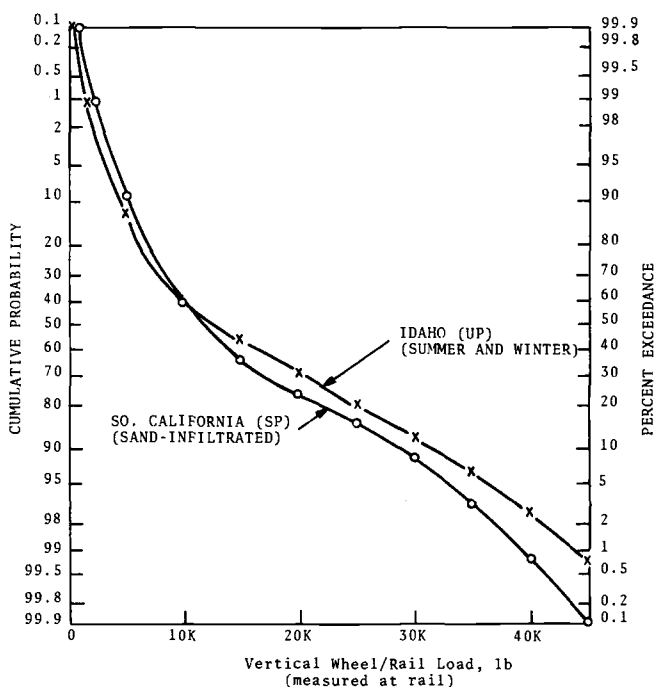


FIG. 8—Cumulative probability levels of peak wheel/rail load under mixed freight traffic as derived from tie plate load measurements [15].

Material Behavior

Oding et al [14] have taken test specimens from the region just below the running surface of rails after different service periods and report that yield and fatigue endurance strengths tend to increase out to 300 million gross tons (metric). Elongation and toughness deteriorate somewhat as might be expected under the influence of cold working. However, as 500 million gross tons is approached, the endurance strength drops somewhat, accompanied by a slight decrease in yield strength. The fatigue strength behavior is shown in Fig. 9. The drops in endurance strength and yield are consistent with the observations of Gervais and McQueen [16] that a cycle softening-like behavior occurred during cyclic indentation testing of a low-carbon ferrite: pearlite steel at 10^7 cycles of loading. The soft region appearing at a depth near 0.25 to 0.5 mm (0.010 to 0.020 in.) in Fig. 4 may be a reflection of this same cycle softening-type behavior, although it could also be an effect of surface decarburization.

Lempitskii et al [17] have summarized the results of Soviet work to improve the resistance of rail to contact zone fatigue. Figure 10 illustrates the fact that, for various pearlitic hardness levels, the resistance to fatigue defects peaks at a hardness of 380 Brinell. The relationship between fatigue

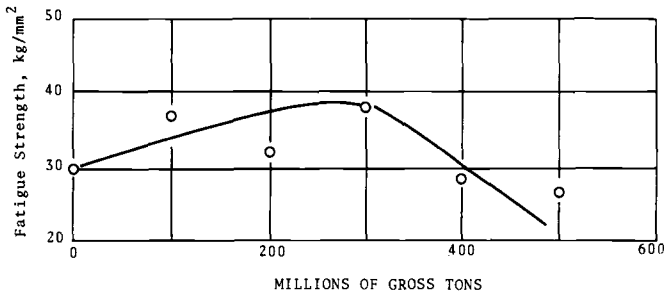


FIG. 9—Variation of limiting fatigue strength (based on 5×10^6 tons of loading cycles) as a function of traffic passed [14].

resistance and ultimate tensile strength is more variable, but generally the stronger the steel, the better its fatigue resistance with hardened rails, both those of conventional composition and those with chromium additions, exhibiting better fatigue resistance, while vacuum-treated rail fell below the norm.

In recent years, information has become available about the fracture

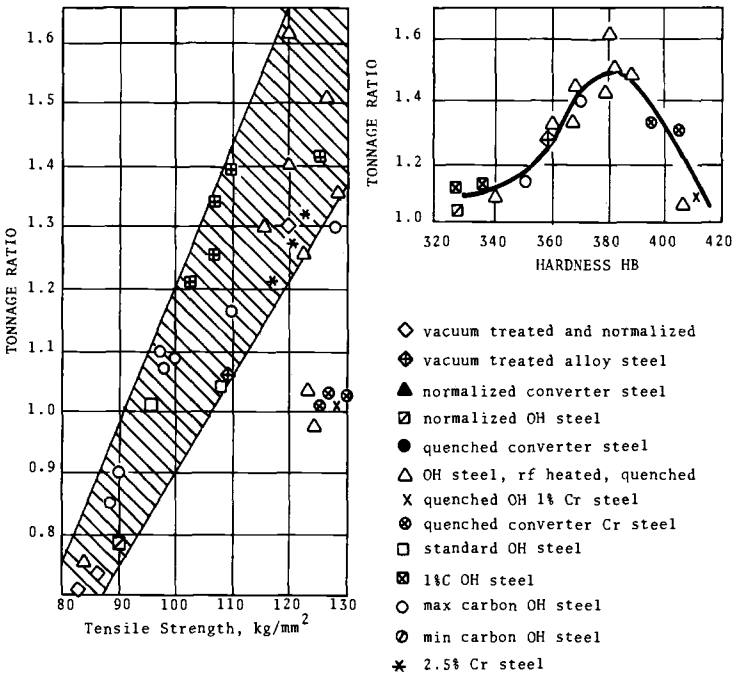


FIG. 10—Resistance of rails to the development of fatigue defects in the contact zone plotted against tensile strength and hardness (tonnage ratio reflects the relative merit of different steels in comparison to standard rail steels) [16].

toughness and fatigue crack growth behavior of rail steels. Although difficulties remain in the use of this type of information to predict explicitly the growth behavior of cracks in actual rails, it can nevertheless be used to provide useful insight into the growth process. An example of this is presented in Appendix II for the case of a transversely oriented crack of radius 5 mm (0.2 in.) embedded within a railhead at an origin depth of 10 mm (0.4 in.) growing under pure opening mode stresses (Mode I) induced by vertical flexure. Wheel loads from 111 kN (25 000 lb) (20 percent exceedance) to 222 kN (50 000 lb) (0.1 percent exceedance) and peak residual tensile stresses up to 172 MPa (25 ksi) are treated. The crack growth behavior at stress ratios $R = \frac{\sigma_{\min}}{\sigma_{\max}} \geq -1$ can be described by the expression

$$da/dN = \frac{5.638 \times 10^{-9} \Delta K^3}{(1 - R) K_{Ic} - \Delta K}$$

where

da/dN = crack growth rate

min = maximum stress

max = minimum stress, and

ΔK = alternating stress intensity factor,

as found by Carter et al [18] for wheel steels and is a close approximation of the upper limit of crack growth behavior for rail steels as shown in Fig. 11. When $R > -1$, the crack growth is expected to respond to only the tensile portion of the stress cycles (that is, $R = 0$). Finally, incorporating the variation of threshold, which is $\sim 8/\text{MN}\cdot\text{m}^{3/2}$ ($\sim 7 \text{ ksi}\sqrt{\text{in.}}$) at $R = 0$ [20], with stress ratio, R , in the fashion found applicable by Cooke and Beevers [20] for British rail steel, that is

$$\Delta K_{\text{threshold}}^{R > -1} = \Delta K_{\text{threshold}}^{R = 0} (1 - R)^\gamma$$

where the constant $\gamma \approx 1$, the results shown in Fig. 12 are obtained. Simply, they show that, except at both very high wheel loads (which have a low occurrence rate) and at very high longitudinal residual tensile stress (which are not that likely), the crack growth rate at small cracks under pure Mode I loading is quite low, and, in fact, at longitudinal residual stresses less than 83 MPa (12 ksi), even 222 kN (50 000 lb) wheel loads would yield negligible crack growth at 5 mm (0.2 in.) radius. Indeed, since both the residual stress and the bending stress diminish as crack front moves downward toward the web, the growth rate probably will remain reasonably low, and one must look to factors other than pure opening Mode I stresses such as the shear stresses or local bending stresses within the railhead to promote growth.

As has been implied several times in these discussions, wear behavior can have both direct and indirect effects upon the stress within the rail, and therefore is a factor of prime importance in assessing the serviceability of rail. Figure 13 is an illustration of rather extreme curve wear and illustrates

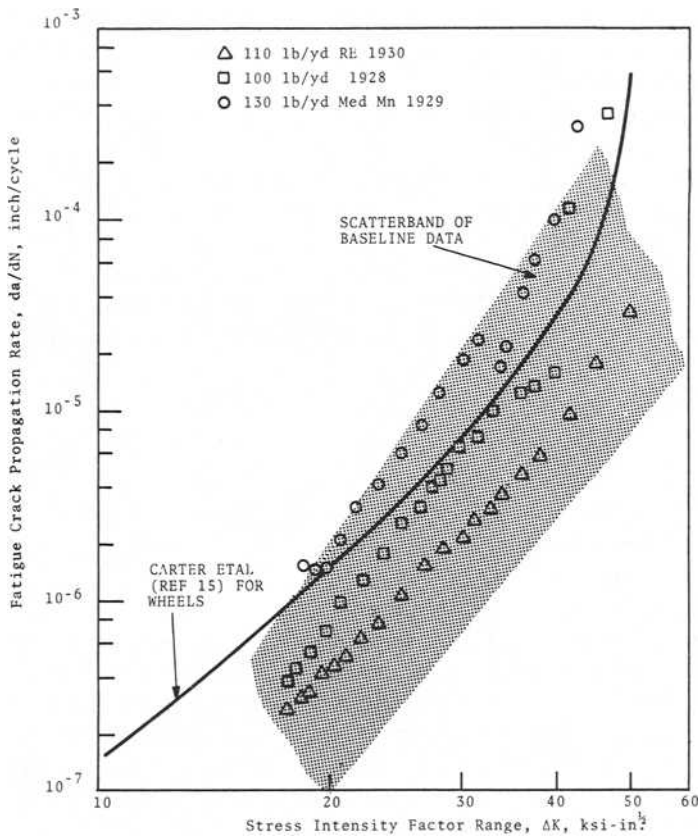


FIG. 11—Variability of fatigue crack propagation rate behavior [19].

how gage control can be lost and stresses significantly increased. Numerous papers have appeared which focus attention on wheel rail wear [21–31].

Recently, work by Kalousek [2] has shown that rail wear generates both spherical and abrasive wear particles. The spherical particles are considered to be the result of a fatigue-dominated wear mechanism. Although it is generally observed that harder (that is, stronger) materials provide better wear resistance, there are some data [32], as shown in Fig. 14, to show that wear resistance is not a single valued function of hardness but can depend upon both composition and heat treatment independently of hardness.

Although better wear resistance is generally associated with greater hardness, the exact functional relationship of wear to mechanical properties will depend upon the operative mechanism of wear. If wear is considered a microfatigue process [15], the approach outlined in Appendix III can be

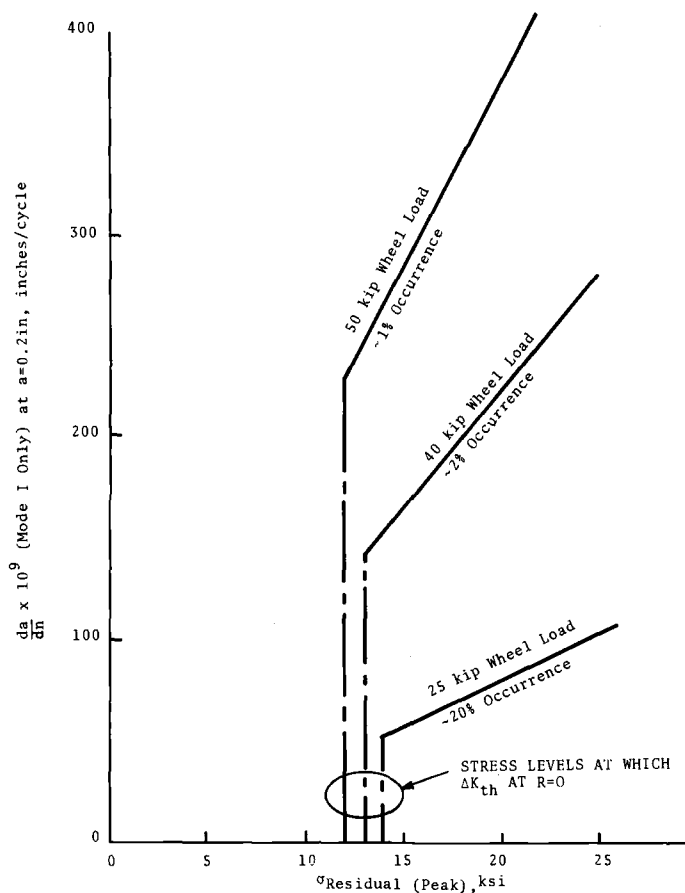


FIG. 12—Effect of peak residual (peak), stress upon transverse fatigue crack growth.

used to show that wear rate, \dot{R} , could be related to several fatigue parameters through the expression

$$\dot{R} = \frac{2 W \cdot h}{\bar{P} \left(\frac{\bar{P}}{P^*} \right)^{1/2}} \left(\frac{P^*}{P_j'} \right)^h$$

where

- \bar{P} = mean pressure dependent upon the cyclic yield strength, that is, $2.6 \sigma'_y$,
- P^* = reflects the increase in effective pressure due to the application of shearing loads,
- W = applied load,
- h = height at the enclave in which fatigue wear is occurring,

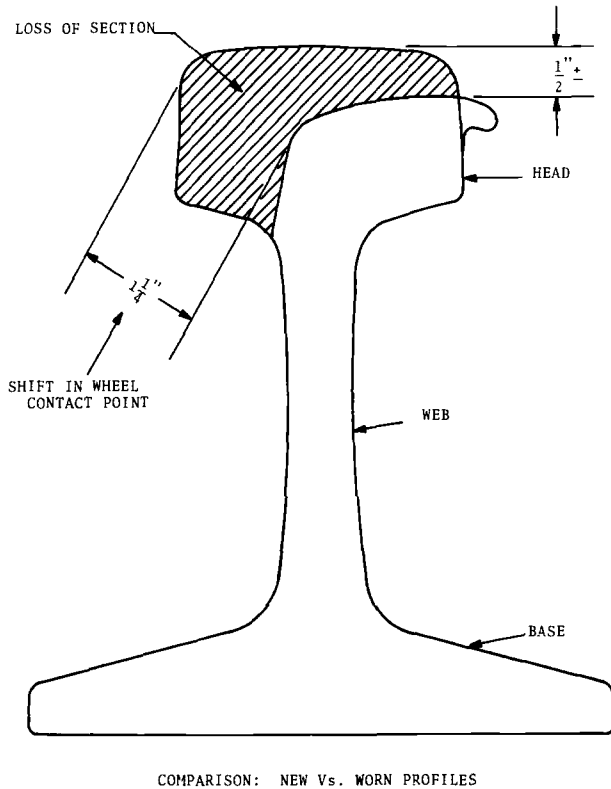


FIG. 13—Loss of rail section due to curve wear.

p'_f = pressure equivalent of the cyclic fracture stress, that is, $\sim 2.6 \sigma'_f$, and

$|b|$ = absolute value of the slope of the log-log stress:life plot.

Thus, the cyclic mechanical characteristics of the material σ'_f , σ_f , and $|b|$ can influence wear rate, recognizing the fact that these characteristics can be altered as the surface undergoes changes during the wear process. For instance, cold working will tend to increase p , reduce $|b|$, and leave p'_f little changed; these changes will reduce the wear rate. On the other hand, after the surface has worked hardened, cyclic softening could occur in some metals and alloys, allowing somewhat of a reduction in p , that is, σ'_f and a possible increase in wear rate. Rail steels are shown [19] to exhibit cyclic softening. Different wear modes, depending upon magnitude of the loads, could be treated by considering that the height of the wear enclave, h , probably is a complex function of load, W , so that the term $W \cdot h$ probably should better be represented as W^q , where q will vary with the mode of wear and possibly with the type of microstructure as is implied by the result shown in Fig. 15.

The performance requirements have to a great extent led to the develop-

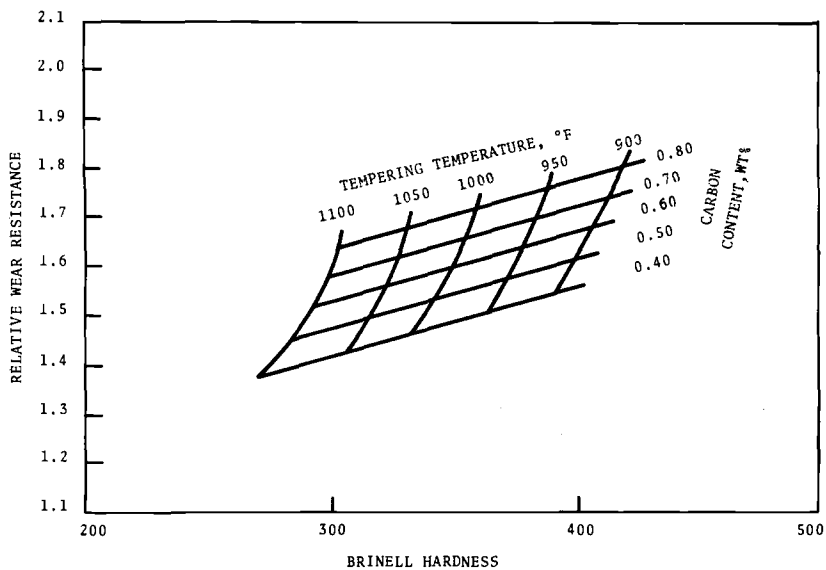


FIG. 14—Relative wear resistance of carbon steels [32].

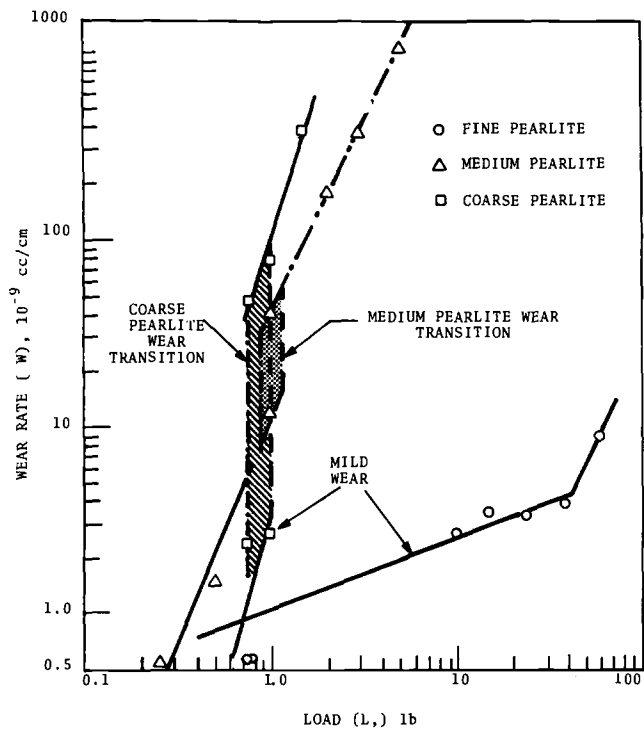


FIG. 15—Wear rate versus load in AISI 1095 steel pearlitic structure [33].

ment of the rail steels presently used. Therefore, in order to strike a reasonable balance between wear resistance and structural strength at acceptable cost, fully pearlitic steels are used with compositions as shown in Table 1, for the manufacture of rails (ASTM Specification for Carbon-Steel Rails (A 1-68a)) [34]. The standard rails are used in the as-rolled condition which produces a steel with the approximate mechanical properties shown in Table 2. However, response of rails to modern service conditions has created problems with excessive wear and crack initiation in standard rails.

Effects of Composition

To meet the needs of these severe service conditions, two classes of improved rails have been introduced. The first class includes rails which have been strengthened through alloy additions. These include high-silicon, intermediate-manganese, and chromium alloy rails. Typical compositions and properties of these steels are given in Tables 1 and 2. The influence of alloys on the mechanical properties of rails has been analyzed using multiple regression analysis. Previously published data for 32 standard, high-silicon and intermediate-manganese rails are used in the analysis [35-45]. The results of the analysis show that the tensile strength, yield strength, unnotched Charpy, and fatigue endurance limit are functions of the chemical composition of as-rolled steels as shown in Table 3. Heller has derived a similar equation of the tensile strength and ductility of as-rolled rails containing chromium [47], and Gladman et al have developed equations relating composition and microstructure to the tensile and impact properties of medium-carbon steels used for rails in Europe [48]. Examination of the equations shows that, while composition changes can increase strength, ductility and impact resistance are decreased.

Effects of Microstructure

The second class of improved steels are heat-treated rails. Rail heat treatments are similar to chromium and chromium-molybdenum alloy additions in that strength is increased by producing a fine pearlite microstructure. Hyzak and Bernstein have shown that heat treating has the advantage of being capable of producing a steel with both improved toughness and strength [49]. This is due to the fact that strength is dependent on the pearlite interlamellar spacing; decreasing the pearlite spacing increases the strength, as seen in Fig. 16. Figure 17 shows that the fracture toughness or impact strength is a function of prior austenite grain size. Since pearlite spacing and austenite grain size may be controlled independently, the strength and toughness may be optimized independently through heat treatment. A comparison of the fracture toughness properties of standard, alloy, and heat-treated rail shows the improved fracture behavior of heat-treated steels [50] (Table 2).

TABLE 1—*Ranges of chemical compositions of rail steels used in North America.*

	Element, Weight Percent				
	Carbon	Manganese	Phosphorus	Sulfur	Silicon
AREA standard ^a	0.69/0.82	0.70/1.00	>0.04	>0.04	0.10 to 0.25
High silicon	0.69/0.82	0.70/1.00	>0.04	>0.04	0.50 to 1.00
Intermediate manganese	0.65	1.37	>0.04	>0.04	0.10 to 0.25
Chromium	0.72	0.78	>0.04	>0.04	0.25
					1.31

^aHeat-treated rails are produced only from this grade.

TABLE 2—Typical mechanical properties of rail steels used in North America at 21° C (75° F).

Rail	0.2% Yield Strength ^a		Tensile Strength ^a		Elongation, ^a %	Dynamic Fracture Toughness ^b	
	ksi	MPa	ksi	MPa		ksi $\sqrt{\text{in.}}$	MN $\cdot \text{m}^{-3/2}$
Standard	69.9	481.9	135.9	937.0	9.5	26.0	28.6
High silicon	70.8	488.2	137.0	944.6	10.3	19.0	20.9
Intermediate manganese	76.2	525.5	133.4	920.1	13.5	27.0	29.7
Chromium	94.9	654.1	161.6	1114.0	9.2	19.0	20.9
Heat-treated	126.1	869.4	176.9	1219.7	9.5	34.0	37.4

^aTests performed with 0.505-in. (12.8-mm) diameter specimens.^bTests performed with precracked Charpy bars.

Effect of Hydrogen

Rail steels are also subject to shatter cracking associated with high hydrogen contents (>3 parts per million) [46]. However, studies by Cramer and his co-workers, who confirmed the connection between hydrogen and shatter cracks, showed that cracking could be suppressed by slow cooling (controlled cooling) between 370 and 150°C (700 and 300°F) as seen in Fig. 18 [51–55]. More recently, Heller et al [46] have shown that various rail grades have different degrees of susceptibility to flake formation. Investigations were made to establish the critical hydrogen contents, above which flakes are formed. These investigations revealed that sensitivity to hydrogen increases with an increasing manganese-carbon ratio, as seen in Fig. 19. Higher sulfur contents reduce susceptibility to the formation of flakes (Fig. 20). A chromium-manganese special grade is less sensitive to flaking

TABLE 3—Regression equations for predicting mechanical properties of non-heat-treated rail steels at 70° F.

Pearlitic rail steels	
Tensile strength, psi	72 750 + 63 324 (%C) + 11 935 (%Mn) + 20 206 (%Si)
Yield strength, psi	38 766 + 34 580 (%C) + 8234 (%Mn) + 12 453 (%Si)
Un-notch Charpy, ft-lb	299 - 365 (%C) + 103 (%Mn)
Endurance limit, psi	48 528 + 9523 (%C) + 3366 (%Mn) + 10 037 (%Si)
Brinell hardness	113 + 162 (%C) + 34 (%Mn) + 38 (%Si)
Chromium rail steels [46]	
Tensile strength, psi	34 185 + 116 175 (%C) + 16 664 (%Mn) + 10 254 (%Si) + 10 592 (%Cr) + 81 619 (%P)

Conversion factors—

1 psi = 1.6894 Pa

1 ft-lb = 1.355 N·m

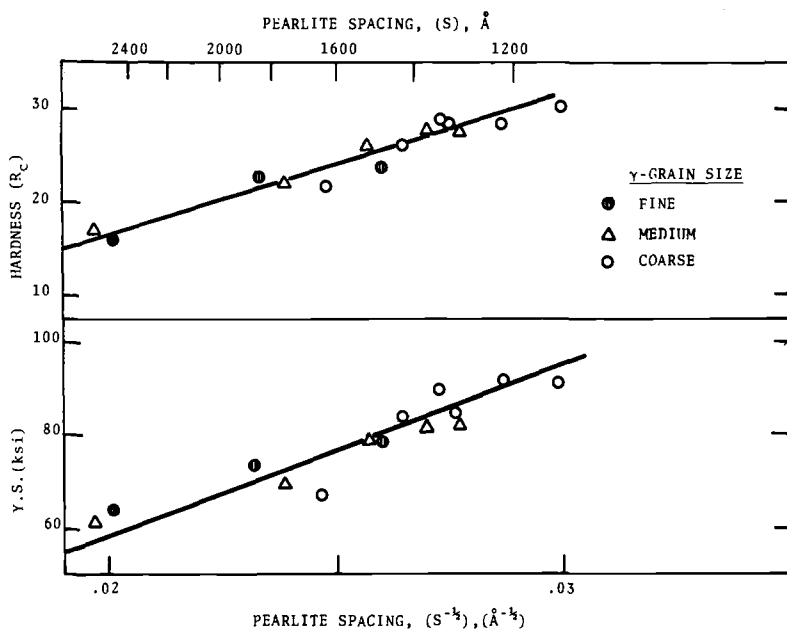


FIG. 16—Yield strength and hardness versus pearlite interlamellar spacing [49].

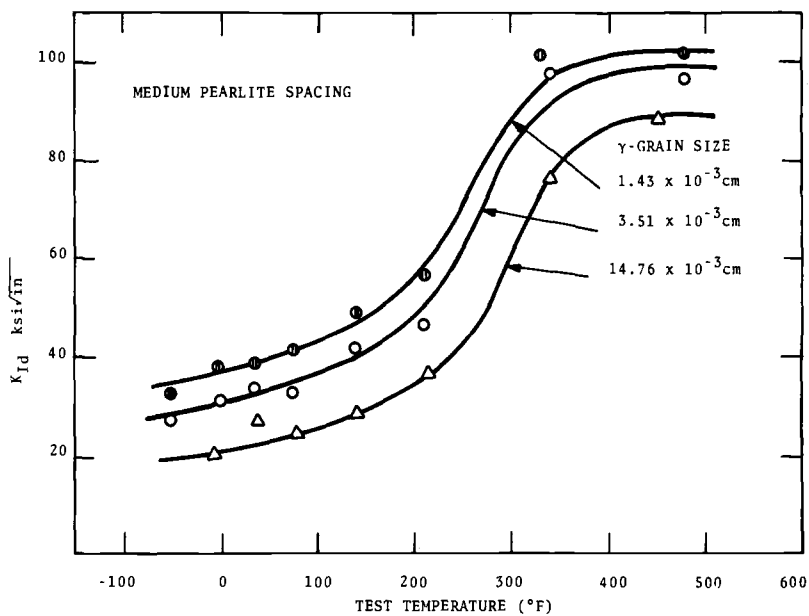


FIG. 17—Dynamic fracture toughness K_{Id} , curves as a function of prior austenitic grain size [49].

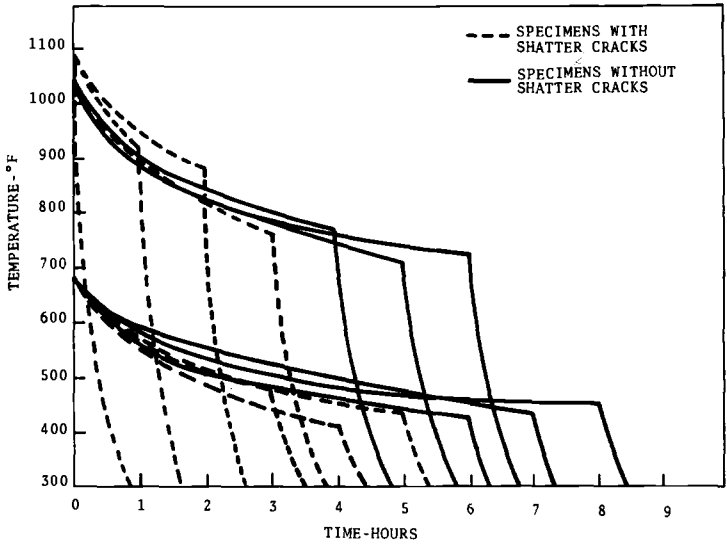


FIG. 18—Effect of cooling rate on shatter crack formation of AREA rail steels [53].

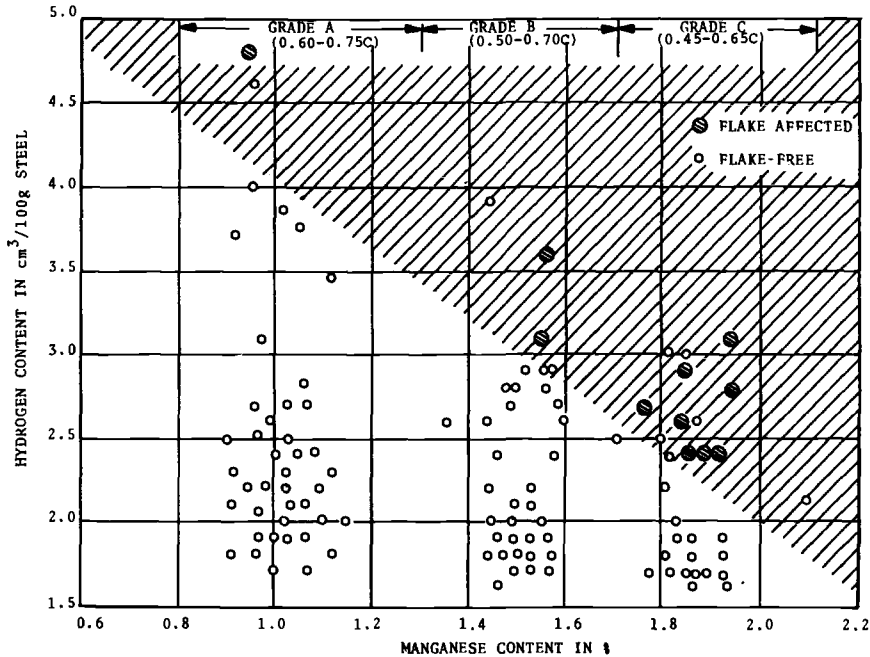


FIG. 19—Manganese content and flakes in wear-resisting rail steels [46].

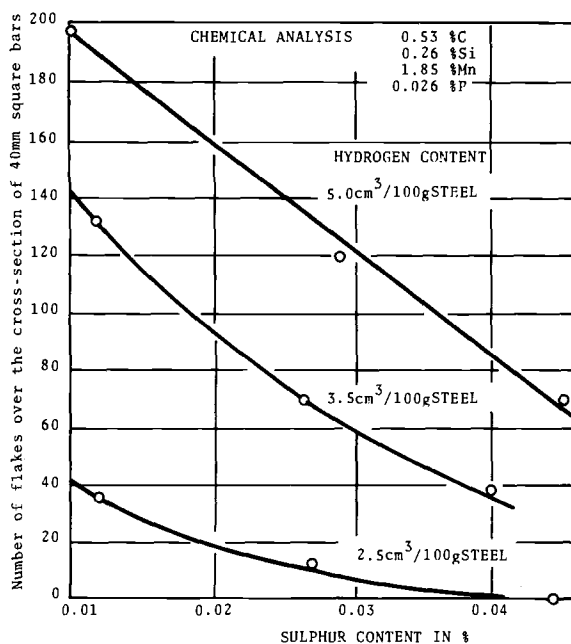


FIG. 20—Flake formation as a function of sulfur content with various hydrogen contents for a Grade C rail steel [46].

than standard carbon rails in spite of having a higher tensile strength. Hydrogen effusion does not differ between the pearlitic grades.

Where higher hydrogen contents lead to flaking, these occur predominantly in segregation lines. Accordingly, the tendency of the various rail steels to form flakes is governed mainly by the content of alloying and accompanying elements in the segregation and, particularly in rails of high carbon and manganese contents, leads to a transformation of the segregation lines to martensite.

Tension tests confirmed the influence of the alloying elements on the hydrogen embrittlement of the pearlitic structure. In the standard tension test, the degree of hydrogen embrittlement increases with increasing manganese contents, and in the multiaxial state of stress of the notched-bar tension test, it increases with higher manganese and chromium contents. Carbon has no effect on hydrogen embrittlement [46].

Conclusion

The continuously increasing service demands placed on the presently used pearlitic steels, which have been developed over the past 75 years, are approaching the limits of the rail's ability to act as an effective part of the track structure. The ability of rail to meet the serviceability demands placed

upon it has been shown to depend upon a number of mechanical properties and characteristics, some of which can undergo alteration as the rail is subjected to use. In spite of much improved knowledge of the mechanical properties, reliable quantitative predictions of rail service behavior are difficult to make. As a result, the amount of research directed at rail steels and rail behavior has increased rapidly over the past five years. In this respect, this paper is intended to provide a background for the following papers by giving the context in which current rail research is performed.

APPENDIX I

For a 84.5 kN (19 000 lb) wheel load, the maximum shear stress occurs at a depth of approximately 2.8 mm (0.11 in.). The calculated contact induced stresses acting in the x , y , and z directions at that point are approximately [56]

$$\begin{aligned}\sigma_x &= -240 \text{ MPa } (-35 \text{ ksi}) \\ \sigma_y &= -207 \text{ MPa } (-30 \text{ ksi}) \\ \sigma_z &= -965 \text{ MPa } (-140 \text{ ksi})\end{aligned}$$

Based on Office for Research and Experiments (ORE) results [9], the residual stresses at that level could be

$$\begin{aligned}\sigma_{xR} &\approx +69 \text{ MPa } (+10 \text{ ksi}) \\ \sigma_{yR} &\approx -207 \text{ MPa } (-30 \text{ ksi}) \\ \sigma_{zR} &\approx -90 \text{ MPa } (-13 \text{ ksi})\end{aligned}$$

Superimposing these stresses upon the contact stresses and solving for the octahedral shear stress (τ_{oct}) using

$$\tau_{\text{oct}} = 1/3 [(\sigma_x - \sigma_y)^2 + (\sigma_y - \sigma_z)^2 + (\sigma_z - \sigma_x)^2]^{1/2}$$

one finds that

$$\tau_{\text{oct}} = 248 \text{ MPa } (36 \text{ ksi})$$

which would be somewhat less than the estimated shear endurance strength of approximately 275 MPa (40 ksi).

APPENDIX II

A transverse crack fully embedded within the head of a rail can be approximately represented by a penny-shaped crack embedded within an infinite solid for which the stress intensity range is given by

$$\Delta K = 1.13 \Delta \sigma \sqrt{a}$$

The stress range, $\Delta \sigma$, can be estimated approximately for the theory for a beam on an elastic foundation. With the lower crack front at a depth of 15 mm (0.6 in.)

(10 mm (0.4 in.) depth at origin and $a = 5$ mm (0.2 in.)), the maximum nominal bending tensile stress and the stress ranges, $\Delta\sigma$, at the crack tip depth are given below:

Wheel Load, kN (kips)	Maximum Tensile Stress, MPa (ksi)	$\Delta\sigma$, MPa (ksi)
111 (25)	15.2 (2.2)	108.3 (15.7)
178 (40)	24.1 (3.5)	173.1 (25.1)
222 (50)	30.3 (4.4)	217.9 (31.6)

If no residual stresses are present, the stress ratio, R , will be much less than $R = 1$ so that only the maximum tensile stress can be considered to drive the crack ($R = 0$). For a 222-kN (50-kip) wheel load, the stress intensity will be

$$\Delta K = (1.13) (30.3 \text{ MPa}) \sqrt{0.005 \text{ m}} = 2.4 \text{ MN}\cdot\text{m}^{-3/2}$$

which is less than the threshold of $8 \text{ MN}\cdot\text{m}^{-3/2}$ ($7 \text{ ksi } \sqrt{\text{in.}}$) at $R = 0$. Thus, without residual tensile stress present, all wheel loads less than $\sim 710 \text{ kN}$ ($\sim 160 \text{ kips}$) will fail to produce sufficient stress intensity to drive a crack of 5 mm (0.2 in.) radius above the threshold level.

In order to incorporate residual stress into the analysis, one must recognize that the residual stress pattern within the railhead will redistribute as the crack enlarges. For simplicity, it will be assumed that a crack originates at that point of peak residual stress at a depth of 10 mm (0.4 in.), and, as it grows downward, the residual stress diminishes linearly to zero at the bottom of the head as shown conceptually in Fig. 21. For each load of peak residual stress, a new stress ratio is calculated by

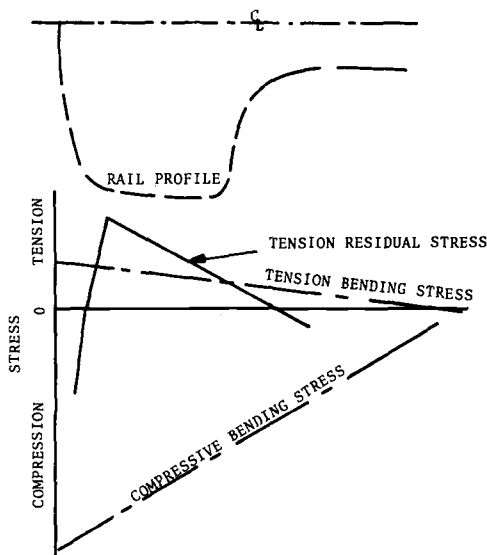


FIG. 21—Location of residual and bending stresses in the railhead.

adding the residual stress at $a = 5$ mm to the peak bending stress at that point, that is

$$R = \frac{\sigma_{\min} + \sigma_{\text{residual}}}{\sigma_{\max} + \sigma_{\text{residual}}}$$

Where $R \geq -1$ the crack growth rate can be calculated from the expression

$$\frac{da}{dN} = \frac{5.638 \times 10^{-9} \Delta K^3}{(1 - R) K_{Ic} - \Delta K}$$

whenever ΔK exceeds the threshold which is calculated from

$$\begin{aligned} \Delta K_{\text{threshold}}^{1 > R > -1} &= \Delta K_{\text{threshold}}^{R = 0} (1 - R) \\ &= 7 (1 - R) \end{aligned}$$

Values of da/dN for a range of wheel loads and tensile residual stress levels are tabulated below:

<i>da/dN</i> for Three Tensile and Residual Stress Levels, m/cycle (in./cycle)			
Wheel Load kN (kips)	103 MPa (15 ksi)	138 MPa (20 ksi)	172 MPa (25 ksi)
111 (25)	$1.5 \times 10^{-9} (5.9 \times 10^{-8})$	$2.0 \times 10^{-9} (8.0 \times 10^{-8})$	$2.6 \times 10^{-9} (10.3 \times 10^{-8})$
178 (40)	$4.3 \times 10^{-9} (16.9 \times 10^{-8})$	$5.6 \times 10^{-9} (22.3 \times 10^{-8})$	$7.1 \times 10^{-9} (28.3 \times 10^{-8})$
222 (50)	$7.3 \times 10^{-9} (28.6 \times 10^{-8})$	$9.5 \times 10^{-9} (37.3 \times 10^{-8})$	$11.8 \times 10^{-9} (46.8 \times 10^{-8})$

APPENDIX III

Some Russian research [56] has suggested that there is a fatigue aspect of wear which combines with adhesion to cause metal transfer on a macroscopic scale. A fatigue model of wear may be developed which predicts behavior consistent with observed behavior by merging concepts of metal contact at rubbing surfaces with a Manson-Coffin view of fatigue.

If wear were to be considered a fatigue process, the wear rate, \dot{R} , could be considered directly proportional to the area of contact at the asperities, A , and inversely proportional to the number of cycles, N_f , necessary to achieve the amount of fatigue damage within an enclave near the surface needed to remove metal from the surface, that is

$$\dot{R} = A \cdot h / N_f$$

where h is the depth of the enclave in which the fatigue damage will occur. The units of \dot{R} are volume/cycle which is reasonable. Now the area of contact depends upon

both the load, W , and the mean pressure, \bar{p} , which can develop within asperities [57] as

$$A = W/\bar{p}$$

thus

$$\dot{R} = W \cdot h / \bar{p} N_f$$

The mean pressure, \bar{p} , is thought to be virtually independent of load, W , having a value dependent on the yield strength. If the surface is rough and loads relatively light, one may hypothesize that asperity contact behavior resembles the metal flow problem of a punch where the thickness-to-width ratio is near unity; in this case, the yield pressure, \bar{p} , is approximately equivalent to the yield strength [58]. On the other hand, when the surface is smoother (after wear in) or the loads higher or both, the situation could resemble that of the flat punch where the thickness-to-width ratio approaches 10 or more; here, \bar{p} would be approximately 2.6 times the yield strength [33]. Thus, the value of \bar{p} may depend upon the conditions of the surface and the loading.

Shear forces applied to the interface have been shown [59] to have a large effect upon the effective pressure, p^* , which develops, that is

$$p^* = \sqrt{\bar{p}^2 + \alpha^2 s^2}$$

where α is reported to have a value of about 10 [59], and s is the applied shear stress. The effect of the shear stresses is to increase the contact area and the effective fatigue stress at the interface.

Considering the increase in area first, if the contact area without shear stress is

$$A = W/\bar{p}$$

then the area with shear stress due to the increase in effective pressure, p^* , might be represented as

$$A = W/\bar{p} \left(\frac{\bar{p}}{p^*} \right)^m$$

Based on reported data (where $\alpha = 10$), if the shear stresses approach the mean pressure, \bar{p} (which is a function of yield strength), the contact area will increase by a factor of three; thus, the power term, m , should be $1/2$. Basically, the ratio $1/[(\bar{p}/p^*)^m]$ is an amplification factor reflecting the increase in applied effective pressure over the yield pressure.

Now, returning to fatigue aspect, Morrow [60] noted that applied stress, σ_a' , and the cycles to failure, N_f , could be related through the equation

$$\sigma_a' = \sigma_f'(2N_f)^b$$

where σ_f' is the cyclic fracture stress and b is the slope on a plot of $\log \sigma_a'$ plotted versus $\log 2N_f$. However, the value of b is related to the cyclic plastic stress-strain curve through the expression

$$b = \frac{-n'}{1 + 5n'}$$

where n' is the slope of the log-log cyclic stress-strain line. Given that σ_a' can be considered to be p^* , then

$$N_f = 1/2 \left(\frac{p^*}{\sigma_f'} \right)^{1/b}$$

where $b < 0$. Substituting into the expression for \dot{R} , one finds that

$$\dot{R} = \frac{2}{P} \frac{W \cdot h}{\left(\frac{p^*}{p_f'} \right)^{1/2}} \left(\frac{p^*}{p_f'} \right)^{1/b}$$

where p_f' is the pressure equivalent of σ_f' .

References

- [1] *Yearbook of Railroad Facts*, Association of American Railroads, Washington, 1976, p. 53.
- [2] Kalousek, J. and Klein, R., *AREA Bulletin*, American Railway Engineering Association, Vol. 17, No. 656, Jan. 1976, pp. 429-448.
- [3] Beck, R. F., "Final Report/US-USSR Track and Metallurgy Information Exchange," Sept. 1976, to be published as National Technical Information Service report.
- [4] Thomas, H. R. and Hoersch, V. A., University of Illinois Engineering Experimental Station Bulletin No. 212, 1930.
- [5] Code, C. J., *AREA Proceedings*, American Railway Engineering Association, Vol. 61, 1960, pp. 1219-1238.
- [6] Frocht, M. M., *Proceedings SESA*, Society for Experimental Stress Analysis, Vol. 14, No. 1.
- [7] Way, G. H., *AREA Bulletin*, American Railway Engineering Association, Vol. 76, June 1975, p. 616.
- [8] "Sperry Railer," Automation Industries, Summer 1975, p. 6.
- [9] "Behavior of the Metal of Rails Under the Repeated Action of Wheels," ORE Report C53/RP9/E, International Union of Railways, Utrecht, 1971.
- [10] Hyler, W. S. and Grover, H. J., *AREA Proceedings*, American Railway Engineering Association, Vol. 55, 1954, pp. 840-854.
- [11] Fowler, G. J., "Fatigue Crack Initiation and Propagation in Pearlitic Rail Steels," Ph.D. Thesis, University of California at Los Angeles, 1976.
- [12] Johns, T. G. and Davies, K. B., BCL Interim Report 30, DOT-TSC-1038, Department of Transportation, June 1976.
- [13] Technical Report DOT-TSC-1038, to be published.
- [14] Oding, I. A., Nickonov, A. G., and Maryanovskaya, T. S., *Russian Metallurgy and Mining*, No. 5, 1964, pp. 59-69.
- [15] Ahlbeck, D. R., Johnson, M. R., Harrison, H. D., and Pause, R. H., BCL Interim Report, DOT-TSC-1051, Department of Transportation, April 1976.
- [16] Gervais, E. and McQueen, H. J., *Journal of the Iron and Steel Institute*, March 1972, pp. 189-198.
- [17] Lempitskii, V. V., Treshevskii, I. S., and Kazarnovskii, D. S., *Stal in English*, No. 11, Nov. 1964, pp. 929-933.
- [18] Carter, C. S., Caton, R. G., and Guthrie, J. L., "Fracture and Fatigue Crack Growth Characteristics of Railroad Wheels and Axles," Technical Report DOT-TSC-617, Boeing Commercial Airplane Co., Seattle, April 1976.
- [19] Feddersen, C. E., Buchheit, R. D., and Broek, D., BCL Interim Report, DOT-TSC-1076, Department of Transportation, July 1976.
- [20] Cooke, R. J. and Beevers, C. J., "Slow Fatigue Crack Propagation in Pearlitic Steels," Research Report, University of Birmingham, Nov. 1972.
- [21] Kilburne, K. R., *Wear*, Vol. 7, 1964, pp. 255-269.

- [22] Deardon, J., *Wear*, Vol. 3, 1960, pp. 43-56.
- [23] Fijinaawa, U., *Railway Gazette*, Vol. 12, 1967, p. 899.
- [24] Munch, W., *Proceedings of the Iron and Steel Institute Meeting on Rail Steels*, London, 23 Nov. 1972, p. 24.
- [25] Schumacher, G., *Proceedings of the Iron and Steel Institute Meeting on Rail Steels*, London, 23 Nov. 1972, p. 43.
- [26] Schoeneberg, K. W., *Proceedings of the Iron and Steel Institute Meeting on Rail Steels*, London, 23 Nov. 1972, p. 52.
- [27] Vinot, J., *Proceedings of the Iron and Steel Institute Meeting on Rail Steels*, London, 23 Nov. 1972, p. 75.
- [28] Dean, J., Jones, E. G., and Babb, A. S., *Proceedings of the Iron and Steel Institute Meeting on Rail Steels*, London, 23 Nov. 1972, p. 47.
- [29] Heller, W., *Proceedings of the Iron and Steel Institute Meeting on Rail Steels*, London, 23 Nov. 1972, p. 115.
- [30] Rougas, M., *12th Annual Railroad Conference 1975 Technical Proceedings*, U. S. DOT-FRA-ORD&D 76-243, U. S. Dept. of Transportation.
- [31] King, F. E., *12th Annual Railroad Engineering Conference 1975 Technical Proceedings*, U. S. DOT-FRA-ORD&D 76-243, U. S. Dept. of Transportation.
- [32] Illinois Institute of Technology Research Institute, unpublished data.
- [33] Bhattacharyya, S., Illinois Institute of Technology Research Institute, Final Report B8054-4, 1965.
- [34] "Specification for Steel Rails," American Railway Engineering Association, 1974.
- [35] Cramer, R. E., *AREA Proceedings*, American Railway Engineering Association, Vol. 50, 1949, pp. 537-539.
- [36] Cramer, R. E., *AREA Proceedings*, American Railway Engineering Association, Vol. 51, 1950, p. 604.
- [37] Cramer, R. E., *AREA Proceedings*, American Railway Engineering Association, Vol. 52, 1951, p. 670.
- [38] Cramer, R. E., *AREA Proceedings*, American Railway Engineering Association, Vol. 53, 1952, p. 903.
- [39] Cramer, R. E., *AREA Proceedings*, American Railway Engineering Association, Vol. 55, 1954, p. 834.
- [40] Cramer, R. E., *AREA Proceedings*, American Railway Engineering Association, Vol. 56, 1955, p. 955.
- [41] Cramer, R. E., *AREA Proceedings*, American Railway Engineering Association, Vol. 57, 1956, p. 851.
- [42] Cramer, R. E., *AREA Proceedings*, American Railway Engineering Association, Vol. 58, 1957, p. 1042.
- [43] Cramer, R. E., *AREA Proceedings*, American Railway Engineering Association, Vol. 59, 1958, p. 976.
- [44] Cramer, R. E., *AREA Proceedings*, American Railway Engineering Association, Vol. 61, 1960, p. 875.
- [45] Cramer, R. E., *AREA Proceedings*, American Railway Engineering Association, Vol. 64, 1963, pp. 535-536.
- [46] Heller, W., Weber, L., Hammerschmid, P., and Schwitzer, R., *Stahl und Eisen*, Vol. 91, No. 19, 14 Sept. 1972, pp. 934-945.
- [47] Heller, W., "Moghchkeiten der Schunenenentwuklung fur einen Hochlustungsschnellverkehr," *Technische Mitteilungen Krupp, Werksberichte*, Vol. 33, No. 2, 1975, p. 74.
- [48] Gladman, T., McIvor, I. D., and Pickering, F. B., "Some Aspects of Structure-Property Relationships in High Carbon Ferrite-Pearlite Steels," *Proceedings of the Iron and Steel Institute Meeting on Rail Steels*, London, 23 Nov. 1972.
- [49] Hyzak, J. M. and Bernstein, I. M., *Metallurgical Transactions*, Vol. 7A, No. 8, Aug. 1976, pp. 1217-1224.
- [50] Stone, D. H., "An Introduction to Fracture Mechanics of Railroad Rails," *Railroad Track Mechanics*, A. Kerr, Ed., Pergamon Press, to be published.
- [51] Cramer, R. E. and Alleman, N. J., *AREA Proceedings*, American Railway Engineering Association, Vol. 38, 1937, pp. 665-672.
- [52] Cramer, R. E. and Bast, E. C., *AREA Proceedings*, American Railway Engineering Association, Vol. 39, 1938, pp. 809-812.

- [53] Cramer, R. E. and Bast, E. C., *Area Proceedings*, American Railway Engineering Association, Vol. 40, 1939, pp. 658–664.
- [54] Cramer, R. E., *AREA Proceedings*, American Railway Engineering Association, Vol. 43, 1942, pp. 617–626.
- [55] Cramer, R. E. and Alleman, N. J., *AREA Proceedings*, American Railway Engineering Association, Vol. 44, 1943, pp. 616–620.
- [56] Kragelskii, I. V., *Friction and Wear*, Butterworths, 1965.
- [57] Moore, D. F., *Principles and Applications of Tribology*, Pergamon, 1975.
- [58] Rowe, G. W., *An Introduction to the Principles of Metalworking*, Arnold, 1975.
- [59] Bowden, F. P. and Tabor, R., *The Friction and Lubrication of Solids*, Clarendon, 1964.
- [60] Morrow, J. in *Internal Friction, Damping, and Plasticity*, ASTM STP 378, American Society for Testing and Materials, 1965, p. 45.

DISCUSSION

*Pierre Vicens*¹ (written discussion)—The development of new steel grades capable of better resistance to the repeated stresses undergone by the rail in service may only lead to an interesting approach of the fatigue problems if it has first been endeavored to eliminate the incidental defects which are detrimental to the performance of the currently used steel grade.

The research studies conducted by Societe Nationale des Chemins de Fer Francais (SNCF), Steel Industry, and the Iron and Steel Research Institute (IRSID) revealed that the fatigue failures in railhead (transverse fissure and horizontal fissure as shown in Figs. 22 and 23) were due to internal heterogeneities, either flakes or nonmetallic inclusions. The elongated manganese silicates or silicoaluminates revealed themselves as especially harmful due to the notch effect at their end; as concerns a standard grade rail steel as per UIC specification, the fatigue limit under alternating torsion may be as low as 12 to 14 kg/square mm, whereas the normal fatigue limit of this grade is 18 to 20 kg/square mm.

The advantage of a nondestructive process allowing the detection of these heterogeneities on all the rails prior to track laying seemed obvious, and therefore IRSID has developed the RALUS process for the continuous ultrasonic testing of railheads.

Briefly, this testing method involves the detection of heterogeneities in the upper part of the railhead, through a 20 mm deep layer (Fig. 24). In fact, the fatigue defects that are to be avoided are located in this zone. The probe is applied on railhead side. It includes two slightly skewed crystals, coupled by means of a water column. The flaw echoes are recorded on a strip chart, the winding of which is controlled by the motion of the rail, shown in Figs. 25 and 26.

For the calibration of the equipment, IRSID has studied the records corresponding to 140 rails removed from the track: 77 rails presented a good behavior and 63 rails revealed poor behavior. Thus, six rail classes have been

¹Ingenieur en chef adjoint, Metallurgie Qualite, Sacilor, France.

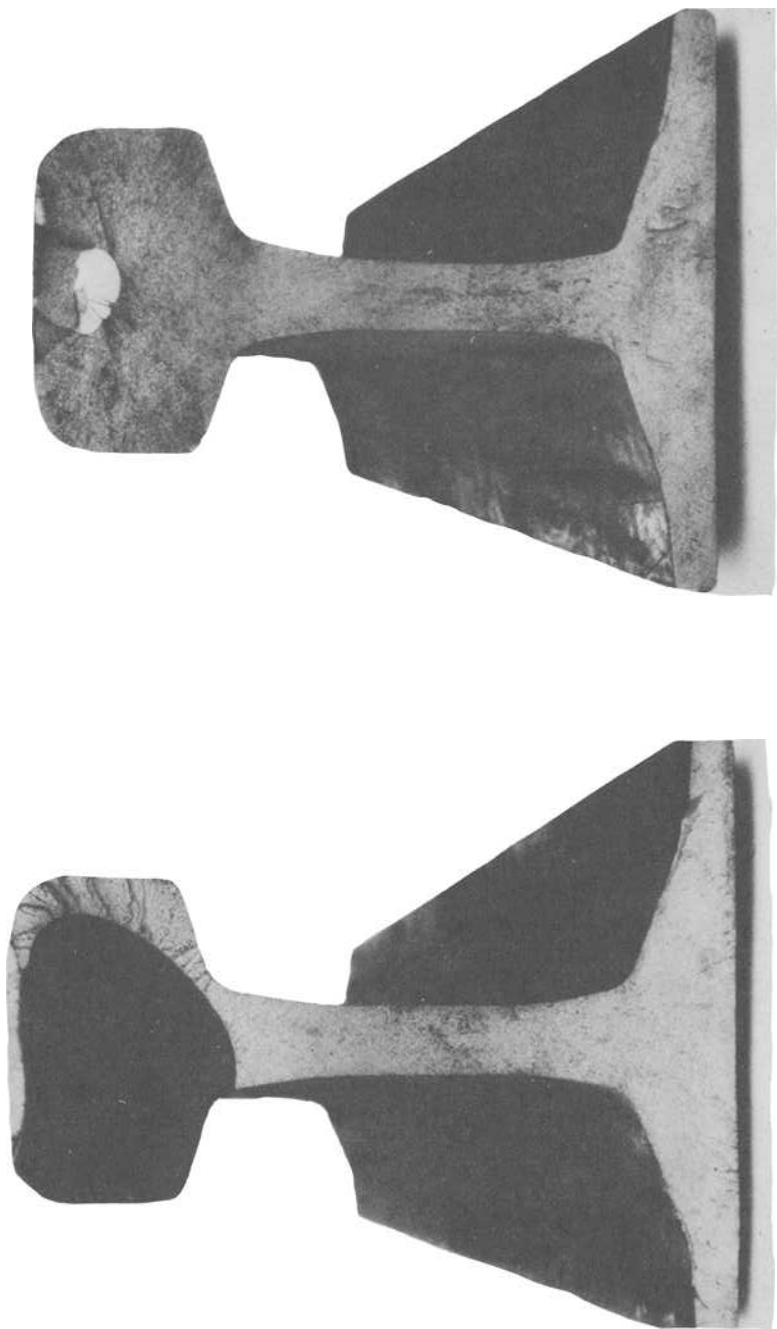


FIG. 22—*Transverse fissure.*

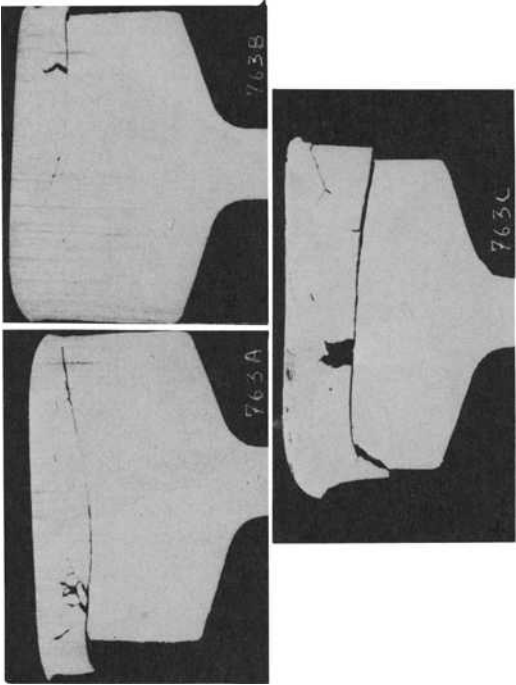
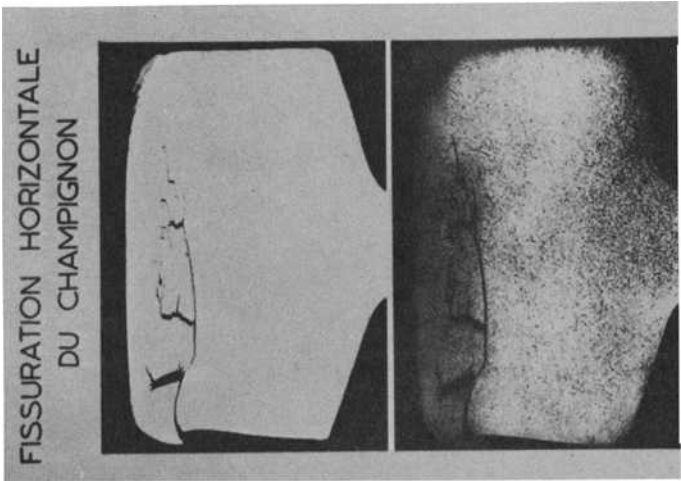


FIG. 23—Horizontal fissure.

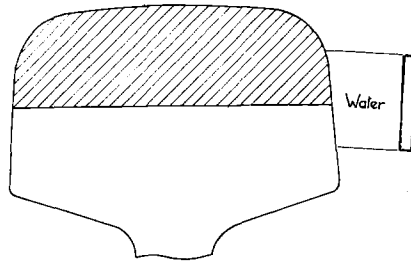


FIG. 24—*RALUS inspected zone.*

defined according to the number and to the height of the peaks above a given threshold. Ninety-six percent of the good rails were included in the first three classes, and 84 percent of the bad rails were included in the last three classes (Table 4).

In order to ascertain the validity of RALUS process, the SNCF proceeded in 1963 to the laying of rails pertaining to the various classes. The test sites were the following:

The Track No. 1 of the Paris-Lyon line between Blaisy and Dijon:

traffic of 70 000 gross tons per day
 speed of 120 km/h
 slope 8 mm/m
 rocky platform

The so-called Grande-Ceinture track near Paris:

traffic of 75 000 gross tons per day
 speed of 80 km/h
 slope 0
 backfilling platform

The axle loads are in general higher on the Grande-Ceinture track, but the dynamical overloads are higher on Blaisy track. The results obtained are shown in Table 5 which proves the validity of the developed criterion.

Since 1966, the rail testing according to RALUS process has been applied in the steel works producing rails for SNCF. The continuous ultrasonic testing of each rail has permitted:

1. Easier study of the parameters having an influence on rail steel internal soundness.
2. Development of the manufacturing methods leading to the best industrial results.
3. Control of the uniformity of production quality.
4. Rejection of bad rails (Class 5) liable to present a short life.
5. Putting aside the poor quality rails (Class 4) in order to use them for subsidiary tracks.

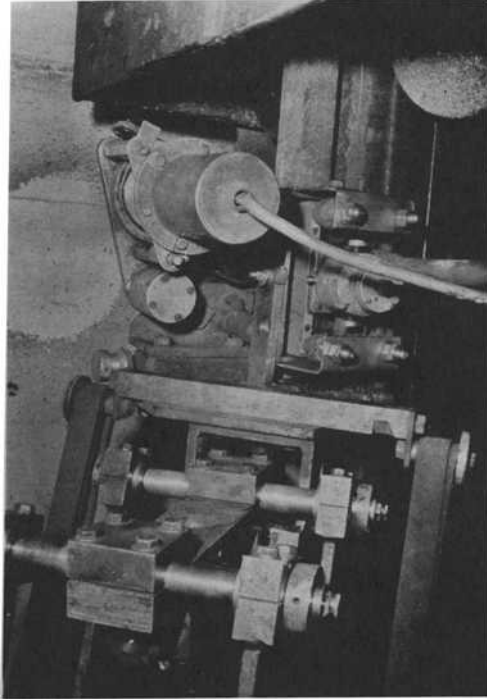
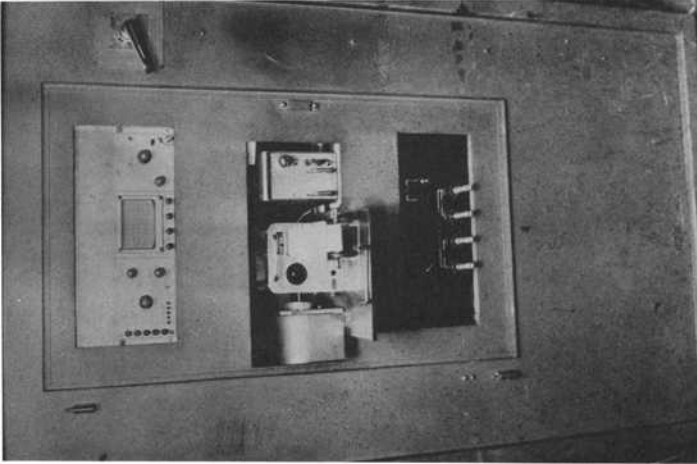


FIG. 25—RALUS apparatus.

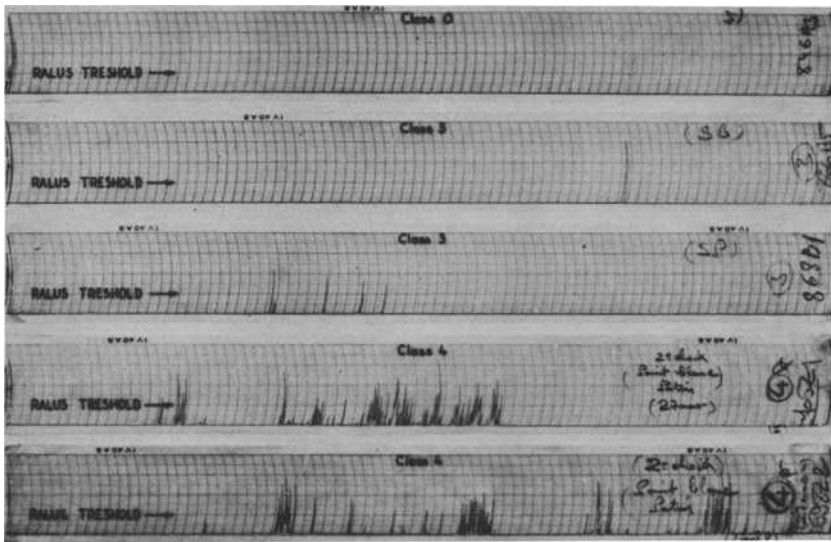


FIG. 26—RALUS record.

6. Since 1971, the best rails, of Classes 0 and 1, which are specially sorted for a laying on main tracks.

Based on the accurate statistical data that SNCF has available in the very comprehensive file pertaining to the life of rails in service, it is possible to define on the diagram shown in Fig. 27 the influence of these actions on rail removal.

In 1974, testing was improved. The main changes are as follows:

1. Extension of the scanned zone to 30 to 5 mm (Fig. 28) under the surface, for two reasons. Previously, hydrogen flakes were not all revealed, as shown in Fig. 29. According to the studies of Office for Research and Experiments (ORE) C 53 Committee, the possible increases in the axle loads are liable to shift inwards toward the zone where the fatigue defects appear.
2. Introduction of a double accounting of the defects. The RALUS accounting system is maintained for Classes 3, 4, and 5, but a second accounting system of the defects has been introduced to take into account a threshold lower than RALUS accounting threshold. Over this threshold, the length and not the number of defects is taken into account (Fig. 30). This is intended with a view to facilitate the quality level of production; in fact, following the improvement in quality, resulting from the fact that the Bessemer converter was replaced by Kaldo and oxygen low pressure (OLP) oxygen processes in 1972, the threshold defined for the RALUS no longer permitted a sufficiently accurate sorting. A recently installed comprehensive automated system is shown in Fig. 31.

TABLE 4—*RALUS classes*

Class	Number of Echos	Height of Echos, mm
0	...	1
1	≤3	≤10
2	>3	≤10
3	≤3	>10
4	>3	>10
5	>6	>20

Class	Good Rails in Track, %	Bad Rails in Track, %
0	96	16
1	96	16
2	96	16
3	4	84
4	4	84
5	4	84

After nearly ten years experience with the continuous ultrasonic testing of the rails, we believe that this process is a very powerful tool which deserves a great interest, either for the knowledge of manufacturing processes and of the parameters having an action on inclusions and flake appearance, or for continuously obtaining a very good behavior of the rails with regard to fatigue in service.

D. H. Stone and R. K. Steele (authors' closure)—The RALUS technique is an effective demonstration of the difference in approach to the problem of hydrogen cracking by the Europeans who do not control cool rails. Mr. Vicens' data indicate that, since 1966, this method has been as effective as

TABLE 5—*Track trials.*

Ralus Class	Blaisy (tonnage carried: 273 million)			Grande Ceinture (tonnage carried: 318 million)		
	Rails Laid	Rails Removed %		Rails Laid	Rails Removed %	
0	786	23	2.9	145	4	2.8
1	739	41	5.5	165	6	3.6
2	316	62	19.6	96	8	8.3
3				144	11	7.6
4				56	21	37.5

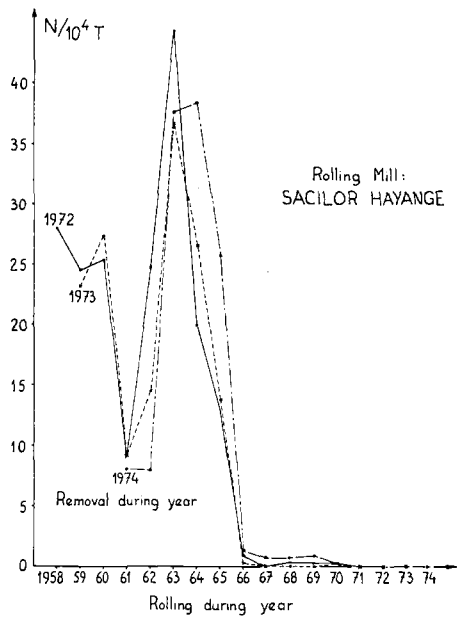


FIG. 27—SNCF tracks.

control cooling. The authors believe that the RALUS technique might reduce the number of rail failures due to its ability to detect harmful nonmetallics.

Herbert Schmedders² (written discussion)—Let me make some comments about quality characteristics of railroad rails under consideration of modern metallurgy in western Europe, especially West Germany.

The increasing traffic volume in connection with the economic growth of the industrialized nations of western Europe after the Second World War

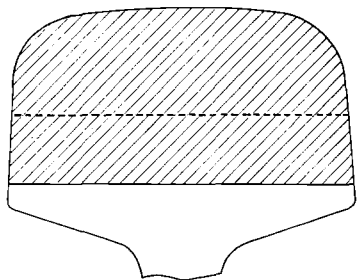


FIG. 28—New inspected zone.

²Manager of Quality Control, August Thyssen-Hütte Aktiengesellschaft, Duisburg, West Germany.

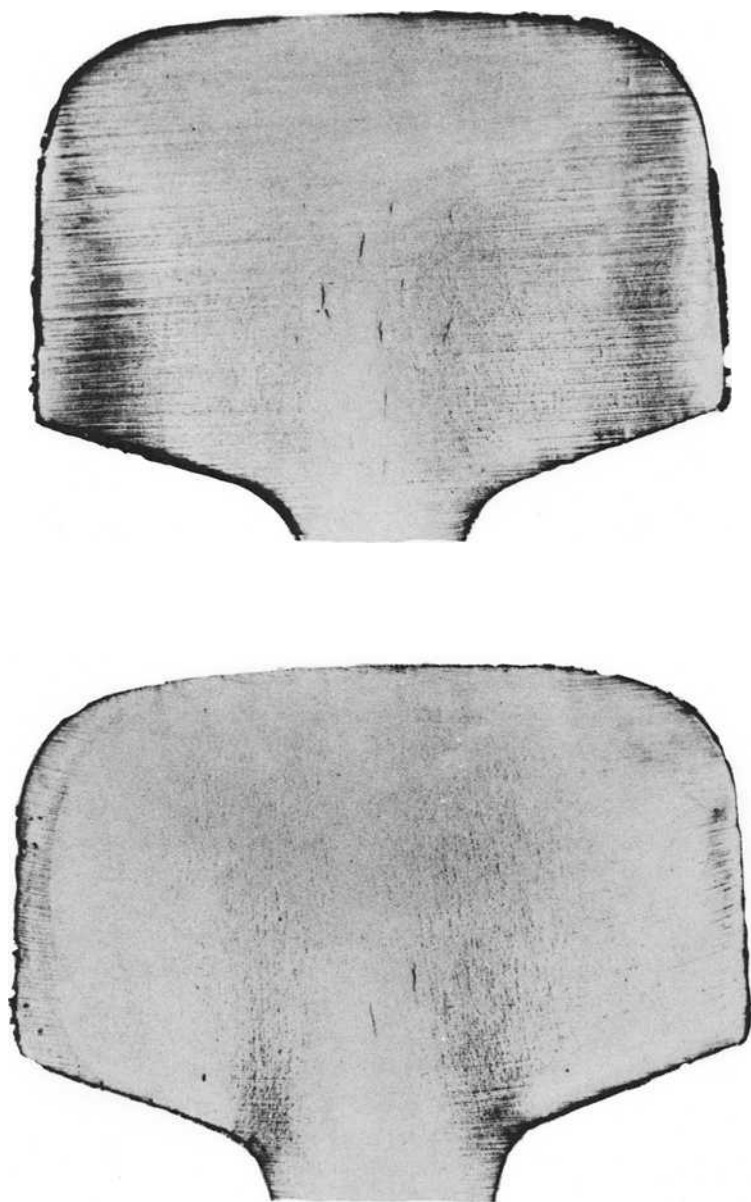


FIG. 29—*Hydrogen flakes.*

could only be accomplished by the railroad companies by means of operational and technical improvements, which meant an increased demand on railroad tracks and roadbeds, particularly on rails themselves.

In this connection, I should point out the increased speed of passenger

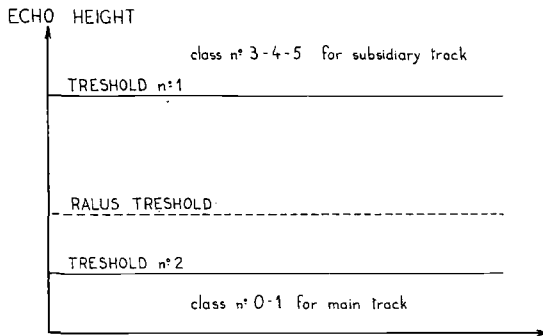


FIG. 30—New U.S. Classes.

trains of up to 100 mph and freight trains of up to 80 mph, the higher axle loads of up to 24 net tons, the more frequent interval of individual trains, the electrification of all main tracks, and the continuous welded rail versus the old joint bar connection method.

The increased loads shortened the lifetime of the rails. In order to improve that lifetime on main tracks, the rail sections were increased from 50 to 60 kg/m (100 to 120 lb/yd), and tensile strengths of the rails were improved from 100,000 to 128,000 psi, according to the UIC 860-V specifications. Besides the tensile strength, the rail quality to achieve trouble-free usage had to be further determined by avoiding shatter cracks and coarse inclusions.

Sufficiently high tensile strength values simultaneously incorporate a high (crushing and) yield strength, and at the same time provide a high resistance to fatigue cracks. They reduce the wear on the outer rail in curves (Fig. 32) and create resistance to head flow on the curved inner rail (Fig. 33).

Shatter cracks (Fig. 34) or coarse nonmetallic inclusions or both (Fig. 35) can lead to transverse or horizontal fissures or vertical split heads (Fig. 36), also called "dark spots." Both the aforementioned failures are to be considered severe safety hazards to rail traffic.

To eliminate shatter cracks, steel mills in the United States invented the controlled cooling of the rail. This method assures effusion of the hydrogen to a noncritical degree prior to reaching a temperature range critical to the development of flake formation. The disadvantage of the controlled cooling is the stalling in the production flow and a loss in tensile properties of about 5,000 psi compared to noncontrolled cooled rails.

Increasingly, the vacuum degassing of the liquid steel, thus reducing the hydrogen to a noncritical degree with regards to the formation of shatter cracks, becomes more popular in modern rail steel production. Predominantly, the Duisburg-Hamborn degassing process has become common practice in the Federal Republic of Germany. The advantage of this computerized vacuum degassing is to control and record all criteria determining the final hydrogen content.

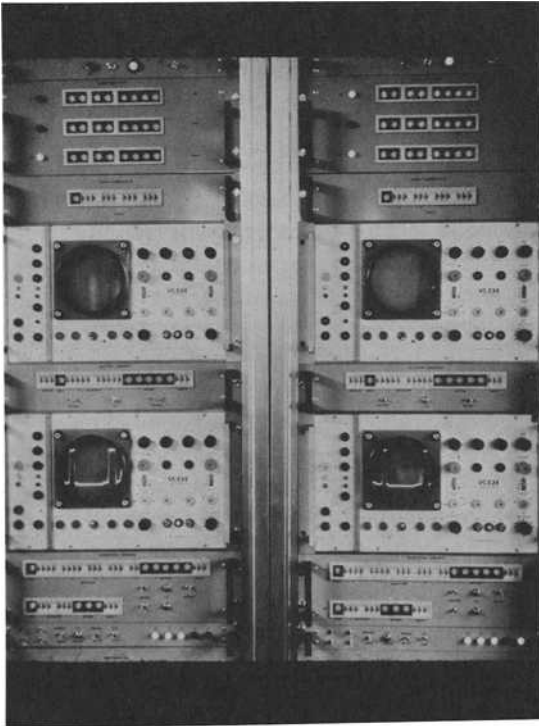
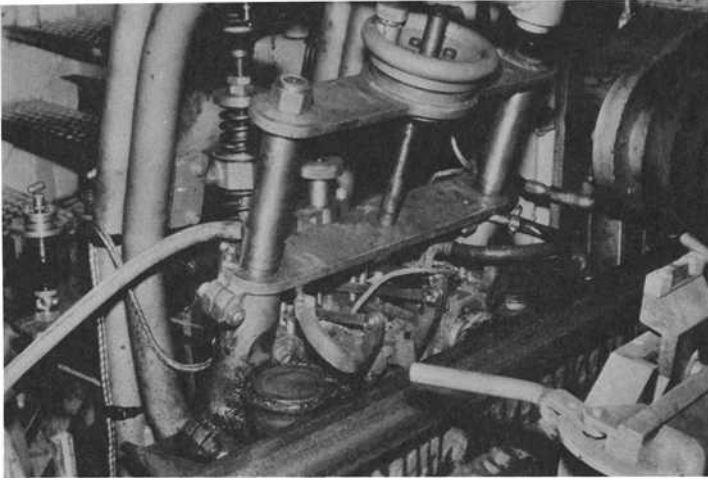


FIG. 31—New ultrasonic apparatus.

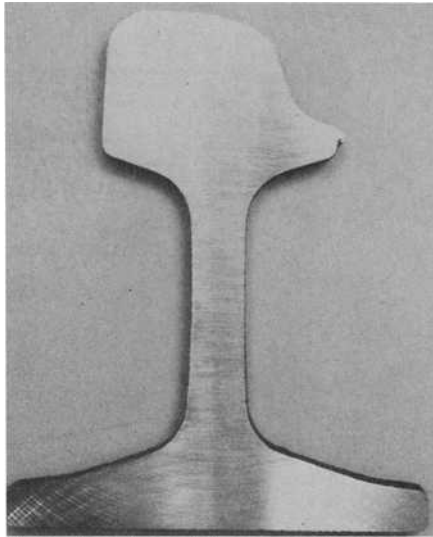


FIG. 32—*Abrasive wear of the railhead.*

In maintaining a very low pressure of less than 1 torr in the vacuum degassing unit for a certain period of time, a very low and noncritical residual hydrogen content level of less than 2.5 ppm is achieved, even in cases with fairly high initial hydrogen levels such as 6 ppm (Fig. 37).

By means of adequate pouring practice, a renewed increase in the

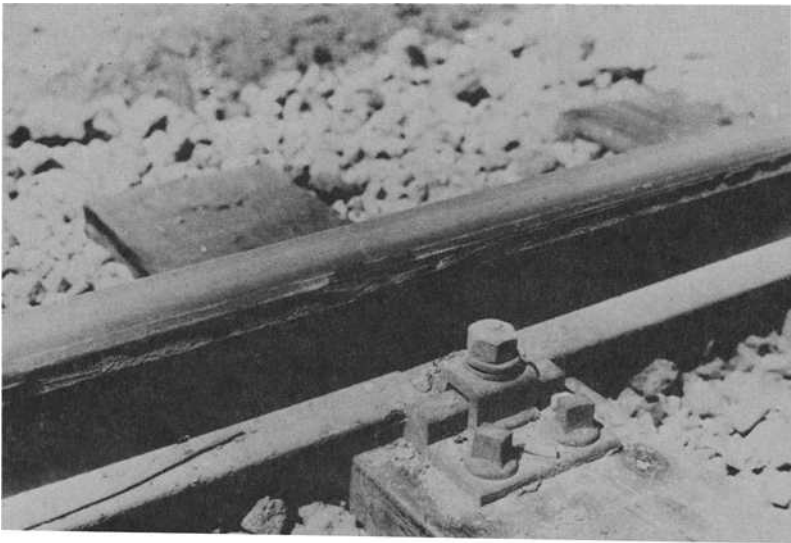


FIG. 33—*Rail with head flowed to side.*

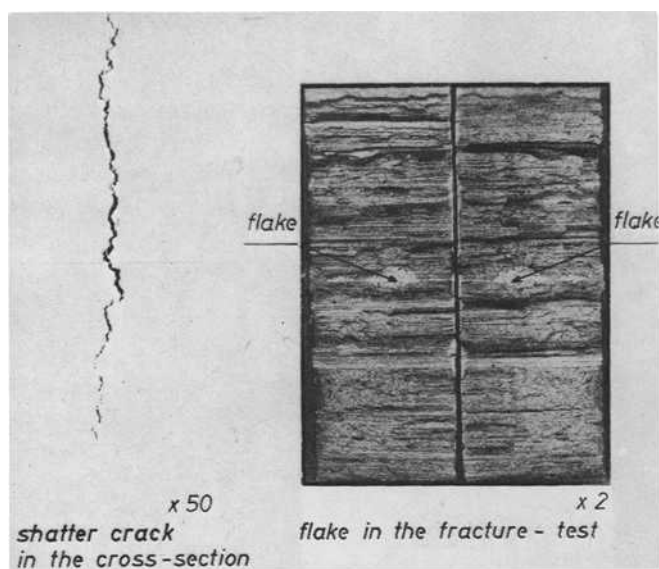


FIG. 34—Shatter crack in the railhead.

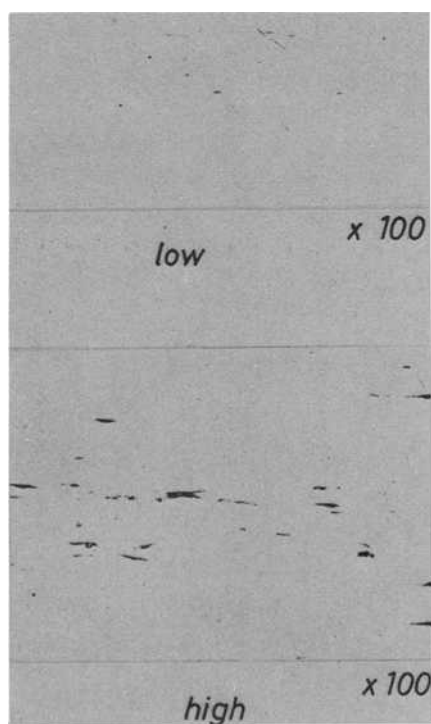


FIG. 35—Inclusion content polished section of the railhead.

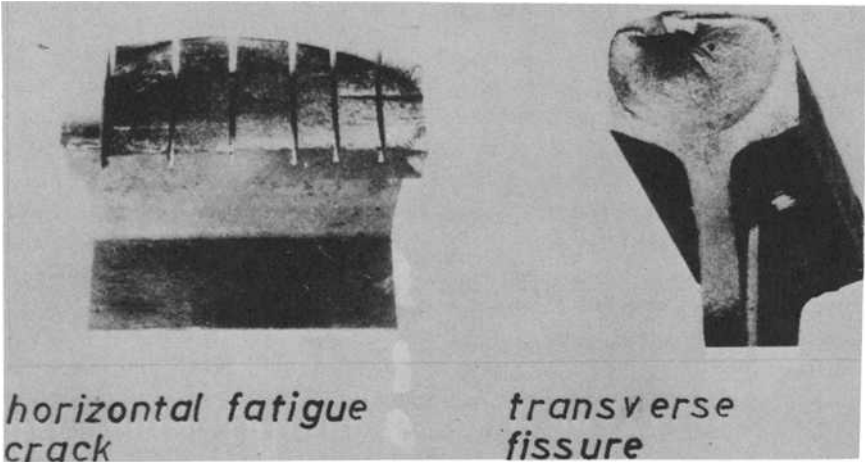


FIG. 36—Fissure in the railheads.

hydrogen level is prevented. Rails, produced from such vacuum degassed steel, can be cooled conventionally without developing flakes. Steps subsequent in the production process are in direct relation in determining the limit of the hydrogen content, above which flaking could possibly occur. The production standards in Germany limit the hydrogen content to 3.5 ppm for the UIC Quality Grade A. For the high wear resistant quality developed by

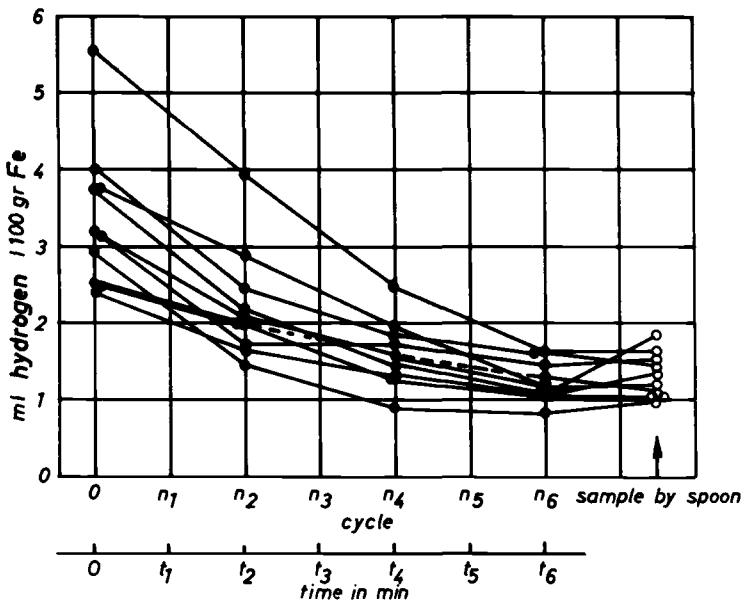


FIG. 37—Hydrogen removal during degassing.

the August Thyssen Mill, the so-called THS 11 rail quality — with 0.7 percent carbon, 10 percent manganese, 1.0 percent chromium, and 0.1 percent vanadium and a tensile strength exceeding 1100 N/square mm = 156,000 psi, the comparable value would be 3.00 ppm.

The degree of purity of the steel concerning nonmetallic inclusions is in direct relation with its oxygen content, that is, low oxygen means a good degree of purity. The vacuum degassing is also efficient in achieving very low oxygen levels, regardless of the oxygen contents in the steel prior to the vacuum degassing operations. After completing the degassing process, oxygen contents of 0.002 to 0.008 percent are achieved in the steel, which then has a degree of purity similar to ball bearing quality steel (Fig. 38).

Since 1963, steel for high-strength rail steels with a minimum tensile strength of 128,000 psi has been produced, utilizing the vacuum degassing method. Approximately 2.5 million tons of rails have been produced accordingly, which were supplied largely to the German Federal Railroad and other federal railroad companies worldwide. All these rails have an excellent performance record, withstanding extreme loads even under poor service conditions. None of these rails developed cracks, which could be attributable to fissures originating from flakes or nonmetallic inclusions.

D. H. Stone and R. K. Steele (authors' closure)—The authors agree with Dr. Schmedders that vacuum degassing is an effective process for the elimination of hydrogen-induced cracking.

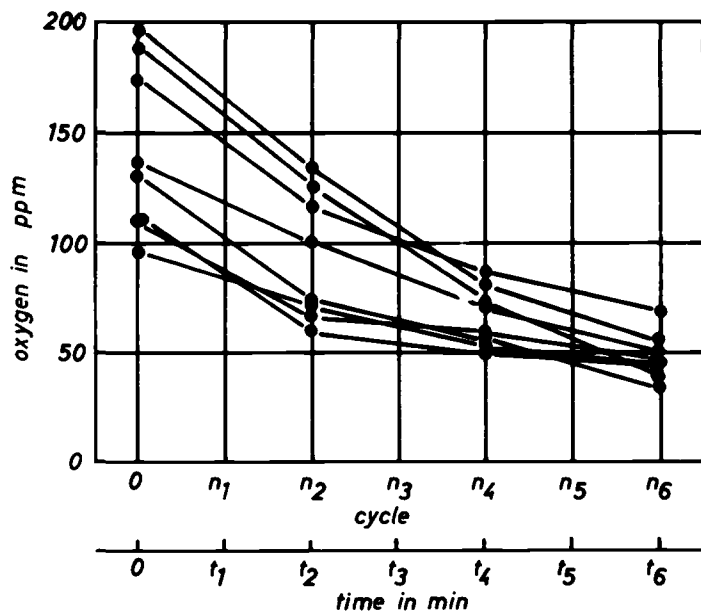


FIG. 38—Removal of oxygen during degassing.

Rail Wear Under Heavy Traffic Conditions*

REFERENCE: Kalousek, J. and Bethune, A. E., "**Rail Wear Under Heavy Traffic Conditions,**" *Rail Steels—Developments, Processing, and Use, ASTM STP 644*, D. H. Stone and G. G. Knupp, Eds., American Society for Testing and Materials, 1978, pp. 63–79.

ABSTRACT: The life of rail in curves under heavy traffic densities and loads is governed either by rail failures or wear. Basic forms of rail wear including rail gage face wear and surface fatigue forms of wear are described and illustrated by metallographical and scanning electron micrographs. The influence of improved rail metallurgical properties and lubrication on wear reduction is discussed. Potential savings arising from the usage of rail with improved metallurgy are estimated.

KEY WORDS: steels, railroad tracks, wear, metallurgy, lubrication

Modern railroads are striving to improve the productivity of their plant by increasing track utilization and employing cars of increasingly greater capacity. In view of these trends, improving or in many instances even maintaining rail service life is a challenging engineering problem.

Rails are replaced either due to rail failures or wear. Wear, as one of the major causes for rail replacement, is responsible for a significant portion of railway maintenance expenditures. The potential savings which may be realized from a better understanding of wear mechanisms are quite significant.

Rail wear has been studied extensively in the past [1–3]³ and more recently has enjoyed renewed interest [4,5]. This paper is intended to present some observations of typical rail wear experienced on Canadian Pacific (CP) rail and the conclusions which have been derived from these observations. Although recognizing that there are also substantial safety risks and expenditures associated with rail failures, it is our intention to confine our remarks solely to rail wear.

*Original experimental data were measured in U.S. customary units.

¹Presently, associated research officer, National Research Council of Canada, Vancouver, B.C., Canada; formerly, research engineer, Technical Research, Canadian Pacific Limited, Research Department, Montreal, Que., Canada.

²Assistant director, Technical Research, Canadian Pacific Limited, Research Department, Montreal, Que., Canada.

³The italic numbers in brackets refer to the list of references appended to this paper.

Basic Forms of Rail Wear

CP rail carries in excess of 30 million gross tons annually on approximately 195 miles of trackage with varying degrees of curvature. While standard carbon rail has a life of approximately 600 million gross tons in tangent track, rail life in curves is reduced on the average to 120 million gross tons due to severe forms of rail wear.

Rail wear can quite broadly be categorized into two types, fatigue and adhesive wear. Both types of wear are apparent on rails removed from service on CP rail in areas of high traffic density and high axle loads.

At the end of the service life on curved trackage, the outer rail is severely worn on the gage side and is shelled or spalled at the gage corner of the running surface. More likely than not, the rail is also corrugated with long wavelength type corrugations. The inner rail in curves usually experiences substantial plastic flow of metal toward the field side; the surface of the rail is flaked across almost the full width of the railhead, and again the rail is often corrugated. Figure 1 depicts the various types of damage which may be observed on rails deleted from service. Flaking, shelling (referred to as checking by some railroads), and spalling are fatigue forms of wear. Gage face wear and a portion of surface wear on the outer rail are predominantly adhesive forms of wear. Delamination and some abrasive types of wear are also present. Let us examine these types of wear more closely beginning with adhesive gage face wear on the outer rail.

Gage Face Wear

Figure 2a shows the lateral components of tread forces acting in the wheel/rail interface under saturated creep in curves of 2 deg or more. The tread forces give rise to forces active between the wheel flange and the gage

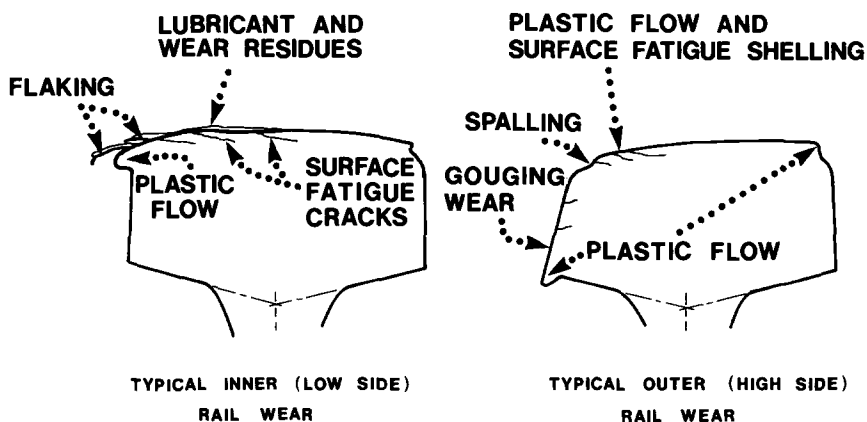


FIG. 1—Wear of rails in curves under heavy traffic conditions.

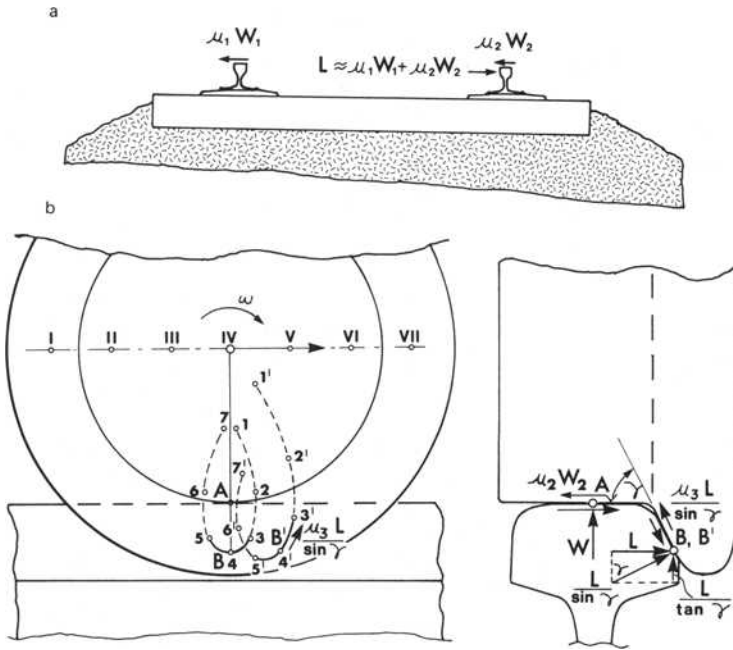


FIG. 2—(a) Lateral tread and flange forces. (b) Sliding trajectories and forces in wheel/flange rail interface.

face of the rail. On the leading wheel sets, the horizontal component of the flange force is equal to the sum of the products of the vertical loads and friction coefficients in each of the wheel/rail interfaces.

Figure 2b depicts the sliding trajectories of flange asperities and the friction forces in the wheel flange/rail interface. As the wheel moves from Positions I to VII, a point (B) on the wheel flange follows the trajectory of an extended cycloid and contacts the rail between Points 3 and 5 if the angle of attack is equal to zero. Although not shown in this figure, the angle of attack is the angle between the vertical plane of the wheel and the vertical plane of the rail at the point of contact. With a positive angle of attack, such as on leading wheel sets of trucks, the zone of flange contact B precedes that of the vertical contact A. In these circumstances, a point (B') on the wheel flange would follow the trajectory between Points 3' and 5'. A scanning electron micrograph (SEM) of a trace of such a trajectory on the gage side of the rail is shown in Fig. 3. An increase in the angle of attack results in an increase in sliding distances, sliding velocities, and higher wear rates.

Apart from the effect of the magnitude of lateral loads and the amount of sliding (that is, amount of lateral and vertical creep), lubrication and rail metallurgy also have a pronounced effect on gage face wear.

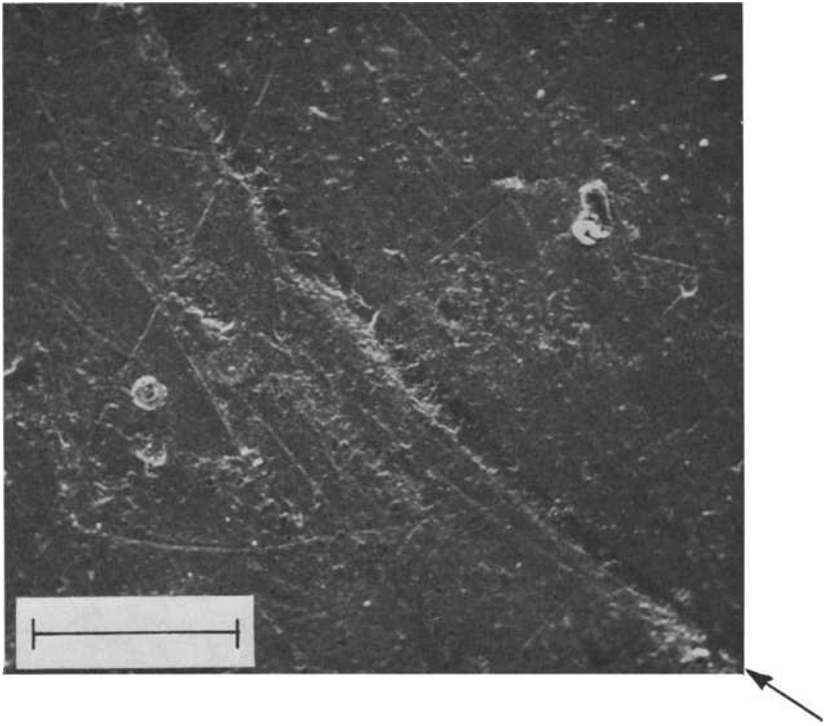


FIG. 3—SEM of a scar left by wheel asperity on the gage side of a rail. Scale mark indicates 100 μm .

Effect of Lubrication on Gage Face Wear

If the wheel flange/rail interface is not lubricated, a severe form of wear referred to as gouging appears on curves with high axle loads and heavy traffic densities. Railroaders also refer to this type of severe wear as snowflaking, because the large number of wear particles generated which fall on ties and tie plates appear to resemble snow. Some of these particles may be very coarse approximately 2 mm across (0.08 in.), but on the average they are approximately 0.1 mm (0.004 in.) across as illustrated in the scanning electron micrograph of particles collected from a nonlubricated outer rail (Fig. 4). If the gage corner of the outer rail is slightly shelled or spalled, numerous and rather large metal flakes about 1 cm (0.40 in.) across may also be found.

The liberal use of lubrication significantly reduces gage face wear rates. Wear particles formed under lubricated conditions are generated in reduced quantities. In addition, their shape and the process by which they are generated changes. A large number of these particles resemble ice floes as shown in Fig. 5, and their formation can be attributed to delamination [6].

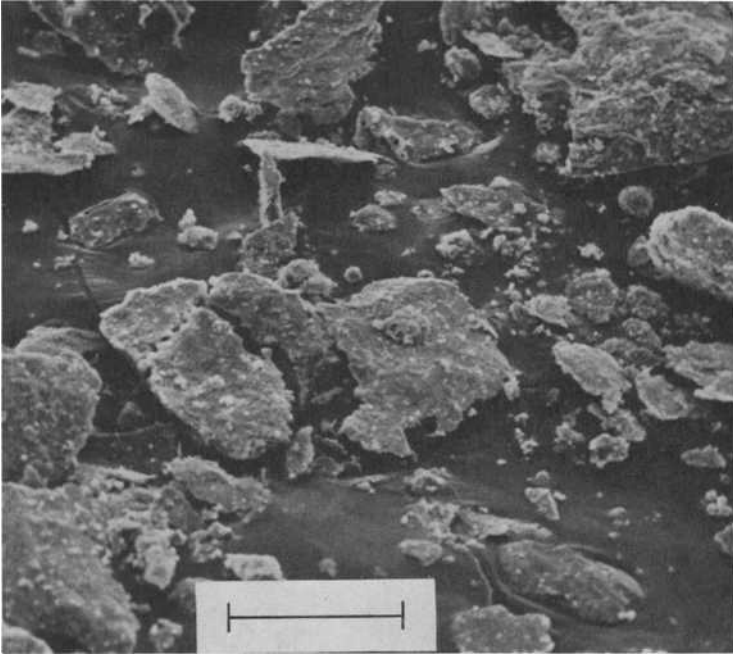


FIG. 4—SEM of wear particles generated in an unlubricated wheel flange/rail interface. Scale mark indicates 100 μm .

These particles were extracted from scrapings collected at the bottom edge of the gage side of an outer rail.

Effect of Metallurgy on Gage Face Wear

The effect of rail metallurgy on gage face wear and the general service performance of rails may be evaluated best by a test in which two rails are placed end to end in a curve. The outcome of such a test, performed by CP on carbon and chromium rail, is shown in Fig. 6. The standard carbon rail⁴ had an average hardness of 265 Brinell hardness number (BHN), while the chromium rail⁵ had an average hardness of 315 BHN. On the outer rail, standard carbon rail gage face wear was almost twice that of the chromium rail. In the illustration shown in Fig. 6, 3.8 cm² (0.59 in.²) of outer standard carbon rail gage face area has been worn away, and 0.25 cm² (0.04 in.²) of material has been displaced due to plastic flow. The comparative chrome rail has worn by 2.1 cm² (0.32 in.²) on its gage face and suffered a displacement

⁴0.80 percent carbon, 0.93 percent manganese, 0.030 percent sulfur, 0.012 percent phosphorus, 0.14 percent silicon.

⁵0.83 percent carbon, 0.51 percent manganese, 0.022 percent sulfur, 0.008 percent phosphorus, 0.30 percent silicon, 1.20 percent chromium.

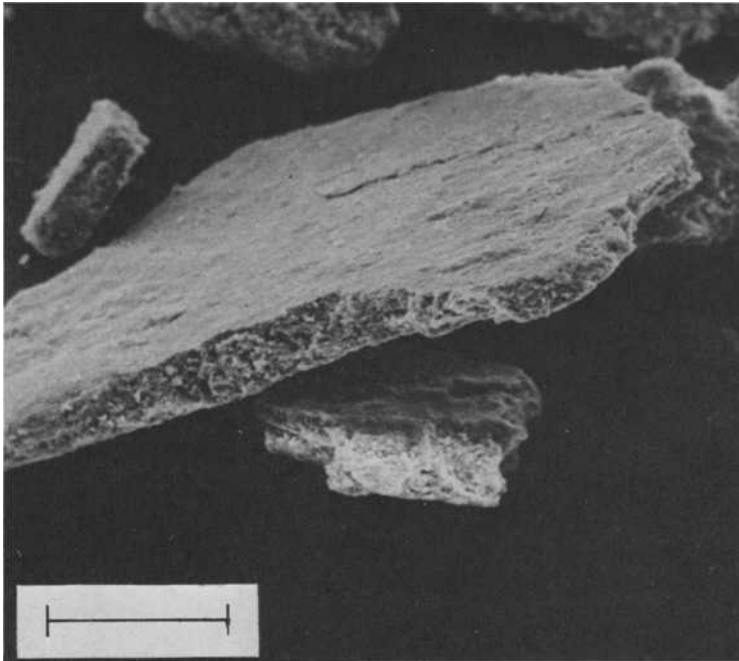


FIG. 5—SEM of ice floe like wear particles. Scale mark indicates 100 μm .

of 0.19 cm^2 (0.03 in.^2) due to plastic flow. At the present time, we are not able to predict wear behavior of rail materials reliably.

Need for Wear Prediction Formula

In the real world, prediction of actual wear rates for the high rail is very difficult, due to the complexity and multidisciplinary nature of the wear processes involved.

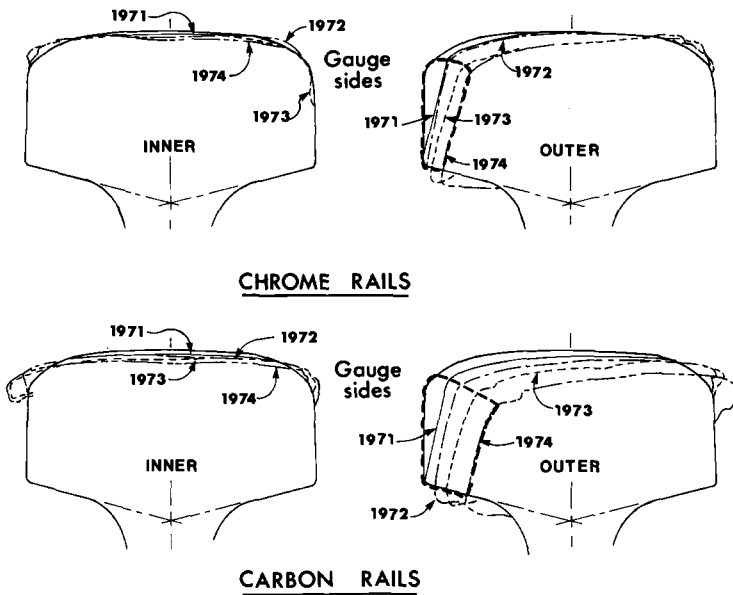
Several wear formulas have been noted while reviewing technical literature [7,8] which attempt to predict gage face wear rates; however, their applicability under heavy traffic conditions is questionable. Railroads, at present, have need for a formula similar to the widely used American Railway Engineering Association (AREA) wear formula for tangent track [3] to provide a reliable prediction of wear rates on outer rails. Such a formula, including the effect of lubrication and rail metallurgy, might take the following form

$$V = \frac{C \eta L}{\sin \gamma H^a}$$

where

V = volumetric wear,

$L/\sin \gamma$ = flange force (force perpendicular to wheel flange/rail interface),



DATA ACQUIRED	SEPT. '69	JUNE '71	MAY '72	JUNE '73	APRIL '74
TONNAGE (MGT)	0	45.8	70.3	101.6	126.2

--- - INDICATES AREA OF GAUGE FACE WEAR

FIG. 6—Ten-degree curve rail wear profiles..

- η = mean value of lateral and vertical creep (increases with angle of attack),
- γ = angle specified in Fig. 2b,
- H = metal hardness,
- C = coefficient dependent upon the type and amount of lubricant in the wheel/rail interface, and
- a = exponent expressing the nonlinear effect of rail hardness on wear rate.

Coefficient C and Exponent a will have to be statistically determined from service data. To collect such data on any single railroad is difficult, since not all rails with different types of rail metallurgy are available to a single railroad company. Many railroads are optimistic that the Facility for Accelerated Service Testing (FAST) will contribute significantly to the generation of such data. It should be pointed out that this formula could not be used exclusively for gage face wear, as it would also include the effect of fatigue (shelling, spalling) wear on the life of an outer rail in curves. In fact, under heavy wheel loads, at high traffic densities, shelling, spalling, flaking,

and plastic flow of railhead material have become the predominant cause of premature rail replacement.

Forms of Surface Fatigue Wear

Surface fatigue is the second type of wear to be discussed in this presentation. Figures 7 and 8 show transverse cross-sectional micrographs of an inner rail flake and outer rail shelling, respectively. The flaking and slight shelling are being formed as the result of the presence of fatigue cracks. Once cracks have initiated, remaining rail life (at least in the case of the inner rail) becomes dependent upon the rate of crack growth. Uncontrolled growth of fatigue cracks leads to the early development of long wavelength rail corrugations. The relationship between contact fatigue and the initiation and deepening of long wavelength rail corrugations has been discussed in detail [9]. Presently, rail grinding is the most widespread technique used by railroads to control the growth of long wavelength rail corrugations. However, it is being acknowledged by an increasing number of railroaders that improved rail metallurgy and lubrication practices can alleviate long wavelength rail corrugation difficulties [10,11].

The initiation of fatigue cracks such as those shown in Figs. 7 and 8 and the origin of fatigue cracks in general have been given considerable attention in recent scientific literature. One source of fatigue crack initiation on rails is small seams or subsurface chains of nonmetallic aluminum oxide, silicates, or other type of inclusions [12].

Even without the presence of the seams or inclusions in the rail, fatigue cracks may still initiate. Many theories have been developed to describe crack initiation processes (see, for example, the review by Plumbridge and Ryder [13]). One plausible explanation for fatigue crack initiation involves the dislocation theory [14]. During work hardening, also referred to as strain hardening, dislocations accumulate mainly at the grain boundaries. This accumulation will eventually create intercrystalline voids or microcracks which may develop in the subsurface layer of the rail. These microcracks can grow into macrocracks which merge with other cracks and reach the surface of the rail [15].

Effect of Rail Strength on Work Hardening of Rail Material

Rail yield strength has an appreciable effect on the nature of work hardening. Wheel/rail lateral tread forces (Fig. 2a) extrude the material above the cracks toward the center of the curve and form flakes on the inner rail or head checks and shelly spots on the outer rail. Due to the action of the passage of wheel flanges on the outer rail, flattened metal fragments generated at head checks and shelly spots are approximately 1 cm (0.4 in.) across. On the other hand, flakes formed on the inner rail can be quite large, several centimetres (1 to 2 in.) wide and tens of centimetres (4 to 8 in.) long.

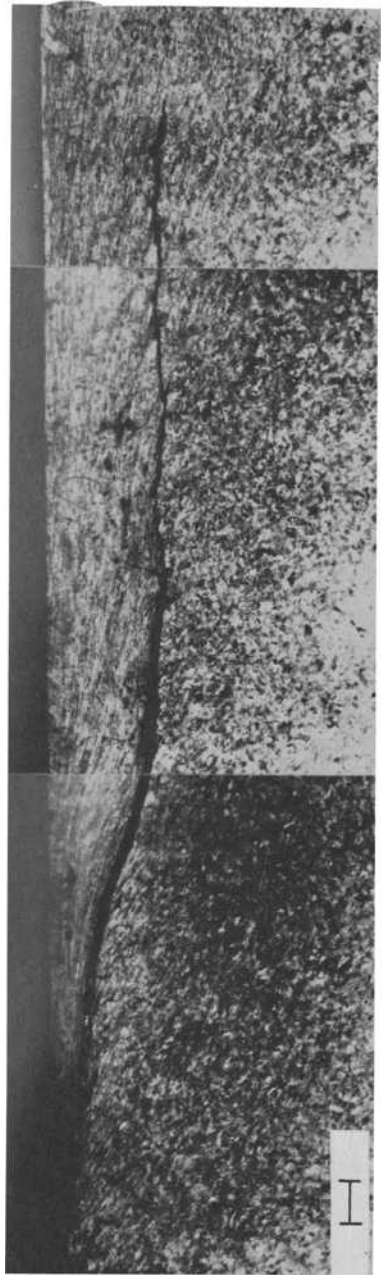


FIG. 7.—Transverse cross-section micrograph of inner or low railhead flake. Scale mark indicates 1 mm.

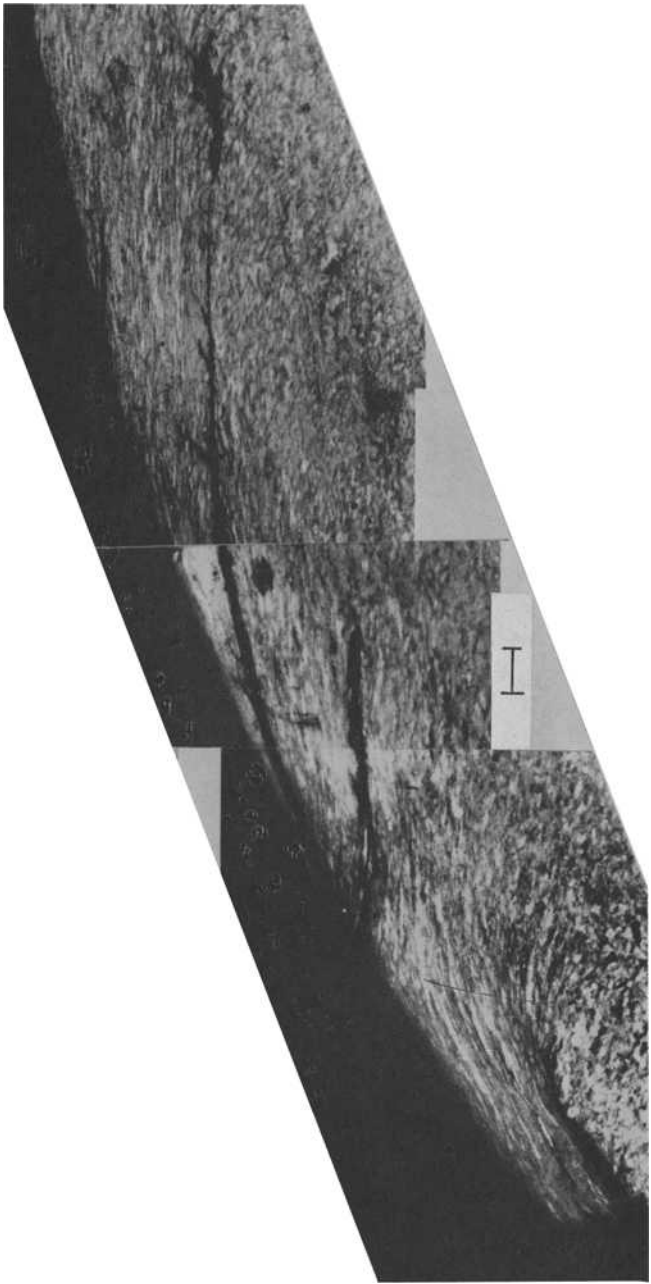


FIG. 8—Transverse cross-section micrograph of slightly shelled outer or high rail.

In the following, the metal fragments originating from head checks and shelly spots will be referred to as "shellings." These should not be mistaken for "shells" or horizontal split heads originating from cracks which develop 1/4 in. or more below the running surface of the rail.

The material in flakes and shellings is heavily work hardened by passing wheel sets, until the ductility reserve of the rail material is exhausted. During this process, the yield stress of metal gradually increases until it equals the ultimate tensile stress and the flakes or shellings become brittle. Rail materials with lower yield strength and hardness generally exhibit a greater degree of work hardening, a thicker work-hardened layer, and deeper and larger flakes and shellings. Rail materials with high yield strength and hardness exhibit shallower fatigue cracks and less severe fatigue damage. This may be attributed to a smaller difference between the yield and tensile strength of high-strength rail steels as compared to standard carbon rail steel.

Effect of Residual Stresses on Surface Fatigue

It is known that the least favorable period of operation of the rails with respect to the formation of fatigue cracks is during the run-in period [16]. Initial strain hardening of the surface layer of rail metal proceeds very rapidly, resulting in the development of substantial tensile stresses acting at the plane of the interface between the work-hardened layer and the nonhardened layer. Consequently, these stresses in conjunction with maximum shear stress due to external contact loading have a stress raising effect, which promotes the creation of fatigue cracks.

Some of the as-manufactured rails may contain tensile residual stresses in the top section of the railhead, which are usually maximum in the longitudinal direction. If these tensile residual stresses are superimposed upon the tensile stresses between the work and non-work-hardened layers, even earlier development of subsurface cracks may result. The adverse effects of tensile residual stresses on contact endurance has been observed, for example, on gear teeth and races of ball bearings [17].

By analogy with surface fatigue failures in other fields of engineering, it is desirable to have a longitudinal compressive residual stress in the top portion of the railhead to delay initiation of fatigue cracks. The beneficial effects of compressive residual stresses may be attributed to, first, a reduction in the value of the tensile stress between work-hardened and parent material layers. Second, it may lead to increased resistance to the development of plastic deformations in the work-hardened layer due to the Bauschinger effect [18]. The Bauschinger effect is concerned with plastic deformation of materials in the tensile compression loading cycle, during which the work hardening is not completely isotropic. The consequence of this nonisotropy is that the initiation of reverse deformation requires less stress [19]. Therefore, rail containing a longitudinal residual tensile stress work hardens more rapidly

due to the compressive nature of the imposed contact stresses than rail which contains a compressive residual stress in the top section of the railhead due to the manufacturing process.

Effect of Lubricant

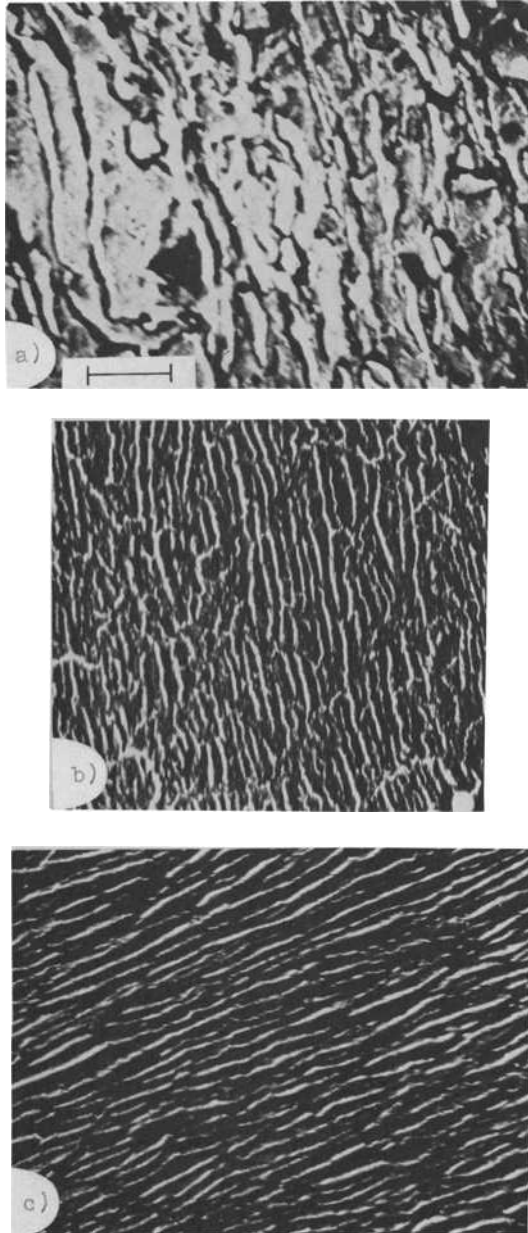
The effect of a lubricant or lubricant residues on the growth of contact fatigue cracks was first described by S. Way [20]. Pressure hydrodynamically transmitted from the wheel/rail interface to the root of the crack via the lubricant adds to the shear mode of crack propagation⁶ and aggravates formation of head checks, shelly spots, and flaking of rails [9].

During the numerous track and rail inspections, the authors noticed a difference between the flakes generated from lubricated track and unlubricated track. The flakes from lubricated track are covered with grease residues and are generally thicker and larger than the flakes from unlubricated track. Flakes from unlubricated track are shiny and quite often have a bluish tint.

Two representative flakes, one from an unlubricated, and the second from a lubricated track, both originating from standard carbon rail, were polished and etched with dilute nital solution. Plastic replicas were prepared for electron microscopy (EM) examination. The results are shown in Figs. 9 and 10. In comparing these two figures, one may see that the pearlite lamellae in a cubic element of unlubricated flake are more closely packed than in the case of the lubricated flake. Providing the original pearlite lamellae spacing was similar in both flakes, it may be concluded that the flake taken from lubricated track is less severely work hardened than the flake from a nonlubricated track. This is consistent with track observations. In addition, one may observe in Fig. 9b the breaking up of the pearlite colony. This is indicative of heavy strain hardening and possible overheating (between 500 and 600°C). We feel that the higher degree of work hardening of flake material in conjunction with reduced crack frequency in unlubricated track results in decreased loss of railhead material via flakes or shellings.

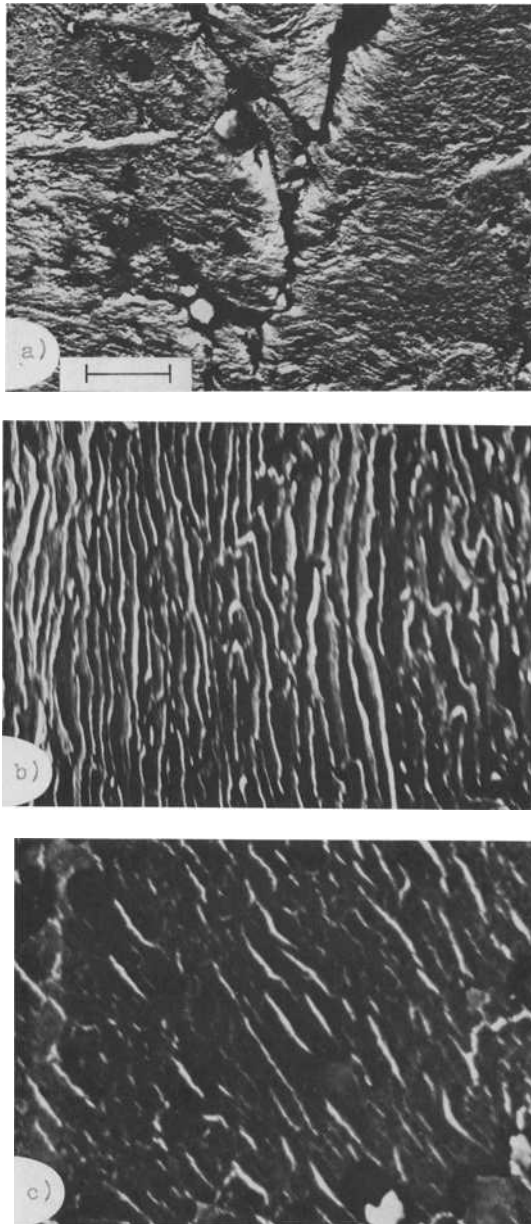
There are two significant implications suggested by the in-track and metallographical observation of flakes. The effect of lubrication should be taken into account by metallurgists when developing new rail materials. Rail metallurgy which performs well under dry conditions may perform poorly under lubricated conditions. Second, railroads must cope with a practical dilemma which demands the lubrication of the gage face of the outer rail while at the same time maintaining the running surfaces of the rail free of lubricant.

⁶In general, the lateral tread force in wheel/rail interface brings the maximum shear stress closer to the interface. The higher the coefficient of friction, the smaller the distance between wheel/rail interface and the location of maximum shear stress [27].



- (a) Surface of the flake.
- (b) Transverse section of the flake.
- (c) Longitudinal section of the flake.

FIG. 9—EM replicas of inner rail flake from nonlubricated track. Scale mark indicates $1\mu\text{m}$.



- (a) Surface of the flake.
- (b) Transverse section of the flake.
- (c) Longitudinal section of the flake.

FIG. 10—EM replicas of inner rail flake from lubricated track. Scale mark indicates 1μm.

Economic Considerations

To achieve increased rail life, the rail material must have increased resistance to surface fatigue, adhesive wear, plastic flow, and brittle fracture. The resistance of rail material to surface fatigue and adhesive wear is increased by higher tensile strength and hardness. Plastic flow and brittle fracture can be alleviated by increased yield strength and improved fracture toughness, respectively. To satisfy these requirements simultaneously poses a number of technical problems for the steel mills and will inevitably result in higher costs.

It would take a detailed study to evaluate the full economic benefits of an improved rail, but for purposes of illustration an order-of-magnitude economic comparison of three types of rail is presented in Table 1. This table is based on the assumptions of average rail life of carbon rail (2 years), chromium rail (3.5 years), and advanced rail (6 years). A projected average traffic density of 49.9 Tg (55 million gross tons)/annum and increased percentage of heavy axle loads as compared to the period of 1969 to 1974 were used in the rail life estimates.

We think it feasible that an advanced eutectoid steel rail with the specified mechanical properties could be manufactured by means of heat treating, alloying, or a combination of both at a reasonable cost. The cost of labor to relay one kilometre (mile) of track was estimated at \$6 215/km (\$10 000/mile). Under these assumptions, for 314 km (195 miles) of curved track, the chromium rail presents, in a six-year period, potential savings of 13 million dollars, and advanced rail savings of 23 million dollars as compared to standard carbon rail. Potential savings of this magnitude should be a

TABLE 1—*Material and labor cost of rail replacement.*

Type of Rail	Carbon	Chromium	Advanced
Tensile strength			
GPa	0.89	1.1	1.31 to 1.39
(ksi)	(130)	(160)	(190 to 200)
Hardness, BHN	260	320	380 to 400
Fracture toughness			
MPa \sqrt{m}	28.6	19.8	33 to 38.5
(ksi $\sqrt{in.}$)	(26)	(18)	(30 to 35)
1976 posted price for rail steel			
\$/Mg	330	430	530
(\$/ton)	(300)	(390)	(480)
Replacement factor for 6-year period	3	1.715	1
Cost of rail for 314 km (195 miles) of track in 6-year period, millions of dollars	40.8	30.2	21.8
Cost of labor to relay 314 km (195 miles) of track, millions of dollars	5.8	3.4	1.9
Total cost, millions of dollars	46.6	33.6	23.7

significant incentive for railways to advance rail developmental and production programs.

Conclusions

Some metallurgical and lubrication aspects of rail wear under heavy axle loads and high traffic densities based on in-track observations and analysis of specimens taken from service rails have been discussed.

As we come to know and better understand the nature of wear mechanisms experienced on rail under heavy traffic conditions, the areas in which we must focus our attention become more defined. Improved rail metallurgy, a better understanding of wheel/rail tribology, and the improved knowledge of the effect residual stresses may have on rail life are areas that clearly demand closer and continuing study.

Acknowledgment

We would like to thank the Transportation Development Agency of the Ministry of Transport of Canada for financially supporting a portion of this work.

References

- [1] Dearden, J., *Wear*, Vol. 3, 1960, pp. 43-59.
- [2] Andrievskii, S. M., "Lateral Wear of Rails on Curves," *Transactions of the All-Union Institute of Railway Transportation*, No. 207, National Research Council of Canada Technical Translation No. 1079, 1961.
- [3] Christianson, H. B., Wascoe, W., Brunn, D. E., Diamond, L. P., Dutton, G. B., Jr., Gray, R. L., Hay, W. W., Huffman, W. H., Mattle, T. J., Meyer, C. J., Nye, F. N., Paul, W. W., Peterson, W. B., Sams, A. L., Sjostrand, T. J., Sooby, C. W., Stark, J. J., Jr., and Van Cleve, P. E., *AREA Proceedings*, American Railway Engineering Association, Vol. 70, Bulletin No. 615, 1969, pp. 75-94.
- [4] Beagley, T. M., *Wear*, Vol. 36, 1976, pp. 317-335.
- [5] Sciammarella, C., Press, M., Kumar, S., Seth, B., Nailsecu, L., and Kalpakjian, S., "Study of Friction and Creep Between Steel Wheels and Rail," Illinois Institute of Technology Report No. IIT-TRANS-76-2, 1976.
- [6] Suh, N. P., *Wear*, Vol. 25, 1973, pp. 111-124.
- [7] Kilburn, K. R., *Proceedings of Conference on Some Aspects of Friction and Wear in Mechanical Engineering*, Kingston, Ont., Canada, National Research Council of Canada, Nov. 1962, pp. 77-91.
- [8] Heumann, H., "Principles of the Lateral Forces Applied to Railway Vehicles," Publication by the Technical University of Munich, British Railways Research Department Translation Service No. 321, Sept. 1961.
- [9] Kalousek, J. and Klein, R., *AREA Proceedings*, American Railway Engineering Association, Vol. 77, Bulletin No. 656, 1976, pp. 429-448.
- [10] King, F. E. and Kalousek, J., *AREA Proceedings*, American Railway Engineering Association, Vol. 77, Bulletin No. 658, 1976, pp. 601-620.
- [11] Read, R. G., *AREA Proceedings*, American Railway Engineering Association, Vol. 74, Bulletin No. 639, 1972, pp. 38-51.
- [12] Littmann, W. E. and Widner, R. L., *Transactions of the ASME, Journal of Basic Engineering*, American Society of Mechanical Engineers, Vol. 88, 1966, pp. 624-636.
- [13] Plumbridge, W. J. and Ryder, D. A., *Metallurgical Reviews*, Vol. 3, 1969, pp. 119-142.

- [14] Mott, F. E., *Acta Metallurgica*, Vol. 6, 1958, pp. 195-197.
- [15] Burghard, H. C., Jr., and Davidson, D. L., "Fracture Mechanics and Fracture Surface Topography," *Proceedings of the 1st International Conference on Fracture*, Sendai, Japan, 1965, pp. 571-596.
- [16] Albrecht, V. G. and Melentiev, L. P., *Rail International*, Vol. 5, 1974, pp. 351-358.
- [17] Mura, H., Tsushima, T., and Nagafuchi, M., *Wear*, Vol. 35, 1975, pp. 261-282.
- [18] Kishi, T. and Tanabe, T., *Journal of Mechanics and Physics of Solids*, Vol. 21, 1973, pp. 303-315.
- [19] Sierakowski, E. L. and Phillips, A., *Acta Mechanica*, Vol. 6, 1968, pp. 217-231.
- [20] Way, S., *Journal of Applied Mechanics*, Vol. 2, 1935, p. A49.
- [21] Johnson, K. L., *Wear*, Vol. 9, 1966, pp. 4-19.

The Assessment of Rail Steels

REFERENCE: Morton, K., Cannon, D. F., Clayton, P., and Jones, E. G., "The Assessment of Rail Steels," *Rail Steels—Developments, Processing, and Use*, ASTM STP 644, D. H. Stone and G. G. Knupp, Ed., American Society for Testing and Materials, 1978, pp. 80–98.

ABSTRACT: Many problems with rails can be attributed to the failure of the steel to withstand the service environment. The successful selection of new and better materials depends upon accurate material evaluation. Realistic laboratory techniques adopted at British Railways for studying material behavior are described in detail, and various results for currently available rail steels are given. The future development of rail steels based on these evaluation methods is discussed.

KEY WORDS: steels, railroad tracks, fatigue (materials), fracture strength, wear

In any developed railway system, the cost of replacing worn and defective rails is a major economic burden. A fractured rail is a serious threat to the safe operation of the railway [1].² Selection of the optimum material for this component is, therefore, of considerable importance. To be successful, however, the material selection process must be based on an understanding of the complex interrelationships between service environment and the material properties.

The service stresses in a rail result from the forces imposed on it and range from the essentially static residual and thermal stresses resulting from manufacture and prestressing practice, respectively, to the high impact forces that can occur as a result of wheel/rail contact at discontinuities in the track or tires. The forces resulting from wheel/rail interaction are normally the most significant. The magnitude of these depends on a number of factors which include the vehicle unsprung mass, rail top profile, rail section, cant and curvature, support conditions, axle load, vehicle speed, and wheel profile.

The strains that the rail steel experiences depend on the magnitude of the applied forces and also on the material response to them. The determination of service strains and the assessment of a material's ability to withstand them are the important factors in any material selection process.

¹Principle scientific officers, senior scientific officer, and senior principle scientific officer, respectively, British Railways Board, Research and Development Division, The Railway Technical Centre, Derby, England.

²The italic numbers in brackets refer to the list of references appended to this paper.

This paper concentrates on the material property evaluation aspect of rail steel development and the prediction of service performance. The methods of assessment which have been adopted by British Railways (BR) in the last few years are described.

Assessment Methods

Much of the available data on rail steel behavior has been produced in full-scale tests or in-service experiments. While there are many advantages associated with this type of approach, there are also serious drawbacks; the effect of noncontrollable service variables on results, the problem of accurate measurements, the long time scale involved, and high cost.

In recent years, there has been a general move in BR towards the greater use of small-scale laboratory tests for the evaluation of material behavior. In this approach, the service trial is reserved for the ultimate test. The following review describes the laboratory tests now used to study both rail failure and rail wear problems.

Rail Failures

The most important rail failures occurring on BR [1] are wheel burns, star cracking at fishbolt holes, taches ovales, thermite weld failures, and failures initiated at corrosion pits in the rail foot. The mechanisms associated with each of these failure types normally involve fatigue crack initiation and growth, followed by rapid fracture when the fatigue crack has reached a critical size. In the case of wheel burn, the initial crack may also be caused by back quenching. In order to understand the role of material properties in rail failures, each of these phenomena need to be studied.

Fatigue Crack Initiation and Early Crack Growth—The most suitable assessment method to use for studying crack initiation and the development of small cracks in components is the “critical location approach” developed by Morrow and Topper and their co-workers [2,3]. This technique relates the behavior of a small element of material at a critical location in a component to that of small, smooth laboratory specimens. The specimens are subjected to an actual or representative service strain history.

In addition to comparing materials, this method may be used to predict the life (in terms of the development of a small crack) of a component from a knowledge of the local strains experienced in service at the critical location and relevant material properties. A cycle counting method (rain flow) is used to reduce the variable service strain record to cycles and reversals suitable for use with a realistic fatigue life curve. A cumulative damage law is then required to predict the life of the component. At BR, the Palmgren-Miner rule has been adopted for this purpose. A schematic representation of this approach is shown in Fig. 1. The basic material properties required in this approach are: (a) cyclic stress-strain relationships and (b) fatigue life

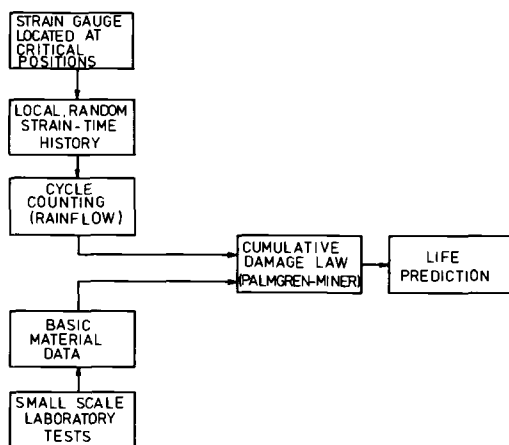


FIG. 1—Schematic representation of critical location approach.

relationships (both strain and stress life relationships are used, but the parameter proposed by Smith et al [4] is also used if variable mean stresses exist in the service record).

Cyclic stress-strain properties—Rails in service are subjected to random loads, and therefore the material's strain response to cyclic loading is important. This information can be obtained from a cyclic stress-strain curve. This has been defined as the locus of tips of the stable hysteresis loops from completely reversed cyclic tests carried out at different strain amplitudes.

There are several methods of determining this curve, but the one most frequently employed is the incremental step test method in which just a single smooth specimen is required [5]. The strain input to the specimen and the resultant hysteresis loops are shown in Fig. 2. The test is performed in a servohydraulic testing machine, and the strain inputs to the specimen are supplied from an on-line tape recorder. Many rail steels have been tested in this way, and some of the results are given in the paper by Dabell, Hill, and Watson in this volume.³

Fatigue life curves—Fatigue crack initiation and growth result from repeated plastic deformation. When comparing materials for components which may develop fatigue cracks, therefore, it is pertinent to consider the relationship between strain and life. This relationship can be evaluated by carrying out constant amplitude, fully reversed fatigue tests using strain control, or alternatively such curves can be predicted using the approach first proposed by Morrow [6]. He defined four fatigue parameters, namely, fatigue strength coefficient and exponent, σ'_f and b , respectively, and fatigue

³Dabell, B. J., Hill, S. J., and Watson, P., this publication, pp. 430–448.

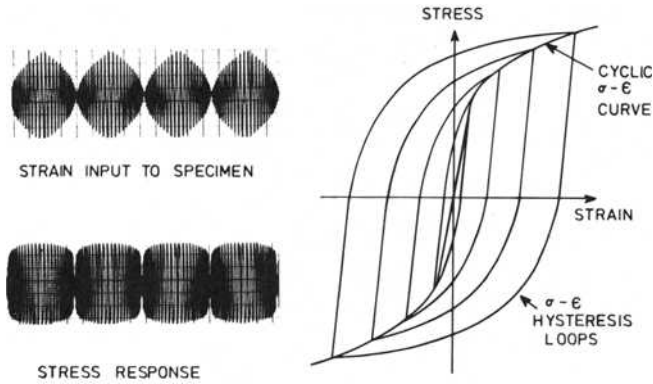


FIG. 2—Cyclic stress-strain curve using the incremental step method.

ductility coefficient and exponent, ϵ'_f and c , respectively. The relationship between applied strain and life can be expressed mathematically by

$$\frac{\epsilon_f}{2} = \epsilon'_f (2N_f)^c + \frac{\sigma'_f}{E} (2N_f)^b$$

where

- ϵ_f = total applied strain range,
- N_f = cycles to failure, and
- E = Young's modulus of elasticity.

Thus only four fatigue parameters are required to predict a strain-life curve. Subsequent work has shown that ϵ'_f and σ'_f are equivalent to the monotonic fracture ductility, ϵ_f , and fracture stress, σ_f , respectively [7], and the two exponents are related to the cyclic strain hardening exponent, n' , which is computed from a cyclic stress-strain curve. The relationships which are most commonly used are those due to Morrow and Fettner [8] which are

$$c = \frac{-1}{1 + 5n'} \quad \text{and} \quad b = \frac{-n'}{1 + 5n'}$$

Thus only two tests, a monotonic test and an incremental step test, are required to predict fatigue life curves.

Strain life curves have been produced for a number of rail steels, and typical examples are shown in Fig. 3. It can be seen from the results that, over the entire life range, there are significant material differences. For example, the fracture tough rail steel is superior to conventional BS11 in the low-cycle region of the curve but appears to be slightly inferior in the high-cycle (fatigue limit) regime. In addition, the austenitic manganese steel is inferior to both the BS11 and fracture tough rail steels in the low cycle region but has a much higher fatigue limit than either. This type of information is

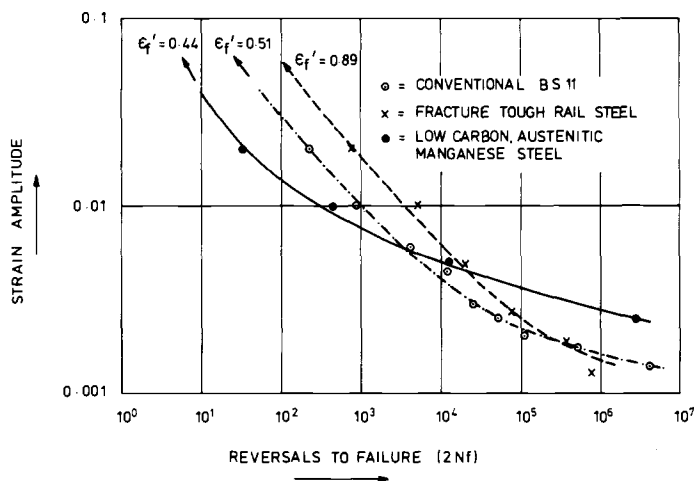


FIG. 3—Strain life curves for some rail steels.

significant in material selection exercises. If high strains are known to occur in service, then steels with high ductility will, in general, be preferred to high-strength steels.

Strain life curves have also been produced for many experimental steels with variations in carbon, silicon, and manganese [9]. This latter series of tests was performed to obtain quantitative relationships between chemical composition, microstructure, and mechanical properties, including the fatigue parameters. These data have been used to predict fatigue curves direct from chemical composition and are of value in assessing new materials for rails.

Crack Growth—Subsequent to the development of a small crack, crack growth can take place until the critical crack size for brittle fracture has been achieved. The best method of quantifying this portion of the failure process is the linear elastic fracture mechanics crack tip stress intensity factor (K) approach first proposed by Paris [10].

Tests are carried out to determine crack growth rates as a function of ΔK on notched specimens tested under load-controlled conditions. At BR, both single-edge-notched and center-hole notched specimens are used, in either a very high frequency vibraphore (Amsler) (frequency 150 to 200 Hz) or a servohydraulic testing machine (frequency 0.1 to 50 Hz). Crack growth is measured either continuously using an electric potential method or at intervals optically.

Results for a number of rail steels using center-notched specimens are shown in Fig. 4. In general, little difference is observed in the crack propagation rates of these steels at similar levels. This implies that the differences in life mentioned in the section on fatigue life curves are determined by the initiation period. The figure shows the scatterband of the

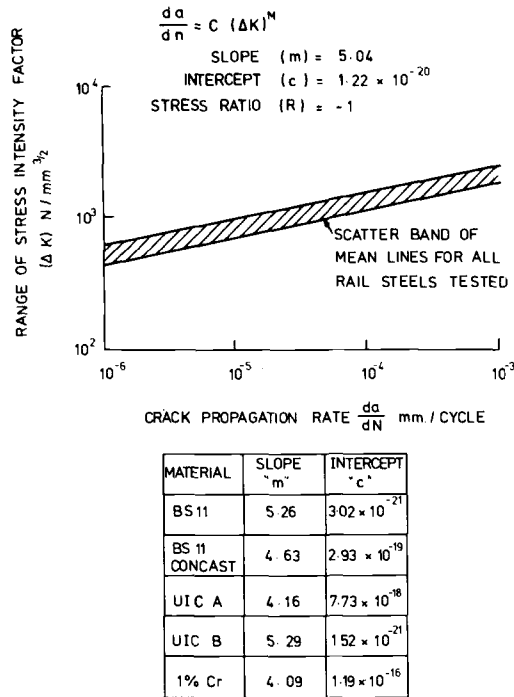


FIG. 4—Crack propagation results for some rail steels.

mean values of the da/dN to ΔK lines produced from an average of six tests on ten rail steels. Overall differences are considered to be of secondary importance and would in practice be masked by scatter of the individual points.

Fracture Toughness—The resistance of a material to rapid crack growth, which is initiated from a preexisting crack or similar defect, is usually referred to as its fracture toughness. Using the principles of linear elastic fracture mechanics, the fracture toughness of a material can be quantified by the critical crack tip stress intensity factor [11, 12] which, for the crack opening mode, is known as K_{Ic} . Under conditions of limited crack tip plastic deformation, K describes the magnitude of the crack tip stress field [13]. Its value is related to the crack length, remote body loadings, and the geometry of the body. Following the measurement of K_{Ic} in a laboratory test, the critical crack length for any given stress in a structure made of the same material may be predicted. Thus, withdrawal criteria and in-service inspection requirements for cracked rails may be determined in a logical, quantitative fashion.

Laboratory tests for determining K_{Ic} are well documented [12], and proposed specifications are also available (ASTM Test for Plane-Strain Fracture Toughness of Metallic Materials (E 399-74), [14]). However, in

making laboratory determinations of K_{Ic} , proper cognizance must be taken of the service environment to be experienced by the material. K_{Ic} is not an invariant material property. Its value is influenced by temperature and strain rate [15,16]. In addition, excessive plastic deformation occurring at the crack tip may affect the determination of K_{Ic} [17,18].

When significant crack tip plastic deformation occurs, alternative methods to quantify fracture resistance may have to be considered. These include modified forms of linear elastic fracture mechanics, crack opening displacement, the J contour integral, and equivalent energy approach [19]. At BR, a modified linear elastic fracture mechanics procedure is used (K_c), but its limit of applicability, as with the other candidate nonlinear fracture parameters, has yet to be fully understood. The value of K_c is usually influenced by the size of the body containing the crack (a constraint effect); therefore, the specimen tested should simulate the service structure.

Fracture toughness tests should be conducted over the entire range of operating rail temperatures and strain rates. On BR rail, temperatures range from about -15 to 50°C and strain rates from 0 to about 2.5 s^{-1} . The highest strain rates and the highest stresses are associated with impact loading. This type of loading is caused when the wheel loses contact with the rail running surface, and this occurs most frequently as a result of wheel flats, wheel burn depressions, and rail joints. This loading rate produces a stress intensification rate (\dot{K}) of $4 \times 10^4\text{ MN} \cdot \text{m}^{-1.5}\text{s}^{-1}$ at the tip of a 5-mm-deep surface embedded crack originating at the running surface of the rail. If it is only possible to perform a limited number of fracture toughness tests, it is advisable to test at the lowest expected temperature and the highest strain rate since a combination of these conditions will result in the lowest operating fracture toughness.

Fracture toughness specimens used at BR range from the standard three-point bend, single-edge-notch specimen machined from the head or web of the rail section to a full rail section type specimen. The web specimen is oriented at 45° so that crack propagation is in the same plane as that occurring in service at this position in the section. The choice of specimen depends upon the toughness of the rail steel being tested. Usually a small specimen is tested first, but if failure is accompanied by significant crack tip yielding, the full section specimens are used in subsequent tests. A K calibration for the full section specimen has been developed at BR using a finite element-energetic approach (Fig. 5). Small standard specimens are tested in servohydraulic machines which generally provide adequate ram displacement rates to cover the range of strain rates expected in service. To achieve the necessary loading rates and fracture loads in the full section specimen, a drop weight machine is used. This machine, which has been described in detail elsewhere [20], consists of a 60-ton steel anvil resting on a 300-ton concrete foundation with tup guides providing a maximum drop height of 9.2 m. The machine is built to take a maximum tup mass of 5 tons. A range of tups can be used, however, and very small masses, down to

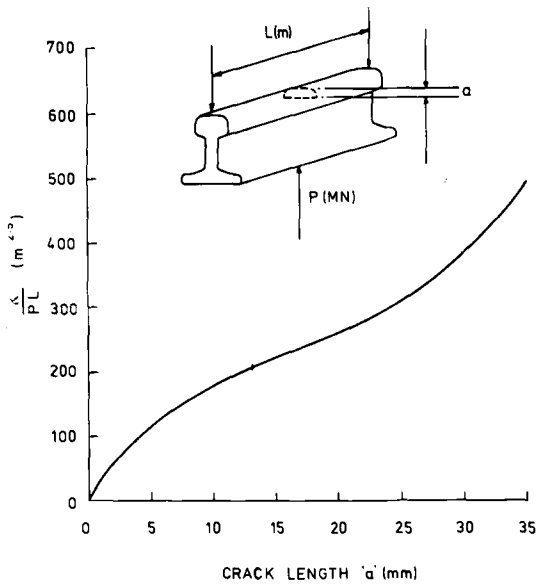


FIG. 5—Rail section K calibration transverse head crack.

1 kg, can be dropped accurately from any height using a duplex tup system. The tups are guided to within 2 mm of their target.

The fracture load in the high strain rate, full section specimen tests is measured by instrumenting each specimen. Two or more sets of strain gages located at different points on the rail section are used (Fig. 6). The outputs from these gages are first measured statically in a bending arrangement similar to that used in the dynamic test. The dynamic strain gage signals are recorded on magnetic tape (maximum frequency response 20 kHz), and they are later replayed to give a detailed and well-defined, strain-time record [20]. By comparing the signals from the various strain gage locations, it is possible to (a) detect the onset of rapid crack initiation, (b) check that the specimen has behaved in a sensibly linear elastic fashion and that the expected stress distribution exists on the crack plane, and (c) determine the load at fracture.

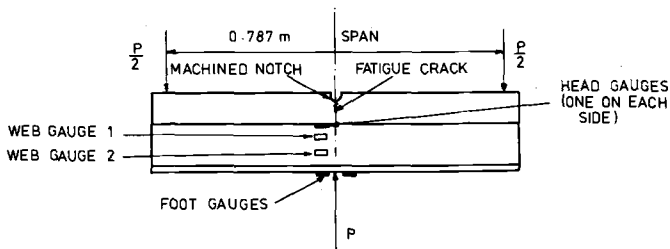


FIG. 6—Rail section specimens instrumented for dynamic testing.

The results of high strain rate tests conducted on BS11 full section rail steel specimens compared favorably with those derived from specimens machined from the rail section and tested conventionally in servohydraulic equipment (Fig. 7). Thus there is some measure of confidence in the full section specimen, dynamic fracture toughness test technique.

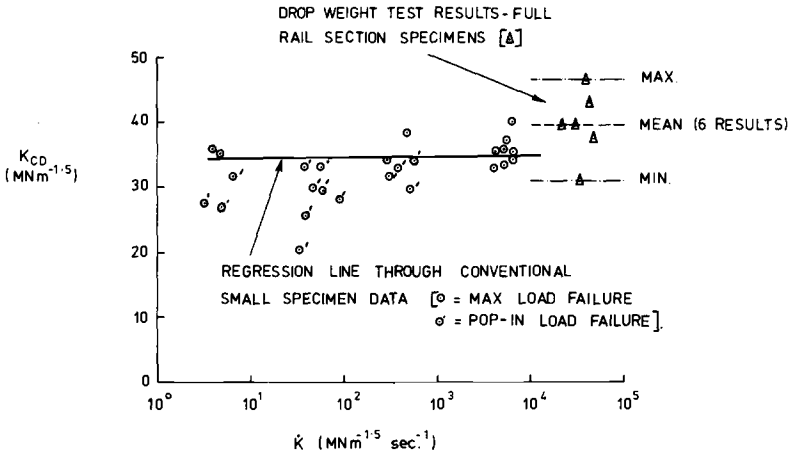


FIG. 7—Effect of strain rate on the fracture toughness of typical BS11 rail steel.

The effects of strain rate and temperature on the fracture toughness of typical casts of BS11 are shown in Figs. 7 and 8, respectively. There is a slight increase in K_{IC} with temperature constant. Most of the fracture toughness data on BS11 rail steel have been determined at $-15^{\circ}C$ and at quasi-static loading rates (Table 1). No consistent trends in fracture toughness have been identified with variations in composition within the specification, with rail position in the ingot or with supplier [21]. The only significant variation observed was that between head and web specimens.

Recently, the British Steel Corporation has changed the production route for BS11 rail steel from acid Bessemer or basic open hearth ingot practice to a basic oxygen continuously cast (concast) process. It was considered that the change of process might possibly influence the level of fracture toughness

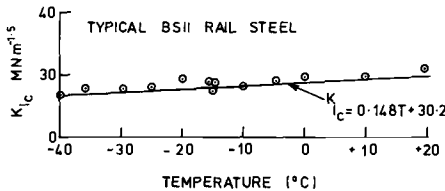


FIG. 8—Effect of temperature on the fracture toughness of BS11 rail steel.

TABLE 1—Summary of valid K_{Ic} data, BS11 rail steel (excluding concast BS11).

Specimen Location	Head	Web
Mean K_{Ic} , $MN \cdot m^{-1.5}$	35.2	31.1
95 percent confidence limits on the mean, $MN \cdot m^{-1.5}$	± 1.51	± 1.23
Standard deviation, $MN \cdot m^{-1.5}$	± 4.0	± 2.77
Number of results	30	23

NOTE—Test temperature -15°C , loading rate quasi-static.

because of higher silicon levels (≤ 0.35 percent), higher proof stresses, and smaller reductions in rolling associated with the concast process.

Fracture toughness tests were performed on specimens machined from the railhead, and these were tested at -15°C under quasi-static loading conditions (assuming that, like conventional BS11, there would be little if any effect of strain rate on toughness). The results showed that there was no significant difference in railhead toughness between BS11 produced by the basic oxygen steel (BOS) concast and the prior process routes (Table 2).

Fracture toughness tests are currently being performed on wear-resistant grades of rail steel. The chemical compositions of these steels and the -15°C , quasi-static loading K_{Ic} determinations are given in Table 3. The results to date are essentially similar to those for BS11.

Rail Wear

BR purchases about 150 000 tons of new rail each year, and a high proportion of this is used to replace rails which have become worn in service. Since the problem of wear has been recognized for centuries, it might be expected that the theoretical basis for its understanding would be similarly

TABLE 2—Summary of valid K_{Ic} data, BS11 rail steel, concast process.

Cast No.	Chemical Composition, percent by weight			Number of Results	Mean K_{Ic} , $MN \cdot m^{-1.5}$
	Carbon	Silicon	Manganese		
1207	0.6	0.3	1.19	5	31.5
2293	0.59	0.31	1.25	3	39.5
2971	0.56	0.30	1.15	6	42.9
3354	0.58	0.29	1.11	6	34.4
3535	0.59	0.32	1.11	4	39.2
3689	0.55	0.35	1.14	4	37.3
3943	0.53	0.27	1.15	2	40.8
2970	0.58	0.36	1.12	2	39.1

NOTE—Test temperature -15°C , loading rate quasi-static. Specimens taken from the head of the rail.

TABLE 3— K_{Ic} data for UIC grades of rail steel.

	Chemical Composition (Spec.), percent by weight						Number of results	Average K_{Ic} , $\text{MN}\cdot\text{m}^{-1.5}$
	Carbon	Silicon	Manganese	Chromium	Sulfur	Phosphorus		
UIC 860								
Grade A	0.6 to 0.75	0.5	0.8 to 1.3	. . .	0.05	0.05	10	32.8
UIC 860								
Grade B	0.5 to 0.7	0.5	1.3 to 1.7	. . .	0.05	0.05	4	36.0
UIC 860								
Grade C	0.45 to 0.65	0.4	1.7 to 2.1	. . .	0.03	0.03	3	30.3
1 percent chromium	0.68 to 0.75	0.2 to 0.5	1.1 to 1.4	1.0 to 1.3	0.04	0.03	4	35.3

NOTE—Test temperature -15°C , loading rate quasi-static. Specimens taken from the head of the rail.

well established. This is not the case mainly because it is not possible to measure the fundamental parameters associated with wear: the stresses, strains, and temperatures at the rubbing surfaces. This problem has been extremely significant in the development of wear life prediction since there is no basic reference point with which to relate laboratory and service environments. Consequently, wear testing can only be used to predict the comparative wear behavior of different materials.

The method most commonly used to obtain wear data for wheel and rail steels involves the attempted simulation of wheel/rail Hertzian contact stresses and creep rates with a twin-disk wear testing device. The approach now being used at BR, however, is based on reproducing the service wear mechanism in the laboratory. To achieve this, it was first necessary to study the mechanisms of wear that rails experience.

The surface topography and subsurface microstructures of a number of worn rails were examined by optical and scanning electron microscopy. In the case of high rail wear on curves, wear debris was also collected and examined in the same way.

This work showed that, although both vertical and lateral wear could be attributed to a plastic deformation and fracture mechanism, there are two factors which complicate the vertical wear of rails. First, the rolling/sliding action of the wheel tread gives rise to surface phase transformations in the rail of a type [22] commonly observed with ferrous materials which have experienced rubbing contact. This does not occur with flange/rail contact on curves. Second, there is the influence of atmospheric corrosion on the fracture process.

So far, only the more straightforward case of lateral rail wear has been studied in the laboratory. This work has been carried out with a pin on a ring wear testing machine which was designed and constructed within the department. This machine is capable of a wide range of testing conditions with linear sliding speeds of 0 to 5 000 cm/s and pin loads of 0 to 200 kg.

One of the major problems encountered in laboratory wear testing, and one which has led to considerable confusion over the comparison of wear data, is the generation of high stable surface temperatures. This can lead to the formation of thick, adherent oxide films, and wear then takes place almost wholly within the oxide layer.

This situation does not arise in service because of the intermittent nature of the wheel/rail contact and the large masses of metal involved. To help reduce this problem in the laboratory test, artificial cooling by dried, compressed air is used.

The machine is fully instrumented and measures ring rotational velocity, total ring revolutions, pin height loss, and frictional force on the pin. These data are scanned at preset intervals of between 10 and 90 s and recorded by a teletype. It was established, by testing BS11 rail steel over the full range of machine conditions, that the required wear mechanism could be achieved with a linear sliding velocity of 40 cm/s and pin loads of 50 to 100 kg.

Several other rail steels were tested under these conditions, and the results for four of these steels, BS11, Union Internationale des Chemins de Fer (UIC) wear-resistant grades B and C, and 1 percent chromium steel, are shown in Fig. 9 in terms of log wear rate against pin load.

It can be seen that these curves form a set of nearly parallel straight lines. For this reason, the wear resistance of each steel can be denoted by a single wear rate figure at constant load. Table 4 shows the wear rates of the four steels at 100-kg pin load, and it can be seen that the relative wear resistance of the four steels compares favorably with the established relative life in the high rails of curves in service.

The wear testing procedure has been used [23] to investigate the relationships between wear resistance, chemical composition, microstructure, and the stress-strain properties of a range of ferrite pearlite steels produced under experimental conditions. This work showed that the wear behavior is best related to the flow properties at high strains. This is illustrated in Fig. 10 which depicts the relationship between wear rate at 100-kg pin load and the values of K' (the cyclic strength coefficient (Footnote 3)), measured by the incremental step test described previously, for six rail steels containing carbon, manganese, and silicon. Small specimens machined from the wear pins were used for the determination of the cyclic stress-strain curves.

This work is being continued to establish the validity and application of the relationships, devised for pearlitic steels, to a wider range of steels by studying the behavior of martensitic, bainitic, and austenitic materials.

Discussion

The introduction of improved rail steels has invariably resulted from the inability of standard steels to withstand the increasing demands of service. In many cases, the improved rail steel has been based on a higher ultimate tensile strength and tested under service conditions. There are several

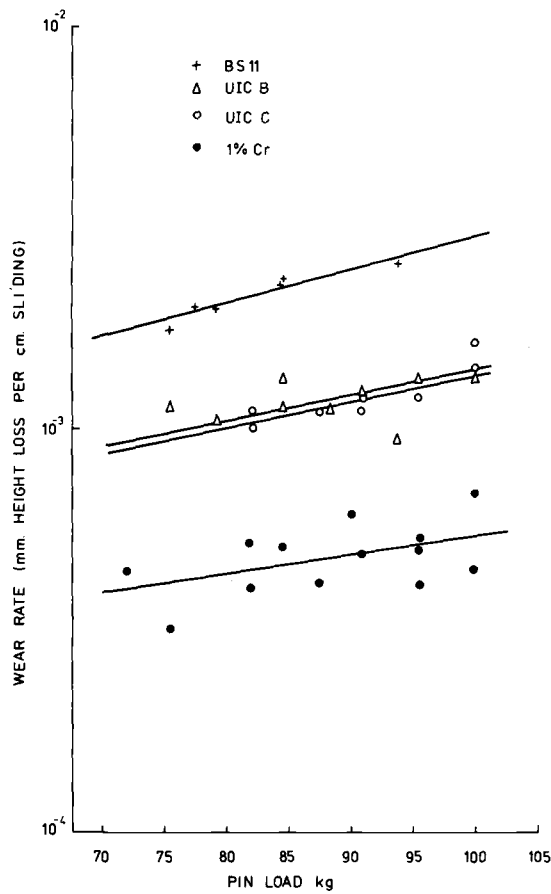


FIG. 9—Wear rate versus pin load for four rail steels.

reasons why this approach to rail steel development is no longer considered the best method available.

It is possible to define materials by much more meaningful parameters than ultimate tensile strength. This term can be used as a rough guide to the wear resistance of a narrow class of microstructures, such as pearlitics, since

TABLE 4—Relative wear of rail steels.

Rail Steel	Approximate Relative Life in Curved Track	Wear Rate in Laboratory Test (100 kg load)	
		Pin Height Loss per cm Sliding mm/cm	
BS11	1	30.0×10^{-4}	
UIC B	2	14.0×10^{-4}	
UIC C	2	13.5×10^{-4}	
1 percent chromium	4	5.5×10^{-4}	

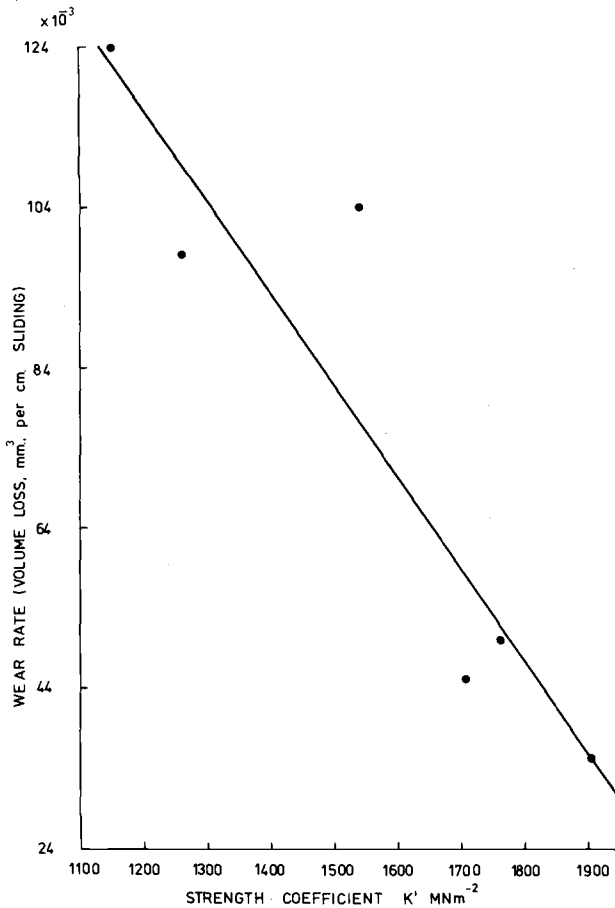


FIG. 10—Wear rate versus K' for six C-Mn-Si rail steels.

the work hardening characteristics of these materials are similar. It would, however, be of little use in comparing the wear behavior of pearlitic steels with austenitic, bainitic, and martensitic steels. Further, it does not reveal anything at all about fracture and fatigue properties.

The use of the service trial as a means of assessing material behavior is fraught with difficulties unless carried out on a very extensive and costly scale, since the many service variables which cannot be controlled can mask even significant material differences.

Results from the assessment methods described in this paper can be used in conjunction with service environmental data to provide predictions of service performance which allow the consequences of introducing new rail steels to be determined.

Escalating labor and material costs have made the repair and replacement

of rails an expensive process and resulted in the need to optimize material properties for specific applications.

For these reasons, considerable attention has been paid by BR to understanding and developing new methods of assessing material behavior so that eventually the specific requirements of a rail steel for curved, straight, continuous welded rail (CWR), and switches and crossings can be well defined.

By taking the work a stage further to study the relationships between relevant material properties and metallurgical variables, it is anticipated that future generations of rail steels will be designed from first principles to meet these specific requirements.

An assessment of the problems in BR track has highlighted three areas in which improved rail steel properties are required.

1. On an economic basis, there is a need to increase the wear resistance of rails. This must be achieved, however, without reducing the resistance to fatigue and fracture shown by BS11 rail steel. Since pearlitic steels are the cheapest to produce, it is unlikely that future plain rail steels will depart from this type of microstructure. Although a lot of work has been carried out on this type of material, there is still some scope for optimization since it has been shown that wear resistance is very sensitive to small changes in composition. Further, there is a growing need to study the relationship between resistance to corrugation formation and other material properties.

2. Failures in switches and crossings have indicated the need for materials with both better strength and ductility than BS11. The majority of common crossings used on BR are constructed by welding or bolting together premachined BS11 rails. These crossings are used in all types of sites, although, in the more severe locations, they have now largely been replaced by crossings manufactured in austenitic manganese steel (AMS). Crossings made from either steel have major disadvantages. BS11 steel crossings suffer from serious wear or gross deformation of the crossing nose and fatigue cracking problems from bolt-holes, whereas cast AMS crossings often contain casting defects which may act as fatigue crack initiation sites. AMS has the additional disadvantage of being difficult to weld, and therefore crossings made in this material cannot be welded into track.

An alternative material must have the following properties:

- (a) High cyclic yield stress or a high cyclic strain hardening exponent or both so that gross deformation is minimized.
- (b) High wear resistance.
- (c) High fracture toughness.
- (d) High fracture ductility for increased low-cycle fatigue resistance (more important in crossings than in plain rail due to the regular impact forces).
- (e) Must be weldable both to itself and BS11 so that crossings can be fabricated and repaired by welding and be capable of being welded into track.

- (f) Relatively cheap. Due to the small quantities of rail involved in producing crossings compared with the plain rail requirement, the cost factor is not as important. However, the use of expensive alloying elements and additional heat treatments must still be kept to a minimum.

One possible method of obtaining these required properties in an as-rolled material is by producing a bainitic microstructure. Such a structure would enable the carbon content of the steel to be reduced to a much lower level than is used for BS11 steel without a reduction in strength and with possible benefits in weldability, ductility, and toughness.

To obtain a bainitic microstructure, the polygonal ferrite reaction should be retarded as much as possible without a marked retardation of the bainite transformation. The mechanical properties of these steels can be adjusted by variations in the carbon, manganese, and chromium contents. A range of steels of this type are currently being evaluated using the small-scale laboratory methods described in this paper.

3. Specific service failure problems can be considered in terms of material selection. An example is the wheel burn problem.

A fracture prediction diagram developed using the principles of linear elastic fracture mechanics for this situation in BS11 rail steel is shown in Fig. 11. Various operating conditions are shown which reflect combinations of residual stress, temperature stress, and fracture toughness (that is, worst expected, average, etc.) Also shown is a typical bending moment which can be induced as a result of impact loading in service. At sites where wheel burn occurs, this type of loading is very common because of the rail running surface depressions caused by wheel slippage. It will be seen that at worst the critical defect size is about 1 mm, and at very best (that is, no residual or

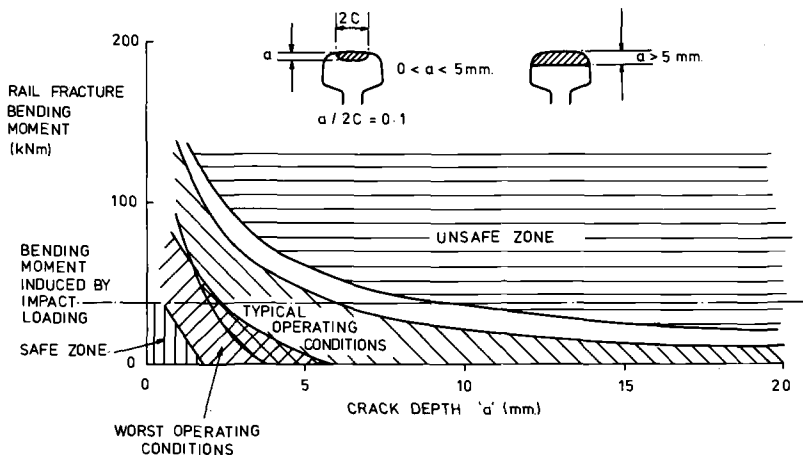


FIG. 11—The effect of railhead surface crack size on fracture bending moment for BS11 rail steel.

temperature stress, best estimate of average fracture toughness, etc.) this is increased to about 10 mm. Because of the possible derailment hazard caused by this type of fracture, it is BR policy to withdraw rails showing evidence of wheel burn. This results in 2000 to 3000 rails being removed annually [1]. If a steel of about twice the toughness of BS11 were used, the critical crack length would be increased to about 15 mm. It would not be necessary, therefore, to withdraw rails which only showed evidence of surface damage. A detailed surveillance of wheel-burned rail in service over a period of almost three years indicates that the vast majority of cracks embedded in the transformed structure of the rail running surface do not propagate beyond the martensite—ferrite/pearlite boundary (usually 2 to 3 mm deep). This is of little consequence with BS11 rail steel since the depth of this layer is sufficient to contain a critical crack; but, in a tougher rail steel, the crack will be required to extend beyond this boundary to produce a crack of sufficient size to be critical. A steel with a K_{Ic} greater than $50 \text{ MN}\cdot\text{m}^{-1.5}$ would ensure this condition. Thus, it would be possible to leave the vast majority of wheel-burned rail in track without impairing safety, and this would result in an economic benefit.

The British Steel Corporation and BR have investigated the possibility of producing a tougher rail steel [2]. Full rail section specimens have been used extensively for fracture testing these experimental steels. The results of fracture toughness tests on one cast at various strain rates and two temperatures are shown in Fig. 12. These results demonstrate the need to test

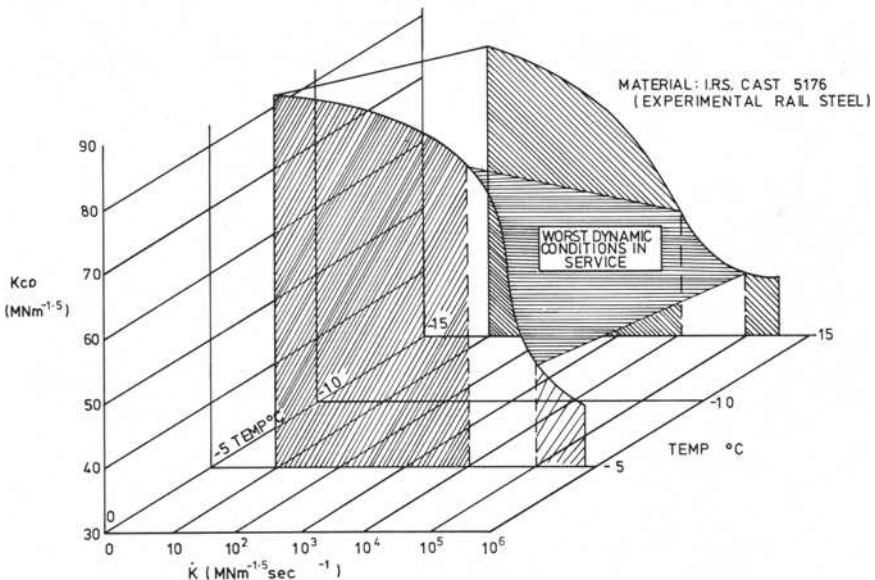


FIG. 12—The effect of temperature and strain rate (\dot{K}) on fracture toughness of an experimental steel.

under conditions which closely simulate the service environment. Approximations could result in either a pessimistic or optimistic assessment of candidate steels. The experimental rail steels produced to date are tougher than conventional rail steels. Further improvement would be desirable, however, to meet requirements at the lowest operating temperature and highest strain rate condition.

Concluding Remarks

This paper has outlined the present-day, small-scale laboratory methods employed at BR for evaluating rail steels. Emphasis has been placed on the use of more sophisticated assessment methods to give a better and more realistic comparison of materials and a clearer understanding of the relationships between metallurgical variables and the important mechanical properties. These procedures have indicated the significant information required about the service environment and the lack of knowledge in this area. In the future, much greater efforts will be needed to obtain relevant service information suitable for application to the new assessment methods and for future development of these techniques.

Acknowledgments

The authors would like to thank the British Railways Board for permission to publish this paper. Contributions from many of our colleagues, namely, P. Watson, J. Chelu, B. J. Dabell, S. J. Hill, R. Allen, and K. Sharpe were also gratefully received.

References

- [1] Davies, J. and Jones, E. G., "Experience with Rails on British Railways and the Requirement for an Improved Rail Steel," Rail Steel Developments Symposium, Iron and Steel Institute, London, 1972.
- [2] Endo, T. and Morrow, J., *Journal of Materials*, JMLSA, Vol. 4, No. 1, March 1969, pp. 159-175.
- [3] Topper, T. H. and Byregowda, C. V., "Local Stress-Strain Approach to Fatigue Analysis and Design," "Design Engineering," ASME Conference, American Society of Mechanical Engineers, Chicago, Ill., May 1970.
- [4] Smith, K. M., Watson, P., and Topper, T. H., *Journal of Materials*, Vol. 5, No. 4, Dec. 1970, p. 767.
- [5] Landgraf, R. W., Morrow, J., and Endo, T., *Journal of Materials*, Vol. 4, No. 1, 1969, p. 1976.
- [6] Morrow, J., "Fatigue Properties of Metals," Manual SAE, ISTC, Div. 4, Society of Automotive Engineers, April 1964.
- [7] Landgraf, R. W. in *Achievement of High Fatigue Resistance in Metals and Alloys*, ASTM STP 467, American Society for Testing and Materials, 1970, pp. 3-36.
- [8] Morrow, J. in *Internal Friction, Damping, and Cyclic Plasticity*, ASTM STP 378, American Society for Testing and Materials, 1965, pp. 45-87.
- [9] Morton, K., Dabell, B. J., and Watson, P., "Techniques for Predicting the Fatigue Performance of Materials," International Conference on Fatigue Testing and Design, Society of Environmental Engineers, City University, April 1976.

- [10] Paris, P. C., Gomez, M. P., and Anderson, W. E., "A Rational Analytical Theory of Fatigue," *Trend in Engineering*, University of Washington, Seattle, Jan. 1961.
- [11] *Fracture Toughness Testing and Its Applications*, ASTM STP 381, American Society for Testing and Materials, 1975.
- [12] Brown, W. F. and Srawley, J. E., *Plane Strain Crack Toughness Testing of High Metallic Materials*, ASTM STP 410, American Society for Testing and Materials, 1967.
- [13] Irwin, G. R., *Transactions of the ASME, Journal of Applied Mechanics*, American Society of Mechanical Engineers, Vol. 24, 1957, p. 361.
- [14] "Methods for Plane Strain Fracture Toughness (K_{Ic}) Testing," BSI Document D.D.3, British Standards Institution, 1971.
- [15] Shabbits, W. O., Pryle, W. H., and Wessle, E. T., "Heavy Section A533 Grade B Class I Steel Plate and Submerged Arc Weldments," Westinghouse Atomic Power Division, WCAP 7414, HSST, Tech. Report 6, Dec. 1968.
- [16] Barsom, J. M., "Effect of Temperature and Rate of Loading on the Fracture Behavior of Various Steels," International Conference on Dynamic Fracture Toughness, Paper 31, London, July 1976.
- [17] Nelson, F. G., Schilling, P. E., and Kaufman, J. G., *Engineering Fracture Mechanics*, Vol. 4, 1972, pp. 33-50.
- [18] Kaufman, J. G. and Nelson, F. G. in *Fracture Toughness and Slow-Stable Cracking*, ASTM STP 559, American Society for Testing and Materials, 1974, pp. 74-85.
- [19] Harrison, J. D., "A Comparison Between Four Elastic-Plastic Fracture Mechanics Parameters," Welding Institute Report E 64/75, March 1975.
- [20] Cannon, D. F., "Fracture Research at High Strain Rates," *Railway Engineer*, Vol. 1, No. 1, Jan./Feb. 1976.
- [21] Cannon, D. F., Walker, E. F., and Barr, R. R., "The Fracture Toughness of Rail Steels," Symposium on Rail Steel Development, Iron and Steel Institute, London, 1972.
- [22] Eyre, T. S. and Baxter, A., *Metals and Materials*, Oct. 1972, pp. 435-439.
- [23] Clayton, P., unpublished work.

A Metallurgical Examination of Control-Cooled, Carbon-Steel Rails with Service-Developed Defects*

REFERENCE: Sonon, D. E., Pellegrino, J. V., and Wandrisco, J. M., "A Metallurgical Examination of Control-Cooled, Carbon-Steel Rails with Service-Developed Defects," *Rail Steels—Developments, Processing, and Use, ASTM STP 644*, D. H. Stone and G. G. Knupp, Eds., American Society for Testing and Materials, 1978, pp. 99-117.

ABSTRACT: A metallurgical analysis was made of 33 carbon-steel rail samples selected from service, 31 of which had service-developed defects. The program was formulated to attempt to establish the metallurgical characteristics that promoted the defects and to establish possible interrelationships among these characteristics, the in-location service stresses, and the defects. This paper describes the results of chemical analyses, hardness and tension tests, and the results of wear, deformation, metallographic, and fractographic analyses. A companion paper in this symposium describes the results of Charpy V-notch impact toughness tests, fracture toughness tests, and fatigue tests.

The results of this investigation showed that (a) all the service-developed defects in the rail samples examined were fatigue cracks, (b) all these fatigue cracks initiated at sharp internal notches such as inclusions, and (c) a correlation between the metallurgical properties of the rail samples and defect formation could not be made.

Overall, it is reasonable to conclude that the service lives of the rails investigated would have been longer if the inclusions responsible for crack initiation had not been present. However, it should be noted that most of these rails had service lives lasting 16 years—454 million metric tons (MMT) (500 million gross tons (MGT)) with one sample lasting 22 years—685 MMT (755 MGT). Furthermore, the service stresses, although unknown, were apparently severe as evidenced in the deformation of the rail-heads.

It appears that of greater importance and interest with respect to the effect of steel quality and properties on defect formation in rails would be a study of defects that form early in the rail life. It is recommended that such studies be conducted.

KEY WORDS: steels, railroad tracks, carbon steels, defects, composition measurement, tensile properties, hardness, metallography, fractography, wear, service life, evaluation

The Ad Hoc Committee on Rail Research, which is composed of representatives of the American Railway Engineering Association (AREA), the Association of American Railroads (AAR), and the American Iron and

*Original experimental data were measured in U.S. customary units.

¹Senior research engineer, project analyst, and chief research engineer, respectively, U.S. Steel Corporation Research Laboratory, Monroeville, Pa. 15146.

Steel Institute (AISI) Committee on Railroad Materials, formulated a program to determine the metallurgical properties and applied stresses that promote service defects in conventional control-cooled, carbon-steel rail, particularly in rails exhibiting short service lives or premature failure. The overall objective of the program was to establish possible interrelationships of material properties, in-location service stresses, and service defects in rails.

As part of this program, U.S. Steel Corporation was awarded a contract to conduct a metallurgical and failure analysis of 33 rails removed from service, 31 of which contained service-developed defects. The specific tasks to be performed are outlined in Table 1. The results of these studies are discussed herein, except for the Charpy V-notch impact toughness, fracture toughness, and fatigue properties, which are discussed in a companion paper in this volume.²

TABLE 1—*Test program tasks.*

-
- | | |
|----|--|
| A. | Chemical analyses |
| B. | Mechanical property analyses |
| 1. | Hardness tests |
| 2. | Tension tests ^a |
| 3. | Wear and deformation analyses |
| 4. | Charpy V-notch impact toughness tests ^b |
| 5. | Fracture toughness tests ^b |
| 6. | Fatigue tests ^b |
| C. | Metallographic analyses |
| 1. | Macrostructural examination |
| 2. | Microcleanliness examination |
| 3. | Microstructural examination |
| D. | Fractographic analyses |
| 1. | Fractographic features determination |
| 2. | Composition and nature of origin |
-

^aConducted by AAR Technical Center, Chicago, Ill.

^bReported in companion paper in this symposium.

Materials and Experimental Work

Materials

Thirty-three control-cooled, carbon-steel rail samples were selected by the Ad Hoc Committee from approximately ninety 2.44 m (8-ft) portions of jointed rails that had been removed from track sites on main line railroads by the AAR. Thirty-one of the samples were removed because ultrasonic inspection had indicated service-developed defects in them. These samples were broken in three-point bending at room temperature at the AAR Technical Center to reveal the service-developed defects, and tensile and Charpy V-notch impact properties were determined by the AAR. One half of

²Barsom, J. M. and Imhof, E. J., this publication, pp. 387-413.

each fractured sample (31 samples) and two samples of rail containing no service-developed defects (for comparison purposes) were sent to the U.S. Steel Research Laboratory.

Information concerning the samples is given in Table 2. Note that the sample distribution was not uniform in that 21 of the rail samples were from one railroad (Railroad A), 28 were produced by one producer (Producer A), and 26 were removed from tangent track. The tie and ballast conditions at the track sites were generally indicated as good by the field group that selected the samples. Although it was desired to have rail samples with prematurely short service lives from traditionally troublesome track locations, rail samples with service-developed defects were not found in these locations. As a result, the field group was only able to select rails with relatively long service lives; most of these (27) had lives between 363 to 545 million metric tonnes (MMT) (400 and 600 million gross tons (MGT)) and the average life was 454 MMT (500 MGT) or 16 years (Table 2). This average service life represents about 15.4 million loading cycles at about 14.7 metric tonnes (16.25 tons) per wheel, well beyond the number of cycles (5 million) generally considered as infinite life in laboratory fatigue tests such as a rolling contact load test. Only three rail samples had lives less than 363 MMT. Twenty-three of the samples contained detail fractures originating from shelling; four contained shelling only; three contained compound fissures; and one contained a horizontally split head. Most rail samples were from B, C, or D cut rails. There were no A cut (top of steel ingot) rails.

Experimental Work

Metallography—The samples of rail were sectioned as shown in Fig. 1 to obtain specimens for chemical analysis, for oxygen analysis, and for metallographic examination. The microcleanliness of 50 unetched fields on each specimen was rated on a quantitative television microscope (QTM) at a magnification of $\times 360$ to determine average inclusion area, highest inclusion area (worst field), and the length factor.³

Because proeutectoid ferrite forms preferentially on the austenite grain boundaries in decarburized layers near the rail surface during cooling after hot rolling, prior austenite grain size was measured on an etched longitudinal section of a specimen taken just below the surface of the lower side of the head of each rail sample (Fig. 2). It should be noted that it was not possible to clearly distinguish prior austenite grain size by any other method. Grain size was determined in accordance with the ASTM Method for Estimating Average Grain Size of Metals (E 112-74).

The pearlite colony size and interlamellar pearlite spacing were obtained by using the scanning electron microscope (SEM) on an etched longitudinal section (Fig. 3). The circular intercept method of Hilliard in ASTM Method

³Length factor is the summation of lengths of inclusions over 125 μm long per 100 fields, divided by 125 μm .

TABLE 2—Rail sample background.

Sample No.	AAR No.	Weight, lb/yd	Rail			Track Location	Service		Defect ^a Type
			Cut	Source	Producer		MGT	Years	
1	1	133	C	A	A	tangent	538	16	D
2	2	133	C	A	A	tangent	574	17	D
3	3	133	C	A	A	tangent	574	17	D
4	4	133	C	A	A	tangent	304	8	S
5	5	133	D	A	A	tangent	547	16	D
6	9	133	D	A	A	tangent	574	17	D
7	21	133	D	A	A	tangent	574	17	D
8	24	133	B	A	A	tangent	304	8	S
9	28	119	F	B	A	high rail—1° 38' ^b	481	15	D
10	29	119	C	B	A	transposed—1° ^c	481	15	S
11	30	119	B	B	A	tangent	481	15	D
12	31	119	E	B	A	tangent	481	15	D
13	38	133	C	A	A	tangent	538	16	D
14	43	133	B	A	A	tangent	381	10	D
15	45	133	E	A	A	tangent	520	17	D
16	46	133	B	A	A	tangent	557	18	D
17	50	133	C	A	A	tangent	520	17	S
18	55	133	E	A	A	tangent	519	17	D
19	60	133	D	A	A	high rail—1°	519	17	D
20	61	133	B	A	A	tangent	557	18	D
21	65	133	C	A	A	high rail—1°	519	17	D
22	67	133	B	A	A	tangent	471	18	D
23	69	133	D	A	A	tangent	755	22	D
24	73	133	B	A	A	tangent	519	17	D
25	75	127	...	C	B	tangent	655	19	D
26	77	119	D	B	A	high rail—1° 16'	496	16	D
27	78	115	...	D	B	tangent	236	19	HSB
28	32	119	E	B	A	tangent	481	15	D
29	83	119	...	B	A	tangent	481	15	none
30	84	133	...	A	A	tangent	519	17	none
31	85	140	C	C	C	low rail—1 °	420	13	CF
32	86	140	B	C	C	low rail—1 °	420	13	CF
33	87	140	C	C	C	tangent	420	13	CF

Conversion factors—

1 lb/yd = 0.5 kg/m

1 MGT = 0.91 MMT

1 deg = 0.07 rad

^aHSH = horizontally split head.

D = detail fracture from shelling.

S = shelling.

CF = compound fissure.

^bRail location on curve and degree of curvature.^cTransposed from high to low side of curve during service.

E 112-74 was used to determine average pearlite colony size at a magnification of $\times 1500$. To determine interlamellar pearlite spacing, 20 fields were examined at a magnification of $\times 3000$, and the smallest observed interlamellar pearlite spacing in each field was then measured at a magnification of $\times 24\,000$ by counting intercepts in a 10-cm line.

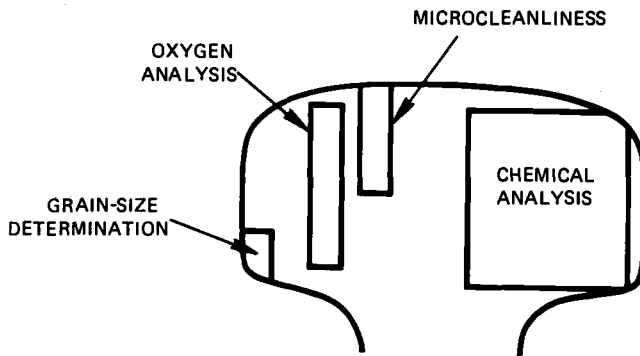


FIG. 1—Location of test specimens in rail samples.

Complete transverse sections of each rail were macroetched in hot 50 percent hydrochloric acid (HCl) in water in accordance with the ASTM Method for Macroetching Metals and Alloys (E 340-68). These samples were examined visually for porosity and inclusions. Sulfur prints were also made on complete transverse sections of each rail, and these were examined visually for the amount and distribution of sulfides.

Fractography—The fracture surface and polished cross sections adjacent to the fracture initiation sites of nine rail samples (No. 1, 2, 6, 8, 23, 27, 31, 32, 33) that were suitable for examination were examined by using the SEM, the energy dispersive spectra (EDS) X-ray analyzer, and the optical micro-

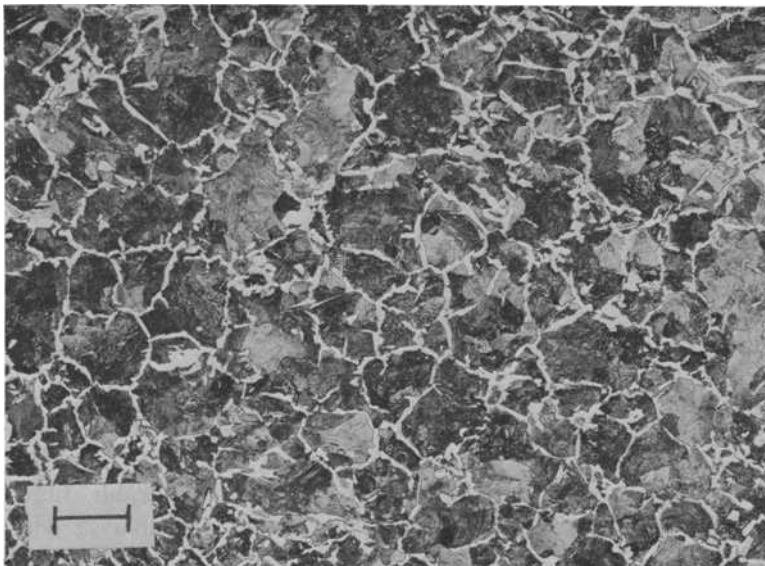


FIG. 2—Prior austenite grain boundaries outlined by proeutectoid ferrite in decarburized zone near rail surface. Etched in 2 percent nital. Sample No. 33. (Scale mark indicates 100 μm .)

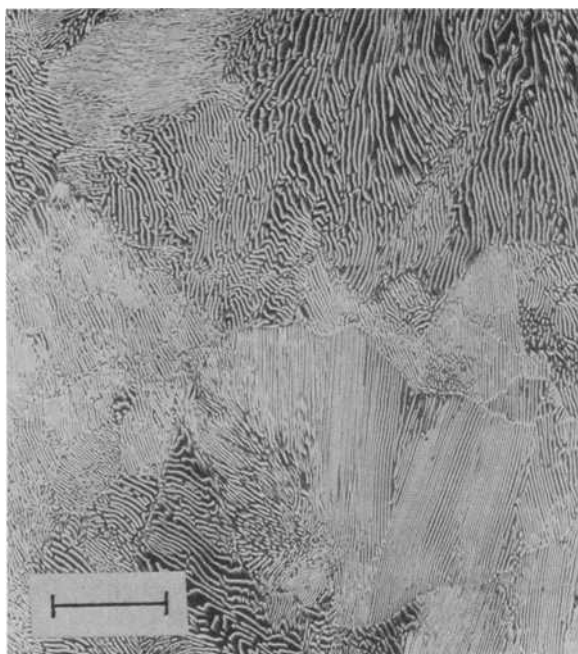


FIG. 3—Typical pearlite colonies and pearlite lamellae. Etched in 2 percent nital-picral (50:50) mixture. Sample No. 11. (Scale mark indicates 10 μm .)

scope to characterize details of the fracture surface and to analyze any particles at the origin of the fracture.

Hardness—Rockwell C hardness tests were made on transverse sections of the head of each rail sample. Tests were made at 0.32 cm (1/8-in.) intervals along a trasverse to the center of the railhead starting 0.16 cm (1/16 in.) from the gage corner surface.

Wear—Profile tracings of the head of each rail sample were made from the macroetch specimens. The profiles were compared with the profile of standard hot-rolled rail sections, and a planimeter was used to determine the decrease in area of the railhead caused by wear in service.

Results

Composition

The chemical compositions of the 33 rail samples and the mean and standard deviation of each element are shown in Table 3. The high and low check-analyses values for each element (underlined in Table 3) covered approximately the entire AREA specified ranges for ladle analysis, with only a few values slightly outside the ladle analysis specification. Generally, carbon and manganese were on the high side of the ladle specifications.

TABLE 3—Chemical composition of rails, percent (check analyses).

Sample No.	C	Mn	P	S	Si	Cu	Ni	Cr	Mo	Al	N	O ^a
1	0.79	0.89	0.021	0.023	0.17	0.073	0.067	0.032	<0.003	0.008	0.004	57
2	0.80	0.96	0.018	0.025	0.20	0.096	0.072	0.022	<0.003	0.008	0.003	59
3	0.82	0.95	0.018	0.023	0.18	0.101	0.068	0.029	<0.003	0.009	<u>0.003</u>	54
4	0.74	0.83	0.019	0.028	0.18	0.066	0.076	0.028	0.007	<u>0.013</u>	0.004	67
5	0.80	0.97	0.014	0.033	0.19	0.078	0.068	0.024	<0.003	0.010	0.003	<u>45</u>
6	0.78	0.92	0.024	0.026	0.18	0.100	0.069	0.025	<0.003	0.006	0.003	75
7	0.79	0.96	0.019	0.026	0.19	0.087	0.068	0.021	<0.003	0.007	0.003	58
8	0.74	0.85	<u>0.045</u>	0.039	0.19	0.096	0.070	0.039	0.003	0.013	0.004	61
9	0.68	0.79	0.016	0.043	0.15	0.101	0.066	0.033	0.003	0.012	0.003	66
10	0.72	0.89	0.018	<u>0.044</u>	0.16	0.076	0.059	0.031	<0.003	0.010	0.003	80
11	0.77	<u>1.06</u>	0.025	0.027	0.20	0.079	0.065	0.038	<0.003	0.009	0.004	60
12	0.79	0.91	0.021	0.030	0.14	0.090	0.073	0.031	<0.003	0.011	0.003	<u>87</u>
13	0.78	0.76	0.019	0.023	0.16	0.071	0.069	0.034	<0.003	<u>0.004</u>	0.004	60
14	0.73	0.82	0.011	0.022	0.18	0.099	0.062	0.039	<0.003	0.009	0.004	65
15	0.77	0.87	0.015	0.026	0.13	0.051	0.072	0.034	<0.003	0.006	0.005	68
16	0.78	0.86	0.011	0.030	0.18	0.060	0.067	0.024	<0.003	0.006	0.003	60
17	0.83	0.97	0.025	0.024	0.16	0.064	0.058	0.023	<0.003	0.005	0.004	62
18	0.69	0.94	<u>0.008</u>	0.028	0.20	0.052	0.069	0.021	<0.003	0.008	0.004	67
19	0.77	1.00	0.023	0.032	0.19	0.089	0.072	0.027	<0.003	0.011	0.004	53
20	0.75	0.83	0.013	<u>0.017</u>	0.21	0.052	0.074	0.026	<0.003	0.006	0.004	80
21	0.79	0.88	0.027	0.032	0.14	0.052	0.069	0.023	<0.003	0.008	0.003	62
22	0.74	0.87	0.010	0.030	<u>0.22</u>	0.073	0.069	0.023	<0.003	0.007	0.003	71
23	0.76	0.84	0.016	0.032	0.12	0.129	<u>0.099</u>	0.037	0.005	0.010	0.003	61
24	0.81	0.85	0.011	0.033	0.16	0.053	0.064	0.023	<0.003	0.009	0.004	54
25	<u>0.66</u>	0.92	0.012	0.032	0.18	0.041	0.015	0.033	<0.003	0.005	0.003	59
26	0.78	<u>0.70</u>	0.012	0.036	<u>0.12</u>	0.150	0.076	0.024	<0.003	0.011	0.003	70
27	0.72	0.79	0.017	0.028	0.15	<u>0.011</u>	<u>0.006</u>	<u>0.013</u>	<0.003	0.006	0.004	67
28	0.75	0.86	0.014	0.033	0.15	0.060	0.065	0.027	<0.003	0.010	0.003	67
29	0.81	0.83	0.011	0.026	0.13	0.126	0.076	0.028	<0.003	0.010	0.003	62
30	0.78	0.89	0.010	0.033	0.16	<u>0.152</u>	0.093	0.031	<u>0.011</u>	0.007	0.004	61
31	0.82	0.81	0.013	0.037	0.17	0.137	0.049	0.055	0.005	0.007	0.006	63
32	0.83	0.81	0.013	0.037	0.16	0.142	0.046	0.056	0.005	0.007	0.004	60
33	<u>0.84</u>	0.81	0.015	0.036	0.18	0.149	0.052	<u>0.057</u>	0.006	0.007	<u>0.007</u>	65
Mean	0.77	0.875	0.017	0.030	0.17	0.087	0.065	0.031	... ^b	0.008	0.0037	63.8
Standard deviation	0.044	0.075	0.007	0.006	0.026	0.035	0.017	0.010	... ^b	0.002	0.0009	8.3

AREA SPECIFICATION FOR LADLE ANALYSES

0.67/ 0.80	0.70/ 1.00	0.04 max	0.05 max	0.10/ 0.25	(for 91/120 lb/yd rail)
0.69/ 0.82	0.70/ 1.00	0.04 max	0.05 max	0.10/ 0.25	(for 121 and over lb/yd rail)

Conversion factor—

1 lb/yd = 0.5 kg/m

NOTE—Highest and lowest values underlined.

^appm.^bNot determined.

Mechanical Properties

The rail samples contained a service-induced, work-hardened region generally within 0.32 to 0.96 cm (1/8 to 3/8 in.) from the gage corner surface of the railheads, as shown in the typical hardness profiles of Fig. 4. Thus, the railheads had been subjected to stresses sufficient to cause yielding at 0.96 cm below the gage corner. The maximum hardness reading near the gage corner surface and the minimum hardness reading near the center of the railhead are shown in Table 4 for all 33 samples, along with the longitudinal tensile properties and the wear rate of the railhead. The highest and lowest values of these properties (underlined values) show that the sampling provided a large range of mechanical properties that are representative of control-cooled, carbon-steel rail. Typical contour profiles of the rail samples, which were used to determine rail wear rates (Fig. 5), illustrate the range of flow and wear observed on the railheads of the samples.

Metallography

The prior austenite grain size, the pearlite colony size, the pearlite interlamellar spacing, and the microcleanliness of the 33 samples are shown in Table 5. The microcleanliness of the rail samples was rated by determining the average inclusion area, worst field, and inclusion length factor. These metallographic values are representative of the range of values expected for

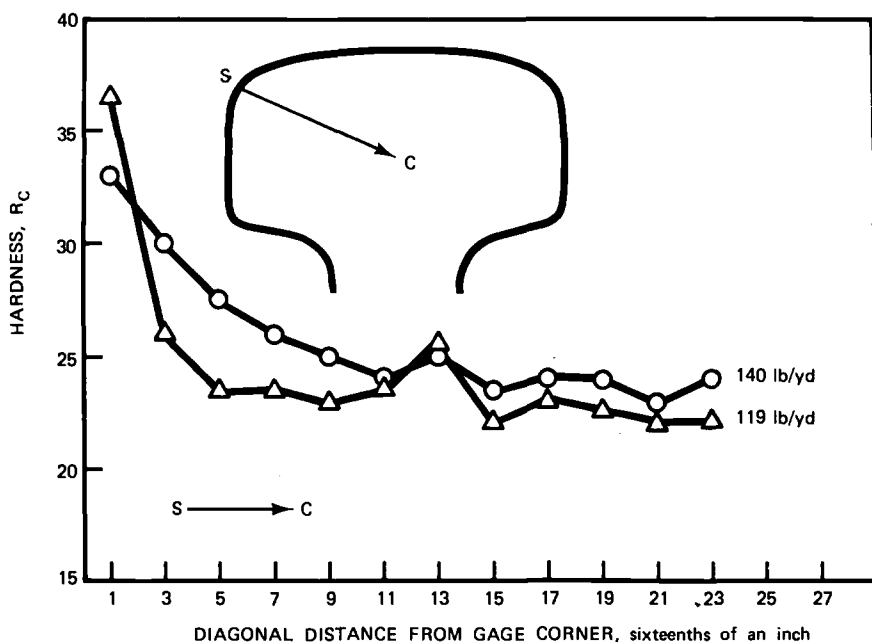


FIG. 4—Typical hardness profiles of railheads.

TABLE 4—Mechanical properties of the rails.^a

Sample No.	Hardness, Rc		0.2% Offset Yield Strength, ksi	Tensile Strength, ksi	Elongation in 1 in., %	Reduction of Area, %	Rail Wear Rate, in. ² / MGT
	Center	Surface					
1	23	33.5	73.2	139	12.5	<u>9.0</u>	4 × 10 ⁻⁴
2	23	34	66.7	135	13.8	10.5	3
3	<u>24</u>	34.5	69.6	139	12.5	9.5	3
4	20	30	65.6	129	10.2	14.3	4
5	22.5	35	67.6	134	10.4	15.5	4
6	21	34	73.0	135	13.9	9.8	3
7	23.5	35	70.5	135	10.7	13.9	<u>1</u>
8	21	<u>29</u>	62.1	130	11.3	16.1	4
9	<u>17.5</u>	35	60.5	121	12.3	17.3	9
10	21	35.5	<u>87.0</u>	140	10.2	13.4	<u>13</u>
11	24	36	<u>77.7</u>	137	9.7	16.4	5
12	22	<u>36.5</u>	68.3	133	9.0	14.1	6
13	21	<u>31.5</u>	64.3	131	10.9	14.5	4
14	19	34.5	65.5	127	10.8	14.9	4
15	22	33	<u>67.5</u>	130	10.5	15.6	4
16	20.5	31	71.1	131	10.2	13.9	4
17	24	35	<u>77.7</u>	<u>141</u>	8.4	11.7	5
18	17.5	33.5	<u>58.3</u>	119	14.3	20.2	5
19	22.5	32	<u>76.6</u>	134	10.3	14.0	5
20	21	30.5	63.9	128	11.0	15.4	2
21	23	36	72.2	132	10.6	14.8	5
22	21	33.5	62.2	127	<u>15.8</u>	11.3	5
23	21.5	31.5	71.6	132	13.8	11.0	4
24	22	32	76.5	132	10.7	14.1	5
25	19.5	30.5	69.7	123	12.6	<u>21.0</u>	5
26	20.5	34.5	68.3	132	9.5	13.3	10
27	18	30.5	62.5	<u>118</u>	12.9	20.9	4
28	20	33	76.8	132	13.7	9.5	8
29	22	35.5	75.6	137	8.8	14.4	7
30	22	36	76.5	134	<u>7.5</u>	11.5	2
31	23.5	32	72.4	139	8.7	14.6	5
32	23	33	70.2	137	8.8	14.3	5
33	24	34.5	73.2	141	8.8	14.2	5
Mean	21.5	33.4	70.1	132.2	11.1	14.1	4.9
Standard deviation	1.8	2.0	6.1	6.0	2.0	3.0	2.3

Conversion factors—

1 ksi = 6.895 MPa

1 in. = 2.54 cm

1 MGT = 0.91 MMT

NOTE—The highest and lowest values are underlined.

^aThe tensile properties were determined at the AAR Technical Center.

control-cooled, carbon-steel rail. Most of the inclusions rated were sulfides, although aluminates and silicates were also observed.

Fractography

Fractographic examination of each type of service-developed defect investigated (Table 6) indicated that they were all fatigue cracks that

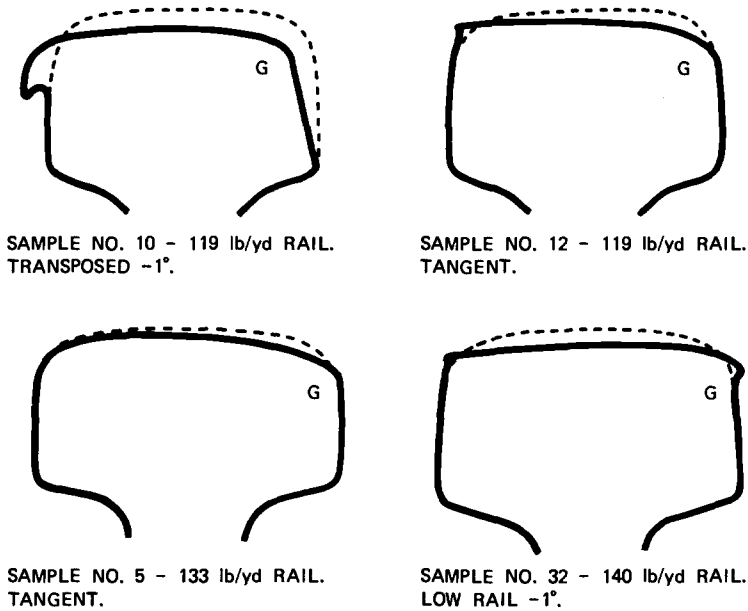


FIG. 5—Rail wear profiles. Dotted line represents the original section profile. G denotes gage corner.

initiated at discontinuous clusters of calcium-aluminate inclusions that formed long stringers which were as small as 1 mil wide and had length-to-width ratios much greater than 10. Several fatigue cracks also initiated at what appeared to be microvoids. The cracks propagated in a horizontal plane to form shelling or horizontally split head defects. In the case of detail fractures from shelling and compound fissures, these horizontal cracks then turned into a transverse plane and continued to grow in this direction. In some instances, it appeared that the crack initiated and then propagated in both of these planes simultaneously.

SEM examination of all the fractures showed that mashing and rubbing of the horizontal surfaces under cyclic wheel loadings caused considerable mechanical damage to the surface details (Fig. 6a). This was even found near the edge of the fatigue fracture surface, adjacent to the laboratory-produced cleavage fracture, where the fatigue crack growth was most recent (Fig. 6b).

The transverse fracture surface contained details that appeared to be striations. However, the orientation and spacing of these were directly related to the orientation and spacing of the pearlite lamella, as shown on the polished and etched cross section perpendicular to the fracture surface (Fig. 7). This relationship was seen in all service-exposed specimens and was also seen in fatigue tests of rail steel in the laboratory. These apparent striations are not related to crack growth direction or rate and cannot be used to

TABLE 5—*Metallographic data.*^a

Sample No.	Prior Austenite Grain Size, ASTM No.	Pearlite		Inclusion		
		Colony Size, cm	Interlamellar Spacing, A	Area, %	Worst Field, %	Length Factor
1	4.5	7.9×10^{-4}	2100	0.30	1.20	58
2	5.5	12.1	1860	0.37	2.25	80
3	5	10.4	1860	0.24	2.50	26
4	4.5	12.4	2400	0.36	1.05	46
5	4.5	7.3	1880	0.36	1.05	47
6	4.5	9.0	1980	0.30	1.25	40
7	4	7.4	1930	0.27	1.00	42
8	6	7.2	2230	0.47	2.10	<u>97</u>
9	<u>2.5</u>	7.7	<u>2410</u>	<u>0.50</u>	<u>4.20</u>	84
10	3.5	8.0	2070	0.43	1.00	48
11	4.5	7.9	2020	0.29	0.90	41
12	4	7.7	2040	0.35	3.10	88
13	6	12.8	1940	0.25	0.77	44
14	<u>6.5</u>	7.3	2380	0.20	0.60	18
15	4	11.1	<u>1690</u>	0.30	1.25	67
16	4	9.1	2070	0.29	0.93	59
17	3.5	8.4	1850	0.26	0.90	60
18	3.5	10.1	2020	0.24	0.91	38
19	3.5	10.0	1830	0.32	1.00	43
20	3.5	12.1	1780	<u>0.18</u>	0.57	20
21	6	10.6	1960	0.30	0.81	33
22	5	7.8	2120	0.28	0.74	54
23	4.5	10.1	2060	0.36	2.65	45
24	5	9.3	2130	0.30	1.00	29
25	3.5	11.5	2020	0.28	0.77	35
26	5	14.5	1930	0.26	0.74	24
27	5.5	11.3	2250	0.26	3.60	56
28	4.5	9.5	2300	0.23	1.00	28
29	4	10.8	2040	0.24	<u>0.57</u>	28
30	5.5	<u>6.3</u>	2090	0.22	0.58	<u>14</u>
31	5	11.5	1990	0.28	1.25	22
32	4.5	<u>15.2</u>	1930	0.31	0.97	47
33	4.5	9.5	1840	0.35	1.30	56
Mean	4.6	9.8	2030	0.30	1.35	46
Standard deviation	0.9	2.1	178	0.07	0.91	20.5

^aThe highest and lowest values are underlined.

locate the origin of the crack. Accordingly, macroscopic features such as beach marks⁴ were used to locate the fracture origins.

An examination of shelling in Sample No. 8 (Fig. 8a) revealed particles containing calcium and aluminum at the origin (Figs. 8b, c). Because of the presence of atmospheric corrosion products on the fracture surface, a

⁴Beach marks represent successive positions of the crack front where arrests of the crack occur as it propagates through the steel. These arrests can be caused by variations in cyclic loading or plastic flow. The marks are composed of slight steps in the fracture surface that are concentric to the initiation site.

TABLE 6—*Results of fractographic examination.*

Sample No.	Defect Type	Initiation Feature	Growth Direction
1	detail fracture from shelling	calcium aluminates	horizontal and transverse
2	detail fracture from shelling	calcium aluminates	horizontal and transverse
6	detail fracture from shelling	calcium aluminates	horizontal and transverse
8	shelling	calcium aluminates	horizontal only
23	detail fracture from shelling	calcium aluminates	horizontal and transverse
27	horizontally split head	calcium aluminates	horizontal only
31	compound fissure	microvoids	horizontal and transverse
32	compound fissure	microvoids	horizontal and transverse
33	compound fissure	microvoids	horizontal and transverse

polished cross section of the origin was prepared (Fig. 8*d*). Discontinuous calcium aluminate inclusion stringers were found on and adjacent to the fracture surface. Similarly, discontinuous calcium aluminate inclusion stringers were also found at the origin of a typical detail fracture from shelling in Sample No. 23 (Fig. 9).

Massive discontinuous calcium aluminate inclusion stringers that were enveloped in iron oxide were found at the origin of a horizontally split head in Sample No. 27 (Fig. 10). The iron oxide resulted from atmospheric corrosion that contaminated the exposed fracture surface.

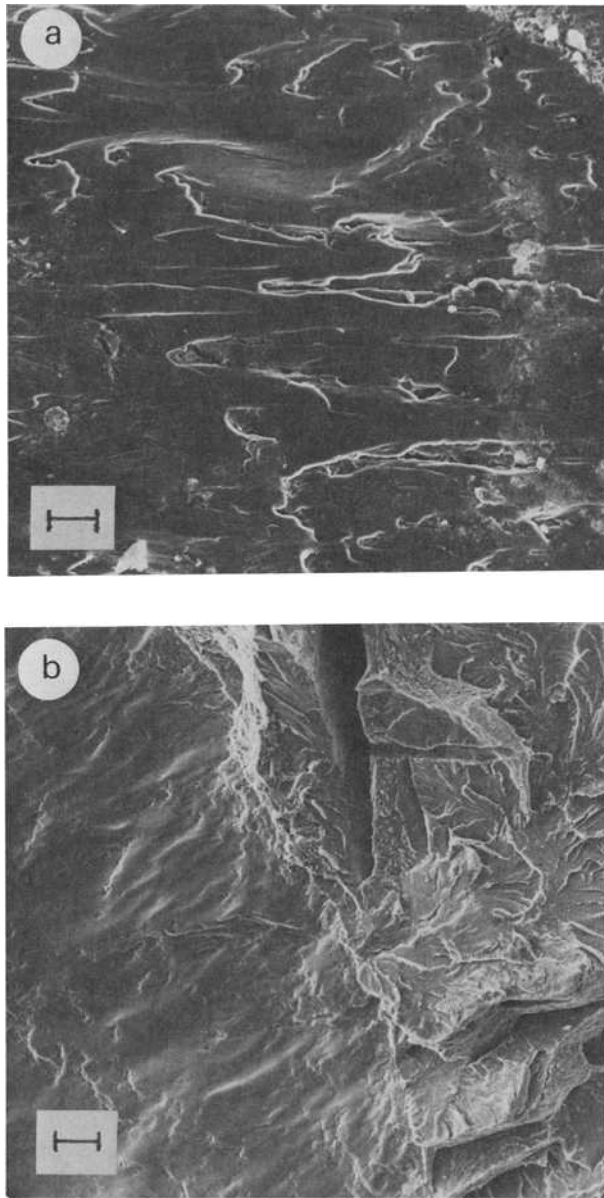
A typical example of a compound fissure (Sample No. 33) is shown in Fig. 11. The initiation site had smooth featureless surfaces (Fig. 11*c*) and what appeared to be microvoids (Fig. 11*d*). The source of these initiation sites is not known.

In the samples studied, sulfides were not responsible for fatigue crack initiation. Studies [1-4]⁵ on bearing steels fatigue tested under rolling contact loading have also shown that sulfides do not cause fatigue crack initiation. Inclusions and porosity have previously been associated with rail failures and have been reported by the AREA Committee on Rails in numerous AREA Bulletins as early as 1947 [5,6].

Linear Multiple Regression Analyses

Linear multiple regression analyses were made to determine any relationships between composition, metallurgical properties, wear, defect formation, and service life of the rail samples. Meaningful relationships were only obtained between composition and hardness, tensile strength, and pearlite interlamellar spacing. As shown in Table 7, both hardness and tensile strength increased as carbon, manganese, and chromium contents increased. These effects have been reported previously in the literature [7,8]. In addition, pearlite interlamellar spacing decreased as carbon and manganese

⁵The italic numbers in brackets refer to the list of references appended to this paper.



- (a) Scanning electron fractograph of fracture surface showing mechanical damage due to wheel loadings. (Scale mark indicates 10 μm .)
 (b) Scanning electron fractograph of fracture surface showing mechanical damage (left) adjacent to laboratory brittle fracture (right). (Scale mark indicates 10 μm .)

FIG. 6—Typical horizontal plane fracture surfaces.

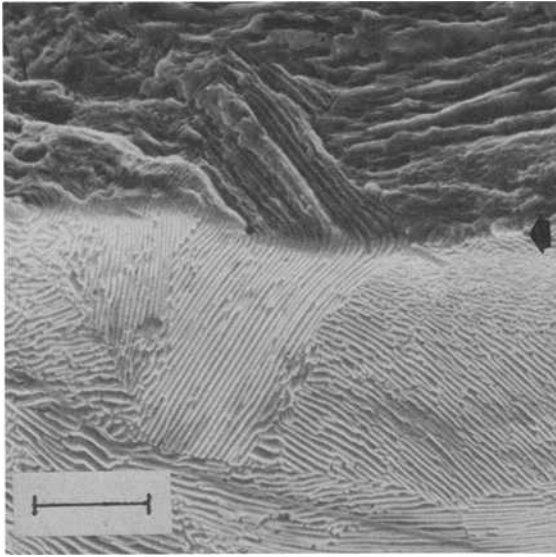


FIG. 7—Scanning electron fractograph of vertical fracture surface of service failure showing striation-pearlite lamella relation. (Scale mark indicates 10 μm .) Top arrow indicates direction of crack propagation. Arrow on right indicates fracture surface edge.

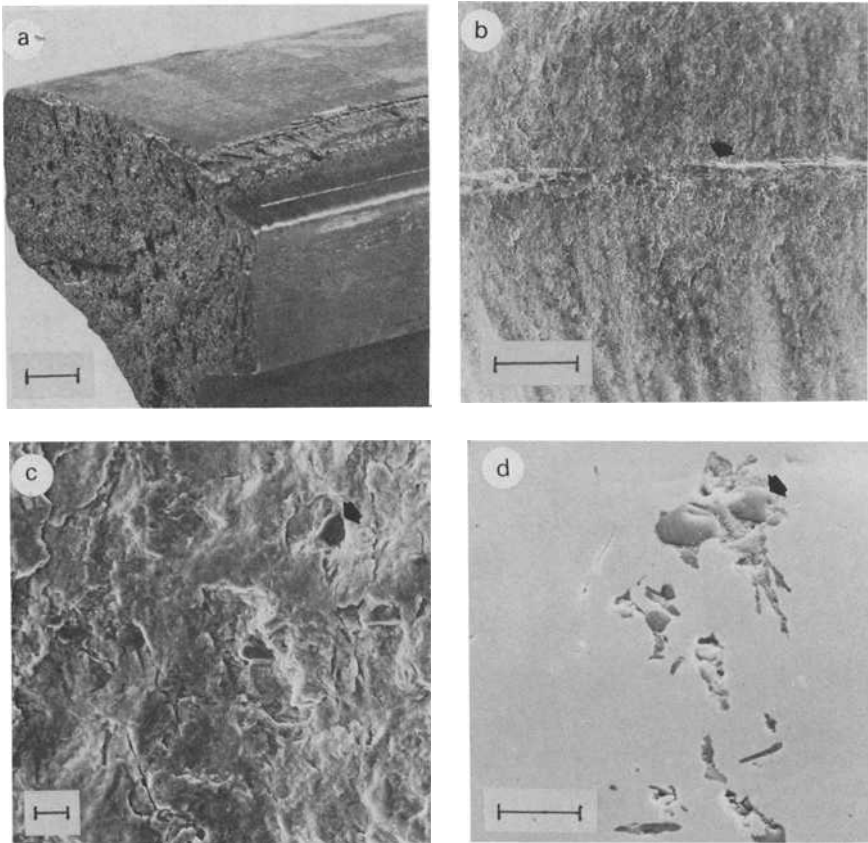
contents increased, and increased as the aluminum content increased. Carbon, manganese, and chromium additions increase the hardenability of steel and allow the steel to cool to lower temperatures before the transformation of austenite to pearlite begins [9]. At these lower temperatures, finer pearlite forms, and, according to prior work [7, 10, 11] this increases the hardness and tensile strength of the rail. Aluminum has an opposite effect [12].

Conclusions

The following conclusions can be made, based on the results of this study:

1. All the service-developed defects in the rail samples examined were fatigue cracks.
2. All of these fatigue cracks initiated at sharp internal notches such as inclusions.
3. A correlation between the metallurgical properties of the rail samples and defect formation could not be made.

Overall, it is reasonable to conclude that the service lives of the rails investigated would have been longer if the inclusions responsible for crack initiation had not been present. However, it should be noted that most of these rails had service lives lasting 16 years—454 MMT (500 MGT), with one



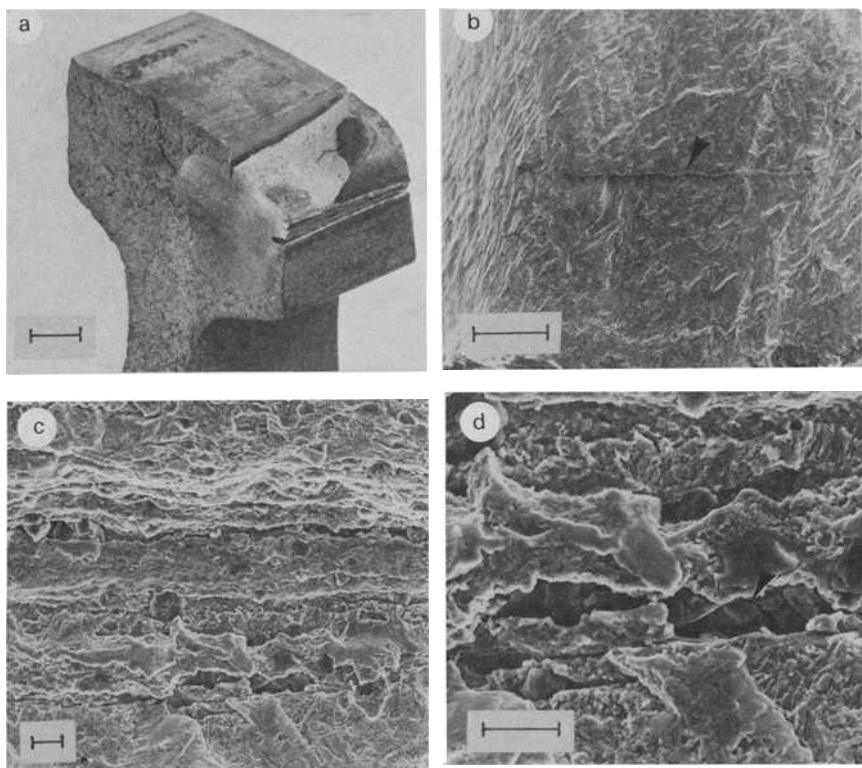
- (a) Rail showing shelling. (Scale mark indicates 1 cm.)
 (b) Scanning electron fractograph of defect origin. (Scale mark indicates 1 mm.)
 (c) Scanning electron fractograph of fracture surface showing calcium aluminate particles on fracture surface. (Scale mark indicates 10 μm .)
 (d) Scanning electron micrograph of transverse cross section showing calcium aluminate inclusions at origin. (Scale mark indicates 10 μm .)

FIG. 8—Shelling in Rail Sample No. 8.

sample lasting 22 years—685 MMT (755 MGT). Furthermore, the service stresses, although unknown, were apparently severe as evidenced in the deformation of the railheads.

It appears that of greater importance and interest with respect to the effect of steel quality and properties on defect formation in rails would be a study of defects that form early in the rail life. It is recommended that such studies be conducted.

It is understood that the material in this paper is intended for general information only and should not be used in relation to any specific



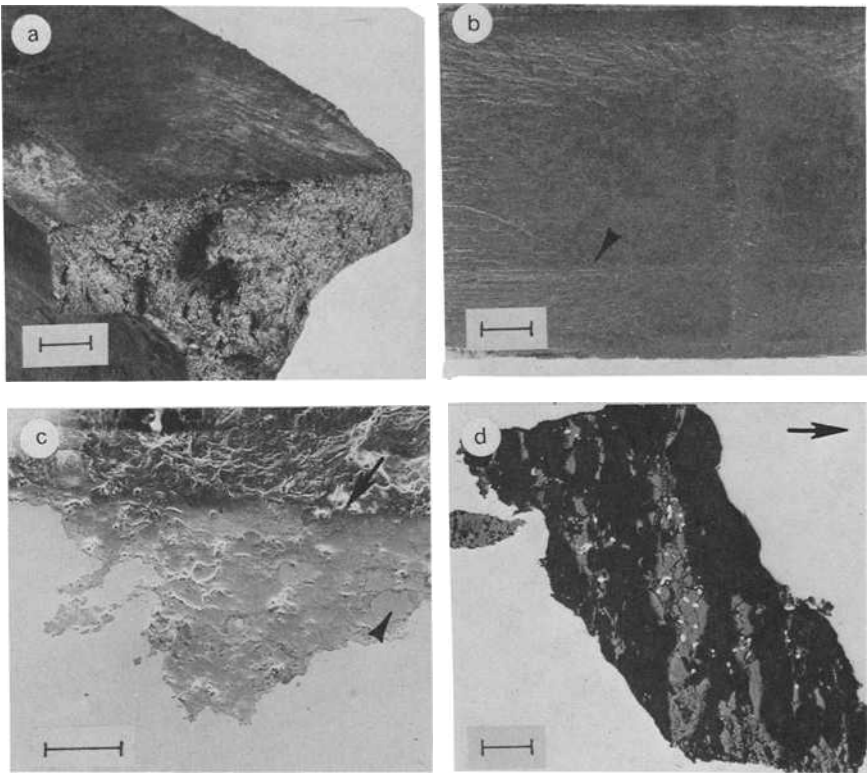
(a) Rail showing detail fracture from Shelling. (Scale mark indicates 1 cm.)
 (b) Scanning electron fractograph of defect origin. (Scale mark indicates 1 mm.)
 (c) Scanning electron fractograph of defect origin. (Scale mark indicates 10 μm.)
 (d) Scanning electron fractograph of calcium aluminate inclusions at origin. (Scale mark indicates 10 μm.)

FIG. 9—Detail fracture from shelling in Rail Sample No. 23.

application without independent examination and verification of its applicability and suitability by professionally qualified personnel. Those making use thereof or relying thereon assume all risk and liability arising from such use or reliance.

Acknowledgment

The authors wish to thank B. K. Stewart, statistician, U. S. Steel Research, for her help in evaluating the complex data.



- (a) Rail showing horizontally split head. (Scale mark indicates 1 cm.)
(b) Photomacrograph of fracture surface showing defect origin. (Scale mark indicates 1 cm.)
(c) Scanning electron micrograph of transverse cross section showing calcium aluminate inclusions in matrix of iron oxide at origin. (Scale mark indicates 50 μm .) Top of figure is fracture surface edge.
(d) Light micrograph of horizontal section parallel to fracture surface through origin showing calcium aluminate inclusions. (Scale mark indicates 100 μm .) Arrow indicates rolling direction.

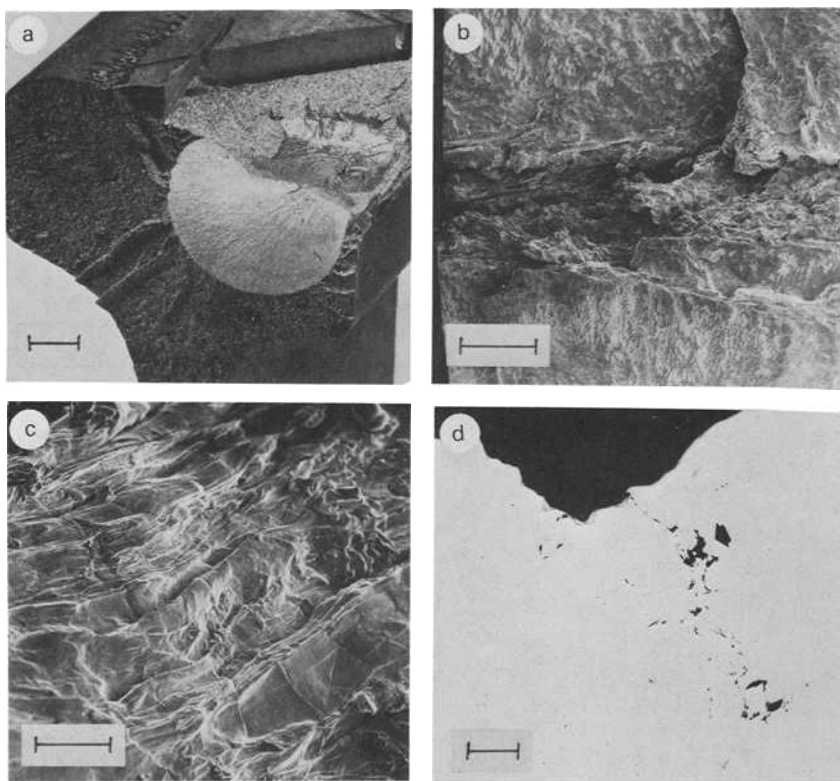
FIG. 10—Horizontally split head in Sample No. 27.

TABLE 7—Linear multiple regression equations.

1. Center hardness, $R_c = -12.7 + 31.8 (\%C) + 9.8 (\%Mn) + 38.2 (\%Cr)$
where ($R^2 = 0.86$, standard error = 0.71 R_c)
2. Tensile strength, ksi = $33.7 + 97.4 (\%C) + 21.6 (\%Mn) + 152 (\%Cr)$
where ($R^2 = 0.74$, standard error = 3.2 ksi)
3. Pearlite interlamellar spacing, $A = 3715 - 1788 (\%C) - 630 (\%Mn) + 29240 (\%Al)$
where ($R^2 = 0.49$, standard error = 133.6 A)

$R^2 \times 100$ = percent of variance explained by equation.

Standard error = mean square deviation of sample points from the estimated regression line.



- (a) Rail showing compound fissure. (Scale mark indicates 1 cm.)
 (b) Scanning electron fractograph of defect origin. (Scale mark indicates 1 mm.)
 (c) Scanning electron fractograph of fissures at defect origin. (Scale mark indicates 50 μm.)
 (d) Light micrograph of transverse cross section showing microvoids at defect origin. (Scale mark indicates 100 μm.)

FIG. 11—Compound fissure in Rail Sample No. 33.

References

- [1] Uhrus, L. O., *Clean Steel*, Iron and Steel Institute Special Report 77, London, 1963, pp. 104–109.
- [2] Murray, J. D. and Johnson, R. F., *Clean Steel*, Iron and Steel Institute Special Report 77, London, 1963, pp. 110–118.
- [3] Tricot, R., *Production and Application of Clean Steels*, Iron and Steel Institute Special Report 134, London, 1972, pp. 192–204.
- [4] Enekes, S., *Production and Application of Clean Steels*, Iron and Steel Institute Special Report 134, London, 1972, pp. 215–220.
- [5] Cramer, R. E., *AREA Proceedings*, American Railway Engineering Association, Vol. 48, 1947, pp. 809–818.
- [6] Cramer, R. E., *AREA Proceedings*, American Railway Engineering Association, Vol. 53, 1952, pp. 902–915.
- [7] Gladman, T., McIvor, I. D., and Pickering, F. B., *Journal of the Iron and Steel Institute*, Vol. 210, 1972, pp. 916–930.
- [8] Heller, W. and Schweitzer, R., *Stahl und Eisen*, Vol. 95, 1975, pp. 1057–1061.

- [9] Manning, R. D., Reichhold, H. M., and Hodge, J. M., *Transformation and Hardenability in Steels*, symposium, University of Michigan, 27-28 Feb. 1967, pp. 169-177.
- [10] Hyzak, J. M. and Bernstein, I. M., *Metallurgical Transactions A*, Vol. 7A, 1976, pp. 1217-1224.
- [11] Gensamer, M., Pearsall, E. B., and Smith, G. V., *Transactions ASM*, American Society for Metals, Vol. 28, 1940, pp. 380-398.
- [12] Bain, E. C. and Paxton, H. W., *Alloying Elements in Steel*, American Society For Metals, Metals Park, Ohio, 1961, p. 164.

Welding of Railroad Rails— A Literature and Industry Survey*

REFERENCE: Hauser, Daniel, "Welding of Railroad Rails—A Literature and Industry Survey," *Rail Steels—Developments, Processing, and Use*, ASTM STP 644, D. H. Stone and G. G. Knupp, Eds., American Society for Testing and Materials, 1978, pp. 118–141.

ABSTRACT: Literature and industrial sources relating to methods for welding of railroad rails are surveyed. The welding processes included are thermite, flash, gas-pressure, and arc welding. Process and procedural descriptions, weldment properties, service performance in track, fabrication costs, and production rates are reviewed.

KEY WORDS: steels, railroad tracks, welded joints, arc welding, flash welding, gas welding, thermite welding

The performance of railroad track structures depends on many factors, one of the most important of which is the integrity of the rail joints. A large proportion of rail failures occurs at the connections between rail sections, particularly at conventional bolted rail joints. The cost of these failures, and the inspection and maintenance performed to reduce their incidence of occurrence, is high. For example, during the decade of 1963 to 1973, 1522 train accidents resulted from rail failures in the joint area or joint failures [1].² The cost of these accidents due to damage of equipment, track, and roadbed only was \$36.5 million. The total cost was much higher. In terms of inspection and repair, nearly 172 000 service and detected rail failures accompanying the inspection of 238 000 miles of track in 1970 were reported, of which over 89 000 occurred in the web-in-joint region [2]. Seventy-two percent of these joint failures were detected by visual or instrument inspection.

A significant reduction of bolted joint failures has been achieved by the adoption of continuous welded rail. Because of the importance of rail welding to the improvement of track performance, the practices used for rail welding are reviewed in this article. The processes surveyed are thermite

*The majority of original experimental data were measured in U. S. customary units.

¹Research metallurgist, Fabrication and Quality Assurance Section, Battelle-Columbus Laboratories, Columbus, Ohio 43201.

²The italic numbers in brackets refer to the list of references appended to this paper.

welding, electric flash butt welding, gas pressure welding, and arc welding. Other methods for joining of rails such as mechanical fastening and adhesive bonding have been reviewed in detail elsewhere [3].

Rail Joints and Adoption of Continuous Welded Rail

Rail joints are connections between continuous sections of rail designed to support vertical and lateral forces imposed under traffic and prevent vertical and lateral movement of the rail ends relative to each other. In conventionally bolted track, joints are designed to permit longitudinal rail movement in order to accommodate thermal expansion and contraction of the rails. Other types of joints must be capable of supporting longitudinal forces. The wear resistance, strength, toughness, and resistance to deflection of the joint should approach that of the rails being connected. For train control using signal block construction, some joints also must provide electrical insulation between the rail lengths.

The service performance of rail connections depends on many interacting factors including the following: (a) the type and quality of the specific connection, (b) speeds, wheel loads, gross tonnage, and nature of traffic, (c) track curvature, superelevation, gage, line, and surface, (d) rail section and rail steel properties, (e) design, quality, and maintenance of the track structure, and (f) range and frequency of ambient temperature changes.

The development and adoption of continuous-welded rail (CWR) has been motivated almost entirely by the reductions of maintenance costs and rail failures and an increase in rail life in comparison with standard bolted joints. The major improvement accompanying the installation of CWR is increased stiffness at the rail joints. The principal advantages of CWR are the following:

1. Elimination of bolted joint maintenance that includes bolt tightening, joint oiling, joint bar and bolt replacement, rail end hardening, rail end buildup or rail grinding to remove end batter, rail end straightening to remove droop; and rail end cropping, re-drilling, and relaying [4-8].

2. Reduction of damage to ties, fasteners, ballast, subgrade, rolling stock, and freight [4-10].

3. Elimination of signal bond installation and maintenance and improvement of track circuit conductivity [6-8].

4. An increase of rail life for 255 km of 637 to 660 N/m rail (158.5 miles of 131 to 136 lb/yd) from 19 to 26 years for 6 railroads on track carrying an average of 164 GN (18.4×10^6 tons) annually [11]. Recent estimates of the increase of life of flash-welded rail in comparison with bolted rail have ranged from 15 to 50 percent.

Because CWR costs more to install than bolted rail, it may not be economical for track that carries low tonnage and low wheel loads or for track that has such very sharp curves that railhead wear determines the need for replacement. On the other hand, CWR has been installed on some lines

that experience many joint failures due to high individual car weights of 890 kN (100 tons) or more even though they carry less than 8.9 GN (1 million gross tons) per year.

Although the savings accrued with the use of CWR in comparison with bolted joints are dependent on many factors, the following figures have been reported:

1. Track maintenance costs are reduced by \$198 to \$1200 per mile per year [6].
2. Thirty to forty percent of bolted track maintenance is at the rail joints, and 45 percent of bolted rail renewal is required because of rail end batter and rail end drooping [6].
3. Surfacing costs were reduced by 40 percent and overall track maintenance costs by 20 percent on the French railway system (SNCF) in 1961 [12].

The reduction of rail joint failures accompanying the installation of CWR is indicated by the reported failure statistics [2]. During 1970, for all rail sections and ages, there were 75.6 rail failures of all types per 161 track km (100 track miles) inspected, of which 37.5 failures per 161 track km (100 track miles) were web-in-joint failures. Of a total of 180 074 service and detected failures covering 383 track Mm (238 078 track miles), 89 396 failures (50 percent) were attributed to the web-in-joint region. It is significant that 64 273 joint failures (72 percent) were detected defects. These figures compare closely with the 46 bolt-hole cracks detected per 161 km (100 miles) of track tested by Sperry Rail Service in 1970 [13]. A total of 119 509 defects were detected in 244 Mm (151 741 miles) of track of which 70 542 were joint defects that represented removal of over 650 km (400 miles) of track. During 1973, Sperry Rail Service detected 126 000 rail defects in 300 Mm (185 000 miles) of track, of which 60 percent (75 000) were joint defects [14]. This is equivalent to 41 joint defects detected per 161 km (100 miles) of track tested.

In comparison to these figures, the accumulative failure rate for flash-welded joints through 1970 was 5.8 per 161 track km (100 miles) and for gas pressure welds was 22.9 failures per 161 km (100 miles) as shown in Table 1. With the available data, a comparison with thermite welds was made on the basis of failures per 100 weld years, which includes the ages of the welds. Compared with flash welds, gas pressure welds failed three times as frequently, and thermite welds failed 85 times as frequently.

During 1971, 54 percent of main line rail defects that developed during service in Japan were at bolt-holes [15]. The portion of the defects that was detected is not known. During the period of 1961 to 1963 on British Railways, there were three rail failures (excluding switch and crossing rails) per 161 track km (100 miles) per year of which 61 percent occurred at rail ends and 30 percent were through bolt-holes [16]. Failure statistics for bolted and welded rail on British Railways during the period of 1968 to 1972 are presented in Table 2 [17]. The weld failure data include both flash and

TABLE 1—Accumulated service and detected rail weld failures to 31 Dec. 1970 [2].

	Flash- Welded Joints ^a	Gas Pressure- Welded Joints ^a	Thermite- Welded Joints ^a
Track kilometers	22 701 ^b	10 200 ^b	. . . ^c
Track kilometer years	111 690 ^b	64 480 ^b	. . . ^c
Failures	817	1 449	358
Failures per 100 track km	3.6 ^b	14.2 ^b	. . .
Failures per 100 track km-years	0.73 ^b	2.25 ^b	. . .
Number of welds, millions	3.82	1.72	0.035
Average weld age, years	4.92	6.32	2.78
Weld years, millions	18.8	10.8	0.097
Failures per 100 weld years	0.00435	0.0134	0.368

^aIncludes new and relay rail.^bDerived from data assuming all joints were between 12-m-long (39-foot-long) rails.^cUnknown.

thermite welds, so that the failure rates of these two processes cannot be compared. The authors noted that the increasing failure rates accompanied the introduction of higher wheel loads and train speeds in 1967.

During the period of 1933 to 1971, about 58 000 track km (36 000 track miles) of CWR were laid [18]. Although flash welding has been used to produce most CWR, oxyacetylene gas pressure welding was used to manufacture increasing amounts of CWR through 1970.

Although there were approximately 81 000 km (50 000 miles) of CWR in track at the end of 1974 [19], which would require 13.5 million bolted joints, this accounts for only about 25 percent of the 332 300 km (206 400 miles) of line-haul [7] and 15 percent of the 553 000 km (343 000 miles) of track in the United States [20]. The remaining 472 500 km (293 470 miles) of bolted track represent about 79 million bolted joints between 12-m-long (39-ft-long) rail sections. The 14 railroads that have the greatest amounts of CWR (1840 to 8770 track km as of 31 Dec. 1975) account for 71 450 km (44 378 miles) of the 79 740 total km (49 527 miles) [21]. Assuming that all CWR is in line-haul track, there remain some 42.5 million bolted joints in this track category. The largest amounts of CWR installed to date were 9950 km (6179 miles) in 1970 and 7140 km (4434 miles) in 1972. During 1975, 4173 km (2592 miles) of CWR were installed and during 1976, 4192 km (2604 miles) of CWR installation were planned.

In summary, CWR has given excellent service performance, and continued installation, particularly in heavily traveled track, will improve the economics of railroad operation. Additional details on the fabrication, installation, performance, and costs of CWR are given in subsequent sections of this article.

TABLE 2—*Bolted and welded rail joint failures on British Railways [17].*

Year	Bolted Track, kilometers	Rail End Bolt-hole Failures ^a	Bolt-hole Failures per 100 Bolted Track Kilometers ^a	CWR Track, kilometers	Weld Failures ^b	Weld Failures per 100 CWR Track kilometers ^b
1968	33 000	667	2.0	6 280	217	3.5
1969	29 800	741	2.5	7 400	195	2.6
1970	27 500	977	3.5	8 530	248	2.9
1971	27 200	1030	3.8	9 500	435	4.6
1972	26 600	1350	5.1	10 300	434	4.2

^aCracked and broken.

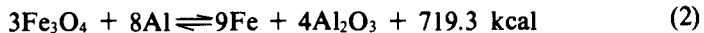
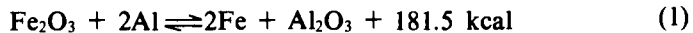
^bFlash and thermite welded.

Current Rail Welding Processes

In the sections that follow, welding processes currently used for joining rails are described and discussed. For each method, procedures, properties, service experience, principal failure modes, process variability, personnel skills, costs, and adaptability to shop and field fabrication are included, depending on the available information. Table 3 summarizes several important characteristics of rail joining processes.

Thermite Welding

Thermite welding is a process that produces coalescence "by heating with a superheated liquid metal and slag resulting from a chemical reaction between a metal oxide and aluminum, with or without the application of pressure. Filler metal, when used, is obtained from the liquid metal" [22]. The most common exothermic chemical reactions used for thermite welding are



The first reaction is used in the Goldschmidt® process (Orgotherm) [23] and the Calorite® and Boutet® (Delachaux) [24] processes. The second reaction is the basis of the Thermit® welding process that was developed in the United States [22].

TABLE 3—A summary of several characteristics of rail joining processes.

	Flash-Welded Joints	Gas Pressure-Welded Joints	Thermite-Welded Joints	Bolted Joints
Number of joints in service, millions	3.82	1.72	0.035	42.5
Rail joining rate, joints per hour	17	5 to 15	1.5	6
Cost per joint, dollars	20	40	65	25
Common joint defects	electrode burns, hot tears, misalignment	lack of fusion	porosity, voids, inclusion, lack of fusion	bolt-hole cracks, loose bolts, rail end batter,
Inspection methods	visual, magnetic particle	visual, magnetic particle	visual, ultrasonic, gamma radiography	visual, ultrasonic

The temperature of the molten metal is about 1925°C (3500°F), which is less than the theoretical temperature of about 2760°C (5000°F). The reduction of temperature results from various heat losses and the addition of other materials to the mixture. These other materials include carbon, manganese, pieces of high-carbon steel, and other alloying elements to increase abrasion resistance and provide weld-metal grain refinement. The alloying elements are added so that the solid weld metal will have mechanical properties similar to those of the rail steel being joined.

Thermite welding is used extensively in the United States and West Germany. This welding process is used almost exclusively for joining rails at the track site. It is attractive for in-track joining because of its portability, low capital investment requirement, and relatively short time for weld completion. Because the mechanical properties of thermite welds usually are inferior to those of welds made by other processes, usage in Japan is largely restricted at present to emergency repairs of CWR, although an effort is being made to improve the weld properties, particularly fatigue resistance.

Thermite Welding Procedures—Although certain procedures used in thermite welding are recommended for specific processes, general procedures for successfully making rail welds can be given. The procedures outlined in the following paragraphs are considered to be the minimal practices needed to provide acceptable weld quality [22–35]:

1. Cut the rail ends perpendicular to the rail axis using a torch, saw, or abrasive disk. Torch cuts should be relatively smooth, and, to prevent rail cracks from initiating at the torch-cut, heat-affected zone, thermite welding should be performed within 1 h of cutting.

2. Clean the rails within about 127 mm (5 in.) of the joint by filing, wire brushing, and solvent wiping to remove dirt, grease, moisture, loose oxide, and slag. Remove burrs and deformed head metal.

3. Separate the rail ends by a gap of 13 to 32 mm ($\frac{1}{2}$ to $1\frac{1}{4}$ in.) depending on the rail section and welding process.

4. Align the rails using a straight edge along the gage side of the railhead.

5. Raise the rails at the joint to compensate for the greater thermal contraction that occurs in the railhead during cooling relative to the web and base regions.

6. Attach the molds to the rail, centered over the joint, and seal the molds to the rail with luting material, according to the equipment supplier's instructions.

7. Insure that the crucible or reaction chamber is clean and dry.

8. Preheat the rail ends sufficiently to provide good fusion with the weld metal. Uniform heating of the rail ends is important and can be judged by visual observation of the rails.

9. Ignite the reaction mixture in the crucible. If the crucible is tapped manually, it is essential that sufficient time be allowed for completion of the reaction and to permit the slag to float to the surface of the molten metal. A stopwatch and observation of slag formation in the crucible are two methods used to time the manual taping operation. This operation is shown in Fig. 1.

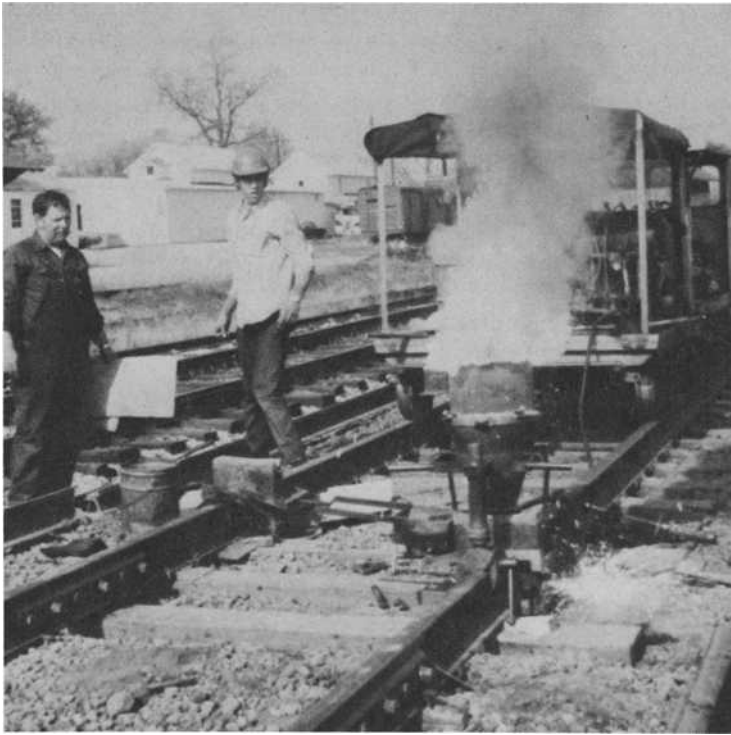


FIG. 1—Reaction of thermite mixture in crucible before pouring into mold.

10. Remove the molds after allowing the weld metal to completely solidify, which requires about 5 min.

11. Chisel and grind off excess weld metal to the rail profile, at least on the top and sides of the head. Final grinding should be performed when the weld and rail have cooled nearly to ambient temperature.

12. Inspect the weld by visual, dye penetrant, and ultrasonic nondestructive methods. Some urban track fabricators have radiographically inspected thermite welds using the Co^{60} isotope for a gamma ray source.

Although detailed procedural descriptions accompany each thermite welding process, railroads have had widely varying degrees of success with the process. This variability is considered to be due to the inherently large amount of human judgement that is required during thermite welding, especially for the rail preparation, torch preheating, and manual tapping steps.

Three approaches have been used to overcome the problem of variable weld quality. The first method is to define the welding procedures in great detail and to supervise closely the welding operation using adequately trained supervisory personnel [34,36].

The second approach to decreasing the variability of thermite welds has

been to modify the process to reduce the amount of human judgement needed. One such judgement associated with external preheating can be eliminated by using a larger and possibly hotter thermite mixture, which preheats the rail ends and melts off a small amount of rail steel as the molten steel washes over the rail ends. This process modification is incorporated into the Thermex Metallurgical Thermit process, the Boutet process, and the Orgotherm "SoV" Quick Welding method. The latter process is used for about 98 percent of field welds for the West German Federal Railroad. The Thermex, Orgotherm, and Boutet processes are used successfully by several U.S. railroads.

A second process modification that partly automates thermite welding permits self tapping of the molten charge. To accomplish this, the Thermex Metallurgical Thermit process includes five metal disks that are placed at the bottom of the crucible and the Boutet process includes a solid plug that is placed in a tapping thimble below the thermite mixture. Both of these tapping devices are designed to prevent the molten steel from entering the rail joint until the reaction is complete and the alumina slag has separated from the melt by flotation in the reaction crucible.

Both of these process modifications appear to improve the service performance of thermite welds significantly. Additional service time in track and accumulation of failure statistics are needed to make adequately supported conclusions.

The third approach to overcoming the problem of uncertain thermite weld quality, which is used successfully by several railroads, has been to reinforce the welds with bolted joint bars. If excess weld metal is not removed from the rail web and base, specially shaped joint bars can be used. If the rail ends are misaligned, grinding may be needed to obtain proper joint bar fit to the rails. Although this method has higher installation and maintenance costs than a joint that is welded only, the uncertainties of weld reliability can be reduced.

The Cost of Thermite Welds—The direct cost of making thermite welds in the fields is estimated to be \$65 based on observations of an eight-man welding gang working on a closed track section. During the 8-h shift, twelve welds were completed and no inspections were performed. The estimated cost is calculated as follows:

Direct labor; 8 men \times 8 h \times \$6/h	\$384
Welding kits; \$30 each \times 12 welds	360
Other consumables and equipment; \$3 \times 12 welds	36
Total cost	\$780
Direct cost per weld	\$65

Including indirect costs, the total cost of welding is expected to be much greater than this. The direct cost is in reasonable agreement with a value of \$55 for thermite welding on the West German Federal Railroad in 1972 [37].

Mechanical Properties of Thermite-Welded Rails—The results of slow

bend tests have been published in Refs 23,38-42 and the results of rolling load tests have been published in Refs 38,39,43-44. These have been collected and summarized in Ref 3.

In general, thermite welds have lower strength and ductility than flash and gas pressure welds which is attributed mainly to the cast, dendritic structure that is typical of thermite welds. Weld defects, such as inclusions and pores, also reduce the mechanical properties of thermite welds.

Service Performance of Thermite-Welded Rail—Because of their lower mechanical properties and greater variability in quality, thermite welds generally do not perform in track as well as flash butt and oxyacetylene gas pressure welds, where performance is considered to be time in track without failure. One measure of this is the accumulation of weld failure statistics published by the American Railway Engineering Association (AREA) [2,45]. These figures, which were collected from the railroads on a voluntary basis beginning in 1962, are incomplete since not all railroads have submitted reports. Although “absolute comparisons and total failure rates cannot be derived from the data,” “trends can be examined” [45]. These trends indicate that thermite welds have a much higher failure rate than flash welds and gas pressure welds.

The most common causes of in-service, thermite weld failures are [46-49]: (a) porosity, voids, and inclusions (mold material or alumina from the thermite mixture) in the weld metal, and (b) gouges and local regions transformed to brittle martensite produced during grinding of the weld and adjacent rail.

In spite of the poorer service performance experienced by many railroads, thermite welding is widely used, and, on at least one railroad, the failure rate is reported to be as low as that for shop-fabricated, flash butt welds. This has been accomplished by developing detailed procedure specifications, closely supervising the welding operation, and carefully inspecting the welded joints. About 3 percent of the welds are rejected and cut out, and the rails are rewelded.

Flash Welding

Flash welding produces coalescence “simultaneously over the entire area of abutting surfaces, by the heat obtained from resistance to electric current between two surfaces and by the application of pressure after heating is substantially completed. Flashing and upsetting are accompanied by expulsion of metal from the joint” [50,51].

Although flash butt welding was first used in 1937, the gas pressure welding process was favored, and it was not until 1955 that any significant number of flash-welded rails were placed in service [9,18]. The flash welding process is used predominantly for plant welding of rails although an in-track welding unit has been developed and evaluated.

Flash-Welding Procedures [6,9,10,15,41,50-60]—In rail plant flash weld-

ing, the rail ends to be welded are cleaned and then polished at the locations of contact with the current-conducting electrodes on the railhead and base. The rails are positioned in the welding machine and held by both vertically and horizontally acting hydraulic clamps in each platen. The rail ends are inclined so that about 1.6 mm (1/16 in.) separates the top of the railhead and each end of the bottom surface of a 914 mm long (36 in. long) straight edge that is centered on the joint. This camber is provided to compensate for the greater thermal contraction that occurs in the railhead relative to the web and base during cooling. Electrode clamps in each platen complete the electrical circuit and are separate from the positioning clamps. The rails are aligned by horizontal or vertical movement of the stationary platen that does not provide longitudinal motion. Some newer machines automatically correct for rail twist to provide accurate alignment of the railhead, web, and base.

During the first step of the welding cycle, which sequences automatically, the movable platen brings the rail ends into contact to permit high current flow; for example, 20 000 to 100 000 A at about 5 to 10 V, which preheats the rail ends. The rails are brought together and separated up to 20 times during the preheating stage, which raises the rail ends to a temperature of 950 to 1100°C (1750 to 2000°F) and flashes off rough points on the rail ends. After the rail reaches the proper temperature, flashing is initiated again by bringing the movable platen and rail forward at a controlled and increasing speed. During the flashing period, which removes from 6 to 25 mm (¼ to about 1 in.) from the end of each rail, high spots on the rail ends contact, are rapidly melted, and the molten globules are expelled from the joint. Atmospheric oxygen is virtually excluded from the joint by molten metal expulsion.

Upon completion of flashing, the movable platen is accelerated so that the rail ends are upset to refusal either with constant platen speed or under impact loading of 530 to 580 kN (60 to 65 tons). A minimum upset of 12.7 mm (0.5 in.) is recommended. The welding current is turned off and the electrodes are released from the rail; but the rail clamping and upsetting forces are maintained at least 10 s while the weld cools sufficiently for safe handling. Monitoring of the welding current, rail movement, and upsetting provide basic quality control.

Depending on the specific flash welding process used, the hot, upset metal can be removed by a shear either at the welding station or at a separate station, 12 m (39 ft) or one rail length beyond the welding station. In some new plants, the shear that is beyond the welding station is positioned by sensing the heat in the weld region. The weld then is finish ground either manually or semiautomatically to produce a smooth profile on the top and sides of the railhead and on the underside of the rail base. In some installations, the rail web also is finish ground. Additional stations at rail length spacings can have facilities for rail straightening and magnetic particle inspection of the completed welds. Flash welds normally are not heat treated. A plant flash weld being made is shown in Fig. 2.

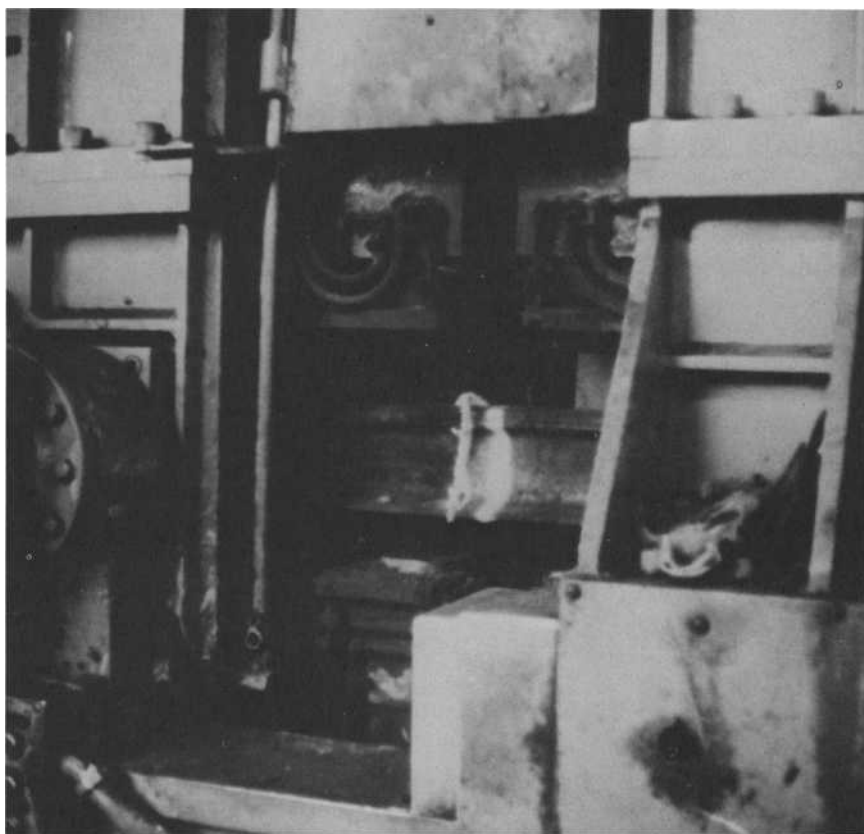


FIG. 2—Plant flash weld showing sheared upset metal pushed off of the hot weld.

Rail end straightness is a significant problem in plant flash welding because, although the central portion of a rail can be straightened by gagging or rolling, these methods are less effective at the rail ends [7,58]. A procedure used by some railroads to avoid the problem of bent rails at the welding plant is to inspect rails for straightness at the steel mill prior to shipment to the welding plant. Variations of rail height and head width also are a problem if final rail grinding is not to consume excessive time. Rail end straightness also is a problem in gas pressure and in-track thermite welding, but this has not been widely reported for these two processes.

Relay rail also is welded at flash welding plants using welding procedures that are essentially the same as for new rail with the addition of dismantling, inspection, and rail end cropping operations. If the rails have been inspected for internal defects in track, this is not required at the welding plant. Cropping of the rail sections, usually 460 mm (18 in.) from each end, can be done automatically.

In some instances, it is not economical to weld relay rail. For secondary lines having low loadings, up to about 71.2 GN (8 million gross tons) per

year, bolted relay rail strings can be transferred directly from main lines. It has been estimated that this method can save \$1500 per mile in comparison with sending the bolted strings through a plant for flash welding [61].

The reported time required for flash welding is in the range of 1 to 2½ min and the welding rate is from about 100 to 160 welds per 8-h shift [54,58–60]. One railroad, using a contractor at a fixed plant and operating two flash welders each 130 h per week produces 2000 acceptable welds per week, 7.7 welds per hour, at a total welding cost of about \$16 per weld. This cost does not include the costs of transporting rail from the steel mill to the welding plant and the costs of transporting welded rail strings to the track site. The cost of the fixed rail welding plant recently built by the Santa Fe Railroad at Amarillo, Texas, was reported to be \$7.9 million, including \$2.7 million for rail loading and unloading units and 4 new rail trains [54]. A contractor's charge for welding rails on a rail train portable plant is \$10 to \$30 per weld depending on the size of the contractor's crew.

In-Track Flash Welding—Flash welding in track has been used in recent years in the United States, Europe, Japan, Italy, Hungary, and the Soviet Union, where the equipment was developed. This unit, which has been used by several railroads in the United States to make about 33 000 welds since 1972, clamps the rails at the rail webs to achieve electrode contact and to transmit the upsetting force to the rails [6,41,62–69]. In some of the work, where bolted rail was converted to CWR, the rail ends were cropped to eliminate batter, bent down ends, and wear from the joint bars. The rails then were aligned both vertically and laterally. The rail ends were elevated to clear the tie plates and to provide camber so that the rail surface would be flat when the weld cooled. The in-track machine flashes continuously during a 3-min automatic welding cycle that is completed by upsetting 13 mm (½ in.), but not to refusal, under a 445 kN (50 ton) force. The weld is held in the upset position while it partially cools. If the rail ends do not butt together closely, they can be manually flashed until arcing reaches the full height of the rail end before the automatic cycle is begun. Upset metal currently is removed from the top and sides of the railhead and from the sides of the rail base. In comparison with plant flash welders, higher operator skill is required, better surface preparation is desirable in order to obtain flashing over the entire joint surface, and the welding time is longer. The in-track welder is shown in Fig. 3.

This unit costs approximately \$500 000 and reportedly is capable of making 8 to 10 welds per hour and 50 to 60 welds in an 8-h shift. In main line track, with about 6½ h actual welding time, the rate has averaged 53 welds; a maximum of 86 welds was recently made in 7 h working time in an 8-h shift. The total cost per weld would be about \$30 for a job requiring 4000 welds. This cost does not include the cost of unspiking, shifting, cropping, and respiking of the rails.

The Soviet in-track flash welder has been used to join long rail strings and to convert conventional bolted rail to continuous-welded rail in track. In the

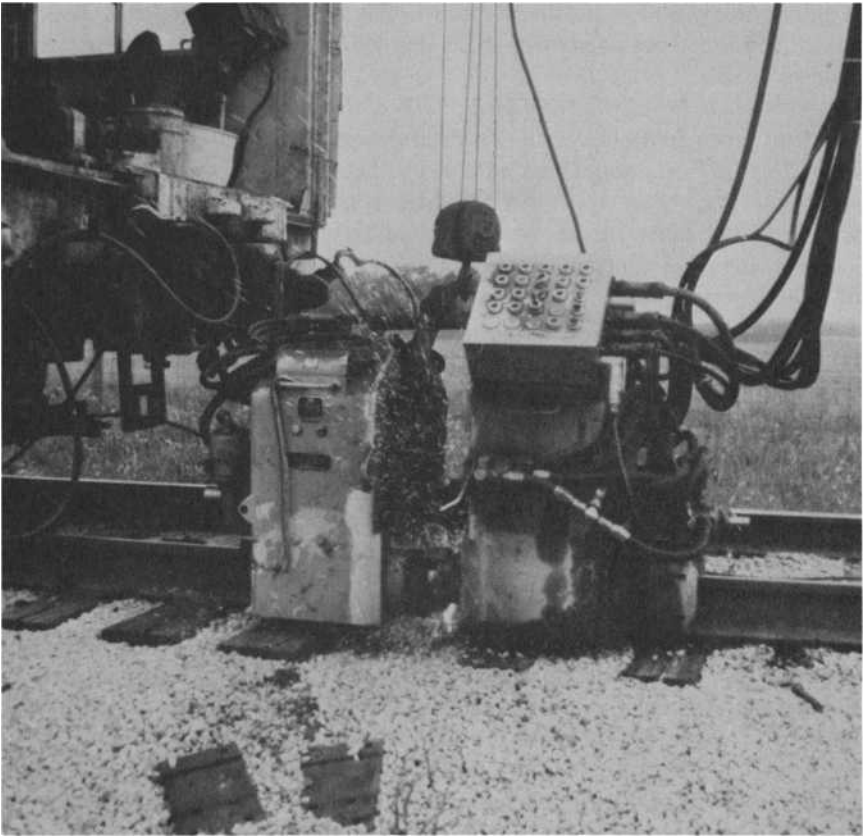


FIG. 3—*In-track flash welder during welding cycle.*

latter application, additional rail sections are added as the gap between the rails, due to cropping and upsetting losses, reaches a convenient length. This unit also has been used to repair sections of continuous-welded rail by removing a short piece and welding in a replacement segment.

The technique used for this in the Soviet Union first involves cutting out a 3-m-long (10-ft-long) piece of rail. A 3.7-m-long (12-ft-long) piece then is welded to the CWR on one end. The CWR on the other side of the short rail is cut so that it overlaps the short rail by 25 mm (1 in.), unspiked for 61 m (200 ft) and bowed laterally so that it contacts the gage side of the opposite rail. During flash welding, ten men lean against the bowed CWR, tending to straighten it, and force the rail to its final position during the forging stage at the end of the welding operation.

Assuming that 460 mm (18 in.) are cropped from each end of a 12-m-long (39-ft-long) bolted rail segment and that each weld is made with 51-mm (2-in.) upset, conversion of each track mile from bolted to welded rail

requires nearly 300 welds and 24 additional pieces of cropped rail. Welding would require three to six 8-h shifts depending on the amount of on-track time available.

Mechanical Properties of Flash-Welded Rails—The results of slow bend tests are given in Refs 41, 42, 70–73 and results of rolling load tests are in Refs 38, 44, 70, and 74. These have been collected and summarized in Ref 3.

Service Performance of Flash-Welded Rail—On the basis of discussions with railroad personnel as well as weld failure statistics given earlier in Table 1, the service performance of flash welds is excellent. The failure rate of 0.0038 service and detected failures per 100 weld years is equivalent to about one failure per 161 km (100 miles) of welded track per year [2]. This failure rate compares favorably with 75.6 rail failures of all types per 161 track km (100 track miles) inspected during 1970, of which 37.5 failures per 161 track km (100 track miles) were web-in-joint failures.

The most common causes cited for flash-weld failures that are associated with the welding process itself, and not the rail steel quality, are electrode burns on the rail base that form brittle martensite on the rail surface and entrapment of oxidized flash particles in the joint. Weld failures occur less frequently due to insufficient grinding that leaves a stress concentration at the upset, hot tearing by straining the weld before it has cooled sufficiently, and formation of surface martensite by excessive grinding. The most common cause for weld rejection at the welding plant is the formation of surface cracks during weld upsetting in rails containing pipe defects, numerous or large inclusions, and segregation [42,46–49,71,75–77]. A second common cause for flash-weld rejection is misalignment, which was discussed previously. Both of these problems can be eliminated by inspecting the rails at the steel mill prior to shipment to the welding plant. Ultrasonic inspection for pipe defects and large inclusions has been found to be very effective in identifying rejectable “A” rails. Defects have been found to extend into “B,” “C,” and even “D” rails.

Although failure statistics have not been obtained, the service performance of the in-track flash welds reportedly has been excellent also. The failures that have occurred have initiated most frequently at the upset, stress concentration on the underside of the rail base.

Gas Pressure Welding

Gas pressure welding is defined [78] as a welding process in which “coalescence is produced simultaneously over the entire area of abutting surfaces, by heating with gas flames obtained from the combustion of a fuel gas with oxygen and by the application of pressure, without the use of filler metal.” Welding occurs in the solid state by grain growth, grain coalescence, and diffusion across the joint interface.

This process for rail welding was first used in the United States in 1939 and was developed to the extent that welds could be made at a lower cost

than that of bolted joints in new rail [4,9]. Because of the longer time required for welding and greater incidence of weld defects, gas pressure welding largely has been replaced by flash butt welding in recent years although gas pressure welding units are still in service [18].

In Japan, where 150 and 200-m long (492 and 656-ft long) rails are produced from 25 and 50-m-long (82 and 164-ft-long) individual rails, both plant gas pressure and flash welding are used. An on-rail, gas pressure welding car was built in Japan but was not considered useful due to its low rate of welding. To overcome a shortage of in-track welding capacity, however, this process was reevaluated, and a welding machine weighing 4450 N (1000 lb) was successfully developed for welding 200-m-long rails in track [15,41]. Details on the operation of this equipment and the performance of the welds were not obtained.

An in-track oxyacetylene gas pressure welder also has been developed in the United States [79,80], but detailed information on its operation and the performance of welded rails has not been obtained.

Gas Pressure Welding Procedures [4,5,10,15,41,78-87]—Although the welding procedures used by railroads differ in some details, the following general procedures have been reported.

Rail ends are prepared by butting the rails together, with the joint slightly elevated, clamping them, and sawing the two ends simultaneously to produce smooth and flat joint surfaces. If welding is not performed shortly after rail end preparation, the surfaces are coated with oil to prevent oxidation. Before welding, the rail ends are cleaned with a suitable solvent, such as carbon tetrachloride. The rails are clamped in the welding machine and an upsetting pressure of 20.7 MPa (3000 psi) over the rail cross-sectional area is applied. Oxyacetylene torches are ignited and oscillated over a 51 mm (2 in.) length to produce uniform heating. Upsetting begins when the rail ends reach about 1100°C (2000°F). When they reach 1230°C (2250°F), the rail steel has softened enough for each rail to move about 9.5 mm (3/8 in.) and produce an upset region. The upset on the railhead is removed by a hydraulic shear on some welders and upset on the web and base are partially removed by cutting torches. At another station, when the rail weld temperature is about 480°C (900°F), it is reheated over about 150 mm (6 in.) to about 840°C (1550°F) with oscillating oxyacetylene torches to normalize the weld. The torches above the rail are directed vertically downward and at 45 deg to the rail length direction so that the softest zones at the ends of the normalized length are gradually contacted by wheel treads. When cool, the rail is ground manually and magnetic particle inspected.

The welding portion of the operation requires 5 to 10 min, depending on the rail size [4,5,87], and normalizing, which is not performed at all facilities, takes an additional 5 min [84]. The welding and normalizing operations can be performed simultaneously at separate stations. In a large welding program, an experienced welding crew can make 40 to 50 welds in an 8-h shift with a welding plant set up at the track site [84]. At a fixed plant using

dual welding and normalizing machines and associated equipment, a rate of 15 finished welds per hour or 120 welds in an 8-h shift has been achieved [4].

For a group of 4078 gas pressure welds made at the track site in 1952 [88], 44.7 man-hours were required per weld including (a) equipping flat cars with rollers, etc. (0.04 man-hours), (b) setting up and dismantling welding equipment (0.08 man-hours), (c) unloading rail (0.24 man-hours), (d) sawing and welding operations (3.53 man-hours), (e) loading welded rail (0.30 man-hours), and (f) employing a watchman (0.28 man-hours). Materials for the sawing and welding operations (\$3.38 per weld) and equipment rental (\$1.01 per weld) would cost about three times as much at the present time as in 1952 or \$13.20 [11]. Assuming an average direct labor rate of \$6 per man-hour, the cost per weld would be about \$40. This does not include indirect costs or the cost of shipping the rail to the welding site.

Mechanical Properties of Gas Pressure-Welded Rails—The results of slow bend and rolling load tests conducted at the Association of American Railroads (AAR) Research Center are given in Refs 38, 39, 71, 74, and 89 and summarized in Ref 3. In comparison with flash welds, the bend test results are somewhat poorer but the rolling load test results are about the same. These gas pressure weld properties generally are better than thermite weld properties.

Service Performance of Gas Pressure-Welded Rails—The service performance of gas pressure welds in rails has been good, as indicated earlier in Table 1. The reported failure rate of welds in new rails during 1970 was close to that of flash welds and about one third of that of gas pressure welds in relay rails.

The most common causes of weld failure appear to be lack of fusion due to insufficient cleaning of the rail ends, lack of parallelism of the joint surfaces, inclusion of mill scale from the rail surface into the interface, insufficient upsetting, and pop out (extinguishing) of the oxyacetylene flame which carburizes the joint surfaces by exposure to excess acetylene [9,42,46,49,76–77]. Using an oxidizing flame rather than a neutral oxyacetylene flame, in order to increase the heating rate and reduce the welding time, also can cause lack of fusion by oxidizing the joint surfaces. As with other welding processes, rail defects, hot tearing, and excessive grinding (which overheats the rails and causes brittle martensite formation) also have been causes of failures. In one instance, a ball of oxidized metal from torch cutting the upset metal adhered to the rail base and provided a stress concentration that was the origin of a failure [49].

Arc Welding

In addition to those processes described previously that are widely used for welding rails, there are several arc welding processes that have been used to a much lesser extent. They include electroslog welding, submerged arc welding, and “enclosed” welding (a shielded metal arc welding technique).

The arc welding processes used for rail welding are reviewed in the following sections.

Electroslag Welding—Electroslag welding is a process in which the electrical resistance of a molten slag held in the joint area furnishes the heat necessary for welding [50,51]. The heat generated melts both the filler metal and the adjacent joint walls. When welding rails, a ceramic or water-cooled copper mold, having essentially the same configuration as the rail, is required to hold the molten slag and filler metal in the joint. The weld is accomplished as the filler metal fills the joint volume from the bottom. The process is used mainly for joining heavy sections. Electroslag welding in its standard form has been used most widely in the Soviet Union for the welding of continuous crane rails [90-92].

In practice, electroslag welding of rails is complicated by the irregular shape of the rail, which makes it difficult to obtain uniform heating without overheating some part of the joint. Also, assembly and dismantling of the mold can be difficult. In spite of these deterrents, successful welds have been made in several sizes of rails. The joints are made without preheating or postheating and require about one man-hour per joint including setup, welding, and finishing.

Electroslag welded crane rails made in the Soviet Union have been shown to have tensile and impact properties equal to or better than those of the unwelded rail. Low-strength, ductile welds with a hardened head area are made by using low-carbon electrode wire for the base and web sections and then adding ferromanganese to the molten metal in the head section. Slightly alloyed welds are made by using different electrode wire compositions and consumable wire guides. There has been no indication that electroslag-welded rails are used anywhere except on crane rails in the Soviet Union.

Combined Submerged Arc and Electroslag Welding—A hybrid process involving the use of both electroslag and submerged arc welding to join rails has evolved from studies of arc welding processes during recent years in Japan. The dual process technique is now referred to as submerged slag welding [15,41,93-95]. This process was developed with the goals of reducing the time required for rail welding and automating the welding process to reduce weld property variability.

In submerged arc welding, the heat for welding is provided by an arc between a bare, consumable metal electrode and the workpiece [50-51]. A layer of granular, fusible flux shields the arc and protects the molten weld metal from atmospheric contamination. The flux also can contain alloying and deoxidizing elements.

This process is applied first to weld the rail base and is followed by the electroslag process to weld the rail web and head. Welding of the entire rail base up to the start of the web requires three passes. Between welding passes, unfused flux and solidified slag are removed from the joint by chipping and wire brushing. When the submerged arc welding is finished, the remainder of the joint is welded using the electroslag welding process. It takes about 30

min to complete a weld by the submerged slag process. No preheat or postweld heat treatments are used.

The ranges of properties of submerged slag rail welds are given in Table 4 along with properties of other types of welds made in Japan with Type 50 rails (102 to 107 lb per yard) [15,41]. The composition of the rail steel is 0.60 to 0.75 percent carbon, 0.70 to 1.10 percent manganese, 0.10 to 0.30 percent silicon, 0.035 maximum percent phosphorus, and 0.040 maximum percent sulfur. Because these results were collected from several sources representing tests performed at different times and places, they show ranges of values and give a rough comparison of the welding processes.

The bending fatigue and static bending properties of submerged slag welds generally are less than those of flash and gas pressure welds but greater than those of thermite welds.

Japan National Railways has constructed a car to make field welds by the submerged slag procedure. This car was used to produce welded rail for two test sites in 1971. Up to the present, only favorable results, based on railhead hardness and profile, have been reported. Refinements of the welding car are being continued by Japan National Railways.

Enclosed-Arc Welding—The enclosed arc welding procedure was developed to adapt shielded metal arc welding to butt joints having large cross-sectional areas [15,41,96,97]. The rails are prepared by cleaning and squaring and then are set with about a 18-mm (0.7-in.) gap. After blocks to retain molten metal are placed around the rail base, the base of the rail is welded by the shielded metal arc process after suitable preheating. Japanese practice involves preheating to about 500°C (930°F), and it is presumed that others also preheat if the particular application and material require it. After the base has been welded, additional blocks are quickly positioned above the rail base and welding is continued. Actual welding time varies with rail size but usually takes less than 1 h. In Japan, postweld tempering at about 700°C (1300°F) for 10 min follows welding.

Enclosed arc rail welding has been practiced widely in Europe, England, and Japan. There are many variations of the same general practice. The success of the procedure depends greatly upon the skill of the welder. The properties of the welds produced are comparable with welds produced in rails by other processes. The Japanese make the comparisons shown in Table 3 for fatigue and bend properties.

During the past eight years, the Swedish Railways have developed shielded metal arc electrodes and enclosed arc welding procedures that result in welds meeting the requirements given below for 490 N/m (101 lb/yd) rails having a nominal ultimate strength of either 786 or 883 MPa (114 or 128 ksi) [98,99]: (a) a fatigue life of 2×10^6 cycles with a load range of 14.7 to 222 kN (3300 to 50 000 lb) with the load applied at the weld, centered in a 1-m span; (b) a minimum bend deflection of 20 mm (0.79 in.) for rails with 883 MPa tensile strength and 24 mm (0.94 in. for rails with 786 MPa tensile strength

TABLE 4—Some results of mechanical tests of welded rails [14].

Property	Weld	Welding Method				Submerged Slag Weld
		Flash Weld	Gas Pressure Weld	Enclosed Arc Weld	Thermite Weld	
Fatigue Strength, rotating bending MPa		227 to 276 290 to 331	283 to 303 331	276	262 to 303 179 to 214	227
Static bending strength ^a	bending strength, HU ^b	1.14 to 1.36	1.19 to 1.34	1.18 to 1.33	0.725 to 0.894	1.08 to 1.14
	MN		1.11 to 1.28		0.970 to 0.983	
	HD ^b	0.970 to 1.16	1.16 to 1.29	0.921 to 1.04	0.832 to 0.930	1.10 to 1.17
	deflection, mm	30 to 97	0.979 to 1.19 25 to 84	28 to 49	0.863 to 0.970 7 to 11	23 to 34
Drop weight strength		13 to 64	23 to 90	15 to 23	17 to 23 9 to 11 11 to 18	29 to 40
	height, m	1.5 to 5.0	2.0 to 3.5 1.0 to 4.0			
	french ^d type	3 to 8 x 5		3 to 8 x 7	2.0 to 3.5 2.5 to 4.0	
	deflection, mm	7 to 69 7 to 57	15 to 53 6 to 74	4 to 50	0.5 to 6.6 4.0 to 9.4	
	french type					

^a1.5-m-long rail is supported with a 1-m (39.4-in) span with the weld in the center. The load is applied with a 127-mm-radius (5-in.-radius) die. The bending strength is the load at fracture and the deflection is that at the center of the span just before fracture.

^bHU = head up. HD = head down.

^cThe span is 914 mm (36 in.) and the tup weighs 8896 N (2000 lb) and has a tip radius of 127 mm (5 in.). The specimen is supported by two springs.

^dThe span is 500 mm (19.7 in.), the tup weighs 3434 N (772 lb), and no springs are used to support the rail. The height of the tup is stepped up at 0.5-m intervals to 4 m (13.1 ft). If the rail does not fracture, the height is increased to 8 m (26.2 ft) in 1-m intervals. If the rail still does not fracture, the test is repeated at 8 m; 8 x 5 means five repetitions at a height of 8 m (26 ft).

with the weld centered in a 1-m span; (c) the same hardness in the upper part of the weld as in the parent rail; (d) high notch toughness.

In the development of welding procedures, which were approved also by the Danish and Norwegian Railways, a fiberglass-covered, baked sand briquette backing was developed to provide a notch-free transition between the weld and the underside of the rail base. In order to improve fatigue properties by reducing residual stresses, the weld is heat treated for about 10 min or at least until the head, web, and base are at a uniform temperature of 590 to 650°C (1100 to 1200°F) over 100 mm (4 in.) on each side of the joint. After this, pads of mineral wool are pressed against the rail web to produce uniform cooling rates. The railhead and sides of the base then are ground to remove any stress concentrations. Although the total time required to complete a rail weld was not given, it is estimated to be about 1.5 h.

Acknowledgments

The preparation of this survey was supported by the U.S. Department of Transportation, Federal Railroad Administration through the Transportation Systems Center, Cambridge, Mass., with R. K. Steele serving as project monitor and capably assisting in the report preparation. Significant technical inputs to this survey were provided by numerous railroads and suppliers of equipment and services. The author appreciates their cooperation and assistance.

References

- [1] "Broken Rails: A Major Cause of Train Accidents," National Transportation Board, Washington, D.C., Special Report NTSB-RSS-74-1, 2 Jan. 1974.
- [2] Bush, R. F., "Rail Failure Statistics," *AREA Proceedings*, Vol. 73, Bulletin 638, 1972.
- [3] Hauser, D., "Methods for Joining of Rails: Survey Report," prepared for the U.S. Dept. of Transportation, Federal Railroad Administration, July 1977, Report No. FRA/ORD-77/16, NTIS No. PB272066AS, available from the National Technical Information Service, Springfield, Va. 22161.
- [4] "Wabash Railroad Proves Economy of Welded Rail," *Welding Engineer*, Vol. 43, No. 2, Feb. 1968, pp. 32-33.
- [5] McKittrick, E. S. and Donalds, W. E., *Welding Journal*, Vol. 38, No. 5, May 1959, pp. 469-474.
- [6] Dick, M. H., *Railway Age*, Vol. 172, June 1972, pp. 34-38.
- [7] "Rail Research and Development," *AREA Proceedings*, American Railway Engineering Association, Vol. 75, Bulletin 644, 1973, pp. 1-38.
- [8] Srinivasan, M., "Continuous Welded Rail," Modern Permanent Way, Somaiya Publications Pvt. Ltd., 20 March 1970.
- [9] Magee, G. M., *Welding Journal*, Vol. 39, Sept. 1960, pp. 881-889.
- [10] Dick, M. H., "Railway Track and Structures Encyclopedia," Simmons Boardman Publishing Corp., New York, 1955.
- [11] Schram, I. H., *AREA Proceedings*, American Railway Engineering Association, Vol. 54, 1953, pp. 1170-1173.
- [12] Myers, E. T., *AREA Proceedings*, American Railway Engineering Association, Vol. 64, Bulletin 577, 1963, pp. 460-463.
- [13] Owen, R. M., *Railway Track and Structures*, Vol. 67, No. 4, 1971, pp. 26-27.
- [14] Dick, M. H. and Dove, R. E., *Railway Age*, Vol. 175, No. 5, 11 March 1974, pp. 16-22.

- [15] Oishibashi, Hirotugu, "Rail Welding Methods," Railway Technical Research Institute, Quarterly Report (Japanese National Railways), Vol. 15, No. 2, 1974, pp. 69-75.
- [16] Dearden, J., *Railway Gazette*, Vol. 121, Feb. 1965, pp. 148-150.
- [17] Jenkins, H. H., Stephenson, J. E., Clayton, G. A., Morland, G. W., and Lyon, D., *Railway Engineering Journal*, Jan. 1974, pp. 2-26.
- [18] *AREA Proceedings*, American Railway Engineering Association, Vol. 73, Bulletin 636, 1972, p. 468.
- [19] *Modern Railroads*, Vol. 29, No. 9, 1974, p. 28.
- [20] Dick, M. H. and Dove, R. E., *Railway Age*, Vol. 175, 11 March, 1974, p. 22.
- [21] "Good Year Seen in 1976 for Welded Rail Programs," *Modern Railroads*, Vol. 30, No. 10, Oct. 1975, p. 19.
- [22] *Welding Handbook*, 6th Edition, Section 3, L. Griffing, Ed., American Welding Society, New York, 1971.
- [23] "Modern Orgotherm Quick Welding Methods," Elektro-Thermite GMBH, Essen, Germany.
- [24] "Calorite—The New Approach to Thermite Welding," AlFex, Inc., St. Jerome, Quebec, Canada.
- [25] "Continuous Welded Rail—Thermite Welding," *AREA Proceedings*, Vol. 68, Bulletin 605, 1967, pp. 398.
- [26] Kannowski, K. H., *AREA Proceedings*, American Railway Engineering Association, Vol. 71, Bulletin 626, 1970, pp. 654-656.
- [27] "Instructions for Thermit Self-Preheat Rail Welding," Thermex Metallurgical Inc., Lakehurst, N.J.
- [28] Kannowski, K. H., *AREA Proceedings*, American Railway Engineering Association, Vol. 69, Bulletin 614, 1968, pp. 914-916.
- [29] Ailes, A. S., *Welding and Metal Fabrication*, Vol. 32, No. 11, Nov. 1964, pp. 414-419.
- [30] *Welding Handbook*, 6th Ed., C. Weisman, Ed., American Welding Society, Section 5, Chapter 89, "Railroads," Miami, Fl., 1973, p. 89.42.
- [31] Ahlert, W., *Schweissen und Schneiden*, Vol. 18, No. 9, 1966, p. 430.
- [32] "Calorite Rail Welding Procedure," AlFex Inc., St. Jerome, Quebec, Canada.
- [33] "Thermite Welding—Rail Joints," Holland Co., Homewood, Ill.
- [34] Clemons, R. E., *Railway Track and Structures*, Vol. 67, Sept. 1971, pp. 28-29.
- [35] "Du-Wel Steel Products Company."
- [36] Dearden, J., *British Welding Journal*, Vol. 15, No. 4, 1968, pp. 158, 169.
- [37] Birmann, F., *Schweissen und Schneiden*, Vol. 24, No. 8, 8 Aug. 1972, pp. 286-290.
- [38] "Continuous Welded Rail—Results of Rolling-Load and Slow-Bend Tests of Butt-Welded Rail Joints," *AREA Proceedings*, American Railway Engineering Association, Vol. 67, Bulletin 598, 1966, pp. 428-437.
- [39] "Rolling-Load and Slow-Bend Test Results of Butt-Welded Rail Joints," *AREA Proceedings*, American Railway Engineering Association, Vol. 68, Bulletin 605, Feb. 1967, pp. 383-396.
- [40] "Rapid Thermit Welding Both With and Without Welding Beads," *Schweissen und Schneiden*, Vol. 15, No. 10, 1963, p. 447.
- [41] Nakamori, Shizuo, "Report on the Survey of Rail Joining Technology in Japan," Mitsubishi Research Institute for Battelle-Columbus Laboratories, Aug. 1974.
- [42] Cramer, R. E., *AREA Proceedings*, American Railway Engineering Association, Vol. 65, Bulletin 584, 1964, pp. 611-614.
- [43] Galbraith, A. H., *AREA Proceedings*, American Railway Engineering Association, Vol. 70, Bulletin 619, 1969, pp. 699-709.
- [44] "AAR Studies of Butt Welded Rail Joints," *AREA Proceedings*, American Railway Engineering Association, Vol. 71, Bulletin 626, 1970, pp. 645-653.
- [45] Case, J. D., *AREA Proceedings*, American Railway Engineering Association, Vol. 72, Bulletin 631, 1971, p. 417.
- [46] "Service and Detected Failures of Butt-Welded Rail Joints," *AREA Proceedings*, American Railway Engineering Association, Vol. 66, Bulletin 591, 1965, pp. 509-513.
- [47] "Continuous Welded Rail Investigation of Service and Detected Butt-Welded Rail Joint Failures," *AREA Proceedings*, American Railway Engineering Association, Vol. 67, Bulletin 598, 1966, pp. 423-428.
- [48] Galbraith, A. H., *AREA Proceedings*, American Railway Engineering Association, Vol. 69, Bulletin 612, Feb. 1968, pp. 574-588.

- [49] Galbraith, A. H., *AREA Proceedings*, American Railway Engineering Association, Vol. 70, Bulletin 619, 1969, pp. 681-698.
- [50] *Welding Handbook*, 6th Ed., A. L. Phillips, Ed., Section 2, 1969.
- [51] *Metals Handbook*, 8th Ed., Vol. 6, "Welding and Brazing," American Society for Metals, Metals Park, Ohio, 1971.
- [52] "Ultramodern Rail-Welding Complex at Nashville," *Railway Track and Structures*, Vol. 67, July 1971, pp. 17-32.
- [53] "Welding a Railroad," *Welding Engineer*, Vol. 56, Nov. 1971, pp. 36-37.
- [54] "Welded Rail All the Way on Santa Fe," *Progressive Railroad*, Vol. 17, No. 9, Sept. 1974, pp. 82-87.
- [55] Gordon, P. H. and Young, W. F., *British Welding Journal*, Vol. 14, No. 12, 1967, p. 619.
- [56] "Continuous Welded Rail—Fabrication," *AREA Proceedings*, American Railway Engineering Association, Vol. 57, 1956, pp. 776-781.
- [57] Galbraith, A. H., *AREA Proceedings*, American Railway Engineering Association, Vol. 67, Bulletin 598, 1966, pp. 420-423.
- [58] Dearden, J., *British Welding Journal*, Vol. 15, No. 4, 1968, pp. 158, 169.
- [59] "Progress in Rail Welding," *Railway Gazette*, Vol. 124, March 1968, pp. 177-179.
- [60] "Flash Butt Welder for Long Welded Rail," A. I. Welders, Ltd., Inverness, Scotland, July, 1974.
- [61] "M/W Probe 1: Close-Up of Policies and Practices, Union Pacific," *Railway Track and Structures*, Vol. 69, No. 6, 1973, pp. 15-38.
- [62] "New Unit Brings Butt Welding to the Track," *Railway Track and Structures*, Vol. 68, March 1972.
- [63] "Machine Welds Rail in Existing Track," *Railway Age*, Vol. 172, 1971, pp. 32.
- [64] Bul'ba, T. C., *Automatic Welding*, Vol. 18, No. 5, May 1965, pp. 55-57.
- [65] Solodovnikov, S. A., Andrybov, L. V., and Eremichev, V. N., *Automatic Welding*, No. 5, May 1971, pp. 60-61.
- [66] "On the Scene with New In-Track Welding Team," *Welding Journal*, Vol. 51, No. 7, 1972, p. 492.
- [67] "Top U.S. Engineers, Researchers, Get Inside Look at Track Practices," *Railway Track and Structures*, Vol. 70, No. 9, Sept. 1974, pp. 20.
- [68] Merz, D. and Winter, H., "Memoranda on Rail Joining Technology in Europe," Battelle Institute-Frankfurt, 30 July 1974.
- [69] Hunziker, R. A., "Welding Continuous Rail In-Track," presented at the 12th Annual Railroad Engineering Conference, sponsored by the U.S. Dept. of Transportation, Federal Railroad Administration, Pueblo, Colo. 22-23 Oct. 1975.
- [70] Cramer, R. E. and Jensen, R. S., *AREA Proceedings*, American Railway Engineering Association, Vol. 55, 1954, pp. 684-694.
- [71] Cramer, R. E., *AREA Proceedings*, American Railway Engineering Association, Vol. 64, Bulletin 577, 1963, pp. 451-459.
- [72] "An Investigation of Welding Used Rail Without Cropping," Association of American Railroads, ER-41, Dec. 1963.
- [73] Kuchuk-Yatsenko, S. I., *Automatic Welding*, April 1961, pp. 28-34.
- [74] Galbraith, A. H., *AREA Proceedings*, American Railway Engineering Association, Vol. 69, Bulletin 612, February 1968, pp. 589-597.
- [75] Wisnowski, M. J. and Magee, G. M., "Metallurgical Examination of Four Electric-Flash Butt Weld Service Failures Submitted by the Florida East Coast Railway," *AREA Proceedings*, American Railway Engineering Association, Vol. 68, Bulletin 605, Feb. 1967, pp. 460-462.
- [76] Kannowski, K. and Magee, G. M., "Investigation of Service and Detected Butt-Welded Rail Joint Failures," *AREA Proceedings*, American Railway Engineering Association, Vol. 68, Bulletin 605, Feb. 1967, pp. 372-383.
- [77] "Investigation of Welded Rails at the AAR Research Center," *AREA Proceedings*, American Railway Engineering Association, Vol. 65, Bulletin 584, 1965, pp. 615-629.
- [78] *Welding Handbook*, A. L. Phillips, Ed., 5th Ed., Section 2, Chapter 22, 1963.
- [79] Bryan, J. F., Jr., "Track Welding System," Trakwork Equipment Company, U.S. Patent 3,726,232, 10 April 1973.
- [80] Bryan, J. F., Jr., "Track Welding System," Trakwork Equipment Company, U.S. Patent 3,802,348, 9 April 1974.

- [81] *Welding Handbook*, C. Weisman, Ed., 6th Ed., Section 5, Chapter 89, 1973.
- [82] Fries, F., *Schweissen und Schneiden*, Vol. 14, No. 6, June 1962, pp. 259-263.
- [83] "New Units Speed Rail Welding," *Iron Age*, Vol. 186, No. 16, 20 Oct. 1960, p. 161.
- [84] Adams, L., *Welding Journal*, Vol. 29, No. 4, April 1950, pp. 283-289.
- [85] Aoyama, S., Kawashima, M., and Hiruma, M., "Propane Gas Pressure Welding of Rails," Railway Technical Research Institute, Quarterly Report (Japanese National Railways), Vol. 7, No. 3, Sept. 1966, p. 23.
- [86] Hastings, D. C., *Welding Journal*, Vol. 34, Nov. 1955, pp. 1065-1069.
- [87] Vladimirkii, T. A., Zharkov, A. F., and Shrylpov, A. K., *Welding Production*, No. 8, Aug. 1960, pp. 36-42.
- [88] Creedle, F. W., *AREA Proceedings*, American Railway Engineering Association, Vol. 54, 1953, pp. 1161-1167.
- [89] Kannowski, K., "Physical Test Results of Oxy-Acetylene Pressure Butt Welds of Heat Treated Rails," Association of American Railroads Report No. ER-8, Feb. 1961.
- [90] Kopetman, L. N. and Mukanaev, Kh.Kh., *Welding Production*, No. 5, May 1967, pp. 32-34.
- [91] Gorozhaninov, N. E., Garyaev, A. L., and Zverev, L. I., *Welding Production*, Vol. 12, No. 9, Sept. 1965, pp. 68-69.
- [92] Svetlopolyanskii, V. I., *Automatic Welding*, Vol. 19, No. 3, March 1966, pp. 58-60.
- [93] Oi, I., Muramoto, T., and Hakamada, S., "Automatic Submerged-Slag Welding of Rails," Railway Technical Research Institute, Quarterly Report (Japanese National Railways), Vol. 7, No. 4, Dec. 1966, pp. 11-12.
- [94] Oshibashi, H., Hakamada, S., Ohara, M., Oi, I., and Muramoto, T., "Automatic Submerged-Slag Welding of Rail," Railway Technical Research Institute, Quarterly Report (Japanese National Railways), Vol. 13, No. 4, Dec. 1972, pp. 235-240.
- [95] Oi, I., Muramoto, T., and Hakamata, S., "Automatic Submerged-Slag Welding of Rails (Report 2)," Railway Technical Research Institute, Quarterly Report (Japanese National Railways), Vol. 8, No. 4, Dec. 1967, pp. 205-209.
- [96] Clevers, J. A. N. and Stemerdink, J. W. A., *Welding Journal*, Vol. 39, March 1960, pp. 223-228.
- [97] Zwirchmayr, Karl, *Schweisstechnik*, Vol. 13, Oct. 1959, pp. 115-117.
- [98] Ljunggren, Jan, *Svetsaren*, No. 2, 1974, pp. 1-5, 8-9.
- [99] Ljunggren, Jan, *Svetsaren*, Vol. 7, No. 1, 1971, pp. 10-16.

Effects of Alloy Additions and Special Processing on Rail Steels

Role of Alloying and Microstructure on the Strength and Toughness of Experimental Rail Steels*

REFERENCE: Bouse, G. K., Bernstein, I. M., and Stone, D. H., "Role of Alloying and Microstructure on the Strength and Toughness of Experimental Rail Steels," *Rail Steels—Developments, Processing, and Use*, ASTM STP 644, D. H. Stone and G. G. Knupps, Eds., American Society for Testing and Materials, 1978, pp. 145–166.

ABSTRACT: Previous studies on eutectoid steel have demonstrated that strength and toughness are essentially independently varying parameters, with the former primarily controlled by the pearlite interlamellar spacing and the latter primarily controlled by the prior austenite grain size. The work has now been extended to study the effect of modest compositional variations on strength and toughness of 17 experimental rail alloys. Carbon, manganese, and silicon levels were varied over ranges to yield eutectoid or hypoeutectoid microstructures. Vanadium was added to some of these compositions, primarily as a grain refiner. These steels were heat treated to produce varying austenite grain sizes and a reasonably constant, fine pearlite spacing. Instrumented impact tests on precracked Charpy bars were performed to determine both the dynamic fracture toughness (K_{Id}), and the Charpy transition temperature. Tensile tests were used to monitor strength and ductility. Mechanical test data were correlated with observed microstructural variations, particularly the austenite grain size and pearlite spacing as well as fractographic studies of the variation of fracture facet size with austenite grain size. These studies led to a general description of the fracture process in such steels.

KEY WORDS: steels, railroad tracks, eutectics, pearlite, lamellar structure, austenite, grain size, fracture properties, crack propagation, impact tests, dynamic tests, toughness, mechanical properties

Within the last 15 years there has been a dramatic change in the transportation practices of American railroads, including higher gross ton miles over prior lighter tonnage lines, and higher average train speeds. Specifically, in the last ten years, the average freight carload has been increased 20 percent. Presently, the railroads are spending more than \$300

*Original experimental data were measured in U.S. customary units.

¹Metallurgist, Steam Turbine Division, General Electric Company, Schenectady, New York.

²Professor of Metallurgy and Materials Science, Carnegie-Mellon University, Pittsburgh, Pa. 15213.

³Manager—Metallurgy, Association of American Railroads Technical Center, Chicago, Ill. 60616.

million annually to correct damages and to maintain existing rail lines.⁴ Such losses have prompted the Association of American Railroads (AAR) to investigate present and future rail material, so that a stronger and tougher rail may be produced at reasonable cost. Since 1972, three programs have been initiated at Carnegie-Mellon University under the auspices of the AAR: structure-property relationships in commercial rail; basic fracture processes in eutectoid (0.8 percent by weight carbon) steel; and structure-property relationships in potential future rail material. The first topic has recently been completed [1],⁵ and the second is currently under active study [2]. This paper deals with the third topic, the evaluation of future rail material.

The first of the studies was performed on U.S. commercial rail which is primarily of a eutectoid composition with a fully pearlitic microstructure. This study successfully identified the thermomechanical processes that affect the strength and toughness of present day commercial rail. The austenitization temperature during hot rolling, the parameter that primarily establishes the prior austenite grain size, controls the Charpy transition temperature, and the cooling rate after austenitization which dictates the pearlite spacing, controls the yield strength. It was thus found that, for commercial rail steel, strength and toughness are essentially independent of one another, and therefore both can be maximized if a low austenitization temperature and fast cooling rate can be employed in rail production.

In the present study, experimental rail steels of a hypoeutectoid composition, containing varying amounts of proeutectoid ferritic were characterized for strength and toughness properties and response to heat treatment. Typical microstructures of one of the experimental alloys are shown in Fig. 1. Such compositions and microstructures are currently being used for rail applications in Europe and Japan, but the more demanding service conditions expected for a U.S. product necessitated an examination of processing schedules to maximize strength and toughness.

Experimental Procedure

Materials

Material for this study came from laboratory heats of 56.7 kg (125 lb), forged and rolled into 32-mm (1.25-in.) -thick plates. The plates were produced in such a manner as to duplicate the deformation in the head of a commercial rail, with rolling reductions on the order of 50 percent. Chemical analyses of these heats are shown in Table 1. To ensure similar levels of the normal residual elements, the procedure known as the split heat technique was used in producing these laboratory heats. More exact details of this study are documented elsewhere [3].

Test specimens were machined from oversized Charpy and tensile blanks,

⁴Association of American Railroads Technical Center, private communication, 1976.

⁵The italic numbers in brackets refer to the list of references appended to this paper.

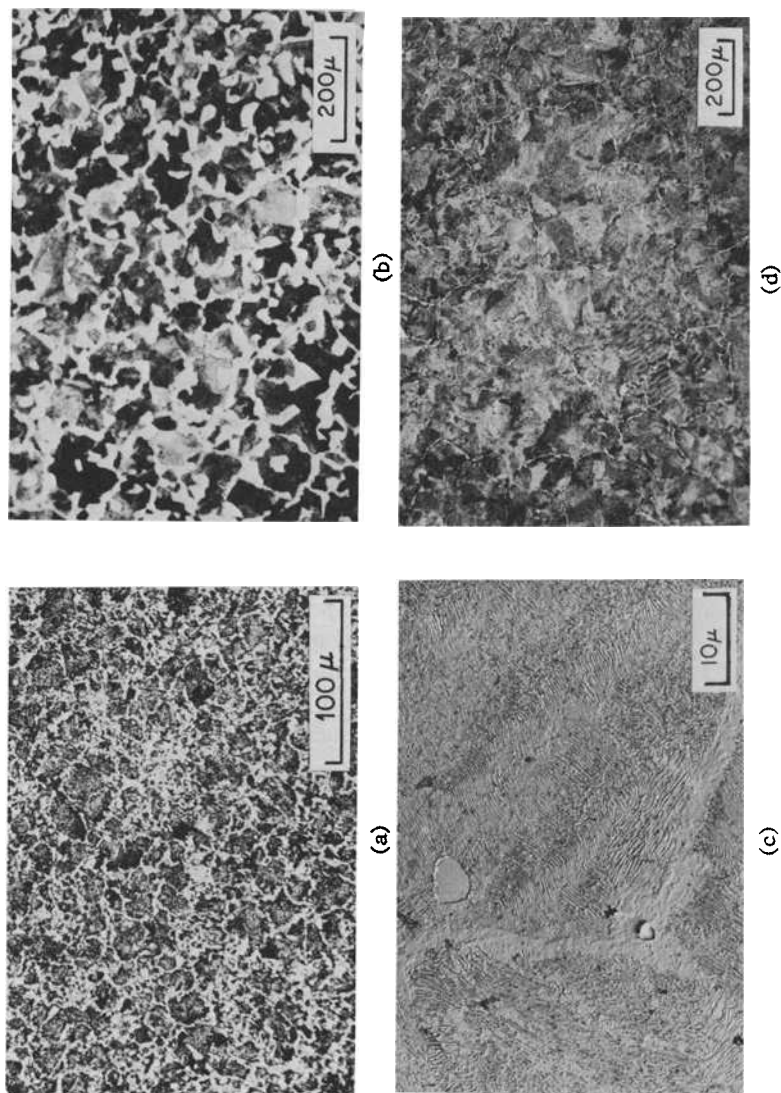


FIG. 1—Microstructures of experimental rail steel, in this case represented by Alloy "I" (0.46C-0.84 Mn-0.64 Si-0.07V). Light areas are proeutectoid ferrite, outlining prior austenite grain boundaries, and dark areas represent pearlite: (a) fine grain size; (b) as-received; (c) austenitized at 1200° C condition (austenitized at 1000° C similar); and (d) carbon replica of the ferrite-pearlite structure.

TABLE 1—*Compositions of experimental rail steel (weight percent of additions)*

Alloy Designation	Carbon	Manganese	Silicon	Vanadium
B	0.56	1.48	0.27	. . .
G	0.41	0.90	0.39	. . .
I	0.46	0.84	0.64	0.07
J	0.45	0.95	0.60	. . .
L	0.44	1.31	0.40	0.08
N	0.66	1.27	0.59	. . .
O	0.44	1.29	0.62	0.08
P	0.44	1.32	0.63	. . .
AREA 133				
16/yd	0.81	0.87	0.17	0.013S 0.018P

NOTE—Other typical elements analyzed include: 0.005 percent phosphorus, 0.023 to 0.032 percent sulfur, 0.05 percent nickel, 0.05 percent chromium.

with the long axis parallel to the rolling direction; the Charpy notch was machined parallel to the plate surface. In all cases, the fracture is expected to propagate in the plane transverse to the rolling direction, a behavior typical of most service failures.

Heat Treatments

Following the results of Hyzak and Bernstein [1], it was decided to vary the toughness systematically, while maintaining an adequate, fairly constant strength level. This procedure was achieved by the use of four heat treatments designed to vary the prior austenite grain size and to hold the pearlite to a nearly constant, fine interlamellar spacing (Table 2). Some variation in pearlite spacing did occur, and the resulting strength changes were monitored. The as-received condition represents the typical American Railway Engineering Association (AREA) control-cooled rail. After a minimum finishing temperature of approximately 1050°C, the commercial

TABLE 2—*Heat treatments.*

Condition	Austenitization Time and Temperature	Isothermal Transformation Time and Temperature
Fine grain size (dual cycle)	900°C, 20 min, oil quench, 800°C, 15 min	550°C, 15 min
As-received	1230°C, 2½ h	finishing temperature 1010 to 1050°C, control cooled
Austenitize 1000°C	1000°C, 45 min	580°C, 15 min
Austenitize 1200°C	1200°C, 60 min	590°C, 15 min

rails are slowly cooled through the transition range (to allow for hydrogen outgassing) to approximately 150°C in no less than 7 h. This results in an austenite grain diameter of approximately 130 μm and a pearlite interlamellar spacing of approximately 1600 Å. To approximate AREA cooling conditions, the experimental alloy plates were buried in vermiculite after rolling and allowed to cool to room temperature. The resulting microstructure exhibited an austenite grain diameter of approximately 65 μm and a pearlite spacing of approximately 2500 Å.

The finest grain size was produced by a thermal cycle treatment similar to that used by Grange [4]. After austenitization, the specimens were isothermally transformed in salt pots; the procedure yielded a grain size of ~ 10 μm and a pearlite spacing of ~ 1800 Å. Two other heat treatments were adopted to extend the data over the grain size range expected in actual commercial rail production. These consisted of austenitization at either 1000 or 1200°C, followed by an isothermal transformation at either 580 or 590°C. The resulting microstructures were characterized by prior austenite grain sizes of ~ 60 and ~ 100 μm , respectively, and interlamellar pearlite spacings of ~ 2000 and ~ 2100 Å, respectively.

Mechanical Testing

Detailed tensile and instrumented precracked Charpy tests were performed on the most promising of the experimental steels. Duplicate room temperature tensile tests were performed on specimens from each heat treatment, using standard ASTM samples with a 6.4 mm (0.252 in.) diameter and a 25.4 mm (1 in.) gage length, and an initial strain rate of 0.01 per minute. The 0.2 percent offset yield strength, ultimate tensile strength, and reduction in area were then determined (Table 3).

For impact tests, standard Charpy V-notch specimens with a fatigue precrack at the root of the notch were tested between temperatures of -46°C and 232°C , using a standard impact machine equipped with an instrumented impact system (Dynatup). Specimens were precracked on a constant deflection precracker (Dynatup); approximately 6 to 8 min was required to create a total crack length of 3.5 to 5.5 mm (0.138 to 0.217 in). The information obtained in these tests, namely the precracked Charpy transition temperature and the dynamic fracture toughness K_{Ia} , is also given in Table 3.

The transition temperature is taken as the value corresponding to a ratio of impact energy to fast fracture area (W/A) of $3.11 \times 10^5 \text{ N/m}^2$ (142 ft·lb/in.²). This represents a value approximately one half the distance between the upper and lower shelf energy, a frequently used measure of the transition temperature [5].

Dynamic fracture toughness values were obtained for tests at -18°C , using a stress intensity rate, \dot{K} , of 3.0 to $5.5 \times 10^5 \text{ N/m}^{3/2} \text{ s}$). These tests, as shall be discussed, have been found to be very sensitive indicators of the role

TABLE 3—*Mechanical properties of experimental rail alloys.*

Alloy	Condition	σ_{ys} (ksi)	σ_{uts} (ksi)	Reduction in area, %	Charpy Transition Temperature, °C	K_{Id} (ksi $\sqrt{\text{in.}}$)
B	fine grain size as-received	95.5	143.7	58.8	52	38
		56.1	115.7	20.7	130	23
G	fine grain size as received	73.5	109.2	62.2	-19	63
		42.6	87.8	39.0	46	31
	austenitize 1000° C	69.2	113.7	53.2	43	35
	austenitize 1200° C	57.8	107.0	45.6	50	29
I	fine grain size as received	85.7	120.4	59.6	-25	63
		60.4	108.8	35.4	106	31
	austenitize 1000° C	87.5	137.5	45.8	103	29
	austenitize 1200° C	85.1	134.9	34.9	108	28
J	fine grain size as received	80.9	121.5	58.2	12	55
		54.3	112.0	35.7	92	30
	austenitize 1000° C	76.1	121.2	56.9	28	50
	austenitize 1200° C	58.4	114.2	40.3	64	28
L	fine grain size as-received	87.7	122.9	60.8	9	44
		63.4	113.1	30.6	148	31
	austenitize 1000° C	94.5	139.4	48.7	110	28
	austenitize 1200° C	85.6	133.6	32.8	121	28
N	fine grain size as-received	100.9	153.9	53.1	108	33
		60.7	126.8	17.1	200	25
O	fine grain size as-received	99.5	132.9	58.2	10	45
		72.0	121.6	36.8	145	28
	austenitize 1000° C	98.2	140.6	49.0	106	30
	austenitize 1200° C	89.2	133.3	37.5	122	25
P	fine grain size as-received	87.4	127.8	62.4	7	62
		55.6	110.0	36.7	100	28
	austenitize 1000° C	80.6	129.8	44.0	70	30
	austenitize 1200° C	69.4	120.6	29.7	100	30

Conversion factors—

$$1 \text{ ksi} = 6.89 \text{ MN/m}^2 = 6.89 \text{ MPa}$$

$$1 \text{ ksi } \sqrt{\text{in.}} = 1.1 \text{ MN/m}^{3/2}$$

of microstructure on fracture toughness, providing a quantitative measure of both the toughness and the crack sensitivity of a specific steel.

Quantitative Metallographic Techniques

Microstructural parameters measured in this study included the austenite grain diameter, the fracture facet diameter, the pearlite interlamellar spac-

ing, and the pearlite colony diameter (Table 4). The latter two quantities were measured on two-stage carbon replicas, while optical microscopy was used to obtain the rest of the parameters. For quantitative metallography, the specimens were etched in 4 percent picral, although other etching techniques [4,6] were used to obtain the austenite grain size. Four samples of each condition were used, and the large number of readings were statistically weight averaged; the results have a standard deviation of about ± 5 percent.

Measurement of the pearlite interlamellar spacing was performed using a technique similar to Brown and Ridley [7]. Secants were drawn perpendicular to the finest spacing observed, being careful to avoid areas near the proeutectoid ferrite where carbon concentration gradients can influence spacing measurements. This method is most likely to project the true interlamellar spacing [1]. Measurement of the austenite grain diameter and pearlite colony diameter was achieved using standard linear intercept techniques (ASTM Method for Estimating the Average Grain Size of Metals (E 112-74)). It should be noted that, due to the uncertainty on how to precisely convert the intercept value to the true grain diameter (ASTM Method E 112-74, [8]), all correlations between mechanical properties and microstructural parameters are based on the linear intercept distance and

TABLE 4—Microstructural parameters of experimental rail alloys.

Alloy	Condition	Pearlite ^a Spacing (Å)	Pearlite ^b Colony Dia. (μm)	Austenite ^b Grain Dia. (μm)	Facet ^b Size (μm)
I	fine grain size	1846	4.4	9.4	...
	as-received	2277	7.8	67.1	86.9
	austenitize 1000	2092	6.0	61.4	51.2
	austenitize 1200	2185	8.3	132.8	94.3
J	fine grain size	1876	5.0	12.9	7.5
	as-received	2588	11.1	79.2	96.0
	austenitize 1000	2219	5.3	23.6	46.0
	austenitize 1200	2671	7.0	135.5	95.8
O	fine grain size	1791	3.4	8.9	9.4
	as-received	2729	8.7	65.9	78.7
	austenitize 1000	1852	5.1	71.9	101.0
	austenitize 1200	2163	6.6	122.2	129.0
P	fine grain size	1180	2.5	10.9	8.0
	as-received	2063	8.6	70.8	119.3
	austenitize 1000	1679	6.3	53.4	57.4
	austenitize 1200	1945	7.2	108.4	96.3
B	fine grain size	1608	6.4	21.7	31.4
	as-received	2649	13.2	68.2	137.1

^aMinimum pearlite spacing.

^bMean linear intercept distance.

not the true grain diameter. This does not affect the results, since comparisons were only made between parameters obtained in the same way.

The fracture facet size was measured on nickel-plated cross sections of fracture surfaces, fractured at -46°C . The length of each uninterrupted cleavage plane was measured and averaged to provide the fracture facet diameter. Measured by this method, the fracture facet diameter is also represented by the linear intercept distance.

Experimental Results

Initially, 17 heats in the as-received condition were evaluated using limited tensile and instrumented impact tests. These results were used to select the nine most promising alloys to receive more intense investigation. Based on their response to heat treatment, five alloys were further selected for detailed microstructural characterization. These five alloys are the only ones that will be discussed in depth.

Microstructural Effects on Mechanical Properties

Results from the investigation on rail steel [1], as well as other studies of structure-property relationships in pearlitic steel [9,10], suggest that the pearlite interlamellar spacing and the prior austenite grain size are the main parameters controlling yield strength and toughness, respectively.

The results of this study lend further support to this conclusion. However, because of compositional variations between alloys and the fact that most of these steels are ferrite-pearlite aggregates with the ferrite normally present in envelopes surrounding the prior austenite grains, scatterbands rather than single-value relationships characterize the supporting data. The following sections will examine the role of pearlite interlamellar spacing, pearlite colony diameter, austenite grain diameter, and fracture facet size on the average mechanical properties of the five alloys.

Pearlite Interlamellar Spacing—With regard to pearlite spacing (S), for the limited range obtained in this study, decreasing the spacing increases the yield strength and does so as a function of $S^{-1/2}$ (Fig. 2). In general, the data follow the Hall-Petch relationship

$$\sigma_{\text{yield strength}} = \sigma_i + k_f S^{-1/2}$$

where

σ_i = friction stress required for dislocations to move through the lattice,
and

k_f = Hall-Petch slope.

Values of σ_i and k_f obtained in this study for nonvanadium steels are -342 MN/m^2 and $0.381 \text{ MN/m}^{3/2}$, respectively, and for the vanadium steels -313 MN/m^2 and $0.436 \text{ MN/m}^{3/2}$, respectively. Karlsson and Linden [11]

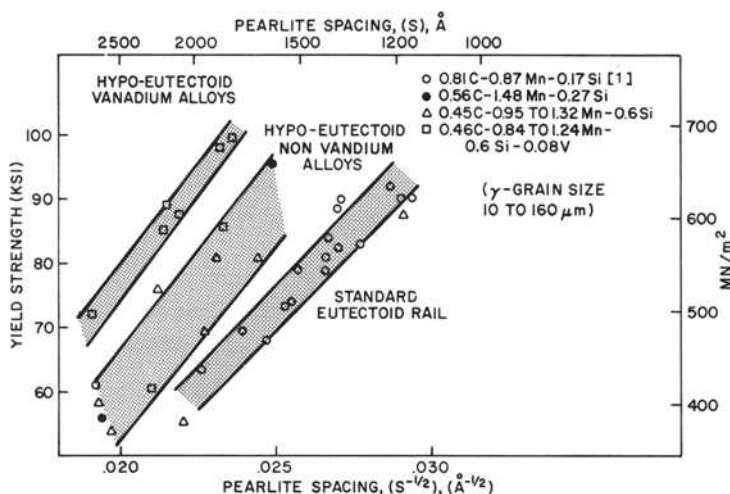


FIG. 2.—Yield strength as a function of the pearlite interlamellar spacing for eutectoid and hypoeutectoid steels.

have summarized existing data for eutectoid steels and suggest a best mean value for k_y at the yield stress of $0.25 \text{ MN/m}^{3/2}$. Apparently, additions of manganese, silicon, and vanadium all help to increase the Hall-Petch slope of the primarily pearlite microstructure. Although negative values for σ_i are inconsistent with definitions of the friction stress, they have been reported elsewhere [1,12–14] and are presented here for comparison purposes only.

As the carbon content decreases, the alloy microstructure becomes a ferritic-pearlitic mixture, and the pearlite can become contained in isolated grains often surrounded by ferrite grains. When this occurs, the dependence of strength on the pearlite spacing drops rapidly.

In the regression analysis of Gladman et al [9] on a variety of carbon steels, the effects of ferrite and pearlite fraction, manganese, silicon, and nitrogen content, and the grain size were examined; a similar k_y value to that found here was obtained, although they found a positive value of the friction stress. The more limited range of microstructure and composition in this study may explain why our results differ in detail from that of Gladman et al [9]. In any event, one of the major conclusions of this study, that when the structure is predominantly pearlite, the strength is dependent almost entirely on the pearlite spacing, is not in question.

Pearlite Colony Size—The results of both this study and that of Hyzak and Bernstein [1] support the conclusion that the effect of colony size on the fracture process is small. The majority of colonies present are contained within a prior austenite grain boundary, although this is not generally the case, as we and others [15] have observed. As first observed by Turkalo [16], while the fracture path can change direction at a colony boundary, it often

continues as a single cleavage facet across a number of pearlite colonies extending over part or, in many cases, one or more prior austenite grain boundaries. Since large changes in grain size accompanied by only modest changes in colony size nevertheless promote large changes in fracture toughness, as discussed later, the colony boundaries in general cannot act as primary barriers to crack growth. Hyzak and Bernstein [1] did find, however, that the statistical fit of regression equations describing the dependence of the Charpy transition temperature on austenite grain size increased at the 10 percent significance level by retaining the term for the pearlite colony size. It is thus suggested that, while the pearlite colony can affect, it does not control the fracture process. A possible reason for its contribution will be considered in a later section.

Prior Austenite Grain Size—Refining the grain size is beneficial in low-carbon steel by promoting an increasing yield strength and a reduction in the Charpy transition temperature [10,17]. For low-carbon steels, the ferrite grain size controls the strength and toughness. In the hypoeutectoid alloys of this study, however, the ferrite is confined to a grain boundary network and, in this condition, has been found to be a minor factor in the control of strength or toughness. Instead, the prior austenite grain size, d , the controlling parameter of the fracture facet unit size (see following) (Fig. 3), has been found to exercise primary control over the toughness of these rail steels. To illustrate, Fig. 4 shows a well-obeyed relationship between the austenite grain size (expressed as $d^{-1/2}$) and the Charpy transition temp-

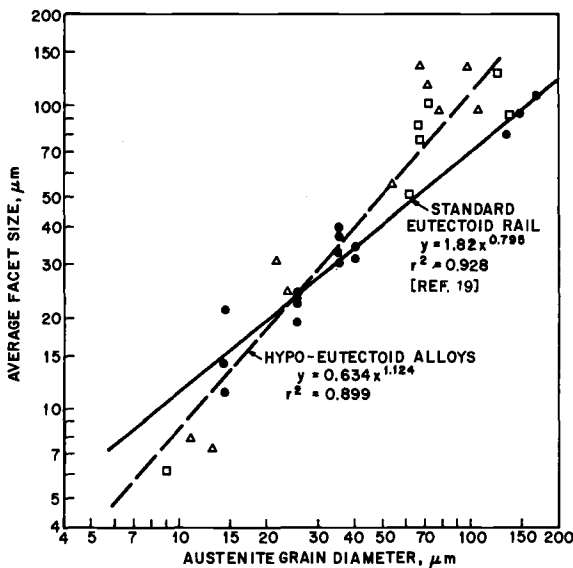


FIG. 3—The fracture facet size as a function of the prior austenite grain size for eutectoid and hypoeutectoid steels.

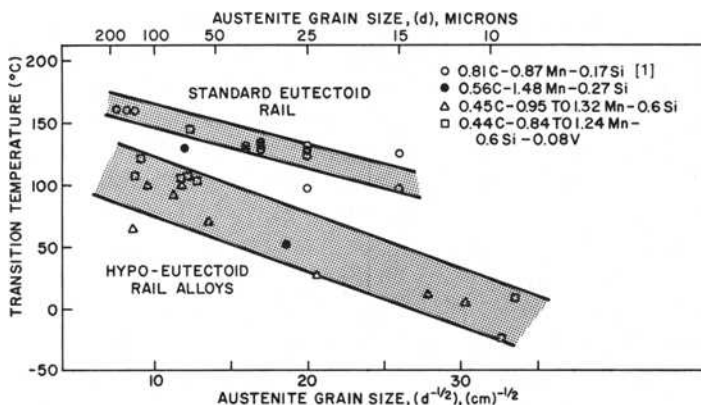


FIG. 4—Charpy transition temperature as a function of the prior austenite grain size for eutectoid and hypoeutectoid steels.

erature, with the scatter due to omission of the minor roles of pearlite colony size and to slight composition variations.

When compared to the existing rail steel, all of the experimental materials evaluated have superior toughness; in general, the nonvanadium steels have the best toughness of all. Equally important, these improvements in toughness have been achieved with either no loss or an actual increase in strength (Table 3, Fig. 2).

Fracture Facet Size—Another and perhaps more direct way to demonstrate which microstructural parameter controls toughness is to measure the fracture facet size and relate it to the microstructure. This type of quantitative metallography is not often reported, the earliest significant work being done by Low [18], and later by Turkalo [16], and most recently by Bernstein et al [19]. In our hypoeutectoid rail alloys, it was found that the fracture facet size was controlled by and was approximately 12 percent larger than the prior austenite grain size (Fig. 3). On the other hand, Bernstein et al [19] found that the facet size in fully eutectoid carbon steel was approximately 21 percent smaller than the prior austenite grain size. Such differences may be due to either the presence of proeutectoid ferrite in the microstructure or to differences in composition. Further work is needed, however, before a conclusion on the slope difference can be made. In any event, in both cases, the austenite grain size controls the facet size, which in turn controls fracture toughness. As discussed elsewhere [1,19], the facet unit has been identified as a region of constant ferrite orientation, whose size changes with the austenite grain size and, to a much smaller extent, with the pearlite colony size.

Compositional Effects on Mechanical Properties

In these experimental rail steels, the total alloy content was kept to a low level; the carbon equivalent (CE) rarely exceeded 0.75 [$CE = C + Mn/6$

+ (Cr + Mo + V)/5 + (Ni + Cu)/15]. In order to regain the strength lost by the reduction of carbon content, traditional solid solution strengtheners, such as manganese and silicon, were added. Vanadium was also added in a few instances to provide strength and grain refinement either from solid solution strengthening or from the precipitation of vanadium carbide and vanadium nitride [20]. In the following sections, we examine the independent role of each of these solutes.

Vanadium—An addition of about 0.08 percent by weight vanadium increased the yield strength about 20 percent over nonvanadium alloys of the same composition, making 85 to 100 ksi a very realistic goal for the yield strength of future rail steels. It is believed that vanadium contributed to the strength in these alloys primarily by solid solution strengthening, since thin foil electron microscopy of Alloy "I" (0.46 percent carbon-0.84 percent manganese-0.64 percent silicon-0.07 percent vanadium) showed that the only precipitates observed were randomly spaced, 50 to 250 Å in diameter, and this only for the as-received, slow-cooled condition. No precipitate row formations were visible in this structure, as is often the case in vanadium-bearing steels [21–23] where these provide the major strength contribution. Their absence in our alloys suggests that, for these high-carbon steels, the nose of the *T-T-T* (time-temperature-transformation) curve for the start of the precipitation reaction was missed even for isothermally transformed specimens.

The addition of vanadium also produces the undesirable effect of increasing the Charpy transition temperature. This, we believe, is due to an undesirable rolling texture. Upon observing the fracture facets, it was noted that there was minimal angular difference between the cleavage facets of neighboring grains. This would allow the crack to propagate more easily, since it would not have to expend considerable extra energy to change direction, as with untextured material. Comparing the texture between Alloys "I" and "J" (0.45 percent carbon-0.95 percent manganese-0.60 percent silicon) obtained by X-ray diffractometry, it was found that the vanadium Alloy "I" contained an approximately 25 percent greater texture in the [110] direction than did "J". The remaining alloys were not examined for texture, although Alloys "L" and "O" behaved similarly in impact testing. Further experiments are needed to examine if or why a strong [110] texture degrades toughness.

Silicon and Manganese—Both silicon and manganese are well-known solid solution strengtheners of ferrite [24]. Additionally, manganese can also reduce both the interlamellar spacing of pearlite and the austenite grain size [9], both of which can be beneficial to strength and toughness.

Comparing Alloys "J" (0.45 percent Carbon-0.95 percent manganese-0.60 percent silicon) and "G" (0.41 percent carbon-0.90 percent manganese-0.39 percent silicon), the silicon addition of ~0.20 percent increased the yield strength from approximately 61 to 67 ksi, or about 10 percent. Silicon had a slight detrimental effect on the toughness, increasing the precracked Charpy

transition temperature about 1°C per 0.01 percent by weight silicon addition. When toughness was measured by dynamic fracture toughness, silicon had no obvious effect.

Comparing Alloys "J" and "P" (0.44 percent carbon-1.32 percent manganese-0.63 percent silicon), the manganese addition of ~0.35 increased strength from approximately 67 to 73 ksi, or about 67 percent. Our data show that manganese slightly reduces the prior austenite grain size. However, due to the deleterious effect of an increasing volume percent pearlite on toughness [9], the precracked Charpy transition temperature increased about 0.6°C per 0.01 percent by weight. As with silicon, manganese had virtually no effect on K_{Id} .

Effect of Fracture Toughness on Alloy Design

In fatigue-precracked Charpy specimens, the measured energy absorbed is due mainly to the propagation of a preexisting crack to fracture. As we have discussed, this propagation energy is very sensitive to the microstructure. As shown in Table 3 and Fig. 4, W/A values are difficult to use directly for the calculation of critical flaw sizes in design applications. A more meaningful parameter is the dynamic fracture toughness, K_{Id} . Because K_{Id} is a plane-strain material condition, only values on the lower energy shelf of the W/A curves were considered valid, although the entire transition curve was determined [3]. The reported value of K_{Id} was taken at -18°C, at a stress intensity rate (\dot{K}) of 3.0 to 5.5×10^5 N/m^{3/2}s (3.0 to 4.0×10^5 ksi $\sqrt{\text{in.s}}$).

For standard Charpy dimensions and the type of loading used in this study [25]

$$K_{Id} = 38.7 Y(P_F)a^{1/2} \quad (1)$$

where

Y = function of a/W ,

P_F = load at fracture before general yield (lb),

a = total crack length (in.), and

W = specimen width (in.).

Once K_{Id} and the axle loads to be encountered on rail lines are known, calculations of the critical flaw size for failures at given temperatures can be found by

$$a_{\text{critical}} = \frac{K_{Id}^2}{(\sigma_{\text{service}})^2} \cdot 2 \cdot \frac{1}{\pi} \cdot g \quad (2)$$

where g is a complex size/geometry factor, dependent on the exact state of stress at the crack tip. This is not known to any great precision for the varying loading conditions on rails. However, on a comparative basis, an apparent increase in allowable flaw size can be used as a predictive tool,

particularly in the area of nondestructive testing. For example, for the best experimental steels "G" and "I" at $69 \text{ MN/m}^{3/2}$ ($63 \text{ ksi } \sqrt{\text{in.}}$) (-18°C) with a realistic service load of 138 MPa (20 ksi), an elliptical surface flaw of 79.8 mm (3.16 in.) can be tolerated. This represents a tenfold increase in the critical flaw size from those in existing rail whose K_{Ia} is approximately $22 \text{ MN/m}^{3/2}$ ($20 \text{ ksi } \sqrt{\text{in.}}$) (-18°C). While this of course is only an estimate based on a surface crack in an infinite plate, it clearly describes a product better able to tolerate flaws and thus one more likely to retain its integrity between inspection periods.

It should be mentioned that controversy exists over the calculation of K_{Ia} from data obtained on specimens fractured after general yielding (not the case at -18°C). The lower bound equivalent energy approach can be used, however, to obtain quite reliable K_{Ia} curves as a function of temperature, as we have done elsewhere [3]. In this technique, if fracture occurs after general yielding, the maximum load, P_F , is converted to new P_F obtained by extrapolation of the elastic region of the load time plot to the time at maximum loading. The operating assumption is that, if the specimen were of valid size for plane strain, a linear elastic type fracture would have occurred [26]. This new lower bound P_F corrected for machine compliance is the value used in Eq 1.

Discussion

The study on standard rail material indicated that higher strength and toughness could be achieved by modifying existing rolling and cooling schedules. However, in practice, existing equipment and constraints on cooling rates make it difficult to only use changes in mill practice to improve rail microstructure, particularly if the improvements are not dramatic. In contrast, the experimental steels having the optimum structure described in this study may not require large changes in finishing procedures. With regard to increased toughness, reducing the grain size or the carbon content or both are two preferred methods. This can be achieved by a lowering of the finishing temperature to at least 1000°C or by a reduction of the carbon content to 0.45 percent.

Considering the latter approach, carbon is the main strengthening element in rail steel, and any reduction would lower the yield strength and perhaps affect wearability. Solid solution or precipitate strengthening would then have to be used to offset this loss in strength. Ideally, such elements should have both a minimal effect on toughness and on the capacity to refine the grain size during hot rolling.

Manganese and silicon were chosen as the two main elements to regain this lost strength. Neither element is seriously detrimental to toughness. If, for example, a high manganese (1.35 percent by weight) and high silicon (0.65 percent by weight) content was used in a 0.45C steel, this material would have an average Charpy transition temperature of 70°C , compared to

30°C for low-manganese (0.90 percent by weight) and low-silicon (0.39 percent by weight) grades. Since the Charpy transition temperature for standard eutectoid rail is $\sim 160^\circ\text{C}$, a substantial benefit in toughness can be achieved, while maintaining an average yield strength of either 79 ksi (high manganese, silicon) or 66.8 ksi (low manganese, silicon) in the heat-treated condition. Whether such grades would have adequate wearability is not yet known.

Vanadium was added because of its potential to refine the grain size during hot rolling and to increase strength. While the strengthening effect has been achieved, vanadium additions did not lead to a refinement of the austenite grain size, probably due to the fact that vanadium precipitates were not formed in sufficient numbers. Studies of precipitation kinetics are needed in medium- to high-carbon steels before the usefulness of vanadium as an alloying addition can be assessed.

In summary, it has been shown that benefits in both yield strength and fracture toughness can be achieved by alloying and microstructural control. For strengthening, specific solute changes in conjunction with an increased cooling rate produced yield strengths near 100 ksi. For toughness, reducing the carbon content and hot rolling at a lower finishing temperature reduced the Charpy transition temperature to as low as -25°C . The most significant aspect of these results, as with the fully eutectoid steels [1], is that strength and toughness are nearly independent of one another, and therefore both can be maximized.

Conclusions

1. Because the steels examined in this study are hypoeutectoid in nature, two factors control the strength: the pearlite spacing and the amount of proeutectoid ferrite. Upon initial yielding, the proeutectoid ferrite, having a lower yield strength and work hardening rate [12], will deform first. Since the small amount of this phase present in most of the alloys studied cannot support the imposed strain, the strength rapidly becomes fully dependent upon the interlamellar spacing. The strength of such steels can thus be increased in at least three ways: solid solution strengthening of the ferrite, the formation of fine precipitates in the proeutectoid ferrite, and refining the pearlite interlamellar spacing. The latter effect dominates in the current steels examined because of their relatively low percentage of free ferrite.

2. Toughness of these steels is controlled by the carbon content and the prior austenite grain size. As the carbon content is reduced, toughness is increased but with a loss in strength. For a given composition, additional toughness can be gained by refining the austenite grain size. Maximum toughness is achieved when the austenite grain size is small and the proeutectoid ferrite has formed a continuous grain boundary network, in which form it is an effective crack blunter.

3. Manganese and silicon strengthen by solid solution hardening. Their

effect on toughness is minimal in the composition ranges studied. Next to vanadium, silicon is the most effective strengthener.

4. Vanadium additions show great potential for improving strength, both in solid solution and as a precipitate. As a grain refiner, its potential has not been realized in this study, since, for the compositions examined, grain growth was not restricted. Further, vanadium appears to lead to an undesirable retained texture. Based on the limited results of this study, vanadium cannot be recommended as an alloy addition.

5. Fracture toughness studies on heat-treated alloys have shown that the critical crack size can be increased by approximately an order of magnitude over existing rail steel, while maintaining or exceeding current strength levels.

6. The effective fracture unit in these hypoeutectoid rail steels is controlled by the prior austenite grain size. It is suggested that a small percentage of preferentially oriented pearlite colonies, perhaps associated with proeutectoid ferrite, near austenite grain boundaries can slightly increase the fracture facet size over that of the grain size. Although a sharp texture may not affect the size of the fracture unit, it does promote closer crystallographic alignment of adjoining cleavage planes leading to crack propagation with less absorption of energy and a corresponding increase in Charpy transition temperature.

Recommendations and Future Research

This study has shown that superior rail properties can be achieved through thermomechanical processing and composition control. The recommended thermomechanical processing is a finishing hot-rolling temperature no higher than 1000°C and a low temperature transformation near 550°C. Thus, in actual mill practice, any lowering of the finishing temperature or increase of the cooling rate will prove beneficial.

The optimum composition for rail steel is still not yet known. Lowering the carbon content to 0.45 percent by weight is desirable from a toughness standpoint. Manganese at 1.35 percent by weight and silicon at 0.60 percent by weight can be tolerated in terms of toughness; when combined, they should give the necessary strength and hardenability required for heavy duty rail service. Wearability effects must be established.

Vanadium, in combination with the heat treatment and alloy contents studied, does not perform to the expected standards, although it has the capability to both increase strength and toughness.

Acknowledgments

The authors would like to acknowledge the generous support of the Association of American Railroads, the National Science Foundation, and the Processing Research Institute of Carnegie-Mellon University, all of

whom sponsored this research. The authors would also like to thank J. M. Hyzak (now at the Air Force Materials Laboratory, Dayton, Ohio) for a smooth transition between this project and the previous AAR-sponsored research. Thanks should also go to Yong-Jin Park whose valuable input during many discussions is greatly appreciated, and to R. H. Van Stone, General Electric Co., who contributed toward the final preparation of this manuscript. The results presented herein were part of a final report, submitted by G. K. Bouse, in partial fulfillment of the requirements for the degree of Master of Engineering at Carnegie-Mellon University.

References

- [1] Hyzak, J. M. and Bernstein, I. M., *Metallurgical Transactions*, Vol. 7A, 1976, p. 1217.
- [2] Park, Y.-J., Ph.D. thesis, Department of Metallurgy and Materials Science, Carnegie-Mellon University, Pittsburgh, Pa., 1977.
- [3] Bouse, G. K. and Bernstein, I. M., "Processing Research Institute Report Number 76-155," Carnegie-Mellon University, Schenley Park, Pittsburgh Pa.
- [4] Grange, R. A., *Metallurgical Transactions*, Vol. 2, 1971, p. 65.
- [5] Dieter, G. E., *Mechanical Metallurgy*, McGraw-Hill, 1961, p. 370.
- [6] Barraclough, *Metallography*, Vol. 6, 1973, p. 473.
- [7] Brown, D. and Ridley, R., *Journal of the Iron and Steel Institute*, Vol. 24, 1966, p. 812.
- [8] Thompson, A. W., *Metallography*, Vol. 5, 1972, p. 366.
- [9] Gladman, T., McIvor, I., and Pickering, F., *Journal of the Iron and Steel Institute*, Vol. 210, 1972, p. 916.
- [10] Burns, K. W. and Pickering, F. B., *Journal of the Iron and Steel Institute*, Vol. 202, 1964, p. 899.
- [11] Karlsson, B. and Linden, G., *Materials Science and Engineering*, Vol. 17, 1975, p. 153.
- [12] Takahashi, T. and Nagumo, M., *Transactions of the Japan Institute for Metals*, Vol. 11, 1970, p. 113.
- [13] Gensamer, M., Pearsall, E. B., Pellini, W. S., and Low, J. R., Jr., *Transactions, American Society for Metals*, Vol. 30, 1942, p. 983.
- [14] Marder, A. R. and Bramfitt, B. L., *Metallurgical Transactions*, Vol. 7A, 1976, p. 365.
- [15] Rathenau, G. W. and Bass, G., *Acta Metallurgica*, Vol. 2, 1954, p. 875.
- [16] Turkalo, A., *Transactions of the American Institute of Mining, Metallurgical, and Petroleum Engineers*, Vol. 218, 1960, p. 24.
- [17] Rosenfield, A. R., Hahn, G. T., and Embury, J. D., *Metallurgical Transactions*, Vol. 3, 1972, p. 2797.
- [18] Low, J. R., Jr., *Fracture*, B. L. Auerbach, M. Cohen, and G. T. Hahn, Eds., Wiley, New York, 1959, p. 68.
- [19] Bernstein, I. M., Park, Y.-J., Bouse, G. K., Hyzak, J. M., and Stone, D. H., *Proceedings of Fourth International Conference on the Strength of Metals and Alloys*, 1976, p. 587.
- [20] Korchynsky, M. and Stuart, H., *Symposium on Low-Alloy, High-Strength Steels*, Nuremberg, 1970, p. 17.
- [21] Batte, A. D. and Honeycombe, R. W. K., *Metal Science Journal*, Vol. 7, 1973, p. 160.
- [22] Davenport, A. T., Brossard, L. C., and Miller, R. E., *Journal of Metals*, Vol. 27, June 1975, p. 21.
- [23] Woodhead, J. H. and Webster, D., *Journal of the Iron and Steel Institute*, Vol. 207, 1969, p. 51.
- [24] *The Making, Shaping, and Treating of Steel*, 9th ed., U.S. Steel Corporation, Herbig and Held, Pittsburgh, Pa. 1971, p. 1136.
- [25] Server, W., Ireland, D., and Wallaert, R., "Strength and Toughness Evaluations From an Instrumented Impact Test," Dynatup Report TR74-29R, Effects Technology, Santa Barbara, Calif., 1974.
- [26] Begley, J. A. and Landes, J. D., *Progress in Flaw Growth and Fracture Toughness Testing, ASTM STP 536*, American Society for Testing and Materials, 1973, p. 246.

DISCUSSION

*Wilhelm Heller*¹(*written discussion*)—Since 1972, the Federal Department of Research and Technology of West Germany has sponsored investigations related to a rapid transit system based on a wheel/rail technique. The investigations have been carried out by a partnership of German industry and universities, and the German Federal Railway. In the course of this research, first the limits of the wheel/rail system had to be investigated; from this newly won knowledge, simulation models were to be developed, and they finally should be translated into the design of test vehicles and track. In the scope of this research project, Fried. Krupp Hüttenwerke Aktiengesellschaft has investigated new high-strength rail steels.

Rail steels for a high-volume rapid transit system should meet the following requirements:

1. High wear resistance.
2. High yield strength.
3. High fatigue strength.
4. Resistance to corrugation and formation of roaring rails.
5. Sufficient toughness.
6. Good weldability.

Altogether, four types of steel have been investigated with respect to their development potential:

1. Pearlitic steels with a guide analysis of about 0.7 percent carbon, 1 percent manganese, and 1 percent chromium, deviations in the carbon, manganese, and chromium content, and additions of at most 0.2 percent titanium, vanadium, and columbium, respectively.
2. Bainitic steels with around 0.3 percent carbon, 3 percent chromium, and 0.5 percent molybdenum.
3. Low-carbon bainitic steels with around 0.1 percent carbon, 4.5 percent manganese, and 0.1 percent columbium.
4. Austenitic steels with around 0.7 percent carbon and 13 percent manganese.

Figure 5 shows the microstructure of the four types of steel. The pearlitic steel exhibits a fine-grained pearlite structure with small interlamellar spacing; the bainitic steel, a bainite structure with finely dispersed carbide precipitations; the low-carbon steel, a coarse acicular bainite structure; and the austenitic steel, an austenite structure with twinning.

For pearlitic steels, the relationships between the structural parameters and the different mechanical properties have been investigated in detail. Accordingly, the 0.2 percent proof stress of pearlitic steels is solely depen-

¹Duisburg, West Germany.

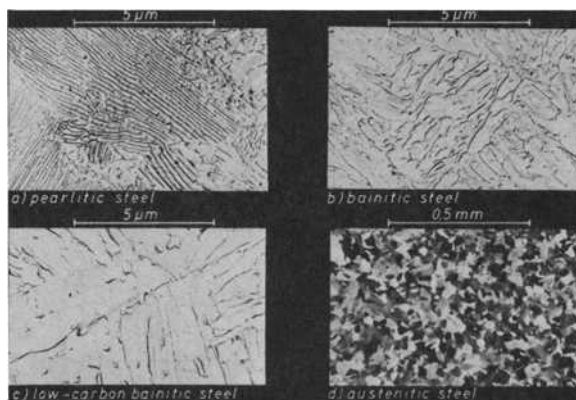


FIG. 5—Microstructure of four types of steel (pearlitic, bainitic, low carbon, and austenitic).

dent on interlamellar spacing (Fig. 6). Above their effect on interlamellar spacing, the alloying elements do not influence the 0.2 percent proof stress. Likewise, tensile strength is mainly dependent on interlamellar spacing. As is illustrated by the mounting of the elastic ratio with increasing tensile strength (Fig. 7), the effect of interlamellar spacing on the 0.2 percent proof stress is somewhat larger than on the tensile strength.

Reduction of area and toughness of pearlitic steels can be plotted as a function of austenite grain size and thickness of cementite lamellae. Both properties improve with decreasing values of austenite grain size and thickness of cementite lamellae, as Fig. 8 shows on the example of the reduction of area.

Pearlitic steel rails obtain a tensile strength of 1150 to 1300 N/mm² and a 0.2 percent proof stress of 650 to 830 N/mm² (Fig. 9). Bainitic steel rails exhibit a tensile strength of 1300 to 1500 N/mm² and a 0.2 percent proof

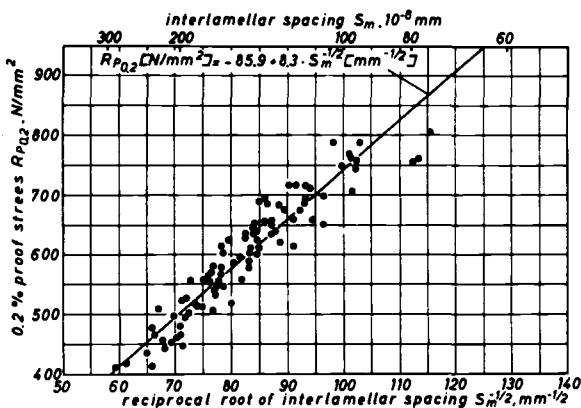


FIG. 6—Relationship between 0.2 percent proof stress and interlamellar spacing.

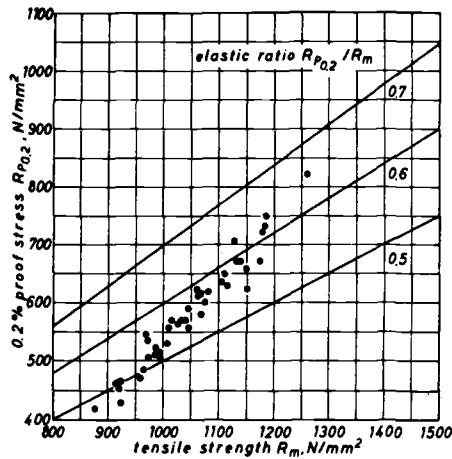


FIG. 7—Relationship between 0.2 percent proof stress and tensile strength.

stress of 1100 to 1300 N/mm², low-carbon steel rails a tensile strength of about 1100 N/mm² and a 0.2 percent proof stress of about 1000 N/mm². Austenitic steel rails having a strong work hardening potential show a tensile strength of about 1000 N/mm² and a 0.2 percent proof stress of about 400 N/mm². The elongation A_5 of the pearlitic steels is of the order of 12 percent, of the bainitic and low-carbon steels of about 16 percent, and of the austenitic steels of about 75 percent.

Bending fatigue strength of pearlitic rail steels amounts to about 400 N/mm², of bainitic rail steels to about 550 N/mm², and of low-carbon rail steels to about 450 N/mm².

Notched bar impact strength of the new pearlitic rail steels is of the same order of magnitude as that of wear-resistant rail steels according to Union Internationale des Chemins de Fer (UIC). For bainitic and low-carbon

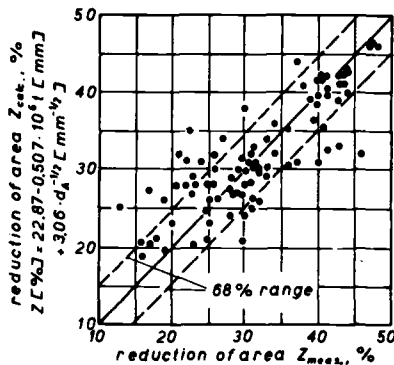


FIG. 8—Reduction of area as measured and calculated from regression equation.

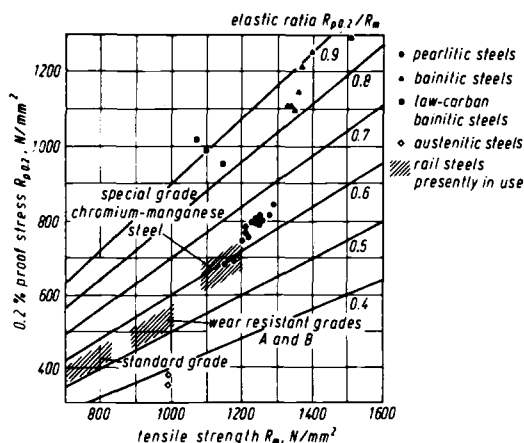


FIG. 9—Tensile strength and 0.2 percent proof stress of rail steels.

steels, three to four times higher values are obtained. As would be expected, austenitic steels proved to be extremely tough. With respect to the impact test, all rails come up to the requirements according to UIC. The fracture toughness of the different rail steels amounts to between 1060 and 1370 $\text{N}/\text{mm}^{3/2}$, independent of the type of steel.

The new rail steels are suited to be welded by flash butt and thermite welding. Naturally, welding terms have to be adapted to the respective type of steel.

To test the service behavior of the new rail steels, the rails have been laid in test tracks with significantly different service conditions (Table 5). The tracks mainly differ in the radius of the curves and the axle load. The results, so far, are positive. But, the duration of the tests are still too short to permit a final judgment.

According to our knowledge, the special grade chromium-manganese steel represents the most advantageous development in rail steels. Beyond it, with pearlitic steels, it is only possible to obtain a relatively small increase in strength. No doubt the other new rail steels could offer some advantages in comparison to the special grade chromium-manganese steel; but, because of their vastly higher manufacturing costs, these steels don't seem to be promising.

G. K. Bouse, I. M. Bernstein, and D. H. Stone (authors' closure)—The authors are pleased to learn of the agreement of Dr. Heller's findings of the effects of prior austenite grain size and pearlite spacing with our work. Further, we wish to congratulate him on showing the effect of cementite thickness which we did not study.

TABLE 5—*Testing of the rails in test track.*

Test Track	Radius of Curves, m	Slope, 0/00	Max Axle load, kN	Max Speed, km/h	Total Load per year, 10 ⁶ t/year	Testing of
DB Mannheim-Karlsruhe		0	220	160	8	susceptibility to corrugation
DB Karlsruhe-Pforzheim	600 and 680	0	220	110	12	wear, fatigue
RBW Tagebau Fortuna	300	0	340	30	66	fatigue, cold deformation, wear
RBW Tagebau Frimmersd.	220 to 300	0	340	30	54	fatigue, cold deformation, wear
SBB Giubiasco-Rivera	290 to 350	5 to 16	200	85	18	fatigue, wear
DB Rohrsen-Systrup		0	220	160	20	susceptibility to corrugation
DB Tostedt-Königsmoor		0	220	160	20	susceptibility to corrugation

Development of High-Strength Alloyed Rail Steels Suitable for Heavy Duty Applications

REFERENCE: Marich, S. and Curcio, P., "Development of High-Strength Alloyed Rail Steels Suitable for Heavy Duty Applications," *Rail Steels—Developments, Processing, and Use, ASTM STP 644*, D. H. Stone and G. G. Knupp, Eds., American Society for Testing and Materials, 1978, pp 167-211.

ABSTRACT: In the first section of the paper, a summary will be given of the various defects which can develop in rails subjected to high axle loads, such as corrugations, gross plastic deformation and abrasive wear of the railhead, checking and spalling, shelling and transverse defects.

The second section of the paper will cover in detail the developmental work on high-strength alloyed rail steels conducted at Broken Hill Proprietary Co. Ltd. Melbourne Research Laboratories. An essential part of the work has been the development of techniques for laboratory simulation of industrial rail production and on-site welding procedures. Various other material properties have also been used in assessing material types.

The major emphasis of the work has been directed to optimizing the mechanical properties of three rail steel types, namely: chromium-columbium-vanadium steels, chromium-vanadium steels, and chromium-molybdenum steels. Fully pearlitic steels exhibiting yield strengths greater than 900 MPa have been developed without adversely influencing other mechanical properties. The steels can be flash butt welded using modified procedures.

KEY WORDS: steels, railroad tracks, deformation, mechanical properties, micro-structure, welding, assessments

The rails used for the transportation of iron ore at Mt. Newman Mining Co. Proprietary Ltd. (and also Hamersley Iron Proprietary Ltd.) in Western Australia are subjected to service conditions which are among the most severe in the world. The action of nine to ten loaded unit trains per day, each consisting of 140 cars with mean axle loads of 300 kN but with peak loads of about 400 kN and each travelling along the single tracks at speeds of up to 60 km/h, has been found to cause rapid deterioration of standard American Railway Engineering Association (AREA) carbon rails of 66 and 68 kg/m sections.

¹Senior research officer and experimental officer, respectively, Broken Hill Proprietary Co. Ltd. Melbourne Research Laboratories, Clayton, Victoria, Australia.

The deterioration of standard rails, which has necessitated very costly inspection, maintenance and rerailling programs, has manifested itself through the development of various problems. The two primary objectives of the rail development program were thus set as follows:

1. To study the metallurgical characteristics of the problems which were occurring in the rails and therefore determine the guidelines to be followed in the alloy development work [1].²

2. To develop new steel alloys suitable for the industrial manufacture of rails and capable of increasing rail life by eliminating or at least minimizing the occurrence of such defects [1].³

The major emphasis of the following text will be on the second of these topics.

Rail Defects

At the Mt. Newman Mining Co. Proprietary Ltd., rail life has been affected adversely by the following defects.

Gross Plastic Deformation and Abrasive Wear of the Railhead

Figure 1 shows the profiles of a new rail and two high rails from a 2-deg curve (837 m radius) which have been subjected to traffics of 100 and 200 million gross tonnes (MGT), respectively. It is evident that the used rails have suffered extensive loss of material, mainly from the gage corner, by both abrasive wear and plastic flow of metal. The deformation and metal loss which occur in low rails of curves and in tangent track are generally much less severe.

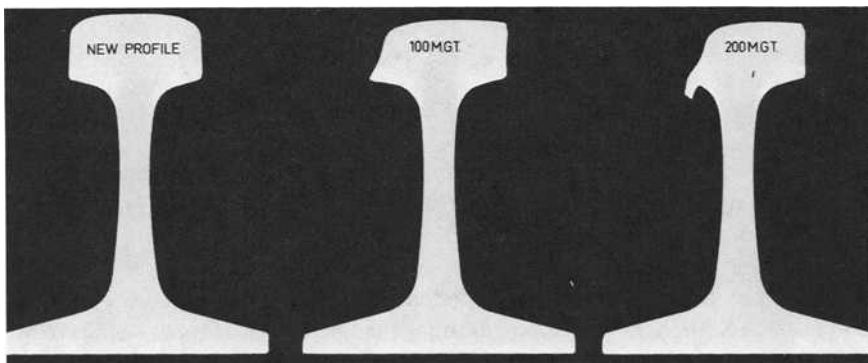


FIG. 1—Standard rail profiles in 2-deg curve (873 m radius).

²The italic numbers in brackets refer to the list of references appended to this paper.

³Defect as used in this paper is the railroad industry's historical usage of the word to characterize service-induced fatigue separations of the metal in rails.

Together with increasing the rate of head loss, deformation of high rails also leads to:

Gage Corner Checking and Flaking—These are surface cracks which initiate at or near the gage corner surface, grow into the railhead to a depth of up to 2 mm below the running surface, and eventually cause thin sections of material to spall off.

Accelerated Wear of Wheels—This occurs from the contact established between rail and wheel flanges.

Subsurface Deformation

The deformation of rails is not confined to the contact surfaces. Thus, as shown in Fig. 2, on taking hardness measurements along the indicated directions, it is found that work hardening of the material occurs up to depth of 8 mm from the running surface in both high and low rails (Traverses 1) and up to a depth of 10 mm from the gage corner in high rails (Traverse 2).

As a result of the subsurface deformation, the inclusions present in the steel (commonly sulfides and silicates) nucleate cracks which may subsequently grow in both longitudinal and transverse directions. These cracks in turn give rise to three further defect types:

Running Surface Checking and Flaking—These are surface cracks which nucleate at silicate inclusions at a depth of 0.3 to 0.8 mm below the running surface of the rails. The cracks grow parallel to the running surface and eventually cause thin sections of material to spall off.

Transverse Defects (Or Detail Fractures)—These nucleate at large inclusions of the silicate type at a depth of 5 to 7 mm below the gage corner of rails. Subsequent crack growth may occur in both longitudinal and transverse directions. Growth in the transverse direction continues until the crack reaches critical size (approximately 80 percent of the railhead), at which time sudden failure of the rail section occurs.

Shelling—Shelly cracks also nucleate at a depth of 5 to 7 mm below the gage corner of rails from both sulfide and silicate inclusions. The cracks grow longitudinally, at an angle of 30 to 40 deg with the running surface, and may run within the railhead for a distance of up to 1 m before breaking out.

Corrugations

As shown in Fig. 3, corrugations are wavelike patterns which develop primarily on the running surface of high rails in curves. If not controlled, they can be up to 1 mm in depth (amplitude). Their formation has been related to the initiation of wheel/rail resonance which gives rise to dynamic loads sufficiently high to cause plastic deformation of the rail steel [2].

In summary, the development of all the rail defects studied could be associated with the occurrence of plastic deformation in the standard rail steel. For this reason, the major emphasis in the alloy development program

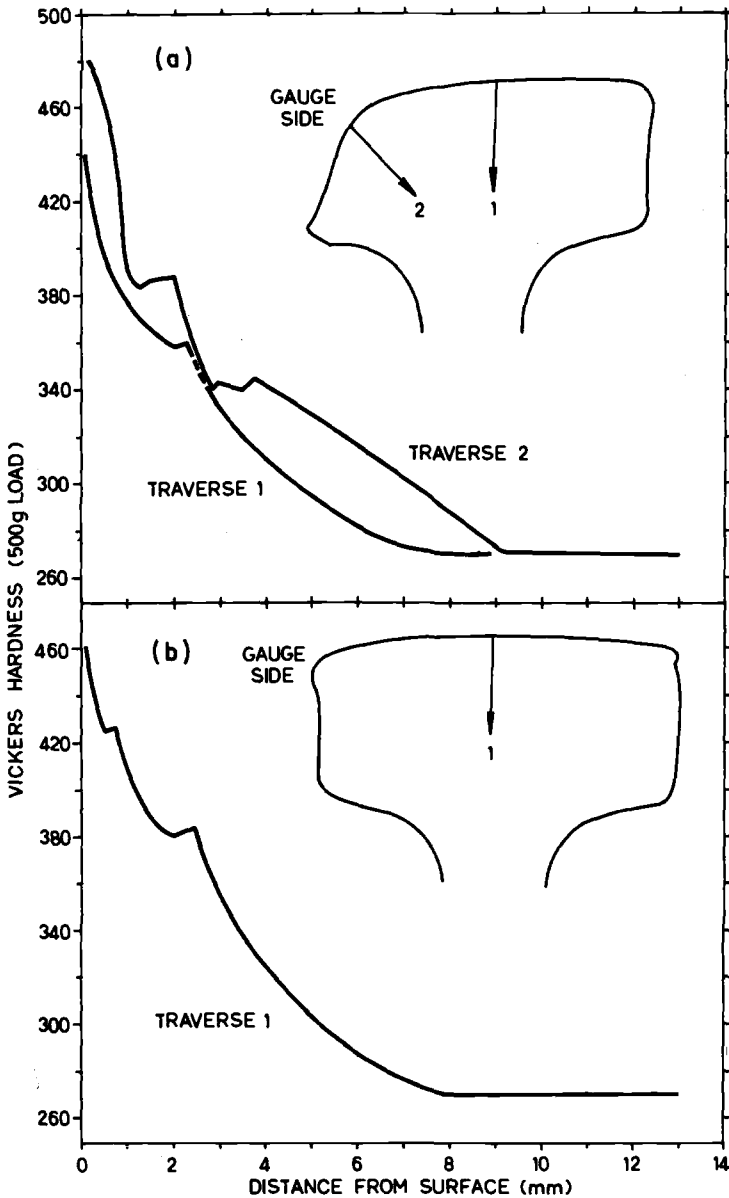


FIG. 2—Microhardness distributions in (a) high and (b) low rails from a 2-deg curve.

was placed on the improvement in yield or proof strength which could be practically achieved in steels suitable for the manufacture of rails. Concurrently, however, a number of other material properties were measured and used to assess the various material types studied.



FIG. 3—*Corrugations.*

Alloy Steel Development

Production and Testing of Equipment Rail Steels

The value of any laboratory investigation is wholly dependent on being able to simulate actual production processes. At the start of the alloy development program, a considerable amount of time was therefore spent altering experimental conditions such that a close agreement would be obtained between the mechanical properties exhibited by the steels produced in the laboratory and those produced at Broken Hill Proprietary Co. Ltd.'s

(BHP) rail manufacturing plant (Australian Iron & Steel Pty. Ltd., Port Kembla).

The first step in the preliminary study was to measure the cooling rate of rails subsequent to hot rolling and then to duplicate this rate in the material hot rolled into plate form under laboratory conditions.

The cooling rate measured by optical pyrometry on the surface of rails of 68 kg/m section was found to be $60^{\circ}\text{C}/\text{min}$, in the temperature range 900 to 740°C . To determine the difference in cooling rate between the surface and the center of the head, chromel/alumel thermocouples were inserted into two rail sections both 750 mm in length, to a depth of 2 to 12 mm below the running surface. The sections were soaked at 950°C for 1 h. One section was then cooled in still air, while the other was cooled in a breeze generated by a fan to simulate windy conditions. The cooling rates obtained in the range 900 to 740°C were as follows: (a) in still air— $43^{\circ}\text{C}/\text{min}$ at a depth of 2 mm and $39^{\circ}\text{C}/\text{min}$ at a depth of 12 mm, and (b) in wind— $60^{\circ}\text{C}/\text{min}$ at a depth of 2 mm and $49^{\circ}\text{C}/\text{min}$ at a depth of 12 mm. It was therefore assumed that, under industrial conditions, the cooling rate in the center of the railhead would be about 4 to $11^{\circ}\text{C}/\text{min}$ lower than that measured at the surface, that is, it would be in the range 49 to $56^{\circ}\text{C}/\text{min}$.

It was then found that a similar cooling rate could be obtained in a plate 32 mm thick on cooling in still air (cooling rate measured in plate was 52 to $58^{\circ}\text{C}/\text{min}$). The following procedure was therefore applied to all alloys manufactured in the laboratory:

Ingot weight	37 kg
Ingot dimensions	95 by 165 by 240 mm
Soaking temperature	1300°C
Soaking time	2 h
Finishing temperature	1000 to 1050°C
No. of passes from ingot to finished plate	7
Reduction per pass	20 percent
Rolled plate dimensions	32 by 190 by 560 mm

Subsequent to rolling, the plates were allowed to cool to 430°C and were then placed into a furnace programmed to cool at a rate of $0.5^{\circ}\text{C}/\text{min}$, that is, in the middle of the range specified by AREA for controlled cooling of rails.

It was also found that a much closer agreement between the properties and particularly the strength of laboratory and plant products (produced without addition of aluminium) could be obtained by adding to the laboratory melts a quantity of aluminium, in the range 0.02 to 0.05 percent. The aluminium additions led to a reduction in strength, presumably by refining the austenite grain size and therefore increasing the transformation temperature. The experimental steels were subjected to the following routine tests:

Tensile—Longitudinal tensile blanks were cut from the center of each plate and machined to round specimens with diameters of 7.3 mm and 5 mm parallel lengths. The tests were conducted at room temperature on an Instron machine using a calibrated extensometer and a crosshead speed of 5 mm/min. Each test was duplicated.

Hardness—Vickers hardness measurements were carried out on the mounted heads of the tensile specimens using a 10 kg load (VHN 10). In each alloy type, ten hardness measurements were taken.

Charpy—At least three full sized longitudinal Charpy specimens, both V-notched and unnotched, were machined from the center of each plate and tested at 200°C (CV200) and 20°C (C20), respectively. At these temperatures, the fracture mode was generally fully ductile. The Charpy data were used only as an indication of the relative impact characteristics of the alloys.

Transformation—The transformation behavior on continuous cooling was determined in each alloy by means of dilatometer specimens machined as hollow cylinders (12.7 mm long, 7.3 mm outside diameter, 1 mm wall thickness). Chromel/alumel thermocouples were spot welded on the surface of each specimen for temperature measurement and control. Further details of the transformation work will be given in a later section.

A number of alloys of widely different composition were manufactured in the laboratory in the manner just described, and their mean tensile, Charpy and hardness properties were compared with the mean properties measured in the head of rails of similar composition. The results obtained are presented in Table 1. In the table, the heat numbers of the experimental alloys are preceded by the letter V.

From the table, it is evident that the mechanical properties of the laboratory and industrial steels are in reasonable agreement. Thus, taking proof stress as an example, and excluding the rail produced at Colorado Fuel and Iron (CF&I), the largest difference was 17 MPa observed in the standard steel, this being due to the lower carbon content of the experimental material.

Heat V1215 was the only experimental steel which did not contain aluminium. It has been included in the table to illustrate the point made previously that aluminium additions lead to a lowering in strength (compare Heat V1226) and properties which are in closer agreement with those of industrial steels. The effect of aluminium also explains the difference observed between Heat V1127 and the rails produced at CF&I. In the latter, aluminium additions were made during steelmaking which led to an aluminium content in the steel of 0.01 percent. Without such additions, it seems likely that the strength would have been higher and therefore much closer to the predicted value.

Weldability of Experimental Rail Steels

At the Mt. Newman Mining Co., rails are flash butt welded into strings of ten rail lengths which are then transported to particular sites on track, laid,

TABLE 1—Composition and mechanical properties of experimental and industrial rail steels.

Alloy Type	Heat No.	Composition										Mechanical Properties							
		C	Mn	Si	P	S	Cr	Cb	V	Mo	0.2 % Proof Stress, MPa	Ulti- mate Tensile Strength, MPa	Elonga- tion, %	Reduc- tion in Area, %	HV10	CV200 J	C20 J		
Standard	V1060	0.71	0.80	0.15	0.02	0.02	461	889	13.5	15.5	252	29	150		
Cr-Cb-V	various	0.80	0.82	0.14	0.02	0.04	478	920	13	16	274	28	140		
	V1215	0.53	1.38	0.20	0.02	0.03	0.62	0.05	0.07	...	730	1105	10.5	29	330	26.5	280		
	V1226	0.55	1.42	0.20	0.02	0.02	0.61	0.06	0.07	...	710	1090	13	33.5	317	27	>285		
Cr-V	265850	0.54	1.38	0.11	0.01	0.01	0.58	0.04	0.05	...	704	1082	15	33	325	32	>285		
	V1070	0.72	1.30	0.18	0.02	0.04	0.80	...	0.11	...	740	1224	11	15	374	15	130		
	2K8711	0.76	1.29	0.36	0.02	0.02	0.82	...	0.12	...	747	1235	10	15	388 ^a	17	125		
Cr-Mo	V1057	0.75	0.88	0.17	0.02	0.03	0.75	0.22	905	1290	8.5	13	398	12	144		
	2K8713	0.73	0.83	0.28	0.02	0.03	0.74	0.21	897	1299	10	19	400	11	140		
	V1127	0.72	0.86	0.17	0.02	0.03	0.82	0.17	863	1247	11	25.5	377	24	285		
	12547 ^a	0.77	0.89	0.20	0.01	0.03	0.76	0.16	804	1217	11	25	352	20	260		

NOTE.—V—precedes experimental alloy heat numbers.

HV10—Hardness Vickers 10 kg load.

CV200—Charpy V-notched at 200°C.

C20—Charpy unnotched at 20°C.

^aRail produced at CF & I

and finally joined by means of thermite welding. In any rail alloy development program, therefore, a knowledge of the welding characteristics of new rail steels is of major importance and particularly their behavior under flash butt welding conditions because of: (a) the higher proportions of such welds in track and (b) the higher cooling rates which are obtained in the heat-affected zone (HAZ). The tendency to form metallurgically deleterious microstructures, such as martensite, is therefore much greater in flash butt welds than in thermite welds. This problem is of course enhanced in those rail materials in which an improvement in properties is achieved by the addition of alloying elements which increase the hardenability of the steel.

As part of the rail alloy development program, a technique has been developed which allows laboratory simulation of flash butt welding conditions in heavy duty rails. The technique has been used to assess the weldability of new rail steels, processed on laboratory scale, in terms of the amount of martensite which forms in the HAZ of welds and the maximum hardness obtained.

The assessment technique has been described in a previous publication [3]. The main aspects can be summarized as follows:

1. The cooling rate, in the temperature range 700 to 400°C, measured near the HAZ center line of rails welded using standard flash butt welding procedures is 0.67°C/s. By applying a postweld current cycle, however, the cooling rate may be decreased to a minimum of 0.41°C/s.

2. The dilatometer specimens machined from the experimental steels are austenitized in a vacuum dilatometer at 1050°C for 10 min and then cooled at linear rates in the range 1.0 to 0.4°C/s. The dilatometer specimens are polished, and the amount of martensite which they contain (if any) is measured together with the associated hardness. The flash butt welding of any alloy steel which forms more than about 5 percent martensite at a cooling rate of 0.4°C/s requires a tempering treatment subsequent to the welding operation.

Alloy Rail Steels Studied

The alloy development program involved a study of three main groups of steel alloys, namely: chromium-columbium-vanadium steels, chromium-vanadium steels, and chromium-molybdenum steels.⁴ For sake of clarity, the results which will be presented in the following text make up only a small fraction of the total number of alloys which were produced in the laboratory. A large number of alloys were rejected on the basis of their production or welding characteristics or both.

A summary of compositions and tensile, hardness, Charpy, and trans-

⁴The development program on the chromium-molybdenum steels was initially suggested by the Climax Molybdenum Company of Michigan. A detailed discussion of the work done at the Climax Research Laboratories has recently been published in Ref 4.

formation properties of the various alloys is given in Tables 2–4. In each table, the properties of the standard rail steel produced in the laboratory have also been included for comparison.

Chromium-Columbium-Vanadium Alloys (Table 2)—The general differences in composition between this group of alloys and standard rail steels are as follows: a higher manganese level, additions of chromium, a lower carbon level, and additions of columbium or vanadium or both.

In the as-rolled condition, the microstructure in most of the alloys containing more than 0.5 percent carbon consists of pearlite with a few isolated pools of ferrite.

The results obtained can be summarized as follows:

1. The two alloys containing either columbium (V1245) or vanadium (V1218) exhibit higher strengths than the standard material (V1060). The increase in strength was due to: (a) a refinement of interlamellar spacings, which resulted from the influence of manganese and chromium on the transformation temperature and (b) the precipitation of columbium carbide (CbC) or vanadium carbide (V_4C_3) in both the ferrite lamellae and the ferrite pools. For example: the mean interlamellar spacing⁵ measured in V1060 was $0.26\text{ }\mu\text{m}$ compared to $0.16\text{ }\mu\text{m}$ in V1245 and $0.21\text{ }\mu\text{m}$ in V1218. Figures 4a, b illustrate the pinning action which the precipitates have on dislocations in both of the steels, while Fig. 4c shows the V_4C_3 precipitates detected under dark-field illumination. The increase in strength and hardness obtained in the alloys was also accompanied by an increase in tensile ductility and Charpy values. This was due to the refinement in the pearlite colony size which was observed in all the lower carbon alloys.

2. A further increase in strength was obtained by adding both columbium and vanadium (V1226). As shown in Fig. 4d, evidence of a precipitate was also found in this alloy. The precipitate was shown to be V_4C_3 , indicating the greater stability of this carbide compared to CbC. The mean interlamellar spacing in V1226 was $0.16\text{ }\mu\text{m}$. The higher strength of V1226 compared to V1218 can thus be related to the decrease in interlamellar spacings which have resulted from the columbium addition. On the other hand, the interlamellar spacings in both V1226 and V1245 are the same, and the only difference between these alloys is the type of precipitate which they contain. It would thus appear that V_4C_3 is the more effective strengthener. Although the increase in strength in V1226 has been accompanied by a slight decrease in both ductility and Charpy values, these still compare favorably with the values measured in the standard steel. From the transformation characteristics of V1226, it can also be seen that the alloy is not expected to form any martensite using standard flash butt welding procedures, that is, at a cooling rate (CR) of 0.7°C/s .

⁵Mean interlamellar spacings were obtained by taking measurements on at least 50 pearlite colonies, photographed at a magnification of $\times 5000$, in which the pearlite lamellae were approximately normal to the plane of polish.

TABLE 2—Cr-Cb-V alloys.

Heat No.	Mechanical Properties										Transformation								
	Composition					0.2 % Ultimate													
	C	Mn	Si	P	S	Cr	Cb	V	Proof Stress, MPa	Tensile Strength, MPa		Elonga- tion %	Reduc- tion in Area, %	HV 10	CV200 J	C20 J	Cooling Rate, °C/s	Ar ₃ , °C	Microstructure ^a
V1060	0.71	0.80	0.15	0.02	0.02	461	889	13.5	15.5	252	29	150	0.5	690	100P	318
V1245	0.53	1.44	0.18	0.02	0.03	0.61	0.07	...	640	989	14	36.5	301	40	>285	0.7	682	100P	320
V1218	0.54	1.39	0.18	0.02	0.02	0.60	...	0.07	606	983	14	38	288	35	>285	0.5	640	98P + 2B	360
V1226	0.55	1.42	0.20	0.02	0.02	0.61	0.06	0.07	710	1090	13	33.5	317	27	>285	0.7	635	90P + 10B	372
V1235	0.53	1.42	0.19	0.02	0.02	0.64	0.04	0.06	621	997	16	49	296	44	>285	0.5	632	90P + 10B	355
V1262	0.49	1.40	0.17	0.02	0.02	0.58	0.06	0.07	611	965	16.5	46	288	53	>285	0.5	635	100P	360
V1114	0.71	1.39	0.17	0.02	0.03	0.70	0.06	0.08	783	1194	8.5	15.5	362	13	78	0.5	626	90P + 5B + 5M	376
V1063	0.53	1.76	0.16	0.02	0.02	0.71	0.07	0.07	765	1063	14.5	33	353	29	>285	0.7	654	90P + 40B + 20M	395
																0.4	640	90P + 3B	395
																0.5	640	90P + 10B	408
																0.7	635	94P + 4B + 2M	356
																0.5	635	15P + 65B + 20M	370
																0.5	635	15P + 35B + 50M	393

^aP—pearlitic, B—bainitic, M—martensitic.

TABLE 3—Cr-V alloys.

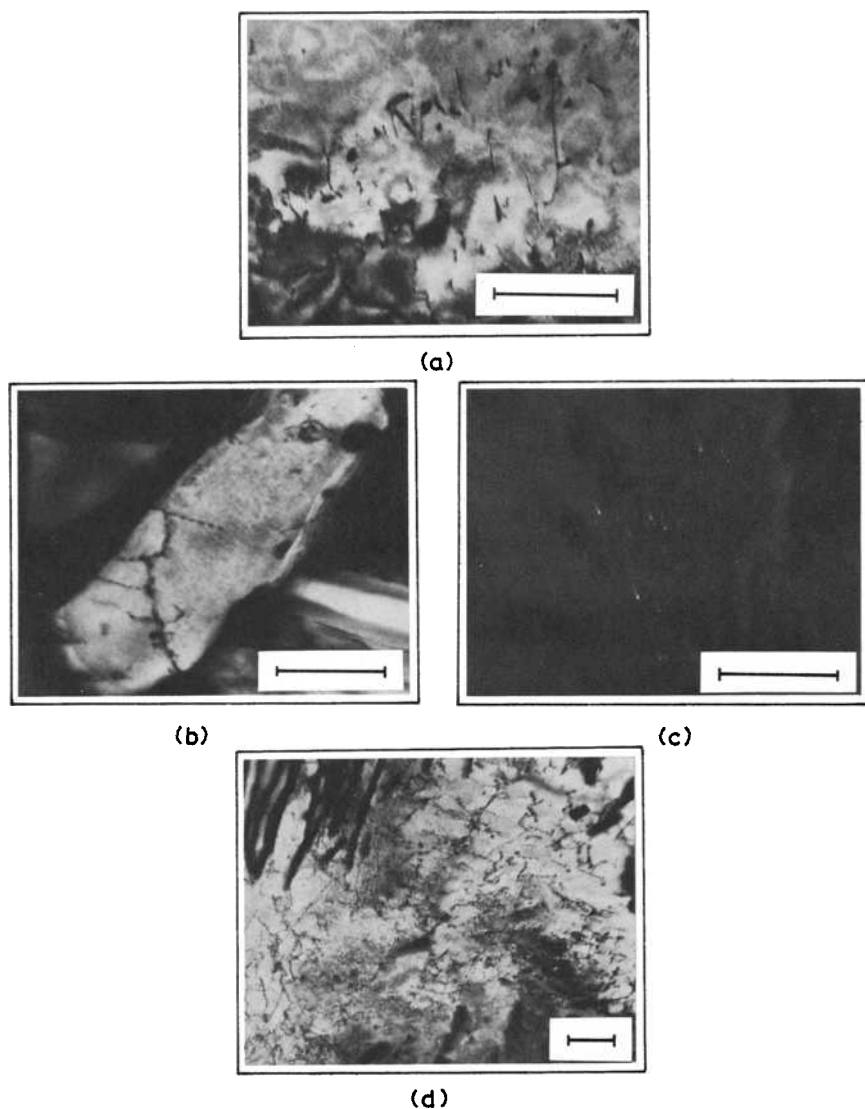
Heat No.	Composition							Mechanical Properties						Transformation					
	C	Mn	Si	P	S	Cr	V	0.2% Proof Stress, MPa	Ultimate Tensile Strength, MPa	Elonga- tion %	Reduc- tion in Area, %	HV10	CV200 J	C20 J	Cooling Rate °C/s	Ar3, °C	Microstructure ^a		HVS
																	Ar3, °C	Microstructure ^a	
V1060	0.71	0.80	0.15	0.02	0.02	461	889	13.5	15.5	252	29	150	0.5	690	100P	318	
V1367	0.71	1.18	0.23	0.02	0.04	0.91	...	645	1053	8.5	14	321	15	154	0.5	656	100P	320	
V1070	0.72	1.30	0.18	0.02	0.04	0.80	0.11	740	1224	11	15	374	15	130	0.5	638	100P	38 ^c	
V1068	0.68	1.49	0.25	0.02	0.04	0.75	0.09	780	1230	12.5	21	375	16	160	0.7	625	70P + 30M	39 ^b	
V1082	0.67	1.76	0.27	0.02	0.02	0.72	0.11	772	1224	16	21	362	15	155	0.4	638	65P + 35M	515	
															0.5	628	45P + 5B + 50M	540	
															0.4	634	45P + 5B + 50M	620	
															0.5	625	35P + 5B + 60M	615	
															0.4	645	35P + 5B + 60M	705	
															0.5	645	35P + 5B + 60M	710	
V1116	0.67	1.33	0.26	0.02	0.03	1.30	0.11	730	1220	11.5	24	362	18	165	0.5	645	25P + 5B + 70M	840	

^ap—pearlite, B—bainite, M—martensite.

TABLE 4—Cr-Mo alloys.

Heat No.	Mechanical Properties										Transformation								
	Composition					Reduction					Cooling Rate, °C/s	Ar3, °C	Microstructure ^a	HV5					
	C	Mn	Si	P	S	Cr	Mo	V	0.2 % Proof Stress, MPa	Ultimate Tensile Strength, MPa					Elongation, %	in Area, %	HV 10	CV200 J	C20 J
V1060	0.71	0.80	0.15	0.02	0.02	461	889	13.5	15.5	252	29	150	0.5	690	100P	318
V1366	0.67	0.89	0.21	0.02	0.03	0.83	608	1014	8.5	18.5	293	24	175	0.7	682	100P	320
V1371	0.73	0.90	0.19	0.03	0.03	0.86	0.08	...	620	1070	11	21	302	19	196	0.5	655	100P	355
V1453	0.69	0.86	0.20	0.02	0.03	0.78	0.13	...	713	1123	12	28.5	353	23	>285	0.7	648	100P	370
																0.5	647	100P	374
																0.7	635	75 + 20B + 5M	395
																0.4	646	95P + 5B	398
																0.5	638	85P + 10B + 5M	405
V1127	0.72	0.86	0.17	0.02	0.03	0.82	0.17	...	863	1247	11	25.5	377	24	285	0.4	634	80P + 20B	420
																0.5	626	66P + 30B + 4M	434
V1057	0.75	0.88	0.17	0.02	0.03	0.75	0.22	...	905	1290	8.5	13	398	12	144	0.4	635	45P + 55B	425
																0.5	625	40P + 50B + 10M	459
V1049	0.72	0.87	0.17	0.02	0.02	0.77	0.27	...	858	1238	6.5	13.5	380	15	174	0.4	625	5P + 80B + 15M	490
																0.5	75B + 25M		512
V1448	0.70	0.93	0.19	0.02	0.02	0.81	0.16	0.05	938	1312	12	31.5	405	22	>285	0.4	634	45P + 50B + 5M	422
																0.5	605	40P + 45B + 15M	460
V1657	0.70	0.95	0.20	0.02	0.03	0.84	0.18	0.06	1030	1393	10.5	30	413	20	280	0.4	632	45P + 45B + 10M	435
																0.5	597	35P + 45B + 20M	418

^ap—pearlite, B—bainite, M—martensite.



- (a) Alloy V1245 (scale mark indicates $0.5 \mu\text{m}$).
 (b) Alloy V1218 (scale mark indicates $0.5 \mu\text{m}$).
 (c) Alloy V1218 dark field (scale mark indicates $0.5 \mu\text{m}$).
 (d) Alloy 1226 (scale mark indicates $0.5 \mu\text{m}$).

FIG. 4—Microstructures in chromium-columbium-vanadium alloys (thin foils).

3. The hot rolling finishing temperature of V1235 was 930°C compared to 1020°C in V1226. From Table 2, it can be seen that the lowering of the finishing temperature has led to a considerable decrease in strength which was due to an increase in the amount of grain boundary ferrite present.

4. A similar decrease in strength was obtained on lowering the carbon level to 0.49 percent (V1262). Again, this was due to an increase in the amount of ferrite.

5. On the other hand, increasing the carbon level to 0.71 percent (V1114) led to a considerable increase in strength due to the absence of grain boundary ferrite and probably to the increase in the proportion of cementite within the pearlite. This alloy, however, also exhibited a considerable reduction in ductility and Charpy values. Furthermore, the hardenability of the alloy was such as to necessitate special cooling precautions on welding.

6. An increase in strength was also obtained by increasing the manganese level to 1.76 percent (V1063) without adversely affecting ductility or Charpy values. However, the manganese has also increased the hardenability of this alloy to such an extent that the microstructure of the steel in the as-rolled condition is fully bainitic. This would lead to production difficulties in meeting AREA specifications for controlled cooling since the bainite transformation takes place in the temperature range 490 to 330°C. Mechanical rather than magnetic cranes would thus have to be used in the transfer of the rails to the cooling pits.

In summary, the "optimum" composition of the chromium-columbium-vanadium alloys is as follows: 0.53 to 0.63 percent carbon, 1.35 to 1.45 percent manganese, 0.10 to 0.20 percent silicon, 0.04 maximum percent phosphorous, 0.03 maximum percent sulfur, 0.55 to 0.65 percent chromium, 0.05 to 0.08 percent columbium, and 0.06 to 0.09 percent vanadium. Rails manufactured in the semikilled condition according to this specification and rolled with a finishing temperature above 1000°C should have a mean 0.2 percent proof stress value of 710 MPa with a minimum value of about 690 MPa, ductilities and Charpy values better than AREA standard rails, and transformation characteristics which would allow the rails to be flash butt welded without the need for special cooling precautions.

Chromium-Vanadium Alloys (Table 3)—These alloys have the same carbon level as the standard steel but have a higher manganese content and contain chromium and vanadium. In the as-rolled condition, they are all fully pearlitic. Relatively little developmental work has been done on this group since, as will become apparent, the hardenability of the steels, and therefore their weldability, has a considerable restricting influence on the scope of the work.

The results in Table 3 may be summarized as follows:

1. The additions of manganese and chromium made to Alloy V1367 have led to an increase in strength due to a decrease in transformation temperature and therefore interlamellar spacings. However, a reduction in ductility and Charpy values has occurred.

2. By increasing the manganese and adding vanadium (V1070), a further increase in strength has been obtained due to further reduction in the transformation temperature and precipitation of V_4C_3 . Both ductility and Charpy values, however, are still below those of the standard steel.

Furthermore, to avoid the formation of martensite during flash butt welding of this alloy, it is necessary to apply a postweld current cycle to reduce the cooling rate in the HAZ to about 0.5°C/s .

3. Strength, ductility, and Charpy values can be increased further by increasing the manganese level (V1068 and V1082). Both of these alloys, however, form a considerable amount of martensite at the slowest cooling rate which can be achieved on flash butt welding, that is, 0.4°C/s , and would therefore require a postweld tempering treatment.

4. Further additions of chromium have no effect on strength (V1116 compared to V1070) but increase hardenability.

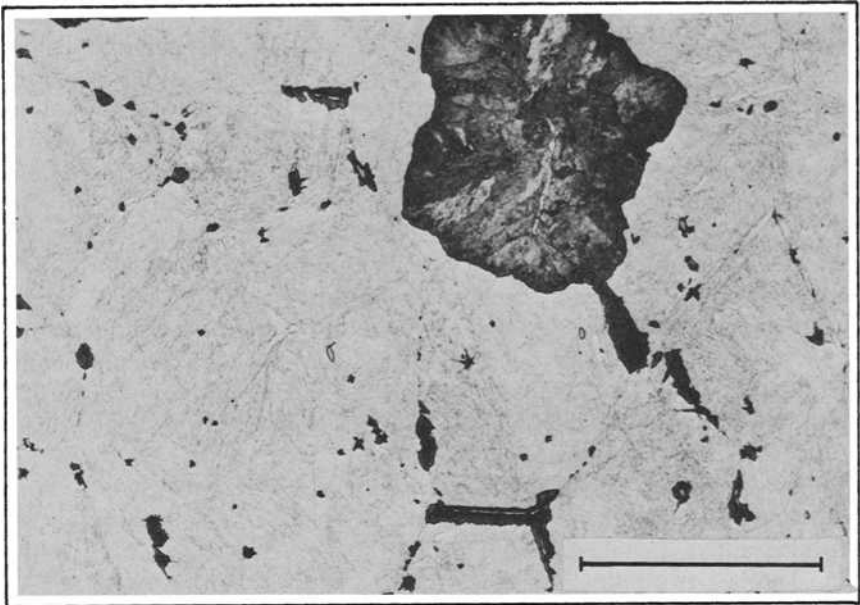
In summary, the "optimum" composition of the chromium-vanadium alloys is as follows: 0.70 to 0.80 percent carbon, 1.25 to 1.35 percent manganese, 0.20 to 0.40 percent silicon, 0.04 maximum percent phosphorus, 0.03 maximum percent sulfur, 0.75 to 0.85 percent chromium, and 0.10 to 0.13 percent vanadium. Rails manufactured in the fully killed condition to this specification should have a mean 0.2 percent proof stress of 740 MPa with a minimum value of 710 MPa. The ductility and Charpy values of the alloy steel would be less than those of standard rails, and the rails would require special cooling precautions on flash butt welding to avoid the formation of martensite.

Chromium-Molybdenum Alloys (Table 4)—The base composition of these alloys, that is, the carbon and manganese levels, is the same as those of standard rail steels. However, they also contain chromium and molybdenum, and some contain vanadium.

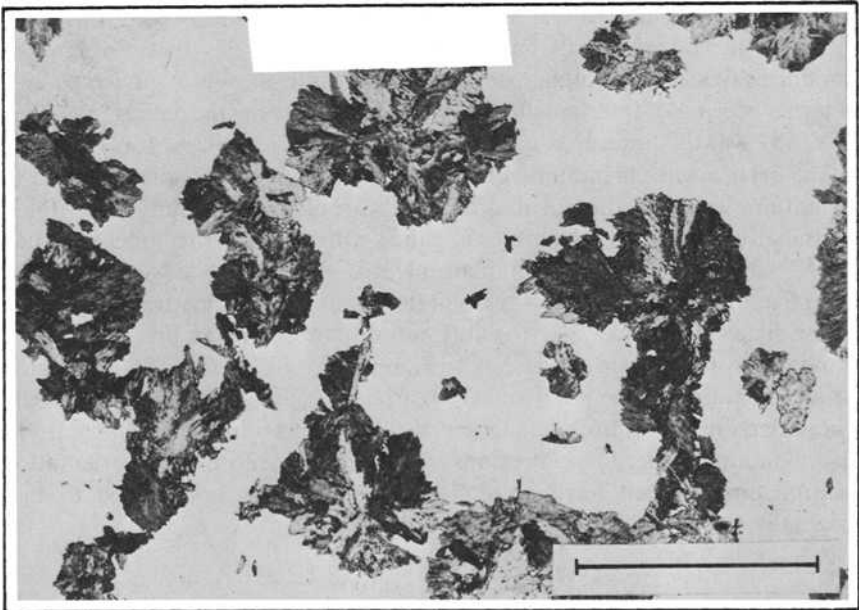
The general trend shown by the series of alloys in Table 4 can be summarized as follows:

1. As was noted in the chromium-vanadium alloys, additions of chromium (V1366) increase the strength by lowering the transformation temperature and therefore refining the interlamellar spacings ($0.16\text{ }\mu\text{m}$ in V1366 compared to $0.26\text{ }\mu\text{m}$ in V1060) but also decrease ductility and Charpy values.

2. Increasing levels of molybdenum up to 0.17 percent (V1366, V1453, and V1127) lead to a considerable increase in strength. For example, the proof stress exhibited by Alloy V1127 is about 120 MPa higher than that of the "optimum" chromium-vanadium alloy. This again is due to a progressive decrease in the transformation temperature and a refinement in interlamellar spacings. Thus, the mean spacing in V1371 is $0.15\text{ }\mu\text{m}$ in V1453 compared to $0.09\text{ }\mu\text{m}$ in V1127. At the same time, however, the elongation and notched Charpy values increase and the reduction of area and unnotched Charpy values become considerably higher than in the standard rail steel. The reason for these "unexpected" trends may be associated with the effect of molybdenum on the growth characteristics of pearlite. The differences in growth behavior can be observed by quenching partly transformed samples. Thus, as shown in Fig. 5, the pearlite in a steel of standard composition grows with a very smooth, almost circular growth front. In contrast, the pearlite in a



(a)



(b)

(a) V1060 (scale mark indicates 100 μm).

(b) V1127 (scale mark indicates 100 μm).

FIG. 5—Growth morphology of pearlite.

steel containing molybdenum grows with a very irregular growth front because of the frequent branching which occurs. The branching leads to a reduction in the pearlite colony size which, in turn, could explain the observed increase in ductility. From Table 4, it is also seen that the transformation characteristics of Alloy V1127 necessitate the use of a postweld cycle to reduce the cooling rate to 0.4 to 0.5°C/s and thus avoid the formation of martensite.

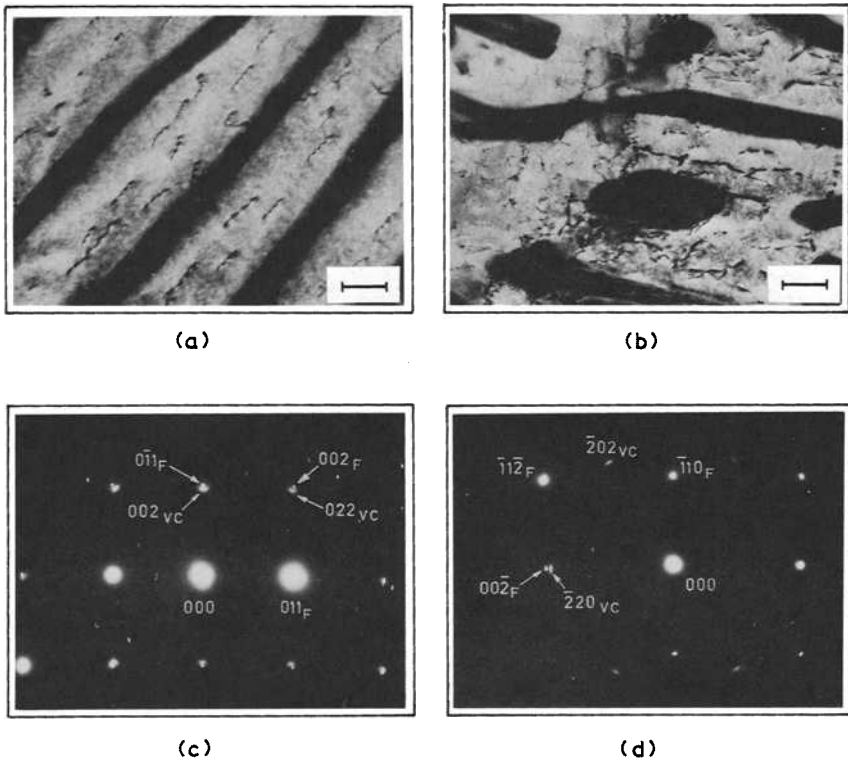
3. A further increase in strength is obtained by increasing the molybdenum content to 0.22 percent (V1057). Such an increase, however, is accompanied by a marked reduction in ductility and Charpy values. Furthermore at this level of molybdenum, traces of a bainitic microstructure were observed in the as-rolled alloy. In rails produced commercially, therefore, a proportion of bainite would be expected to form near the surface of the rails, that is, in regions which cool at a faster rate than the plates produced in the laboratory.

4. Increasing the molybdenum content up to 0.27 percent (V1049) led to a reduction in strength. This was due to the presence of about 40 percent in the as-rolled alloy.

5. The last two alloys in Table 4 (V1448 and V1657) have very similar compositions to V1127. However, they also contain vanadium. It is evident that, in both of these alloys, a considerable increase in strength has been achieved without adversely influencing ductility and Charpy values. Indeed, the reduction of area and Charpy values are much higher than those of the standard rail steel. The higher strength of these alloys could not be explained in terms of smaller interlamellar spacings. Thus, the mean spacing measured in V1657 was 0.09 μm , that is, the same as in V1127. However, as discussed in the section on chromium-columbium-vanadium alloys, the presence of vanadium leads to the formation of a carbide precipitate. To simplify examination procedures by increasing the width of the ferrite lamellae, Alloy V1657 was cooled in a vacuum dilatometer at a rate of 0.1°C/s. As shown in Figs. 6 *a, b*, the dislocation patterns in the ferrite were indicative of a pinning action by a precipitate. Electron diffraction patterns taken on the thin foils showed the precipitate to be V_4C_3 . Figures 6*c, d* illustrate the diffraction patterns obtained from (100) and (110) orientated ferrite grains, respectively. The reflections from both ferrite and V_4C_3 have been indexed. The patterns also contain numerous reflections from the cementite. The orientation relationship between ferrite and V_4C_3 was found to correspond to that originally proposed by Baker and Nutting [5]

$$\begin{array}{lll} (100)\alpha & \parallel & (100)_{\text{V}_4\text{C}_3} \\ [011]\alpha & \parallel & [001]_{\text{V}_4\text{C}_3} \end{array}$$

From Table 4, it is also seen that the chromium-molybdenum-vanadium alloys may form up to 10 percent martensite in the HAZ of flash butt welds, even on applying a postweld cycle to reduce the cooling rate to 0.4°C/s. As



(a) V1657 (scale mark indicates $0.1 \mu\text{m}$).
 (b) V1657 (scale mark indicates $0.1 \mu\text{m}$).
 (c) 100_F ferrite electron diffraction pattern.
 (d) 100_F ferrite electron diffraction pattern.

FIG. 6—Microstructure and diffraction patterns of chromium-molybdenum-vanadium alloy (thin foils).

yet, there has not been sufficient work done to assess whether such a quantity of martensite can be tolerated in welds. The problem, however, may be solved by one of the following procedures: (a) tempering of the HAZ after welding, or (b) adding to the steel a quantity of aluminium to obtain austenite grain refinement, that is, 0.01 to 0.05 percent, which would lead to a lower hardenability, but, as pointed up in a previous section, it would also result in a decrease in strength.

In summary, the work on the chromium-molybdenum alloys has indicated two steel chemistries which appear most suitable for the production of heavy duty rails: (a) 0.70 to 0.80 percent carbon, 0.8 to 0.9 percent manganese, 0.10 to 0.30 percent silicon, 0.04 maximum percent phosphorus, 0.03 maximum percent sulfur, 0.75 to 0.85 percent chromium, and 0.16 to 0.20 percent molybdenum, and (b) 0.65 to 0.75 percent carbon, 0.8 to 0.9 percent manganese, 0.10 to 0.30 percent silicon, 0.04 maximum percent phosphorus, 0.03 maximum percent sulfur, 0.75 to 0.85 percent chromium, 0.16 to 0.20

percent molybdenum, 0.05 to 0.08 percent vanadium, and possibly 0.01 to 0.04 percent aluminium.

Rails manufactured in the fully killed condition according to the first specification should have a mean 0.2 percent proof stress of about 860 MPa, ductilities and Charpy values generally better than AREA standard rails, and transformation characteristics which necessitate the use of a postweld cycle after flash butt welding to avoid the formation of martensite.

An increase in mean proof stress up to about 980 MPa may be obtained in rails of the second chemistry. Rails of this strength, however, may require a tempering treatment after flash butt welding or additions of 0.01 to 0.04 percent aluminium, in which case, they will exhibit a reduction in strength.

Further Tests

In the alloy development program described in the previous section, the assessment of the alloys was made primarily on the basis of tensile, Charpy, and transformation characteristics. It is felt, however, that the reliability of such an assessment can be improved considerably by the simultaneous use of various other testing procedures. Some of the procedures which have been used at BHP MRL for this purpose are described briefly in this section. It should be noted that most of the data which will be presented have been obtained from specimens of rails produced commercially. For details of the various steels, reference should be made to Table 1.

Hot Working Characteristics—The assessment of hot working characteristics of experimental steel grades is an important phase of any alloy development program since the data obtained can be used to predict the necessary roll separating forces, roll torques, and drive motor loadings necessary to roll an experimental alloy in a commercial rolling mill, that is, whether the alloy is capable of being rolled in a particular mill. The technique used to obtain such data under laboratory conditions has been described in a previous report [6].

The range of rail rolling conditions at Australian Iron and Steel Pty. Ltd. is as follows: bloom temperatures are 1025 to 1100°C, finishing temperatures 960 to 1015°C, reduction per pass 5 to 30 percent and strain rate 2.5 to 8.5 s⁻¹. The laboratory rolling trials were thus carried out over a range of similar conditions, namely, temperatures from 950 to 1150°C, at 20 and 30 percent reduction per pass and at a strain rate of 5 s⁻¹. The hot strength of each alloy steel is expressed in terms of a mean yield stress value. This value is calculated from the measured roll separating force and represents the resistance to deformation of a steel to any pass through the rolling mill.

The mean yield stress results obtained are shown in Fig. 7 plotted as a function of rolling temperature for the two percentage reductions used. It can be seen that each of the experimental steels is stronger than the standard steel. The actual percentage increases in strength were as follows:

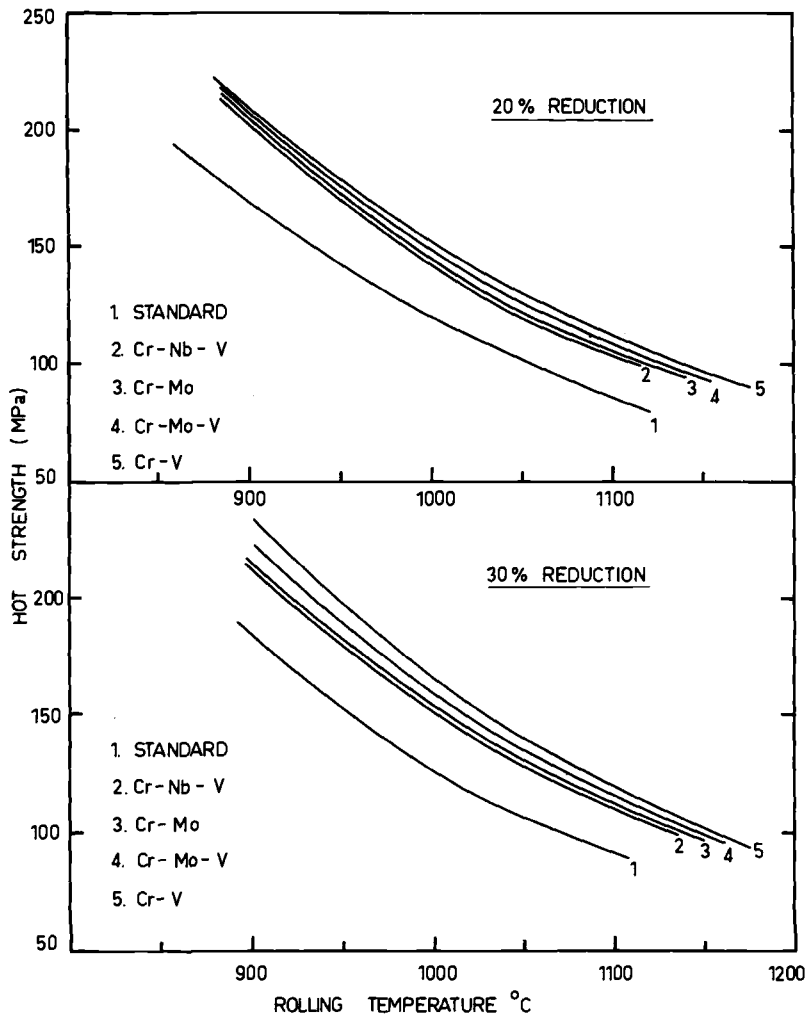


FIG. 7—Hot strength characteristics.

Chromium-columbium-vanadium (Heat 265850)	22 to 25 percent
Chromium-Molybdenum (Heat 11406)	22 to 26 percent
Chromium-Molybdenum-Vanadium (Heat V1657)	23 to 27 percent
Chromium-Vanadium (Heat 2K8711)	24 to 28 percent

The rolling mill at Australian Iron and Steel Pty. Ltd. was therefore capable of hot rolling all of these alloys.

Effect of Rail Type on Wheel Wear—There has been a general belief among track personnel that the use of high-strength rail steels will have a detrimental influence on the abrasive wear rates of wheels.

A laboratory test has been developed at British Steel Corporation (BSC) [7, 8] which greatly exaggerates differences in abrasive wear rates that result from different wheel type/rail type combinations under rolling load conditions. Contrary to the traditional belief, the experiments at BSC have shown that increasing the hardness of either component reduces both its own wear rate and that of the mating component.

A similar test has been used at BHP MRL to determine the effect of the experimental alloy rail steels on the wear of wheels and vice versa. The various alloy rail steels were tested against specimens machined from near the running surface of wrought BS Class C wheels.

The amounts of wear measured in the rail and wheel specimens have been plotted in Figs. 8*a*, *b*, respectively, as a function of revolutions of the wheel specimens. The data show that the abrasive wear of the rail steels is considerably reduced in the high-strength alloys, particularly those of the chromium-molybdenum type. It is also apparent that the high-strength steels have all led to a reduction in the wear rate of the wheel specimens, with the chromium-molybdenum steel again exhibiting the best characteristics.

Figures 9 and 10 show the running surfaces of the wheels and the mating rail types, respectively. It is evident that the mating surfaces are very similar in appearance. It has therefore been suggested that the reduction in wheel wear observed with the higher strength rails may be associated with the reduction in surface deformation obtained on both wheel and rail sample. Indeed, one may expect that the contact between two surfaces such as shown in Figs. 9*a* and 10*a* would enhance the wear process.

Work Hardening—It is evident that the work hardening characteristics of rail steels play a major role in determining their in-track behavior. Laboratory procedures were thus devised to determine such characteristics.

Specimens from various rail steels were subjected to varying amounts of prestrain by means of cold rolling (up to 80 percent reduction). Each specimen was then deformed further under controlled uniaxial plane strain compression conditions. The testing procedure adopted thus eliminated the considerable Bauschinger effect which is exhibited by high-carbon steels on testing under reversed loading conditions (for details of tests, see Ref 9).

The following relationships were established: true stress versus true strain (Fig. 11*a*) and hardness versus true strain (Fig. 11*b*). From Fig. 11*a*, it is evident that, at true strains of less than 0.2, the steels can be listed in order of increasing strength and work hardening rate as follows: standard, chromium-columbium-vanadium (Heat 265850), chromium-vanadium (Heat 2K8711), and chromium-molybdenum (Heat 12547).

Hardness profiles were then taken along the Traverse 1 shown in Fig. 2 on worn standard high and low rails, from a 2-deg curve which had been subjected to traffics of 90, 150, and 210 MGT. The results from the 90 and 150 MGT conditions are shown in Fig. 12, with the omission of the various hardness plateaux which were observed.

The three sets of data have been combined to predict the hardness

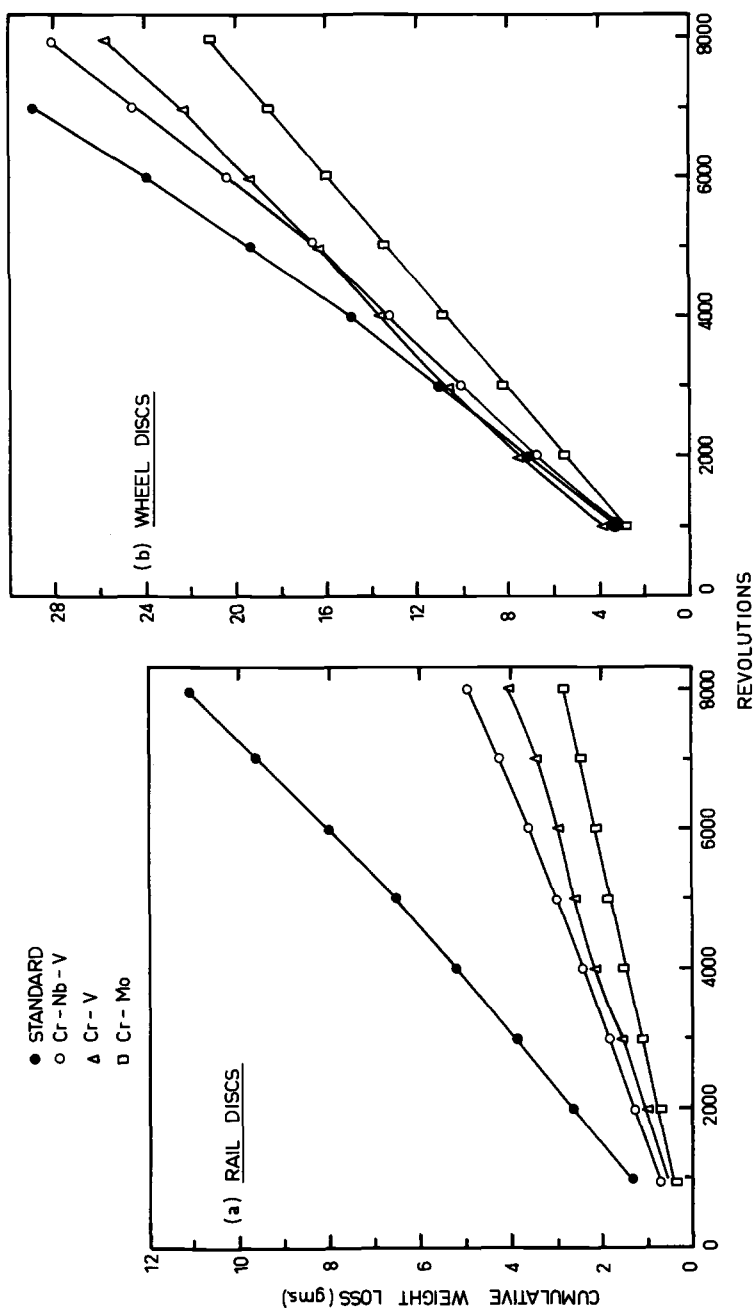
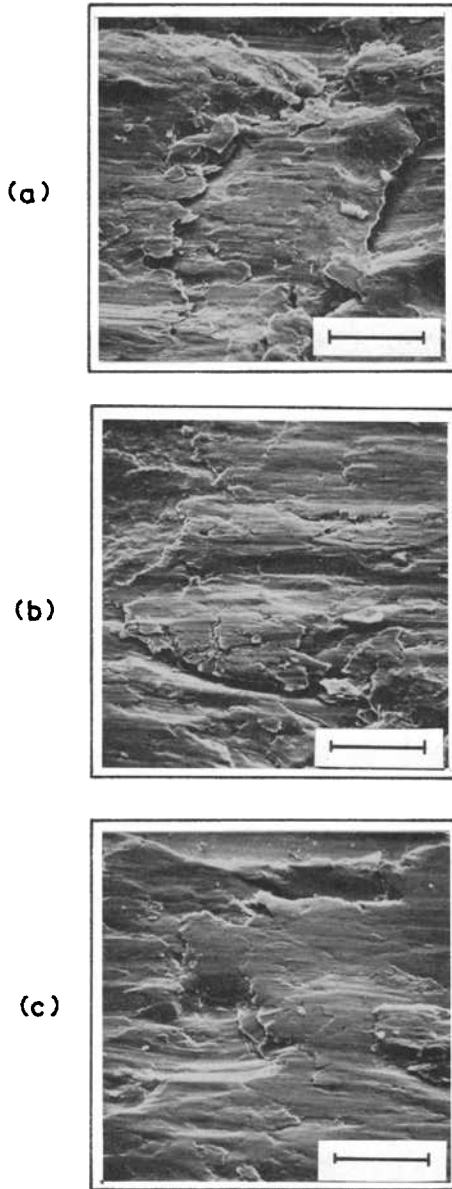


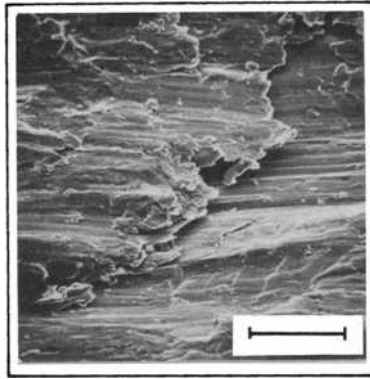
FIG. 8- Abrasive wear characteristics of rails and influence on wear of wheels.



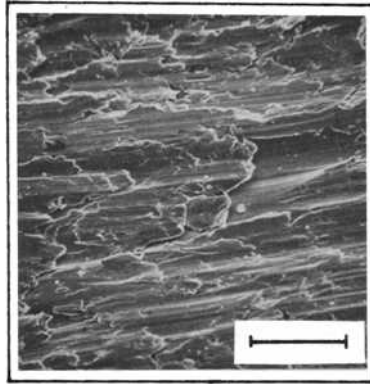
(a) Standard (scale mark indicates 50 μm).
(b) Chromium-columbium-vanadium alloy (scale mark indicates 50 μm).
(c) Chromium-molybdenum alloy (scale mark indicates 50 μm).

FIG. 9—*Running surfaces of rail disks.*

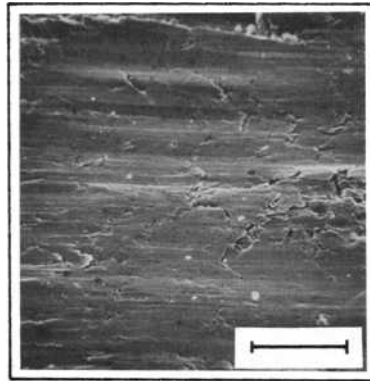
(a)



(b)



(c)



- (a) Standard (scale mark indicates 50 μm).
(b) Chromium-columbium-vanadium alloy (scale mark indicates 50 μm).
(c) Chromium-molybdenum alloy (scale mark indicates 50 μm).

FIG. 10—*Running surfaces of wheel disks.*

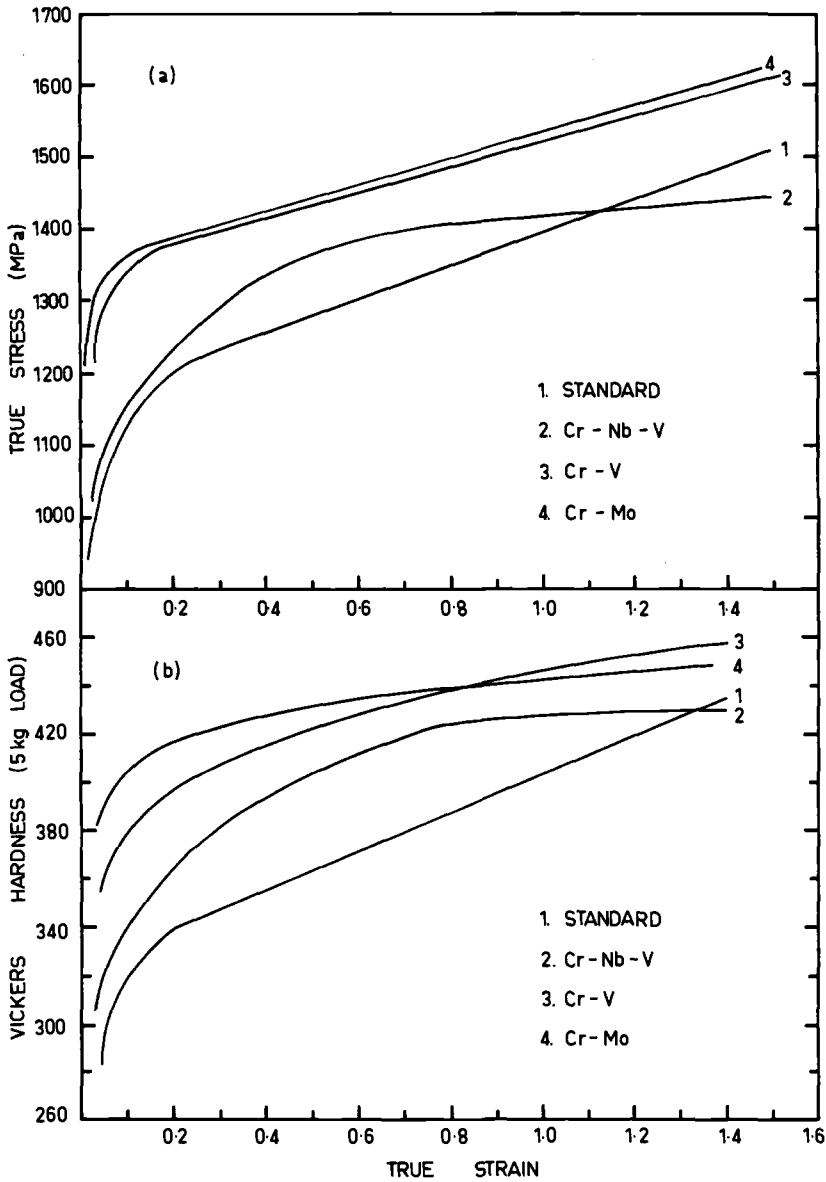


FIG. 11—Work hardening characteristics.

distribution, the depth of hardening, and the depth of microstructural deformation which will develop in the experimental steels when these are placed in 2-deg curves and are subjected to a traffic within the range covered, that is, 90 to 210 MGT. The procedure is best illustrated by using the known behavior of a standard steel to predict the behavior of a chromium-columbium-vanadium steel as a high rail after 90 MGT.

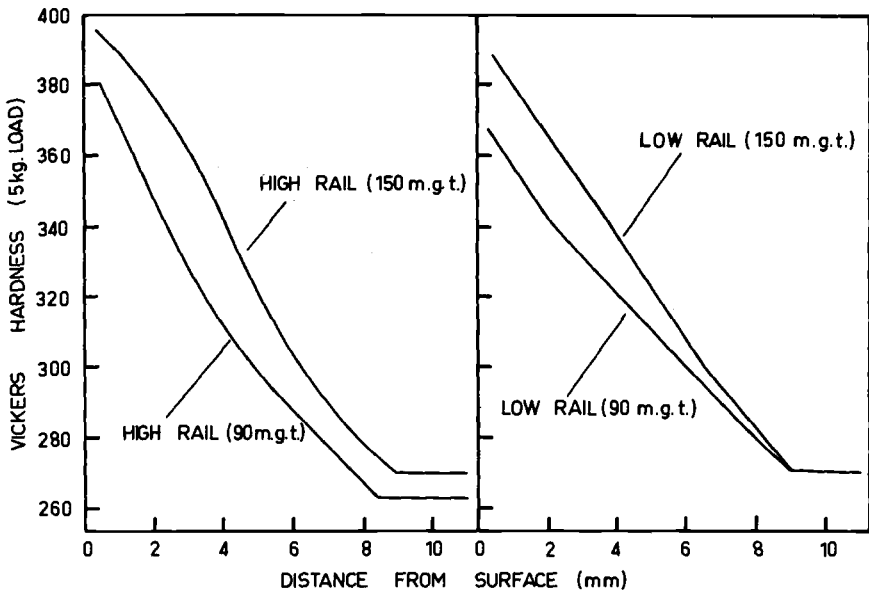


FIG. 12—Hardness profiles in worn standard rails.

The mean base hardness of the alloy steel studied was 307 VHN. The dotted horizontal reference line shown in Fig. 13 can thus be drawn. At approximately 2 mm below the surface, the hardness of the standard rail (Fig. 12) is 350 VHN. To obtain this hardness, a true strain of 0.33 is required (Fig. 11*b*). In turn, such a strain is obtained at a true stress of 1240 MPa

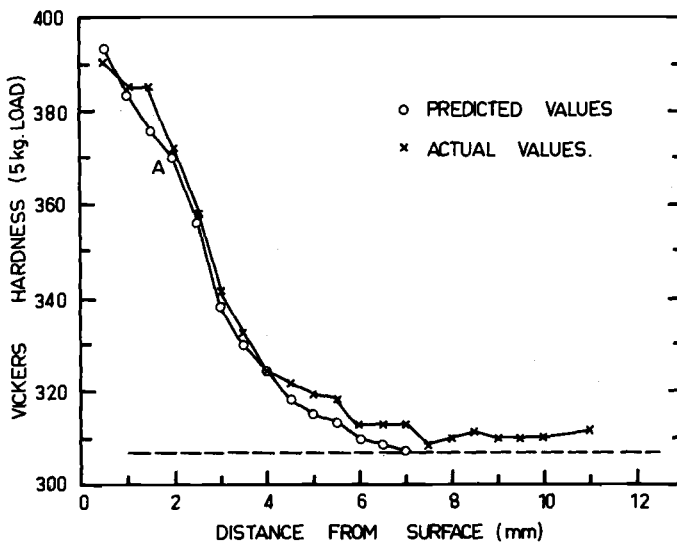


FIG. 13—Predicted and actual hardness profiles in chromium-columbium-vanadium rail.

(Fig. 11a). At the same depth below the surface, a similar stress level should exist in a chromium-columbium-vanadium rail (or indeed in a rail of any composition). In this alloy, a stress of 1240 MPa will lead to a strain of 0.22 which in turn will give a hardness of 370 VHN (from Fig. 11b). This value has been plotted as Point A in Fig. 13. By repeating this procedure, a prediction has been made of the total hardness distribution. Figure 13 also shows the actual hardness distribution observed in a chromium-columbium-vanadium high rail from a 2-deg curve after a traffic of 90 MGT. It is evident that the two sets of values are in excellent agreement.

The procedure has been applied to all the alloy rail types for a traffic of 150 MGT and for high rails. The results are presented in Fig. 14 together with actual data obtained in a standard rail . In terms of increasing depth of hardening, the steels can be listed as follows:

Chromium-molybdenum	3.5 to 4 mm
Chromium-vanadium	4.5 to 5 mm
Chromium-columbium-vanadium	7 to 7.5 mm
Standard	9 mm

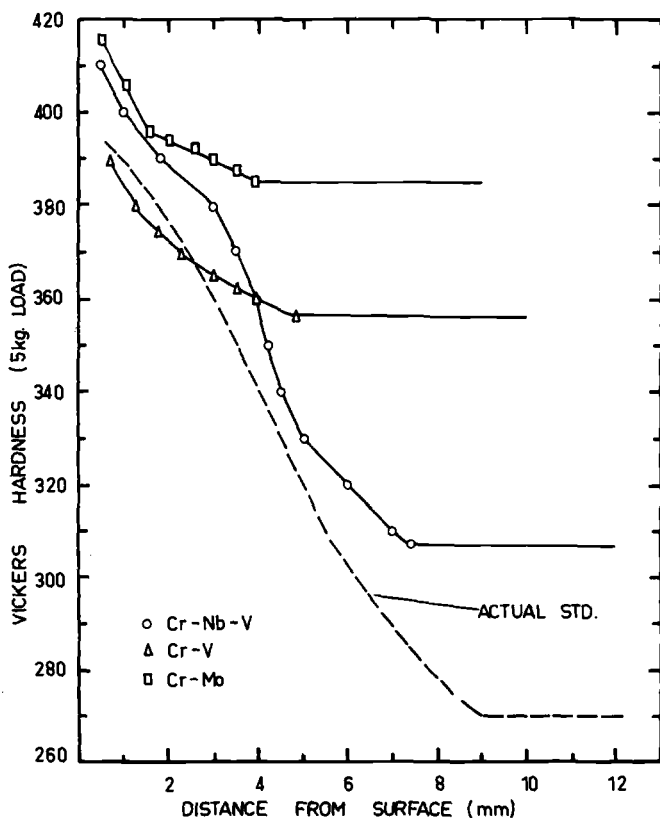


FIG. 14—Predicted hardness profiles in alloy rails after 150 MGT.

As mentioned in a previous section, the depth of microstructural deformation would be even less than these figures.

The major beneficial effect which is expected from such decreases in depth of deformation is the reduction in the number of inclusions which, because of the subsurface deformation, become cracked or give rise to cracks and consequently become potential nucleation sites for shells and transverse defects. Indeed, it may be speculated that the expected decrease in the occurrence of such defects, particularly in the chromium-molybdenum and chromium-vanadium alloys, would be further enhanced by the fact that, at the depth at which a maximum shear stress occurs (5 to 7 mm), there would be no nucleation sites for such defects.

Fracture Toughness and Fatigue Crack Growth—Both the rate at which fatigue cracks grow and the critical crack size are important material characteristics when assessing experimental rail steels. In the current alloy development program, some preliminary work was conducted on the determination of both of these properties, which was then used simply as a means of rating the various rail alloys. The work is continuing with the objective of relating these properties to actual in-track performance.

The static plane strain fracture toughness (K_{Ic}) of standard and alloy rail steels was determined using standard compact tension specimens, 25 mm in thickness and with all other dimensions as given in ASTM Test for Plane-Strain Fracture Toughness of Metallic Materials (E 399-74). The specimens were machined from the head of rails with the plane of the fatigue crack normal to the rolling direction, that is, similar to the growth which occurs in a transverse defect.

The K_{Ic} values of the various steels are shown in Table 5 together with the respective critical crack diameters (d_c) which have been calculated as follows: for a crack of the transverse defect type, d_c is given by

$$d_c = \frac{2}{\pi} \left(\frac{K_{Ic}}{\sigma} \right)^2$$

Assuming that, in standard rails, d_c is 40 mm, that is, about 80 percent of the railhead, then d_c for the alloy rails is given by

$$d_c (\text{alloy}) = \frac{K_{Ic}^2 (\text{alloy}) \times 40}{K_{Ic}^2 (\text{standard})}$$

TABLE 5—Fracture toughness of standard and alloy rail steels.

Alloy Type	Heat No.	K_{Ic} MPa $\sqrt{\text{m}}$	d_c , mm
Standard	...	49.4	40
Cr-Mo	12547	52.5	45
Cr-Cb-V	265850	44.1	32
Cr-V	2K8711	38.5	24

K_{Ic} type specimens were also used for fatigue crack growth determinations. The specimens were subjected to minimum and maximum tensile loads of 1000 and 19 500 N, respectively.

The results obtained are shown in Fig. 15. Thus, in order of increasing crack growth rate, the rails could be listed as follows: chromium-molybdenum, standard and chromium-columbium-vanadium, and chromium-vanadium. Furthermore, it is more evident that the chromium-vanadium steel failed at a crack length which was considerably smaller than in the other rail steels.

The work on fatigue crack growth rate will be continued under stress conditions which simulate more closely those which develop in track.

Summary and Conclusions

A detailed study of the various defect types which develop in standard rails subjected to high axle loads has shown that all of the defects are associated with yielding and plastic deformation of the rail materials. A reduction in the occurrence of such defects would thus require primarily the use of materials exhibiting higher yield strengths.

Techniques have been developed which allow industrial rail production and on-site flash butt welding procedures to be simulated in the laboratory. Using these techniques, an alloy development program has been conducted on three rail steel types, namely, chromium-columbium-vanadium steels, chromium-vanadium steels, and chromium-molybdenum steels. All of these alloys exhibit strengths higher than standard rails.

The alloys have been assessed in terms of the following material properties and characteristics:

- Tensile strength and ductility
- Hardness
- Weldability
- Hot strength
- Impact resistance
- Work hardening
- Influence on wheel wear
- Fracture toughness and fatigue crack growth

Fully pearlitic steels exhibiting a range of yield strengths up to 1000 MPa have been developed without adversely influencing, and frequently improving, other mechanical properties.

The welding of rails has been the major restricting influence on further developments. This restriction, however, may be relaxed to some extent by modifying flash butt welding procedures. A further relaxation may be obtained by including in the welding procedure a tempering process.

A number of the alloys have been produced commercially and are currently undergoing in-track assessment at both the Mt. Newman Mining

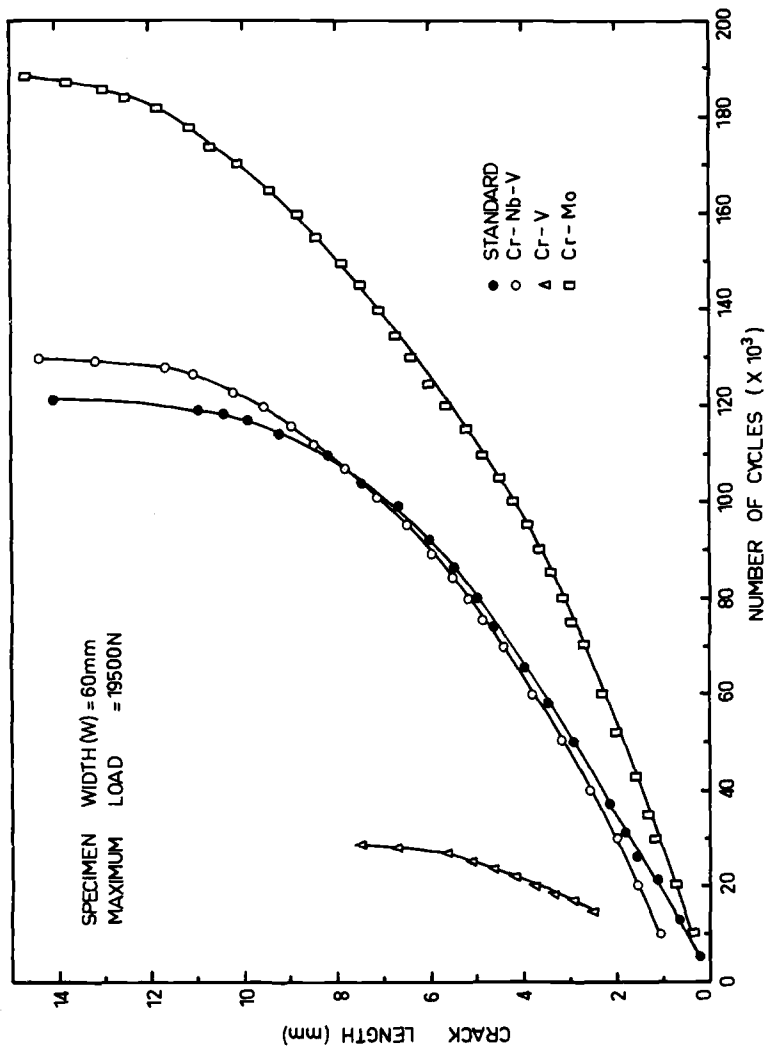


FIG. 15— Fatigue crack growth rates in rail steels.

Co. and Hamersley Iron. The primary objective of the in-track program is to carry out a cost/benefit analysis which will include increase in rail life versus increase in production and welding costs of the new materials.

Acknowledgments

This study was conducted as part of a cooperative program between Mt. Newman Mining Co. Proprietary Ltd. and The Broken Hill Proprietary Co. Ltd. on the development of rail tracks for heavy axle loads. The support and assistance of R. Murphy, railroad manager, and R. A. Jupp, technical superintendent, Railroads, with site observations and samples is gratefully acknowledged. The contribution of plant personnel at Port Kembla Works, notably B. P. Barnsley, assistant manager, Technical Services, and J. K. MacDonald, principle research officer, Products, is also acknowledged. Finally, several colleagues at MRL, notably Dr. R. Moller, R. Boelen, and R. Clark, have given valuable assistance in the laboratory studies.

References

- [1] Marich, S. and Curcio, P., "Development of High Strength Alloyed Rail Steels Suitable for Heavy Duty Applications," BHP Melbourne Research Laboratories Report MRL/083/76/015, June 1976.
- [2] Mair, R. I. and Jupp, R. A., "Rail Track for Heavy Unit Train Operations," presented at the Annual Technical Conference of the Institution of Engineers, Australia, May 1976.
- [3] Marich, S., "Flash Butt Welding of Heavy Duty Rails—Laboratory Simulation and On-Site Experience," presented at the Annual Assembly of the International Institute of Welding, Sydney, Australia, Aug. 1976.
- [4] Smith, Y. E., Sawhill, J. M., Cias, W. W., and Eldis, G. T. *AREA Bulletin*, June-July 1976, Vol. 77, pp. 621-651.
- [5] Baker, R. G. and Nutting, J., "Precipitation Processes in Steel," Iron and Steel Institute Special Report No. 64, 1959, pp. 1-22.
- [6] Moller, R., "Measurement of Resistance to Hot Deformation in Steel," BHP Melbourne Research Laboratories, Report MRL 59/1, April 1972.
- [7] Babb, A. S. and Lee, J., "The Laboratory Wear Testing of Tyre Wheel Steels," 4th International Wheelset Congress, Paris, July 1972, pp. 16-30.
- [8] Babb, A. S., "Testing Techniques for Railway Materials," British Steel Corporation Research Report Prod/Eng/7063/73/A.
- [9] Marich, S. and Curcio, P., "Work Hardening of Standard and Alloy Rail Steels," BHP Melbourne Research Laboratories Report MRL/083/76/010, Jan. 1976.

DISCUSSION

*E. Koerfer*¹ (*written discussion*)—In a few sentences, I would like to report on the experiences and results achieved by the Klockner mill with regard to this topic.

Since 1900 until approximately ten years ago, alloyed steels were used in

¹Klockner-Werke AG, West Germany.

tee rails and grooved rails as a compound material. Therefore, to resist wear in the railhead, steels containing approximately 1 percent chromium were used. Rail web and base were built up through a soft ductile steel as shown in Fig. 16. This patented process was achieved by pouring both steels in a ratio of 1:2 into an ingot mold. The rolling into rails followed the commonly accepted practice.

The chemical composition of the compound casted rails was as follows:

	Carbon, %	Silicon, %	Manganese, %	Phosphorus, %	Sulfur, %	Chromium, %
Hard railhead	0.55	<0.35	0.50	<0.05	<0.05	1.0
Soft web and base	0.35	<0.35	0.50	<0.05	<0.05	...

The railhead had a tensile strength of 160,000 psi (1100 N/mm²) and an elongation exceeding 8 percent. The microstructure was fully perlitic with small interlamellar spacings.

These compound-casted rails under unusually heavy service showed a fivefold life span as opposed to normal rail steel. This was also proven true in the United States. The expenditures involved in finishing the rails at the mill and certain welding problems was an inducement to justify production

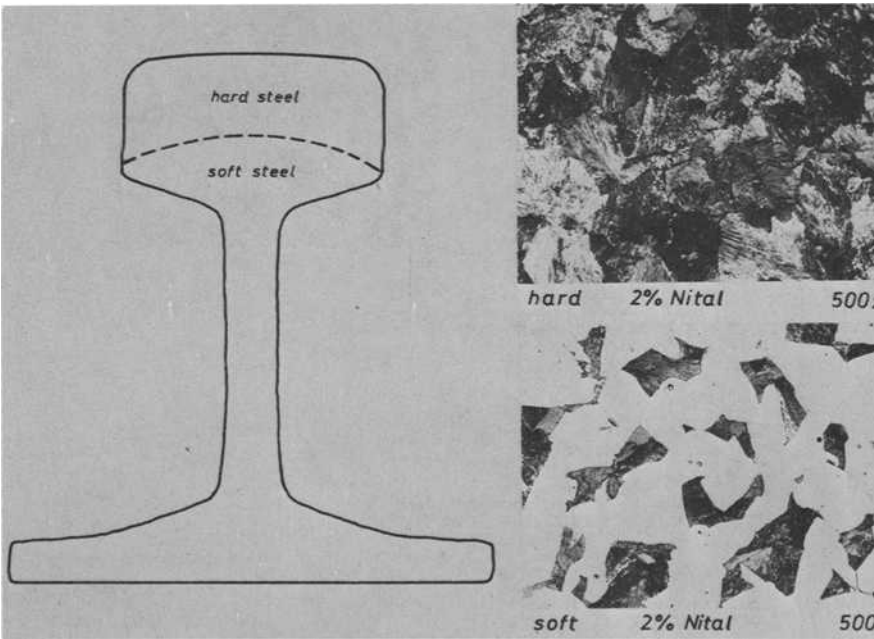


FIG. 16—Klockner compound rail.

of high tensile type rails economically. Thereby, improvements in steel metallurgy—deoxidation, vacuum degassing, ingot mold geometry, and casting aid agents—could be utilized.

The highly wear resistant alloy rail with an appropriate chemical analysis and inherent mechanical properties follows the natural sequence of further development of the compound material. This is shown by the following data:

Chemistry						
Carbon, %	Silicon, %	Manganese, %	Phosphorus, %	Sulfur, %	Chromium, %	Molybdenum, Vanadium, % ^a
0.7	0.5	0.8	0.03	0.03	1.0	0.1 0.1
Tensile strength			1.00 N.mm ² (160,000 psi min)			
Yield point			650 N.mm ² (95,000 psi min)			
Elongation			10 percent			

^aMolybdenum and vanadium mill's option.

The microstructure consists of sorbite/troostite and is free of ferrite as shown in Fig. 17.

Rails of this type can be produced with current steelmaking and rolling procedures which are less complex than those required in the production of

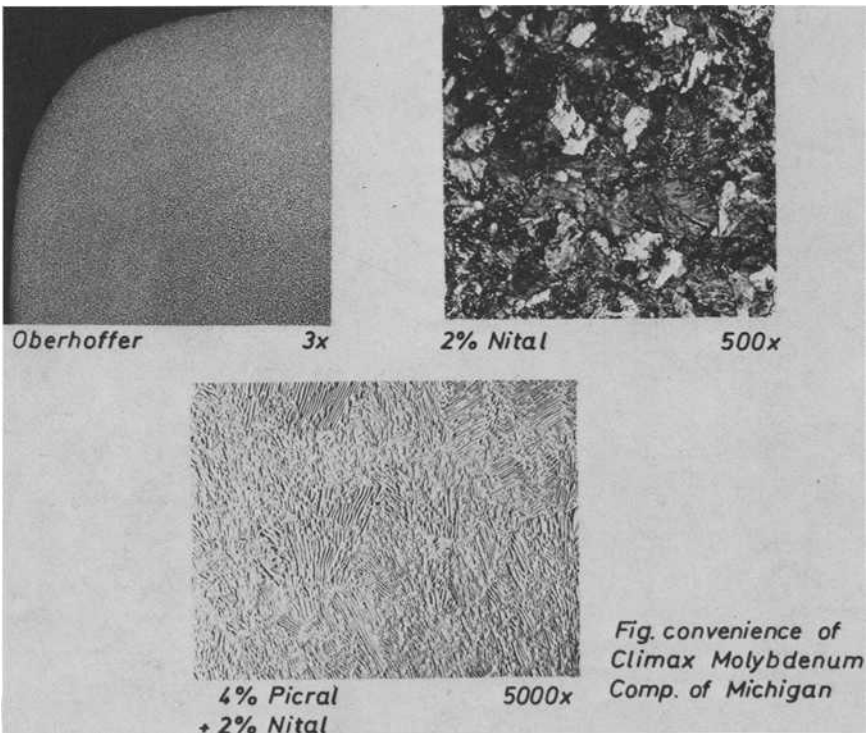


FIG. 17—Macro- and microstructures of steel for rails in Special Quality KVS 610.

compound-casted rails. Delivery terms can therefore be met without limitations if the chemical analysis and mechanical properties are adjusted accordingly. The question of weldability has also been resolved. The welding parameters need to be adjusted according to the chemical composition.

The thermal cycle must be adjusted such that cooling after the welding will not lead to transformation to hard bainitic or martensitic microstructures or both in the heat-affected zones. This will be achieved when more than 7 min are allowed for cooling of the heated area from 800 to 500°C (1472 to 932°F). To achieve this, the course of action would be a series of preheating prior to welding or a delay in cooling insulation against loss of heat such as reheating.

A service time of more than ten years, not only in Germany, but throughout the world, is evidence that this type of rail is generally accepted.

For heat-treated rails similar in their composition to compound-casted rails—wear resistant hard steel in the railhead and soft steel in the web and base—it may be beneficial to merely use C steel. Additional work procedure must surely be used for handling heat-treated materials. One must expect reductions in the ordered lengths. Even though this type of carbon steel welds well, annealing effects in the weld area can occur which would then have an irregular effect on the track surface with unpleasant consequences.

With alloyed rail steel, one will notice that the tensile strength in the area of the edge of the rail base will sometimes be a little higher than in the railhead, but, because of the refinement in the grain structure, which results from the several rolling operations, sufficient ductility is maintained. Exceptions to this have not been made known.

Since 1965, continuous cast rails, rolled by Klockner, have been tested by the German Federal Railroad. Prior to rolling, the blooms' dimensions were 280 by 280 mm, and they were shaped into rails in nine passes using the commonly accepted practice. The end result was a section S54 with an area of 6948 mm². The forming ratio was 11.2 fold. The 30 m lengths were then welded into 120 m lengths utilizing flash welding. In the field, thermite procedure was followed when welding the lengths to the existing track.

All chemical and mechanical conditions according to UIC 860 for wear resistant quality rail steel were met. Also all criteria for testing were met. During macrotesting, one could notice the original material as being continuous cast, that is, segregation of the original core zone.

These continuous cast rails are still in use today on the main line of the German Federal Railroad. In the ten years that these rails have been in use, mixed passenger and freight traffic consisting of 300 million metric tons have rolled over them. The passenger trains roll over this section at 160 kph.

No difference in behavior was noticeable in the test section from the adjoining rail sections produced in the commonly accepted manner.

S. Marich (author's closure)—As pointed out in a recent publication,² I am in complete agreement that the microstructure of a steel plays a major

²Marich, S., AREA Bulletin 663, Vol. 78, June/July 1977, pp. 594–610.

role, together with hardness and tensile strength, in determining the wear resistance.

I also agree that modern rail steel metallurgies, steelmaking, and rail rolling techniques can at least minimize the occurrence of fatigue defects associated with flakes, inclusions, and segregation. However, the ability to do so is also a function of the loads applied to the rails. Thus, as axle loads increase, the critical crack size of defects in the steel will decrease, and, therefore, further improvements in material properties and processing practices will become necessary.

It is my opinion that the formation of shells in rails depends on both steel cleanliness and material properties such as yield and tensile strengths, fatigue resistance, and work hardening characteristics. The effect of inclusions would be primarily associated with the nucleation stage of the fatigue crack while material properties would have a major influence on the growth stage. Unfortunately, although numerous general studies on this phenomenon have been reported in the literature, the number of studies that have included detailed microscopic examination of the nucleation of shells has been negligible.

The "hollow cavities" shown in Fig. 3 are due to the formation of a martensitic type phase on the surfaces of the shelly crack. This phase forms because of friction effects between the surfaces and is very brittle. On sectioning of samples, spalling of this phase occurs, giving the impression of large cavities associated with the shelly crack.

E. Koerfer (written discussion)—Please allow me to make a few comments on the strength and safeguarding against breakage of rail steels and fatigue in rail steels from the German point of view. The requirements on steel for rail in service with regard to the head, web, and base of rail are quite distinct. For the rail producer, it is therefore important to find the optimum compromise.

The governing factor for the wear resistance of rail steel is the tensile strength and hardness. Yet, it must be pointed up that it is not enough to have tensile strength and hardness; a specific microstructure is also necessary. Experience has shown that, at the same tensile strength and hardness level, a microstructure of pearlite/sorbite gives less wear than a microstructure of bainite or tempered martensite achieved by hardening or quench and tempering.

Internal defects in the head of the rail, such as flakes, macroinclusions, and segregation, enhance the formation of fatigue cracks as a result of the stresses developed by the wheel/rail interaction which sooner or later create rail breaks. Due to modern improvements in steel metallurgy, steelmaking, and rail rolling practice, the rail will be able to avoid the aforementioned failure.

Shelling is of a peculiar nature. Numerous examinations have proved that often shelling is not the result of internal defects in the material, but the result of the inability of the material to withstand the applied loads. In Fig.

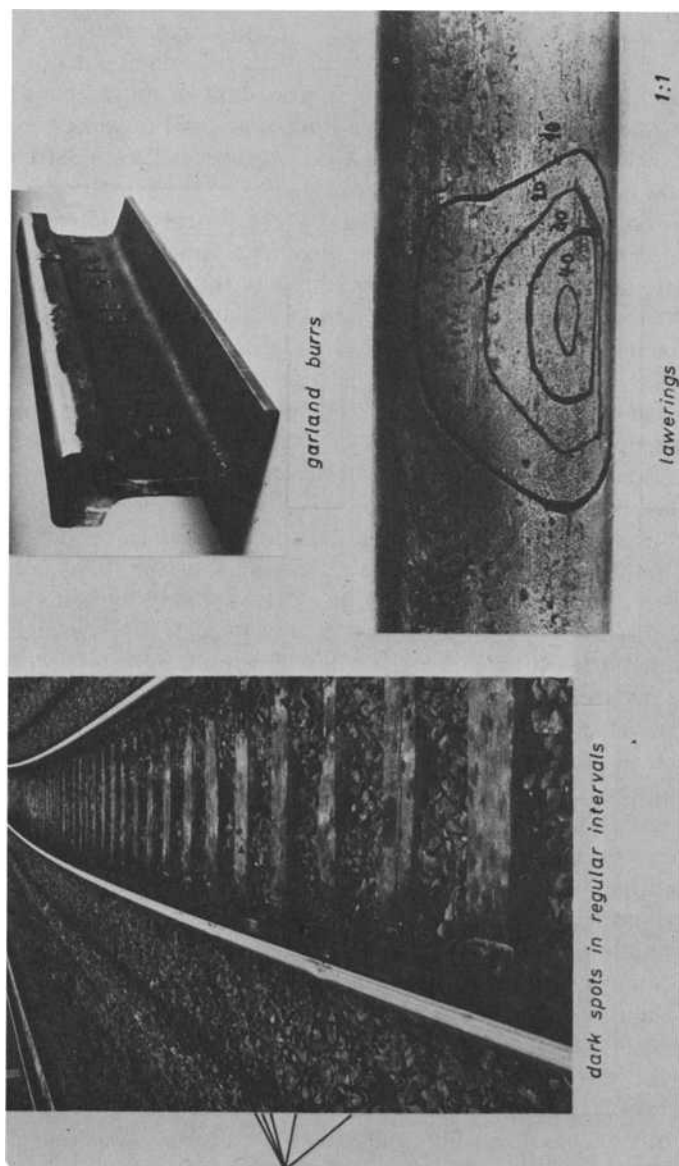


FIG. 18—Shelling Section S64, Quality UIC-C.

18 on the higher rail in a curve, noticeable dark spots are evident in more or less regular intervals on the rail surface which are typical for the beginning of shelling. They show a local narrow lowering of the running edge where the wheels no longer made full contact. This lowering of the running edge can be as much as 0.5 mm. The running edge is reduced to something resembling a garland. As shown in Fig. 19, sectioned damaged areas indicate a crack oriented at an angle to the running surface of the rail and at a depth of 6 to 10 mm under the running edge. Figure 19 also shows a noticeable deformation of the material which has led to a limited amount of work hardening underneath the running edge of the rail. Cracking occurs once the strength of the steel is exhausted. In several instances, due to service conditions, hollow cavities were created as illustrated in Fig. 20. The process of deformation of the material can be observed from the dendritic structure.

The question of consistency in rail quality and the load application with regard to the formation of shelling was proved in an experiment. In a curve with a radius of 1800 m, on which both high-speed trains and heavy freight traffic travelled, the outside rail was replaced with a section S54 which had a tensile strength of only 520 N/mm² (75 000 psi), whereas the remaining rail had a tensile strength of 880 N/mm² (127 000 psi). After a short period of service, a noticeable difference in the surface condition of the two rail types could be observed. The lower strength rails showed severe damage on the running surface as can be seen in Fig. 21, while the adjacent rails showed normal wear. Most noticeable was the periodicity of the damage.

The height of the profile, the width of the running surface, and the hardness of the running surface are depicted in Fig. 22. Likewise, the crack zones are noted. Clearly evident is the periodicity of the deformation and the relationship between deformation hardening and crack formation. Figure 23 shows a transverse rail section cut through a damaged area illustrating the crack and structural damage observed under the running edge.

The conclusions can be drawn that shelling is greatly influenced by a rail's tensile strength. Therefore, rail failure can occur without material defects such as large slag inclusions, clinker, or poor material purity of steels if the service conditions are greater than the rail quality.

Generally speaking, insufficient rail web behavior can be traced back to piping, lamination, and large inclusions. Simple metallurgical preventive measures or, in exceptional cases, an ultrasonic examination of the rail web can bring about the best results. For an undisturbed stress transfer from railhead to web to the rail base, rails should show a great transition radius. An acceptable surface finish is a matter of course.

For the transmission of dynamic stresses, the area of the rail base should be as smooth as possible. Through suitable roll design, cracks on the underside of the rail base can surely be eliminated.

Statistics indicate that the proportion of rail breaks increases as service time is extended. Often, brittle vertical breaks have occurred in which the origin cannot be determined with the bare eye. On more detailed examination, it is often found that many fatigue cracks have nucleated and grown

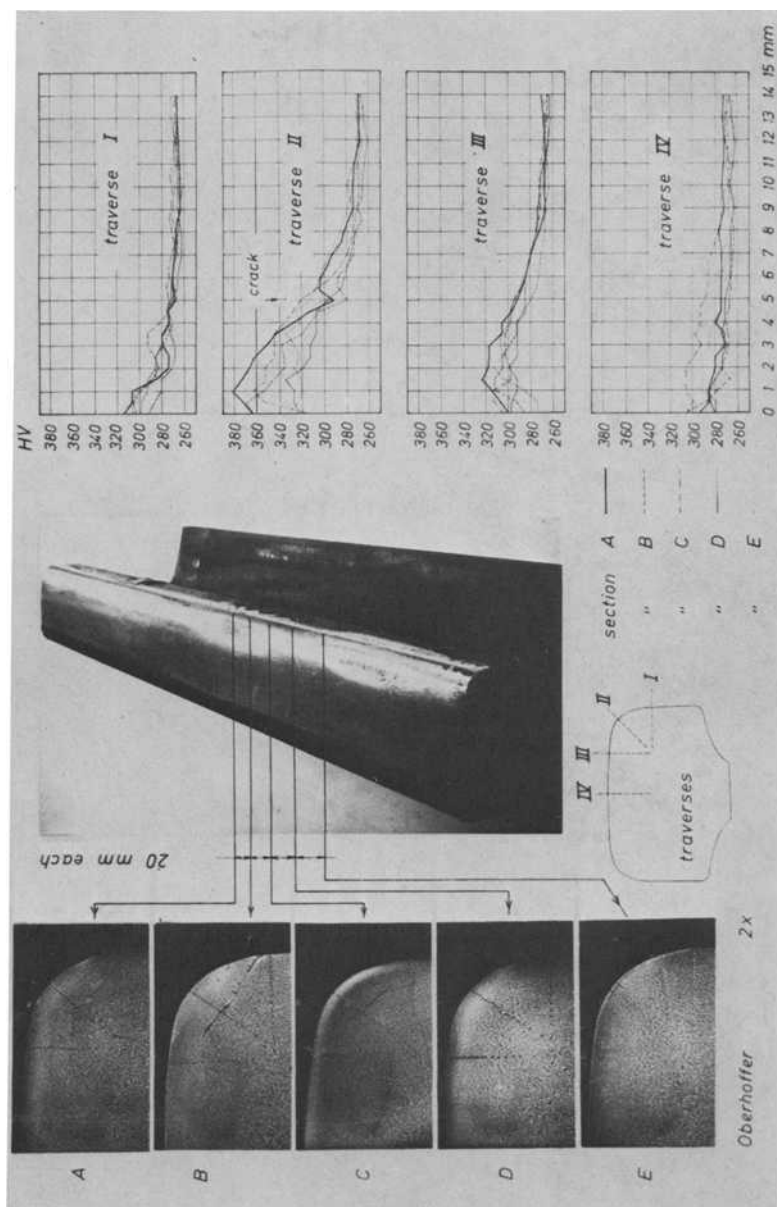


FIG. 19—Shelling, structure, hardness.

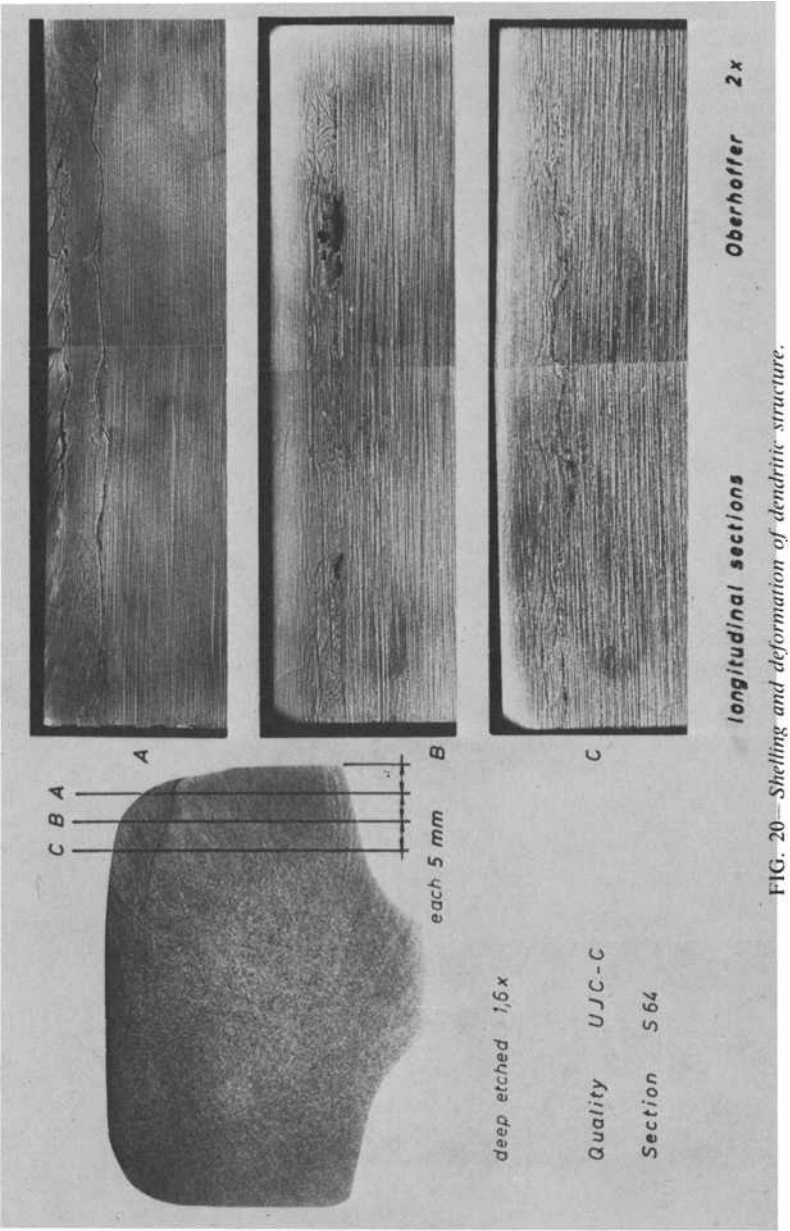


FIG. 20—Shelling and deformation of dendritic structure.

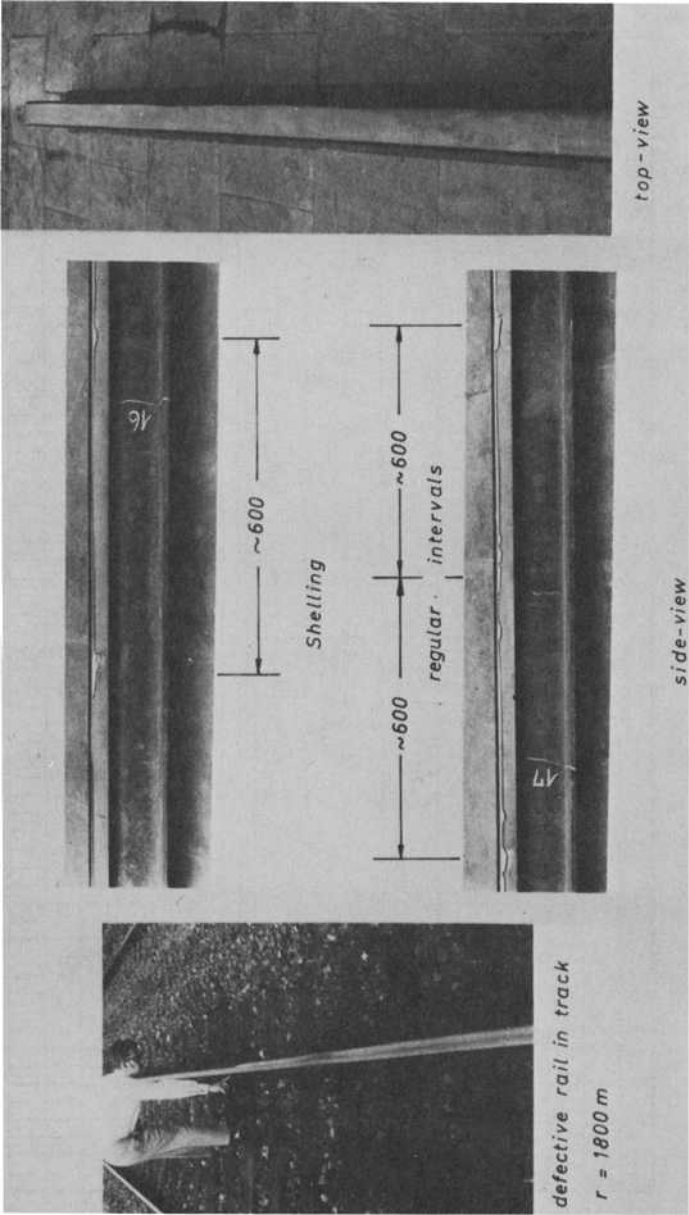


FIG. 21— Defects on running edge of rail.

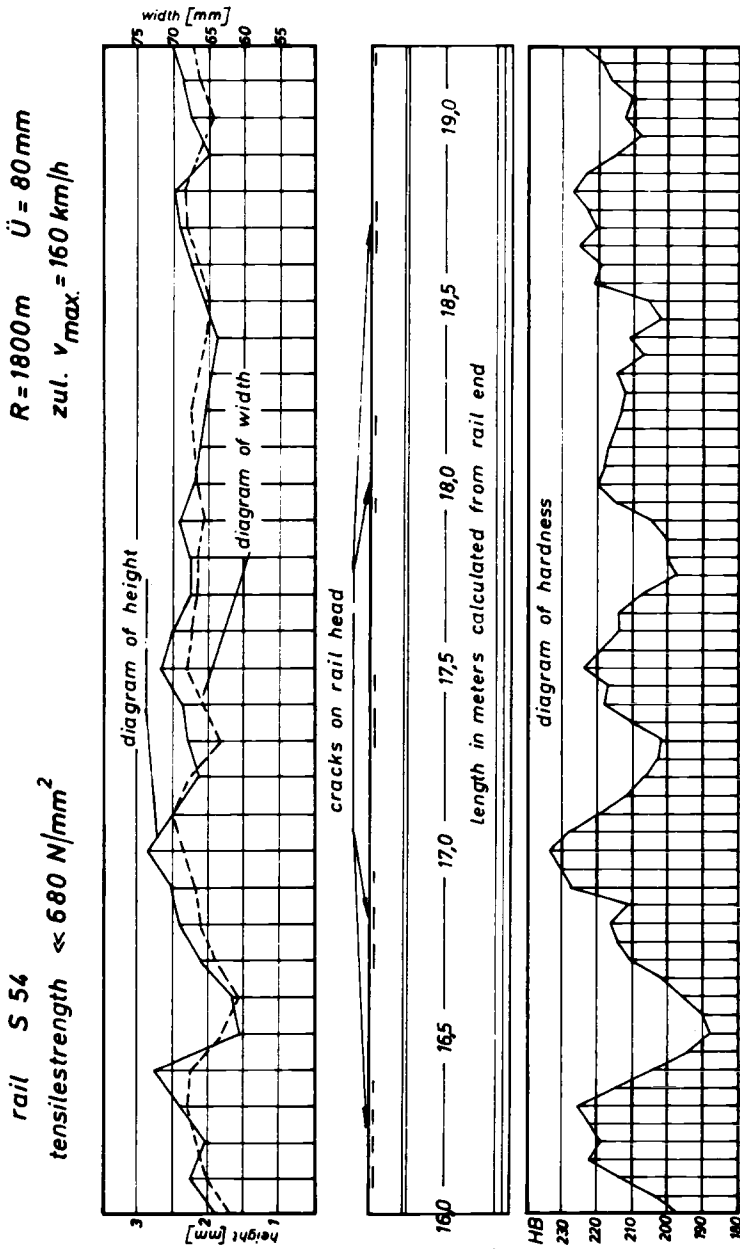


FIG. 22- Diagrams of height, width, and hardness of the running surface.

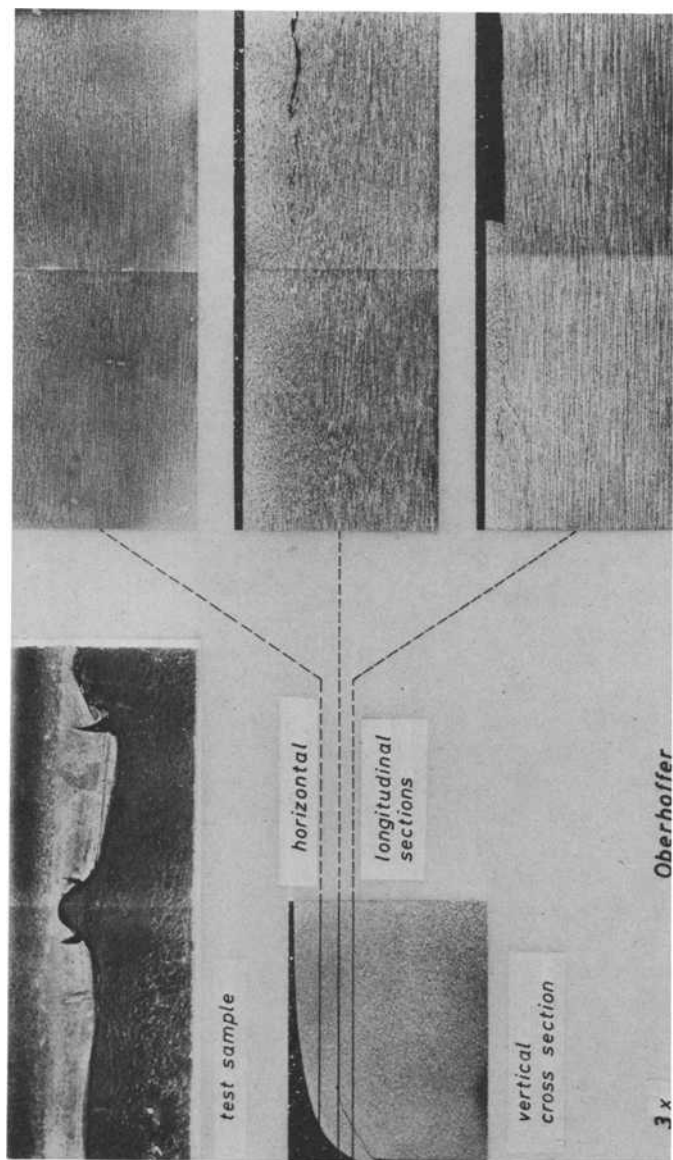


FIG. 23—Crushing, shelling.

from the underside of the rail base prior to the catastrophic failure of the rail. Figure 24 shows a vertical rail failure which resulted from numerous corrosion fatigue cracks nucleated on the underside of the rail base. A further improvement in rail life could thus be realized by minimizing the corrosion susceptibility of the rail steel.

S. Marich (author's closure)—It is recognized that the formation of a hard and brittle microstructure in the heat-affected zone of welds could be deleterious to the in-track performance of welds. The formation of martensite should therefore be prevented as Dr. Koerfer suggests by reducing the cooling rate in the heat-affected zone subsequent to welding. However, it is felt that the same does not apply to a bainitic microstructure which, in these alloy types, is considerably softer and more ductile than martensite.

Dr. Koerfer appears to suggest the use of "standard" carbon steel for the production of heat-treated rails. This has indeed been the practice for many years in countries producing rails of this type, such as the United States, Japan, and Russia. The production of heat-treated rails does require special production facilities. However, heat treatment procedures do not influence the "ordered" rail length. For example: in both Japan and Russia, rails of 25 m length are produced in the heat-treated condition. Under high axle load conditions, welds in heat-treated rails do have a tendency to form "soft spots." This behavior is more prevalent in heat-treated rails consisting of bainitic or quenched and tempered martensitic microstructures.

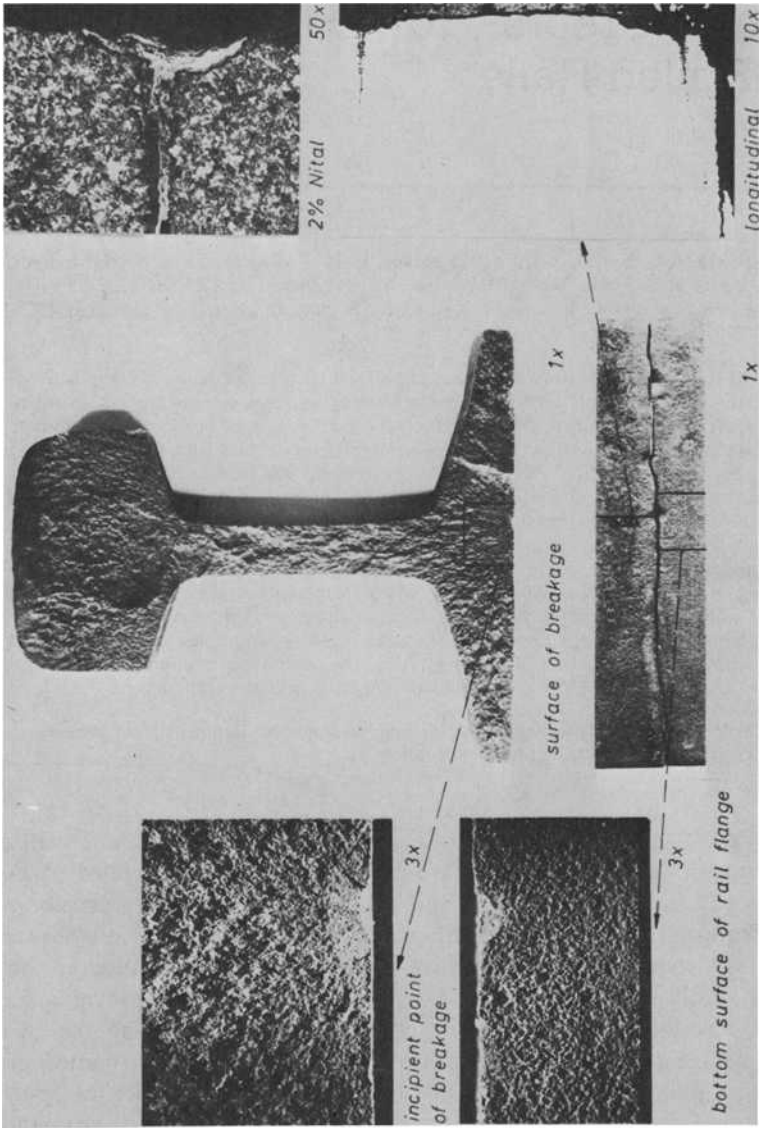


FIG. 24— Brittle breakage on S49 fatigue fractures due to corrosion.

Alloy Steels for High-Strength, As-Rolled Rails*

REFERENCE: Smith, Y. E. and Fletcher, F. B., "Alloy Steels for High-Strength, As-Rolled Rails," *Rail Steels—Developments, Processing, and Use, ASTM STP 644*, D. H. Stone and G. G. Knupp, Eds., American Society for Testing and Materials, 1978, pp. 212-232.

ABSTRACT: A laboratory study was conducted on a broad range of compositional variations of chromium-molybdenum steels for application as high-strength, as-rolled rails. A series of experimental heats was prepared and processed to simulate commercial production of as-rolled 65-kg/m (132-lb/yd) rail, with regard to cooling rate and transformation characteristics. Test specimens were evaluated in terms of hardness, tensile properties, and microstructure. The mechanical properties are related to the observed microstructures. Increasing the molybdenum content of the steel is highly effective in increasing yield strength by refining the pearlite; the appearance of coarse bainite reduces the yield strength. Vanadium contributes additional strengthening, but only under certain conditions where the pearlite is refined. Lowering carbon and adding columbium produces microstructural changes that are not beneficial to the mechanical properties. These results make possible some tentative conclusions regarding the optimization of composition for the commercial production of as-rolled rails in the 760 to 1170 N/mm² (110 to 170 ksi) yield strength range.

KEY WORDS: steels, railroad tracks, high strength steels, mechanical properties, microstructure, pearlite, molybdenum alloys

A recent publication described the laboratory and commercial-scale development of high-strength, chromium-molybdenum, as-rolled 65-kg/m (132-lb/yd) rails for main line and mineral railways.² This development arose from a growing demand for higher strength rails, as well as a need for a means of producing such a product without heat treatment because of the limited worldwide capacity of existing equipment. The previous paper briefly described some of the observed relationships among the critical parameters, namely, steel composition, cooling rate, transformation products and microstructures, and hardness and tensile properties. Further laboratory studies have been directed at a more complete understanding

*Original experimental data were measured in U.S. customary units.

¹Research supervisor and senior research associate, respectively, Climax Molybdenum Company, Ann Arbor, Mich. 48106.

²Smith, Y. E., Sawhill, J. M., Jr., Cias, W. W., and Eldis, G. T., *American Railway Engineering Association Bulletin*, June/July 1976.

of the physical metallurgy of prospective high-strength, as-rolled steels for rail applications. This paper summarizes the results of the work to date in an investigation that is continuing.

Experimental Methods

Steelmaking

Steels were produced by induction melting in 25 to 57-kg (55 to 125-lb) heats that were aluminum killed. Common commercial impurity contents of sulfur and phosphorus were added to each heat. Since the research described in this paper spans a three-year period, there has been some evolution in procedure over the period. Initially, the heats were melted under either argon or vacuum, as designated by either a prefix P or V in the heat number (Table 1). However, air melting was adopted relatively early, so most of the steels in the composition list of Table 1 do not carry this prefix. The variation in melting practice is not considered to be significant with respect to the comparisons that will be made in this study. Two to four ingots per heat were chill cast in tubular steel molds.

Specimen Preparation and Testing

The ingots were forged into billets which were subsequently hot rolled into approximately 22-mm (7/8-in.) round bars that were cut into tensile specimen blanks. Since this study was directed toward developing higher hardness in the heads of 65-kg/m (132-lb/yd) rail, the processing of all test specimens incorporated a final cooling cycle that simulated the cooling of the heads of as-rolled 65-kg/m (132-lb/yd) rail. Common commercial practice in North America involves air cooling the rail on cooling beds to below 540°C (1000°F), after which the rail is placed in an insulated box to reduce the cooling rate and thus ensure against hydrogen-induced cracking. The rails then take over 10 h to cool below 175°C (350°F). With respect to the laboratory tests, only the cooling rate to the temperature at which transformation is complete is of significance.

Information from several (unpublished) sources indicates that the commercial finish rolling temperature is around 1010°C (1850°F) and the time required for 65-kg/m (132-lb/yd) railheads to cool from 925 to 705°C (1700 to 1300°F) is between 5 and 6 min. For most of the steels, this natural cooling rate was attained by making bundles of seven 22-mm (7/8-in.) bars and using the center bar as the specimen. The temperature of the specimen bar was monitored with a thermocouple attached to the surface at the longitudinal center. The bundle was heated to 1010°C (1850°F), air cooled to between 480 and 540°C (900 and 1000°F), and furnace cooled to near room temperature.

Specimens of the last six steels in Table 1, which involves an evaluation of

TABLE 1—Compositions of experimental steels.

Steel No.	Heat or Ingot No.	Element, %										
		C	Mn	Si	Cr	Mo	V	Cb	P	S	Al	N
1	P995A	0.77	0.82	0.13	0.70	0.18	(0.015) ^a	(0.015)	(0.04)	ND ^b
2	V1096A	0.73	0.83	0.16	0.75	0.21	(0.015)	(0.015)	(0.04)	ND
3	V1095A	0.78	0.88	0.17	0.79	0.24	(0.015)	(0.015)	(0.04)	ND
4	P995C	0.76	0.92	0.14	0.81	0.28	(0.015)	(0.015)	(0.04)	ND
5	P925	0.75	0.81	0.17	0.73	0.40	(0.015)	(0.015)	0.04	0.007
6	P995D	0.76	0.92	0.13	0.80	0.28	0.06	...	(0.015)	(0.015)	(0.04)	ND
7	5770C	0.77	0.86	0.20	0.74	0.26	0.05	...	(0.022)	0.023	0.03	ND
8	5814C	0.68	0.88	0.28	0.82	0.24	0.019	0.026	0.07	0.011
9	5814B	0.64	0.88	0.28	0.82	0.24	0.019	0.026	0.07	0.011
10	5814A	0.60	0.88	0.28	0.82	0.24	0.019	0.026	0.07	0.011
11	5815A	0.73	0.92	0.88	...	0.24	0.019	0.024	0.09	0.011
12	5815C	0.71	0.93	0.88	0.44	0.24	0.019	0.024	0.09	0.011
13	5772	0.79	0.86	0.21	0.74	0.19	0.021	0.023	0.04	0.009
14	5770A	0.76	0.85	0.21	0.72	0.19	0.05	...	0.022	0.023	0.04	0.009
15	5773A	0.80	0.89	0.53	0.58	0.19	0.021	0.023	0.04	ND
16	5773B	0.79	0.89	0.54	0.59	0.19	0.06	...	0.021	0.024	0.04	ND
17	5625A	0.76	0.86	0.44	0.79	0.003	0.10	...	0.021	0.026	(0.06)	ND
18	5627A	0.74	1.25	0.30	0.81	0.03	0.10	...	0.020	0.025	(0.06)	ND
19	5814D	0.66	0.88	0.28	0.82	0.24	...	0.02	0.019	0.026	0.07	0.011
20	5868A	0.68	0.61	0.26	0.51	0.30	0.020	0.024	0.09	0.012
21	5868B	0.68	0.61	0.26	0.51	0.30	...	0.02	0.020	0.024	0.09	0.012
22	5868C	0.68	0.61	0.26	0.51	0.30	...	0.04	0.020	0.024	0.09	0.012

^a Parentheses indicate unanalyzed aim composition.^b ND = not determined.

the influence of columbium, were produced according to a slightly different processing schedule. It was expected that a columbium-containing steel would be more sensitive to variations in the hot working and reheating schedule; therefore, a schedule was devised that even more closely approximates the mill processing of rail. The forged billets of these steels were hot rolled into plates with an imbedded thermocouple. Hot rolling was completed at 1010°C (1850°F), and the plates were mildly insulated so that they cooled at the same rate as the bar bundles previously described, down to 480 to 540°C (900 to 1000°F), after which they were furnace cooled. This schedule eliminated the cooling and subsequent reheating after hot working experienced by the specimen bars of the other steels.

Standard tensile specimens having a 13 mm (1/2 in.) diameter by 51-mm (2in.)-long gage section were prepared from the processing blanks. Tensile testing was performed at room temperature with strain rates of 18 and 300 percent/h in the elastic and plastic ranges, respectively.

Tensile bars were cut to produce longitudinal sections for metallographic observation. The specimens were mechanically polished and etched with 4 percent picric acid and 1 percent nitric acid in ethanol. They were then given a gold-palladium coating under vacuum for evaluation by scanning electron microscopy, and photographs were taken at a specimen tilt angle of 35 deg. This angle is in the vertical plane, perpendicular to the plane of the photomicrographs presented in this paper. Therefore, the magnifications of the scanning electron micrographs are accurate only in the horizontal direction.

Results and Discussion

Influence of Molybdenum

Chromium has been employed for some time in rail steels as a pearlite refiner for increasing yield strength into the range of 585 to 690 N/mm² (85 to 100 ksi). The addition of molybdenum to a rail steel composition that includes about 0.75 percent chromium provides a further refinement of the pearlite. Pearlite refinement, that is, smaller interlamellar spacing, is influenced by both elements by a lowering of the transformation temperature. With the continuous cooling conditions being fixed, increasing the molybdenum content reduces the transformation temperature until ultimately the mode of transformation changes from pearlitic to bainitic. This effect is demonstrated by the data of Table 2 and Figs. 1 and 2 for Steels 1 through 5. Mechanical properties and microstructural characteristics are presented in Table 2. The yield and tensile strengths are plotted in Fig. 1 as a function of molybdenum content. The strength of this 0.75C-0.8/0.9Mn-0.15Si-0.7/0.8Cr base composition increases with molybdenum content up to about 0.3 percent; at the 0.4 percent molybdenum level, strength is lower. The photomicrographs of Fig. 2 show the changes that take place in the

TABLE 2—Mechanical properties and microstructures of specimens cooled at indicated rates to simulate commercial production of 65 kg/m (132 lb/yd) as-rolled rails.

Steel No.	Heat or Ingot No.	Specimen No.	Cooling Rate ^a	Recalcescence Temperature, °C (°F)	Microstructure ^b	Hardness, HB	Yield Strength, N/mm ² (ksi)	Tensile Strength, N/mm ² (ksi)	Reduction of Area, % ^c
1	P995A	...	2	...		307	605	1060 (88)	29
2	V1096A	...	1	...		330	690	1125 (100)	39
3	V1095A	...	1	...		361	825	1310 (120)	37
4	P995C	...	2	...		418	940	1310 (136)	41
5	P925	...	1	820	1140 (119)	31
6	P995D	...	2	...		430	1115	1455 (211)	37
7	5770C	4	2	605 (1125)		392	1000	1380 (200)	32
		5	2	615 (1140)		394	960	1335 (194)	29
8	5814C	3	1-2	580 (1080) ^d		423	1170	1530 (222)	17
		3	1	None		340	820	1150 (167)	20
		5	2+	625 (1160)		322	705	1115 (162)	35
9	5814B	...	1-2	None		354	875	1195 (173)	28
10	5814A	...	1	None		328	800	1080 (157)	39
11	5815A	...	2	620 (1145)		322	660	1095 (159)	27
12	5815C	...	1	625 (1155)		335	685	1130 (164)	31
13	5772	...	1	670 (1240)		303	585	1060 (154)	26
14	5770A	3	1-2	670 (1240)		334	635	1110 (161)	21
		4	2	675 (1245)		318	620	1095 (159)	22
		5	1-2	665 (1225)		326	695	1150 (167)	28
15	5773A	8	1	670 (1235)		298	605	1105 (160)	21
		10	1	670 (1240)		317	605	1105 (160)	23
16	5773B	9	1	645 (1195)		326	695	1160 (168)	28
17	5625A	...	2	620	1090 (158)	22
18	5627A	...	2	585	1060 (154)	21
19	5814D	1	1-2	605 (1120)		344	795	965 (140)	46
		3	1-2	625 (1155)		334	740	1130 (164)	43
		1	2	610 (1130)		345	835	1180 (171)	38
20	5868A	2	1	none		360	855	1180 (171)	27

21	5868B	1	2	615 (1135)		321	800	(116)	1160	(168)	39
		2	1	none		368	860	(125)	1195	(173)	28
22	5868C	1	2	580 (1075) ^d		356	925	(134)	1260	(183)	25
		2	1	none		302	715	(104)	1005	(146)	26

^aCooling Rate 1 is a 5-min natural cool between 925 and 705°C (1700 and 1300°F).

Cooling Rate 2 is a 6-min natural cool between 925 and 705°C (1700 and 1300°F).

Cooling Rate 1-2 is intermediate between these two rates.

^bPearlite: ; Transitional Pearlite: ; Bainite: .

^cElongation ranged from 10 to 15 percent.

^dThermal arrest with no recalcence.

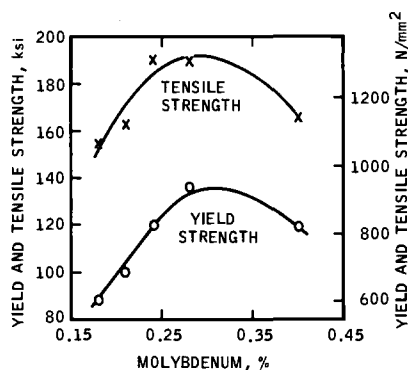
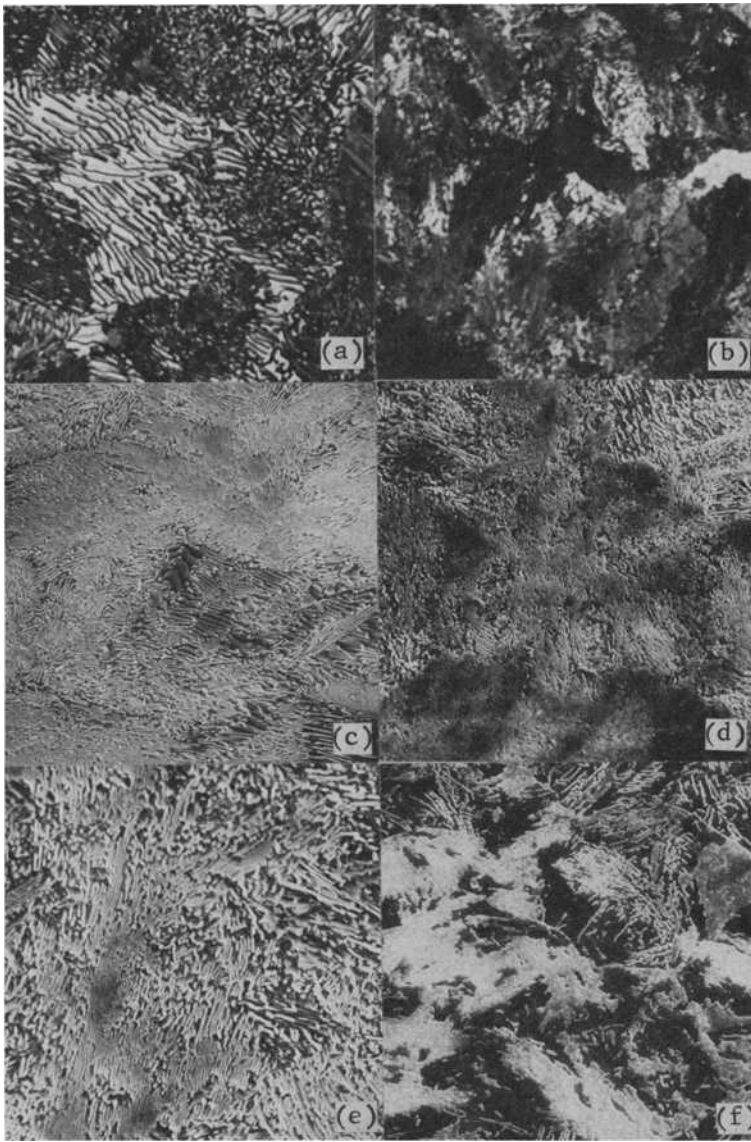


FIG. 1—Influence of molybdenum content on strength of chromium-molybdenum rail steels of grain size ASTM 10.

microstructure as a result of increasing the molybdenum. A typical microstructure of a conventional 0.75C-0.81Mn-0.15Si rail steel is shown in Fig. 2a for reference. This pearlitic structure, which is easily resolved at $\times 1000$, has a yield strength of about 480 N/mm² (70 ksi). The 0.24 percent molybdenum steel of Fig. 2b is composed of a finer pearlite that is unresolved at this magnification. This microstructure may be seen clearly in the higher magnification scanning electron micrograph of Fig. 2c. At the slightly higher molybdenum content of 0.28 percent in Steel 4, the microstructure is even finer, as shown by Figs. 2d, e. In addition, most of the structure is different from an orthodox lamellar pearlite. The lamellae are disordered, and the transformation is bordering on going bainitic, but the change has only partially taken place. For lack of an established term to describe this peculiar structure, it will be referred to as transitional pearlite because it more closely resembles pearlite than bainite. This microstructure is obviously highly desirable, as it produces a higher yield strength than the coarser, orthodox pearlite. Increasing the alloy content further causes the transformation to become bainitic, which generates a much coarser carbide distribution and a correspondingly lower hardness and strength. It is noteworthy that the high-strength transitional pearlite of Steel 4 also has the highest ductility, that is, a reduction of area of 41 percent.

Influence of Carbon

In the interest of improving weldability, the feasibility of using lower carbon contents was investigated in the chromium-molybdenum steel. Since the eutectoid carbon content of this alloy steel is estimated to be about 0.55 percent, there was no concern about the possibility of ferrite formation in the 0.6 to 0.7 percent carbon range. Steels 8, 9, and 10 were prepared accordingly. As the carbon content was reduced to a minimum of 0.60



- (a) Optical micrograph of AREA standard rail ($\times 1000$).
- (b) Optical micrograph of Cr-0.24Mo Steel 3 ($\times 1000$).
- (c) Scanning electron micrograph of Cr-0.24Mo Steel 3 ($\times 2000$).
- (d) Scanning electron micrograph of Cr-0.28Mo Steel 4 ($\times 2000$).
- (e) Scanning electron micrograph of Cr-0.28Mo Steel 4 ($\times 5000$).
- (f) Scanning electron micrograph of Cr-0.40Mo Steel 5 ($\times 2000$).

FIG. 2—Microstructures of chromium-molybdenum rail steels of varying molybdenum contents in comparison with AREA standard rail.

percent, the microstructure became more bainitic (Fig. 3). Specimen 5 of Steel 8 at 0.68 percent carbon transformed to pearlite when cooled at a rate slightly slower than Rate 2 of Table 2, as shown in Fig. 3a. Specimen 3 of this same steel, cooled slightly faster, transformed to transitional pearlite and bainite as demonstrated by Figs. 3b, c which show different areas of the specimen. The high-temperature region of the cooling curves for these two specimens is shown in Fig. 4. Specimen 5 exhibits recalescence, as would be expected from a pearlitic transformation on continuous cooling, while Specimen 3 does not. Further reduction in carbon to 0.64 percent in Steel 9 resulted in the microstructure of Fig. 3d, which is about 80 percent bainite with a small amount of transitional pearlite. This steel was cooled at Rate 1-2, as shown in Fig. 4. A final reduction of carbon content to 0.60 percent produced a completely bainitic microstructure, as shown in Fig. 3e.

The yield strengths of the lower carbon rail steels varied somewhat inconsistently with carbon content. In general, fine transitional pearlite tends to increase the yield strength and bainite tends to decrease it, although bainite can be stronger than coarse pearlite.

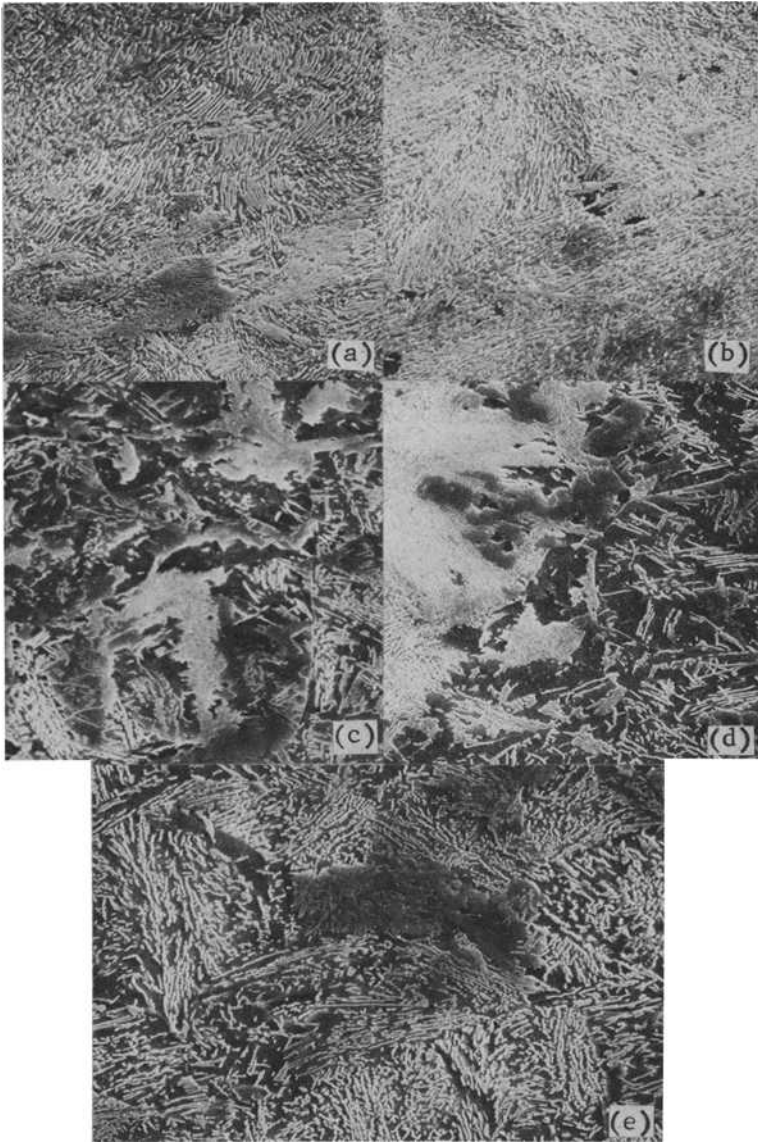
An explanation of the delay of pearlite transformation with reduced carbon content can be proposed on the basis of the manner in which these steels transform isothermally. Isothermal transformation at the temperature of the pearlite nose of the *TTT* curve takes place with very rapid pearlite growth, such that the transformation appears to be nucleation controlled. Also, excess carbides are formed isothermally, although excess carbides are not found in significant quantities on continuous cooling. If the pearlite is carbide nucleated in these hypereutectoid compositions, which would be consistent with the thinking of Nicholson,³ a reduction of carbon content would lower the nucleation rate.

The observed increase in hardenability with reduced carbon content suggests that the composition could be favorably balanced by reduction of both carbon and alloy contents. However, it should be noted that the most desirable microstructural change did not take place as hardenability increased. In the molybdenum series described previously, the microstructure went completely to transitional pearlite as hardenability was increased before it went bainitic. On the other hand, transitional pearlite and bainite appeared together in the carbon series. It may be that a large volume fraction of transitional pearlite can only be obtained in the high-carbon range. Since this microstructure appears to be the most desirable for its mechanical properties, this may be an argument for maintaining the high (hypereutectoid) carbon content.

Influence of Silicon and Chromium Variation

Steels 11 and 12 were prepared to investigate the feasibility of substituting silicon for either part or all of the chromium in the basic chromium-

³Nicholson, M. E., *Transactions AIME*, American Institute of Mining, Metallurgical, and Petroleum Engineers, Vol. 200, 1954, p. 1071.



- (a) Specimen 5 of Steel 8 containing 0.68 percent carbon (slower cooling) ($\times 2000$).
- (b) Specimen 3 of Steel 8 containing 0.68 percent carbon (faster cooling) ($\times 2000$).
- (c) Specimen 3 of Steel 8 containing 0.68 percent carbon (faster cooling) ($\times 2000$).
- (d) Steel 9 containing 0.64 percent carbon ($\times 2000$).
- (e) Steel 10 containing 0.60 percent carbon ($\times 2000$).

FIG. 3—Scanning electron micrographs of chromium-molybdenum rail steels of varying carbon contents.

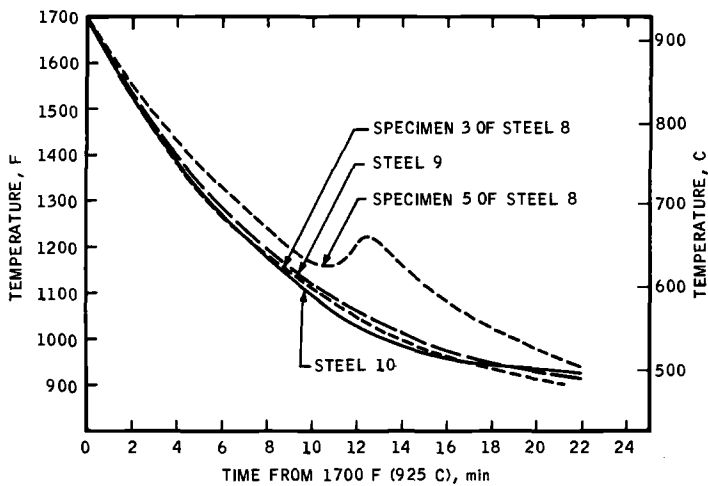


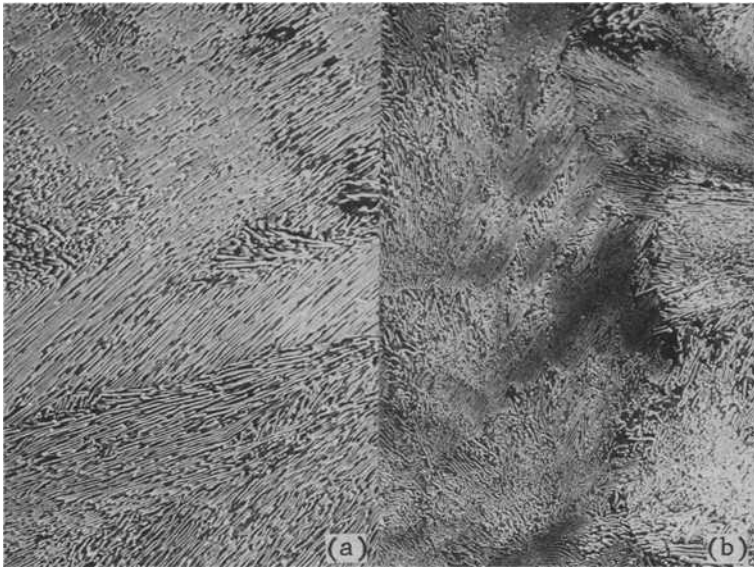
FIG. 4—Cooling curves of specimens of Steels 8, 9, and 10 with carbon contents of 0.60 to 0.68 percent.

molybdenum composition. A 0.24 percent molybdenum content was used in order to aim for a minimum of about 760 N/mm² (110 ksi) yield strength. The resulting strength and hardness of these two steels are similar, with the chromium-containing steel having a slight advantage (Table 2). The recalcrescence points are virtually identical, suggesting pearlitic structures of approximately equal fineness as confirmed by the microstructures of Fig. 5. The substitution of silicon for chromium was not completely successful in that the yield strength was about 70 to 105 N/mm² (10 to 15 ksi) lower than intended.

Influence of Vanadium

Chromium-molybdenum-vanadium rails have been produced commercially in Europe. The effect of adding vanadium to the chromium-molybdenum steel of maximum strength is shown by the difference between Steels 4 and 6, which are both from the same heat. The addition of 0.06 percent vanadium results in notably higher hardness and strength with no significant loss of ductility (Table 2). The strength change is apparently caused, at least in part, by a refinement of the transitional pearlite microstructure, as may be observed by comparing Fig. 6a with Fig. 2d. Vanadium may also have introduced some precipitation strengthening, but attempts to extract vanadium carbide or nitride precipitates were not successful.

Steel 7 was prepared as a check on the outstanding properties observed in Steel 6. Thermocouples were employed during cooling of all of the bar bundles to provide more complete results than were available on Steel 6. The

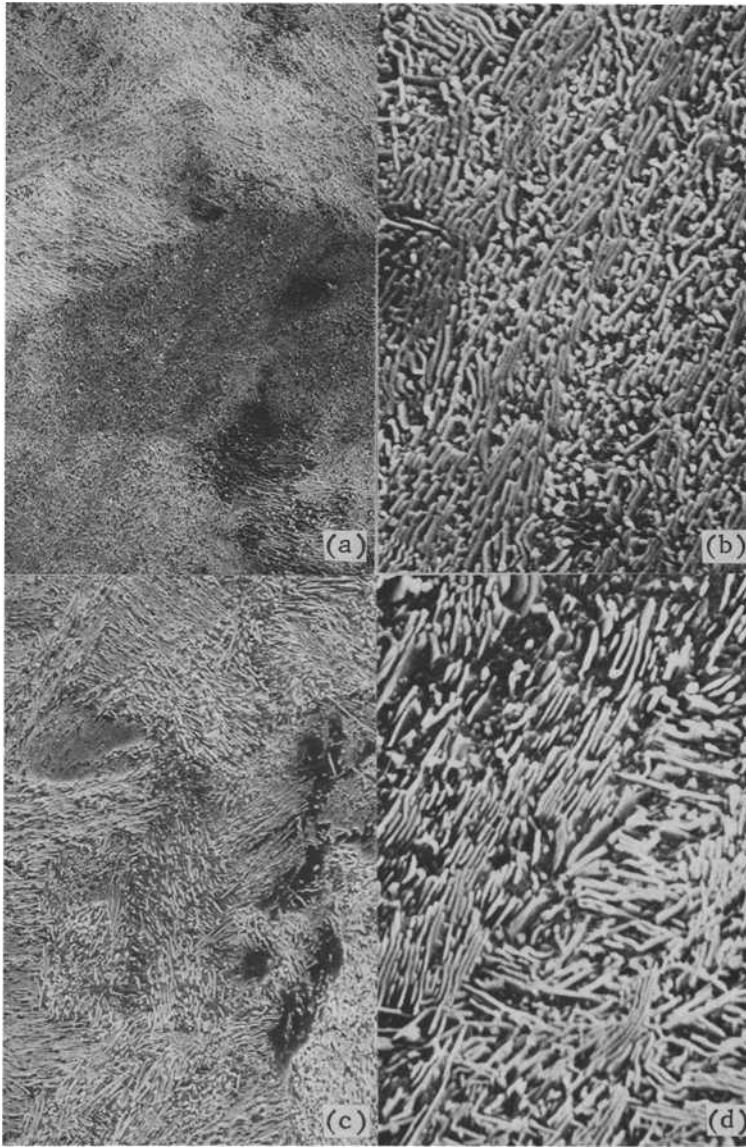


(a) Steel 11 without chromium ($\times 2000$).
 (b) Steel 12 with 0.44 percent chromium ($\times 2000$).

FIG. 5—Scanning electron micrographs of 0.88Si-0.24Mo rail steels with and without chromium.

cooling curves for the three specimens of Steel 7 are presented in Fig. 7. Specimens 4 and 5 experienced identical cooling rates and very similar recalescence temperatures. The tensile properties are correspondingly similar; however, they are not quite as high as those of Steel 6. The microstructure of Specimen 4 of Steel 7 is shown in Figs. 6c, d. It consists of fine transitional pearlite. Specimen 3 was cooled at a slightly faster rate, such that transformation to pearlite did not start quite fast enough to cause recalescence. A thermal arrest occurred at about 580°C (1080°F), allowing transitional pearlite to form at a relatively low temperature; but the absence of recalescence also allowed about 25 percent bainite to form (Fig. 8b). The highly distorted transitional pearlite is shown in Fig. 8b. Some extremely fine, moderately distorted pearlite is shown surrounded by bainite in Fig. 8c. This pearlite has an interlamellar spacing of less than 500 \AA . The yield strength of this mixed structure is 1170 N/mm^2 (170 ksi), but the reduction of area is only 17 percent, much lower than that of Steel 6. No specific explanation was found for the low ductility of this steel, although the presence of bainite is believed to contribute.

The influence of adding vanadium to a chromium-molybdenum steel at the lower strength level may be observed by comparing the two pairs of steels, Steels 13 and 14 with Steels 15 and 16. The first pair involves adding



(a) Steel 6 with 0.28 percent molybdenum and 0.06 percent vanadium ($\times 2000$).
 (b) Steel 6 with 0.28 percent molybdenum and 0.06 percent vanadium ($\times 10\,000$).
 (c) Specimen 4 of Steel 7 with 0.26 percent molybdenum and 0.05 percent vanadium ($\times 2000$).
 (d) Specimen 4 of Steel 7 with 0.26 percent molybdenum and 0.05 percent vanadium ($\times 10\,000$).

FIG. 6—Scanning electron micrographs of chromium-molybdenum-vanadium rail steels.

averaging about 70 N/mm^2 (10 ksi) higher than the steel without vanadium. The completely pearlitic microstructures of Steels 13 and 14 are shown in Figs. 9a,b, respectively. A similar gain in strength was attained by a

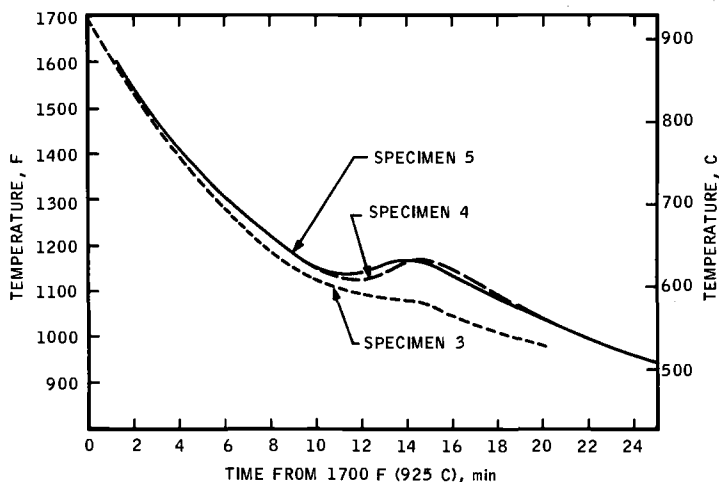


FIG. 7—Cooling curves of specimens of Steel 7 (0.2 percent molybdenum, 0.05 percent vanadium).

0.05 percent vanadium to a 0.19 percent molybdenum steel. The triplicate specimens of Steel 14 are in the 620 to 690 N/mm² (90 to 100 ksi) range, vanadium addition to a 0.25 percent molybdenum steel with silicon substituted for a portion of the chromium. The recalescence temperature of Steel 16 is somewhat lower than that of the other vanadium Steel 14, but the strength is about the same. The microstructures of Steels 15 and 16 are shown in Figs. 9c,d, respectively. The pearlite interlamellar spacing appears to be about equal for the two.

Vanadium without Molybdenum

Steels 17 and 18 are chromium-vanadium steels containing different levels of manganese. Both steels contain 0.1 percent vanadium. The tensile properties of Table 2 show that vanadium without molybdenum is not very effective in developing a fine pearlitic microstructure. The microstructures are strictly orthodox pearlite (Table 2), as would be expected from the modest strength levels attained.

Influence of Columbium

A preliminary evaluation of the use of columbium was made by adding 0.02 percent to the last ingot of Heat 5814, Steel 19. The microstructure of Specimen 1 of Steel 19 is presented in Fig. 10a. A comparison of the tensile properties of this steel with those of Steel 8 in Table 2 shows that no benefit was derived from the columbium, except that the reduction of area was improved. Columbium was further investigated in Steels 20, 21, and 22, which are three ingots from the same heat. Columbium increases from 0 to



(a) $\times 2000$.
 (b) $\times 10\ 000$.
 (c) $\times 10\ 000$.

FIG. 8—Scanning electron micrographs of Specimen 3 of Cr-0.26Mo-0.05V rail Steel 7.

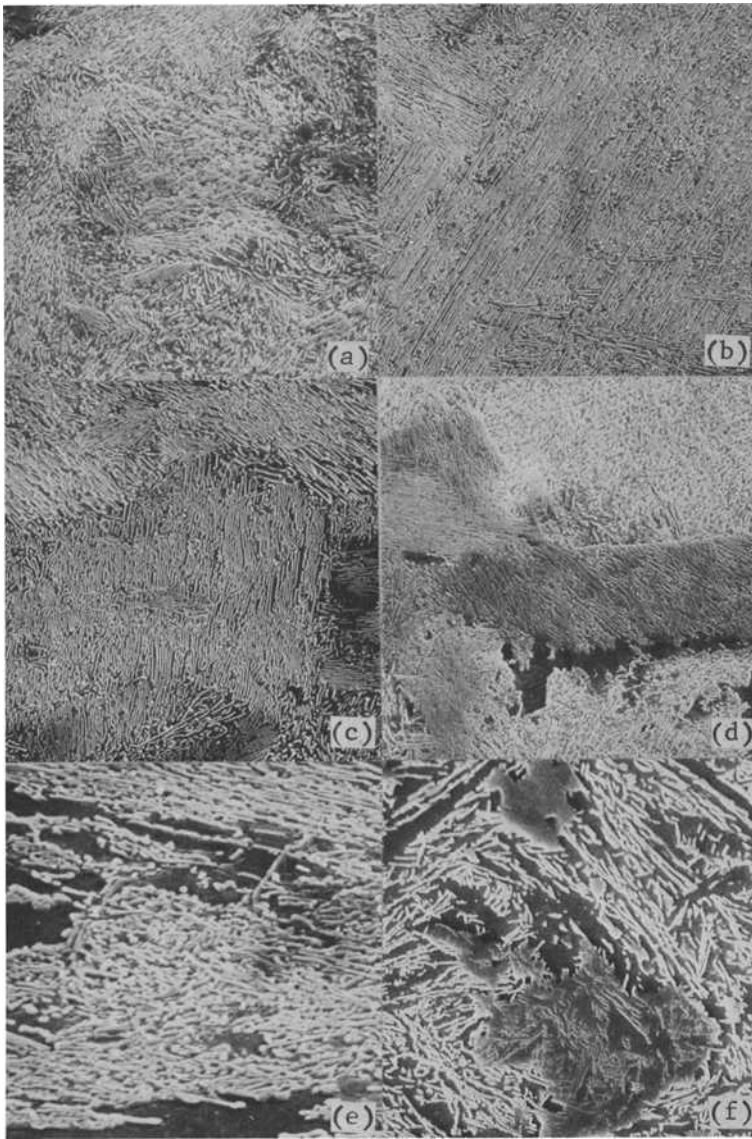
0.4 percent within the heat, but the average tensile properties for the two specimens of each steel are virtually unchanged as a result of the columbium addition. The two slightly different cooling rates employed for the specimen



- (a) Steel 13 with 0.19 percent molybdenum ($\times 2000$).
 (b) Specimen 4 of Steel 14 with 0.19 percent molybdenum and 0.05 percent vanadium ($\times 2000$).
 (c) Specimen 8 of Steel 15 with 0.19 percent molybdenum ($\times 2000$).
 (d) Steel 16 with 0.19 percent molybdenum and 0.06 percent vanadium ($\times 2000$).

FIG. 9—Scanning electron micrographs of chromium-molybdenum and chromium-molybdenum-vanadium rail steels.

pairs produced some notable differences in microstructure which were only reflected by the mechanical properties at the highest columbium content.



- (a) Steel 19 with 0.24 percent molybdenum and 0.02 percent columbium ($\times 2000$).
- (b) Specimen 1 of Steel 20 with 0.30 percent molybdenum ($\times 2000$).
- (c) Specimen 1 of Steel 21 with 0.30 percent molybdenum and 0.02 percent columbium ($\times 2000$).
- (d) Specimen 1 of Steel 22 with 0.30 percent molybdenum and 0.04 percent columbium ($\times 2000$).
- (e) Specimen 1 of Steel 22 with 0.30 percent molybdenum and 0.04 percent columbium ($\times 10\ 000$).
- (f) Specimen 2 of Steel 22 with 0.30 percent molybdenum and 0.04 percent columbium ($\times 2000$).

FIG. 10—Scanning electron micrographs of chromium-molybdenum and chromium-molybdenum-columbium rail steels.

Specimen 1 of Steel 20 is largely a mixture of orthodox and transitional pearlite with a small amount of bainite. This microstructure is shown in Fig. 10*b*. Specimen 2, which was cooled slightly faster, is about 50 percent bainite, as shown in the microstructure column in Table 2. A similar difference exists between the two specimens of Steel 21, this time with the higher bainite specimen being slightly stronger. Specimen 1 is shown in Fig. 10*c*. Specimen 1 of Steel 22 is also about 40 percent bainitic, and it has the highest strength of the group. This microstructure is shown in Figs. 10*d,e*. Specimen 2 is practically all bainite and has the lowest strength of the group. This microstructure is presented in Fig. 10*f*. With regard to the microstructure/mechanical property relationship, it is noteworthy that a very high fraction of bainite must be developed before the strength is significantly reduced.

Strength, Ductility, and Microstructure

A scatter plot of yield strength versus reduction of area is presented in Fig. 11. Taking all of the points into consideration, there is a mild tendency for the ductility to increase as the yield strength increases. This is a most encouraging observation from a practical point of view. It probably is a manifestation of the fact that the strength is being increased in these steels by development of finer microstructures. The finer structures have higher ductility despite their higher strength. Selected points in Fig. 11 are coded to

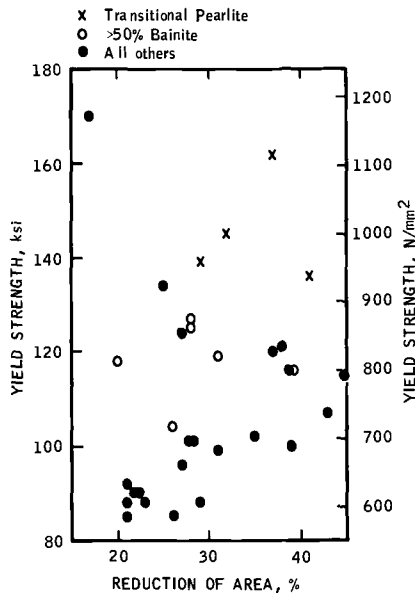


FIG. 11—Scatter plot of yield strength versus reduction of area as influenced by microstructure in alloy rail steels.

indicate the influence of microstructure on the trend. A high proportion of bainite does not necessarily indicate either higher or lower ductility. On the other hand, the specimens that have virtually completely transformed to transitional pearlite exhibit both high yield strength and high ductility.

General Discussion

On the basis of the detailed observations described previously, it is possible to arrive at recommendations directed at an optimization of composition for 65-kg/m (132-lb/yd) alloy rails. The molybdenum content can be taken directly from Fig. 1 depending on the desired yield strength, if the same carbon and other alloy contents are retained as in this first series of steels. This molybdenum content must be adjusted for a grain size difference between laboratory and commercial heats, as will be discussed later. The chromium-molybdenum composition is effective without further alloy addition up to the high yield strength range, 760 to 895 N/mm² (110 to 130 ksi).

An effort was made to reduce the carbon content in this chromium-molybdenum base composition. It was found that the hardenability was increased by lowering the carbon content, possibly due to an influence on pearlite nucleation. It was suggested that the total alloy content might be reduced to compensate for this change. As carbon was reduced, however, the transformational change to a bainitic product occurred differently than at the higher carbon content. As hardenability was increased in the molybdenum series, complete transformation to transitional pearlite occurred before the shift to bainite. At the lower carbon level, only partial transformation to transitional pearlite was obtained. The same result was observed in the columbium series, which was at 0.68 percent carbon. It may be that the higher carbon hypereutectoid composition is more effective in promoting transformation to fine transitional pearlite, which has the best combination of strength and ductility.

A yield strength of 1100 to 1170 N/mm² (160 to 170 ksi) was only attainable with the addition of vanadium. Vanadium was employed in these steels with the aim of developing increased strength due to precipitation. Goldshteyn et al⁴ have shown that the ferrite lamellae of pearlite in a 0.67C-0.85Mn-0.07V steel contain vanadium carbide precipitates. The addition of vanadium to Steel 4, to produce Steel 5, resulted in a finer transitional pearlite. A portion of the 180 N/mm² (26 ksi) increase in yield strength is attributable to this refinement. A search for vanadium carbide particles in an extraction replica of a sample of Steel 7 that was cooled at the railhead cooling rate was not successful. While it is expected that vanadium carbide (probably V₄C₃) must precipitate to some degree at this cooling rate, it was concluded that the particles must be less than 20 Å in size. Of course, 10 to 15-Å carbides would be adequate to cause significant strengthening.

⁴Goldshteyn, M. I., Kolosova, E. L., Susloparov, G. D., and Murayev, Y. A., *Fizika Metallov Metallovedenie*, Vol. 23, No. 2, 1967, p. 347.

The results of including vanadium in Steels 14 and 16 are believed to be more decisive in evaluating the precipitation-strengthening potential of vanadium at the railhead cooling rate. These two steels should have been strengthened accordingly if the potential exists at this cooling rate, and they clearly were not. In this study, vanadium only caused a notable increase in strength when it was involved in the formation of the large volume fraction of transitional pearlite.

The addition of up to 0.04 percent columbium in this type of steel was not found to be beneficial. This is not surprising, considering that the solubility of columbium at such a high carbon content must be very limited. According to Irvine et al.,⁵ the solubility of columbium in 0.25 percent carbon steel is 0.4 percent at 1315°C (2400°F), and this solubility decreases rapidly with increasing carbon content. At 0.75 percent carbon, the columbium solubility can reasonably be expected to be between 0.01 and 0.02 percent. Furthermore, only a fraction of that dissolved at the ingot soaking temperature could be expected to be in solution at the transformation temperature. Therefore, the most important role of columbium is expected to be related to the columbium that is precipitated in the austenite and to its influence on austenite recrystallization during hot rolling.

It was noted previously that, when these alloy rail steels are made commercially, an adjustment must be made in the composition to provide commercial steels with the same transformation characteristics as the laboratory steels; the same composition made commercially would be slightly higher in hardenability than a laboratory steel. This difference in hardenability is due to a difference in grain size between commercial aluminum-killed heats and laboratory aluminum-killed heats. The small induction furnace heats made in the laboratory are high in nitrogen and very homogeneous in prior austenite grain size at ASTM 10. Aluminum-killed commercial heats of chromium-molybdenum alloy rail steel made thus far were about 0.05 percent lower in molybdenum than would be indicated by the data of this study for an equivalent level of strength, because the grain size of the commercial heats was ASTM 8. In addition, some further reduction in alloy content would be appropriate if the commercial heats were made to a semikilled practice, because of the expected still larger grain size, or if lighter rail sections were involved than the 65-kg/m (132-lb/yd) section represented by the cooling rates in this study. Fracture grain sizes of the steels in the earlier paper (Footnote 2) were reported to be ASTM 6 to 7. It has subsequently been determined that these fracture grain size measurements do not show the true prior austenite grain size.

Summary

A series of experimental steel compositions was produced in the laboratory and evaluated for potential application as as-rolled 65-kg/m (132-lb/yd)

⁵Irvine, K. J., Pickering, F. B., and Gladman, T., *Journal of the Iron and Steel Institute*, Vol. 205, Feb. 1967, p. 161.

rails. The steels were variations of a 0.75 percent carbon, 0.8 percent manganese, 0.8 percent chromium, 0.2 percent molybdenum base composition. It was found that increasing molybdenum to 0.30 percent raised the yield strength to about 930 N/mm^2 (135 ksi) by developing a highly refined transitional pearlite microstructure; additional molybdenum resulted in bainite formation and a decrease in strength. Reducing the carbon content in the base composition to the 0.6 to 0.7 percent range increased hardenability, which resulted in a mixed microstructure of transitional pearlite and bainite. This behavior suggests that the conventional carbon level aids in the formation of a high percentage of fine transitional pearlite. The addition of vanadium was effective in further refining the microstructure to attain a yield strength in the range of 1100 to 1170 N/mm^2 (160 to 170 ksi) if the molybdenum content was high enough to develop a sufficiently low transformation temperature. Otherwise, the vanadium addition resulted in only a modest change in microstructure and a correspondingly small increase in yield strength. Chromium-vanadium steel without molybdenum did not develop a very fine pearlitic microstructure. Columbium was not effective in improving the properties of the chromium-molybdenum steel. The steels investigated in this laboratory study would require slightly lower alloy contents for commercial heats. In terms of the laboratory compositions, it may be concluded that a $0.75\text{C}-0.85\text{Mn}-0.75\text{Cr}-0.24\text{Mo}$ steel is best suited to the 760 to 895 N/mm^2 (110 to 130 ksi) yield strength range, while a $0.75\text{C}-0.9\text{Mn}-0.75\text{Cr}-0.28\text{Mo}-0.06\text{V}$ steel appears potentially feasible for the 895 to 1170 N/mm^2 (130 to 170 ksi) range. About 0.05 percent less molybdenum would be required in aluminum-killed, commercially melted steel for 65-kg/m (132-lb/yd) rails.

H. Masumoto,¹ K. Sugino,¹ S. Nisida,¹ R. Kurihara,² and S. Matsuyama²

Some Features and Metallurgical Considerations of Surface Defects In Rail Due to Contact Fatigue

REFERENCE: Masumoto, H., Sugino, K., Nisida, S., Kurihara, R., and Matsuyama, S., "Some Features and Metallurgical Considerations of Surface Defects in Rail Due to Contact Fatigue," *Rail Steels—Developments, Processing, and Use*, ASTM STP 644, D. H. Stone and G. G. Knupp, Eds., American Society for Testing and Materials, 1978, pp. 233–255.

ABSTRACT: Two unique types of surface defects resulting from contact fatigue have been observed in rail used in high-speed lines in Japan (speed greater than 150 km/h). One of these results from the dark spots which randomly appear on the running surface and develop into transverse defects, and the other is the head check which arises at the gage corner.

An experimental simulation of these defects was attempted through rolling contact fatigue tests. The resulting defects were similar to those found on the running surface. For their initiation, a slip component of load was necessary, in addition to the normal load. Examinations of these defects indicated that they initiated on the contact surface, as did those found in rail, and not at the subsurface where the shear stresses are maximum due to Hertzian contact.

To investigate the effects of microstructure on the initiation and propagation behavior of these defects, coarse pearlitic, fine pearlitic, and tempered martensitic structures were examined. The fatigue limit of each structure showed a good correlation with its tensile strength. In the rolling contact fatigue tests, the fine pearlitic structure exhibited the longest lifetime. However, the tempered martensite had the lowest crack growth rate. Therefore, it is concluded that, to optimize the durability of rail steels, the effect of microstructure should be considered in addition to the tensile properties.

KEY WORDS: steels, railroad tracks, fatigue (materials), surface defects

In Japan, since successful completion of the Tokaido Shinkansen line, travel by rail systems has again been recognized as the most desirable means of passenger transportation. In accord with national planning, the Shinkansen lines extend for about 7000 km. In recent years, however, the increases

¹Managers and assistant manager, respectively, Technical Research Office, Yawata Works, Nippon Steel Corporation, Yawata higashi-ku, Kitakyushu-shi, Japan.

²Researcher and senior researcher, respectively, Steel and Alloy Laboratory, Railway Technical Research Institute, Japanese National Railways, Hikari-Cho, Kokobunji-Shi, Japan.

in traffic speed and frequency on these lines have led to the development of two unique problems concerning rail steels. One is the wear behavior along curved track of small radius, and the other is the appearance of a new type of railhead defect.

In this study, the features of both types of surface defects and the mechanisms of crack initiation are discussed. Based on this work, recommendations for the development of more durable rail steels can be made.

Morphology of Surface Defects on the Railhead

Contact fatigue defects, known as “shelling,” have been found to occur in rails, especially those that were heat treated, which are subject to heavy loads. However, recently, two types of contact fatigue defects, unique because of their lack of correlation with metallurgical factors, have appeared in track subject to relatively light loads (less than eight tons), in contrast to shelling defects. These defect types shall be referred to as “head checks” and “dark spots.”

Head Checks

Groups of S-shaped defects are found to occur at intervals of 2 to 3 mm on the gage corner, as shown in Fig. 1, regardless of traffic speed. These defects are usually found on the elevated outside rail in curves of radius larger than 1000 m and occasionally on the inside rail and in straight track. In curves of smaller radius, it appears that the defects do not grow to a critical size but rather are worn away rapidly. The propagation process of the defect can be divided into four stages, as shown in Fig. 2. The defects become visible with the passage of less than ten megatons traffic and are usually arrested in Stage I, as shown in Fig. 1a. Under certain conditions, however, a few of these cracks propagate toward the outside corner (Fig. 1b). The probability of propagation beyond Stage II is very small and occurs only locally, in the vicinity of 200 to 300 mm along the railhead. In this range, no depressions develop on the running surface as there are no horizontal cracks. In Stage III, these cracks propagate until the outside corner along the running surface is hardened due to wheel contact. After that, in Stage IV, one of the cracks spreads vertically downward through the rail section, causing rapid rail failure. Examination of the fracture surface resulting from such a catastrophic failure reveals the presence of typical beach marks (Fig. 1c). Failure generally occurs when the defect size approaches 35 to 40 percent of the railhead section.

Since the development of defects within Stage I may be unavoidable, it is recommended that, after a surface crack is observed to have grown through the center line of the running surface, the rail be kept under close observation. The conditions necessary for propagation beyond Stage II are not yet understood; however, it is reasonable to assume that unusually high

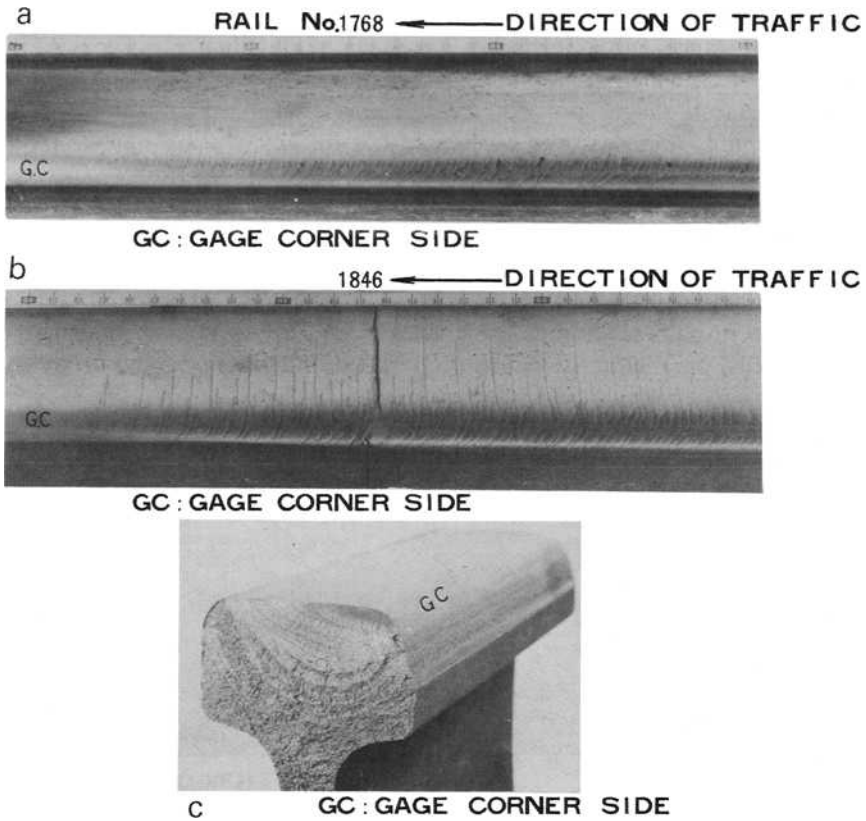


FIG. 1—Examples of (a) head checks in Stage I, (b) crack growth spread beyond Stage II, and (c) transverse fracture from a head check (compare to Fig. 2).

tensile stresses along the running surface, arising from track structural irregularities or local lifting up of a rail, are responsible.

Dark Spots

These defects occur on the running surface of high-speed track sections (speeds greater than 150 km/h) in isolated instances rather than in groups.

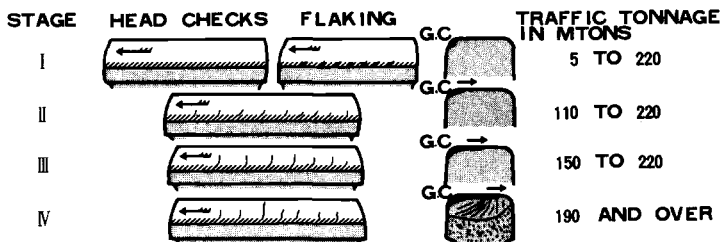


FIG. 2—Propagation process of a head check divided into four stages.

The origin of these defects has no obvious correlation with track parameters. Their appearances in the formative stages can be classified into Types A, B, and C, (Fig. 3) which are found to occur, respectively: near the gage corner in an inverse V shape; along the central area of the running surface, in a circular shape; and near the outside corner, in a V shape.

Figure 4 shows the distribution of initial positions on the running surface, as a function of distance from the center, for each type of defect. Separation of the surface layer just above a horizontal crack reveals the presence of a progressed crack, as shown in the fracture surface of Fig. 5. It is noted that the cracks seem to initiate at the surface. Figure 6 shows a longitudinal/vertical section taken through the crack origin. The main crack propagates horizontally, parallel to the direction of traffic, under the running surface. A

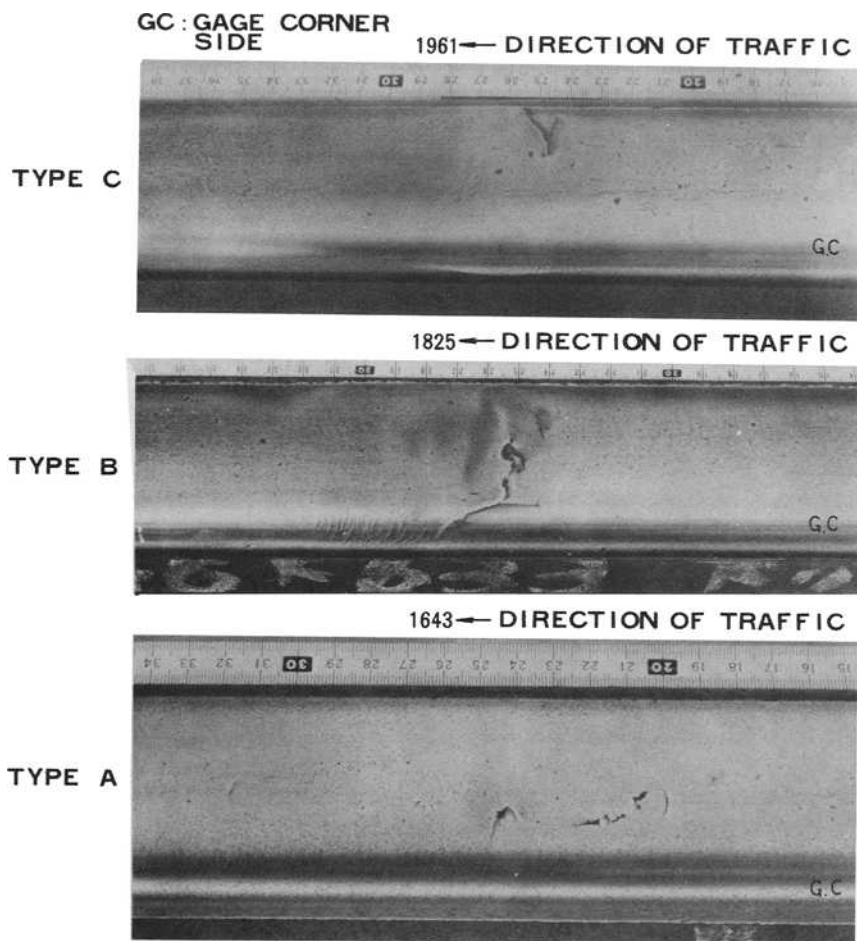


FIG. 3—Principal types of dark spots in the early stages (compare to Fig. 4).

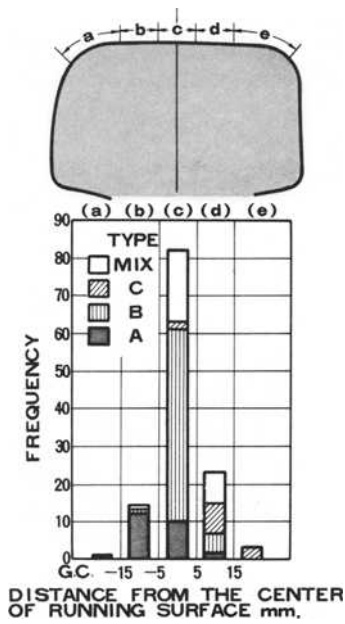


FIG. 4—Distribution of initial positions of dark spots on the running surface.

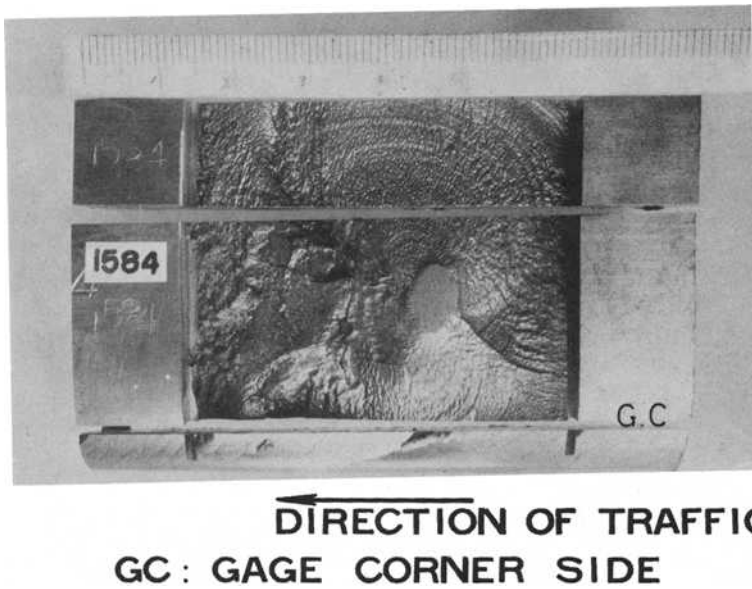


FIG. 5—Fracture surface of horizontal crack revealed by separation of the surface layer.

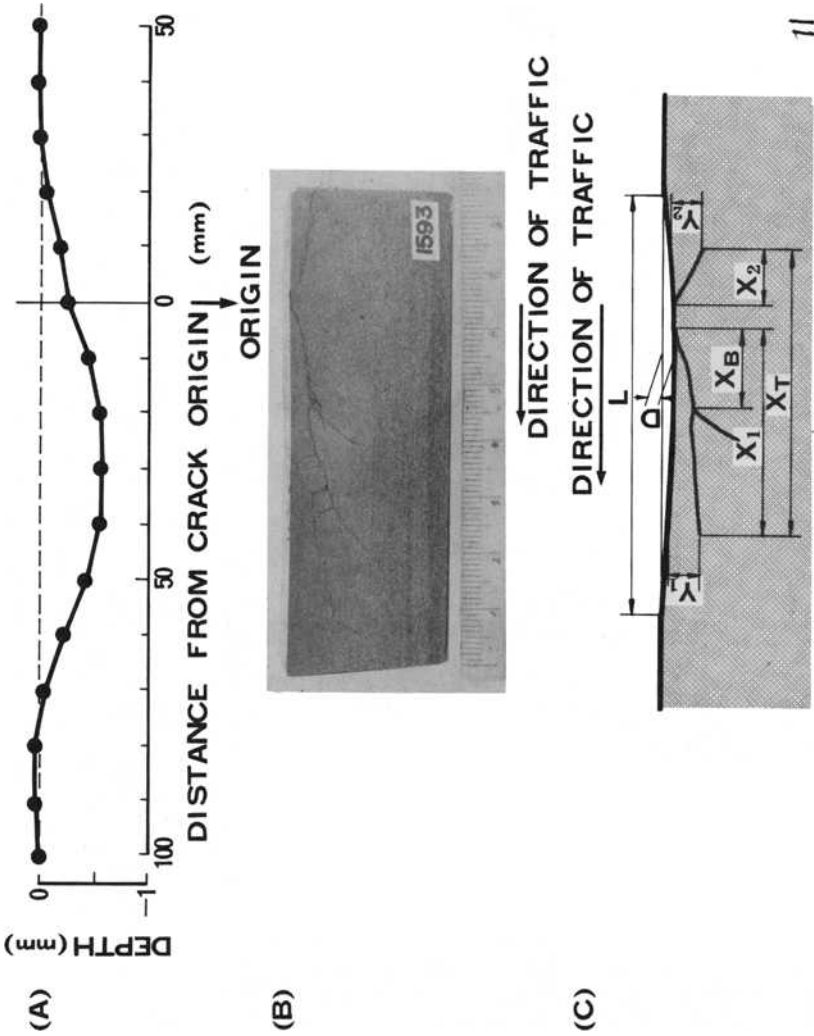


FIG. 6—(a) Surface depression, (b) longitudinal/vertical section through crack origin, and (c) dimensional parameters for Figs. 9–12.

secondary horizontal crack, propagating in the opposite direction, has a shorter length than the former and cannot turn nor branch to form a transverse brittle fracture.

The propagation process of a primary crack along the traffic direction can be divided into four stages, as shown schematically in Fig. 7. In Stage I, the crack, which has initiated at the running surface, spreads horizontally under the surface. In Stage II, this crack branches. Although sometimes the running end of the horizontal crack turns down, in general, the branch crack is observed to turn more rapidly. In a few instances, it has been observed that the horizontal crack turns up after running for a considerable distance with or without branching, and then flaking of the surface can occur. Also, fissuring of the surface layer above a horizontal crack can produce flaking. In Stage III, the branch crack turns down, forming a defect similar in appearance to a tache ovale. In the final stage, after growth of this defect to approximately 70 percent of the railhead area, brittle failure occurs, as shown in Fig. 8.

As the horizontal crack develops, a depression of the running surface occurs with simultaneous appearance of a dark spot and widening of the bright running stripes known as contact widening which indicate the presence of this defect (Fig. 3). The depth, D , and the length, L , of the depression increase with increasing length of the horizontal crack. Figure 9 illustrates the relationship between D and L in each stage of this defect. It can be seen that, in the later stages of defect growth, the distributions in Fig. 9 become narrower, approaching a limit. This suggests that the impact force produced by the wheel on the rail depends on the geometry of the depression, and therefore, a transverse branch crack will grow under some optimum combination of values of D and L . Figures 10a,b show the relationships between depth and length of horizontal cracks both along and opposite to the traffic direction.

In Fig. 11, the relationship between the distance from a crack origin to the first branching position and the primary horizontal crack length along the

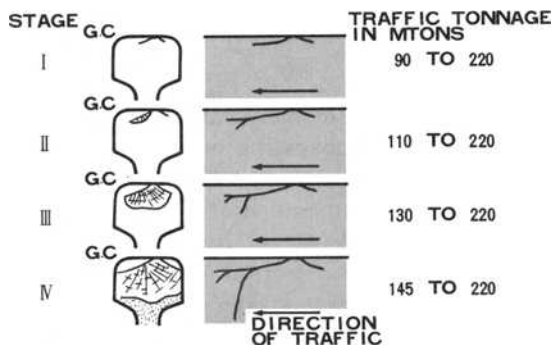


FIG. 7—Propagation process of dark spots divided into four stages.

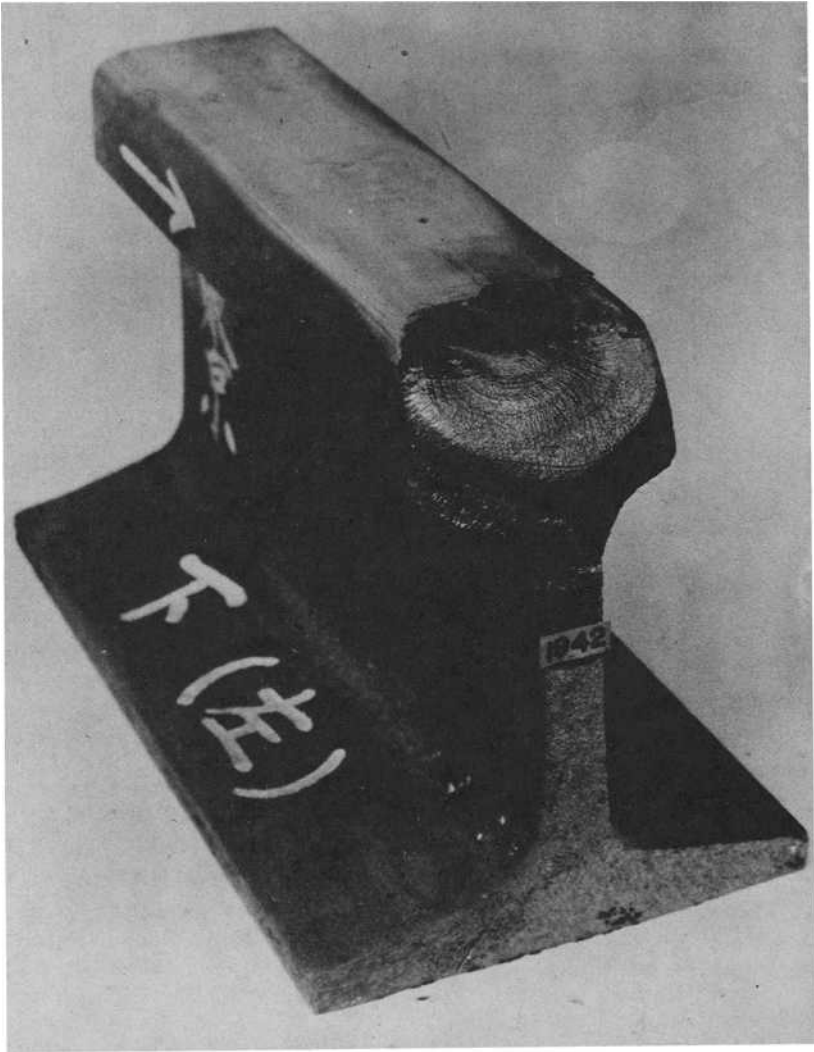


FIG. 8—Transverse fracture showing detailed fracture similar to a *tache ovale*.

traffic direction is presented. In many cases, the branch crack forms a dangerous transverse crack propagating underneath the horizontal crack and therefore remaining shielded from detection by an angular ultrasonic probe. Within the limits of this investigation, it has been found that the first branching of a horizontal crack occurs at a distance greater than 10 mm from the initial position of the defect, as shown in Fig. 11, and that the surface depression length is always greater than the total horizontal crack length, as shown in Fig. 12. Therefore, a tolerance criterion may be defined for a length of 30 mm for a dark spot corresponding to the minimum length of 10 mm for a latent horizontal crack.

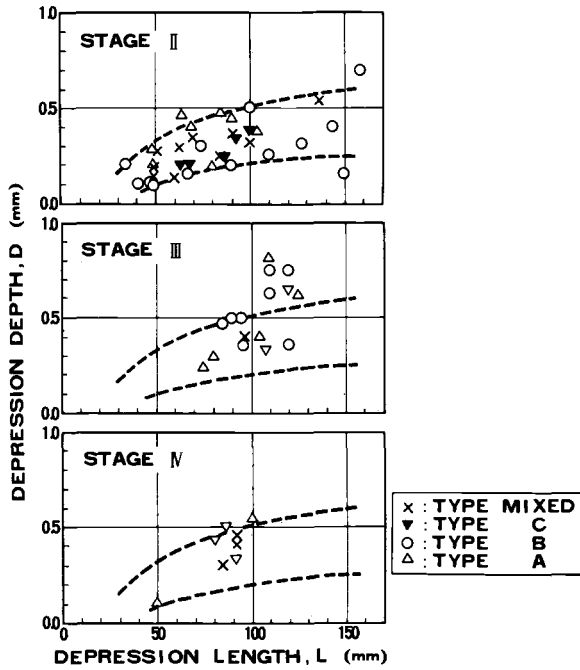


FIG. 9—Relationship between depth and length of the surface depression through various stages of dark spots.

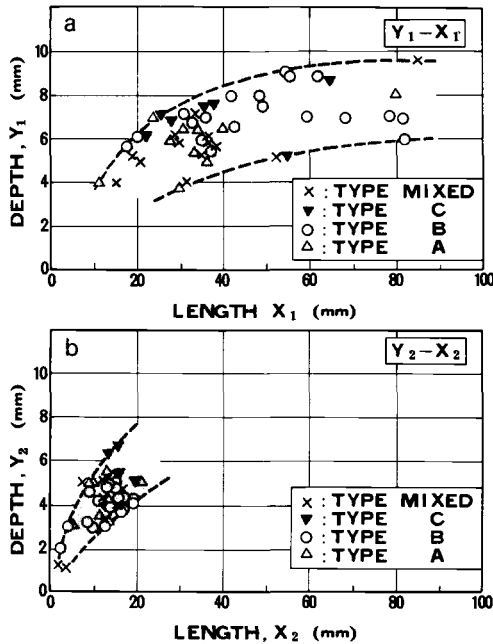


FIG. 10—Relationships between depth and length of horizontal crack (a) in traffic direction and (b) in the opposite direction.

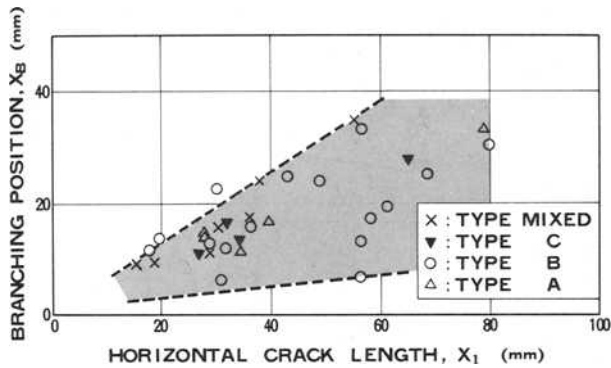


FIG. 11—Relationship between the distance from crack origin to first branching position and the main horizontal crack length in traffic direction.

The uniqueness of these defects lies in the fact that they are not directly correlated with macroscopic metallurgical flaws, gross nonmetallic inclusions, or martensitic formation. The observation that they tend to occur in situations of high-speed traffic suggests that wheel slipping plays an important role in their development. This will be discussed in detail in a later section.

Experimental Reproduction of Surface Defects

The surface defects previously described appear to result from metallic fatigue processes. Therefore, the fatigue strength of rail steels should be important in understanding the factors responsible for occurrence of these defects and subsequently controlling their development. However, the

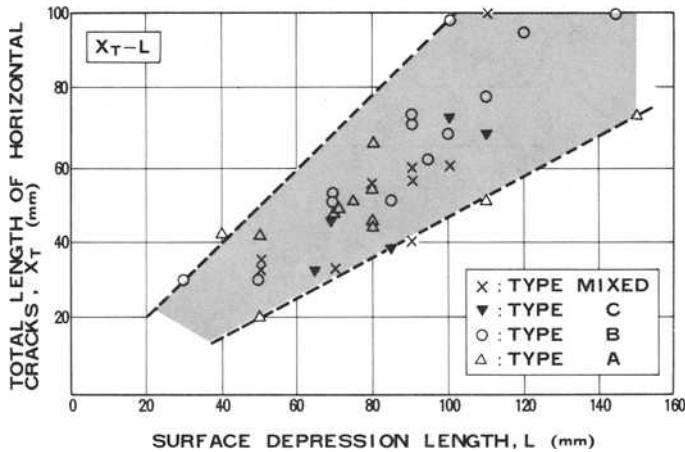


FIG. 12—Relationship between horizontal crack length and the surface depression length.

results of simple fatigue tests such as experiments under conditions of rotating bending or repeated torsion are insufficient to provide complete understanding of this behavior because they do not consider the contact stresses resulting in the rail from wheel loads.

The authors attempted to reproduce these defects, especially the dark spots, experimentally, through rolling contact fatigue (RCF) tests by using the procedure illustrated in Fig. 13. This test consists of two disklike

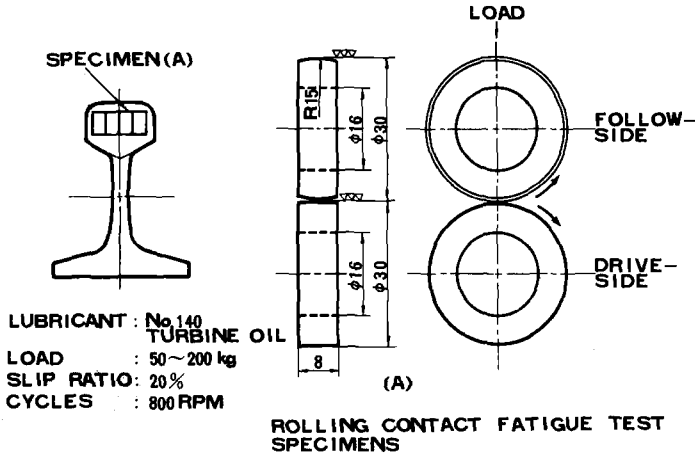


FIG. 13—Rolling contact fatigue test, specimens, and test method.

specimens subject to a normal load representing the wheel load with tangential slip occurring at the surface. The slip component was added to simulate wheel slipping which is assumed to occur in high-speed sections of track. Each specimen is in contact with the other and is driven separately, rotating in the opposite direction to the other specimen. Since the drive-side specimen rotates faster than the follow-side one, slipping on the contact surfaces is generated by the difference in circumferential speed.

The shape of the specimens was determined by preliminary experiments. The curvature of the contact surface of the follow-side specimen was needed to raise the stress by narrowing the contact tread width, thus keeping the contact stable. Lubrication of the contact surfaces with turbine oil was employed to avoid temperature increase and wear.

Figure 14 shows a cross section through the follow-side specimen after the RCF test. Many cracks can be observed, mainly originating in the contact patch on the specimen surface and growing obliquely inwards. The direction of crack growth was always opposite to the direction of specimen rotation, that is, parallel to the movement of the loading point. It was remarkable that these cracks occurred only on the follow-side specimen. The shapes and growth of these cracks were similar to those of the dark spots observed on the running surface of a rail; therefore, the authors concluded that the RCF

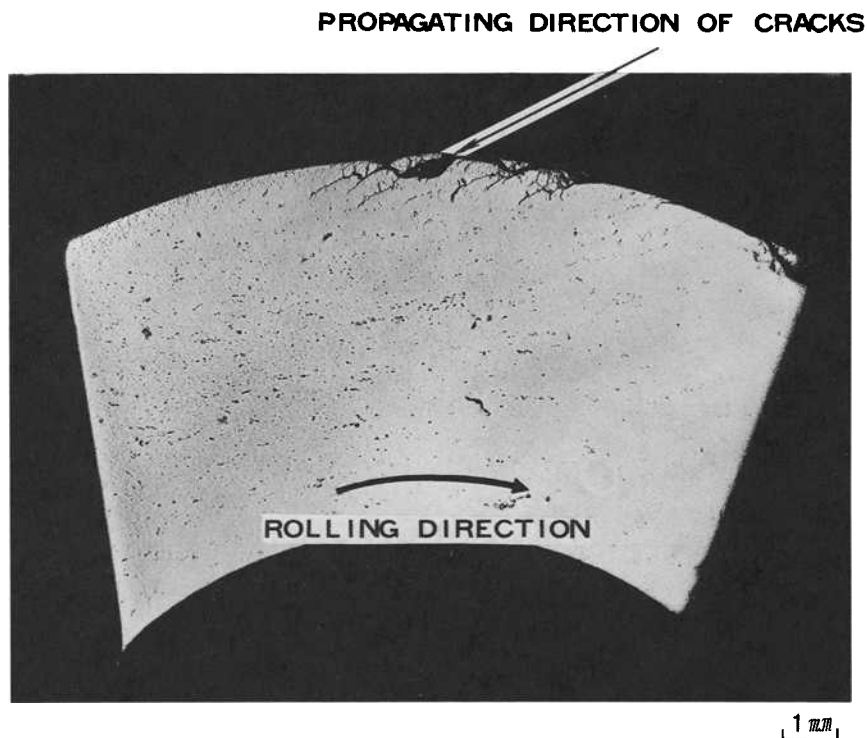


FIG. 14—Tangential section of specimen failed by rolling contact fatigue test.

test could successfully reproduce these defects and adopted this procedure to examine the initiation behavior of rail steels. In the experimental tests to be discussed, the procedure included visual inspection of the specimens, *in situ*, every 5×10^4 cycles to detect the occurrence of defects.

Results of Fatigue Tests and the Effects of Metallurgical Factors on Fatigue Properties

Since improvements in fatigue properties should be a fundamental goal in preventing rail defects, the authors investigated the influence of metallurgical factors on several fatigue properties in an attempt to establish values of those properties leading to the greater durability of rail steels in service.

The following fatigue tests were performed: RCF tests for surface defect initiation, rotating bend (RB) tests for general property determination, repeated torsion (RT) tests for property determination, and tests for the measurement of fatigue crack propagation (CP) rate.

Specimen Preparation

Details of the specimens used are in Table 1, Figs. 13 and 15. Three types of microstructures were selected as typical of rail steels in use. R-1 was an as-

TABLE 1—Chemical composition and mechanical properties of tested specimens.

%					
C	Si	Mn	P	S	
0.67	0.21	0.85	0.015	0.018	
Specimens	$\sigma_{0.2}^a$ kg/mm ²	σ_B^b kg/mm ²	Elevation, %	Reduction of Area, %	VHN
R-1	50.0	93.0	13.5	21.5	271
R-2	75.5	115.9	14.0	50.9	357
R-3	133.6	140.5	11.8	42.5	447

^a $\sigma_{0.2}$ = 0.2% proof stress.

^b σ_B = tensile strength.

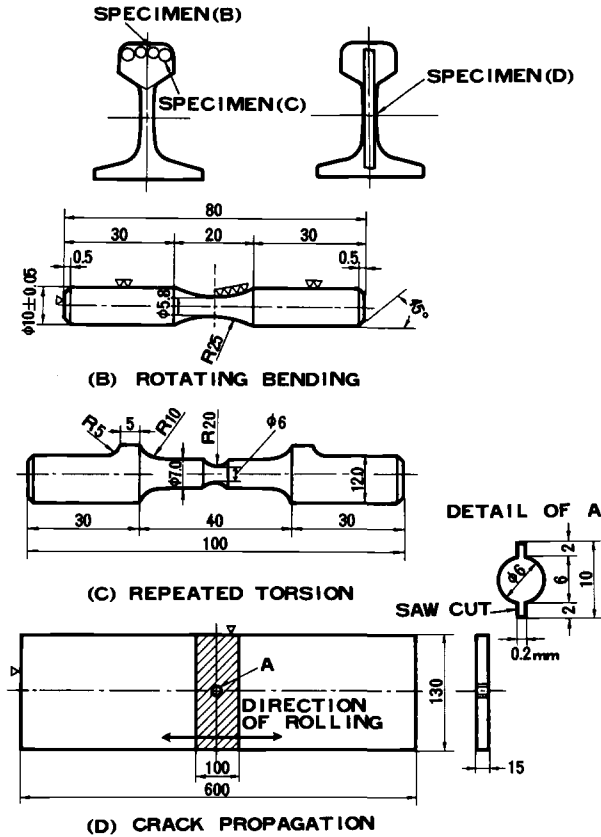


FIG. 15—Three fatigue specimens.

rolled carbon rail steel containing coarse pearlite with a small amount of proeutectoid ferrite; R-2 was a fine pearlitic steel representative of slack quenched rail; and R-3 was a tempered martensitic steel representing quenched and tempered rail steels. Specimens other than those for the CP tests were cut from the railhead of R-1 steel, while those for the CP tests were removed from the entire section of rail due to the necessarily large width of the specimens used.

Specimens were heat treated by induction heating according to the procedure shown in Table 2, then machined as shown in Figs. 13 and 15. Representative microstructures are shown in Fig. 16. Tensile properties were changed because of the heat treatments (Table 1).

TABLE 2—*Procedure of heat treatment of three specimens.*

Specimens	Heat Treatment
R-1	as rolled
R-2	1100°C—cooled to 650°C at 6.2°C/s—WQ ^a
R-3	950°C WQ, 450°C tempered

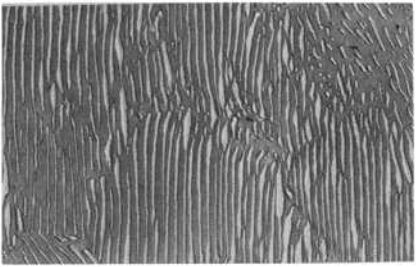
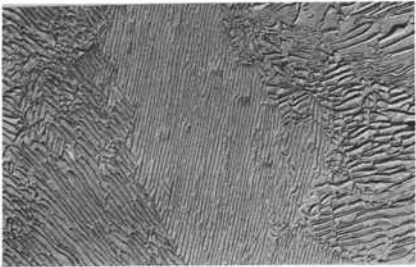
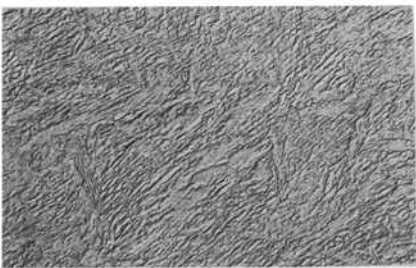
^aWQ = water quenched.

Test Results

The results of the RCF tests are shown in Fig. 17 as load versus N diagrams where N = number of cycles. In this test, like other fatigue tests, the characteristic curves and endurance limits can be obtained for each structure. R-2 shows the longest lifetime among the three structures. The fairly long lifetime of R-1 in the high load region may be due to the relative decrease in contact stress caused by broadening of the contact tread, as shown in Fig. 18. This broadening was presumed to occur as the result of plastic deformation of the specimen surface caused by heavy loads and the relatively low yield strength of R-1. Taking into account track broadening, the authors calculated the approximate contact stress using Hertz's equations for the contact stress on circular cylinders.³ The calculated stress versus N curves are shown in Fig. 19. In this case, R-1 exhibits the shortest lifetime due to its low yield strength, since the higher the yield strength, the longer the lifetime. But when discussing the durability of rail steel, wheel loads are generally used as a major factor; hence Fig. 17 plotted in terms of load seems more suitable for determining the initiation properties of defects than Fig. 19. Therefore, the structure of R-2, namely, fine pearlite, is the most preferable against initiation despite its rather low yield strength.

Figures 20 and 21 show the results of RB and RT tests, respectively. R-3 is the highest in fatigue strength in both tests. As shown in Fig. 22, the fatigue limits of each specimen correlate well with tensile strength. Hence, the fatigue limits obtained by these tests are not influenced by microstructure.

³Timoshenko, S. and Goodier, J. N., *Theory of Elasticity*, McGraw-Hill, 1951, p. 372.

Specimens	Structure
R - 1	
R - 2	
R - 3	

2 μ

FIG. 16—Electron micrographs of tested specimens.

From the results of the CP tests, the relationships between variations in range of stress intensity factor, ΔK , and the crack propagation rate are shown in Fig. 23. ΔK was calculated by the following equation⁴

$$\Delta K = \Delta \sigma \sqrt{W \tan \frac{\pi L}{W}}$$

⁴Irwin, G. R., "Fracture Mechanics," *Structural Mechanics*, Proceedings of 1st Naval Symposium, Pergamon Press, 1960, p. 247.

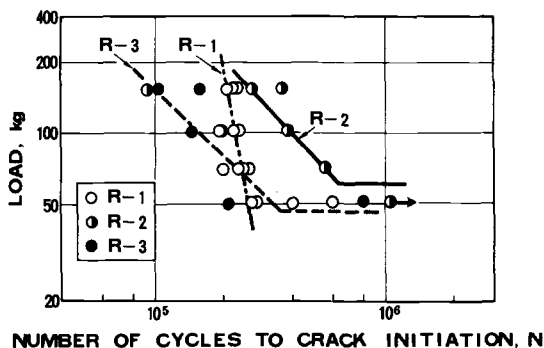


FIG. 17—Effect of normal load on cycles to failure of tested specimens in rolling contact fatigue test.

where

W = specimen width,

$\Delta\sigma_\gamma$ = gross stress range, and

$2L$ = crack length on the surface.

The average of the crack lengths measured on both surfaces of a specimen was adapted for the crack length, $2L$, used in the equation. It is seen that a linear relationship exists between the propagation rate and ΔK for each specimen and that every specimen has a nearly equal gradient. The results of these tests show that R-1 has the highest CP rate and R-3 the lowest despite its high strength.

Figure 24 shows the appearances of fatigue cracks in the different steels. The fatigue crack always proceeds internally rather than along the surface. At localized areas in the fatigue crack region where ΔK is larger, brittle fracture is observed. Considering the results of the CP tests, it seems desirable to increase the strength for retardation of fatigue crack propagation. But the brittle appearance in the fatigue region indicates that the fracture toughness of the material also plays an important role in the propagation, and this toughness may vary with microstructure. All the results of the fatigue tests are summarized in Table 3.

Discussion

Mechanisms of Initiation and Propagation of Surface Defects

Though the shapes and the propagation processes of head checks and dark spots are very complicated, it is assumed that these defects originate at the railhead surface. For contact fatigue, it has been asserted that the cracks initiate at the point of maximum shear stress several millimetres below the contact point, but no indications of such behavior were observed in this investigation.

The effects of slipping on the initiation of cracks in the RCF tests are




Specimens	FOLLOW-SIDE, DRIVE-SIDE	NUMBER OF CYCLES	TREAD WIDTH
R-1		F : 21.5×10^4 (FAILED) D : 26.9×10^4	3.0 mm
R-2		F : 9.6×10^4 (FAILED) D : 12.0×10^4	2.4 mm
R-3		F : 10.9×10^4 (FAILED) D : 13.6×10^4	1.5 mm

FIG. 18—View of tested specimens showing different tread widths.

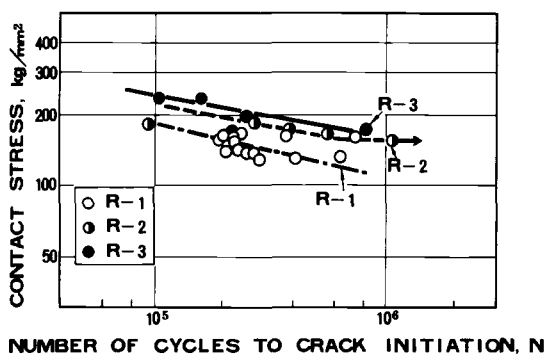


FIG. 19—Calculated contact stress versus cycles to failure of tested specimens.

shown in Fig. 25. The greater the amount of slip, the shorter the lifetime to crack initiation. This result emphasizes the importance of slipping on initiation:⁵ the slip at the surface seems to force the point of maximum shear stress to move toward the contact surface.

The reason why the cracks always originate only on the follow-side specimen in RCF test is proposed as follows: the tangential stress in the forward direction of travel creates a large tensile stress adjacent to the rear of the contact region.⁶ This tensile stress, which is a maximum at the running surface, could enhance the possibility of crack initiation at this location.

Details of the RCF tests such as loads, rotation cycles, slip, etc., are schematically illustrated in Fig. 26 in relation to the wheel and rail. When the train is accelerated or the wheels are driven, the wheel acts as the drive-side specimen and the rail acts as the follow-side one; therefore, the crack will originate on the running surface of the rail. The higher the speed of the train, the larger the slip ratio and tangential force and the greater the number of

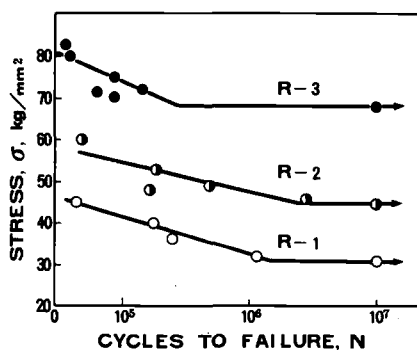


FIG. 20—Stress versus cycles to failure of tested specimens in rotating bending test.

⁵Soda, N., Yamashita, M., and Osora, K., *Lubrication* (in Japanese), Vol. 16, No. 8, 1971, p. 41.

⁶Lipson, C. and Jurinall, R. C., *Handbook of Stress and Strength*, MacMillan, 1963, p. 66.

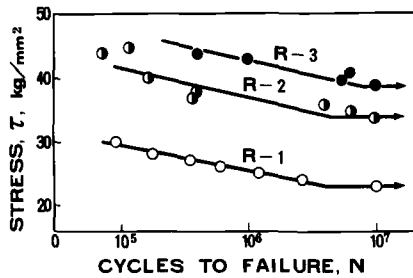


FIG. 21—Stress versus cycles to failure of tested specimens in repeated torsion fatigue test.

cracks found in sections of track subjected to such traffic. This supports the assumption that dark spots tend to originate in rails subject to speeds above 150 km/h. The reason why dark spots grow along the direction of traffic is not evident, but it must have some relation to the relative movement of contact point and must be influenced by track conditions, axial and residual stresses in rail, etc.

Effects of Metallurgical Factors on Fatigue Strength

With an increase in tensile strength, the fatigue limits of the RB and RT tests must also increase linearly, just like other steels, while fatigue crack propagation rates decrease. Therefore, an increase in the tensile strength is recommended as a means of improving the fatigue properties of rail steels. For the prevention of crack initiation, fine pearlite has been preferable to tempered martensite despite its low strength. The higher durability of a fine pearlitic structure is assumed to result from its greater resistance to localized plastic deformation of the surface layer by the applied tangential forces. The lamellar arrangements of ferrite and hard cementite in pearlite of very

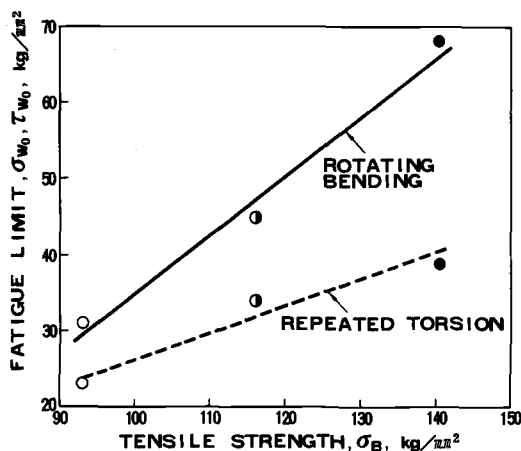


FIG. 22—Effect of tensile strength on fatigue limit.

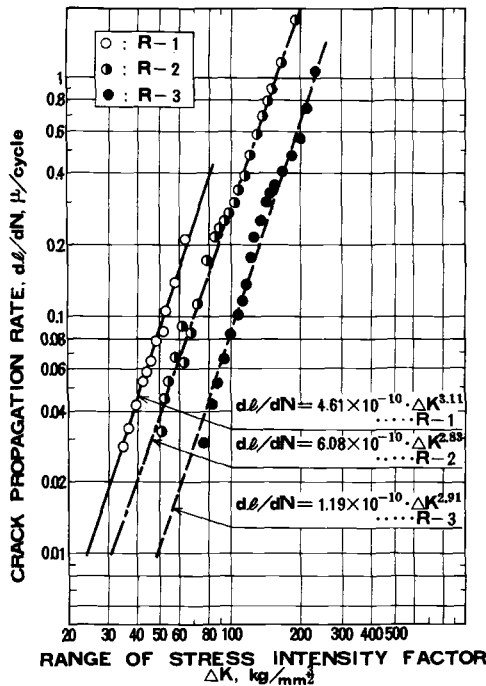


FIG. 23—Crack propagation rate of tested specimens.

narrow spacing seem more resistant to metal flow than a tempered martensitic structure or ferritic matrix with a dispersion of spheroidized cementites.

The good crack propagation properties of tempered martensite seem to depend not only on its strength, but also on its structure or toughness. Considering the brittle appearance observed in CP specimens, notch toughness should never be ignored in investigations of fatigue crack propagation behavior. Fine pearlite is preferable to tempered martensite for crack initiation, and the reverse for crack propagation, although each of these properties is associated with an increase in strength. Both of these findings should be considered in recommendations for the improved durability of rail steels.

Conclusions

From the foregoing investigations, the following conclusions were obtained.

1. Recently, two unique types of rail steel defects have been observed in track subject to relatively small wheel loads and high traffic speeds. One is known as the head check, which originates at the gage corner independent of traffic speed. The others referred to are the dark spots that originate on the running surface of rail subject to traffic speeds greater than 150 km/h. Their

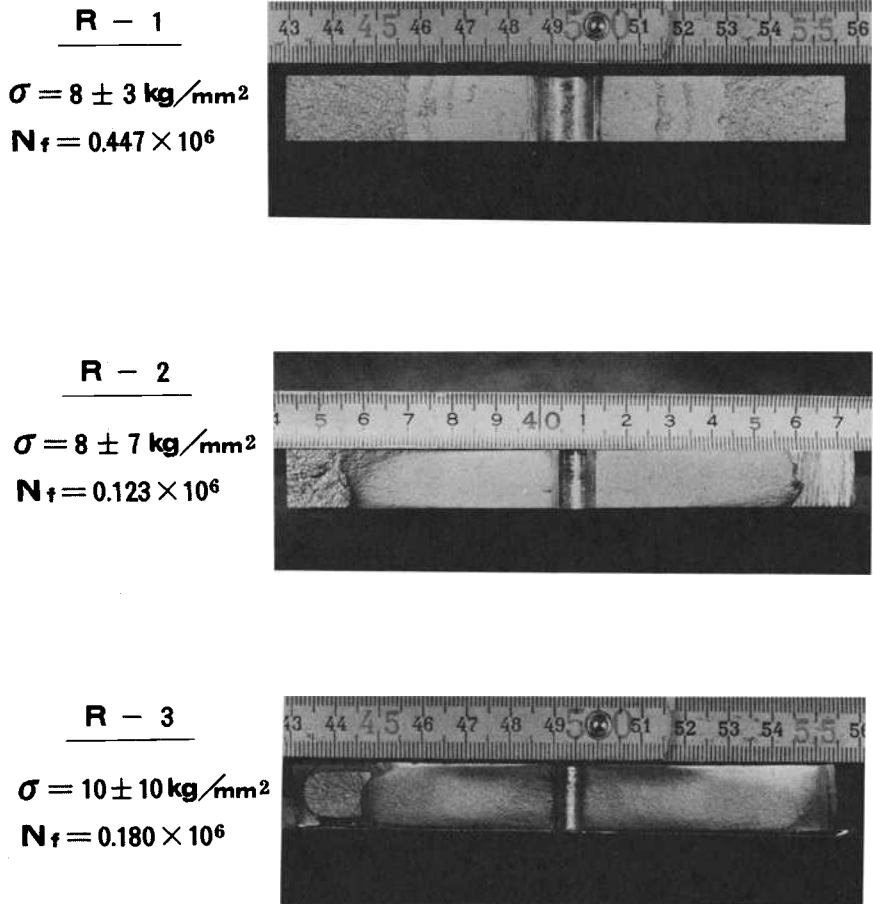


FIG. 24—Appearance of fatigue cracks.

TABLE 3—Summary of fatigue testing data.

Specimens	σ_B^a kg/mm ²	σ_{W0}^b kg/mm ²	τ_{W0}^c kg/mm ²	dl/dN^d		K_{fc}^e kg/mm ^{3/2}
				C	m	
R-1	93.0	31.0	23.0	4.61×10^{-10}	3.11	139.0
R-2	115.9	45.0	34.0	6.08×10^{-10}	2.83	288.0
R-3	140.5	68.0	39.0	1.19×10^{-10}	2.91	407.0

^a σ_B = tensile strength.

^b σ_{W0} = fatigue limit of rotating bending.

^c τ_{W0} = fatigue limit of repeated torsion.

^dC, m = constants in the equation to calculate the fatigue crack growth rate in the form of $dl/dN = C \times \Delta K^m$.

^e K_{fc} = critical stress intensity factor in fatigue.

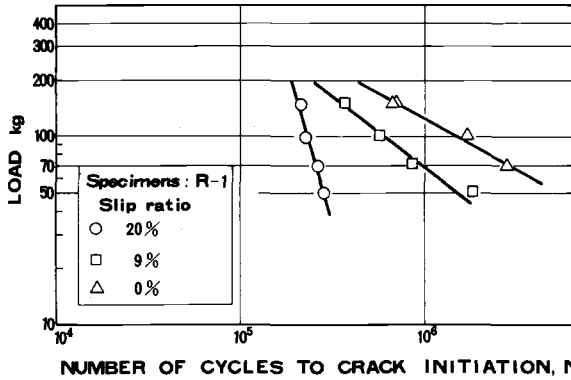


FIG. 25—Effect of slip ratio on cycles to failure in rolling contact fatigue test.

growth processes can be divided into four stages. Both types of defects are suggested to have surface origins, rather than internal origins.

2. Rolling contact fatigue tests have been conducted successfully for the simulation of dark spots. For surface initiation, slipping on the contact surface is necessary, in addition to a normal load. These defects grow in the direction of motion of the load.

3. Not only an increase in tensile strength, but consideration of the role of microstructures, are necessary for an improvement of the durability of rail steels. Fine pearlite was suitable for the prevention of crack initiation, whereas tempered martensite is preferable for retardation of fatigue crack propagation. Therefore, the effects of microstructure on fatigue properties must be considered to optimize rail steel durability further.

The authors think that fine pearlitic rail steel is preferable for their practical purpose, because the initiation always precedes the propagation.

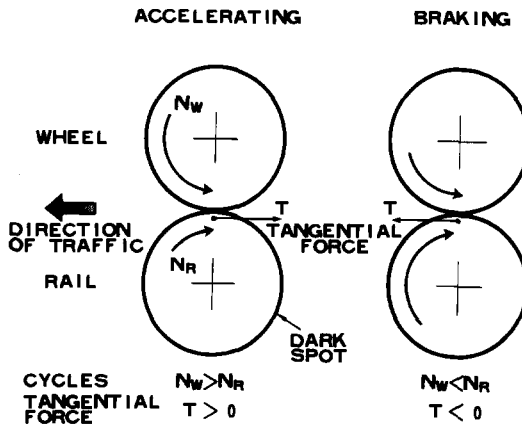


FIG. 26—Schematic correspondence of experimental results on wheel and rail.

Acknowledgment

The authors wish to thank the Japanese National Railways and Nippon Steel Corporation for permission to publish this paper. The authors also acknowledge A. Ito and H. Kido, Nippon Kokan K. K., for their valuable discussions. Fatigue tests were greatly assisted by the constant efforts of C. Urashima and H. Kageyama in the Yawata Works.

In this report, the investigations of rail defects were done by R. Kurihara and S. Matsuyama, and the fatigue tests were performed by H. Masumoto, K. Sugino, and S. Nisida.

United Kingdom Development of Rails Rolled from Continuously Cast Blooms

REFERENCE: Young, J. D., "United Kingdom Development of Rails Rolled from Continuously Cast Blooms," *Rail Steels—Developments, Processing, and Use*, ASTM STP 644, D. H. Stone and G. G. Knupp, Eds., American Society for Testing and Materials, 1978, pp. 256–284.

ABSTRACT: The development of rails rolled from continuously cast blooms in the United Kingdom is described. Results of pilot (seven tonne) trials which were begun in 1962 are discussed. These trials evolved into larger scale experiments and eventually into routine processing routes and rail evaluations.

Production experience, mechanical test data, and the results of metallurgical evaluations of rails from the new continuously cast steel process route in various steel grades totalling over 300 000 tonnes are given. Because of the new nature of the process, special testing of the rails was undertaken. These tests included fracture toughness testing and wear tests which compared rails from continuously cast blooms with conventional rails. A program to survey hydrogen content and the development of retarded bloom cooling for shatter crack prevention is reviewed.

KEY WORDS: railroad tracks, steels

Modern track conditions associated with higher traffic speeds and axle loads, and the widespread use of continuously welded track demand the highest possible rail quality standards consistent with economic manufacture. Throughout the world, continuous casting has been established as a beneficial manufacturing process on a wide variety of steel products. Using this background experience supported by many years of investigation and production trials, the British Steel Corporation (BSC) has established standard routine continuous casting procedures for the full range of normal carbon-manganese rail steels. Work is in process to include alloy rail steels. Indeed, the BSC's Workington Mill is probably unique in rolling only rails and track products and in its feedstock being almost entirely basic oxygen steel (BOS), which has been continuously cast into blooms. Extensive checking of mechanical and metallurgical properties has been carried out, and typical examples are quoted in this report, demonstrating that rails

¹Manager, Technical Services, British Steel Corporation, Teesside Division, Workington Works, Cumbria, England.

rolled from continuously cast blooms are at least equivalent, and in some cases superior, to the conventional ingot route product of similar chemical composition. Rail specification amendments have been negotiated to permit the use of continuously cast rail blooms. Slow cooling of the blooms after continuous casting has proved an effective alternative to pit or box cooling of rolled rails for the prevention of shatter cracks.

Process Development Trials

Reasons for Investigations

In the United Kingdom, rails have in the past been manufactured from open hearth and acid Bessemer steel (and in more recent years electric arc) cast into semikilled (or balanced) open-top ingots, which were then hot charged to soaking pits and rolled to rails in one heat. By the early 1960s, it was becoming apparent that semikilled, open-top ingot practice would be inadequate to meet future rail quality requirements. Replacement of the BSC's Workington steelmaking plant was being considered, and technical and economic benefits being achieved on other steel products through the use of continuous casting led to this process being examined as a future rail production process route.

Initial Pilot Plant Trials

Considerable experimental experience had already been gained on a wide range of steel compositions on a continuous casting pilot plant at BSC's Barrow Works. Hence in 1962, the initial series of trials (approximately 100 tonnes) commenced, the pilot plant being fed from a seven-tonne electric arc furnace, the bloom size being 230 mm (9 in.) square and the rolling reduction 7.5:1.

The rail steel qualities used in these initial trials and various subsequent experiments were to the chemical compositions listed in British Standard Specification 11:1959 (BSS 11) known as "normal" quality or "medium manganese," International Union of Railways Specification 860-0 (UIC 860-0), wear-resisting Grades A, B (UIC 860-0A and UIC 860-B) (Table 1). The rails produced were used entirely for metallurgical testing, which proved that they fully met the requirements of the specifications. The relatively small bloom cross section for the roll pass design used caused inadequate filling of the flange tips, and these initial trial rails could not be put into track service.

Limited Production Trials

During the middle to late 1960s, several thousand tonnes of rails had been rolled at BSC's Shelton Works and put into main line service on British Rail (BR). Rationalization of rail making led to Shelton ceasing rail production. However, based on the encouraging results of the Barrow pilot plant trials

TABLE 1—Rail specifications.

Specification	Composition Limits							
	Carbon		Silicon		Manganese		Sulfur	
	min	max	min	max	min	max	max	Chromium
BSS 11								min max
Basic oxygen process ^a	0.50	0.60	0.05	0.35	0.95	1.25	0.06	0.06
Open hearth	0.50	0.60	0.05	0.35	0.95	1.25	0.06	0.06
Electric	0.45	0.55	0.05	0.35	0.95	1.25	0.06	0.06
Acid Bessemer	0.40	0.50	0.05	0.35	0.95	1.25	0.06	0.06
UIC 860-0								
Normal ^a	0.40	0.60		0.35	0.80	1.20	0.05	
A ^a	0.60	0.75		0.50	0.80	1.30	0.05	
B ^a	0.50	0.70		0.50	1.30	1.70	0.05	
C	0.45	0.65		0.40	1.70	2.10	0.03	
AREA ^{a,b}	0.55	0.68		0.35	0.60	0.90	0.05	
110 kg/mm ² chromium ^a	0.68	0.78	0.20	0.50	1.10	1.40	0.05	1.0 1.3
90 kg/mm ² chromium ^a	0.52	0.60		0.35	1.10	1.30	0.05	0.75 1.10

^aQualities produced by continuous casting.

^bAs for 70/80 lb/yd section, with silicon increased to accommodate continuously cast material.

and Shelton's previous experience, 600 tonnes of continuously cast blooms of 413 by 230 mm (16.25 by 9 in.) section in BSS 11 rail quality were obtained in 1970/71 from Shelton Works and rolled to 113 A (113 lb/yd) rails at Workington Works. The steel was produced in 60-tonne Kaldor converters. The reduction of area in rolling was 13:1.

Metallurgical structure and mechanical properties all met the specification requirements. However, some of the rails produced from this second trial contained large inclusions and also surface defects arising from severe corner cracks in the blooms. Investigations proved that modification of the Shelton continuous casting machine to specialize in mild steels rendered it unsuitable for use in relatively small trial tonnages of rail steel. Following stringent quality control testing and inspection, a 200-tonne batch of these rails was put into main line service by BR. Service experience to date has been entirely satisfactory.

Full-Scale Production Trials

In 1970, the decision was made to close the Workington steelmaking plant eventually and concentrate rail rolling at the Workington Mill, the steel being supplied from BSC's Lackenby Works (South Teesside) in 260-tonne heats of continuously cast blooms. During the detailed design stage of the Lackenby Continuous Casting Plant, full reference was made to the results of earlier trials and experience with continuously cast rail steels.

After commissioning the new continuous casting plant at Lackenby, one 260-tonne heat of BSS 11 rail steel was produced each week and rolled to rails at Workington. The collation of rail rolling and metallurgical results with continuous casting data enabled standard manufacturing procedures and parameters to be evolved.

In July 1974, the Workington steelmaking plant was closed, ingot supplies terminated, and the mills immediately commenced the rolling of rails almost entirely from continuously cast blooms. To date, over 300 000 tonnes of rails have been rolled at Workington from continuously cast blooms produced at Lackenby Works.

The following sections of this report will concentrate on the results achieved from this new routine process route.

Current Manufacturing Procedure

Rail steel is produced by the well-established BOS top lancing process, based on a static model computer control. Each 260-tonne heat is tapped into a single ladle, which is then flushed with either nitrogen or argon gas to ensure uniformity of both temperature and chemical composition. Twin sliding gate nozzles in the ladle bottom ensure the pouring of slag-free metal into two tundishes, each feeding four casting strands. The C-type continuous casting machine is fitted with curved molds and has a casting radius of 10 m

(33 ft). The machine control system was designed to cater for a range of steel qualities (including rail steels), and various mold cross section sizes may be used from 483 by 305 mm (19 by 12 in.) to 254 mm (10 in.) square. The standard mold used for rails is 330 by 254 mm (13 by 10 in.), this optimum being established by a series of investigations.

After straightening, the blooms are flame cut to the ordered weight/length and allowed to cool before despatch to the rolling mills. Blooms in rail steel qualities least susceptible to shatter crack formation, for example, BSS 11 and UIC 860 "normal," are air cooled, but blooms in the more hydrogen-susceptible grades, for example, UIC 860 A and B and American Railway Engineers Association (AREA) heavy section qualities, may be slow cooled to prevent shatter crack formation.

At the rail rolling mills, the blooms are reheated in gas-fired walking beam type furnaces and rolled to the ordered section and hot sawn to length. Currently, the maximum rail length finished is 18.28 m (60 ft). All rails are roller straightened, and either milled or sawn to finished length.

Rail rolling in BSC is mainly concentrated at Workington Works, with the flexibility of additional capacity at Cargo Fleet Works (South Teesside) and Glengarnock Works (Scotland). All three rail manufacturing works have had their quality control systems checked and audited by an independent Ministry of Defense Quality Assurance assessment team. All have been approved and certified as being capable of releasing rails for despatch without the need for independent customers' inspection.

Rail Quality

Metallurgical Structure

Macrographic examination of rails rolled from continuously cast blooms made to standard procedure gives excellent results. The piping, excessive central segregation, and dispersed (or spotty) segregation commonly found in rails rolled from conventional ingot material is not encountered. A typical structure is illustrated in Fig. 1.

Abnormal features sometimes encountered include minor segregation in the rail web (Fig. 2) and the occasional presence of small streaks associated with the bloom corner positions (Fig. 3). These features were associated with steel sulfur content, mold design, and cooling parameters [1],² and were confirmed by a small-scale trial using an unsatisfactory mold design (Fig. 4).

The minor streaks on macrographs have been proved by metallographic, microprobe analysis and electron microscopy to be fully pearlitic regions associated with pockets of manganese sulfide inclusions. Microsegregation of manganese of the order of 35 to 80 percent of the base level has been

²The italic numbers in brackets refer to the list of references appended to this paper.



FIG. 1—*Typical sulfur print of a rail rolled from a continuously cast bloom.*

detected, being similar to but less severe than quoted by other workers [2]. Under very carefully controlled acid pickling conditions, a ghost of the original cast structure can occasionally be observed. Rails from ingot material may occasionally show a similar effect which is not considered detrimental to rail quality or performance.

The finished railhead grain size of ASTM 3 to 4, is identical to that obtained with conventional ingot practice.

Cleanliness

Microscopic Results—A linear traverse counting method (see Appendix I) proved the superior cleanliness of the continuously cast product compared



FIG. 2—Sulfur print showing abnormal feature in web of a rail rolled from a continuously cast bloom.

with ingot material. Both the incidence and sizes of oxide inclusions are lower in the continuously cast product (Fig. 5, Table 2). Further confirmation of the superior cleanliness of continuously cast rail steel was provided by quantitative television microscopic analysis; typical results are shown in Table 3.

Ultrasonic Testing Results—A high proportion of heavy rails are ultrasonically tested for pipe and inclusions (see Appendix II). None of the rails from continuously cast blooms have been rejected for pipe, and, from the last 10 000 tested, only one was downgraded for its inclusion content, which compares very favorably with the already excellent result of only 12 rails in 10 000 being downgraded on the alternative BOS-killed ingot rails.

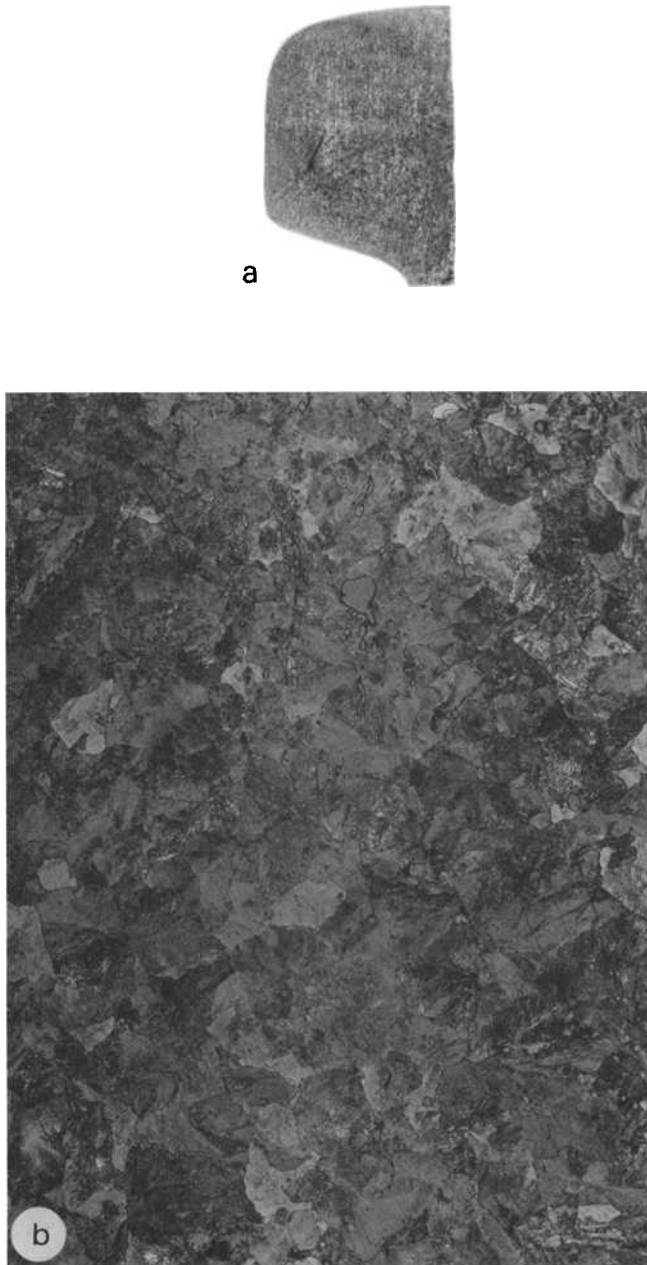


FIG. 3—Sulfur streak in head of a UIC 860-B rail. (a) Sulfur print. (b) Nital etch $\sim \times 270$.

Chemical Composition—Homogeneity

The excellent homogeneity of continuously cast material is demonstrated by the following results.

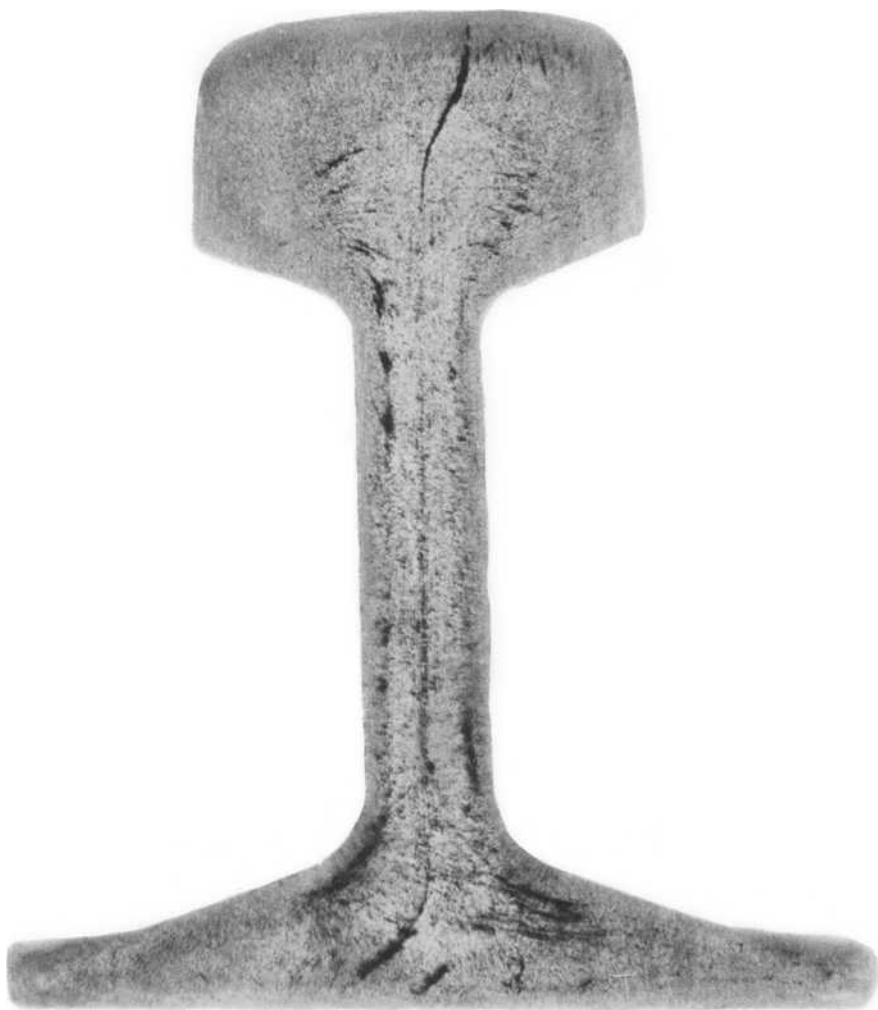


FIG. 4—Unsatisfactory sulfur print from a rail rolled from a special trial 406 by 203 mm (16 by 8 in.) mold with modified cooling conditions.

Bloom Samples—The chemical composition of drillings taken from several positions on the bloom cross section on a large number of samples shows a slight degree of negative segregation of carbon and sulfur at the bloom center—in the case of carbon averaging 0.025 percent lower than the mean (Table 4).

Rail Samples—Typical examples of web center carbon and manganese contents compared with the standard head sample positions are given in Table 5. Additionally, several hundred rail samples have been analyzed from within a heat, using the standard head sample position. No significant

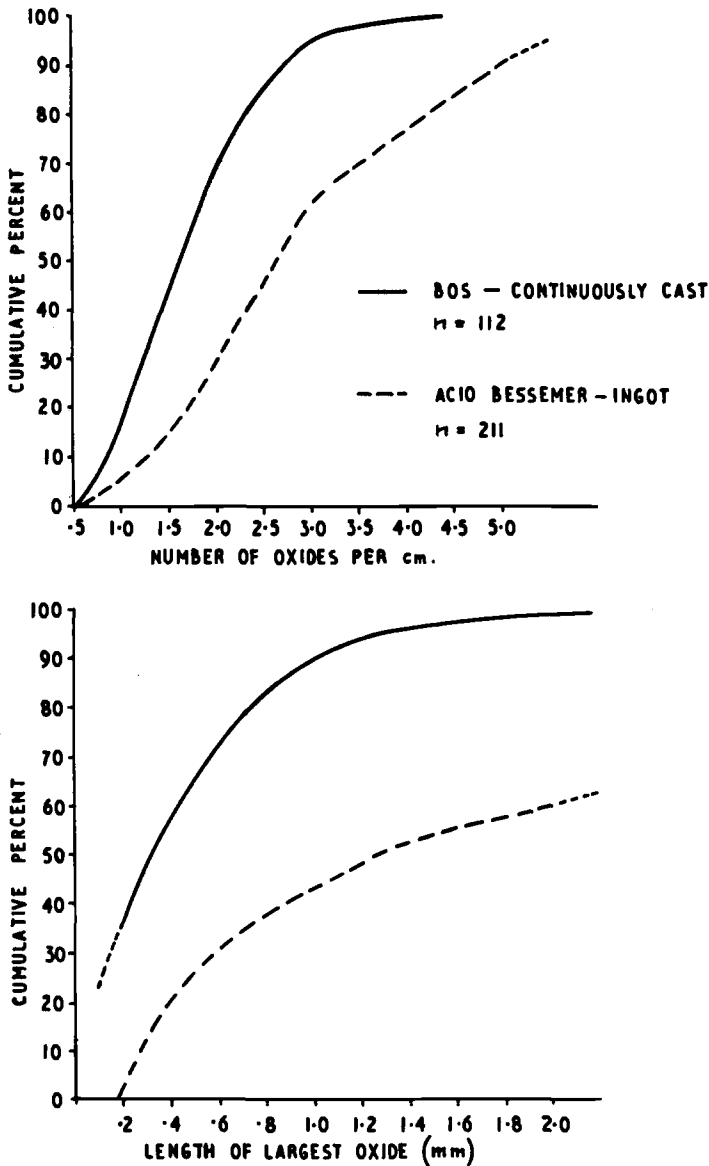


FIG. 5—Oxide inclusion content and size for steel made by the BOS—continuously cast and acid Bessemer—ingot routes.

differences are found between top and bottom of a strand, or between strands within a single heat. Within a single heat, all carbon analyses were within ± 0.02 percent of the mean, with a standard deviation of 0.0041 percent. Manganese contents were all within -0.06 to $+0.03$ percent of the mean, with a standard deviation of 0.0093 percent.

TABLE 2—Oxide inclusion length.

	Proportion of Samples with the Maximum Oxide Stringer Length, %	
	Below 1 mm	Above 2 mm
Continuously cast	89	2
Conventional ingot	42	39

In sequence continuous (or continuous continuous) casting, good mixing occurs in the intermediate blooms between adjacent heats. This was clearly defined by the addition of copper as a trace element (Fig. 6). Sequence casting is now a regular practice, and extensive work has been done to identify the intermediate blooms.

Routine Mechanical Tests

Tensile Tests—Tensile properties have been entirely in accordance with the specifications used, the results from continuously cast material being at least equivalent, and in many cases superior, to those obtained from conventional ingot material of similar chemical compositions (Table 6, Figs. 7–9). Variability of tensile properties within a single heat is negligible, again confirming the homogeneity of continuously cast material (Table 7).

Statistical analysis of chemical compositions and tensile strengths obtained on BSS 113 A rail section in BSS 11 quality has proved a reliable predictive equation, namely

$$\begin{aligned}
 &\text{ultimate tensile strength (UTS), N/mm}^2 \text{ (tonnes/in.}^2\text{)} \\
 &= 122 \text{ (7.9)} \\
 &= +782 (+50.67) \times \text{percent carbon} \\
 &= +218 (+14.13) \times \text{percent manganese} \\
 &= +118 (+7.64) \times \text{percent silicon} \\
 &95 \text{ percent confidence limits } \pm 26 (\pm 1.7)
 \end{aligned}$$

Falling Weight Tests—A comparison of the falling weight test requirements of various rail specifications is given in Table 8, and to date all rails produced from continuously cast blooms have fully met these requirements.

Surface Quality

Since establishing standard liquid steel and continuous casting conditions at Lackenby, the surface quality of both blooms and rails have been excellent and markedly superior to previous ingot experience [3]. Current initial inspection results (from which short rails may be recovered) for continuously cast rails are given in Table 9 and compare extremely favorably with past ingot experience.

Occasionally, small longitudinal corner cracks may occur on the bloom

TABLE 3—Typical inclusion content of ingot and continuously cast BSS 11 rail steel determined by quantitative television microscopic analysis.

	Ingot		Continuously Cast	
	min	mean	min	max
Oxide volume fraction	0.003	0.0374	0.001	0.071
Sulfide volume fraction	0.066	0.2664	0.027	0.268
No. of inclusions per square mm				
Size				
2 to 4 μm	9	73.57	9	63
4 to 6 μm	4	33.24	2	50
6 to 8 μm	2	15.50	0	7
> 8 μm	2	22.45	0	0

TABLE 4—*Variation in chemical composition across a continuously cast bloom section 330 by 254 mm (13 by 10 in.).*

Variation from Average of Quarter Diagonal Position								
	Carbon, %				Sulfur, %			
	min	mean	max	s	min	mean	max	s
Corner	-0.033	-0.010	+0.017	0.0092	-0.0034	-0.0014	+0.0026	0.00079
Center	-0.073	-0.025	+0.067	0.0235	-0.0034	-0.0009	+0.0026	0.0010

surface when the continuous casting mold requires machining or is nearing the end of its life. Blooms containing these small corner cracks may be dressed by grinding, and our limited experience shows that the resultant rails have a surface defect rate less than 0.5 percent.

Special Test Results

Various nonroutine tests, not included in rail specifications have been carried out, and these indicate that rails of continuously cast material are at least equivalent, or in some cases superior, to the conventional ingot produced.

Charpy Impact Properties—Notched-bar Charpy impact properties from continuously cast material were slightly superior to conventional material at temperatures below 40°C and comparable up to 100°C (Fig. 10). The impact strength was virtually identical in the longitudinal and transverse directions.

Fracture Toughness—Fracture toughness tests using a method essentially comparable to ASTM Test for Plane-Strain Fracture Toughness of Metallic Materials (E 399-74) (see Appendix III) on 13 heats gave a K_{Ic} value of $36.73 \pm 1.12 \text{ MN} \cdot \text{m}^{-3/2}$ similar to that of ingot material of $35.97 \pm 1.59 \text{ MN} \cdot \text{m}^{-3/2}$. The test temperature was -15°C.

Transverse and Longitudinal Tensile Properties—Rails from continuously cast material having received an 11.7:1 rolling reduction showed more uniformity between transverse and longitudinal tensile properties than conventional ingot material (Table 10). This improved uniformity should be an advantage in service, providing some improvement in transverse shear stress service behavior.

Wear—A laboratory abrasive wear test (see Appendix IV) showed continuously cast material to have a similar or possibly slightly superior wear resistance to ingot material of comparable chemical composition (Table 11).

Further Developments

Continuous casting is particularly suited to long production runs on standard qualities and is less attractive for special steel grades in small tonnages.

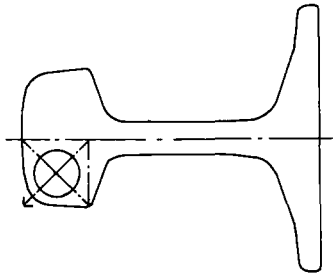


TABLE 5—Variation in chemical composition in the 113 lb/yd rail section.

Heat No.	Standard Head Position		Center of Web ^a	
	Carbon, %	Manganese, %	Carbon, %	Manganese, %
632	0.570	0.99	0.575	0.97
649	0.570	1.07	0.570	1.07
650	0.565	1.09	0.560	1.06
832 ^b	0.575	1.12	0.580	1.12

^aMidheight of web, 3.17 mm (1/8 in.) drill dia.

^bThis rail is illustrated in Fig. 2.

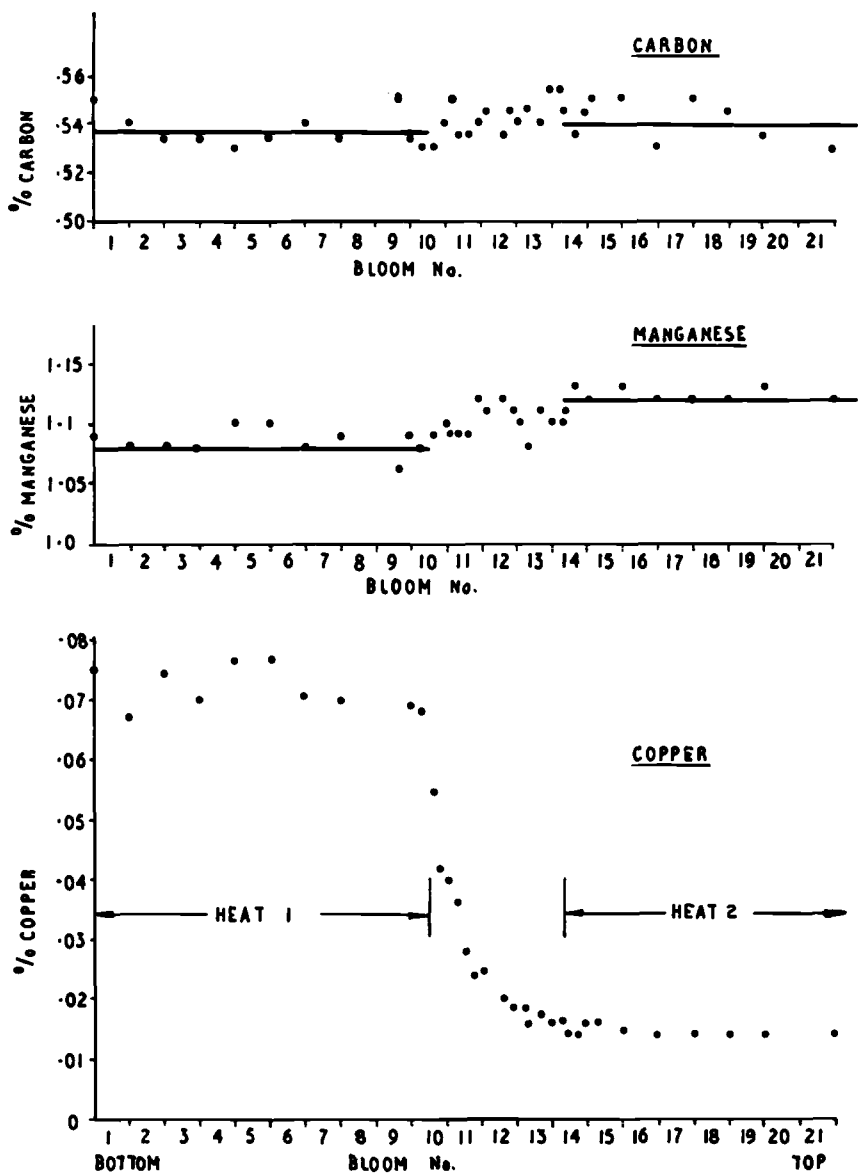


FIG. 6—Change in chemical composition between sequence casts. BSS II quality.

While a heat of 11 to 14 percent manganese austenitic rail steel was successfully cast on the Barrow pilot plant, cracking problems were experienced during the reheating and initial stages of rolling. The rolled 11 to 14 percent manganese rails are used in relatively small tonnages in switches and crossings and severe service applications. The established process route includes electric arc steelmaking and ingot casting.

TABLE 6—*Tensile properties.*

Rail Quality	UTS						No. of Casts	Specification Minima		
	N/mm ²		Long Tons/in. ²		Elongation, %			UTS		
	\bar{x}	<i>s</i>	\bar{x}	<i>s</i>	\bar{x}	<i>s</i>		N/mm ²	tons/in. ²	Elongation, %
BSS 11	824	26.0	53.3	1.68	14.8	1.27	409	710	46	9
UIC 860 A	942	27.1	61.0	1.75	12.9	0.98	54	883	57.1	10
UIC 860 B	947	24.4	61.3	1.58	12.9	0.89	38	883	57.1	10
AREA (80 lb/yd)	831	24.4	53.8	1.58	15.3	1.15	49

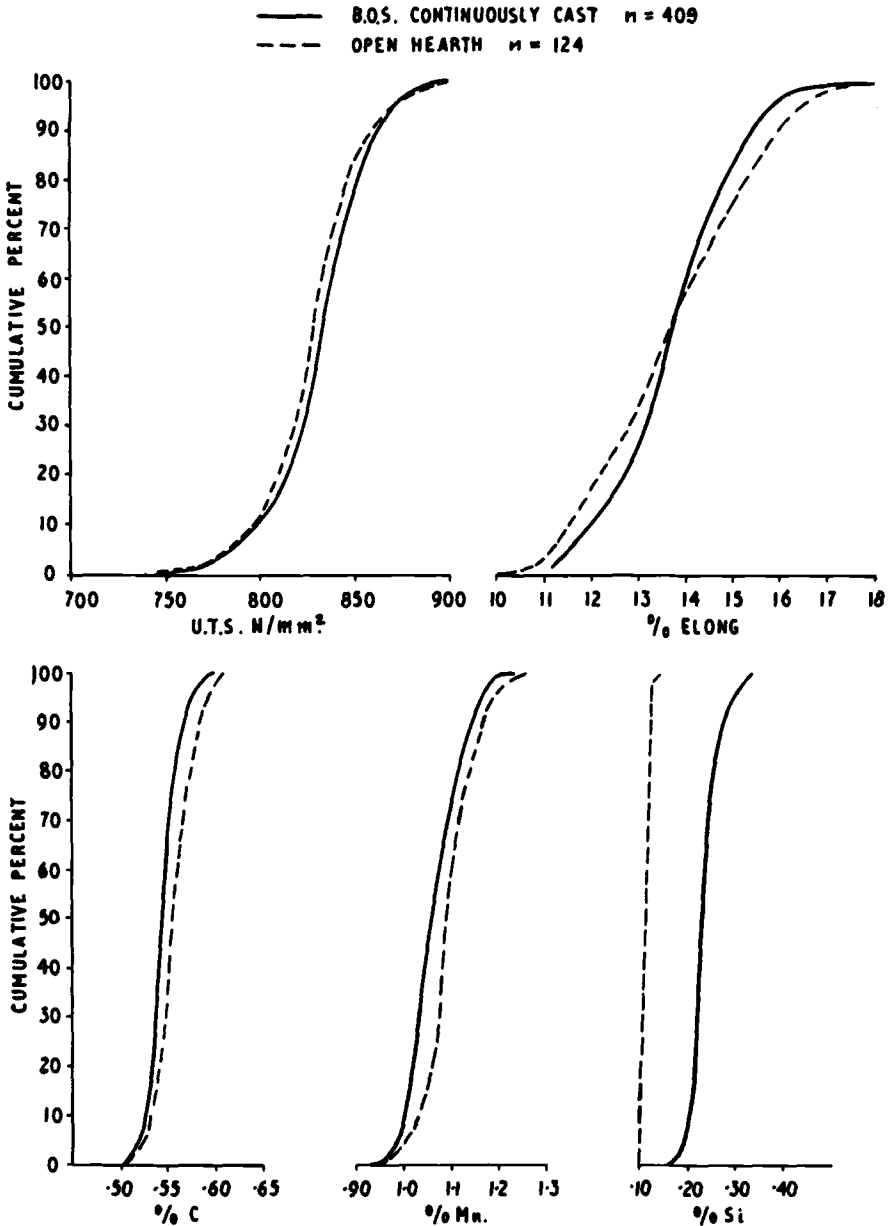


FIG. 7—Distribution of tensile properties and chemical composition—BSS 11 material, BSS 113 lb/yd section.

Some pilot plant trials were successfully completed with UIC 860-C quality rail steel (1.7 to 2.1 percent manganese). A single heat has also been continuously cast on the production plant at Lackenby, in the standard 330 by 254 mm (13 by 10 in.) bloom section. Some microsegregation of

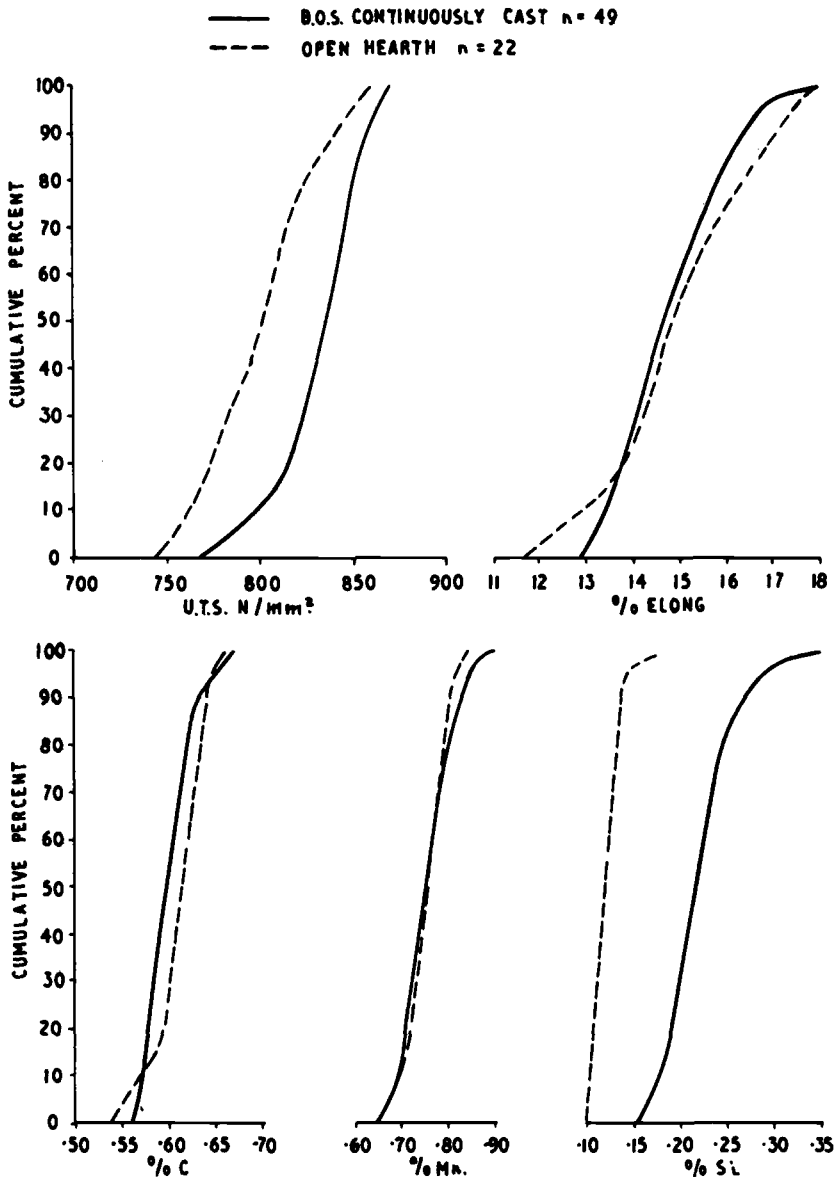


FIG. 8—Distribution of tensile properties and chemical composition—AREA material, 80 lb/yd section.

manganese was found in the rolled rail, similar to severe problems recently experienced with large ingot practice, which has resulted in this grade being deleted from the UIC 860 specification.

Development work is in hand with the continuous casting of chromium rail steels, which have been previously manufactured by the conventional ingot process. Results from two heats are encouraging.

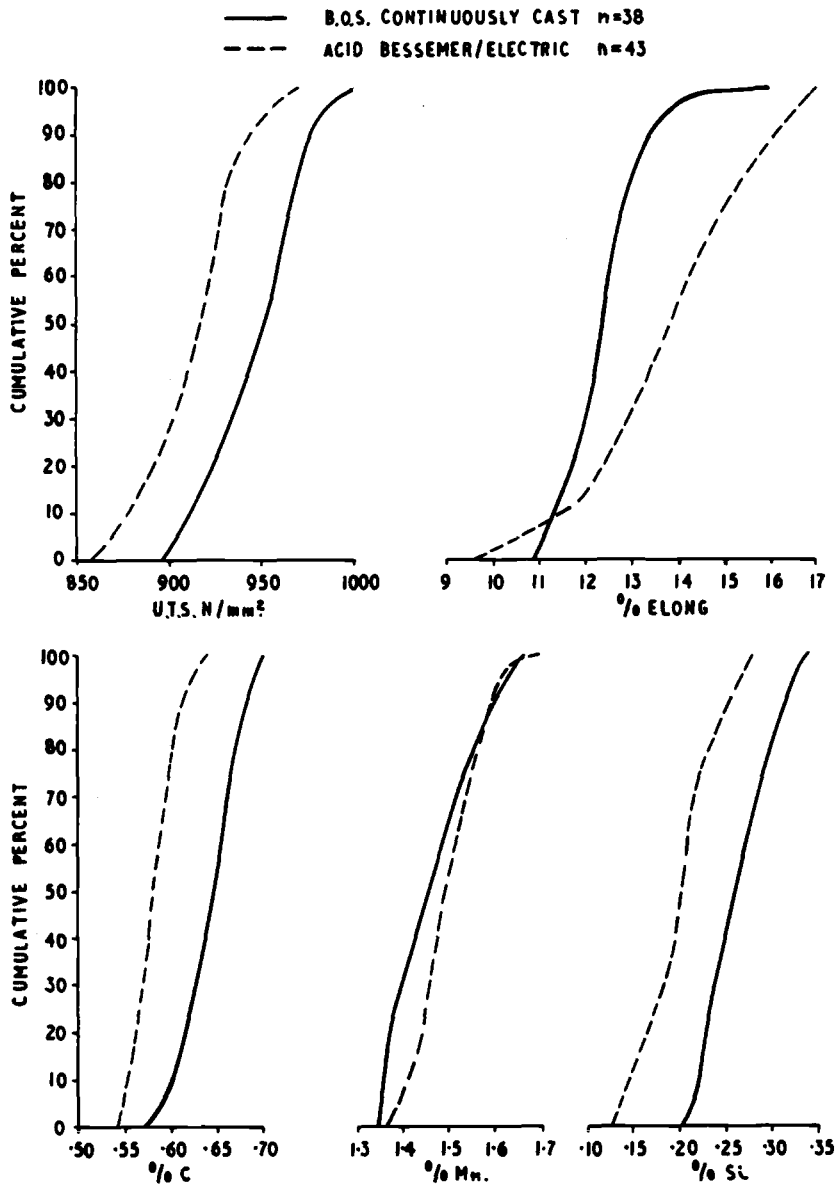


FIG. 9—Distribution of tensile properties and chemical composition—UIC 860 B material, BSS 113 lb/yd section.

Hydrogen Removal by Controlled Cooling of Blooms

The higher tensile rails to the UIC 860 A, B, and AREA specifications are prone to shatter cracking if their hydrogen contents are high. Safe levels have been quoted for the UIC 860 A and B qualities in the range 2.5 to 3.5 ppm [4,5] (Table 12).

TABLE 7—*Variation in tensile properties within a continuously cast heat.*

	UTS		Elongation	
	Range About Mean	s	Range About Mean	s
BSS 11 quality	-40 to +32 N/mm ² -2.6 to +2.1 long tons/in. ²	11.63 0.75	-3.4 to +3.9%	1.41

The normal practice in the United Kingdom has been to slow cool such rails in insulated pits as stipulated in the AREA Part 2 Specification. As the new process route includes a reheating stage, advantage was taken of the preceding bloom cooling stage to retard this cooling rate, to allow more hydrogen to diffuse out. On several trial casts, the continuously cast blooms were held on the cooling racks for about 1 h, then lifted by magnet and stacked in an insulated pit. The blooms were allowed to cool from around 600 to 650°C to 250 to 350°C over three to six days, that is, a cooling rate of the order of 2 to 4°C/h, similar to those achieved on ingot material at Sacilor [5]. The final hydrogen results on an initial eight BSS 11 casts were successfully reduced, and a further 32 casts of UIC 860-B quality confirmed the success of the technique on achieving hydrogen levels in the final rail of below 2 ppm. The results are shown graphically in Figs. 11 and 12 and summarized in Table 13 as obtained by the hot vacuum extraction technique.

BSC plans to incorporate slow cooling of continuously cast blooms in the standard process route for those steel qualities demanding control of hydrogen content. This development will reduce constraints in rail rolling and subsequent handling operations.

Rail Specification Amendments Associated With Continuous Casting

The interrelated and mutually dependent development of railways and the steel industry over the past 100 years and their interest in the safety of the

TABLE 8—*Comparison of drop test parameters for a 113 lb/yd rail section.*

	AREA	UIC 860-0	BSS 11
Weight of tup			
lb	2000	2205	2800
kg	907	1000	1270
Bearer spacing			
ft	4	3.28	4
m	1.22	1.0	1.22
Height of drop			
ft	20	1 27.59	26.5
m	6.1	2 19.21	
Anvil foundation	springs	8.4 5.9 solid	8.1 solid

TABLE 9—*Rail initial mark out for surface defects.*

Origin	Percent of Rails Marked Out	
	Continuously Cast	Ingot
Bloom/ingot surface crack	0.60	4.21
Nonmetallic material		
entrapped in surface	0.64	1.15
Subsurface blowholes	0.01	2.86
Total	1.25	8.22

travelling public led to many rail specifications being very detailed with respect to testing procedures and process routes.

The successful adoption of continuously cast blooms for rail manufacture has necessitated the amendment of rail specifications. Amendment Slip No. 3 to BSS 11:1959 covers single heats of continuously cast rail steel and as an interim measure considers the product of a single strand as the equivalent of an ingot. However, the use of sequential continuous (or continuous continuous) casting of rail steel invalidates this analogy. Draft specifications incorporating sequential continuous casting are being prepared by three major standards organizations, namely: International Standards Organization (ISO), International Union of Railways (UIC), and the British Standards Institution (BSI). All these draft specifications incorporate similar principles and philosophies for rails rolled from continuously cast steel, and these align closely with the recommended procedures published by American Iron and Steel Institute (AISI) [6].

The major changes proposed include:

1. Blooms known to be entirely from a single heat are designated main heat blooms. Blooms which arise from the changeover from one heat to the next are designated intermediate blooms.

2. For heat identification, a heat is considered to commence with the first bloom known to be entirely from that heat. Intermediate blooms are classed as part of the previous heat. These intermediate blooms and the rails produced from them must be capable of being properly identified.

3. Acceptance test samples, taken at an agreed frequency, shall be randomly selected from main heat blooms only. This random sampling will produce test results representative of the rails being used in service, rather than the previous philosophy used for ingot material, of testing the suspect and nonrepresentative portions, that is, ingot top or bottom positions.

Achieving satisfactory results from two adjacent main heats in a sequence means that the associated intermediate material must also be satisfactory. If a heat within a sequence is withdrawn or rejected, then the adjacent intermediate material must either be scrapped, or progressively retested to define the demarcation between rejected and accepted material.

4. When a conventional rail specification specifies a minimum reduction

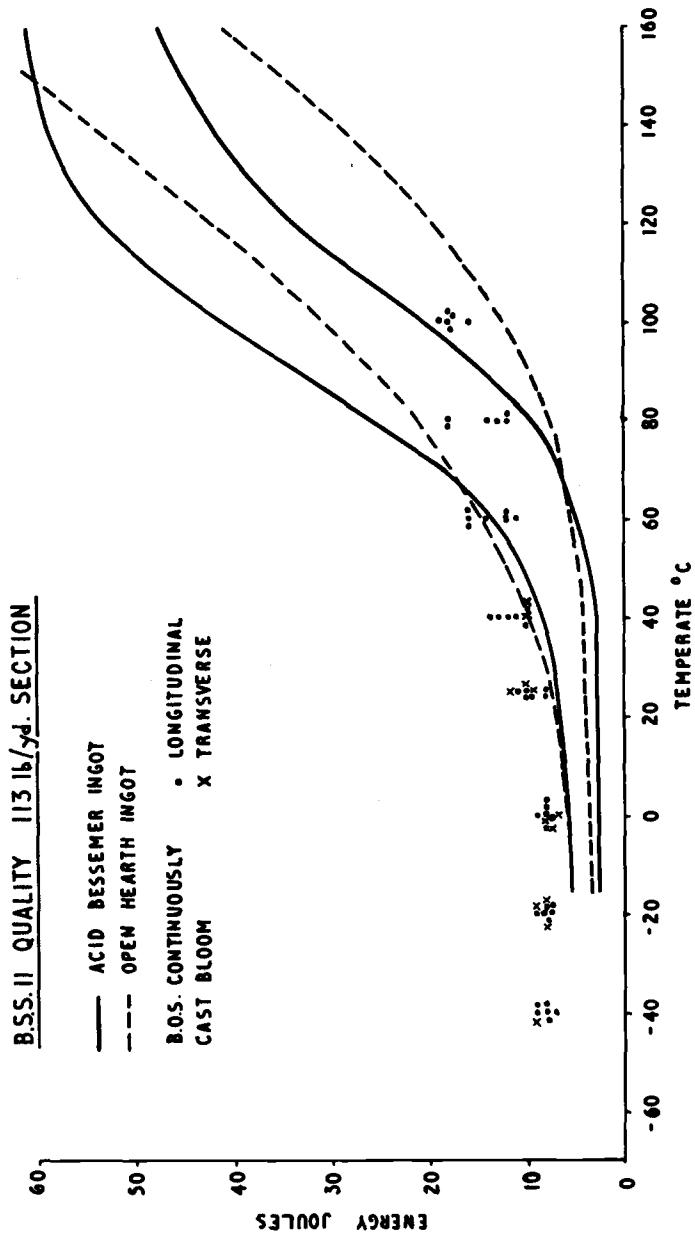


FIG. 10—Charpy impact properties of continuously cast and conventional ingot material.

TABLE 10—*Comparison of typical longitudinal and transverse tensile properties.*

Manufacturing Process	Test Direction	Average UTS, N/mm ²	Average Elongation, %
Continuously cast	longitudinal	833	17
	transverse	831	13
Killed ingot	longitudinal	793	18
	transverse	766	8

in cross-sectional area between the ingot and rail, for example, 20:1 or 25:1, this clause should either be eliminated or modified to a lower ratio for continuously cast material. From BSC's experience, a minimum ratio of 8:1 is acceptable.

5. As fully killed steel is a prerequisite for successful continuous casting, the silicon specification for rail steel should be raised to at least 0.35 percent silicon maximum.

6. Arising from the large heat sizes being used and the various bloom handling and stocking operations, marshalling of blooms for rolling in casting order is almost impossible. Hence, simplification of hot stamping requirements has been adopted whereby a heat number, bloom code number (in rolling sequence), and rail position within each bloom are hot stamped on the rail. This can, if required, be collated with strand and bloom position within the strand in the inspection or despatch documentation.

Discussion

The new process route using basic oxygen steelmaking and continuous casting adopts the most up-to-date techniques for rail manufacture. The data quoted in this paper are typical examples of the extensive experience accumulated during both development trials and full-scale operation. These data and considerable experience in service prove that rails rolled from continuously cast steel are at least equivalent, and probably superior, to conventional rails.

The inherent homogeneity of continuously cast rails and the consistently high standards of surface and internal quality are not merely of economic advantage to rail producers, but must eventually be beneficial to customers

TABLE 11—*Typical laboratory abrasive wear test results in BSS 11 rails.*

Manufacturing Process	Position in Chemical Composition Range	Typical Wear Rate, mg/m slip
BOS—continuously cast	mid to high	32.2
Acid Bessemer—ingot	mid to high	53.5
Open hearth—ingot	mid to high	37.3

TABLE 12—*Maximum hydrogen content to avoid shatter cracks.*

	ppm H ² [4]	ppm H ² [5]
UIC 860-A	3.3	3.0 to 3.5
UIC 860-B	2.5	2.5 to 3.0

in service reliability and reduction of track failures and defects.

Continuous casting enables the economic advantages of large-scale iron and steelmaking to be fully exploited, using increasing heat sizes, and simultaneously to achieve improvements in quality control and standards.

The adoption of retarded bloom cooling after continuous casting takes advantage of a natural break in the process line. This effectively removes excess hydrogen at the earliest stage in the new process route, after which there is no likelihood of further hydrogen pickup. In eliminating the need for pit (or box) cooling of the rails, the retarded bloom cooling process will facilitate the production of longer rail lengths, and may remove constraints on the rail rolling and subsequent handling operations.

It is predicted that the use of continuously cast blooms for rail production will be widely adopted by other rail producers within the next few years.

Conclusions

1. To date, BSC has produced over 300 000 tonnes of rails from continuously cast blooms and these have proved fully satisfactory in service such that this is now the standard process route, with ingot production being retained merely as support capacity.
2. Basic oxygen steelmaking combined with continuous casting is a proven process route for the production of rails, offering many advantages over the conventional ingot route, for example, improved process control, higher product yield, and better bloom quality. This process route has only been established after exacting examination of the rails at all stages of manufacture and under service conditions.
3. The rails produced from continuously cast blooms are in many respects superior to conventional ingot steel, namely:
 1. Internal and surface quality are improved considerably.
 2. Both the incidence and size of oxide inclusions are reduced.
 3. There is a higher degree of chemical homogeneity which results in closer control of physical properties.
 4. The transverse and longitudinal properties are more uniform.

In all other aspects, the continuously cast product is at least equal to ingot material.
4. It is possible to control the rail hydrogen levels to acceptable values by slow cooling of the continuously cast blooms as an alternative to pit cooling of the rolled rails.

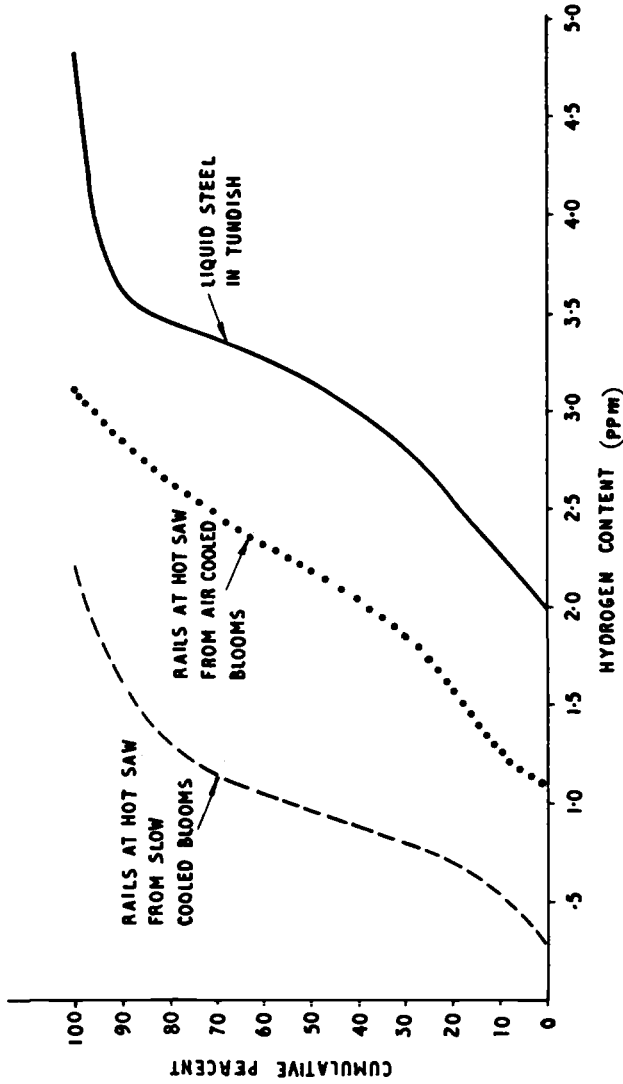


FIG. 11—Effect on hydrogen content of slow cooling continuously cast blooms BSS 11 quality.

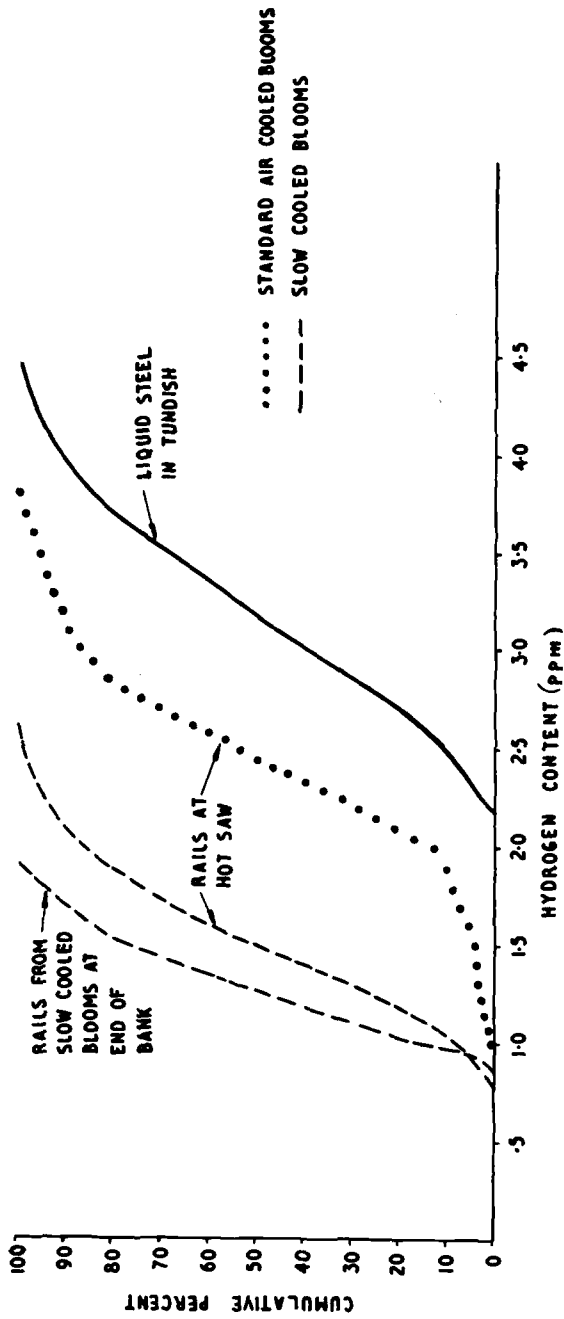


FIG. 12—Effect on hydrogen content of slow cooling continuously cast blooms UIC 860 B quality.

TABLE 13—Hydrogen content of rails rolled from slow-cooled continuously cast blooms.

	H ² Content in Liquid Steel, ppm				H ² Content at Hot Saw Stage, ppm								H ² Content in Cold Rail, ppm							
					Slow-Cooled Blooms				Air-Cooled Blooms				Slow-Cooled Blooms							
					min		mean		max		s		min		mean		max		s	
	min	mean	max	s	min	mean	max	s	min	mean	max	s	min	mean	max	s	min	mean	max	s
BSS 11	2.1	3.13	4.0	0.50	0.4	1.05	2.2	0.42	1.2	2.21	3.1	0.54								
UIC 860 B	2.3	3.25	4.1	0.55	0.8	1.57	2.6	0.39	1.0	2.53	3.8	0.52	0.9	1.36	1.9	0.28				

5. The advent of continuous casting has necessitated amendments to rail specifications, and draft specifications incorporating sequential continuous casting are being prepared by major standards organizations.
6. While current development work indicates that chromium rails can be produced successfully by the continuous casting route, it is probable that 11 to 14 percent manganese austenitic quality will continue to be produced from ingot for the foreseeable future.
7. BSC development of continuous casting for rail production has stimulated much interest and investigation among other rail producers. It is predicted that adoption of this modern process route will increase markedly in the future.

Acknowledgments

The author wishes to thank the British Steel Corporation for permission to publish this report and to acknowledge the generous cooperation and assistance afforded by many colleagues at various works and research establishments over the long period of investigation and development. Special recognition must be made of the help given by the technical staffs of BSC Lackenby and Workington Works in preparing this report.

APPENDIX I

Microscopical Cleanness Assessment

This assessment is carried out by traversing a minimum of 10 cm, along the vertical, longitudinal plane of the railhead, at a magnification of $\times 400$, counting the number of inclusions of specified type passing the crosswires. The length of the largest oxide in the sample is also recorded.

APPENDIX II

Ultrasonic Cleanness Assessment

Rails are manually ultrasonically tested under three operations:

1. A full-length examination from the running surface at a rate of 30 cm (1 ft)/s for inclusions and pipe.
2. If responses are recorded in the head, then the relevant area is tested from the side of the head.
3. If responses are recorded in the web, then the relevant area is tested from the side of the web.

Testing for hydrogen cracks is carried out from the side of the head.

The techniques are capable of detecting inclusions of 1 mm length and pipe of 20 mm height.

APPENDIX III

Fracture Toughness Test

The fracture toughness test carried out was a three-point bend test on a rectangular specimen in which a crack has been developed from a machined notch. The K_{Ic} plane strain fracture toughness property is the critical value of the elastic stress field intensification at the crack tip at which the first significant extension of the crack occurs under the influence of a rising force under conditions of high constraint to plastic deformation. The test is comparable to ASTM Test for Plane-Strain Fracture Toughness of Metallic Materials (E 399-74).

APPENDIX IV

Laboratory Wear Test

The test employed is a test of abrasive wear. It utilizes two disk specimens cut from a rail and tire, respectively. The disks are rotated in contact under a stress of 541 N/mm^2 (35 long tons/in.²), with a 25 percent slip induced by driving the tire disk at a 25 percent greater peripheral speed than that for the rail disk. Axial oscillation of the tire disk ensures an even wear distribution across both disk peripheries. Results are recorded as a weight loss per metre of slip.

References

- [1] Ushijima, K., "Continuously Cast Steel Billets," Iron and Steel Institute Special Report No. 89 Continuous Casting of Steel.
- [2] "Investigation of Rails Made From Continuously Cast Blooms by Algoma Steel Corporation," Association of American Railroads Research and Test Department Report No. R-104.
- [3] Morgan, E. L., "Factors Influencing Surface Defects on Rails Produced by the Acid Bessemer Process," *Journal of the Iron and Steel Institute*, Vol. 206, Jan. 1963.
- [4] Heller, W., Weber, L., Hammerschmid, P., and Schweitzer, R., *Stahl Eisen*, Vol. 92, No. 19, 1972, pp. 934-945.
- [5] Vicens, P., *Revue de Metallurgie*, Vol. 72, May 1975, pp. 387-402.
- [6] "Generally Accepted Procedure in North America for the Identification and Analysis of Strand Cast Steel," American Iron and Steel Institute document.

Strength and Fracture of Rail Steels

Mechanism of Cleavage Fracture in Fully Pearlitic 1080 Rail Steel

REFERENCE: Park, Yong-Jin and Bernstein, I. M., "Mechanism of Cleavage Fracture in Fully Pearlitic 1080 Rail Steel," *Rail Steels—Developments, Processing, and Use*, ASTM STP 644, D. H. Stone and G. G. Knupp, Eds., American Society for Testing and Materials, 1978, pp. 287–302.

ABSTRACT: Under service conditions, final failure of rails is usually caused by impact. To elucidate the phenomenon, the mechanism of impact-initiated cleavage fracture has been studied in fully pearlitic rail steel. The study has demonstrated that the early stages of cracking probably occur by strain localization in the ferritic lamellae. By direct correlation studies of fracture surface and microstructure, it has been further shown that a crack usually does not change direction at pearlite colony boundaries. Rather, the prior austenite grain size is the controlling agent for the more effective obstacle to crack propagation, namely, the cleavage facet size. The data show that the facet size is dependent on the prior austenite grain size, although it is always somewhat less, particularly for the larger grain size materials. The reasons why it is an effective parameter to represent the toughness of eutectoid steels are discussed.

KEY WORDS: steels, railroad tracks, microstructure, fractures (materials), surfaces, cleavage, pearlite, austenite, grain boundaries, crack initiation, crack propagation, toughness

There has been considerable research on the fracture toughness of pearlitic steels [1–6].³ It is now reasonably well established that the presence of pearlite has a deleterious effect on impact properties. With an increasing proportion of pearlite, the ductile-to-brittle transition temperature (DBTT)⁴ increases, and the upper shelf energy decreases [4]. However, there have been conflicting results reported in the literature as to the effects of pearlite interlamellar spacing [1,2], pearlite colony size [5] and prior austenite grain size [3] on the toughness of fully pearlitic steels. Recently, the prior-austenite grain size has been demonstrated to be the dominant microstructural factor controlling the fracture toughness in fully pearlitic rail steel, with this behavior relatively independent of pearlite spacing and colony size [6]. The

¹Presently, Association of American Railroads Research Center, Chicago, Ill. 60616; formerly, graduate student, Carnegie-Mellon University, Pittsburgh, Pa. 15213.

²Assistant professor, Carnegie-Mellon University, Pittsburgh, Pa. 15213.

³The italic numbers in brackets refer to the list of references appended to this paper.

⁴This temperature is generally equivalent to the fracture appearance transition temperature (FATT).

present study has been carried out to identify the specific roles of both pearlitic and prior austenite grain structures on the mechanism of cleavage fracture. Since it is likely that crack propagation rather than nucleation is the critical event for cleavage fracture in steels [7], this former aspect has received the bulk of attention in this study.

Materials

Most experiments were performed on a section of the standard rail steel used in the United States (Steel A). The materials for mechanical testing and subsequent fractography were taken from the head of the rail. In addition to use of this steel, an experimental higher purity eutectoid steel was also prepared and used for supplementary studies (Steel B). The chemical compositions of the two steels are shown in Table 1.

TABLE 1—*Chemical compositions of steels (in weight percent).*

Steel	C	Mn	Si	P	S
A	0.81	0.87	0.17	0.018	0.013
B	0.75	0.55	0.18	0.021	0.017

Oversized blanks of the rail steel were austenized either in a salt pot or in a tube furnace over a temperature range from 800 to 1200°C (1073 to 1473 K). After austenitizing, specimens were isothermally transformed in salt pots held at various temperatures in the range of 550 to 675°C (823 to 948 K), producing a fully pearlitic microstructure. Transformation times were chosen to ensure complete transformations, without the complication of appreciable spheroidization. Pearlitic spacings from 1000 to 3000 Å, and prior austenite grain sizes from 15 to 150 µm were attained. The isothermal heat treatments produced no significant changes in colony size, which was in the range from 4.3 to 7.1 µm. After heat treatment, standard ASTM Charpy bars were machined from the blanks. Dynamic instrumented impact tests were performed on fatigue precracked Charpy specimens to obtain both impact energies and dynamic fracture toughness, K_{Id} , values as a function of temperature and microstructure. More detailed heat treatment and mechanical testing procedures have been previously documented [6]. For supplementary studies, a coarse pearlitic structure was prepared from Steel B after austenitization for 1 h at 800 to 1000°C (1073 to 1273 K), followed by furnace cooling. Fracture surfaces from broken Charpy bars were used for establishing direct relationships between the fracture surface and the microstructure. Examinations were performed on JSM-2 and JSM-35 scanning electron microscopes.

Experimental Procedures and Results

Fracture Mode

Fracture surfaces of fatigue precracked Charpy specimens broken at temperatures well below the DBTT were characterized by electron fractography as predominantly transgranular cleavage (Fig. 1). Sectioned, nickel-plated fracture surfaces showed that some cleavage facets were not completely flat and contained small steps. In some cases, curved facets associated with heavy localized deformation were found (Fig. 2). As shown in previous studies [8,9], it was observed that, during the process of crack propagation, microcracks had been nucleated ahead of the main crack front. Since such microcracks are probably on a different level from the main crack, they can account for much of the observed ductile tearing when the two cracks join [8]. It was also shown that inclusions did not, in general, have much influence on crack propagation. While microcracks were sometimes nucleated from inclusions located near the fatigue crack tip (Fig. 3), this was not a common observation. By using the energy dispersive X-ray analysis capability of the scanning electron microscope (SEM), the inclusions were found to be either manganous sulfide (MnS) (perhaps associated with manganous oxide (MnO)) or a metallic compound containing manganese

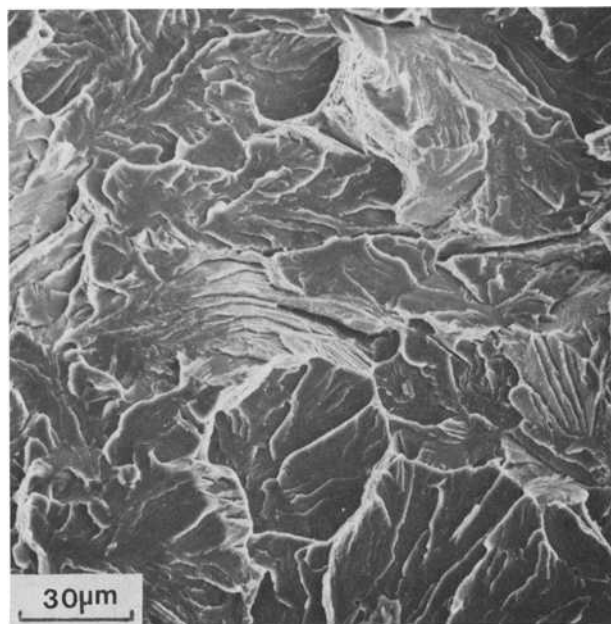


FIG. 1—Scanning electron fractograph of rail steel fractured at -45°C .

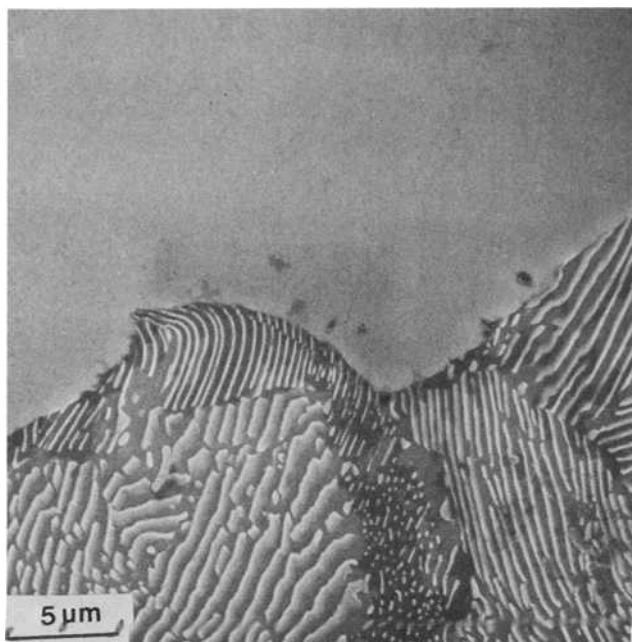


FIG. 2—Micrograph showing a curved facet.

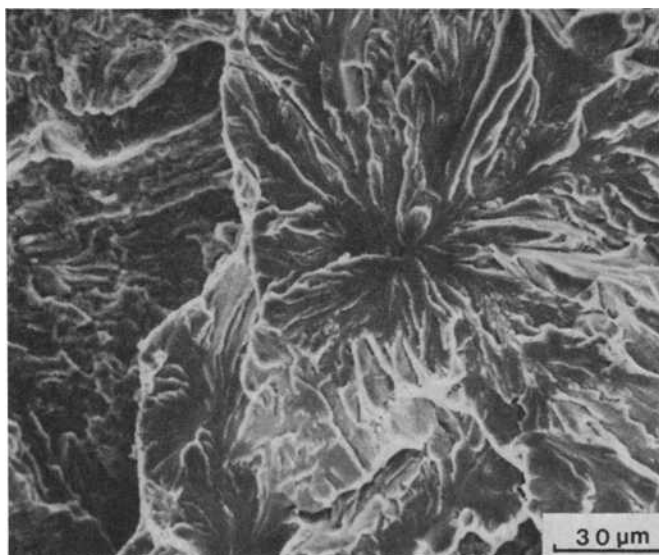


FIG. 3—Crack nucleation from an inclusion. Arrows indicate tip of fatigue precrack.

with some titanium, silicon, and a little aluminum. This latter inclusion is most likely an oxide.

Early Stages of Cracking

In order to investigate the origin of crack initiation, the fracture surfaces were examined by SEM. Two types of initiation sites were observed. The predominant one was cleavage facets with no associated plastic deformation; such microcracks are not unexpected, and little could be learned from detailed studies of their morphology. Another type, with associated plastic deformation, was more carefully studied utilizing microcracks near the fracture surfaces. Since brittle fracture in impact tests involves catastrophic crack growth, only a few of these microcracks could be detected. However, when specimens were etched in Villela's reagent, additional microcracks appeared. Figure 4a shows several of these near the fracture surface. Figure 4b shows the one in the lower right corner of Fig. 4a at higher magnification. An interesting feature is the appearance of holes in ferrite, with apparently continuous cementite. These microcracks, while perhaps of secondary importance in impact fracture, are expected to be of more importance as the ductility of the material increases. In such a case, these microcracks may mirror the early stages of crack formation and perhaps stable crack growth. It thus seemed worthwhile to perform a serial sectioning study on one of the microcracks. Figure 5a shows the microcrack etched initially by Villela's reagent, where the cementite appears continuous with holes in the ferrite. After removal of 6 μm of material from the surface, it was shown that these holes are associated with heavy plastic deformation of lamellae (Fig. 5b). The same area was then carefully polished until the holes disappeared when examined on an unetched surface or one etched by saturated Picral. Only a faint line was evidence of the existing crack. This line is believed to be due to the offset of microstructure. Figure 5c further illustrates that the cementite was fractured and was displaced due to the presence of slip band in the ferrite. When the same area was again etched by Villela's reagent, the holes reappeared along the same line (Fig. 5d). It is therefore concluded that these holes are revealed by the preferential etching ability of Villela's reagent. The formation of a localized slip band in the ferrite must act as the precursor event for crack formation and may also contribute to stable crack growth associated with microcrack linking.

Direct Correlations Between Fracture Surface and Pearlitic Structure

This next aspect is concerned with the role of specific metallurgical features on the ease of cracking. When structure/property relationships are studied in steels, it is often difficult to isolate experimentally single microstructural variables. Therefore, it has been found useful to examine the fracture surface and microstructure simultaneously and to thus relate the microstructure directly to features on the fracture surface. Recently, several

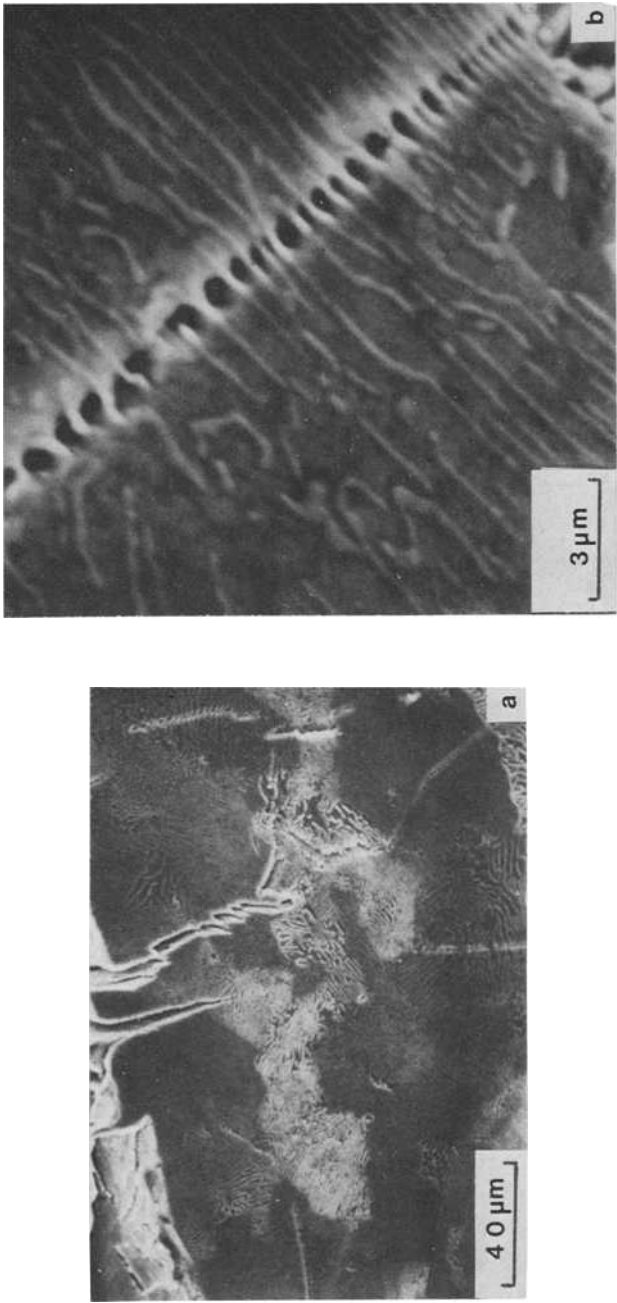


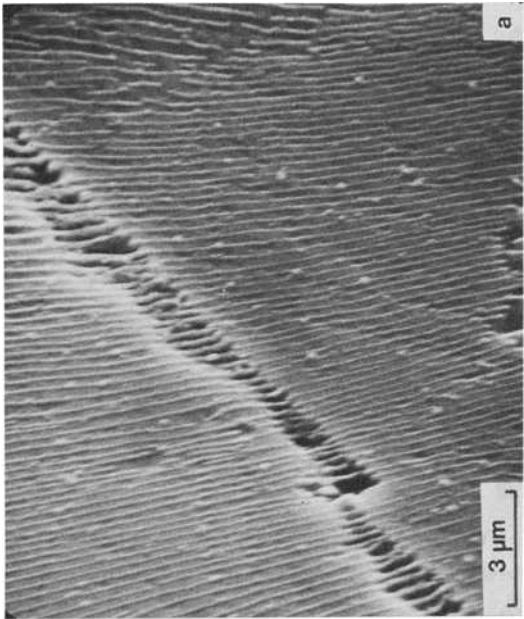
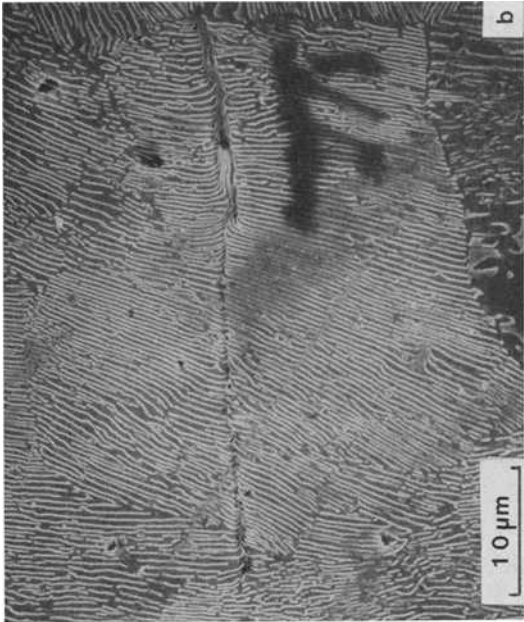
FIG. 4—Microcracks near the fracture surface of Steel B.

techniques [10–12] have been developed, providing additional information on the interaction between microstructure and the propagating crack. In this study, two different methods were used to establish correlations between the pearlitic structure and the fracture surface.

The first method is a modification of the technique devised by Almond et al [10]. A fractured specimen was mounted in a thermally plastic lucite and sectioned at an angle to the fracture surface. The surface that made an obtuse angle with the fracture surface was then polished and etched by normal metallographic procedures, and the lucite was dissolved away with acetone. The edge between the fracture surface and etched surface was then examined by SEM. This method clearly revealed the role of pearlite colony boundaries on the process of brittle transgranular fracture. While in some cases it was observed that the fracture path changed direction at colony boundaries, more often than not the crack traversed several pearlite colonies as a single cleavage facet (Fig. 6). The second method involves direct and careful etching of the fracture surface with saturated Picral so as to not destroy the fine features of the fracture mode [11]. By this method, the pearlitic structure was revealed on the fracture surface, and the majority of individual cleavage facets were observed to consist of a number of pearlite colonies (Fig. 7).

Direct Correlations Between Fracture Surface and Prior Austenite Grain Structure

Since the prior austenite grain boundaries are no longer present in the transformed steel, these techniques could not reliably differentiate between prior austenite and pearlite colony boundaries. In an attempt to investigate more directly the role of prior austenite grain boundaries on crack propagation, thermal etching in vacuum [13] has been used. A small specimen of rail steel having a surface polished by conventional metallographic methods was sealed in an evacuated quartz capsule. This specimen was furnace cooled after austenitizing at 1100°C (1373 K) for 20 min. Austenite grain boundaries were clearly revealed on the polished surface (Fig. 8). A notch was oriented so that a crack would run through the thermally etched surface, and the sample was fractured by hammer impact at -45°C (228 K). The edge between fracture surface and thermally etched surface was then examined by SEM. It was found that a crack could often be obstructed at a prior austenite grain boundary, but this was not always the case. Figure 8a shows a one-to-one correspondence between cleavage facets and austenite grains; Fig. 8b illustrates an austenite grain consisting of several facets; Fig. 8c shows the case where a single cleavage facet could cover more than one austenite grain. In order to investigate whether this latter observation is due to the fact that pearlite colonies can grow across austenite grain boundaries [14], the specimen was etched by saturated Picral to reveal the pearlitic structure. From etched fracture surface studies of this type, two different pearlite



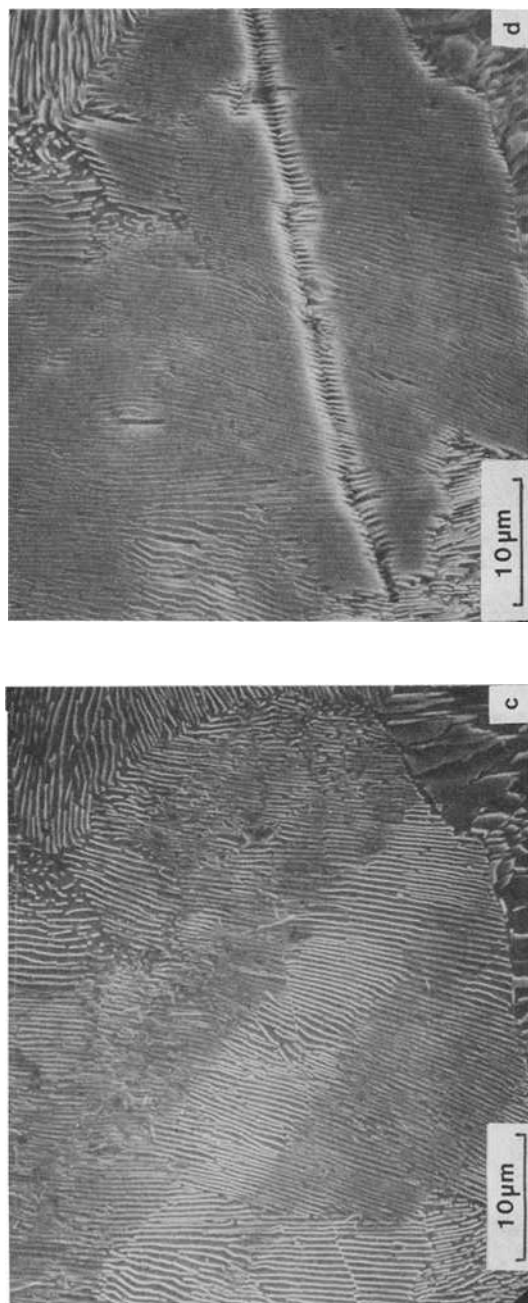


FIG. 5—Scanning electron micrographs showing results of serial sectioning on a microcrack.

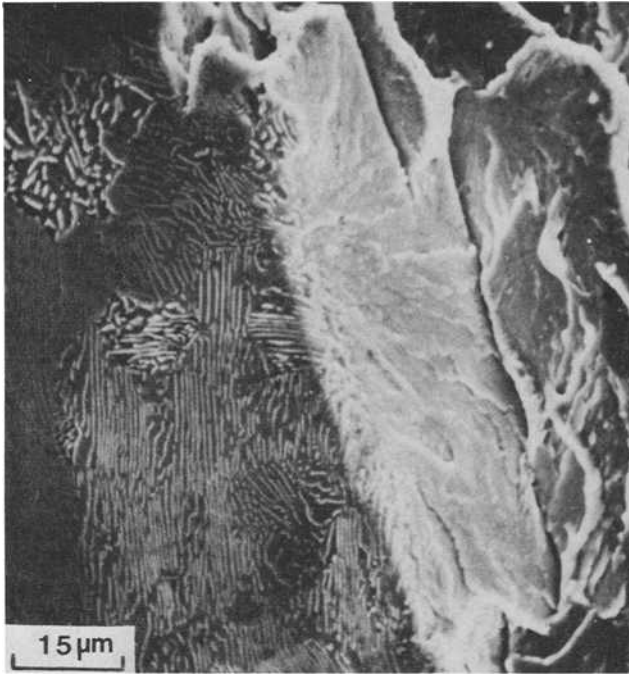


FIG. 6—The fracture and microstructural details on a specimen of Steel B.

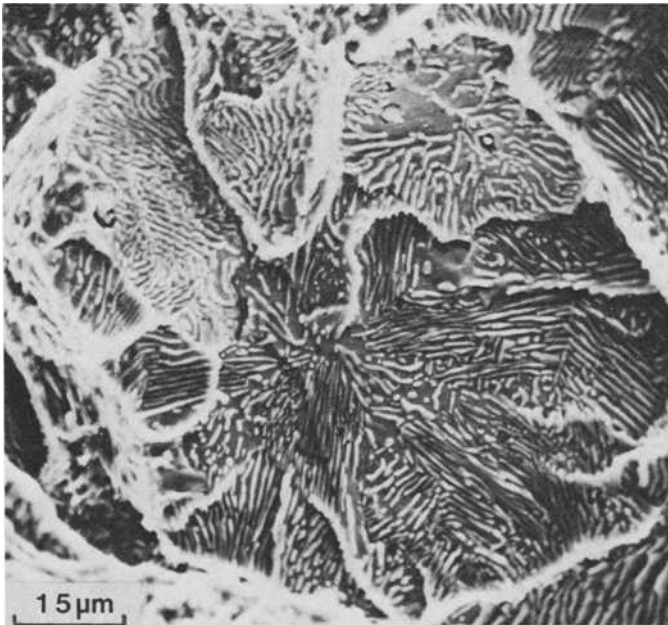


FIG. 7—The fracture surface of Steel B after etching by saturated Picral.

colonies were often observed across those prior austenite grain boundaries where the crack was not obstructed (Fig. 8*d*). This implies that the ferrite orientation in both colonies is similar, as will be discussed.

Cleavage Facet Size

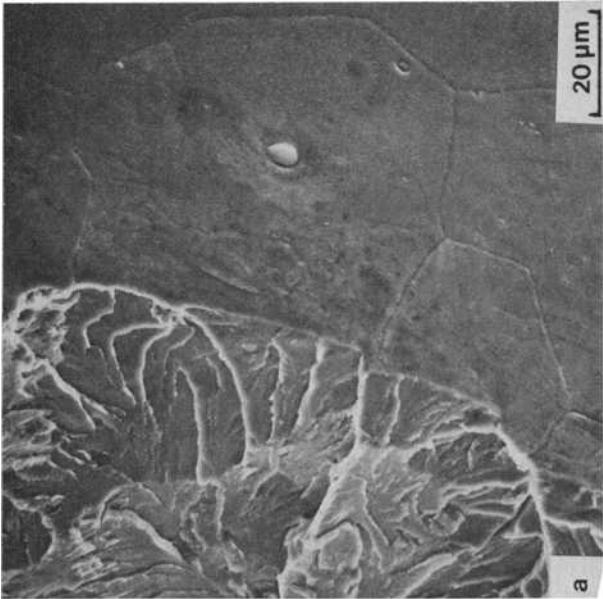
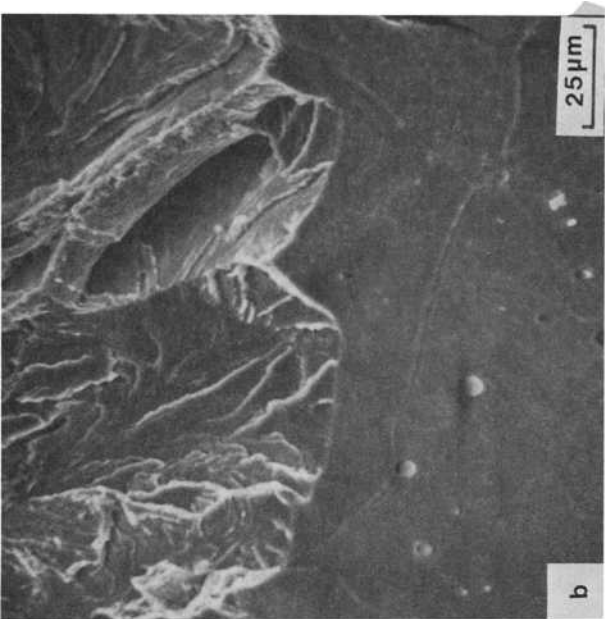
The lack of a direct correspondence between fracture facet and austenite grain size suggests that the cleavage facet size is a more meaningful parameter to represent the toughness of materials [9,15]. On a qualitative basis, since most of the energy-absorbing processes for a propagating crack are associated with boundaries where the crack changes direction [8], one would expect that, the finer the facet size, the more difficult would be the process of crack propagation.

The average cleavage facet size in fractured, precracked Charpy specimens of rail steels was measured on stereo pairs of microfractographs, using the linear intercept method. The result showed that, while the average facet size is a strong function of the prior austenite grain size, it is always somewhat less, particularly for the larger prior austenite grain size materials (Fig. 9).

Discussion

Early Stages of Cracking

The shear cracking of pearlite has been shown to be an important contributor to the fracture of pearlitic steels over a range of carbon content [16–18]. The concentrated stress at the tip of an impinging slip band either in adjacent proeutectoid ferrite or in the ferrite within a pearlite colony could lead to cracking of the carbide. These previous studies were performed on the specimens which exhibited appreciable macroscopic ductility and very likely ductile regions on the fracture surfaces. In the present study, although the specimens were fractured in a much more brittle manner, the process of crack initiation can be similar to the previous results [16–18], although brittle microcracks are probably more dominant. When localized shear cracks are important, it is concluded from the observations of Fig. 5 that the early stages of cracking are associated with the presence of a slip band in the ferrite, impeded by carbide lamellae. After the cementite lamellae have cracked, these initial cracks link up to form fibrous cracks, as described by Miller and Smith [18]. When the microcracks become large enough, they act as Griffith-type cracks in initiating unstable cleavage fracture [19]. These cleavage cracks will propagate catastrophically, often linking up with other moving cracks. If local plasticity is suppressed, the crack process is initiated by the growth of a brittle cleavage unit, probably triggered by cementite cleavage.



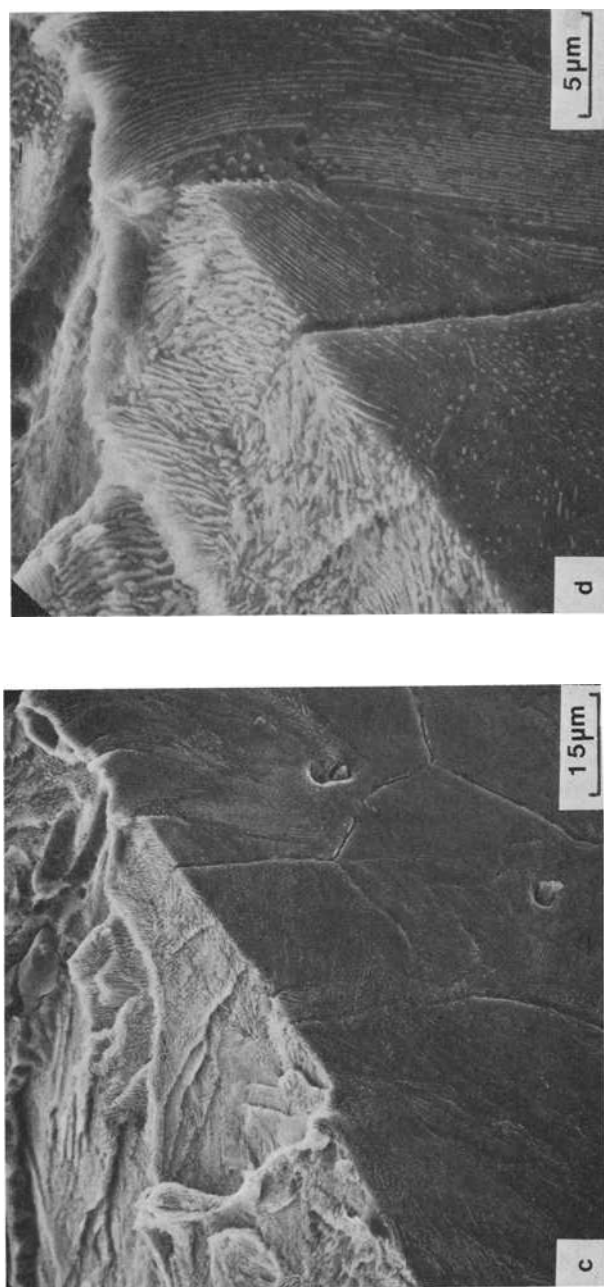


FIG. 8—Direct correspondence of fracture surface to the prior austenitic structure.

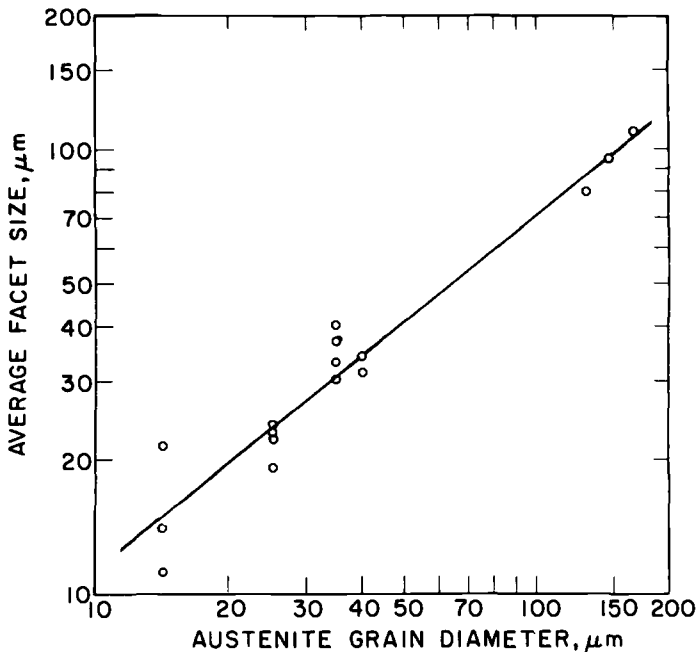


FIG. 9—Relationship between cleavage facet size and prior austenite grain size.

Mode of Crack Propagation and Correlation with Structure

By direct correlation of fracture surface and microstructure, it was shown that a crack could often be obstructed at a prior austenite grain boundary. This phenomenon is believed due to the discontinuous nature of ferrite orientations across the boundary. Since the pearlite colonies usually nucleate at prior austenite grain boundaries, and the constituents of pearlite bear specific orientation relationships with the parent austenite grain, pearlite colonies across an austenite grain boundary can thus often have different ferrite orientations. It was further observed that, while a crack could change direction at pearlite colony boundaries, more often it continued as a single cleavage facet across several pearlite colonies. Since a crack propagates along $[100]$ cleavage planes of ferrite in pearlitic steels [9], the latter observation suggests that the cleavage planes in these colonies must be continuous. In support of this, thin-foil transmission electron microscopy [20] has shown that $[100]$ cleavage planes of ferrites were closely aligned across a number of pearlite colonies to an extent compatible with the facet size. These colonies are expected to lead to a single cleavage facet. The cleavage facet size can therefore be considered as an effective parameter to describe the toughness of materials with the same microstructure. Since the average facet size is a strong function of the prior austenite grain size, these considerations support the results of a previous study [6] which show that

the fracture toughness in fully pearlitic rail steel is primarily dependent on the prior austenite grain size.

The results of this study also suggest that, if there is any preferred orientation in the microstructure, this could lead to cleavage facets and a deterioration of toughness. Therefore, in designing rail steels with better toughness, alloying elements and processing schedules should be carefully selected to minimize the formation of a strong texture.

Conclusions

1. In fully pearlitic rail steel, initial cracking occurs either by cleavage of cementite lamellae or when the concentrated stress at the tip of a slip band in lamellar ferrite leads to cracking of the cementite against which the slip band impinges.

2. The cleavage facet size, which can be considered as an effective parameter to represent the toughness of materials, is a strong function of the prior austenite grain size, but it is always somewhat less, particularly for the larger grain size materials.

3. The fracture unit is determined by those colonies which share a common ferrite orientation, allowing easy passage of a single cleavage crack.

Acknowledgments

The authors would like to thank D. H. Stone, Manager of Metallurgy, Association of American Railroads Research Center, and J. M. Hyzak and G. K. Bouse, former graduate students at Carnegie-Mellon University, for their help, encouragement, and for many useful discussions throughout this study. This research has been supported by the Association of American Railroads and the Processing Research Institute of Carnegie-Mellon University.

References

- [1] Gross, J. H. and Stout, R. D., *Welding Journal*, Vol. 34, 1955, pp. 117s-122s.
- [2] Burns, G. and Judge, C., *Journal of Iron and Steel Institute*, Vol. 182, 1956, pp. 292-300.
- [3] Turkalo, A. M., *Transactions, Metallurgical Society of the American Institute of Mining and Metallurgical Engineers*, Vol. 218, 1960, pp. 24-30.
- [4] Burns, K. W. and Pickering, F. B., *Journal of Iron and Steel Institute*, Vol. 202, 1964, pp. 899-906.
- [5] Gladman, T., McIvor, I. D., and Pickering, F. B., *Journal of Iron and Steel Institute*, Vol. 210, 1972, pp. 916-930.
- [6] Hyzak, J. M. and Bernstein, I. M., *Metallurgical Transactions*, Vol. 74, 1976, pp. 1217-1224.
- [7] Cottrell, A. H., *Transactions, Metallurgical Society of the American Institute of Mining and Metallurgical Engineers*, Vol. 212, 1958, pp. 192-203.
- [8] Low, J. R., Jr., *Progress in Materials Science*, Vol. 12, 1963, pp. 1-95.
- [9] Ohtani, H. and Terasaki, F., *Tetsu-to-Hagane*, Vol. 58, 1972, pp. 67-80.
- [10] Almond, E. A., King, J. T., and Embury, J. D., *Metallography*, Vol. 3, 1970, pp. 379-382.
- [11] Inckle, A., *Journal of Materials Science*, Vol. 5, 1970, pp. 86-87.

- [12] Shechtman, D., *Metallurgical Transactions*, Vol. 7A, 1976, pp. 151-152.
- [13] Lozinskii, M. G., *High Temperature Metallography*, Pergamon Press, New York, 1961, pp. 241-318.
- [14] Rathenau, G. W. and Baas, G., *Acta Metallurgica*, Vol. 2, 1954, pp. 875-883.
- [15] Naylor, J. P. and Krahe, P. R., *Metallurgical Transactions*, Vol. 5, 1974, pp. 1699-1701.
- [16] Rosenfield, A. R., Votava, E., and Hahn, G. T., *Transactions*, American Society for Metals, Vol. 61, 1968, pp. 807-815.
- [17] Barnby, J. T. and Johnson, M. R., *Metal Science Journal*, Vol. 3, 1969, pp. 155-159.
- [18] Miller, L. E. and Smith, G. C., *Journal of the Iron and Steel Institute*, Vol. 208, 1970, pp. 998-1005.
- [19] Lindborg, U., *Transactions*, American Society for Metals, Vol. 61, 1968, pp. 500-504.
- [20] Park, Y. J. and Bernstein, I. M., *Proceedings of the Fourth International Conference on Fracture*, Waterloo, Canada, Vol. 2, 1977, pp. 33-40.

Fracture Mechanics Analysis of Rails with Shell-Initiated Transverse Cracks*

REFERENCE: Besuner, P. M., "Fracture Mechanics Analysis of Rails with Shell-Initiated Transverse Cracks," *Rail Steels—Developments, Processing, and Use*, ASTM STP 644, D. H. Stone and G. G. Knupp, Eds., American Society for Testing and Materials, 1978, pp. 303–329.

ABSTRACT: This report develops a fracture mechanics model for railhead transverse defects, specifically detail fractures from rail shell. The model is applied to calculate the failure strength of 71 rail segments which were rejected by inspection, removed, and tested by the Association of American Railroads in three-point bending. Utilizing the defect measurements for each rail, reasonable agreement is obtained between observed failure loads and failure loads calculated from the stress and fracture mechanics analyses. The fracture mechanics analysis is then extended to obtain preliminary estimates of the fatigue performance of defective rails in service. Specifically, the crack tip stress intensity factor is calculated for transverse defects under various types of in-service loading. The fracture mechanics solutions are utilized to calculate conservatively the remaining lifetime of the rail as a function of defect size and magnitude of wheel load. Using a simplified two-dimensional stress analysis and a three-dimensional fracture mechanics analysis, it is calculated that the shear stress reversal experienced as the wheel passes from one side to the other side of a transverse crack is the dominant stress component causing fatigue crack propagation. Recommendations are made for additional analytical developments and experimental programs required to refine the fatigue life predictions and incorporate them into rail risk assessment and reliability optimization programs.

KEY WORDS: steels, railroad tracks, crack propagation, fatigue life, stresses, structural analysis

Over 100 million dollars is expended annually to replace more than 0.9 million metric tons (one million tons) of worn or rejected rail. Some rails fail before defects are detected, and some of these failures lead to derailments. Service failures and detector car findings suggest that current trends toward heavier wheel loads, higher speeds, and aging rail might be aggravating the problem [1].² Additional information is required to enable the most effective approach to improved safety at minimum cost. As part of the Truck Train Dynamics Research Program, the Association of American Railroads (AAR) has developed methods for estimating the risk associated with

*Original experimental data were measured in U.S. customary units.

¹Senior analytical engineer, Failure Analysis Associates, Palo Alto, Calif. 94304.

²The italic numbers in brackets refer to the list of references appended to this paper.

operation of rails containing imperfections. These methods will enable decisions to be based on cost-risk trade-offs which select the optimum inspections, operation and repair conditions. In order to implement the risk assessment methodology, it is necessary to develop improved stress analyses and fracture mechanics analyses, as well as materials data to evaluate structural fatigue performance of defective rails. The AAR rail research program contains laboratory testing of both conventional specimens and rail sections that had been rejected by standard inspections [2] and removed from service. The failure loads and fracture surface details, including size and orientation of the shell and transverse defect, were determined by the AAR [3].

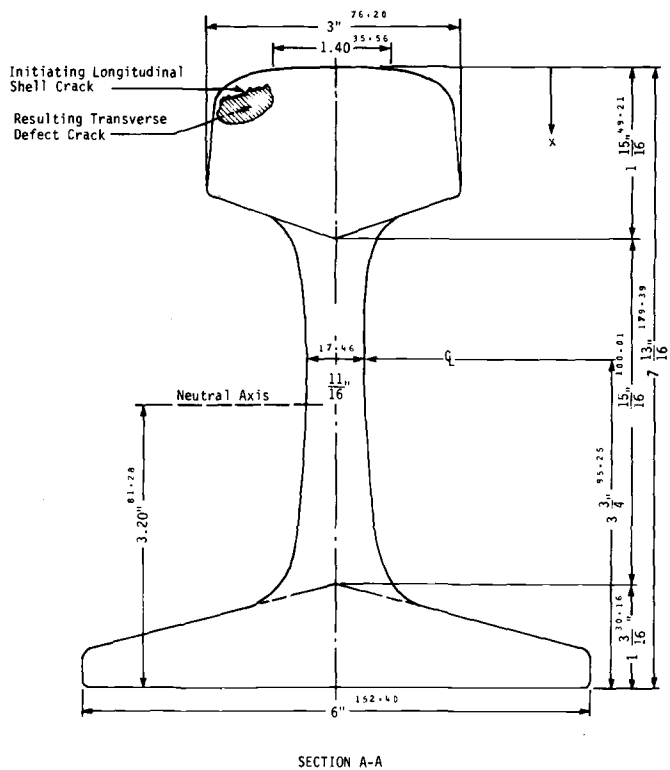
The major objectives of this analysis of the AAR data are to (a) develop a fracture mechanics model for transverse railhead defects, specifically detail fractures from shell, (b) apply the model to calculate failure loads from postfracture defect measurements for each of the three-point bend tests performed by the AAR on defect-containing and retired rail, (c) extend the model to obtain preliminary estimates of the fatigue performance of defective rails in service, and (d) define and recommend approaches to meet data/analysis needs to improve the fatigue performance estimates.

The AAR rail bending experiments are outlined and a detailed description is given of the analytical fracture mechanics technique and its application to predict successfully the onset of static, brittle failure in flawed rail. Then, these crack evaluation techniques are applied to stress fields encountered in service as the wheel passes over the transverse plane of the railhead defect. It is calculated that the shear stress reversal experienced as the wheel crosses the crack plane is the dominant stress component causing fatigue crack propagation. A preliminary fatigue analysis is performed to define the remaining lifetime of the defective rail.

Experimental Results

Rail Bending Tests

Figure 1 shows schematically the test configuration used to apply the three-point bending failure loads to the 94-cm (37-in.) rail sections. The sections are taken from rails which had been found defective during in-track nondestructive inspection. Figure 1 also shows the vertical failure, or fracture plane, of the rail and the transverse defect responsible for detail fracture from shelling in 42 of the 71 rail sections tested and analyzed. In all cases, the fracture plane was within 10 cm (4 in.) of the position ($z = 0$) of the applied load P and maximum bending moment M . The failure load, deflection, position of the fracture plane, characteristics and geometric outline of the defect, and rail size were recorded, and photographs of the fracture surface also were taken. In addition, standard tensile specimens and notched Charpy impact specimens were machined out of most rail sections and tested. The results of these tests were provided by the AAR along with



- NOTES: 1. Section A-A is the plane of eventual fracture and usually contains a fatigue crack.
2. Section A-A is shown in its upright position although the rail is tested in an upside down position.

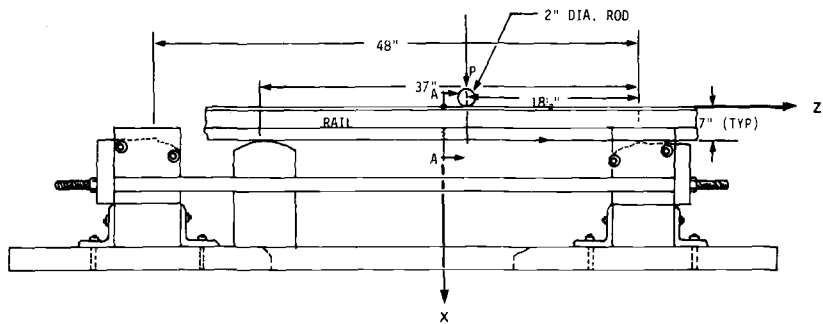


FIG. 1—Schematic of loading configuration of AAR three-point bend tests of rail section.

significant facts regarding the history of the rail. These included age, tonnage life, time of last inspection, and the general tie, ballast, and roadbed conditions at the rail location.

In preparation for the fracture mechanics analysis described in the next

section, the dimensions and calculated areas of all transverse defects were measured. Table 1 lists the failure loads and transverse defect dimensions for all 71 rails. All but two of the 42 defect-containing rails failed at low loads (less than 890 kN (200 kips)). The remaining 29 rail sections, 27 with no measurable transverse defects, and two with relatively small defects, all failed by plastic hinge mechanism at relatively high loads (1112 to 2002 kN (250 to 450 kips)).

TABLE 1—Crack dimensions and three-point bend failure loads for 71 rail sections.

Fracture No.	Rail Size (lb/yd)	PTD Area (sq. in.)	Crack Depth (in.)	Crack Length (in.)	Collapse Load (lb)
1	133	0.80	0.91	1.17	104 500
2	133	1.85	1.25	1.83	90 500
3	133	0.70	0.82	1.13	114 900
4	133	0.00	0.00	0.00	307 200
5	133	0.70	0.75	1.25	104 000
6	0	0.00	0.00	0.00	0
7	133	0.19	0.32	0.63	323 700
9	133	0.42	0.74	0.79	131 400
10	133	0.95	0.05	0.25	119 300
11	133	0.91	0.95	1.35	100 400
13	133	0.00	0.00	0.00	396 500
14	0	0.00	0.00	0.00	0
16	0	0.00	0.00	0.00	0
20	133	1.10	1.10	1.50	94 500
21	133	0.40	0.70	0.80	116 200
24	133	0.00	0.00	0.00	357 100
26	133	1.55	1.08	1.80	109 600
28	119	2.21	1.60	2.04	87 000
29	119	0.00	0.00	0.00	250 200
30	119	3.42	1.75	2.64	42 000
31	119	1.17	0.98	1.26	87 700
32	119	2.95	1.89	2.38	59 700
34	133	2.67	2.05	2.65	61 200
35	133	0.96	1.05	1.25	115 650
36	133	1.25	1.10	1.40	132 100
37	133	2.15	1.55	2.00	84 600
38	133	0.96	1.00	1.22	116 900
41	133	2.04	1.53	1.82	78 500
42	133	1.49	1.10	1.75	107 500
43	133	1.56	1.25	1.60	117 000
44	133	0.83	0.90	1.50	119 500
45	133	0.95	0.97	1.30	129 400
46	133	1.74	1.22	1.75	90 900
47	133	0.08	0.17	0.45	178 300
48	133	0.00	0.00	0.00	336 800
49	133	0.00	0.00	0.00	354 300
50	133	0.00	0.00	0.00	349 500
51	133	1.11	1.05	1.55	114 700
52	133	0.49	0.68	0.94	126 000
53	133	1.25	1.15	1.55	81 500
54	133	0.04	0.12	0.45	178 700
55	133	0.97	1.01	1.29	137 100
56	133	0.00	0.00	0.00	367 700
57	133	0.00	0.00	0.00	410 700

TABLE 1—*Continued.*

Fracture No.	Rail Size (lb/yd)	PTD Area (sq. in.)	Crack Depth (in.)	Crack Length (in.)	Collapse Load (lb)
58	133	0.00	0.00	0.00	275 100
59	133	0.05	0.18	0.45	272 000
60	133	0.08	0.26	0.47	196 400
61	133	0.91	0.90	1.34	135 900
62	133	0.00	0.00	0.00	362 900
63	133	0.00	0.00	0.00	335 100
64	133	0.00	0.00	0.00	353 000
65	133	0.08	0.24	0.50	171 100
66	133	0.07	0.40	0.50	241 700
67	133	3.56	2.60	2.65	10 000
68	133	0.00	0.00	0.00	341 800
69	133	1.10	0.97	1.46	135 500
70	133	0.00	0.00	0.00	308 900
71	133	0.00	0.00	0.00	319 200
72	133	0.00	0.00	0.00	265 000
73	133	1.40	1.16	1.55	107 200
74	133	0.00	0.00	0.00	340 200
75	127	1.20	1.09	1.50	96 000
76	0	0.00	0.00	0.00	0
77	133	0.00	1.40	1.70	100 000
78	0	0.00	0.00	0.00	0
79	0	0.00	0.00	0.00	0
80	0	0.00	0.00	0.00	0
81	0	0.00	0.00	0.00	0
82	0	0.00	0.00	0.00	0
83	0	0.00	0.00	0.00	0
84	0	0.00	0.00	0.00	0

Conversion factors—

1 lb/yd = 4.96 g/cm

1 in.² = 6.45 cm²

1 in. = 2.54 cm

1 lb = 4.45 N

NOTE—The zero entry refers to either no transverse crack or the lack of data.

Fracture Toughness Data

Dynamic fracture toughness tests were performed³ on two precracked Charpy specimens from most of the rails of Table 1, and a limited number of static fracture toughness values were also obtained.

Barsom and Rolfe [4] have derived an empirical formula relating static fracture toughness K_{Ic} with Charpy V-notch energy values (CVE) in the lower shelf and transition temperature range

$$K_{Ic} \text{ (CVE)} = (2E \text{ (CVE)}^{3/2})^{1/2} = 643\,428 \text{ (CVE)}^{3/4}$$

$$(K_{Ic} \text{ (CVE)} = (2E \text{ (CVE)}^{3/2})^{1/2} = 7750 \text{ (CVE)}^{3/4}) \quad (1)$$

³Stone, D. H., Association of American Railroads, and Fowler, G., Failure Analysis Associates, private communication, giving dynamic toughness results of specimens machined from the rail section of Ref 3, received Oct. 1975.

for K_{Ic} in units of $N/mm^{3/2}$ ($psi \sqrt{in}$), $E = 206\,295\, MN/m^2$ ($30\,000\,000\, psi$), and CVE in $N\cdot m$ (foot-pounds). Figure 2 compares the static toughness results from three sources: (a) calculated from Charpy notched data using Eq 1, (b) calculated from the average of two measured dynamic precracked Charpy values for each rail section (Footnote 3, [5]),⁴ and (c) measured by Fowler.⁵ As seen, the agreement between the notched and precracked Charpy static toughness calculations is poor. This could be partially because none of the seven steels used to formulate the empirical formula in Ref 4 were eutectoid rail steel although the box-like cluster of data indicates that no systematic relationship exists between CVE and K_{Ic} .

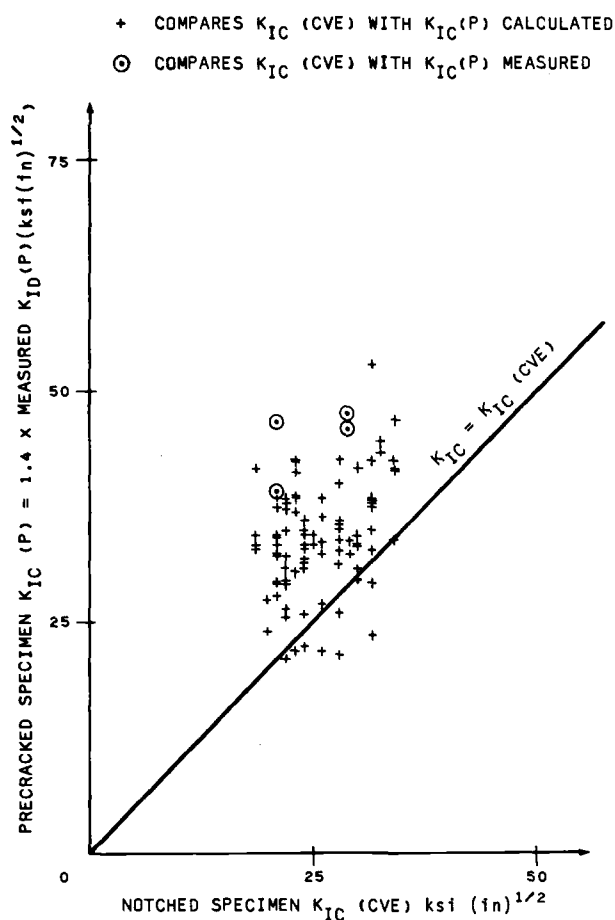


FIG. 2—Comparison of static fracture toughness calculated from two types of dynamic results: Charpy V-notch impact energy (CVE) and precracked Charpy load (P).

⁴Stone, D. H., Association of American Railroads, personal communications, July–Nov. 1975.

⁵Fowler, G., Failure Analysis Associates, personal communication, Nov. 1975.

Because the AAR three-point bend loads were applied slowly enough to be considered quasi-static (Footnote 4), K_f , the calculated K at failure, should be compared with static fracture toughness, K_{Ic} , rather than with the dynamic toughness, K_{Id} . In order to accomplish the K_f versus K_{Ic} comparison in the absence of K_{Ic} data for most of the tested AAR rail segments, data generated by Tetelman and Stone [5] are used to estimate

$$K_{Ic} = 1.4 K_{Id} \quad (2)$$

Equation 2 is accurate to within 5 percent for the twelve K_{Ic} and K_{Id} data points for the temperature range -46 to 66°C (-50 to 150°F).

Stress Intensity Factor Calculation For AAR Three-Point Bend Tests

Stress Analysis Methods and Results

The stress intensity factor calculations to be described later require knowledge of the stress field for the uncracked rail at the crack locus. Initially, it was believed that the linear beam theory solution might not accurately predict this "uncracked stress field" near the fracture plane ($-10\text{ cm} < z < 10\text{ cm}$) ($-4\text{ in.} < z < 4\text{ in.}$), due to the proximity of load P (Fig. 1). Therefore, additional stress analyses were performed. Figure 3 shows the two-dimensional elastic idealization used to compute the uncracked stress field. The stress was computed using three methods: (a) Fourier series analysis, similar to those performed by Timoshenko [6], (b) finite element analysis [7], using a constant rail thickness, and (c) finite element analysis [7], using variable thickness to simulate head-web-base variations as shown in Fig. 3. The stress analysis results are given in Fig. 3 for all numerical methods and for elementary beam theory. Note that the three numerical results match well, but they show a 2 to 15 percent lower stress than that derived using elementary beam theory in the area of concern, $x < 5\text{ cm}$ (2 in.), due to the proximity of load P . The Fourier series stress analysis results are used next to compute stress intensity factors using linear interpolation of the dimensionless stress, $\sigma_{zz}(x)$, in Fig. 3.

Crack Models of Rail Defects

Figures 4 and 5 illustrate the technique used for modeling the rail defects whose dimensions are given in Table 1. The embedded elliptical crack and corner, quarter-elliptical cracks are used to bound K for all defects whose depth (a_x) is less than 2.5 cm (1 in.) (Region I). A through-thickness edge crack is used to model cracks of depth greater than 9.9 cm (3.9 in.) (that is, Region III, crack has passed the rail's neutral axis and has broken through the thickness). For intermediate depth cracks (Region II), transition curves are drawn between the accurate solutions in Regions I and III. Figure 6 shows this curve, which is based in part on results from Refs 8 and 9 which quantify the effect of free surfaces on buried and surface elliptical cracks.

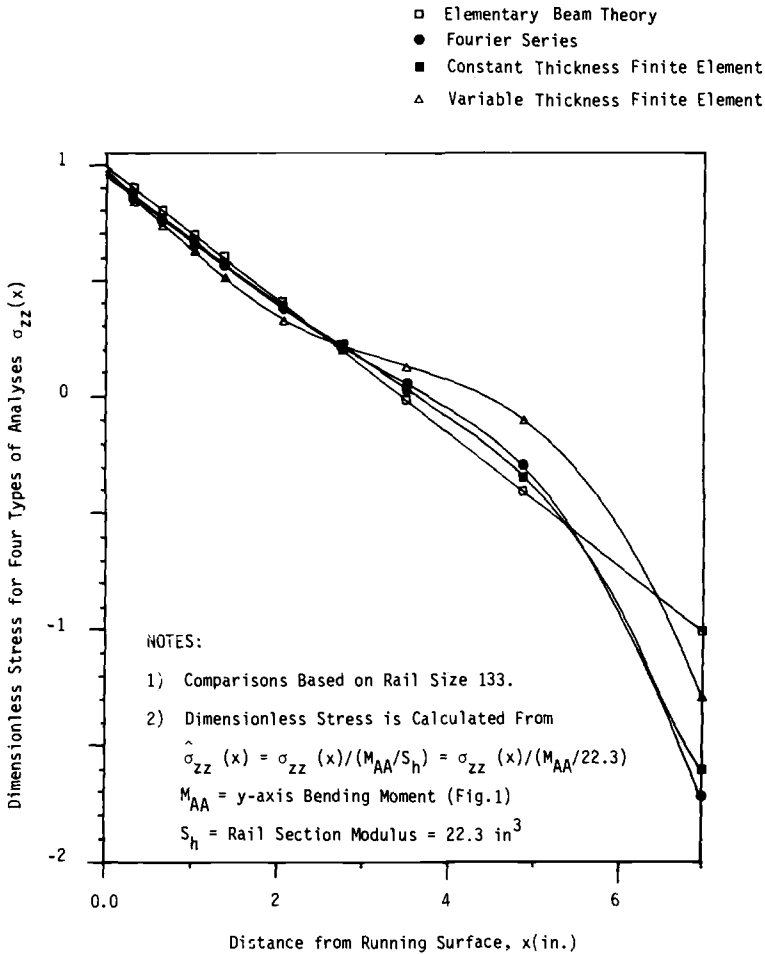


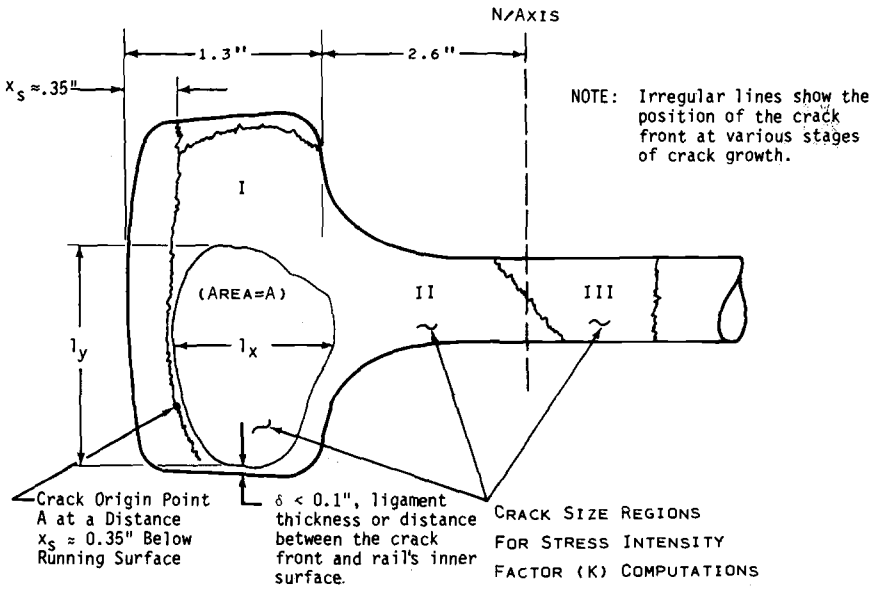
FIG. 3—Uncracked stress results for rail under three-point bending.

Stress Intensity Factor Solution Method

The influence function (IF) method has been used to compute, accurately and inexpensively, the redistribution of the uncracked stress field caused by the defect/crack, as reflected by the parameter K and as just modeled. The IF method has been described previously in Refs 10–14 for two-dimensional elastic crack problems and in Refs 14–18 for three-dimensional problems.

For two-dimensional problems, the equation for stress intensity factor is given by

$$K = \int_{L_a} dK(x) = \int_{L_a} h(x, \text{geometry, constraints}) \sigma_z(x) dx \quad (3)$$



REGION I

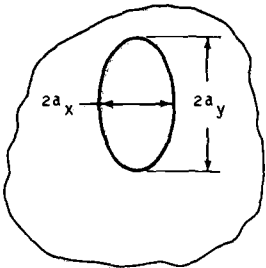
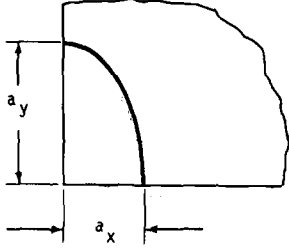
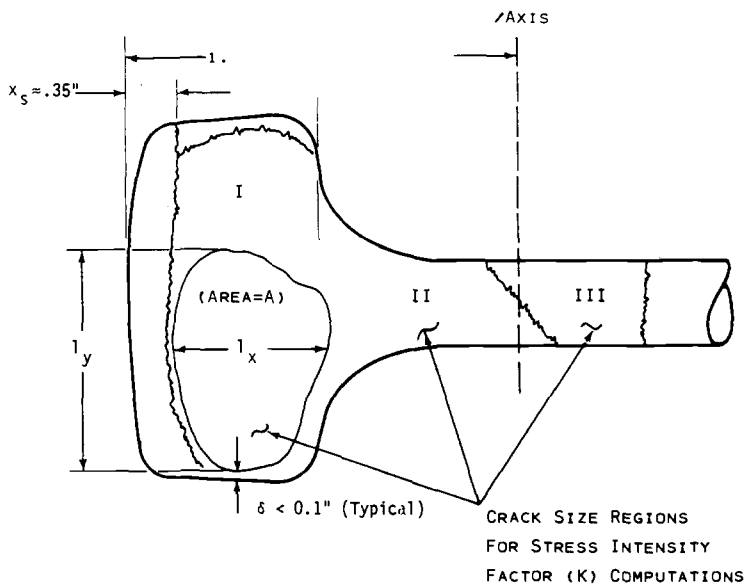
LOWER BOUND K	UPPER BOUND K
FOUR DOF BURIED ELLIPTICAL CRACK	TWO DOF QUARTER-ELLIPTICAL CORNER CRACK
 <p>MODEL a_x, a_y FROM $\frac{a_y}{a_x} = \frac{l_y}{l_x}$ $\pi a_x a_y = A$</p>	 <p>$\frac{a_y}{a_x} = \frac{l_y}{l_x}$ $\frac{\pi}{4} a_y a_x = A$</p>

FIG. 4—Region I modeling procedure for stress intensity factor computations for crack depths less than 3.3 cm (1.3 in.).

where L_a is the straight crack face boundary parallel to the x axis and perpendicular to the z loading direction, and h , the influence function, is the stress intensity factor caused by a unit z -direction opening load on the crack face at position x . Finally $\sigma_z(x)$, termed the uncracked stress field, is the crack locus stress in the uncracked solid.



REGION III
THROUGH-THICKNESS CRACK

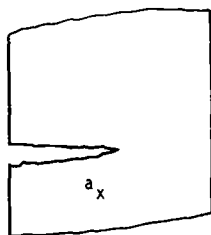


FIG. 5—Region III modeling procedure for stress intensity factor computations for crack depths more than 9.9 cm (3.9 in.).

The approximate [17, 19] formula used to compute K for the specific two-dimensional, through-thickness edge crack shown in Fig. 5 is

$$K = \frac{1}{t(a)} \int_0^a h(x, a, W) \sigma(x) t(x) dx \quad (4)$$

where $t(x)$ is the variable thickness, and $h(x, a, W)$ is given explicitly in Ref 12 for $a/W < 0.5$.

The IF method is particularly advantageous for computation of stress intensity factors for three-dimensional problems. The IF procedure developed in Ref 15 treats the three-dimensional cracking complications of complex crack shape, crack shape change during growth, and stress intensity

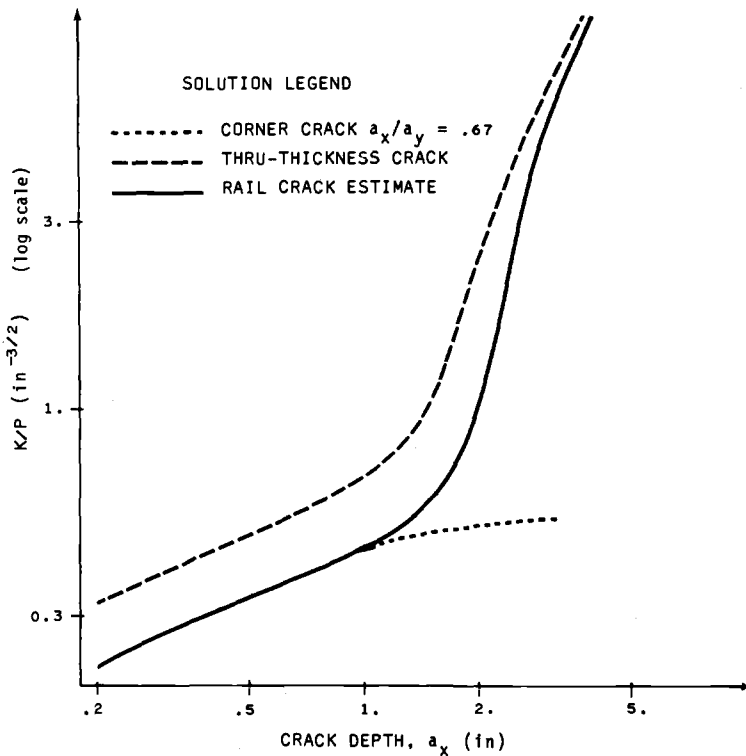


FIG. 6—Stress intensity factor solutions for shell-transverse defect crack in 133# rail section under three-point bending (Fig. 1 ($x_s = 0.8 \text{ cm (0.3 in.)}$)).

factor variation along the crack front. The actual crack is modeled with any prescribed mathematical shape with a finite number n of key variable parameters or degrees of freedom (DOF) $a_i, i = 1, n$. The unstable growth or stable cyclic growth rate of each DOF a_i is assumed to be controlled by its associated stress intensity factor K_i . Each K_i is defined in terms of the strain energy release rate $\partial U / \partial a_i$, where U is the strain energy, caused by perturbation of the single DOF, holding the other DOF constant. This definition, demonstrated in Ref 15 to be reasonable in its own right, is especially compatible with an advantageous influence function theory derived to compute stress intensity factors. The crack size and shape can then be computed as a function of load levels or load cycles by use of the usual linear elastic fracture mechanics modeling of crack growth.

The influence function theory requires only the characterization of the crack opening displacements for various values of the DOF and structural dimensions for any single simple reference loading, such as a uniformly pressurized crack. These closed form or numerical results are then applied to analytically derive all required values of influence functions and stress intensity factors for any other stress state, such as that due to the presence of a local notch or mechanical contact. References 16 and 17 develop the

required influence functions for a 2-DOF quarter-elliptical corner crack and a 4-DOF elliptical buried crack used to analyze the rail defects. The solution for the three-dimensional problem of the quarter-elliptical corner crack, oriented in the x - y plane, for which the two DOF are the semiaxes of the ellipse, a_x and a_y , is given in the form of area integrals over the crack locus A

$$\begin{aligned}\overline{K}_x &= \iint_A h_x(x, y, a_x, a_y, \text{geometry, constraints}) \sigma(x, y) dx dy \\ \overline{K}_y &= \iint_A h_y(x, y, a_x, a_y, \text{geometry, constraints}) \sigma(x, y) dx dy\end{aligned}\quad (5)$$

As with two-dimensional problems, once the h have been evaluated, the three-dimensional K computation is reduced to solution of the uncracked problem and the numerical integration of Eq 5. Reference 17 documents comprehensively the references, procedures, and methods required for accurate computation of h for the models utilized here and for a variety of additional geometries sufficient to solve a majority of structural problems.

Predicting Failure Loads for Three-Point Bend Rail Sections

Figure 7 represents a comparison of actual (P_f) and calculated (P_c) failure loads, using the fracture toughness data for each rail segment and the IF technique to obtain P_c from analysis of Mode I stresses induced by bending. The scatter bands reflect the difference in the corner crack (lower bound P_c) and buried crack (upper bound P_c) models sketched in Fig. 4. The correlation between calculated and measured failure loads is good for loads less than 846 to 890 kN (190 to 200 kips) and crack depths (a_x) larger than 0.89 cm (0.35 in.). The correlation between calculated and actual failure loads is not good for crack depths less than 0.89 cm (0.35 in.), corresponding to failure loads greater than 890 kN (200 kips). There are several possible causes for calculated stress intensity factors to be significantly less than measured material critical stress intensity factors for crack depths less than 0.89 cm (0.35 in.). The small cracks mark the directional transition of a shell to a transverse defect and, therefore, may be: (a) blunt-tipped and not initially crack-like, (b) somewhat shielded from the applied stress by the long shell crack, or (c) shielded by neighboring small transverse defects that are simultaneously emanating from the shell crack. According to the source cited in Footnote 4, the rail fracture surfaces will be analyzed to see if the small cracks, whose failure loads could not be well predicted by the P_c calculations, are fundamentally different from the larger cracks (depth greater than 1.8 cm (0.70 in.)) whose rail bending failure loads have been well predicted by linear elastic fracture mechanics.

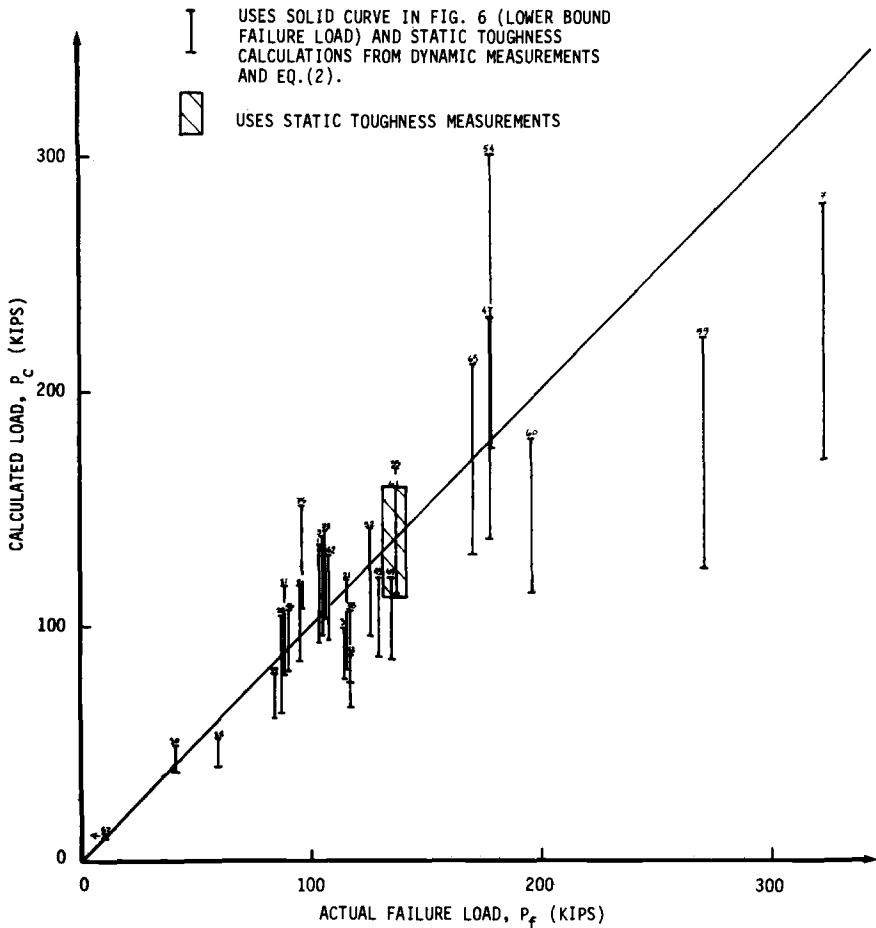


FIG. 7—Comparison of measured and calculated failure loads for rail sections with shell-transverse defect cracks under three-point bending.

Stress Intensity Factors for Actual Service Conditions

The previously described and utilized influence function method was applied to compute stress intensity factors for a variety of stress states which have significance in the study of railroad rail fatigue and fracture [20]. The stress states considered were: (a) railhead tension stresses due to essentially pure bending caused by remote wheel loads, and (b) local shear stress reversal distribution caused by passage of a single wheel over the vertical crack plane. The K results of stress distributions (a) and (b) are used to perform a preliminary railhead fatigue analysis. Based on the correlations

obtained for the calculated versus predicted failure loads described in the previous section, it is expected that the K factors for the following analyses are reasonably accurate for crack depths greater than 0.89 cm (0.35 in.) but may be too large (that is, too conservative) for defects with depths less than 0.89 cm (0.35 in.).

For many of the stress fields considered next, the wheel is in close proximity to the defect, and the actual railhead stress field is compressive. If a crack is subjected solely to a stress state which results in a negative K value, crack closure will result, and additional negative K excursion value will not be felt at the crack front. However, the negative K values may (a) be superimposed with K values calculated from other existing states of stress, and (b) are useful input for empirical relationships (for example, as in Ref 21), which account for crack closure in fatigue crack growth.

Stress Intensity Factors Under Pure Rail Bending

Figure 8 illustrates the results of corner crack (upper bound) stress intensity factor calculations using a pure bending stress field which can be expressed by the equation

$$\sigma_{zz}(x) = \sigma_0 (1 - 2x/h) \quad (6)$$

In the source cited in Footnote 4, z is the longitudinal direction and x is the distance below the running surface as indicated in Fig. 1. Also, $\sigma_0 = M/S$, M is the bending moment, which may be negative, S is the rail section modulus, and h is the rail height. In Fig. 8, as done previously for the three-point bend specimen, two models were used, and a transition curve is drawn between the two to obtain the K solution for cracks of various sizes under pure rail bending.

An Initial Study of Shear Mode Stress Intensity Factors

Because a transverse defect is subjected to shear reversal as the wheel passes over the crack plane, we must consider whether the Mode II and, to a lesser extent, Mode III crack sliding stress intensity factors, K_{II} and K_{III} , contribute significantly to the growth of the crack. Although little or no rigorous influence function methodology is as yet available for Mode II or III analysis of three-dimensional cracking under nonuniform shear stress, some approximate calculations have been based on the strain energy release rate, using the relationship

$$K_{II \text{ effective}} = K_{IIe} \equiv (K_{II}^2 + \alpha K_{III}^2)^{1/2}$$

$$\text{where } \alpha = \frac{(1 + \nu)}{(1 - \nu^2)} = 1.43 \quad (7)$$

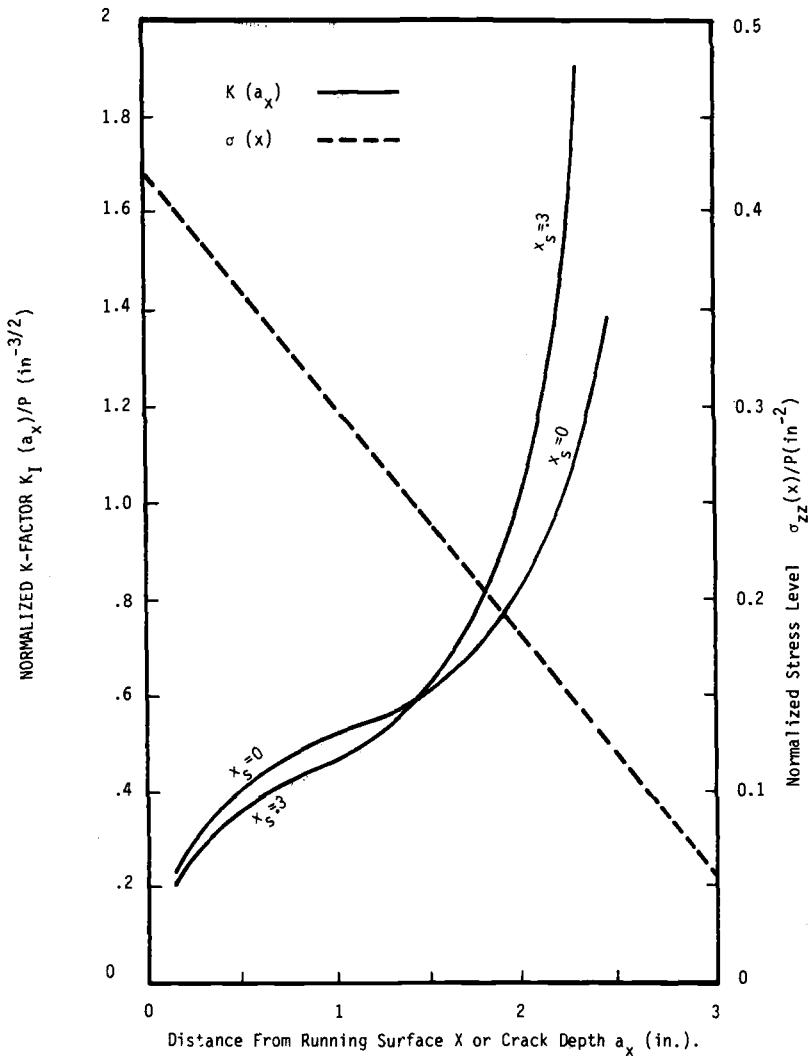


FIG. 8—Calculated stress and stress intensity factors for 133# rail under pure bending moment $M = 103P$ (cm-N) (9.125P (inch-pounds)) where, for convenience, the 103 (9.125) factor is taken from the three-point bending configuration of Fig. 1.

where e denotes “effective,” and ν is Poisson’s ratio. In Ref 5, K_{II} and K_{III} are calculated using the Mode I influence functions. This approximation is felt to be fairly accurate because the influence functions given in Ref 11 for two-dimensional problems are independent or nearly independent of the mode if the crack is small compared to the overall structural dimensions.

Figure 9 shows the shear stress distribution $\tau_{zx}(x)$, computed from a simplified two-dimensional Fourier stress analysis, discussed in more detail

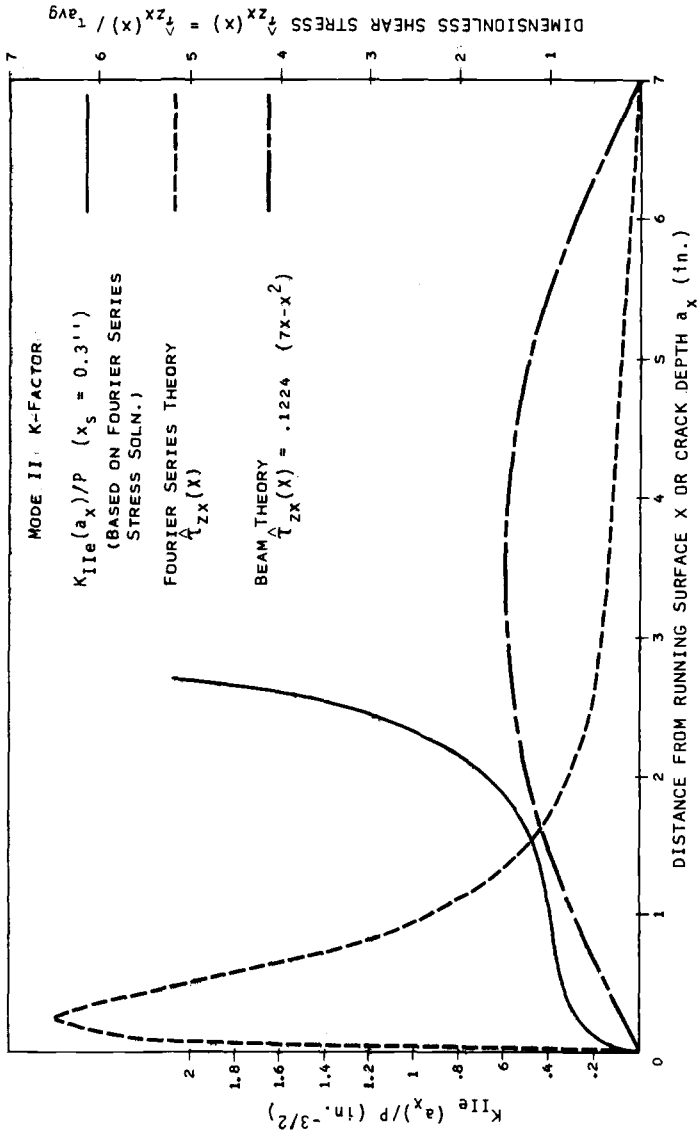


FIG. 9—Fourier series shear stresses and stress intensity factors $z = 0.89$ cm (0.35 in.) away from center of vertical wheel load P .

later. The shear stress, and the resulting factor $K_{IIe}(a)$, are for a crack located 0.76 cm (0.3 in.) below the running surface ($x_s = 0.76$ cm (0.3 in.)) and 0.89 cm (0.35 in.) ($z = \pm 0.89$ cm (± 0.35 in.)) from the center of the 1.3 cm (0.5-in.) vertical wheel/rail contact load indicated in Fig. 10. This location maximizes $K_{IIe}(a)$ for most of the range of concern of crack size, 0.64 cm $< a_x < 3.8$ cm (0.25 in. $< a_x < 1.5$ in.). In Fig. 9, note the large difference between the calculated railhead shear stress distribution and the beam theory (parabolic), stress distribution, and the resulting large values of K_{IIe} calculated for the railhead crack. The next section will explore the relationships between the cyclic or alternating values of K_I and K_{IIe} and their implications on fatigue crack growth.

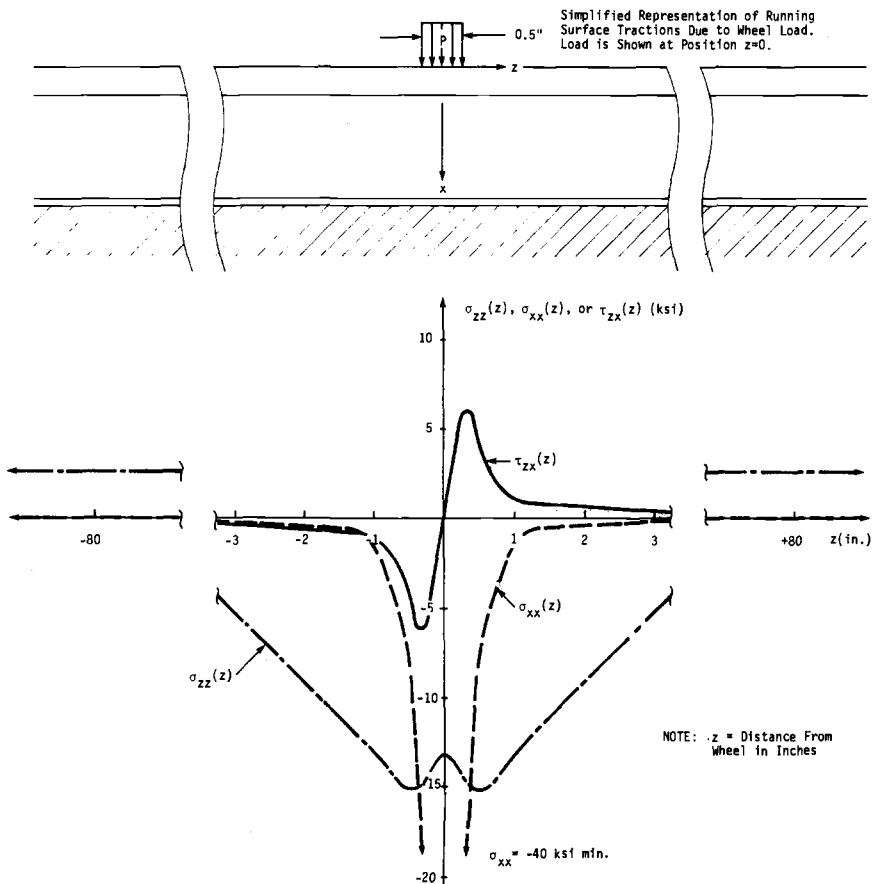


FIG. 10—Calculated stress cycles at a point 0.89 cm (0.35 in.) below running surface for a 111 kN (25 kip) vertical wheel load.

Preliminary Fatigue Analysis of a Transverse Rail Crack

Crack Growth Rate Estimation

The K computations of the previous section have been used to calculate the residual fatigue life with various transverse rail cracks. The three-dimensional fracture mechanics-based residual life prediction technique was developed in Refs 15–17. Briefly, the stress intensity factor associated with each degree of freedom of the crack is assumed to control the fatigue crack propagation rate of the corresponding degree of freedom. The relationship between crack growth rate and stress intensity factor (both mean and alternating components) is obtained from crack growth data using planar crack growth specimens, such as obtained in the source cited in Footnote 5 for rail steel. The fatigue crack growth data generated in the source cited in Footnote 5 is described by

$$da/dN = 1.6 \times 10^{-11} \Delta K^{4.06}$$

for the range of concern of ΔK , (8)

$$8.8 < \Delta K < 38.6 \text{ MN/m}^{3/2}$$

$$(8 < \Delta K < 35 \text{ ksi } \sqrt{\text{in.}})$$

obtained at room temperature, at $R = K_{\min}/K_{\max} \approx 0$, and cyclic frequency of 5 cycles per second (cps).

In order to account for the effects of multimode fatigue crack growth and crack closure under compressive stresses, we make two conservative⁶ assumptions. First, an effective alternating Mode I stress intensity factor is defined as

$$\Delta K_I = K_{\max} - 0.1 K_{\min} \quad (9)$$

where

$$K_{\max} > 0 > K_{\min}$$

The 0.1 factor is based on analysis of the data of Ref 21 which suggest that, due to crack closure, the crack tip “feels” at most 10 percent of the compressive excursion of the normal stress cycle. To account for multimode fatigue crack growth, define

$$\Delta K_{Ie} \equiv (\Delta K_I^2 + C \Delta K_{IIe}^2)^{1/2} \quad (10)$$

where C is a constant. A Von Mises criterion suggests a value $C = 3$, which worked well in a previous mixed mode fatigue analysis [22]. A strain energy release rate criterion [11] suggests the value $C = 1$. Since we now seek a conservative estimate in this preliminary analysis, $C = 3$ is used in the

⁶Leading to shorter calculated fatigue life than alternative assumptions.

following. Experimental programs are in progress to define more accurately the rate of fatigue growth for the complex, mixed mode K variation encountered in railheads.

Preliminary Analysis of Stress Cycle

Consider the case of passage of a single wheel as represented in Fig. 10 by a moving (but quasi-static) load of magnitude P distributed uniformly over a 1.3 cm (0.5 in) length. A two-dimensional, beam on elastic foundation analysis gives shear loads V and bending moments M at the vertical crack plane resulting from a wheel load P located at a distance $z > 0$ from the plane as

$$V(z) = (P/2)e^{-\beta z} \cos \beta z, \quad z > 0 \quad (11)$$

$$M(z) = (P/4\beta) e^{-\beta z} (\cos \beta z - \sin \beta z) \quad (12)$$

where

$$\beta = (k/4EI)^{1/4} \quad (13)$$

Using values obtained from Timoshenko [23] of (a) foundation modulus $k = 10.35 \text{ MN/m}^2$ (1500 psi) (a low, but conservative, value used to avoid underestimating M), (b) elastic modulus $E = 206\,925 \text{ MN/m}^2$ (30 000 000 psi), and using (c) y-axis bending moment of inertia $I = 36 \text{ m}^4$ (86.4 in.⁴) for 133# rail, $\beta = 0.0495 \text{ cm}^{-1}$ (0.0195 in.⁻¹) is calculated.

Equations 11-13 are used to obtain moments and loads, and the Fourier series analysis is used to determine stresses σ_{zz} , σ_{xx} , and τ_{zx} at various positions (x, z) for various moment and shear loads at z . Figure 10 shows schematically the variation in the stress components at a point 0.89 cm (0.35 in.) below the running surface as the wheel moves across (Point A in Fig. 4). Note the large shear stress reversal near $z = 0$ as the wheel passes over the point. Note also that the normal stresses are compressive during the large shear stress cycle and reach small peak tensile levels only when the wheel is 203 cm (80 in.) away.

Limitations of the Preliminary Analysis of Wheel/Rail Stress Cycles

The analysis just discussed combines a two-dimensional beam on elastic foundation analysis to estimate y-axis bending moments and vertical shear loads, and a two-dimensional Fourier series analysis to estimate the stress state in the vicinity of a wheel/rail contact load. Consequently, this is a highly simplified analysis which neglects a series of factors:

1. Railhead residual stresses due to plastic flow of the head which may impose a significant tensile component on the longitudinal railhead stress.
2. The local bending of the head due to eccentric vertical and lateral loads which probably contribute to the compressive stress in the gage corner of the

rail where shell defects initiate but can also induce tension fields which may influence the growth of a larger crack.

3. Shear stresses induced by horizontal running surface shear traction at the wheel/rail interface, which are expected to contribute significantly to subsurface shear stress components.

Consequently, the stress analysis must be regarded as preliminary, and further work is required to obtain more accurate estimates of the relative contributions of shear and normal cyclic stresses. However, it is believed that the two-dimensional analysis is in qualitative agreement with recently available three-dimensional studies (for example, Ref 24) and demonstrates that the shear stress reversal is, at least, a significant contributor to the stress cycle and, therefore, to the growth of transverse cracks.

Cyclic Life Predictions

It is believed from the magnitude of the stresses in Fig. 10 and from fatigue calculations and fractographic evidence discussed later that the shear stress τ_{zx} cycle is the major driving force for fatigue crack growth. The relatively modest tensile excursion of σ_{zz} in Fig. 10 is believed to contribute only minimally to crack growth.

At first impression, it might seem that we are ignoring the observation that fatigue cracks in steel grow in a plane perpendicular to the maximum principle stress σ_1 (that is, 45 deg from the maximum shear stress planes). However, this observation has been made for stress fields which have significant cyclic tensile principle stresses, as opposed to cyclic shear stresses. For the unusual, complicated stress cycle in the railhead, if the cyclic principal stresses are primarily compressive,⁷ then there is no reason for a crack to align itself at right angles to a compressive σ_1 . In fact, no data are available at present with which to reliably predict crack growth rates and directions when σ_1 is primarily compressive. Another way of looking at this situation is shown in Fig. 11. The (x - z) Mohr's circle at Point A ($x = 0.89$ cm (0.35 in.) below running surface (Fig. 4)) is shown for the wheel location of peak shear stress and K . The transverse plane is only 1 to 2 deg from the maximum shear stress plane. Mohr's circle for the wheel location of maximum tensile stress is also shown. Thus the preliminary stress analysis indicates that the large reversal of shear and the absence of a large tensile stress at any time in the cycle cause the crack to grow in the transverse plane. Preliminary checking stress calculations, similar to those in Ref 23 show that the proximity of other wheels does not affect significantly the ratio of cyclic shear to cyclic tensile stress.

Incidentally, the hypothesis that cyclic shear stress drives the fatigue crack can explain the observation from fracture surface photographs that trans-

⁷Martin's three-dimensional analysis in Ref 24 indicates that σ_{yy} (his σ_x), the stress component not considered in our two-dimensional Fourier series analysis, is also deeply compressive at the point of shear reversal due to wheel passage.

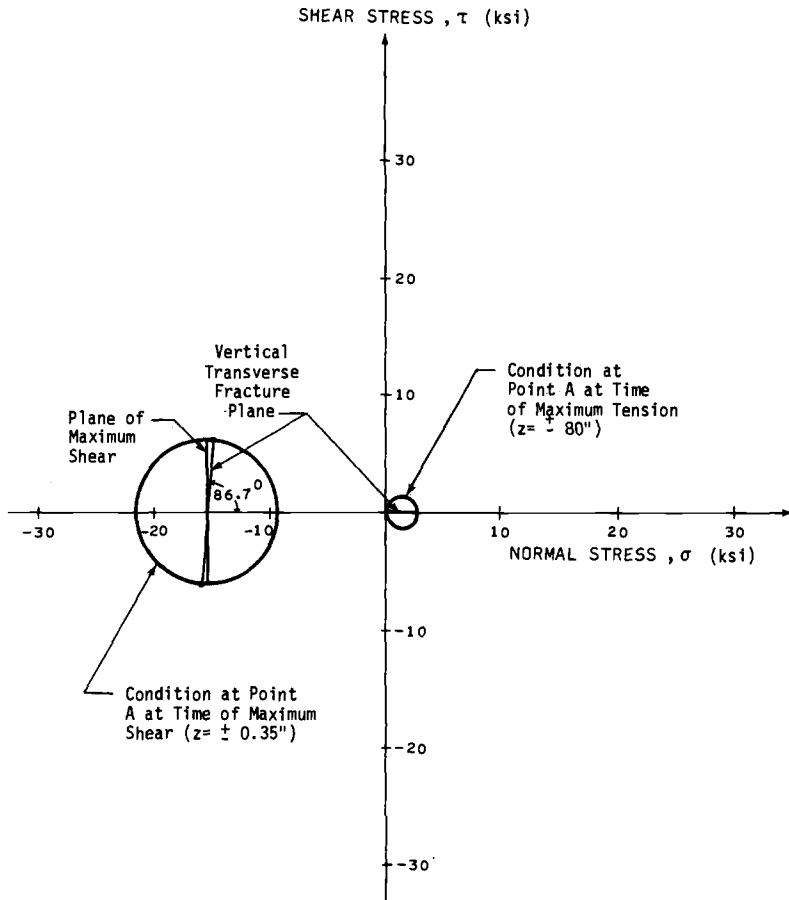


FIG. 11—Mohr circle diagrams for a point 0.89 cm (0.35 in.) below rail running surface for (a) maximum shear stress time point, and (b) maximum tensile stress time point in the x-z plane.

verse defects do not readily approach and break through any railhead surfaces (see schematics of Figs. 1, 4, and 5 and photographs in Ref 25, which show the small ligament dimension of <0.25 cm (0.1 in.)) because the major component of the crack plane shear stress must drop to zero at all railhead surfaces, except where the wheel makes contact. It has been hypothesized that the decreased crack growth rate as the crack approaches the surface is due to compressive residual surface stresses which inhibit Mode I growth. This author believes that this hypothesis is unlikely because (a) as previously stated, railhead residual stresses should be tensile and (b) the crack slows down as it approaches all railhead surfaces, including those remote from the gage corner and running surface where high residual surface stresses are unlikely. In summary, the precise evaluations of the relative contributions of shear and normal stresses to crack growth requires

refined experimental and analytical work, but there is a strong indication that the contribution of shear stress is significant, if not dominant.

Proceeding with the fatigue calculation procedure, we substitute the τ_{zx} and σ_{zz} stress field into equations of the form of Eq 5 to compute K . The resulting K values are utilized in Eqs 8–10 to obtain fatigue crack growth rates for each elliptical crack dimension, and the fatigue analysis program numerically integrates (Eq 8) to obtain the residual fatigue life, N , as a function of wheel load, P , initial crack depth, a_i , and final crack depth, a_f , calculated from the assumed fracture toughness of $55.2 \text{ MN/m}^{3/2}$ ($50 \text{ ksi}\sqrt{\text{in.}}$). The $55.2 \text{ MN/m}^{3/2}$ ($50 \text{ ksi}\sqrt{\text{in.}}$) value is high relative to most of the data in Fig. 2. A value of $K_{Ic} = 22 \text{ MN/m}^{3/2}$ ($20 \text{ ksi}\sqrt{\text{in.}}$) reduces the lives calculated herein by, at most, 50 percent.

Figure 12 shows the effective alternating K factor as a function of crack depth for a 111 kN (25 kip) wheel load. Figure 13 presents the calculated remaining fatigue life from four initial crack sizes as a function of wheel load for values ranging from $P = 55.6$ to 267 kN (12.5 to 60 kips). Note that, above 111 kN (25 kips) wheel load, if wheel load is doubled, the remaining life decreases by a factor of 12.

From the data of Stone and Schoenberg [3], it is noted that the rails were subjected to 200 to 400 million gross tons (MGT) usage per rail without failure (one million metric tons = 1 MGT). This observation indicates that our fatigue analysis is, in fact, conservative, as demonstrated by the dashed curves representing 100, 100, and 400 MGT usage (for example, twenty million repetitive cycles of a 89 kN (20 kip) wheel loading corresponds to 200 MGT). Recommendations for additional work required to remove some of the conservatism are presented next.

Recommendations for Improving the Preliminary Fatigue Analysis

Both the cyclic stress field and the fatigue behavior of detailed transverse cracks and fractures from shells are quite complicated [24], but it is felt that there is a good possibility that an accurate algorithm for fatigue life prediction can be developed if some of the recommendations discussed next are implemented.

To better characterize material crack growth under combined mode loading caused by shear stress reversal, the use of special specimens developed in Ref 26⁸ are recommended. These specimens are capable of describing fatigue crack growth under conditions combining Modes I and II or Modes I and III for a more accurate assessment of combined Mode crack growth than performed previously in the absence of experimental data. To evaluate the effect of the assumptions in Eq 10, fatigue analyses have been performed using $C = 1$, rather than $C = 3$, and significantly longer lives than those observed on the test rails have been calculated. Therefore, the generation of data to better model combined mode crack growth and the

⁸Rau, C. A., Failure Analysis Associates, personal communication. Oct.–Nov. 1975.

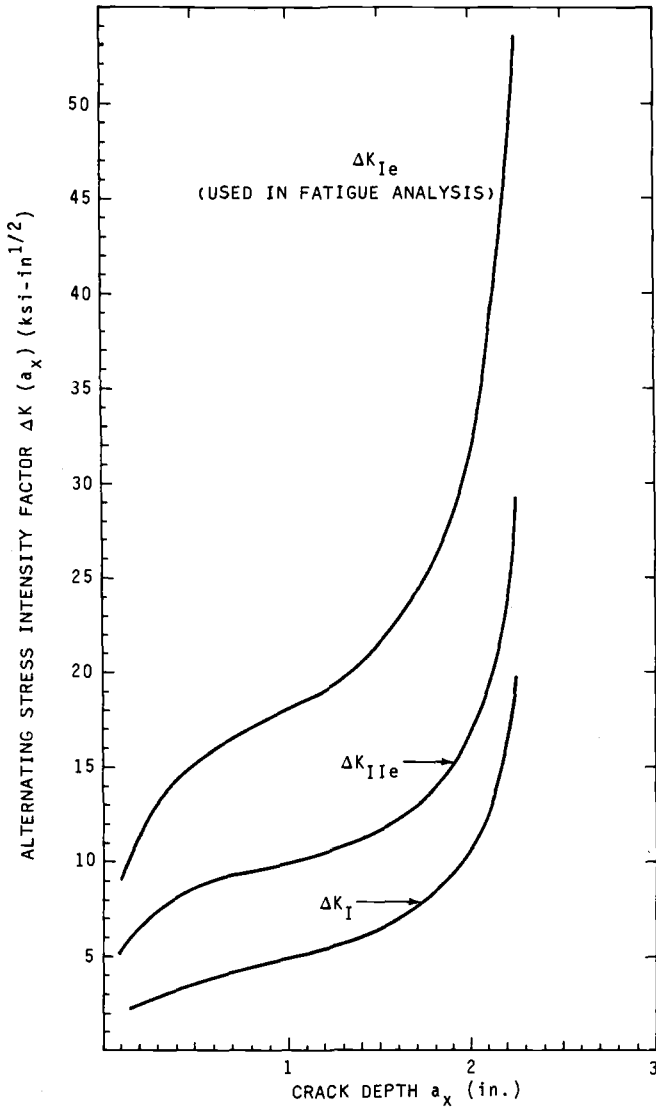


FIG. 12—Alternating cyclic stress intensity factors for a transverse defect located $x_s = 0.8$ cm (0.3 in.) below running surface subjected to passage of a 111 kN (25 kip) wheel load.

effects of superimposed compressive stress is a high-priority recommendation.

To better analyze the uncracked stress, we recommend the use of three-dimensional models as conducted in Ref 24. The results of Refs 24 and 27 could be combined with analysis or measurements of other types of rail loading (including running surface shear tractions, residual stress, eccentric

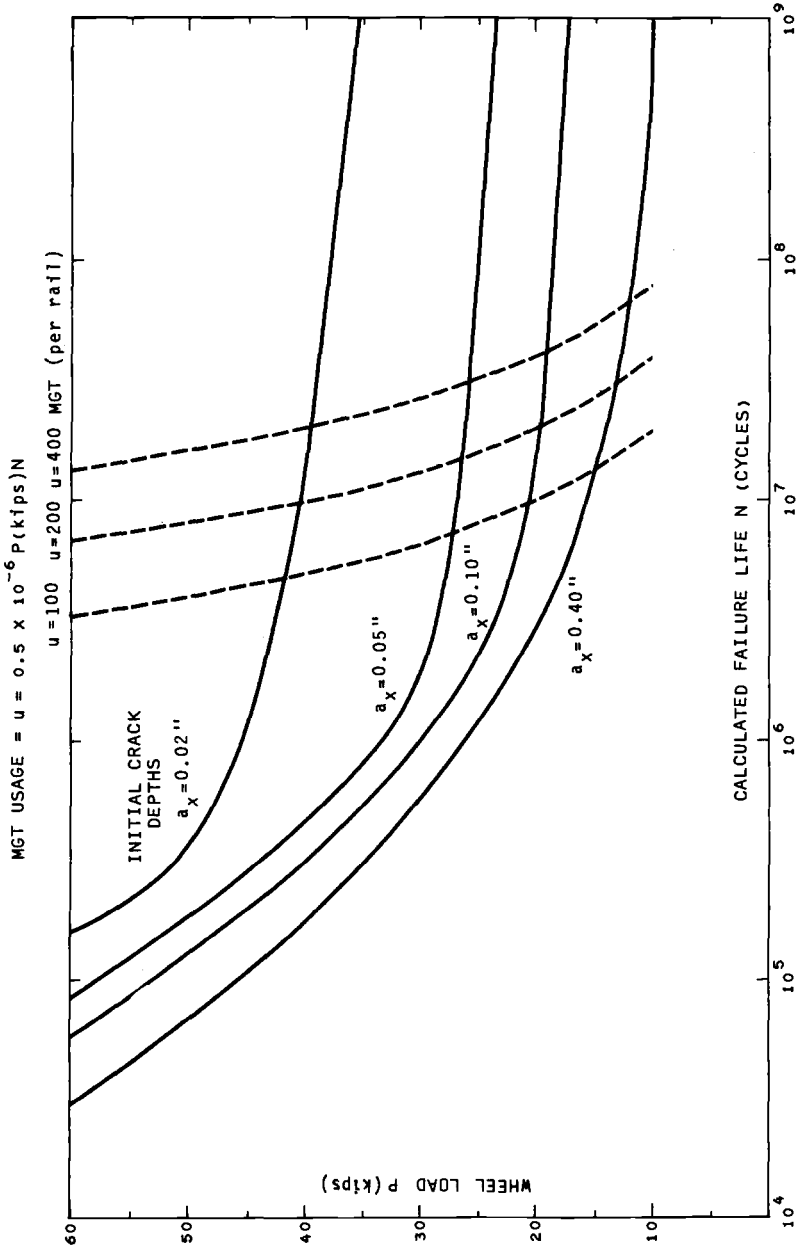


FIG. 13—Preliminary life predictions as a function of initial crack depth a_x and single wheel load P .

bending, and the interaction of neighboring wheels) in order to better calculate uncracked stress states with which to compute K . Recall that the preliminary uncracked stress analysis was two-dimensional, and, although it presented some of the salient features of the stress field (such as the significance of shear stress reversal), a more accurate fatigue analysis should incorporate the stress gradients due to all significant rail loads.

To better calculate the stress intensity factor, it is recommended that three-dimensional influence functions be developed for shear loading of the crack. For reasons discussed in the previous section, this is considered to be a relatively low-priority item. A more important item for investigation is the effect of compression on the K_{II} and K_{III} stress intensity factors caused by shear stress reversal as the wheel passes over the crack plane. As demonstrated by the currently incomplete [25] analyses which consider crack face friction, the rubbing together of the crack face surfaces could substantially reduce the crack sliding and alternating shear stress intensity factors and lead to longer fatigue lifetime predictions than shown in Fig. 13.

To incorporate actual rail loads, it is recommended that the modest literature survey [23,27] be extended in order to better define vertical loads and lateral loading of the rail. Measured static and dynamic loads could then be used for life calculations for specific main line tracks. As an example of possible utility, note that the preliminary fatigue analysis indicates that small decreases of the bending stress will have little effect on transverse defect growth (and might actually accelerate it), while decrease of the shear stress should significantly slow transverse railhead crack growth.

Conclusions

The results of this study have led to the following four conclusions:

1. Failure loads calculated from fracture mechanics analysis of AAR three-point bend tests of retired and defect-containing rail sections agree reasonably well with measured failure loads for railhead transverse crack depths larger than 0.89 cm (0.35 in.).
2. For transverse crack depths less than 0.89 cm (0.35 in.), calculated failure loads are smaller than the measured failure loads.
3. In-service railhead steady and cyclic stresses are markedly different than the tensile railhead stresses imposed by the laboratory tests in three-point bending.
4. Specific fatigue crack growth experiments and analysis should be conducted to improve fatigue life prediction capabilities because they can significantly improve rail inspection and failure prevention programs.

A number of conclusions have been inferred from the preliminary simplified stress and fatigue analysis. The range of applicability cannot be assessed until a more extensive stress analysis is completed and incorporated into the fatigue analysis. These specific conclusions are:

1. In-service railhead stresses include a large shear stress reversal super-

imposed on triaxial compression when the wheel passes over the transverse plane. The peak tensile stress is produced in the railhead when the wheel is about 203 cm (80 in.) away, and the tensile stress magnitude is small compared to the compressive or shear stresses.

2. The shear stress reversal probably causes the majority of in-service fatigue crack propagation of transverse defects. The small tensile excursion plays a minor role in driving the crack while the large triaxial compression may actually reduce the rate of shear-induced crack growth by increasing crack face friction which inhibits relative sliding of the crack faces.

3. The subsurface initiation of shells and transverse cracks from shells and the reluctance of growing transverse cracks to approach free surfaces are consistent with a shear stress-dominated fatigue crack growth.

Acknowledgments

The author would like to acknowledge the significant contributions of B. Prasad and R. Cipolla who provided stress analysis and computer programming support, and Drs. C. Rau, Jr., D. Stone, W. Kucera, G. Fowler, and A. Tetelman, who provided valuable data inputs, suggestions, or editing of this paper and its companion Association of American Railroads report [25].

References

- [1] "Broken Rails; A Major Cause of Train Accidents," Special Study, NTSB-RSS-74-1, National Transportation Safety Board, Washington, D.C., Jan. 1974.
- [2] "Sperry Rail Service," Automation Industries, Inc., Danbury, Conn., April 1971.
- [3] Stone, D. H. and Schoenberg, K. W., "Data Display of Rail Specimens Used for AAR-AISI-AREA Rail Research Program," Technical Report, Association of American Railroads, Chicago, Ill. (to be published).
- [4] Barsom, J. and Rolfe, S., in *Impact Testing of Metals, ASTM STP 466*, American Society for Testing and Materials, June 1969, pp. 281-302.
- [5] Tetelman, A. S. and Stone, D. H., "An Introduction to the Fracture Mechanics of Rail Materials," AAR Research and Test Department, Report No. R-157, Association of American Railroads, Chicago, Ill., May 1974.
- [6] Timoshenko, S. P. and Goodier, J. N., *Theory of Elasticity*, 3rd Edition, McGraw Hill, New York, 1951, p. 138.
- [7] DeSalvo, G. J. and Swanson, J. A., "ANSYS Engineering Analysis System User Information Manual," developed by Swanson Analysis Systems, available through Control Data Corporation, Palo Alto, Calif., Dec. 1972, Ref. C, Oct. 1974.
- [8] *Computational Fracture Mechanics*, a collection of papers by the American Society of Mechanical Engineers, AMD, Vol. 11, 1975.
- [9] Kobayashi, A., "Corner Crack at the Bore of a Rotating Disk," submitted for publication by the American Society of Mechanical Engineers, 1975.
- [10] Bueckner, H. F., *Transactions of the American Society of Mechanical Engineers*, Aug. 1958, pp. 1226-1230.
- [11] Paris, P. C., Gomez, M. P., and Anderson, W. E., "A Rational Analytic Theory of Fatigue," *The Trend in Engineering*, Vol. 13, No. 1, University of Washington, Seattle, Wash., Jan. 1961.
- [12] Bueckner, H. F., "Weight Functions for the Notched Bar," General Electric Report No. 69-LS-45, 1969.

- [13] Besuner, P. M., "The Application of the Boundary-Integral Equation Method to the Solution of Engineering Stress Analysis and Fracture Mechanics Problems," ASME-AMD-Vol. 11, American Society of Mechanical Engineers, March 1975.
- [14] Rice, J. R., *International Journal of Solids and Structures*, Vol. 8, 1972, pp. 751-758.
- [15] Besuner, P. M., in *Mechanics of Crack Growth*, ASTM STP 590, American Society for Testing and Materials, 1976, pp. 403-419.
- [16] Cruse, T. A. and Besuner, P. M., Symposium on Propulsion System Structural Integration and Engine Integrity, Monterey, California, Sept. 1974, *AIAA Journal of Aircraft*, April 1975, p. 369.
- [17] Besuner, P. M., "The Influence Function Method for Fracture Mechanics and Residual Fatigue Life Analysis of Cracked Components Under Complex Stress Fields," EPRI-217-1-TR2, Electric Power Research Institute-Failure Analysis Associates, July 1975.
- [18] "Analysis of Nuclear Reactor Pressure Vessel Feedwater Nozzle Cracks," Contract RP 498-1, Electric Power Research Institute-Teledyne Materials Research, Inc., July 1975.
- [19] Labbens, R., Pellissier-Tanon, A., and Heliot, J. in *Mechanics of Crack Growth*, ASTM STP 590, American Society for Testing and Materials, 1976, pp. 368-384.
- [20] Johnson, D. P. and Besuner, P. M., "Engineering Cost-Risk Analysis of Defective Rail Based on Fracture Mechanics and Statistical Analyses," Failure Analysis Associates-Association of American Railroads Draft Report 75-1-1(A), April 1976.
- [21] Yuen, A., Hopkins, S. W., Leverant, G. R., and Rau, C. A., "Correlations Between Fracture Surface Appearance and Fracture Mechanics Parameters for Stage II Fatigue Crack Propagation in Ti-6Al-4V," *Metallurgical Transactions* 5, Aug. 1974.
- [22] Tetelman, A. S., Besuner, P. M., and Rau, C. A., "Failure Analysis of a Pitman Arm," Failure Analysis Associates, Jan. 1975 (analytical results of this reference compared favorably with unpublished Feb. 1975 experimental results by A. S. Tetelman).
- [23] Timoshenko, S. and Langer, B., "Stresses in Railroad Track," ASME APM-54-26, American Society of Mechanical Engineers, Nov. 1931 (earliest presentation date).
- [24] Martin, G. and Hay, W., "The Influence of Wheel-Rail Contact Forces on the Formation of Rail Shells," ASME 72-WA/RT-8, American Society of Mechanical Engineers, Nov. 1972.
- [25] Besuner, P. M., "Fracture Mechanics Analysis of Rails with Shell-Initiated Defects," Failure Analysis Associates-Association of American Railroads Report 75-1-1(B), Nov. 1975.
- [26] Iosipescu, N., *Journal of Materials*, Vol. 2, No. 3, Sept. 1967, pp. 537-566.
- [27] "Railroad Accident Report," NTSB-RAR-71-2, National Transportation Safety Board, Washington, D.C., 1971.

S. G. Sampath,¹ T. G. Johns,¹ P. M. McGuire,¹
and K. B. Davies¹

Stresses Around Transverse Fissure Flaws in Rails Due to Service Loads*

REFERENCE: Sampath, S. G., Johns, T. G., McGuire, P. M., and Davies, K. B., "Stresses Around Transverse Fissure Flaws in Rails Due to Service Loads," *Rail Steels—Developments, Processing, and Use*, ASTM STP 644, D. H. Stone and G. G. Knupp, Eds., American Society for Testing and Materials, 1978, pp. 330–341.

ABSTRACT: The paper describes analysis related to cracks in rails using the finite element method. Attention has been focused on transverse fissure type of defects in railheads, although the approach is more generally applicable. Elastic stress intensity factors are calculated using the crack closure method and compared against values computed directly from node "opening" displacement. Analyses using idealized polynomial type of stress distributions for embedded cracks are viewed in the light of finite element results. A discussion of stresses that can occur in railheads with flaws for some load situations is included.

KEY WORDS: steels, railroad tracks, cracks

In recent years, railroads in the United States have annually experienced over 800 derailments attributable to broken rails which have resulted in over 60 million dollars of damage each year [1].² The largest percentage of derailments caused by broken rails has been due to the growth of transverse fissure in the railhead. A transverse fissure is an approximately elliptical or egg-shaped crack whose crack face is in the transverse plane of the rail (Fig. 1). Available information [2] suggests that a transverse fissure may grow slowly to be somewhat more than 20 percent of the cross sectional area of the railhead before growth becomes rapid and sudden rupture of the entire rail occurs.

In order to predict the reliability of rail in track, a methodology must exist for calculation of the crack growth rate of such flaws. One portion of this methodology is a mathematical description of the stresses around

*Original experimental data were measured in U.S. customary units.

¹Staff researcher, projects manager, and researchers, respectively, Battelle Columbus Laboratories, Columbus, Ohio 43201.

²The italic numbers in brackets refer to the list of references appended to this paper.

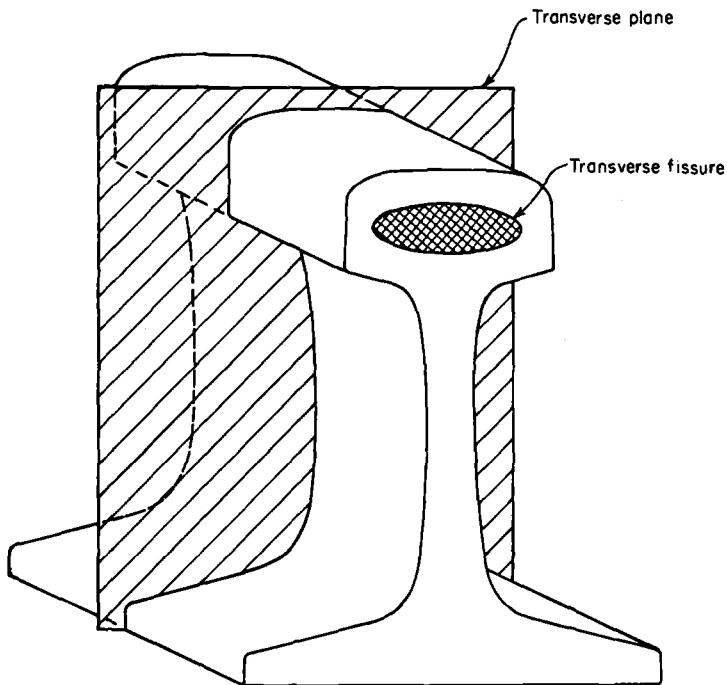


FIG. 1—*Transverse fissure in a railhead.*

specific flaws due to the service load environment. Several finite element models of the track structure and the rail have been developed for this purpose. In this paper, the finite element model of the transverse fissure will be presented in some detail. The supporting finite element models of the rail and track structures are only briefly described since the details concerning these models are to be presented elsewhere.

Stress History in Rails

The stresses induced in rails due to passing vehicles are the combined results of three basic loading mechanisms, flexural actions, local contact stresses, and residual stresses. Flexural stresses produced by vertical wheel/rail loads are the result of vertical bending of the rail on the subgrade foundation and bending and compression of the head on the elastic foundation provided by the web. Local contact stresses are the result of deformation of the rail adjacent to and beneath the loaded area between the wheel and rail. Residual stresses are the result of plastic flow of railhead due to repeated rolling loads. The plastic flow occurring with each wheel passage will decrease and theoretically stop and be elastic thereafter if the service load remains below a limit load called the shakedown limit.

Whether or not this flow stops within the lifetime of the rail is the subject of other ongoing research.

Thermally induced stresses are also sometimes referred to as residual stresses in rails. These stresses, however, are not locked in and could be released by permitting longitudinal expansion at bolted joints.

Mathematical Models

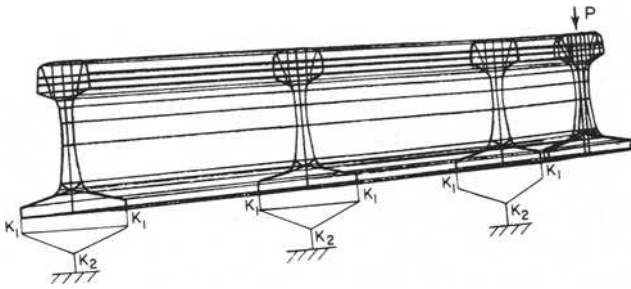
In order to evaluate the stresses in rails due to various service load environments, several mathematical models were constructed using the general purpose finite element program ADINA. For the computation of stresses away from the immediate vicinity of the loaded contact area, a three-dimensional rail section model has been constructed (Fig. 2). The model is supported at each tie seat by a system of springs that simulate the vertical stiffness and torsional rigidity of the ties and subgrade. The vertical stiffnesses of the springs are determined from a multilayer subgrade and ballast model developed in another research program. The torsional rigidity is determined assuming that the rail is rigidly attached to the tie and determining the response of the tie when a moment is placed at the rail seat location. For this, the tie is assumed to be a beam on an elastic foundation.

To compute stresses adjacent to the contact area between the wheel and rail, a refined finite element model of this region was developed. In addition, the computer program FRAC3D developed by Bell [3] was also used to determine stresses in the contact region. The contact pressure distribution between the wheel and rail was computed using the analysis procedure of Johns and Leissa [4].

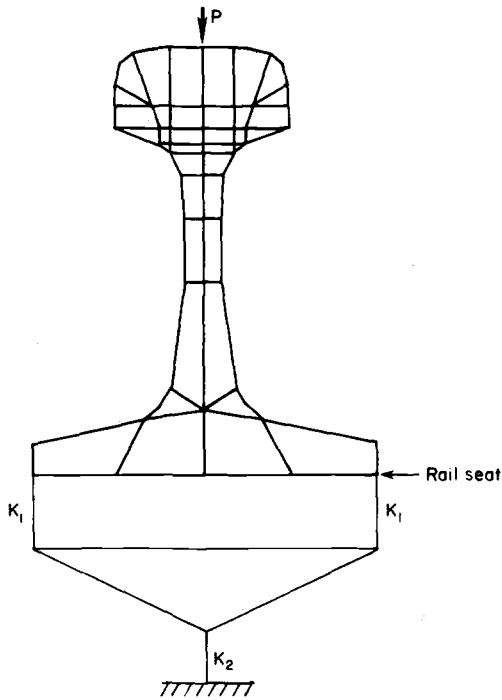
Computed Stress Histories

When a vehicle approaches to within 1.82 to 3.64 m (6 to 12 ft) of a particular point in the railhead, that location experiences a tensile bending stress due to the flexural action of the rail on the elastic foundation of the ties, ballast, and subgrade (Fig. 3). As the vehicle load moves closer, longitudinal stresses within the head become compressive close to the wheel/rail contact point, and the railhead experiences bending action due to compression of the web (Fig. 4). Within the railhead, this bending action causes tensile stresses to occur at some distance directly beneath the wheel.

When the wheel is within 0.0076 to 0.127 m (0.3 to 0.5 in.) of a point in the railhead, large contact stresses develop due to the local deformation of the railhead near the region of application of wheel load (Fig. 4). These stresses are in general much larger in magnitude than the flexural stress components. The contact stresses are, in general, compressive with the exception of a transverse shearing stress component which completely reverses as the wheel passes. The contact stresses developed in the proximity of the wheel/rail contact zone can frequently exceed the yield stress of the



Three-Dimensional Finite Element Full Rail Model



Section Through Rail Finite Element Model

FIG. 2—Three-dimensional finite element, full rail model.

material under normal freight traffic, and residual tensile stresses build up in the railhead in a region adjacent to the tread surface (Fig. 5). This region extends deep within the railhead.

Stresses Around Transverse Fissures

Transverse fissure defects vary in position and geometry but generally appear as elliptical or egg-shaped flaws occurring in the central head

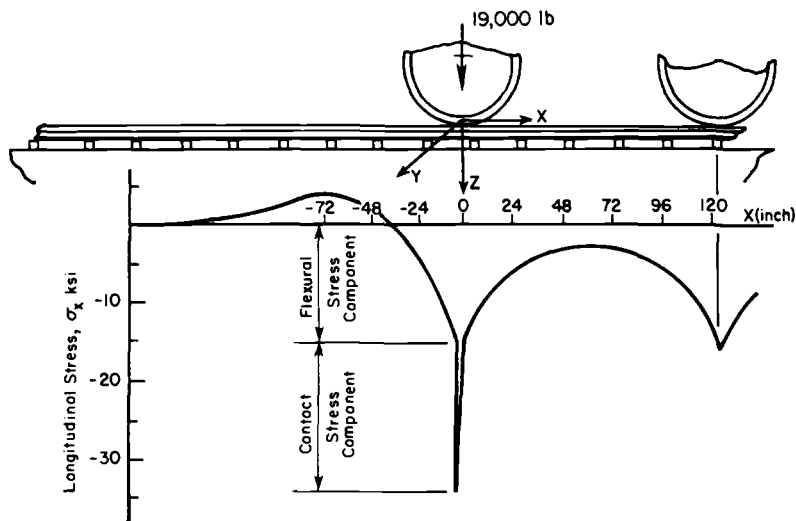


FIG. 3—Longitudinal stress on the running surface.

region or toward the gage corner. For this analysis, a centrally located flaw was assumed. Its cross section was taken as elliptical with aspect ratio (width to height ratio) of 1.33. This crack geometry was found to approximate actual transverse fissures taken from service.

Due to the existence of residual stresses and gradients in the operating stress field, it is not expected that the flaw grows uniformly. In fact, it is known that there is a definite tendency for the crack to grow away from the running surface. This is probably due to the large compressive residual stress field at that location. It is believed, though, that, by determining the stress intensity factors for flaws in an advanced stage of development, an accurate enough evaluation of the crack growth can be made to provide an estimate of the residual life for a reliability analysis of the rail.

Computational Procedure

A finite element model of the railhead including an elliptical flaw has been developed using the general purpose program ADINA. The basic element used was the 20-node isoparametric brick, but advantage was taken of the variable number of midside nodes option to economize on the number of degrees of freedom in the model. The substructuring concept was used to limit the axial length of the rail model containing the flaw (Fig. 6). The external loads for the model were drawn from the stress results of detailed studies made of uncracked rail configurations.

The "quarter point" singularity method was used [5] in order to simulate the unboundedness of the stresses at the crack tip. Although it appears from the work presented in Ref 6 that more accurate measures of the stress

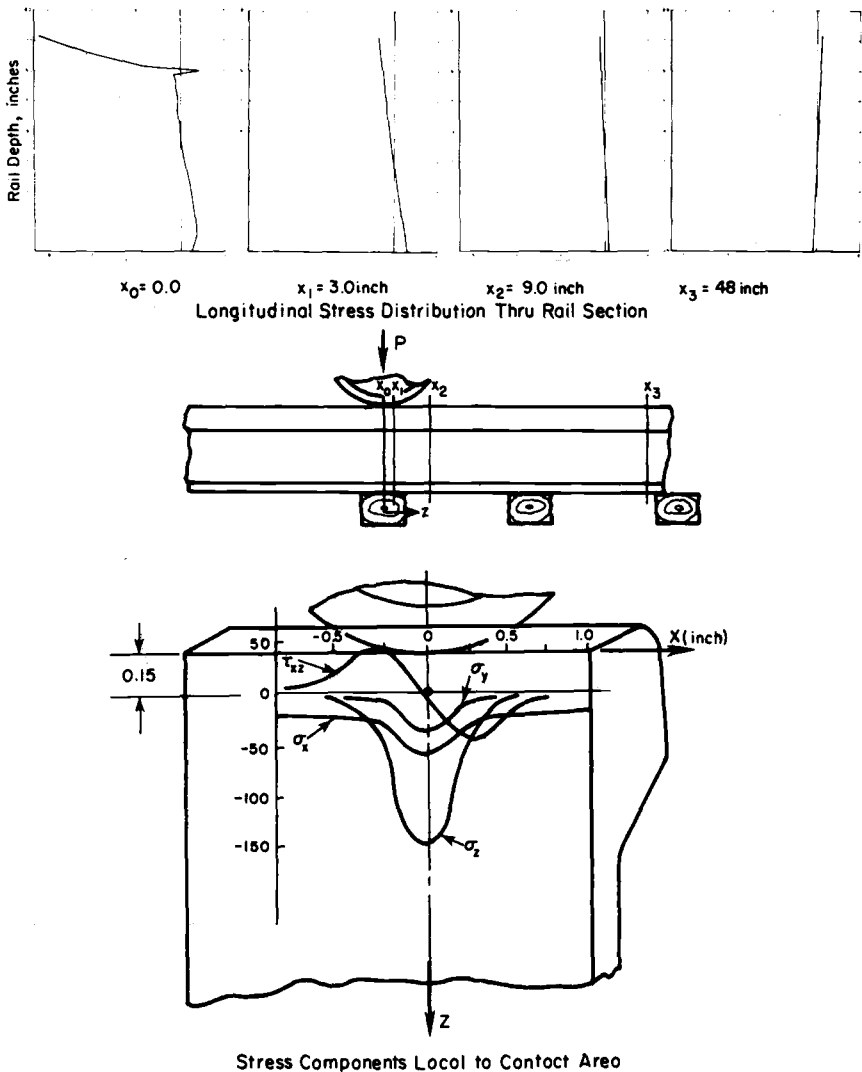


FIG. 4—Load history of the stress (in 132-lb rail, foundation modulus 10 000 psi, 20 000 lb wheel load).

intensity factors (SIF) are obtained if the elements bounding the tip are wedges rather than six-faced bricks, the expense involved in solving the resulting massive problem was believed to outweigh such an advantage.

The crack closure method was employed to calculate the stress intensity factors. The method was chosen for the advantage it offers for multiple load cases as well as its ability to distinguish the three modes of deformation [7,8] in the linear elastic case. In a three-dimensional displacement field, the closure has to be affected in such a way that compatibility is

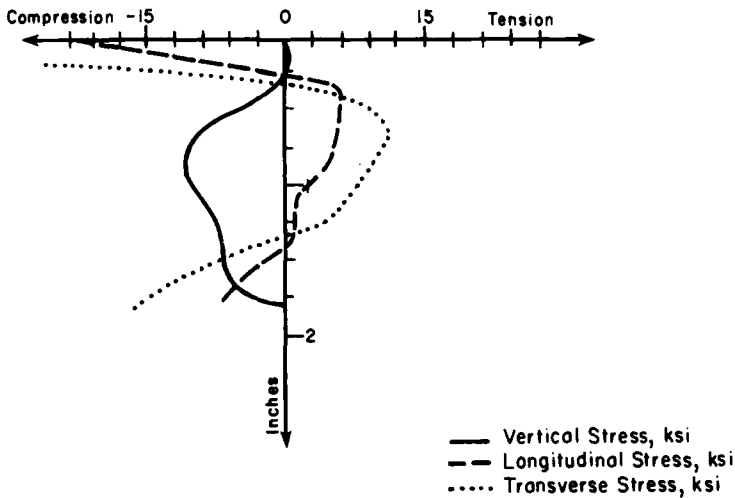


FIG. 5—Longitudinal, vertical, and transverse residual stress in new and used rail beneath the centerline of contact.

preserved around the entire periphery of the crack front. Consequently, the calculation of the closure forces at each node around the crack tip involves the computation of influence functions at each node and subsequent solution of a set of simultaneous equations. Following the suggestion in Ref 8, midside nodes were included in calculating the closure integral. Each of the SIF nodes are calculated separately in this fashion by considering only the displacement component associated with the particular mode. But the K_{II} and K_{III} modes are coupled if the displacement components are with respect to a Cartesian system of coordinates.

The crack closure integral was evaluated on the assumption that the eccentricity of the elliptical flaw for an incremental crack front advance remains unchanged. It is recognized that this assumption linearizes the problem of the variation of SIF around the crack. Some aspects of this problem will be reported elsewhere.

It is well known that the SIF calculated around the crack front for any general external loading on the body is equivalent to the SIF computation for the case where only the crack surface is loaded by the stresses calculated for the position of the crack for the uncracked body [9]. With this convenient equivalence, Shah and Kobayashi [10] have presented SIF results for a general cubic polynomial pressure distribution on an elliptical planar crack surface in an infinite body. Smith and Sorenson [11] have likewise calculated the factors for shear stress distributions on the crack, assuming again a cubic variation. It has been noted by Parmerter [9] that the boundary effect on the SIF manifests itself only for small ligament widths.

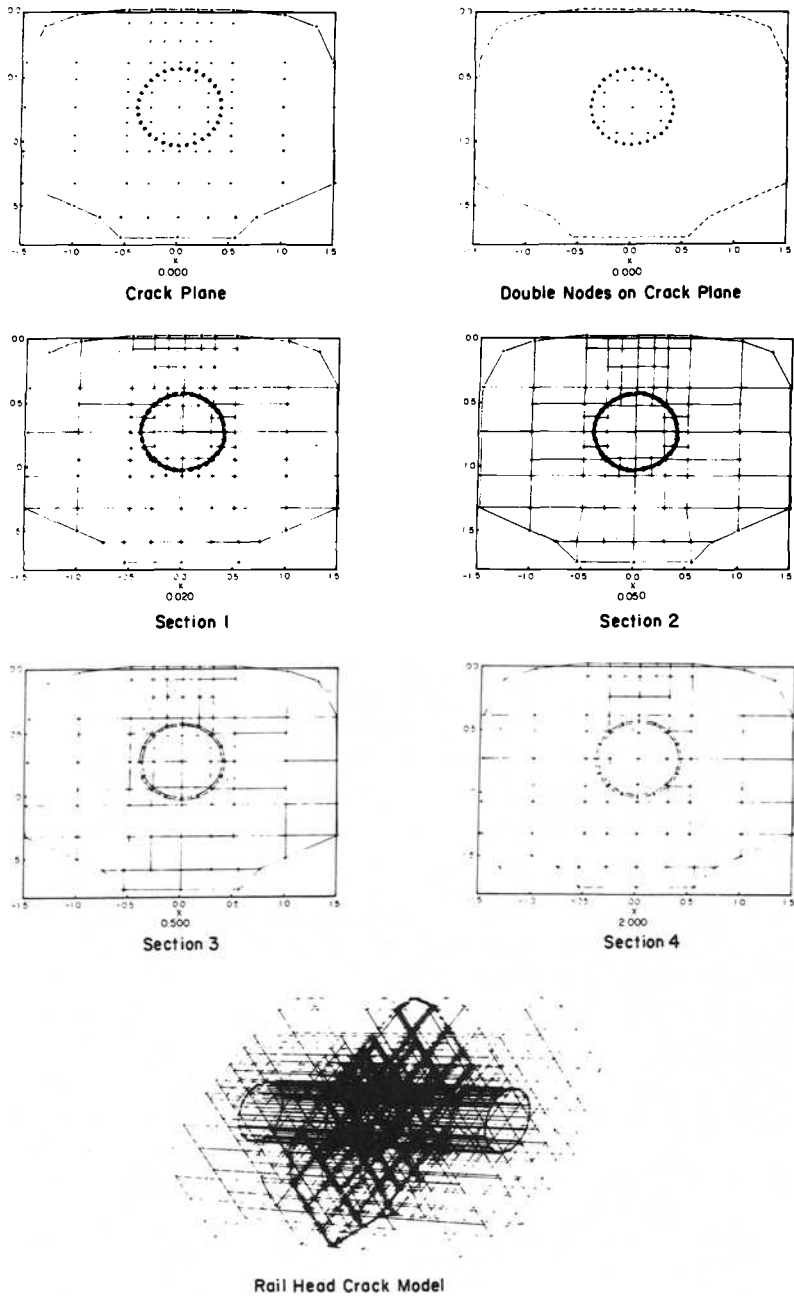


FIG. 6—Sections through finite element model containing a transverse fissure.

For cases of slowly varying stress fields, as occurs in rail sections away from contact load positions, a cubic representation can be expected to hold reasonably well. If so, the methods outlined in Refs 10 and 11 can be used to achieve an economic purpose since finite element analyses of three-dimensional configurations with cracks or the method outlined in Ref 12 are generally expensive. The accuracy of results obtained using the simple method of Ref 10 is demonstrated for one example.

Numerical Results

Stresses on the boundaries of the finite element substructure containing the flaw were determined from the previously described finite element model of the entire rail. These stresses were placed upon the railhead with the flaw in several positions with respect to the location of the wheel. Figures 7, 8, and 9 show the stress intensity factor K_I plotted around the elliptical transverse fissure for the load directly above the flaw, for the load such that the edge of the wheel/rail load patch is directly above the flaw, and for the load several ties away from the flaw. It must be pointed out that, in these calculations, the web stiffness has probably been over-

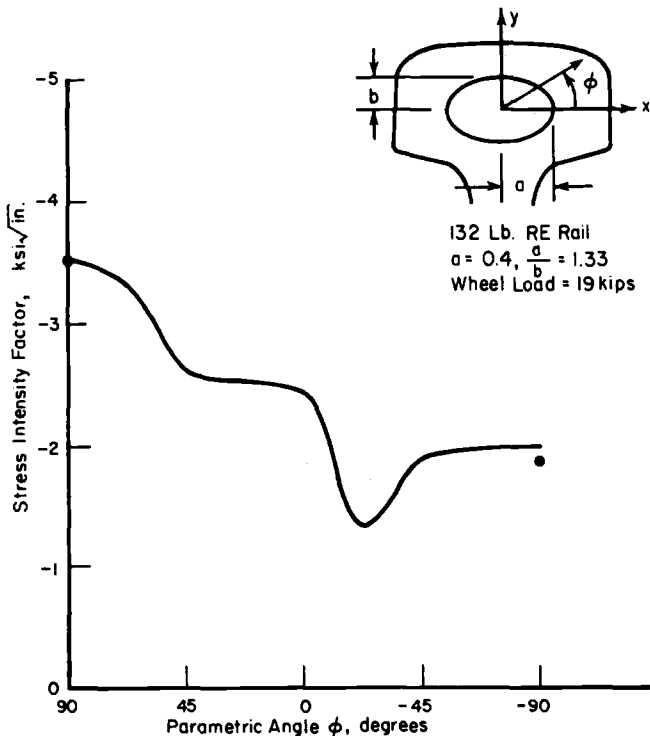


FIG. 7—Stress intensity factor as a function of parametric angle for load over the crack.

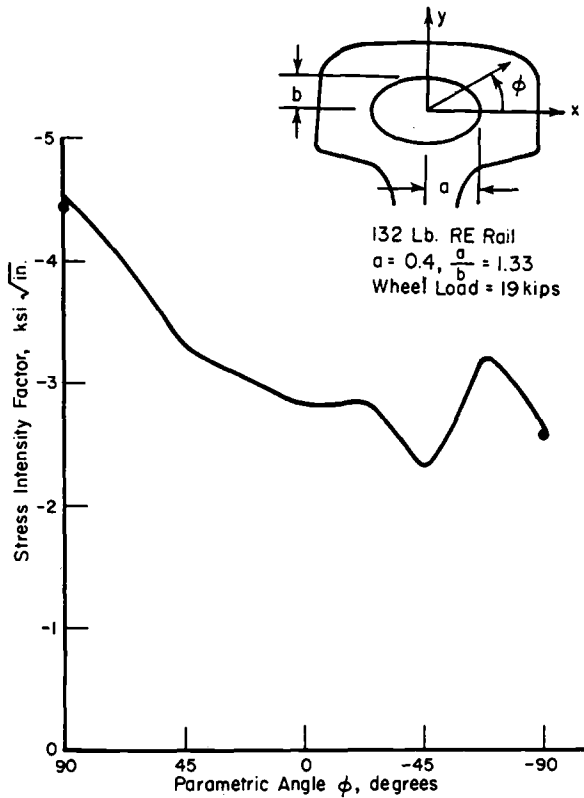


FIG. 8—Stress intensity factor as a function of parametric angle for load near the crack (offset 0.27 in.).

estimated due to the coarseness of the finite element mesh used for generating the boundary conditions applied to configuration in Fig. 6.

With the load directly above the flaw, much of K_I is negative, indicating that, for this loading case, much of the crack closes. It must be noted that, if the residual stress state (Fig. 5) [12] were superimposed upon these stresses, a physically realizable crack opening displacement may result. In this position, not shown here, as the crack becomes slightly larger, K_I at the bottom of the crack becomes positive, which reflects the tensile longitudinal stresses developed by the local bending of the head on the web (Fig. 4).

When the load is such that the edge of the wheel/rail load patch is directly above the flaw, the flaw experiences the maximum reversed transverse shearing stress (Fig. 4). This is a problem similar to the one solved by Besuner [13], except that the transverse shearing stress is smaller in this case since the flaw has been placed deeper within the rail.

For the case of the wheel, several ties from the location of this flaw, a

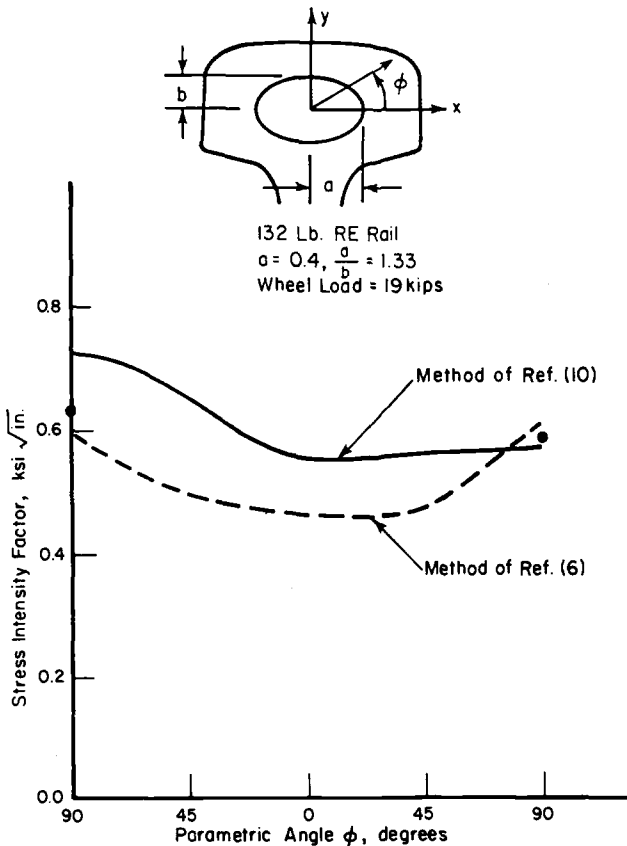


FIG. 9—Stress intensity factor as a function of parametric angle for load far from crack (offset 48 in.).

tensile bending stress is experienced due to reversed bending of the rail on the elastic foundation of the ties, subgrade, and ballast. In Fig. 9, which represents this case, the results obtained by using the method of Ref 10 is included.

Conclusions

The finite element method is very versatile for determining the stress-intensity factors in three-dimensional geometries; however, it also is quite an expensive procedure in spite of various economies being affected. For regions away from contact loaded positions, where the stress field is indeed tensile, the methods of Refs 10 and 11 offer an economical alternative.

Acknowledgments

The authors gratefully acknowledge the guidance of Donald McConnell and Roger Steele of the Transportation Systems Center during this work

and the financial support of the United States Department of Transportation.

References

- [1] Anonymous, "Bulletin No. 141, Summary and Analysis of Accidents on Railroads in the United States," Federal Railroad Administration, Office of Safety, Dec. 1972.
- [2] "Rail Defect Manual," Sperry Rail Service, 1964.
- [3] Bell, J. C. and Batra, S. K., *Surface Mechanics*, American Society of Mechanical Engineers, 1974, pp. 144-163.
- [4] Johns, T. G. and Leissa, A. W., "The Normal Contact of Arbitrarily Shaped Multi-layered Elastic Bodies," Symposium on the Contact of Deformable Bodies, International Union of Theoretical and Applied Mechanics, University of Twente, Dnschede, Aug. 1974.
- [5] Henshall, R. D. and Shaw, K. G., *International Journal For Numerical Methods In Engineering*, Vol. 9, 1975, pp. 495-507.
- [6] Shih, C. F., deLorenzi, H. G., and German, M. D., *International Journal of Fracture Mechanics*, Vol. 12, No. 4, 1976, pp. 647-651.
- [7] Rybicki, E. F. and Kanninen, M. F., "A Finite-Element Calculation of Stress-Intensity Factors by a Modified Crack-Closure Integral," submitted for publication in *International Journal of Engineering Fracture Mechanics*, 1975.
- [8] Hellen, T. K. and Blackburn, W. S., "The Calculation of Stress-Intensity Factors in Two and Three-Dimensions Using Finite Elements," *Computational Fracture Mechanics*, E. F. Rybicki and S. E. Benzley, Eds., ASME-PVP Publication, American Society of Mechanical Engineers, San Francisco, 1975.
- [9] Parmeter, R. R., "Stress-Intensity Factors for Three-Dimensional Problems," Air Force Rocket Propulsion Laboratory Dept., AFRPL-TR-60-30, April 1976.
- [10] Shah, R. C. and Kobayashi, A. S., *International Journal of Engineering Fracture Mechanics*, Vol. 3, 1971, pp. 71-96.
- [11] Smith, F. W. and Sorenson, D. R., "Mixed Mode Stress-Intensity Factors for Semi-elliptical Surface Cracks," NASA Cr-134684, National Aeronautics and Space Administration, 1974.
- [12] Office for Research and Experiments, "Study of Fatigue Phenomena of the Rail in the Contact Zone with the Wheel," *Rail International*, Vol. 3, No. 13, Sept. 1973, pp. 741-794.
- [13] Besuner, P. M., "Fracture Mechanics Analysis of Rails with Shell-Initiated Transverse Defects," Failure Analysis Association Dept. FAA-75-1-1(B), prepared for the American Association for Railroads, Nov. 1975.

Prediction of Rail Steel Strength Requirements—A Reliability Approach

REFERENCE: Mair, R. I. and Groenhout, R., "Prediction of Rail Steel Strength Requirements—A Reliability Approach," *Rail Steels—Developments, Processing, and Use*, ASTM STP 644, D. H. Stone and G. G. Knupp, Eds., American Society for Testing and Materials, 1978, pp. 342–360.

ABSTRACT: The determination of rail yield strength levels to support increased wheel loads is usually based on empirical adjustments to the Hertzian equations for contact stresses. A formulation is given, based on reliability theory, which enables a more refined analysis to be carried out and incorporates the material property variations, provided these can be approximated as Gaussian normal distributions.

Application has been made to unit train operations and estimates made of strength levels required for mean wheel loads in excess of 150 kN. The results indicate the importance of rail/wheel tangential forces on rail damage in curves and show that, while variations in wheel loads about the mean have an influence on performance, the effects are not highly significant. Spread of steel strength also has only a marginal influence within the bounds of accepted steelmaking control.

A comparison has been made between the predicted strength level and service trials which indicates that the suggested procedure provides conservative results.

KEY WORDS: railroad tracks, steels, mechanical properties, yield strength, statistical analysis, reliability

Head crushing, shelling, and long pitch corrugations are frequent forms of rail damage resulting from overloading. Metallurgical examinations of the rail cross section reveal in each case a high level of material inelastic deformation. Prevention of damage by excessive plastic deformation can be achieved by adjusting the ratio of material flow resistance to applied contact stress. The three procedures available to increase the ratio are: (a) reducing applied loading, (b) increasing contact area, or (c) increasing rail strength level.

The deterministic relationships between loading, contact geometry and rail stress levels have been evaluated by numerous authors [1–3].² Equating the calculated stress levels to the material yield stress provides a limiting

¹Engineering research manager, Product Engineering, and research officer, respectively, Broken Hill Proprietary Co. Ltd. Melbourne Research Laboratories, Clayton, Victoria, Australia.

²The italic numbers in brackets refer to the list of references appended to this paper.

value of the applied load to prevent yield for a specific material strength. In general, the calculated load limits are known from experience to be excessively conservative, and an improved estimate can be obtained if limited deformation is permitted until the system achieves a shakedown limit [4,5].

Since deterministic solutions to the problem relate individual load and strength levels, it is necessary to adopt conservative design load and strength values. Operating experience has provided a basis for adjusting the chosen values to give acceptable combinations of properties for wheel loads up to, say, 125 kN. Beyond this level, available operating experience is limited, and the metallurgical complications associated with increased strength levels necessary to match the loads are significantly increased.

As an alternative to the deterministic approach, this paper considers a probabilistic formulation wherein the actual statistical distributions of load, strength, and contact geometry are combined according to the principles of reliability analysis to give a predetermined probability that the applied stress will not exceed the permissible stress. Formulation of the reliability analysis approach was undertaken to obtain a better understanding of the significance of load distribution on the performance of rail steel and thereby obtain a less conservative estimate of the necessary strength level to avoid corrugations. Application of the procedure is made to the unit train system of the Mt. Newman Mining Co. operating on a mean wheel load of 150 kN with peak values above 200 kN.

The paper is based on Ref 6 to which readers are directed for additional data and detailed mathematical derivations. Copies are available on request.

Relationship Between Loading, Contact Geometry, and Stress State at Shakedown

The local region of contact between a rail and wheel can be treated as the contact between two doubly curved elastic half spaces. The dimension of the contact surface ellipse and the three dimensional stress states can be calculated by known methods [7]; however, these solutions are limited to elastic conditions.

In order to utilize existing analyses of the stress states beyond the elastic range, the contact conditions have to be reduced to a more tractable two dimensional representation. Detailed studies of the deformation of rolling bodies above the yield point suggest that the stress state is adequately approximated by conditions of plane strain with a rectangular contact area [8-10]. For a specified width of contact, w , the contact length along the rail can be calculated from Hertz's formula [3] and eliminated from the expression for the maximum normal stress on the contact surface to give

$$\sigma_{\text{app}} = \left[\frac{0.16EP}{(1 - \nu^2)rw} \right]^{1/2} \quad (1)$$

where

- σ_{app} = maximum normal contact stress, MPa,
- P = wheel load, kN,
- r = wheel radius, m,
- w = contact width across railhead, m,
- E = Young's modulus, GPa, and
- ν = Poisson's ratio.

In association with the normal loading, the region of contact is generally subjected to a tangential loading. Two conditions must be distinguished in the consideration of tangential forces between bodies in rolling contact: partial slip and complete slip. The former case characterizes the condition where the tangential traction only reaches a limiting value (slip) over part of the contact region [11,12]. On the other hand, a condition of complete slip implies an appreciable relative velocity between the contacting surfaces with the tangential force, T , at its limiting value, μP . The condition of complete slip is inherently simpler to analyze and has been considered in the elastic range by Smith and Liu [3]. It is usually assumed that the tangential traction is directly related to the normal Hertzian pressure at all points on the contact surface, with a maximum value

$$q = \mu \sigma_{app} \quad (2)$$

where

- q = maximum tractive stress, MPa, and
- μ = coefficient of contact friction.

For undriven ore car wheels, the tangential loading is generated primarily in curves due to differential wheel rolling distances, lateral slip associated with an angle of attack between wheel and rail [13], and lateral forces associated with axle bending motions during vehicle vertical motions [14].

Extension of the elastic analysis to the postyield condition has been carried out by Johnson and Jefferis [5] for an elastic-plastic material. Beyond initial yield, the maximum contact load which can be sustained by a body in rolling contact, with limited plastic deformation, is known as the shakedown limit. Adopting the von Mises yield criterion, the effect of tangential slip on the limit of elastic behavior and on the shakedown limit is shown in Fig. 1. Thus, for a prescribed tangential/normal force ratio, the limiting ratio of the maximum normal stress, σ_{all} , to the material yield stress in shear, k , is defined on the ordinate axis.

The shakedown limits in Fig. 1 are conveniently defined in terms of surface loads only, without reference to the detailed stress distribution below the surface. However, it must be appreciated that the addition of a tangential force introduces a severe state of stress at the surface, and, for values above $0.37P$, shakedown will be controlled by the surface stresses rather than the subsurface conditions [5].

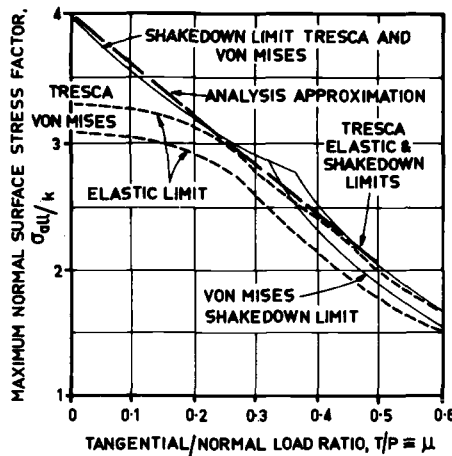


FIG. 1—Yield and shakedown limits in plane strain with combined normal and tangential loading [5].

For practical application, the curve defining the shakedown limit may be approximated by the linear relationship

$$\sigma_{all} = 2.31 (1 - T/P)Y \quad (3a)$$

or, allowing for the conservative condition of complete slip

$$\sigma_{all} = 2.31 (1 - \mu)Y \quad (3b)$$

where

- σ_{all} = maximum normal stress to achieve shakedown, MPa, and
- Y = yield stress in tension, MPa
- = $k\sqrt{3}$ (von Mises).

Equations 1 and 3b provide the deterministic relationships between applied loading, contact geometry, and the shakedown limit from which the maximum permissible wheel loading may be determined. To apply these to the distributions of loading noted in practice, it is necessary to reformulate the expressions in a probabilistic format.

Formulation of a Reliability Function

Since rail defects due to gross plastic deformation are the result of cumulative damage, it is not necessary to preclude the exceedance of the shakedown limit by the applied stress, but it is necessary to ensure that the frequency with which it occurs is sufficiently small such that rail replacement takes place for other reasons prior to the development of an unacceptable degree of deformation. Diagrammatically, this means that the overlap

between the distributions of applied contact stress, σ_{app} , and the maximum permissible contact stress, σ_{all} , has to be limited to a predetermined level (Fig. 2). Expressed mathematically, it is required to determine the reliability, R , against yield such that the contact stress between the wheel and rail will not exceed the shakedown limit of the material, whereby

$$R = \text{prob} (\sigma_{all} > \sigma_{app}) \quad (4)$$

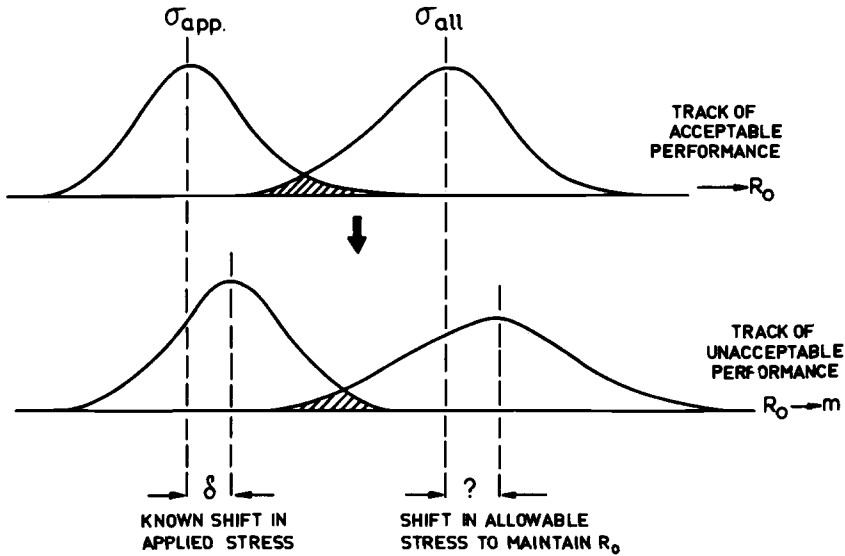


FIG. 2—Interaction between applied contact stress and allowable stress at constant reliability level, R_o .

However, the analysis is more readily accomplished by calculating the probability of yield, Q , (represented by the region of overlap) given by

$$Q = 1 - R \quad (5)$$

$$\begin{aligned} &= \text{prob} (\sigma_{all} \leq \sigma_{app}) \\ &= \int_{-\infty}^{\infty} \text{prob} (\sigma_{all} \leq z) \text{prob} (z \leq \sigma_{app} < z + dz) dz \\ &= \int_{-\infty}^{\infty} F_{all}(z) f_{app}(z) dz \end{aligned} \quad (6)$$

in which $F_{all}(z)$ is the allowable stress cumulative probability distribution function and $f_{app}(z)$ is the applied stress probability density function.

Now, the allowable stress cumulative probability function is given by

$$\begin{aligned} F_{all}(z) &= \text{prob} (\sigma_{all} \leq z) \\ &= \text{prob} (2.31 Y - z / (1 - \mu) \leq 0) \end{aligned} \quad (7)$$

If we assume Y and $1/(1 - \mu)$ to be normally distributed, then, for a given z , $(2.31 Y - z/(1 - \mu))$ is the difference of two normal random variables and is itself normally distributed. Thus, Eq 7 reduces to

$$F_{\text{all}}(z) = F_u \left(\frac{(zm_{\mu'} - m_Y)}{\sqrt{s^2_{Y'} + z^2 s_{\mu'}^2}} \right) \quad (8)$$

where

$$Y' = 2.31 Y,$$

$$\mu' = 1/(1 - \mu), \text{ and}$$

$$F_u = \text{cumulative distribution function of the standard normal variable with mean zero and standard deviation of one.}$$

The argument may be evaluated using the relationships

$$\begin{aligned} m_{Y'} &= 2.31 m_Y & m_{\mu} &= \frac{1}{1 - m_{\mu}} \\ s_{Y'}^2 &= (2.31)^2 s_Y^2 & s_{\mu'}^2 &= \frac{s_{\mu}^2}{(1 - m_{\mu})^2 [(1 - m_{\mu})^2 + s_{\mu}^2]} \end{aligned}$$

in which m and s denote the mean and standard deviations, respectively, of the subscripted variables.

For the applied stress, Eq 1, the material parameters E and ν can be treated as constants, and the wheel radius has a sufficiently small variation to be treated as a constant. Hence, if it is assumed that w and P are independent normal variables, then the derivation of the density function $f_{\text{app}}(z)$ involves the derivation of the density function for the quotient of two independent random variables. Consequently, it can be shown (see Appendix) that

$$f_{\text{app}}(z) = \frac{2z(\lambda^2 m_w s_P^2 s_w^2 z^2)}{\sqrt{2\pi(\lambda^2 s_P^2 + s_w^2 z^4)^3}} \exp \left[\frac{-(\lambda m_P - m_w z^2)^2}{2(\lambda^2 s_P^2 + s_w^2 z^4)} \right] \quad (9)$$

in which $\lambda = 0.16E/[(1 - \nu^2)r]$. Thus, substitution for $F_{\text{all}}(z)$ and $f_{\text{app}}(z)$ from Eqs 8 and 9, respectively, into Eq 6 defines the probability of yield, Q , for specified values of the load, strength, and geometry parameters. Solution of Eq 6 can be accomplished by numerical integration and the reliability level obtained from Eq 5. Alternatively, if a desirable reliability R_0 is prescribed, Eq 6 may be solved iteratively for any parameter in terms of the other parameters which may be adjusted to achieve that reliability. This is the case of interest.

Derivation of the reliability function is based on the assumption that each of the material 0.2 percent proof stress, Y , the applied wheel load, P , the wheel/rail contact width, w , and the wheel/rail friction parameter, $1/(1 - \mu)$, are normally distributed. A review of available data on these parameters applicable to unit train operations is covered in Ref 6 to which the reader is

referred. Within the limits of the data, the assumptions are acceptable at the reliability level of around 90 percent determined later since the results of the analyses are little influenced by the shape of the extremes of the tails of the distribution function adopted at this reliability level.

The assumption of independence between P and w recognizes the more significant variation in w due to wear of the wheel and rail profiles in comparison with changes due to variation of P about the mean value.

Determination of Rail Strength Level

To apply the foregoing analysis to the determination of the rail strength level necessary to overcome gross plastic flow, it is necessary to have specified an acceptable reliability, R_0 , around which the system parameters may be adjusted. In the case of the operations of the Mt. Newman Mining Co., gross plastic deformation and railhead corrugation are almost entirely limited to curved track. Thus, the loading and strength parameters observed in tangent track may be substituted into Eq 6 to evaluate R_0 , a procedure which also compensates for nonproportional damage which may arise due to high loads of the spectrum since tangent track will have experienced similar conditions. The objective is to achieve this same reliability in curved track by adjusting the material strength properties as shown in Fig. 2.

So far, no account has been taken of the fact that, under rail traffic, the material near the running surface of a rail undergoes work hardening during plastic deformation. A measure of the degree of work hardening for tangent track on the Mt. Newman operations has been obtained by correlating microhardness plots of deformed rails with material which has been deformed under controlled conditions.³ Comparisons were also made of the deformed microstructure in both instances to ensure a similar mode of material deformation behavior [15]. Plots of the hardness-depth relationships for tangent and curved track are given in Fig. 3, the significant difference being severe deformation near the surface of the latter.

Since it has been implied that the degree of deformation experienced in tangent track is acceptable in that corrugations are not generally evident in tangent track, then the same margin of strength increase beyond the 0.2 percent proof stress should be provided in curved track to compensate for work hardening. As the work hardening rates of standard rail and higher strength rails are dissimilar, it is necessary to adjust the predictions of strength level based on the 0.2 percent proof values. Selection of the required higher strength steel involves the evaluation of the work hardened strength level at the level of deformation found in tangent track rails.

Usually, the necessary data are not available to do this; however, an adequate approximation can be made from a knowledge of the 0.2 percent proof/ultimate tensile strength ratio. Thus, if we assume

$$(F_u)_{\text{high strength}} = (F_u)_{\text{standard}} + \alpha \quad (10)$$

³Marich, S. and Curcio, P. this publication, pp. 167-211.

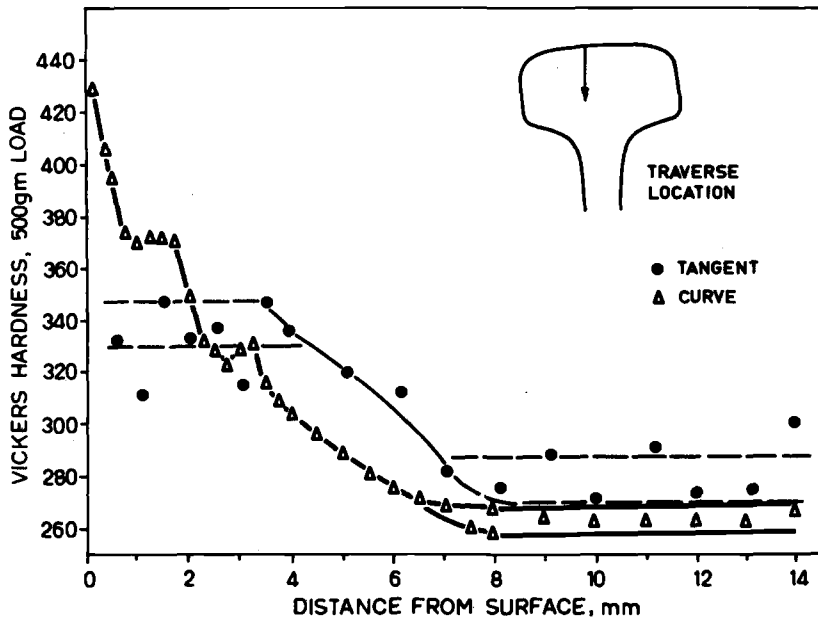


FIG. 3—Microhardness distributions below the rail running surface.

then

$$(Y)_{\text{high strength}} = \frac{(Y)_{\text{high strength}}}{(F_u)_{\text{high strength}}} [(F_u)_{\text{standard}} + \alpha] \quad (11)$$

where

F_u = ultimate tensile strength, MPa,

Y = 0.2 percent proof stress, MPa, and

α = strength increment at 0.2 percent proof stress level, MPa.

Referring to Fig. 4 which relates measured 0.2 percent proof stress/ultimate tensile strength ratios for rail steels and adopting the conservative relationship given, then the resulting expression for the determination of required 0.2 percent proof stress of high-strength rail steel allowing for differences in work hardening rate becomes

$$(Y)_{\text{high strength}} = \frac{1206400 Y_s + 580\alpha Y_s + 33640\alpha}{1206400 - \alpha Y_s - 580\alpha}, \text{ MPa} \quad (12)$$

where $Y_s = (Y)_{\text{standard}}$, MPa.

Application of Reliability Analysis

Formulation of the reliability analysis approach was undertaken to obtain a better understanding of the significance of load distribution on the performance of rail steel and thereby obtain a reasonable estimate of the

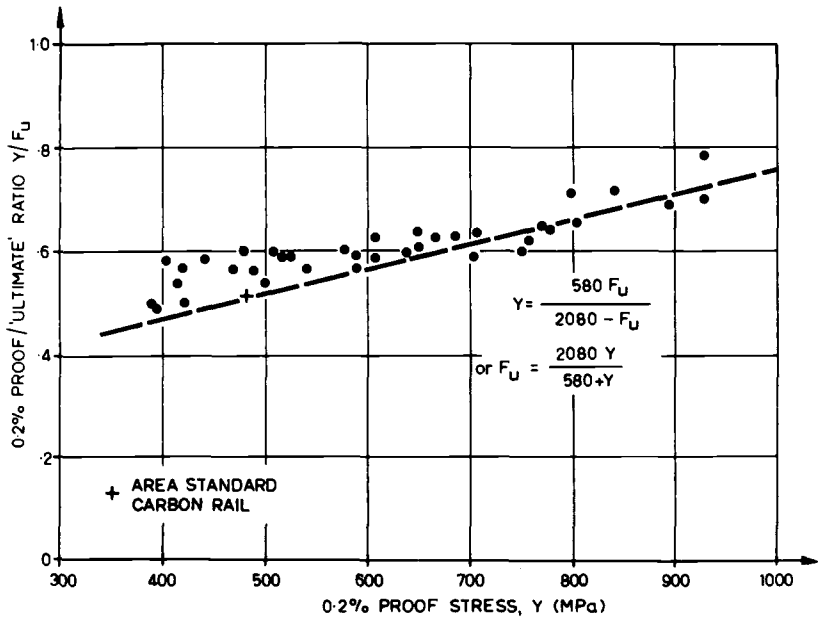


FIG. 4—Variation of Y/F_u with Y for a range of as-rolled rail steels (Footnote 3, [16–18]).

necessary strength level to avoid corrugations on the Mt. Newman Mining Co. rail system. Table 1 lists the measured standard deviations of the loading and geometry parameters adopted for curved and tangent track on that system. Substitution of the tangent track parameters into Eq 6 gives a reliability value, R_0 , of 92 percent for adoption in curved track.

No increase in vertical wheel load has been incorporated between tangent and curved track. Generally, loaded train wheel loading was well balanced between high and low rails as determined by track measurements; however, Fig. 5 specifies the adjustment to rail strength if the loading is not balanced. A mean coefficient of friction of 0.3 has been adopted for curves based on available data, and a mean value of 0.0 (that is, no surface tangential loads) has been conservatively adopted for tangent track, although it is unlikely that this is actually the case for all ore cars. The standard deviation of the 0.2 percent proof stress for the high-strength rail has been taken as 40 MPa, the

TABLE 1—Design values of loading and geometry parameters for determination of required mean yield stress (mean, standard deviation).

Parameter	Tangent	Curves
Vertical load, P (kN)	(151, 16.4)	(151, 16.4)
Coefficient of friction, μ	(0.0, 0.02)	(0.3, 0.02)
Contact width, w (mm)	(12, 2)	(12, 2)
Yield stress, Y (MPa)	(500, 40)	(?, 40)

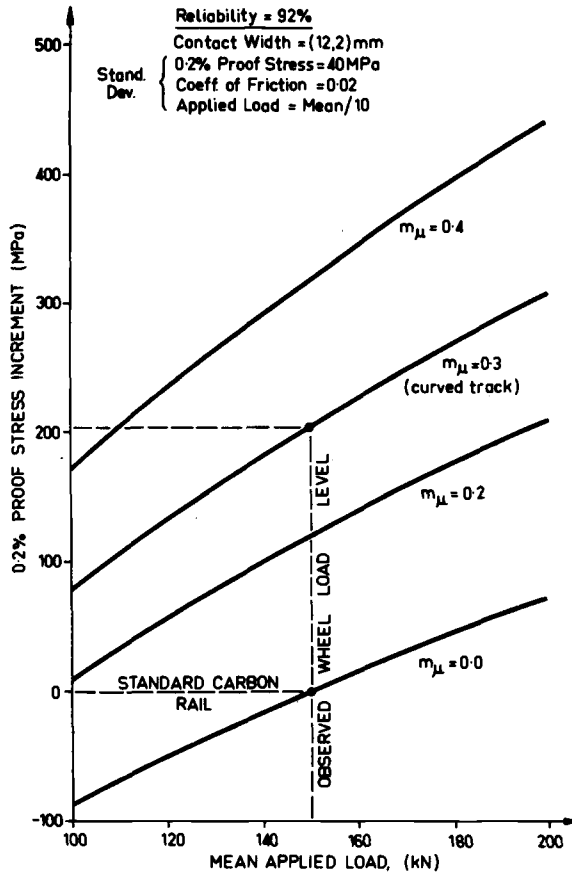


FIG. 5—Interaction between mean wheel load, surface traction, and 0.2 percent proof stress increment.

same as the standard material, based on laboratory tests. Thus, the only unknown parameter is the mean 0.2 percent proof value of the higher strength rail steel. Figures 5–8 indicate the sensitivity of the unadjusted 0.2 percent proof stress increment to variations in contact area, mean applied wheel load, coefficient of friction, spread of wheel loads, and the spread of the rail steel strengths.

The interaction between the three most significant parameters, namely, the mean wheel load, the coefficient of friction, and the mean 0.2 percent proof stress, is given in Fig. 5 from which the strength level increment for high-strength rail steel to minimize plastic flow which can lead to corrugation development is noted to be 205 MPa.

(Previous literature supports the need for plastic deformation in the development of long pitch corrugations [14,19,20], however, plastic flow alone is not sufficient. It has been suggested [21,22] that excitation of

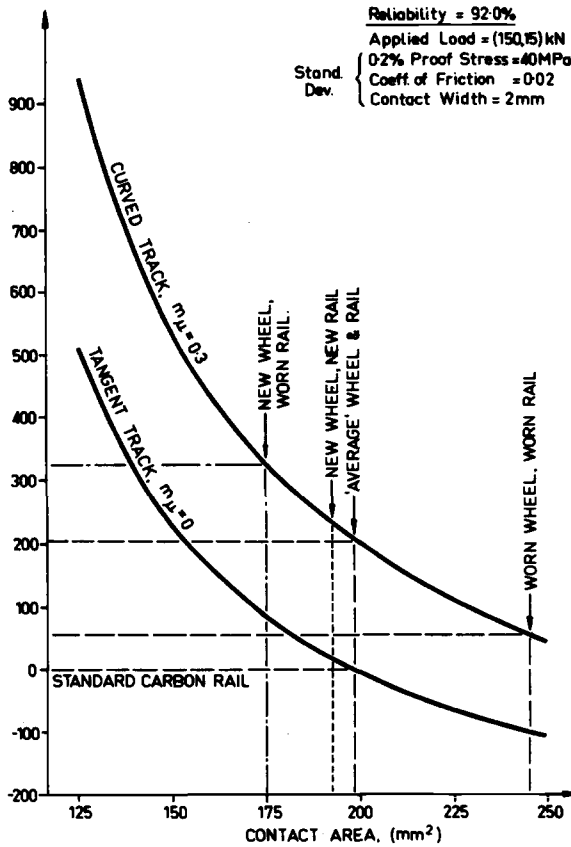


FIG. 6—Interaction between wheel/rail contact area and 0.2 percent proof stress increment for tangent and curved track.

resonance of the track/vehicle system is also necessary to generate the characteristic deformation pattern. Alternative factors including railhead fatigue damage [23] contribute by increasing the vibration input which induces resonance. Conversely, avoidance of gross plastic deformation is sufficient to suppress corrugation formation and can be confirmed from observations on tangent track for rail operations noted to have corrugations in curves and on curves where higher yield strength rails have been installed of a sufficient strength to suppress corrugation formation (see following section.)

The presence of tangential friction forces has an obviously large influence on the required strength level. Any modification which can be introduced to reduce the friction level, even if only partially, will be beneficial in lowering the probability of yield and corrugation development. However, it is difficult to quantify the magnitude of the tangential friction forces and thus evaluate the beneficial effects of any modifications on a limited scale.

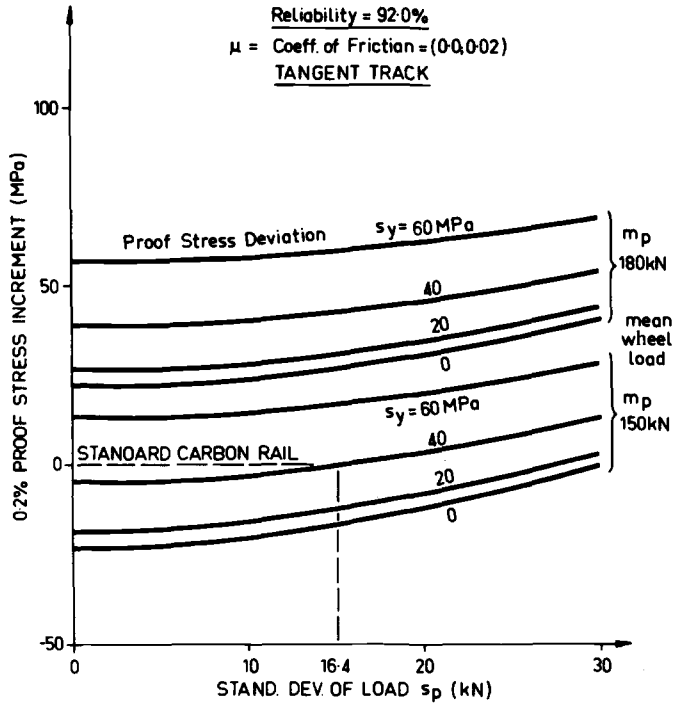


FIG. 7—Interaction between spread of wheel load and 0.2 percent proof stress increment in tangent track.

The other important parameter, the contact area, has an influence on rail strength requirement as shown in Fig. 6. It is readily appreciated that there is a wide variation in contact areas between wheels and rails, but this is not so significant in terms of rail strength levels. Nevertheless, it is important to note from Fig. 6 that the worn wheel/worn rail condition requires a lower mean 0.2 percent proof stress increase for curves, and the new wheel/worn rail condition requires a higher 0.2 percent proof stress increase than for the average conditions adopted. The nominal increments in 0.2 percent proof stress for the conditions shown are:

Mean Wheel/Rail Condition	0.2 Percent Proof Stress Increment (MPa) Above Tangent Track Values
New wheel/new rail profiles	210
New wheel/worn rail profiles	240
Worn wheel/worn rail profiles	155
Average wheel/rail profiles	205

The average wheel/rail combination is adopted for the purpose of rail strength evaluation, giving an increment of 205 MPa for the case under consideration. Both extreme profile combinations tabulated in the preceding

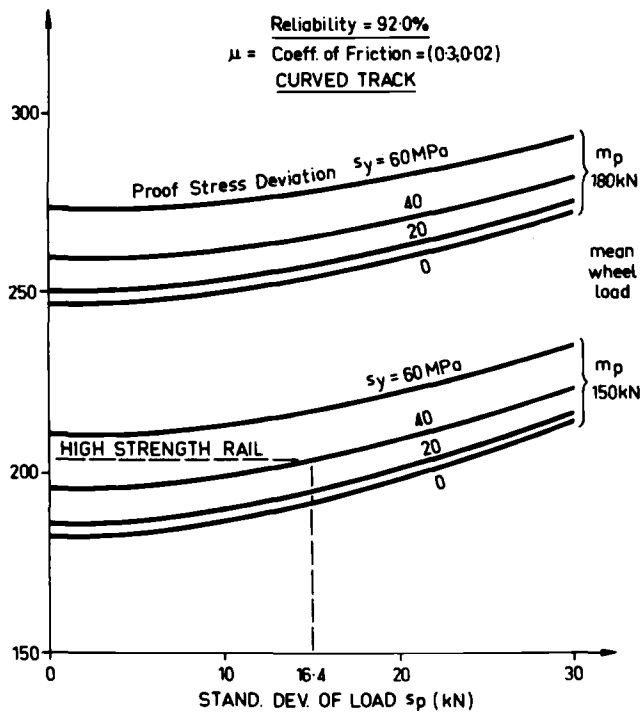


FIG. 8—Interaction between spread of wheel load and 0.2 percent proof stress increment in curved track.

table are included in the normal distribution of contact widths (areas) specified by the standard deviation of 2 mm and thus influence the strength increment in proportion to their relative frequency. Where worn wheel and rail profile data are not available, the new profile values can be substituted with only a marginal shift in strength requirements.

The advantage of the probabilistic solution over the purely deterministic procedure, in addition to the establishment of a rational reliability level based on tangent track performance, is the ability to evaluate the significance of the distribution of various parameters. Figures 7 and 8 present the relevant data for the two principal distributions: the spread of wheel load and the spread of strength values for tangent track ($m_\mu = 0.0$) and curved track ($m_\mu = 0.3$) conditions. The effect of a change in mean wheel load from 150 kN is also shown.

Several points are evident from an examination of the plotted data.

1. An increase in the standard deviation of either the 0.2 percent proof stress or the wheel load increases the mean 0.2 percent proof stress necessary to maintain the tangent track reliability level (that is, 92 percent).
2. The dependence on standard deviation of wheel load is greater in

curves than in tangent track. An increase in the standard deviation from 15 to 30 kN requires an additional mean 0.2 percent proof stress increase of 20 MPa.

3. The dependence on absolute standard deviation of proof stress level is lower in curves where the mean proof stress is higher for the same reliability. An increase in standard deviation of proof stress from 40 to 60 MPa requires an additional mean 0.2 percent proof stress increase of 15 MPa.
4. Reductions in the standard deviations have a much smaller influence on the required mean 0.2 percent proof stress level.

Overall, the necessary 0.2 percent proof stress increment for high-strength rails above the value for standard rail for the Mt. Newman Mining Co. is of the order of 205 MPa, without making any allowance for possible wheel profile changes. Thus, the unadjusted mean 0.2 percent proof stress level for high-strength rails in curves should be 705 MPa, and, employing Eq 12, the corresponding adjusted 0.2 percent proof stress is 745 MPa. This is the mean value. For the purposes of steel supply, it is preferable to specify the minimum 0.2 percent proof value which may be taken as the 5 percentile level given by

$$\begin{aligned}(Y)_{\min} &= (Y)_{\text{mean}} - 1.96s_y \\ &= 670 \text{ MPa}\end{aligned}\tag{13}$$

For the Mt. Newman Mining Co. operations, the actual minimum 0.2 percent proof stress value recommended was 690 MPa. This is marginally higher than the value obtained from Eq 13 because of an adjustment to compensate for estimates made in arriving at the standard deviation of the strength values listed in Table 1 from a limited number of tests.

Service Performance Results

High-strength rail steels have been installed in track for service evaluation (Footnote 3). Initial observations have been obtained from a 2-deg (870-m-radius) curve prone to corrugation and the railhead profile compared with adjacent lengths of standard carbon rails to American Railway Engineering Association (AREA) chemistry. Figure 9 plots the railhead vertical profile at two connecting welds between the standard and high-strength rails and illustrates the difference in performance observed [24]. The measured material properties are shown in Tables 2 and 3.

Corrugations are evident on the standard rail string on the port side of a thermite weld, whereas the high-strength material of 630 MPa proof stress is free from corrugation. Conversely, the corrugation pattern which exists at the start of the standard rail string (four rails) is substantially diminished at the exit end, whereas minor evidence of corrugation is notable in the high-strength rail of 690 MPa, presumably as a carry-over from the standard material.

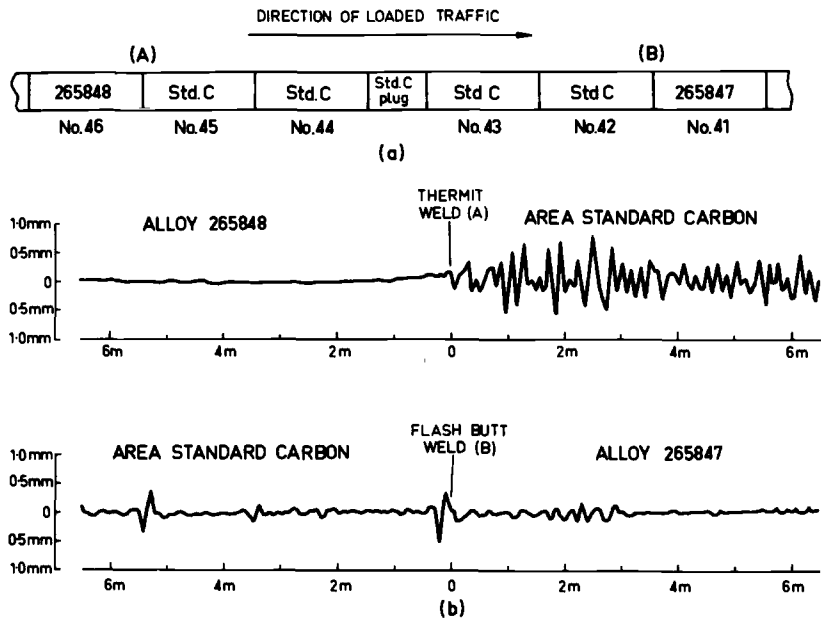


FIG. 9—Rail performance in 870-m curve: (a) rail configuration, (b) running surface profile at connecting welds.

On the basis of the available test results, a material 0.2 percent proof stress of 670 MPa as predicted is adequate to avoid corrugation formation on the Mt. Newman Mining Co. operations and provide a margin against flow equivalent to tangent track. Indeed, the limited test data indicate that a lower proof stress value may prevent corrugation, but the tests may not represent the most severe conditions.

As a further evaluation, a series of measurements of the zone of apparent wheel/rail contact were recorded from a range of high-strength alloy rails after approximately 35 million tonnes gross (Fig. 10). The test rails are installed in curves up to 3 deg (580 m radius) and represent different service conditions. It is apparent from the variation of contact zone width with 0.2 percent proof stress that the initial spread of the railhead is dependent on the rail strength level and approaches a minimum value at the higher strengths. By comparison, the mean 0.2 percent proof stress recommended represents a value close to the minimum contact zone width condition.

TABLE 2—Chemical composition of rails in 11.7-km curve.

Type	Carbon	Manga- nese	Silicon	Phos- phorus	Sulfur	Chro- mium	Colum- bium	Vanadium
Standard	0.75	0.83	0.13	0.02	0.03
265847	0.59	1.30	0.07	0.03	0.02	0.37	0.035	0.066
265848	0.63	1.30	0.08	0.03	0.03	0.61	0.036	0.070

TABLE 3—Tensile properties of rails in 11.7-km curve.

Type	0.2 Proof Stress, MPa	Ultimate Tensile Strength, MPa	Elongation, %	Reduction in Area, %
Standard	470	945	13	15
265847	688	1103	11	16
265848	633	1060	14	30

Further test data at higher tonnages will enable an improved evaluation of the prediction procedures. The current procedure provides a conservative estimate of rail strength requirements at heavy axle loads to limit plastic flow and avoid rail corrugation development and may be used with confidence for other rail systems.

Conclusion

An analysis procedure has been developed to predict the proof stress requirements of rail steels in curves with a predetermined reliability against the formation of gross plastic deformation. The procedure is based on shakedown under rolling contact with empirical adjustment of the results to allow for work hardening. Application of the procedure has been made to the unit train operations of the Mt. Newman Mining Co.

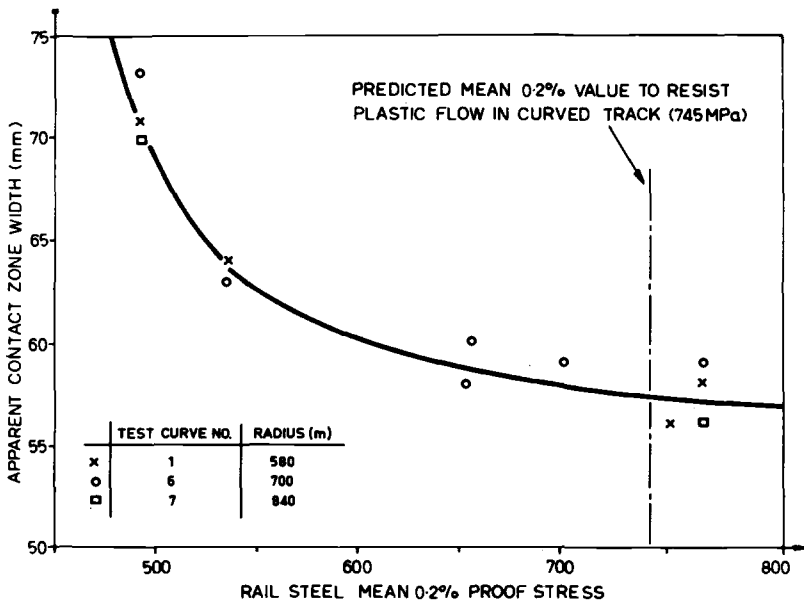


FIG. 10—Relation between contact zone width and mean 0.2 percent proof stress.

The most significant parameter leading to the development of plastic flow and corrugation in curves is the traction force at the wheel/rail interface. A large standard deviation of either the applied loading or the material proof stress contributes to the requirement for an increase in the mean proof stress level, but, within the range of standard deviations of loading and material properties generally recorded, neither variation is as significant as the mean wheel load level. Additional data on contact geometry and wheel/rail friction conditions are required to increase the accuracy of the analysis procedure.

For the Mt. Newman operation at 150-kN wheel load, it was calculated that a minimum 0.2 percent proof stress of 670 MPa is required to suppress gross plastic deformation and corrugation on the high rail of curves. Experimental confirmation of the prediction method shows that it is conservative.

Acknowledgments

This study was conducted on behalf of Mt. Newman Mining Co. Pty. Ltd. as part of investigations into the behavior and design of rail tracks for heavy axle loads. The support and assistance of R. Murphy (Railroad Manager) and R. A. Jupp (Technical Superintendent Railways) is gratefully acknowledged.

APPENDIX

Density Function of Quotient of Two Independent Random Variables

Consider two independent random variables X and Y . Let $Z = Y/X$, then the joint density of X and Z may be written [25]

$$h(x, z) = f_X(x) \phi(z/x)$$

where $\phi(z/x)$ is the conditional probability function of Z given X . Thus

$$f_Z(z) = \int_{-\infty}^{\infty} h(x, z) dx = \int_{-\infty}^{\infty} x f_X(x) f_Y(xz) dx$$

If X and Y are normally distributed with means m_1 , m_2 and standard deviations s_1 , s_2 , respectively, then

$$\begin{aligned} f_{Y/X}(z) = f_Z(z) &= \frac{1}{2\pi s_1 s_2} \int_{-\infty}^{\infty} \exp \left[- \left[\frac{(x - m_1)^2}{2s_1^2} + \frac{(xz - m_2)^2}{2s_2^2} \right] \right] dx \\ &= \frac{m_1 s_2^2 + m_2 s_1^2 z}{\sqrt{2\pi(s_2^2 + s_1^2 z^2)^3}} \exp \left[- \frac{(m_2 - m_1 z)^2}{2(s_2^2 + s_1^2 z^2)} \right] \end{aligned}$$

Since $f_{\sqrt{P}}(v) = 2vf_i(v^2)$ for any random variable V , and substituting

$$\begin{array}{lll} Y = \lambda P & m_2 = \lambda m_p & s^2 = \lambda s_p \\ X = w & m_1 = m_w & s_1 = s_w \end{array}$$

then

$$f_{\text{app}}(z) = f_{\frac{\lambda P}{w}}(z) = \frac{2z(\lambda^2 m_w s_p^2 + \lambda m_p s_w^2 z)}{\sqrt{2\pi(\lambda^2 s_p^2 + s_w^2 z^4)^3}} \exp \left[\frac{-(\lambda m_p - m_w z^2)^2}{2(\lambda^2 s_p^2 + s_w^2 z^4)} \right]$$

References

- [1] Thomas, H. R. and Hoersch, V. A., "Stresses Due to the Pressure of One Elastic Solid Upon Another," Bulletin 212, Engineering Experimental Station, University of Illinois, 1930.
- [2] Beliaev, N. M., "The Calculation of Maximum Stresses at the Compression of Bodies," Leningrad Institute of Railway Engineering No. 102, 1929, pp. 151-174 (in Russian).
- [3] Smith, J. O. and Liu, C. K., *Transactions of the ASME, Journal of Applied Mechanics*, American Society of Mechanical Engineers, June 1953, pp. 157-166.
- [4] Johnson, K. L., *Proceedings of the U. S. National Congress on Applied Mechanics*, Vol. 2, 1963, pp. 971-975.
- [5] Johnson, K. L. and Jefferis, J. A., *Fatigue in Rolling Contact*, Session 2, Paper 5, Institution of Mechanical Engineers, 1963, pp. 54-65.
- [6] Mair, R. I. and Groenhout, R., "Balanced Loading of Rails—A Probabilistic Approach," BHP Melbourne Research Laboratories Report MRL/181/75/010, Dec. 1975.
- [7] Paul, B., "A Review of Rail-Wheel Contact Stress Problems," Report MEAM 75-1, Dept. of Mechanical Engineering and Applied Mechanics, University of Pennsylvania, April 1975.
- [8] Eisenmann, J., *Proceedings*, American Railway Engineering Association, Vol. 71, 1970, pp. 24-59.
- [9] Andrews, H. I., *Wear*, Vol. 2, No. 6, 1958/1959, pp. 468-484.
- [10] Andrews, H. I., "The Creep of Locomotive Driving Wheels, Part 1," *Rail Engineering International*, Vol. 5, No. 1, 1975.
- [11] Carter, F. W., "On The Action of a Locomotive Driving Wheel," *Proceedings of the Royal Society, A*, Vol. 112, 1926.
- [12] Poritsky, H., *Transactions of the ASME, Journal of Applied Mechanics*, American Society of Mechanical Engineers, Vol. 72, 1950, pp. 191-201.
- [13] Marta, H. A., Mels, K. D., and Itami, G. S., "The Friction Creep Phenomenon of Adhesive Between Steel Wheels and Rails," *Rail Transportation Proceedings*, American Society of Mechanical Engineers, 1971.
- [14] Peterson, L. A., Freeman, W. H., and Wandrisco, J. M., "Measurement and Analysis of Wheel-Rail Forces," ASME Paper No. 71-WA/RT-4, 1971.
- [15] Marich, S. and Curcio, P., "Work Hardening of Standard Rail Steels", BHP Melbourne Research Laboratories Report MRL/083/75/006, April 1975.
- [16] Marich, S., *Rail Track Materials Seminar*, BHP Melbourne Research Laboratories, Oct. 1971, pp. 91-109.
- [17] De Sy, A. L., Dilewijn, J., and Goethals, G., "Development of a High Yield Strength Cu-Ni-Cr-Nb Rail Steel," *Rail Steels*, Iron and Steel Institute Meeting, London, Nov. 1972.
- [18] Cannon, D. F. et al., "The Fracture Toughness of Rail Steels," *Rail Steels*, Iron and Steel Institute Meeting, London, Nov. 1972.
- [19] Meacham, H. C. and Ahlbeck, D. R., "A Computer Study of Dynamic Loads Caused by Vehicle-Track Interaction," ASME Paper No. 69-RR-1, American Society of Mechanical Engineers, 1969.

- [20] Meacham, H. C. and Ahlbeck, D. R., "Wheel-Rail Dynamics of Loaded Ore Cars on the QCM and BLE Railroads," Project Report, Quebec Cartier Mining, Oct. 1970.
- [21] Mair, R. I. and Jupp, R. A., *Annual Engineering Conference*, Institution of Engineers, Australia, May 1976, pp. 383-387.
- [22] Groenhout, R. and Mair, R. I., "Spectral Analysis of Rail Corrugations at 217.9 km," BHP Melbourne Research Laboratories Report MRL/081/75/012, Dec. 1975.
- [23] Kalousek, J., "Rail Corrugations," Dept. of Research, Canadian Pacific Ltd., Rep. No. 5488-57, Feb. 1975.
- [24] Marich, S. and Curcio, P., "The Examination of Rails from 11.7 km Curve after 94 M.G.T.," BHP Melbourne Research Laboratories Report MRL/083/75/009, Nov. 1975.
- [25] Haugen, E. B., *Probabilistic Approaches to Design*, J. Wiley and Son, 1969.

Fatigue in Rail Steels

The Effect of Grain Boundary Ferrite on Fatigue Crack Propagation in Pearlitic Rail Steels

REFERENCE: Fowler, G. J. and Tetelman, A. S., "The Effect of Grain Boundary Ferrite on Fatigue Crack Propagation in Pearlitic Rail Steels," *Rail Steels—Developments, Processing, and Use*, ASTM STP 644, D. H. Stone and G. G. Knupp, Eds., American Society for Testing and Materials, 1978, pp. 363–386.

ABSTRACT: Fatigue crack growth has been examined in pearlitic rail steels to determine the effect of grain boundary ferrite and nonmetallic inclusions on the rates of crack propagation under Mode I loading at ambient temperature. The influence of alternating and maximum stress intensity on fatigue crack propagation in these materials has also been evaluated. The data were obtained using single-edge notch specimens machined from the head of rails and the web of wheels. Cyclic loading was performed on a hydraulic test machine at various R ratios.

As the maximum stress intensity, K_{max} , approaches the fracture toughness, K_{IC} , increasing amounts of cleavage bursts occur and the crack growth rates increase. In steels containing ferrite at the prior austenite grain boundary, the amount of cleavage is reduced at a given K level and the growth rates are reduced by an order of magnitude. The results show that traces of grain boundary ferrite (~2 to 4 percent by volume) can reduce crack growth rates by a factor of two at intermediate and low growth rates ($<5 \times 10^{-4}$ mm/cycle).

Increasing R ratio is shown to increase significantly the fatigue crack growth rate near K_{IC} , due to the increase in percent cleavage, while little effect of R ratio is observed at intermediate growth rates. Stable fatigue growth is observed above K_{IC} and is explained in terms of a pop-in model.

Inclusions were observed occasionally at the initiation site of a stable cleavage burst that occurred during fatigue. However, nonmetallic inclusions do not significantly affect the fatigue crack growth rates in rail steels within the range of inclusion content from 0.097 to 0.318 percent by area.

KEY WORDS: steels, railroad tracks, fatigue (materials), crack propagation, microstructure, fracture, inclusions

A frequent cause of rail failure is plastic deformation of the railhead due to heavy rolling loads transmitted through the wheel/rail contact surface [1,2].² Horizontal cracks called shells or shelly spots develop, usually on the gage corner of the railhead. Shells can then act as nucleation sites for vertical

¹Postgraduate research engineer and professor of engineering, respectively, Materials Department, University of California, Los Angeles, Calif. 90024.

²The italic numbers in brackets refer to the list of references appended to this paper.

crack formation and extension by fatigue called "detail fracture from shelling." In addition to shells and detail fractures, rail failures occur by other failure modes [3]. One common feature that most of the failures possess is the occurrence of crack extension by fatigue.

Fatigue crack propagation is a progressive form of crack extension that occurs under the action of cyclic loading. The crack advances an incremental amount during the loading cycle until the crack reaches a critical length, whereupon unstable fracture occurs. Incremental crack growth per cycle, da/dN , is generally plotted as a function of the change in stress intensity factor, ΔK , on a double logarithm plot. Typically, the crack growth curve (da/dN versus ΔK) is sigmoidal in shape and bounded at the lower end by a threshold stress intensity, ΔK_{th} , and at the upper end by the critical stress intensity factor, K_{Ic} . Ideally, ΔK_{th} defines the lower value of ΔK below which the crack will not propagate, and K_{Ic} defines the condition for unstable crack propagation.

The crack growth curve can be divided into three regions depending on the mechanism involved in propagating the crack [4]. The mechanisms of crack propagation vary with stress intensity level and can be influenced by secondary variables such as loading ratio ($R = K_{min}/K_{max}$), frequency, and environment. At values of ΔK near ΔK_{th} (Region A), the fracture mode is sensitive to the microstructure and exhibits a combination of planar facets in the form of intergranular fracture [5], and interlamellar pearlite separation [6], and areas of fatigue striations. The occurrence of the planar facets in steels and titanium alloys has been shown to commence when the reverse plastic zone size is approximately equal to or less than the microstructure unit size, for example, ferrite grain size [7,8]. Robinson and Beevers [7] have proposed a two-component mechanism for crack extension in Region A based on the separate effects of ΔK and K_{max} . Experimental work performed on low-alloy steels has shown that crack growth in this region is sensitive to K_{max} [6,7]. As ΔK increases, the size of the reverse crack tip plasticity exceeds the microstructure unit size, at which point structure insensitive striation growth occurs (Region B). Various mechanisms of striation formation have been proposed based on reverse crack tip plasticity [9,10]. Because the reverse crack tip plasticity during striation formation depends primarily on ΔK , it is expected that K_{max} will not have a strong influence in Region B. As K_{max} approaches K_{Ic} , the crack growth rate deviates from the double logarithm linear relation and accelerates for many metals (Region C). Fractographic examination of these fatigue surfaces shows that the mechanism of crack extension changes from exclusively striation formation to a combination of striations mixed with intergranular separation [5], microcleavage [4,11], and void coalescence [12]. The crack growth rate in Region C is strongly K_{max} dependent.

The influence of nonmetallic inclusions on the fatigue crack propagation rate depends upon the stress intensity level. Broek [13] has shown that the crack propagation rate in aluminum alloys is not influenced by the presence of

inclusions until high growth rates are achieved, whereupon inclusions promote microvoid formation ahead of the crack and linkup with the main crack front by ductile tearing. Shik and Araki [14] conclude that the crack growth rate in high-strength carbon steel is dependent on the total inclusion content but is probably independent of the inclusion type. Their conclusions were reached after examining data from the high growth rate region (Region C). In general, inclusions appear to have an effect in the high growth rate region without a significant effect on Region B crack mechanisms.

The purpose of the present work is to examine the effect of grain boundary ferrite and nonmetallic inclusions on the rate and mechanism of fatigue propagation in pearlitic rail and wheel steels. Nonmetallic inclusions are introduced into rail and wheel materials during manufacturing and are generally deformed into different shapes depending on the rolling conditions and the properties of the inclusions. The effect of the nonmetallic inclusions on the rate of crack propagation has not been examined for rail steels currently used today. In addition, variations in carbon content slightly below 0.8 percent by weight result in a layer of ferrite outlining the prior austenite grains. Because some rail and wheel steels do not contain a layer of ferrite, the resulting effect on crack growth rate is of importance.

Experimental Procedures

The material used in this investigation was fully pearlitic steel commonly used as a railroad track and Class U wheels. Rails and wheels are produced by hot rolling directly from an ingot and subsequently cooled by a controlled cooling process [3,15]. Five representative rail steels and two wheel steels were selected by D. H. Stone of the Association of American Railroads, based on the inclusion content and microstructure, after examining 50 rails and 4 wrought steel wheels. For convenience, the rail material is labeled Rail 1 to Rail 5 and the wheel material is Wheel 1 and Wheel 2. The composition of the steel is shown in Table 1.

The microstructure of Rails 1 to 3 and Wheel 1 consisted of a fully pearlitic structure as shown in Fig. 1a. Rail 5 and Wheel 2 contained a ferrite layer along the prior austenite grain boundary with a thickness of approxi-

TABLE 1—*Chemical composition of the steels tested.*

Steel	C	Mn	Si	S	P
Rail 1	0.74	0.85	0.17	0.030	0.025
Rail 2	0.79	0.85	0.18	0.030	0.025
Rail 3	0.76	0.92	0.15	0.042	0.012
Rail 4	0.72	0.73	0.14	0.018	0.010
Rail 5	0.69	0.73	0.12	0.034	0.013
Wheel 1	0.74	0.68	0.27	0.040	0.018
Wheel 2	0.69	0.70	0.13	0.040	0.020

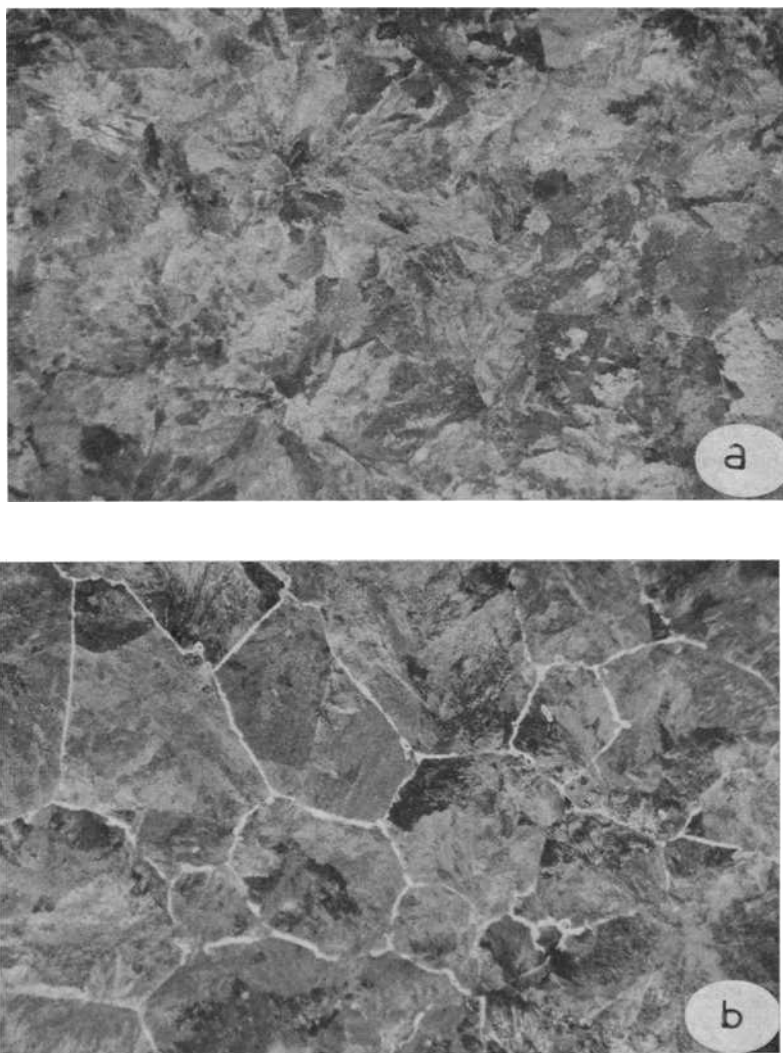


FIG. 1—Microstructure: (a) pearlitic structure typical of Rail 1 to Rail 3 and Wheel 1 ($\times 100$) and (b) ferrite along prior austenite grain boundary in Rail 5 ($\times 100$).

mately 5.0×10^{-3} and 2.5×10^{-3} mm, respectively, as shown in Fig. 1b. Rail 4 contained traces of ferrite that partially outlined some of the prior austenite grain boundaries but was not continuous. The pearlite colony size and prior austenite grain size were determined by comparing them to an ASTM optical grain size comparator. This procedure gave the ASTM grain size number which was then converted to an average size diameter. The pearlite colony size is 5.0×10^{-2} and 1.1×10^{-1} mm for the rail and wheel steel, respectively. The prior austenite grain size for Rail 5 and Wheel 2 is $2.0 \times$

10^{-1} and 2.8×10^{-1} mm, respectively. The prior austenite grain size was not determined for those steels that did not contain a continuous ferrite layer. The pearlite spacing for all the steels was determined by a line intercept method and was found to be approximately the same. The spacing varied within the bounds of 2.0×10^{-4} to 1.3×10^{-3} mm, with the majority of the grains having a spacing of 2.5×10^{-4} mm. The tensile properties were determined using a standard ASTM 0.505 tensile specimen (ASTM Standard Methods of Tension Testing of Metallic Materials (E 8-69)) and are shown in Table 2.

TABLE 2—*Tensile properties.*

Steel	0.2% Offset Yield Strength, MN·m ^{-2a}	Ultimate Tensile Strength, MN·m ⁻²	Reduction in Area, %
Rail 1	482	936	11.9
Rail 2	556	952	9.4
Rail 3	476	934	14.2
Rail 4	451	872	14.9
Rail 5	417	836	17.3
Wheel 1	495	840	5.3
Wheel 2	526	879	8.8

NOTE—Values represent average of two samples tested.

^a1 MN·m⁻² = 0.145 ksi.

Quantitative assessment of the inclusion content was made using an image analysis system (Bausch and Lomb Omnicon). The quantitative results are given in Table 3. The railhead contained mostly sulfide stringer inclusions aligned parallel to the rail axis (Fig. 2a). The wheel steels contained mostly sulfide inclusions that were of a spheroidal shape (Fig. 2b). Both groups of materials contained a smaller portion of oxide-type inclusions which were generally encapsulated by sulfide inclusions.

The specimens used for the crack growth rate studies were machined either from the head of rails or from the plate region of the wheels, all of which had been in service for 5 to 20 years. The rail specimens were oriented such that the crack plane was in the traverse railhead plane and the crack propagation direction was from one side of the railhead to the other side. The crack direction for the wheel samples were in a circumferential direction in the wheel plate.

Single-edge-notched, pin-loaded specimens of nominal dimensions 10 by 40 by 170 mm were fatigue tested on a hydraulically driven machine (MTS 810). A sinusoidal load was applied at an average frequency of 10 Hz. The crack lengths were optically measured using a $\times 25$ microscope with 0.1-mm divisions scribed on the lens. The threshold value of the stress intensity factor, ΔK_{th} , was determined by reducing the load in increments corres-

TABLE 3—Quantitative metallography of inclusion content.

Steel	Average Area Percent Per Field ^{a, b}	Number of Fields ≥0.5 Area Percent ^c
Rail 1 ^c	0.185	29
Rail 2	0.137	10
Rail 3	0.253	64
Rail 4	0.143	27
Rail 5	0.318	97
Wheel 1	0.205	84
Wheel 2	0.097	33

^a500 fields taken for each steel.^bTotal area of field is 26 439 μm^2 at $\times 440$.^cTransverse plane for rail steels.

ponding to 1.0 to 1.5 $\text{MN}\cdot\text{m}^{-3/2}$. ΔK_{th} was defined as the value of ΔK where crack growth was not observed in 10^6 cycles. ΔK was determined by substituting the value of the alternating load into the expression for the stress intensity factor. The details of the experimental procedure have been described previously in greater detail [16].

Experimental Results

Fatigue crack growth rates for the five rail and two wheel steels ($R = 0$) are presented in Fig. 3 as determined from two specimens from each steel. The crack growth rate diminishes at low values of ΔK near ΔK_{th} , the threshold value determined for $da/dN \leq 1.0 \times 10^{-7}$ mm/cycle.³ Additionally, da/dN increases rapidly as ΔK ($= K_{max}$) enters Region C.

Deviations from the linear growth rate of Region B at low values of ΔK occur at an approximately constant value of $da/dN = 2.0 \times 10^{-6}$ mm/cycle for all materials. Threshold values varied from 7.5 to 9.3 $\text{MN}\cdot\text{m}^{-3/2}$. Since the threshold values were determined to the nearest 1.0 to 1.5 $\text{MN}\cdot\text{m}^{-3/2}$, there is not a significant difference in ΔK_{th} for these steels. The same consistency of deviation from the linear rates was not observed at high values of ΔK . The growth rates generally began to increase rapidly within the range 5.0×10^{-4} to 2.5×10^{-3} mm/cycle.

The data presented in Fig. 3 show that two materials, Rail 5 and Wheel 2, have a substantially slower crack growth rate for a given value of ΔK . A comparison of Rail 5 and Wheel 2 with the other steels shows that the only difference in microstructure is the presence of a continuous layer of ferrite along the prior austenite grain boundary. Rail 4 contained discontinuous traces of grain boundary ferrite but did not exhibit a slower crack growth rate.

³ 1 mm/cycle = 3.94×10^{-2} in./cycle. 1 $\text{MN}\cdot\text{m}^{-3/2} = 0.910 \text{ ksi}\sqrt{\text{in.}}$

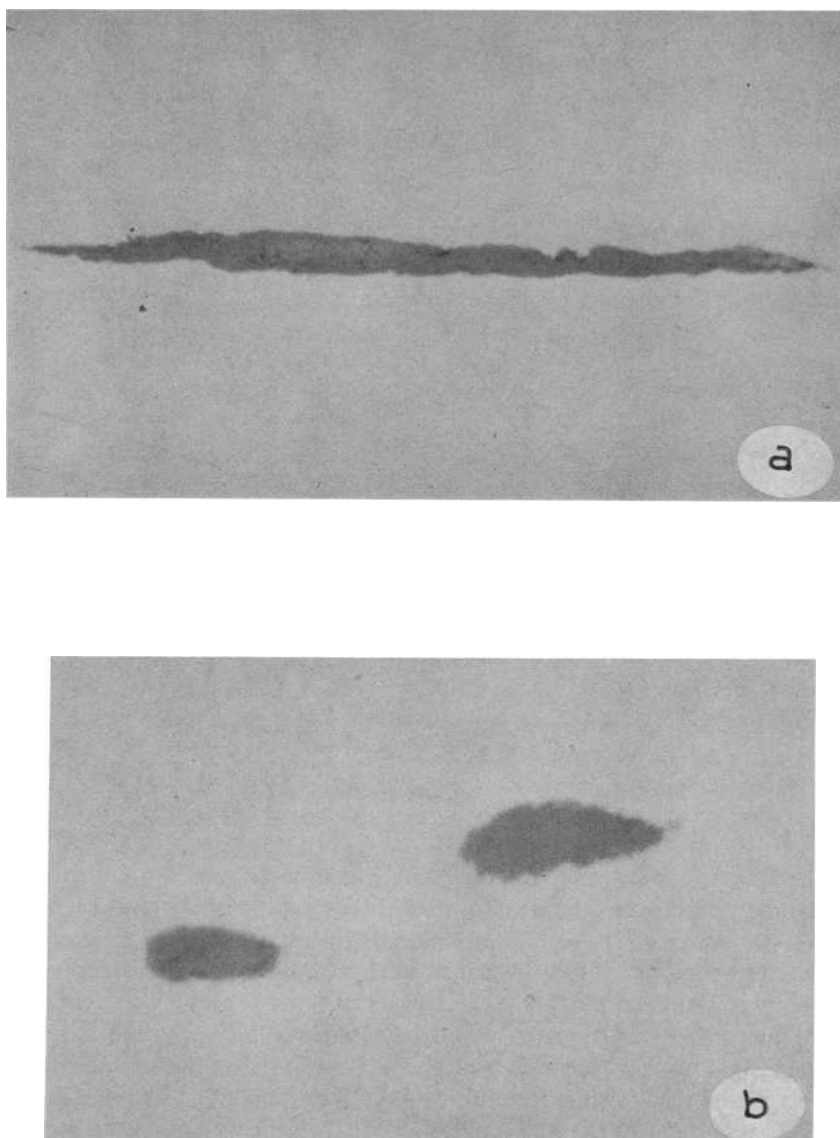


FIG. 2—Shape of sulfide inclusions in (a) railhead ($\times 1100$) and (b) wheel plate ($\times 2000$).

Variations in da/dN as a function of ΔK and K_{\max} for several R ratios are shown in Fig. 4 for Wheel 1. The data show that there is not a significant difference in crack growth rates for Region B when $R \leq 0.2$ and that da/dN can be described by the single ΔK parameter. However, for $R = 0.5$, the overall growth rate increases by approximately threefold, indicating that K_{\max} is strongly influencing crack extension.

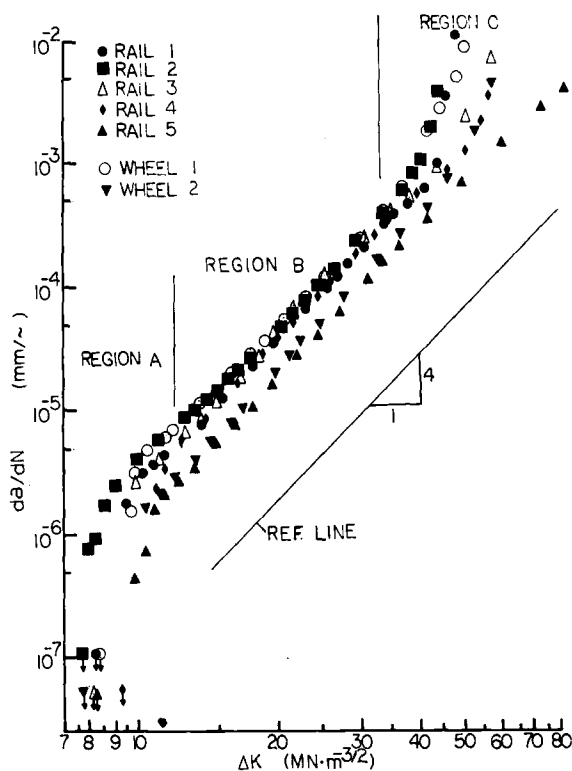


FIG. 3—Fatigue crack growth rates in rail and wheel steels. ($R = 0$, thickness = 10 mm.)

The fracture appearance in Region A was generally the same for all the steels and consists of a mixture of planar facets mingled among the striae. Figure 5a shows a typical region containing a planar facet surrounded by striae characteristic of fully pearlitic steel [16]. These planar facets are a result of interlamellar pearlite separation. Rail 5 and Wheel C also contained some intergranular separation at low ΔK values.

The fatigue appearance in Region B consists of randomly oriented regions of hills and valleys with respect to the overall propagation as shown in Fig. 5b. The alignment of the hills/valleys varies from being parallel to perpendicular to the macroscopic crack direction. This appearance will be referred to as striae although they bear only a slight resemblance to the classical fatigue striations in ductile alloys. The general fracture appearance and random orientations of these striae suggests that their orientation is the same as the ferrite/cementite lamellae orientation in each pearlite colony. The striae have been shown to consist of the underlying pearlitic microstructure by examination of these areas before and after etching [16] and do not necessarily indicate the direction of crack propagation.

The macrofracture appearance changes from a dull grey surface appear-

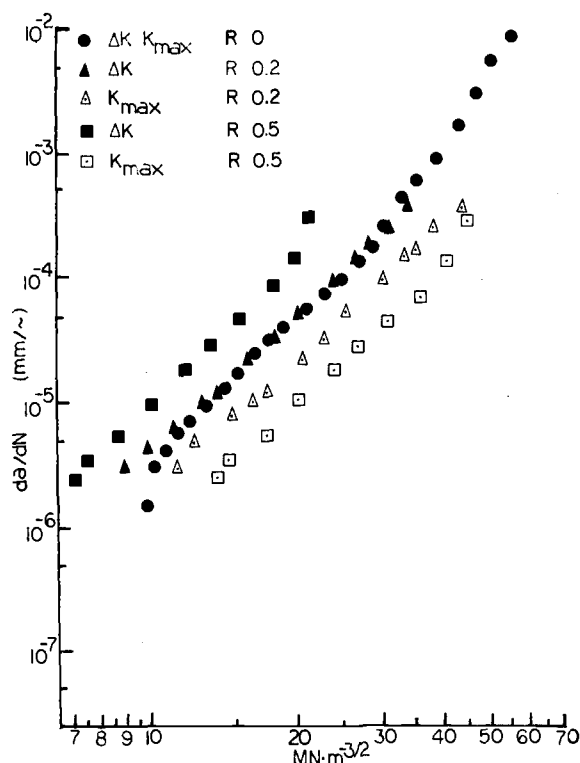


FIG. 4—Fatigue crack propagation rates as a function of ΔK and K_{max} for various R ratios in Wheel 1.

ance (Region B) to one containing a mixture of dull grey and highly reflective areas (Region C). The highly reflective areas are shown to be cleaved grains when examined in the scanning electron microscope (SEM). Figure 5c shows a typical single cleavage facet surrounded by striae. Crack extension by stable cleavage bursts during cyclic loading is a transient fracture mode which terminates at the first unfavorable boundary, such as a pearlite colony boundary where the lamellae change orientation.

Stable cleavage bursts are rarely observed in Rail 5. Instead, regions of intergranular ductile rupture were observed at values of K_{max} approaching K_{Ic} . Figure 5d shows a typical region of ductile failure through the prior austenite grain boundary ferrite. The grain boundary ferrite was most likely the microstructural constituent that prevented cleavage formation. Additionally, cleavage bursts were rarely observed in Wheel 2, although intergranular ductile rupture did not occur.

Crack profile studies show that Region B fatigue crack propagation does not strongly depend on the ferrite/cementite lamellae orientation as shown in Fig. 6. In some pearlite colonies, the crack propagated at approximately right angles to the lamellae. However, many different crack-plane-to-

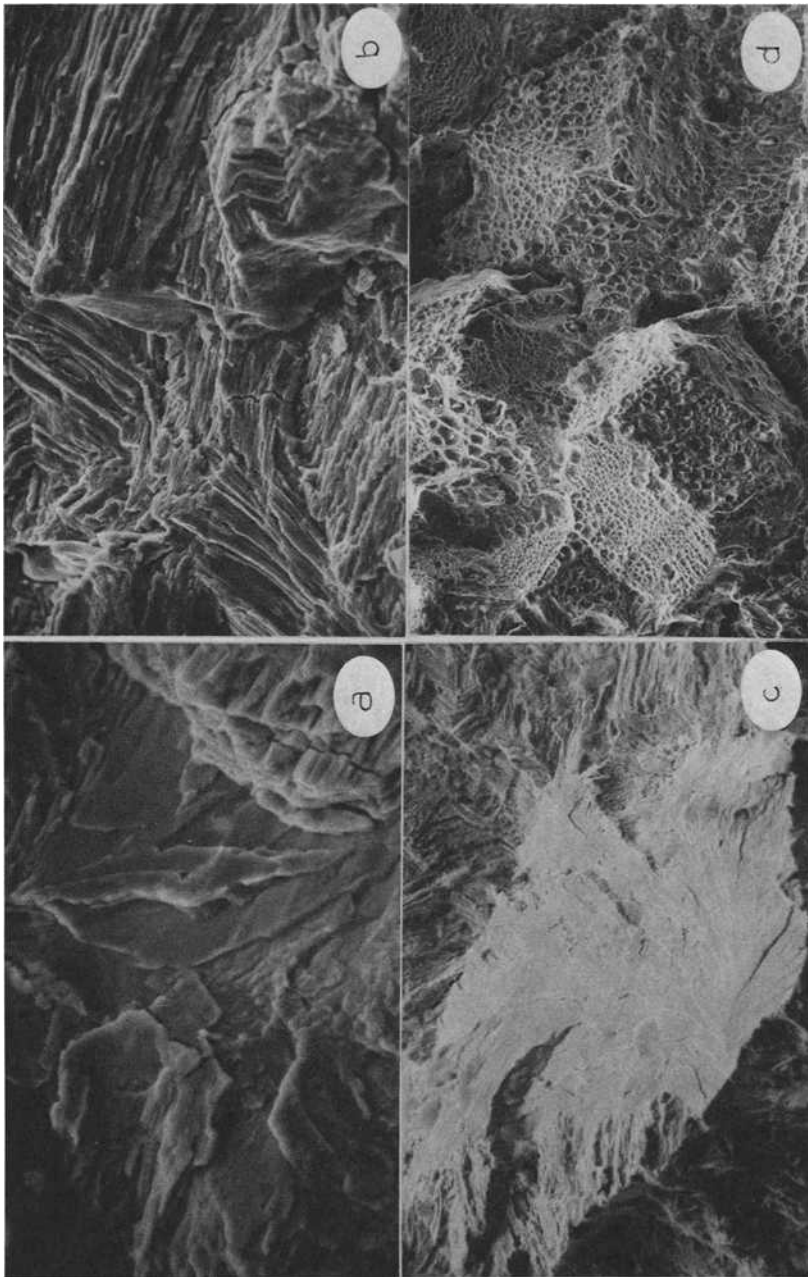


FIG. 5—Fracture modes: (a) Region A—interlamellar pearlite separation ($\times 1743$), (b) Region B—fatigue striae ($\times 934$), (c) Region C—cleavage facet ($\times 353$, $K_{max} = 27 \text{ MN} \cdot \text{m}^{-3/2}$), (d) Region C—intergranular fracture in Rail 5 ($\times 133$).

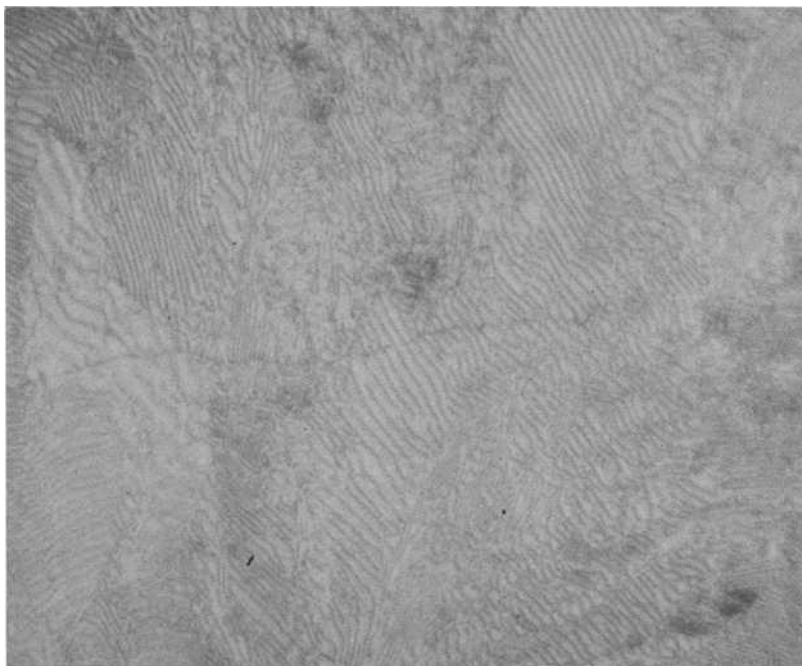


FIG. 6—Crack tip in fully pearlitic steel. ($\times 1540$, $\Delta K = 20 \text{ MN}\cdot\text{m}^{-3/2}$)

cementite-lamellae angles were observed mostly in the range of 45 to 90 deg. Crack-plane-to-lamella angles less than 45 deg were observed less frequently, and only at low values of ΔK did crack extension occur parallel to the lamellae (Region A mechanisms). Figure 6 shows the tip of a fatigue crack after final cyclic loading of $\Delta K \sim 20 \text{ MN}\cdot\text{m}^{-3/2}$. There does not appear to be any damage ahead of the crack tip in the form of cementite cracking or void formation in the ferrite. Similar results were observed upon examination of a specimen fatigued at $\Delta K \sim 34 \text{ MN}\cdot\text{m}^{-3/2}$. One final point of interest is that there was not any evidence (in the form of sheared cementite platelets) that extensive shear occurred along planes 45 deg to the crack plane, that is, planes of maximum shear stress, which would be expected from the operation of the classical striation mechanisms [9,10].

Discussion

Effect of R Ratio

Figure 4 clearly demonstrates that increasing the R ratio can have a significant effect on the overall growth rate in Region C mainly due to the dependency of the cleavage component on K_{\max} . Similar effects are observed in Region A [6] due to the influence of K_{\max} on the two-component fracture

process. However, it is less certain what the effect of K_{\max} is, if any, on the fatigue mechanism of Region B.

Figure 4 illustrates that values of $R \leq 0.2$, at least, do not significantly accelerate the fatigue crack growth rate in Region B, however, an increase in da/dN is observed for $R = 0.5$. An examination of the fracture surface for the specimen tested at $R = 0.5$ showed a mixture of fatigue striae, cleavage, and interlamellar separation at values of $\Delta K = 13$ to $20 \text{ MN} \cdot \text{m}^{-3/2}$ ($K_{\max} = 26$ to $40 \text{ MN} \cdot \text{m}^{-3/2}$). Below this approximate range, interlamellar separation and fatigue striae were predominant, and, above this range, the cleavage mode mixed with the striae was more apparent.

The occurrence of these two K_{\max} -dependent mechanisms, that is, cleavage and interlamellar separation, over the intermediate range of da/dN can account for the slight increase in growth rate at $R = 0.5$ during Region B. Because cleavage fracture depends on K_{\max} , the conditions will be satisfied at values of $K_{\max} \geq 26 \text{ MN} \cdot \text{m}^{-3/2}$. However, interlamellar separation can only occur when the reverse plastic zone size is less than the pearlite colony size [6]. This condition is satisfied when $\Delta K \leq 20 \text{ MN} \cdot \text{m}^{-3/2}$. Therefore, the conditions for cleavage and interlamellar separation are both satisfied during the range $\Delta K = 13$ to $20 \text{ MN} \cdot \text{m}^{-3/2}$ ($K_{\max} = 26$ to $40 \text{ MN} \cdot \text{m}^{-3/2}$) for $R = 0.5$. The result is an acceleration in the overall growth rate during Region B. When $K_{\max} = 40 \text{ MN} \cdot \text{m}^{-3/2}$, pop-in occurs, which is then followed by stable fatigue growth along the specimen edges before final failure.

The Effect of Nonmetallic Inclusions on Fatigue Crack Propagation

The role of nonmetallic inclusions in the fracture process for the three regions of crack growth has been examined. Figure 7 shows an inclusion that is exposed to the fracture surface after the passing of a fatigue crack. The crack plane for the rail samples was oriented perpendicular to the stringer inclusions. As shown in Fig. 7, the crack propagated through the stringer inclusions in a brittle manner, judging by the smooth flat fracture surface on the inclusion. Crack propagation in the wheel material occurred around the inclusion by debonding of the inclusion from the matrix.

At intermediate values of ΔK , the surrounding fracture surface still shows the characteristic fatigue appearance (Fig. 5b). Because distinct striations do not appear on the fracture surface, it is not possible to determine from the fractographs if the inclusions influenced fatigue growth on a microscale, as is sometimes observed in aluminum alloys. At higher values of ΔK , inclusions are occasionally found at the origin of a cleavage facet. The possibility of inclusions participating in this fracture process should not be precluded. However, it is unlikely that they have much of an effect, as many cleavage origins were found without an association to an inclusion. Once a cleavage crack initiated, its path was not affected by stringer inclusions, and the crack propagated through them.

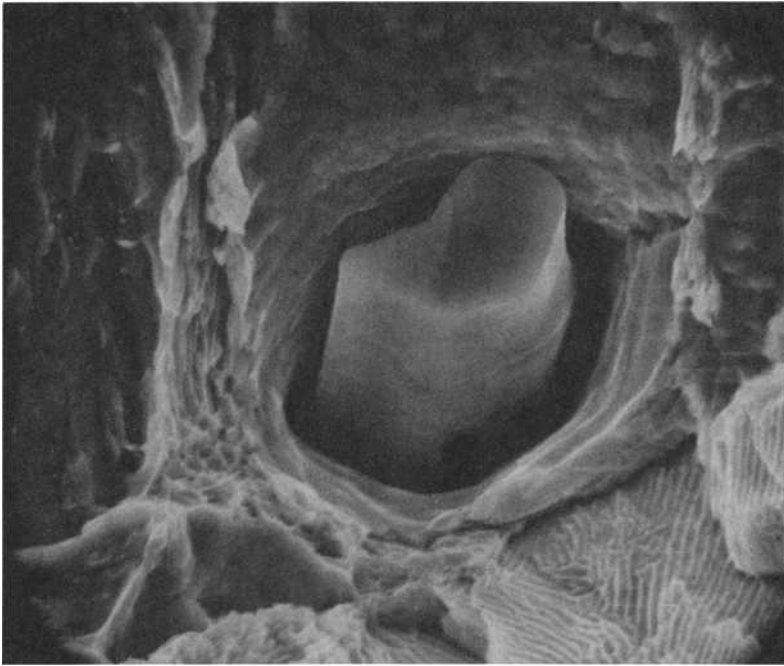


FIG. 7—Sulfide stringer inclusion exposed to the fracture surface ($\times 4500$).

It is doubtful that the inclusion content has a significant effect on the overall crack growth rate. A consistent change of ΔK_{th} with inclusion content was not observed and probably did not influence the limiting value of crack propagation. Additionally, inclusions were not associated with the planar facets found in Region A, indicating that the operation of this mechanism is independent of inclusions. Figure 3 shows that the growth rate in Region B is very similar for all materials except for those steels with ferrite at the prior austenite grain boundary. Rail 5 had the largest total inclusion content for the rail material, and Wheel 2 had the least for the wheel material; however, both steels show an overall growth rate lower than the other materials. This indicates that the presence of ferrite in the boundary retards fatigue crack growth and demonstrates that the inclusion content does not have an observable effect on the overall crack growth rate.

The Effect of Grain Boundary Ferrite at Intermediate Growth Rates (Region B)

Figure 8 shows a profile of the crack path in Rail 5. The effect of a ferrite layer along the prior austenite grain boundary causes crack growth on discontinuous levels, from one grain to an adjacent one. The crack propagates through a pearlite colony on one level (A in Fig. 8) before it

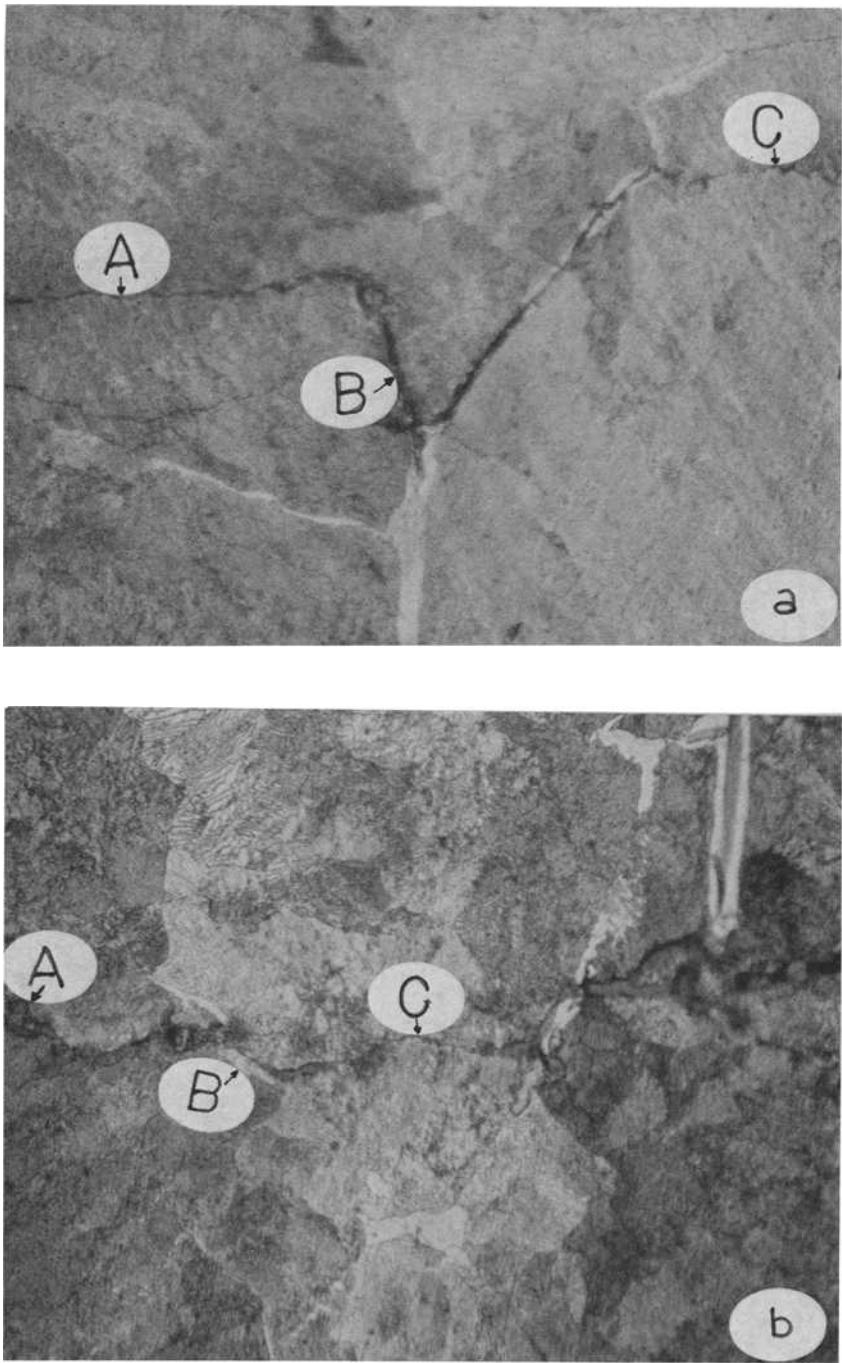


FIG. 8—Profile of fatigue crack in Rail 5 (overall direction of crack growth is from left to right): (a) $\times 500$ and (b) $\times 500$.

encounters a ferrite layer. The crack path is then deflected along the ferrite layer (B). Examination of this region in the scanning electron microscope revealed a flat featureless surface. When the orientation of the ferrite layer becomes unfavorable for forward growth, the crack then reinitiates in the adjacent prior austenite grain on another level (C) and proceeds until another ferrite layer is encountered. Grain boundary deflection was only observed in those steels that contained a complete ferrite layer at the prior austenite grain boundary. In Rail 4, the volume percent of ferrite was not sufficient to cover the prior austenite grains, and crack deflection did not occur. Crack deflection was not observed in the pearlite colony ferrite, indicating that some minimum thickness of ferrite is required for crack deflection.

It has been observed that the forward growth of a fatigue crack in a laminar composite material may be stopped temporarily at a laminate interface oriented perpendicular to the crack plane [17]. The arrest is due to the crack blunting that arises from secondary interfacial splitting perpendicular to the direction of main crack propagation. The continuous ferrite layer surrounded by hard pearlite is analogous to a soft layer in a composite material, and it produces a similar effect in retarding crack growth. Figure 9 shows a schematic diagram of the crack growth retardation process. Consider a crack that has just encountered a ferrite layer. During the beginning of the tensile portion of the loading cycle, slip occurs along planes

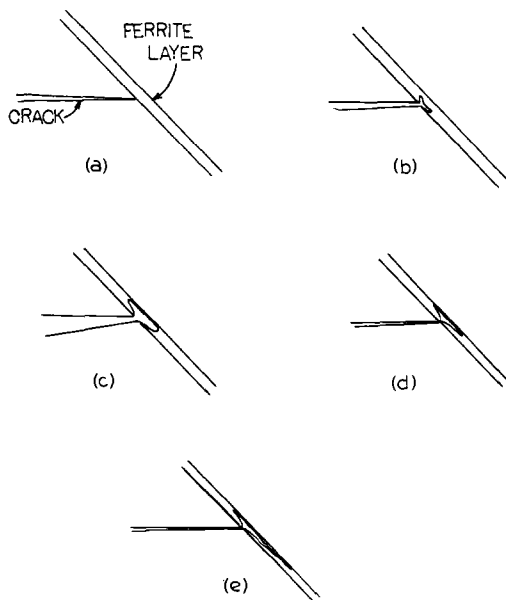


FIG. 9—Fatigue crack mechanism in ferrite layer: (a) zero load (crack encounters ferrite layer), (b) small tensile load, (c) maximum tensile load, (d) zero load, (e) after several cycles.

at 45 deg to the plane of the crack. Since slip is more difficult in front of the crack tip due to the harder pearlite colony, the reverse slip process occurs preferentially in the ferrite, thus preventing the crack from extending forward into the colony. This causes crack propagation to occur in the ferrite layer, resulting in preferential growth along the prior austenite grain boundaries, possibly by a mechanism similar to Stage I fatigue initiation [18]. The crack grows in the ferrite until forward growth can occur by reinitiation in the adjacent pearlite grain.

Since the overall crack growth rate is reduced by a factor of 2 (compared to the steels without grain boundary ferrite), twice as many cycles are required to produce the same extent of crack growth. A simple calculation indicates that the relative velocity of crack propagation in the ferrite as compared to the velocity in pearlite is f/A , where A is the size of the prior austenite grain and f is the extent of crack growth in the ferrite. An estimate of this ratio can be determined by examining the micrograph shown in Fig. 8. For one prior austenite grain, the extent of crack growth in the ferrite is approximately 0.016 mm and in the pearlite is 0.072 mm (bottom micrograph). Therefore

$$\frac{V_f}{V_p} \cong 0.2$$

where V_f and V_p are the crack velocities in the ferrite and pearlite, respectively. This indicates that the blunting effect produces a five-fold decrease in crack growth rate.

Figure 10 shows a comparative plot of crack growth data for steels with varying pearlite (carbon) contents. The data illustrate that the beneficial effect of grain boundary ferrite does not increase as the thickness (or volume percent) of the ferrite increases. When a crack encounters a thick ferrite layer, it will be able to advance through the ferrite by a standard striation mechanism without deflection until the next pearlite colony is encountered. As the amount of ferrite becomes the major microstructural constituent, then the growth mechanism would be characterized by the properties of the ferrite. In Region B fatigue, the crack growth rate is determined primarily by the elastic modulus E ; hence, the crack growth rates of fully pearlitic and ferritic/pearlitic steels are comparable. However, beneficial effects can be achieved by the presence of small amounts of the ferrite phase continuously distributed along prior austenite grain boundaries.

Stable Fatigue Crack Growth above K_{Ic}

Cyclic crack growth occurred at values of the maximum stress intensity factor K_{max} that are greater than the material's fracture toughness. As shown in Table 4, K_{max} could be as high as 1.52 K_Q where K_Q is defined as the tentative value of the fracture toughness. This observation appears to contradict conventional linear-elastic fracture mechanics (LEFM) theory which predicts that unstable fracture (pop-in) occurs when $K_{max} = K_{Ic} = (K_Q$

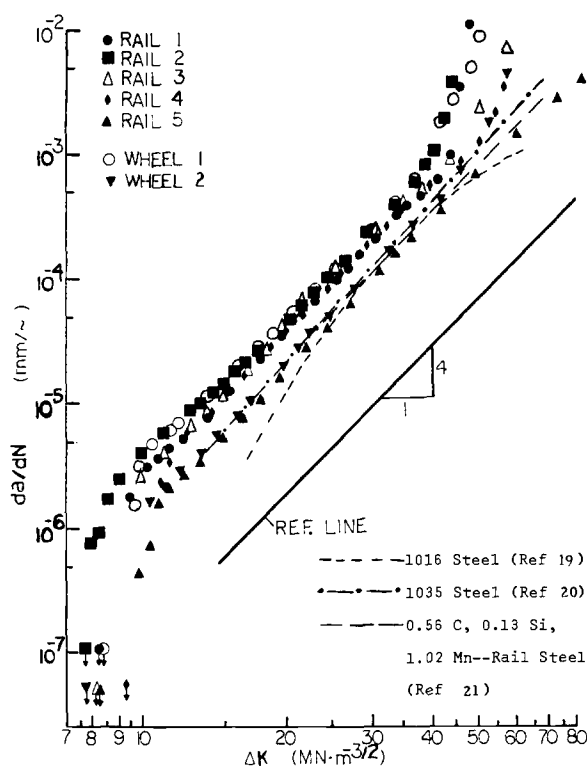


FIG. 10—Fatigue crack growth rates in rail and wheel steels compared with other ferritic/pearlitic steels.

for a valid test according to ASTM Test for Plane-Strain Fracture Toughness of Metallic Materials (E 399-74)). These test specimens have a low ratio of fracture toughness to thickness, and the entire fracture surface was flat, plane strain fracture. Consequently, the occurrence of stable fatigue growth at $K_{\max} > K_Q$ is not related to shear lip effects.

The fracture toughness is determined from the pop-in load, P_Q , which is about 15 to 20 percent less than the maximum load of fracture, P_{\max} for these steels. Table 4 contains the values of K_Q based on P_Q and values of $K_{P(\max)}$ based on P_{\max} . Additionally, the values of K at (a) the first occurrence of isolated cleavage bursts during fatigue testing, K_{OC} , (b) the occurrence of the first major burst of cleavage (greater than 20 percent of the fracture surface), K_F , (c) the deviation of da/dN from the linear growth rate curve, K_{DL} , and (d) the maximum extent of stable fatigue crack growth immediately prior to unstable specimen fracture, $K_{I(\max)}$, are listed in Table 4. Values of K_{OC} and K_F were determined from the observed crack length on the fracture surface where the first isolated burst and pop-in occurred, respectively. There is good agreement between the values for K_Q , K_{DL} , and K_F , suggesting that the value of K_Q for pop-in during plane strain toughness testing, the occurrence

TABLE 4—Values of *K* taken from fatigue and fracture toughness test.

Steel	First Burst of Cleavage, <i>K</i> _{OC}	Cyclic Pop-In, <i>K</i> _F	Fracture Toughness Based on <i>PQ</i> ASTM E-399, <i>K</i> _{DL}	<i>da/dN</i> Deviates from Linearity, <i>K</i> _Q	Fracture Toughness Based on <i>P</i> _{max} , <i>K</i> _{P(max)}	Maximum Value of <i>da/dN</i> , <i>K</i> _{f(max)}
Rail 1	26 MN·m ^{-3/2}	41	41	38.7 ^a	44.5	56
Rail 2	24	35	37	35.7 ^b	44.1	49
Rail 3	33	45	46	45.5 ^{a,b}	52.8	69
Rail 4	31	51	49	49.9 ^{a,b}	62.0	75
Rail 5	1. small burst:57 2. no burst on second sample	did not occur	did not occur	<i>PQ</i> = <i>P</i> _{max}	98.5 ^b	93

NOTE—Values represent average of two samples tested. Values of *K*_{OC}, *K*_F, *K*_{DL}, and *K*_{f(max)} are within $\pm 2 \text{ MN}\cdot\text{m}^{-3/2}$. $1 \text{ MN}\cdot\text{m}^{-3/2} = 0.910 \text{ ksi } \sqrt{\text{in.}}$.

^aInvalid according to ASTM Standard E 399 due to *P*_{max}/*PQ* being greater than 1.10.

^bInvalid according to ASTM Standard E 399 due to insufficient size.

of a major cleavage burst during fatigue testing of these steels, and linear crack growth deviation are related.

A simple model based on the parameters measured from the fracture toughness test can explain the occurrence of crack growth at *K* levels above *K*_Q. As the fatigue crack progresses forward, isolated patches of cleavage fracture occur along the crack front in favorably oriented grains (Fig. 11a). These isolated patches do not produce a noticeable deviation from the linear

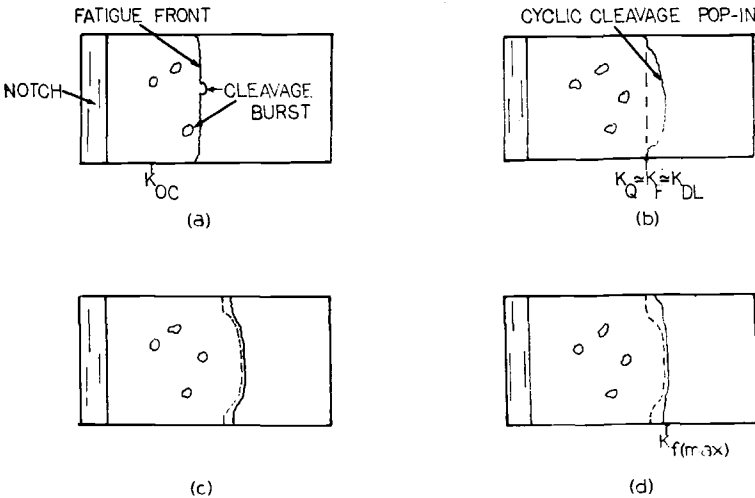


FIG. 11—Illustration of cyclic pop-in model to explain stable fatigue above *K*_{IC}.

growth rate. As the crack grows in fatigue under constant load, the crack length increases. When K_{\max} reaches K_Q , one large pop-in (or several smaller ones) can occur within a short time. At this point, a situation analogous to pop-in during a standard fracture toughness test occurs, as illustrated in Fig. 11b. Unlike the case of the fracture toughness test conducted under rising load, the load is quickly returned to P_{\min} during cyclic loading associated with fatigue testing, and the P_{\max} value required for unstable cleavage of the entire specimen is not reached. During subsequent cyclic loading, the remaining ligament along the sides, which is in a state of reduced constraint, supports fatigue crack propagation at an accelerated rate due to an increase in stress intensity in that region (Fig. 11c). Striae-type formation occurs along the edges of the specimen. At this point, a deviation from the linear rate occurs. After continued cyclic loading, additional large cleavage bursts can occur, and final unstable fracture can intervene. In Rail 5, which contained ferrite at prior austenite grain boundaries, pop-in did not occur during fracture toughness testing or during fatigue testing. As a result, stable fatigue growth above K_Q was not observed, although K_Q was much higher than for the other rail steels.

Table 4 also indicates that the maximum value of K for stable fatigue crack growth, $K_{f(\max)}$, is greater than $K_{P(\max)}$ determined from the fracture toughness test. This observation can be misleading for the following reasons:

1. The thickness, B , of the fatigue specimens was 10 mm, and the thickness of the fracture toughness specimens was 19 mm. As discussed elsewhere [16], $K_{f(\max)}$ (and $K_{P(\max)}$) is dependent on the specimen thickness and generally increases as the specimen thickness decreases. This partially explains why $K_{f(\max)}$ (based on $B = 10$ mm) is greater than $K_{P(\max)}$ (based on $B = 19$ mm).

2. Additionally, $K_{P(\max)}$ is determined from the length of fatigue precrack as required by the ASTM. $K_{f(\max)}$ is determined from the crack length after precracking, pop-in, and some additional fatigue growth (Fig. 11d). Thus, the crack length at $K_{P(\max)}$ (determined from the fatigue precrack length before pop-in) will be less than $K_{f(\max)}$ (determined from the crack length after pop-in). Therefore, for a given thickness and fracture load, the maximum value of K recorded in a fatigue propagation test will be slightly greater than the value determined from the fracture toughness test. These factors together can explain the observation that $K_{f(\max)} > K_{P(\max)}$ shown in Table 4.

Conclusions

1. In pearlitic rail and wheel steel, the presence of grain boundary ferrite can reduce the crack growth rate by a factor of 2 at intermediate and low growth rates. At growth rates above 10^{-3} mm/cycle (Region C), the effect is even greater due to the less frequent occurrence (or the elimination) of cleavage bursts.

2. The effect of increasing R ratio for $R \leq 0.2$ is mainly seen in Region C due to the operation of K_{\max} -dependent stable cleavage bursts. When $R = 0.5$, the overall growth rate increases over the entire growth rate curve. This is attributed to the occurrence of Region A planar facet mechanisms and Region C cleavage mechanisms during Region B growth.

3. Nonmetallic inclusions do not significantly affect the mechanisms of fatigue growth and therefore do not affect crack growth rate within the range of inclusion content from 0.097 to 0.318 percent by area as determined at $\times 440$.

4. Stable fatigue crack growth above K_Q can occur along the specimen sides after pop-in. At this point, the growth rate greatly accelerates and deviates from the double logarithm linear growth rate.

Acknowledgments

The authors wish to thank D. H. Stone of the Association of American Railroads for providing the material and technical advice. Appreciation is also given to Dr. C. A. Rau for his valuable discussions.

References

- [1] Schoenberg, K. W., "Present Performance of American Rail Steels," presented at the Iron and Steel Institute Conference on Rail Steels, London, Nov. 1972.
- [2] Wilcox, R. C., "Failure Analysis of Rails," School of Engineering, Auburn University Auburn, Ala., Contract 2380-01-0814.
- [3] *Railway Track Materials*, American Iron and Steel Institute, New York, Nov. 1961.
- [4] Beevers, C. J., Cooke, R. J., Knott, J. F., and Ritchie, R. D., *Metal Science*, Vol. 9, No. 3, March 1975, pp. 119-126.
- [5] Birkbeck, G., Inckle, A. E., and Waldron, G. W. J., *Journal of Material Science*, Vol. 6, No. 4, April 1971, p. 319-323.
- [6] Cooke, R. J. and Beevers, C. J., *Material Science and Engineering*, Vol. 13, No. 3, March 1974, p. 201-210.
- [7] Robinson, J. L. and Beevers, C. J., *Metal Science Journal*, Vol. 7, Sept. 1973, pp. 153-159.
- [8] Cooke, R. J. and Beevers, C. J., *Engineering Fracture Mechanics*, Vol. 5, No. 4, Dec. 1973, pp. 1061-1071.
- [9] Laird, C. and Smith, G. C., *Philosophical Magazine*, Vol. 7, No. 77, May 1962, pp. 847-857.
- [10] Tomkins, B. and Biggs, W. D., *Journal of Material Science*, Vol. 4, No. 6, June 1969, pp. 532-553.
- [11] Ritchie, R. O. and Knott, J. F., *Material Science and Engineering*, Vol. 14, No. 4, April 1974, pp. 7-14.
- [12] Griffiths, J. R., Mogford, I. L., and Richards, C. E., *Metal Science Journal*, Vol. 5, July 1971, pp. 150-154.
- [13] Broek, D., in *Fracture 1969*, P. L. Pratt, Ed., Chapman and Hall, London, 1969, pp. 754-765.
- [14] Shih, T. and Araki, T., *Transactions, Journal of the Iron and Steel Institute*, Vol. 13, No. 1, 1973, pp. 11-18.
- [15] "Wrought Steel Wheels & Forged Railway Axles," American Iron and Steel Institute, New York, Sept. 1973.
- [16] Fowler, G. J., "Fatigue Crack Initiation and Propagation in Pearlitic Rail Steels," Ph.D. Dissertation, School of Engineering and Applied Science, University of California, Los Angeles, Calif., 1976.
- [17] Mandell, J. F. and Meier, U. in *Fatigue of Composite Materials*, ASTM STP 569, American Society for Testing and Materials, 1975, pp. 28-44.

- [18] Laird, C. in *Fatigue Crack Propagation*, ASTM STP 415, American Society for Testing and Materials, 1967, pp. 131-180.
- [19] Richards, C. E. and Lindley, T. C., *Engineering Fracture Mechanics*, Vol. 4, No. 4, Dec. 1972, pp. 951-978.
- [20] Egan, G. R., "An Engineering Analysis of the Risk of Brittle Fracture of the Carquinez West Bridge," Failure Analysis Associates Report No. 75-7-02-1, 1975.
- [21] Evans, P. R. V., Owen, N. B., and Hopkins, B. E., *Journal of the Iron and Steel Institute*, Vol. 208, Pt. 6, June 1970, pp. 560-567.

DISCUSSION

*Pierre Vicens*¹ (written discussion)—The fatigue tests carried out by ourselves and by the Société Nationale des Chemins de Fers Français (SNCF) in cooperation with IRSID with a view to defining the fatigue behavior of several rail steel grades were twofold:

1. Determination of fatigue limit under alternating torsion test and under other types of stresses within the scope of the studies of C53 Committee of Office for Research and Experiments (ORE), Union Internationale des Chemins de Fers (UIC).

2. Determination of the rate of growth of fatigue cracks and of the values of the critical stress intensity factor.

Fatigue Limits

The investigated grades, whose compositions are given in Table 5, were the following: (a) standard grade of UIC specification, (b) wear-resistant Grade B of UIC specification, and (c) chromium-silicon grade.

The specimens were taken from the railhead of UIC 60 profile in the as-rolled condition, after straightening on roller type machines.

Two grades were obtained by thermal hardening in a pilot plant; the UIC 60 profile rails were induction heated and rapidly cooled over their whole section by means of water sprayed through compressed air. One rail hardened at 100 kg/mm². One rail hardened at 120 kg/mm². The samples were cut from the railhead after treatment and straightening on roller type machines.

TABLE 5—Steel grades.

	C, %	Mn, %	Si, %	Cr, %	P, %	S, %	Al, %
UIC Standard	0.500	1.010	0.135	...	0.063	0.031	
UIC-B	0.616	1.396	0.341	...	0.036	0.024	0.012
Cr-Si	0.689	0.955	0.774	0.850	0.025	0.027	0.015
Induction full hardened							
1	0.606	0.850	0.308	...	0.031	0.024	0.003
2	0.794	0.756	0.272	...	0.030	0.007	0.010

¹Ingenieur en Chef Adjoint, Metallurgie Qualité, Sacilor, France.

²Ritchie, R. O., *Journal of Engineering Materials and Technology*, July 1977, pp. 195-204.

For these steels, which all present a pearlitic structure (Table 6), the higher the tensile strength, the higher the fatigue limit. The thermal hardened steel has, however, for the same tensile strength, a better fatigue limit than the chromium-silicon steel.

TABLE 6—Mechanical properties.

	Yield Strength, 0.2 %, N/mm ²	Ultimate Tensile Strength, N/mm ²	Elongation, %	Reduction in Area, %	Endurance Limit, Alternating Torsion, N/mm ²
UIC Standard	. . .	762	16	. . .	±187
UIC-B	503	936	13.8	22.9	±232
Cr-Si	633	1064	11.5	21.7	±302
Induction full hardened					
1	592	1002	16.6	41.3	±303
2	838	1259	14.0	29.4	±400

We decided to determine the fatigue limits under alternating torsion stressing in order to obtain a comparison on metal behavior under shearing. According to our opinion, the shearing stresses are mainly responsible for the failure of the rail in service.

For a number of grades investigated by C 53 Committee of ORE, other fatigue limits depending on other stress patterns have been determined (Fig. 12). These measurements are intended to control the fatigue criterion proposed by Dang Van (M. Dang Van is with the Laboratoire de Mecanique des Solides de l'Ecole Polytechnique). According to this criterion, a linear relationship exists between the hydrostatic pressure and the part of shearing which is variable along the cycle. The following formula applied

$\sigma + \alpha p = \text{constant}$

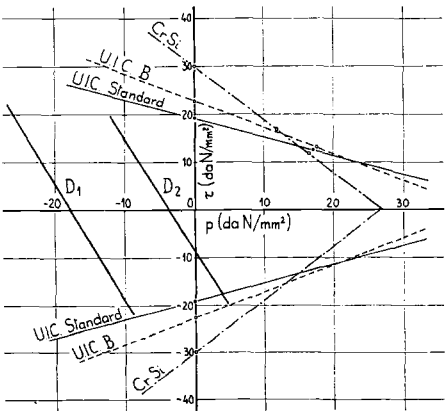


FIG. 12—Dang Van diagram.

in the plane with the poorest orientation when the fatigue failure occurs.

Thus, one can define a field of failure at the outside of two symmetrical lines obtained in conducting fatigue tests according to different stress patterns.

Failure Crack Propagation

The best solution consists of avoiding the occurrence of any fatigue crack by the means of a high fatigue limit. However, as it is difficult to be entirely sure that possible overstressing will never give rise to a failure, it is worth studying fatigue crack propagation for the different grades.

IRSID has especially studied the three harder grades: chromium-silicon steel and induction full hardened steel, 100 and 120 kg/square mm.

The specimens were cut from UIC 60 railhead, straightened on a roller machine. The sampling was carried out in such a manner that the fatigue crack would grow in a transverse direction to railhead (Fig. 13).

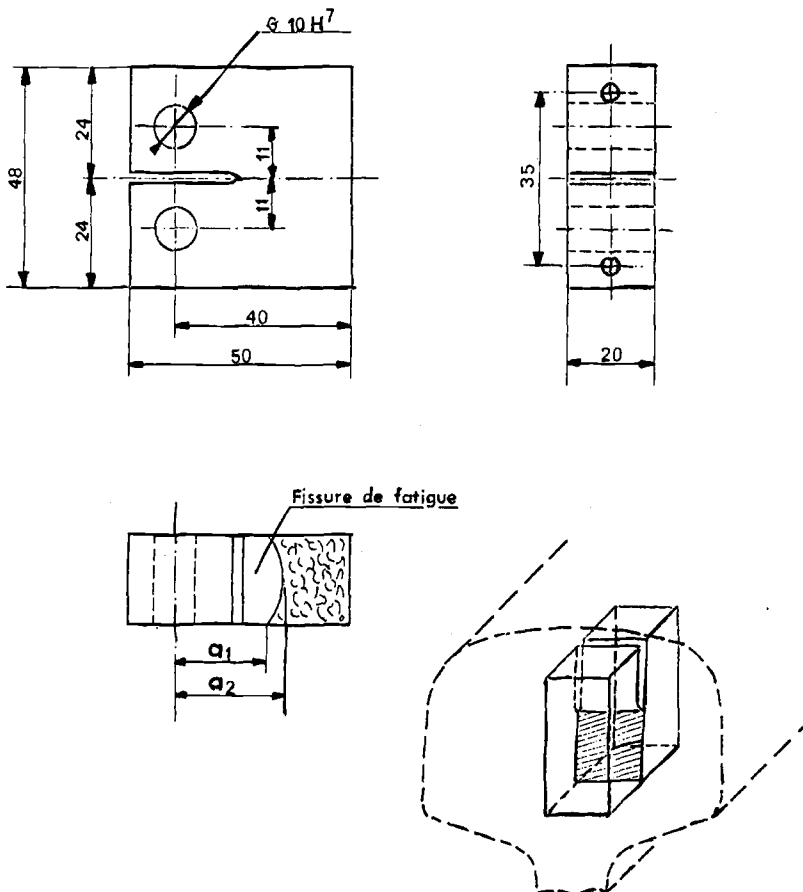


FIG. 13—Specimen design and orientation.

The results (Fig. 14) show the advantage gained from a thermal hardening with regard to the hardening obtained through the addition of alloy elements.

1. The no-crack ΔK_s threshold is higher for the thermal hardened steels.
2. The rate of growth of fatigue crack is more rapid for the chromium-silicon grade.
3. K_{Ic} is the lower for the chromium-silicon grade.

G. J. Fowler and A. S. Tetelman (authors' closure)—The data on crack growth presented by Mr. Vicens represent alloy and heat-treated steels which were not covered in our study.

It is generally accepted that the fatigue endurance limit of steels will increase as the ultimate tensile strength increases, as shown by the trend in Mr. Vicens' data presented in Table 6. However, the endurance limit is also strongly influenced by the microstructure and the nonmetallic inclusion content. Additionally, the crack growth rate near ΔK_{th} (Region A) has been shown to be dependent on the grain size, environment, load ratio, and strength level.² The effect of microstructure on the growth rate is also observed at values of K_{max} approaching K_{Ic} (Region C growth). Perhaps an explanation of the results can be obtained by examining these variables.

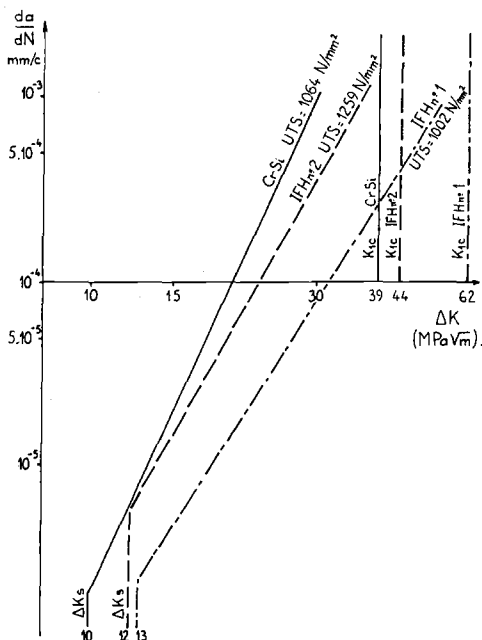


FIG. 14—Crack propagation.

Fatigue and Fracture Behavior of Carbon-Steel Rails*

REFERENCE: Barsom, J. M. and Imhof, E. J., Jr., "Fatigue and Fracture Behavior of Carbon-Steel Rails," *Rail Steels—Developments, Processing, and Use*, ASTM STP 644, D. H. Stone and G. G. Knupp, Eds., American Society for Testing and Materials, 1978, pp. 387–413.

ABSTRACT: The Ad Hoc Committee on Rail Research, which is composed of representatives from the American Railway Engineering Association (AREA), the Association of American Railroads (AAR), and the American Iron and Steel Institute (AISI) Committee on Railroad Materials, formulated a program to investigate the effects of metallurgical properties, mechanical properties, and applied stress conditions on the service fracture behavior of carbon-steel rails. This paper presents the fatigue and fracture behavior of five rails having extremes in room-temperature tensile properties and Charpy V-notch toughness, and an analysis of the effect of this behavior on the in-service useful life of carbon-steel rails. These five rails were removed from service after 15 to 18 years of operation and were selected from a population of about 90 rails that were removed from service because they contained service-developed defects. A companion paper in this symposium describes the results of chemical analysis, hardness and tension tests, and the results of wear, deformation, metallographic, and fractographic analysis.

The results of the fractographic investigation conducted under AAR-AISI contract that are presented in part in the companion paper showed that in-service fatigue cracks initiated from inclusions having a width of about 0.03 mm (1.25 mils). The results of the present investigation showed that fatigue crack initiation from such small discontinuities occurs when the magnitude of the stress fluctuations applied to the railhead with the passage of each wheel are equal to about the tensile strength of the steel. The cost of the steelmaking practices required to eliminate such small discontinuities is believed to be economically prohibitive. Moreover, the detection of such discontinuities is beyond the capabilities of presently available nondestructive inspection procedures. The results also showed that the fatigue crack propagation behavior of various carbon-steel rails is essentially identical and is independent of chemical composition or mechanical properties. Moreover, the dynamic fracture toughness of these rails at the minimum operating temperature of about -35°C (-30°F) was about $27.5 \text{ MPa} \sqrt{\text{m}}$ ($25 \text{ ksi} \sqrt{\text{in.}}$), and a significant increase in the fracture toughness of the rail would result in a negligible increase in the useful fatigue life of the rail. Significant increase in the fatigue life of rails can be achieved by decreasing the wheel load, by maintaining the roadbed, by changes in the design of rails, and by establishing a residual compressive stress field in the upper portion of the railhead which can be accomplished, for example, by induction hardening. Consequently, it is suggested that the safety and reliability of rails can be ensured best by

*Original experimental data were measured in U.S. customary units.

¹Section supervisor and senior research technician, respectively, United States Steel Corporation, Research Laboratory, Monroeville, Pa. 15146.

decreasing the magnitude and fluctuation of the stresses in the rail and by periodic nondestructive inspection of rails.

KEY WORDS: steels, railroad tracks, metallurgy, mechanical properties, stresses, fracture, fatigue

The Ad Hoc Committee on Rail Research, which is composed of representatives from the American Railway Engineering Association (AREA), the Association of American Railroads (AAR), and the American Iron and Steel Institute (AISI) Committee on Railroad Materials, formulated a program to investigate the effects of metallurgical properties, mechanical properties, and applied stress conditions on the service fracture behavior of carbon-steel rails. The Ad Hoc Committee selected four track sites on main line railroads where above-normal incidence of rail cracking had been documented. Thirty-three rail samples were selected by the Ad Hoc Committee from approximately ninety 2.44-m (8-ft) segments of joined rails that had been removed by the AAR from the track sites. Thirty-one of the samples were removed because ultrasonic inspection had indicated that they contained service-developed cracking. The samples were broken in three-point bending at room temperature at the AAR Technical Center to reveal the origin and extent of cracking. They also determined the room-temperature tensile and Charpy V-notch (CVN) impact properties of all 90 of the original rail segments. One half of each fractured segment (31 samples) and the other two that did not contain cracks were sent to U.S. Steel Research for further investigation under AAR-AISI contract. Although it was desired to have rail samples with prematurely short service lives from traditionally troublesome track locations, rail samples with service-developed defects were not found in these locations. As a result, the field group was only able to select rails with relatively long service lives; most of these (27) had lives between 363 and 545 million metric tonnes (MMT) (400 and 600 million gross tons (MGT)), and the average life was 454 MMT (500 MGT) or 16 years (Table 1). This average service life represents about 15.4 million loading cycles at about 14.7 metric tonnes (16.25 tons) per wheel, well beyond the number of cycles (5 million) generally considered as infinite life in laboratory fatigue tests such as a rolling contact load test. The investigation of the thirty-three segments included chemical analysis, tensile properties, metallographic analysis (macrostructural and microstructural examination and microcleanliness), fractographic analysis (fracture surfaces and composition, and nature of fracture origin), and contour profile wear and deformation. The results of this investigation are presented in a companion paper in this symposium.²

In addition, the Ad Hoc Committee selected five of the rail segments for an investigation by U. S. Steel Research of the fatigue and fracture behavior of carbon-steel rails having extremes in mechanical properties. These five

²Sonon, D. E., Pellegrino, J. V., and Wandrisco, J. M., this publication, pp. 99-117.

TABLE 1—AAR-AISI rail program sample selection.

Chemical Composition, %																	
AAR Fracture No.	USS Sample No.	Rail Weight, lb/yd	Service Time, year	Service Tonnage, MGT	C	Mn	P	S	Si	Cu	Ni	Cr	Mo	Total			N ₂ , ppm
High CVN	28	749	15	481	0.68	0.79	0.016	0.043	0.15	0.101	0.066	0.033	<0.003	0.012	0.003	66	
High tensile	29	750	15	481	0.72	0.89	0.018	0.044	0.16	0.076	0.059	0.031	<0.003	0.010	0.003	80	
Intermediate	46	756	18	557	0.78	0.86	0.011	0.030	0.18	0.060	0.067	0.024	<0.003	0.006	0.003	60	
Low CVN	50	757	17	520	0.83	0.97	0.025	0.024	0.16	0.064	0.058	0.023	<0.003	0.005	0.004	62	
Low tensile	55	758	17	519	0.69	0.94	0.008	0.028	0.20	0.052	0.069	0.021	<0.003	0.008	0.004	67	

Mechanical Properties									
AAR Fracture No.	USS Sample No.	Rail Weight, lb/yd	Service Time, year	Service Tonnage, MGT	Yield Strength, ksi	Tensile Strength, ksi	Elongation in 1 in., %	Reduction of Area, %	Charpy V-Notch Toughness, ft-lb
									<div>Transverse</div> <div>Longitudinal</div>
High CVN	28	749	15	481	60.4	121.4	12.3	17.3	6.0
High tensile	29	750	15	481	87.0	140.2	10.2	13.4	3.5
Intermediate	46	756	18	557	71.1	130.5	10.2	13.9	5.0
Low CVN	50	757	17	520	77.6	141.2	8.4	11.7	5.0
Low tensile	55	758	17	519	58.2	119.3	14.3	20.2	6.5

Conversion factors—

- 1 lb/yd = 0.5 kg/m
 1 ton = 0.907 metric tonne
 1 ksi = 6.895 MPa
 1 in. = 25.4 mm
 1 ft-lb = 1.36 J

rail segments were selected from the total population (approximately 90 segments); the five rail segments were characterized as having (a) highest room-temperature tensile strength, (b) lowest room-temperature tensile strength, (c) highest room-temperature CVN energy absorption, (d) lowest room-temperature CVN energy absorption, and (e) intermediate tensile strength and CVN energy absorption at room temperature.

This paper presents the results of the fatigue and fracture behavior studies of the five rail segments and an analysis of the effect of this behavior on the in-service useful life for carbon-steel rails.

Material

The chemical composition and mechanical properties of the five rails investigated are presented in Table 1. This table also presents the years of service life and the tonnage (in million tons) transported over these rails prior to their removal from service.

Experimental Work

The investigation was conducted by using the various specimens. The geometry and orientation for these specimens are shown in Fig. 1. To facilitate the machining of these specimens, the edges of the rail flange and railhead were removed by machining. The remaining head-web-flange rail section was surface ground to a smooth flat plate.

Rotating Beam Specimens

Smooth 4.6 mm (0.180 in.) diameter rotating beam specimens (Fig. 2) were machined from each of the five rails investigated. The tests were conducted on a 15.8-J (140-in.-lb) capacity Krouse rotating beam fatigue testing machine. Conventional $S-N$ curves in air were obtained at testing speeds of 2500 to 6000 cycles per minute (cpm). The terminal conditions for each test correspond to specimen fracture in the testing machine.

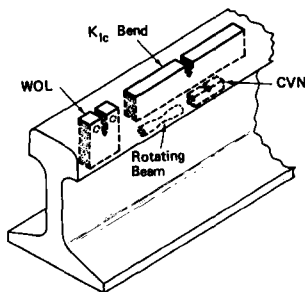


FIG. 1—Various specimens used in the present investigation.

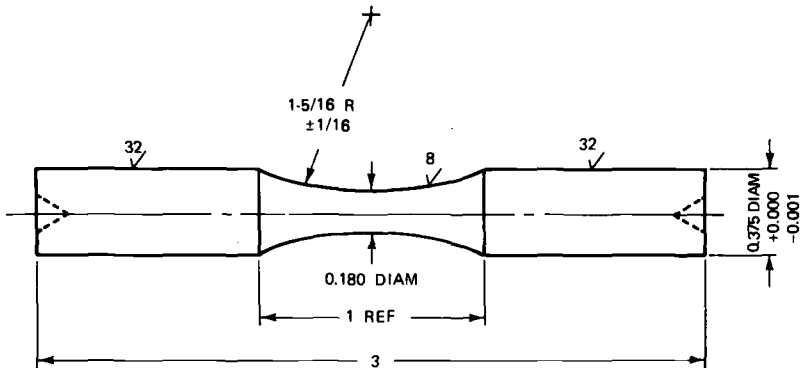
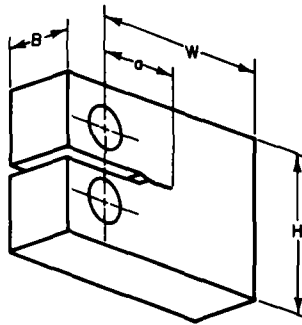


FIG. 2—Smooth rotating beam specimen.

Wedge Opening Loading (WOL) Specimens

The fatigue crack propagation tests in the present investigation were conducted on 13.8-mm (0.545-in.)-thick WOL specimens (Fig. 3). The specimens were machined with the fatigue crack propagation plane oriented transverse to the rail axis (Fig. 1). Two specimens were tested from each rail, one with the crack propagating from the railhead toward the web, and one with the crack propagating from the flange into the web.



a - CRACK LENGTH
 B - SPECIMEN THICKNESS
 W - SPECIMEN WIDTH
 H - SPECIMEN HEIGHT

NOMINAL DIMENSIONS

$a = 1.0$ inch (25.4 mm)
 $B = 0.55$ inch (14 mm)
 $W = 2.55$ inches (64.77 mm)
 $H = 2.48$ inches (62.99 mm)

FIG. 3—Geometry of wedge opening loading (WOL) specimen used in the present investigation.

The stress-intensity factor, K_I , at the tip of a crack in this specimen geometry is given by the equation

$$K_I = \frac{C_3 P}{B\sqrt{a}} \quad (1)$$

where

P = applied load,

B = specimen thickness,

a = crack length measured from the loading plane, and

C_3 = a function of the dimensionless crack length, a/W , where W is the specimen length measured from the loading plane.

For the range $0.35 \leq a/W \leq 0.75$, C_3 can be expressed in the polynomial form as follows

$$\left[30.96 \left(\frac{a}{W} \right) - 195.8 \left(\frac{a}{W} \right)^2 + 730.6 \left(\frac{a}{W} \right)^3 - 1186.3 \left(\frac{a}{W} \right)^4 + 754.6 \left(\frac{a}{W} \right) \right] \quad (2)$$

The specimens were machined to ± 0.05 -mm (± 0.02 -in.) tolerances on all dimensions. An 0.18-mm (0.007-in.) root radius notch was then made with an electrical discharge machine (EDM). The specimen surface was polished to allow for visual identification of the crack tip. To provide a means of measuring the rate of crack extension, two rows of diamond-shaped hardness indentations were made on one of the specimen surfaces (with a Vickers pyramid hardness testing machine) parallel to and 2.3 mm (0.09 in.) from the plane of the crack and in the direction of crack extension. The distance between neighboring indentations was 0.25 ± 0.005 mm (0.01 ± 0.002 in.). Finally, the specimens were cleaned by immersion in an ultrasonically agitated bath.

Testing was done in air at room temperature and at a cyclic stress frequency of 300 cpm in a 222.4 kN (50-kip) materials testing systems (MTS) machine. Alignment was achieved by careful machining of specimens and other auxiliary parts, and by loading the specimens through universal joints.

In all tests, the fatigue crack was initiated and propagated under tension-to-tension sinusoidal loading at a constant maximum load and a constant minimum load, both of which were controlled within ± 1.0 percent. The two load ranges used were 8.9 kN (2000 lb) maximum to 0.89 kN (200 lb) minimum and 7.6 kN (1700 lb) maximum to 0.89 kN (200 lb) minimum. Prior to making crack-length measurements, the fatigue cracks were extended about 5.8 mm (0.23 in.) from the machined notch root at a frequency of 300 cpm. Thus, at the time crack-length measurements were begun, the total crack length, a , was approximately equal to 25.4 mm (1 in.).

Fatigue crack extension was measured optically at $\times 17$ magnification with a microscope (M-101 Gaertner) mounted in a micrometer slide. The

accuracy of measurement of any crack length was approximately ± 0.05 mm (± 0.002 in.).

Fatigue-Cracked K_{Ic} Bend Specimens

For fracture toughness, K_{Ic} , measurements slow-bend, fatigue-cracked specimens were tested in three-point loading according to the ASTM Test for Plane-Strain Fracture Toughness of Metallic Materials (E 399-74). The long axis of the specimen was oriented along the rail length, and the plane of the fatigue crack was transverse to the rail length (Fig. 1). Because of the limited material that was available, some of the specimens were machined from the railhead while others were machined from the rail web. The specimens had a nominal thickness of 12.7 mm (1/2 in.) and were about 33 mm (1.3 in.) wide. They were tested in three-point bending with a ratio of loading span, S , to specimen width, W , equal to 4.0. The specimens were fatigue precracked at room temperature at a maximum stress intensity factor level less than 14.3 MPa \sqrt{m} (13 ksi $\sqrt{in.}$).

The K_{Ic} tests were conducted in the temperature range -45 to $+65^\circ\text{C}$ (-50 to $+150^\circ\text{F}$). The stress intensity factor, K_I , was calculated from the equation (ASTM Method E 399-74)

$$K_I = \frac{PS f\left(\frac{a}{W}\right)}{BW^{3/2}} \quad (3)$$

where

$$\begin{aligned} W &= \text{specimen depth and} \\ f\left(\frac{a}{W}\right) &= \text{a function of relative crack length in ASTM Method} \\ &\quad \text{E 399-74.} \end{aligned}$$

The fracture toughness in terms of K_{Ic} and K_Q was calculated using ASTM Method E 399-74, and from the area under a load-crack opening displacement curve using J -integral procedures [1].³

Charpy V-Notch Specimens

The CVN specimen was the standard specimen, Type A of ASTM Methods and Definition for Mechanical Testing of Steel Products (A 370-76). The long axis of the specimens and the axis of the notches were oriented the same as for the K_{Ic} specimens (Fig. 1). The CVN specimens were machined from ends of fractured K_{Ic} specimens and were tested in the temperature range -60 to $+230^\circ\text{C}$ (-75 to $+450^\circ\text{F}$) according to ASTM procedures.

Results and Discussion

General Discussion

The safety and reliability of structures are governed by many interrelated factors. Fracture of a structural detail can occur as a result of improper

³The italic numbers in brackets refer to the list of references appended to this paper.

material properties, design, fabrication, inspection, erection, and operating conditions. These parameters govern the initiation, subcritical crack propagation, and unstable propagation of cracks under operating conditions. The sum of the elapsed cycles required to initiate a fatigue crack and to propagate the crack from subcritical dimensions to the critical size represents the fatigue life of cyclically loaded structural components. Consequently, an understanding of crack initiation behavior, subcritical crack propagation behavior, and unstable crack propagation behavior can be used to develop a fracture control plan to ensure the safety and reliability of structures. Discussion of the parameters that govern the behavior for each of the stages in the life of cyclically loaded structural details is presented elsewhere [2]. The effect of these parameters on the safety and reliability of carbon-steel rails is presented in the following sections.

Fatigue Crack Initiation

Conventional procedures used to design structural components subjected to fluctuating loads provide (a) a design fatigue curve (*S-N* curve), which is based on the prediction of cyclic life from data on nominal stress (or strain) versus elapsed cycles, and (b) a design fatigue chart (Goodman chart), which indicates the maximum and minimum stresses that can be applied to specimens at any given stress ratio, R ($\sigma_{\min}/\sigma_{\max}$), and at any selected fatigue life. Data used for plotting a curve or chart are usually obtained by testing unnotched specimens and represent the number of cycles required to initiate a crack in the specimen plus the number of cycles required to propagate the crack from a subcritical small size to a critical dimension. The dimension of the critical crack required to cause terminal fracture depends on the magnitude of the applied stress, the specimen geometry, and the specific testing conditions used.

Figure 4 is a schematic *S-N* curve divided into an initiation component and a propagation component. The number of cycles corresponding to the endurance limit represents initiation life primarily, whereas the number of cycles expended in crack initiation at a high value of applied alternating stress is negligible. As the magnitude of the applied alternating stress increases, the total fatigue life decreases and the percent of the fatigue life to initiate a crack decreases and that to propagate a crack increases. Consequently, *S-N*-type data do not provide complete information regarding safe life predictions in structural components, particularly in components having surface irregularities different from those of the test specimens and in components containing crack-like discontinuities, because the existence of surface irregularities and crack-like discontinuities reduces and may eliminate the crack initiation portion of the fatigue life of structural components.

The initiation of fatigue cracks occurs usually in regions of stress concentrations as a result of stress fluctuations. Notches, changes in cross-sectional area, and material discontinuities such as inclusions all cause

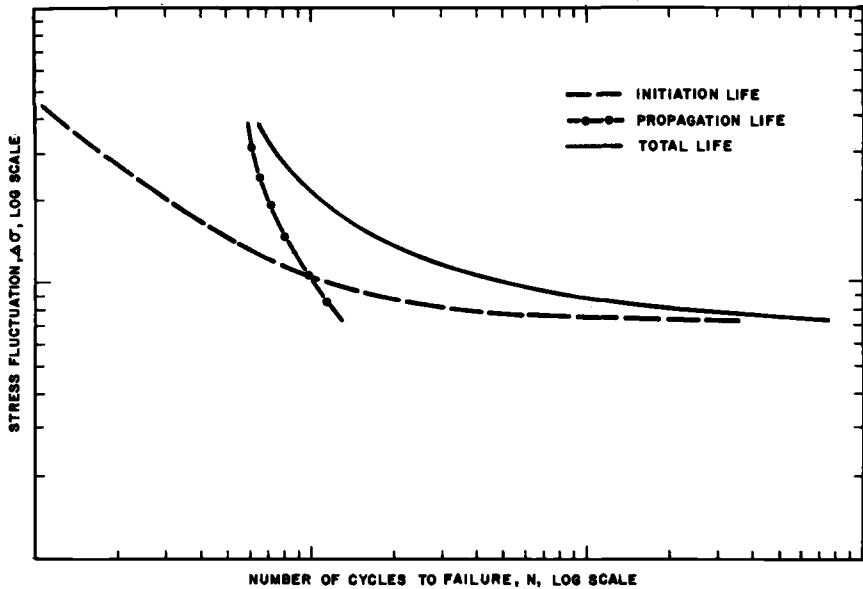


FIG. 4—Schematic S-N curve divided into initiation and propagation components.

localized stress intensification. For example, the material element at the tip of a notch in a cyclically loaded structural component is subjected to the maximum stress, σ_{\max} , and to the maximum stress fluctuations, $\Delta\sigma_{\max}$. Consequently, this material element is most susceptible to fatigue damage and is, in general, the origin of fatigue crack initiation. It has been shown that the maximum stress range (or maximum stress) on this material element can be related to the stress concentration factor, k_t , and to the stress intensity factor range (or stress intensity factor) as follows [2]

$$\Delta\sigma_{\max} = \Delta\sigma k_t = \frac{2}{\sqrt{\pi}} \frac{\Delta K_I}{\sqrt{\rho}} \quad (4)$$

where ρ is the notch tip radius and $\Delta\sigma$ is the applied nominal stress range. Although this equation is considered exact only when ρ approaches zero, Wilson and Gabrielse [3] showed that this relationship is quite accurate for relatively blunt notches.

Experimental data for steels of various yield strengths (Fig. 5), tested at various stress ratios, R (ratio of minimum stress to maximum stress) indicate that the fatigue crack initiation threshold, $(\Delta K_I/\sqrt{\pi})_{th}$ (the value of the parameter $(\Delta K_I/\sqrt{\pi})$ below which fatigue cracks do not initiate) can be estimated

$$\frac{\Delta K_{total}}{\sqrt{\rho}}_{th} = 10 \sqrt{\sigma_y} \quad (5)$$

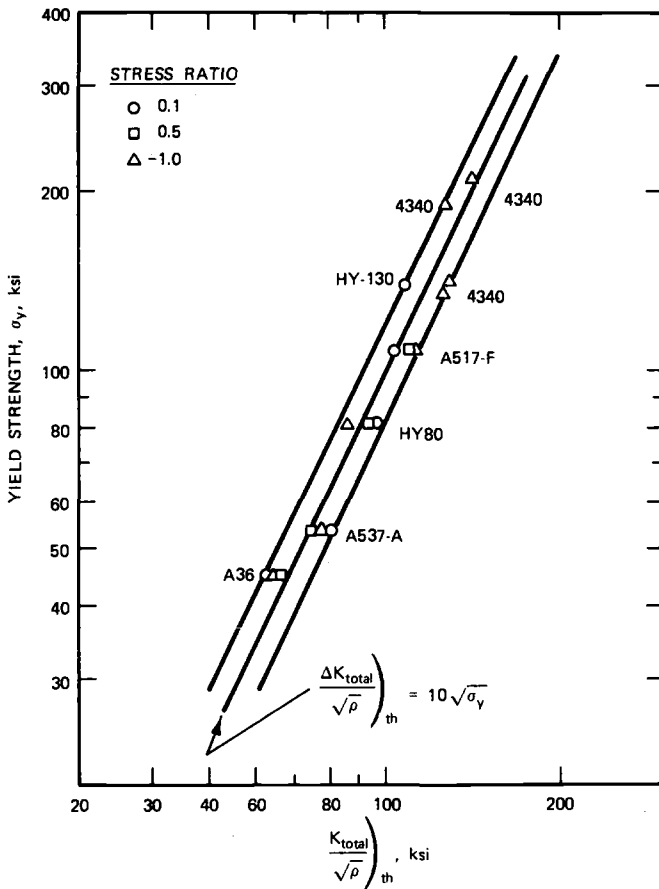


FIG. 5—Dependence of fatigue crack initiation threshold on yield strength.

from where ΔK_{total} is the stress intensity factor range calculated by using the sum of the tension and compression stress range and σ_y is the yield strength of the material.

The number of cycles corresponding to the endurance limit obtained by testing smooth rotating beam specimens represents fatigue crack initiation life primarily. Combining Eqs 4 and 5 and extrapolating the applicability of these equations to smooth rotating beam specimens suggest that the endurance limit should occur when the total range of stress is equal to $11.3\sqrt{\sigma_y}$ and the corresponding alternating stress, σ_{alt} , which is equal to $1/2$ ($\Delta\sigma_{max}$) for a rotating beam specimen, is equal to $5.65\sqrt{\sigma_y}$. The predicted values of alternating stresses corresponding to the endurance limit for the rail carbon steels investigated [$400 \leq \sigma_y < 600$ MPa ($58 \leq \sigma_y < 87$ ksi)] are about 10 percent lower than the experimental values (Fig. 6).

The present data, as well as data published elsewhere [2], show that the

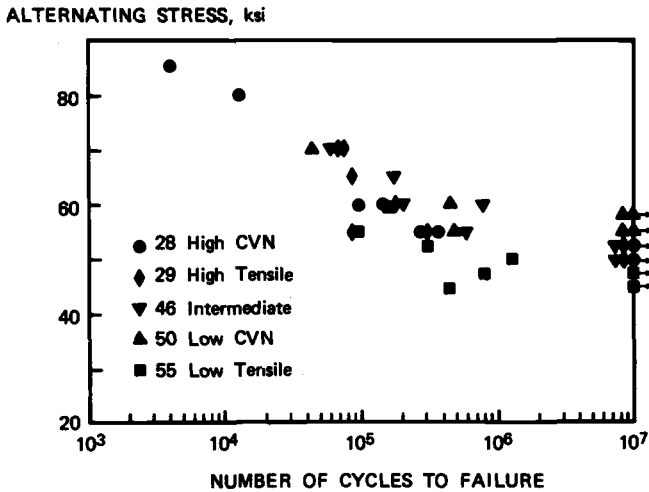


FIG. 6—Rotating beam fatigue results for carbon-steel rails.

value of the fatigue crack initiation threshold increases with increased yield strength or tensile strength of the steel. The published data show also that the fatigue crack initiation life of a component subjected to a given nominal stress range increases with increased yield or tensile strength of the steel; however, the effect of strength decreases with increased magnitude of the stress concentration factor.

Fatigue Crack Propagation

General Behavior—Most fatigue crack growth tests are conducted by subjecting a fatigue-cracked specimen to constant-amplitude, cyclic load fluctuations. Incremental increase of crack length is measured, and the corresponding number of elapsed load cycles is recorded. The data are presented on a plot of crack length, a , versus total number of elapsed load cycles, N (Fig. 7). An increase in the magnitude of cyclic load fluctuation results in a decrease of fatigue life of specimens having identical geometry (Fig. 8). Furthermore, the fatigue life of specimens subjected to a fixed constant-amplitude, cyclic load fluctuation decreases as the length of the initial crack is increased (Fig. 9). Consequently, under a given constant-amplitude stress fluctuation, most of the useful cyclic life is expended when the crack length is very small. Various a -versus- N curves can be generated by varying the magnitude of the cyclic load fluctuation or the size of the initial crack, or both. These curves reduce to a single curve when the data are represented in terms of crack growth rate per cycle of loading, da/dN , and the stress intensity factor range, ΔK_I , because ΔK_I is a single-term parameter that incorporates the effect of changing crack length and cyclic load magnitude. The parameter ΔK_I is representative of the mechanical driving

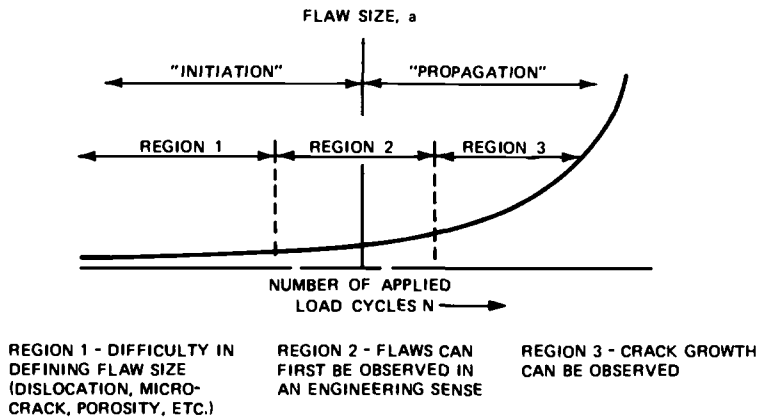


FIG. 7—Schematic showing relation between "initiation" life and "propagation" life.

force and is independent of geometry. The most commonly used presentation of fatigue crack growth data is a log-log plot of the rate of fatigue crack growth per cycle of load fluctuation, da/dN , and the fluctuation of the stress intensity factor, ΔK_I .

The fatigue crack propagation behavior for metals can be divided into

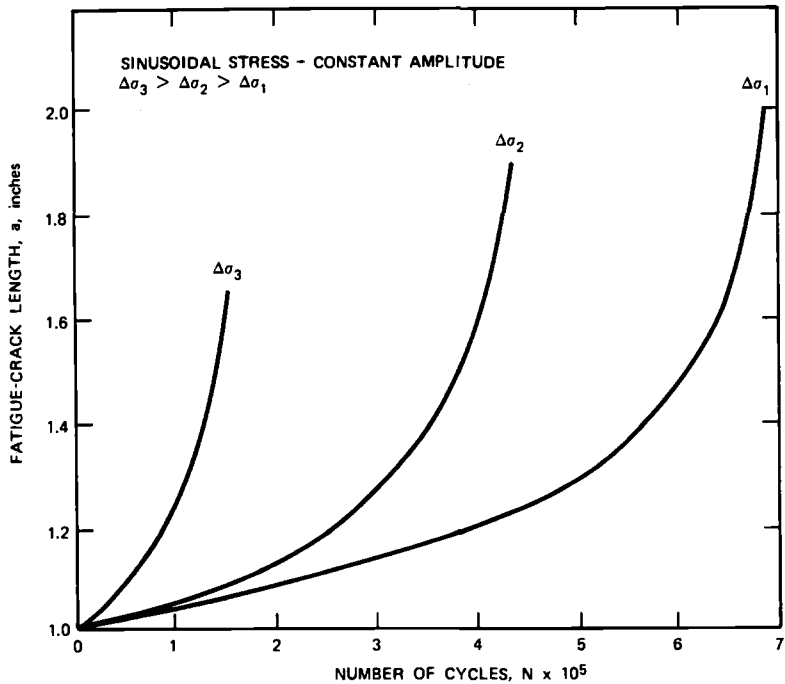


FIG. 8—Schematic showing effect of cyclic stress range on crack growth.

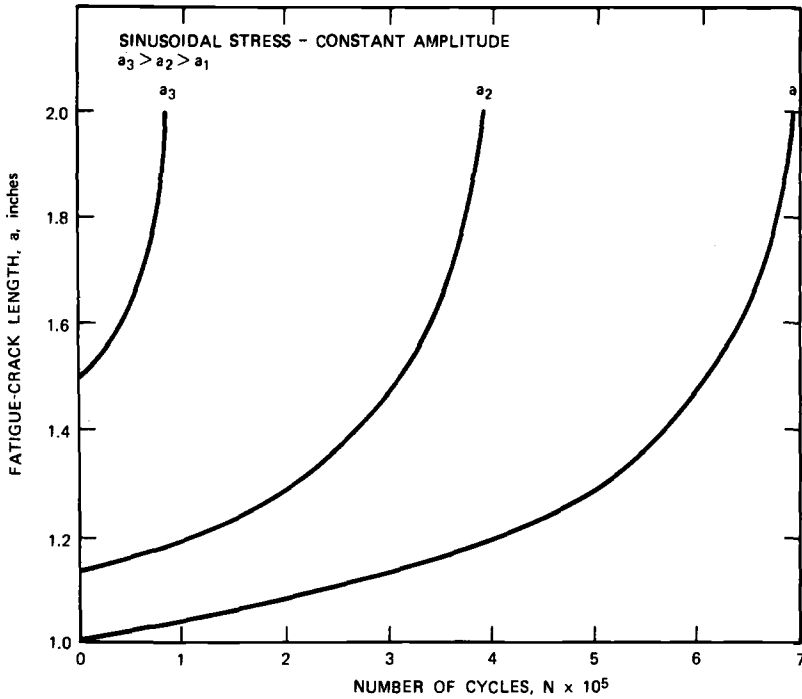


FIG. 9—Effect of initial crack length on crack growth.

three regions (Fig. 10). The behavior in Region I involves a fatigue crack propagation threshold, ΔK_{th} which corresponds to the stress intensity factor range below which cracks do not propagate under cyclic stress fluctuations. An analysis of experimental results published on nonpropagating fatigue cracks shows that conservative estimates of ΔK_{th} for various steels subjected to various stress ratio, R , values can be predicted from Ref 2

$$\Delta K_{th} = 6.4 (1 - 0.85 R) \text{ for } R \geq +0.1 \quad (6)$$

$$\Delta K_{th} = 5.5 \text{ ksi}\sqrt{\text{in.}} \text{ for } R < +0.1$$

where ΔK_{th} is in $\text{ksi}\sqrt{\text{in.}}$

Equation 6 indicates that the fatigue crack propagation threshold for steels is primarily a function of the stress ratio and is essentially independent of mechanical properties and of chemical composition.

The behavior in Region II (Fig. 10) represents the fatigue-crack propagation behavior above ΔK_{th} , which can be represented by

$$\frac{da}{dN} = A (\Delta K_I)^n \quad (7)$$

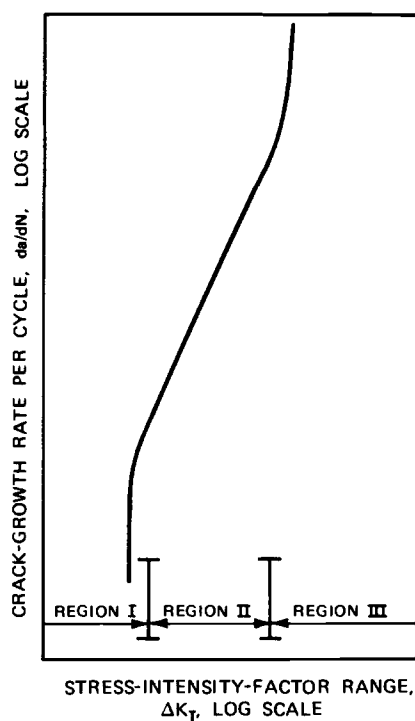


FIG. 10—Schematic representation of fatigue crack growth in metals.

where A and n are constants. This behavior is discussed further in the following section.

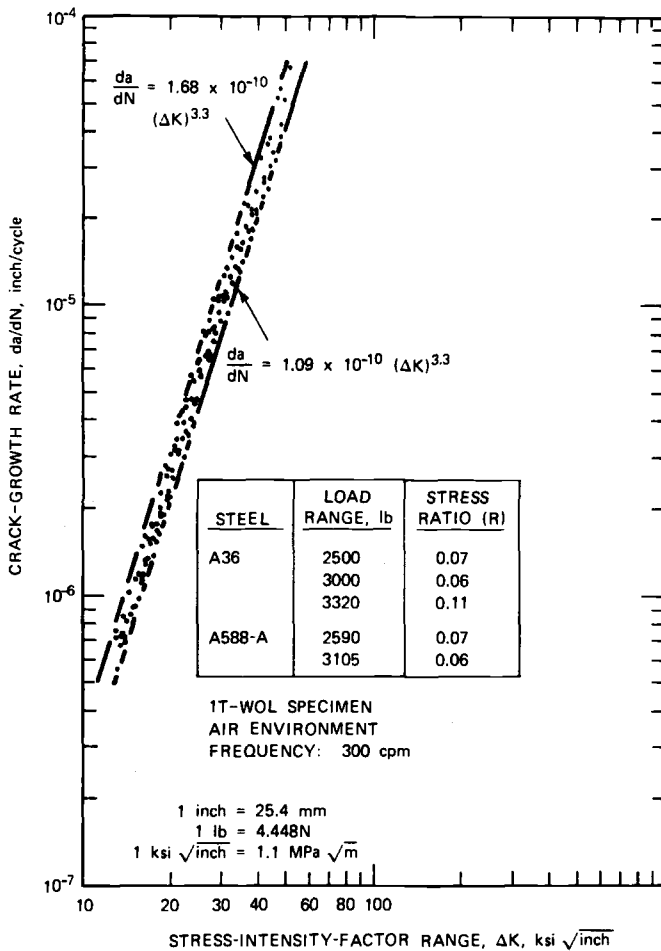
Rail Steels—Extensive fatigue crack growth rate data for various steels show that the primary parameter affecting growth rate in Region II is the range of fluctuation in the stress intensity factor, and that the mechanical and metallurgical properties of these steels have negligible effects on the fatigue crack growth rate in a room-temperature air environment. The data for ferrite-pearlite steels, including A36, A572, A588, ABS-C, A302-B, and A537-A steels fall within a single band [2,4] as shown in Fig. 11 [4], and the upper bound of the scatter of the fatigue crack propagation rate data for these steels in an air environment can be calculated from Ref 4

$$\frac{da}{dN} = 1.68 \times 10^{-10} (\Delta K_I)^{3.3} \quad (8)$$

where

$$a = \text{in.}, \text{ and} \\ \Delta K_I = \text{ksi } \sqrt{\text{in.}}$$

The stress ratio, R , and mean stress have only a small effect on the rate of crack growth in Region II [2]. However, as has been discussed already, they have a significant effect on the behavior in Region I.



FATIGUE-CRACK-PROPAGATION DATA FOR A36 AND A588-A STEELS

FIG. 11—Fatigue crack propagation data for A36 and A588-A steels.

The fatigue crack propagation data for the rail carbon steels investigated are shown in Fig. 12. Superimposed on the data is the upper scatterband line for ferrite-pearlite steels that corresponds to Eq 8. The data show that the fatigue crack propagation rates were identical for the rail carbon steels investigated, regardless of their chemical composition or mechanical properties, and that their propagation behavior was the same as that of the ferrite-pearlite structural steels previously studied despite the large differences in chemical composition and mechanical properties.

Fracture Toughness

Charpy V-Notch Behavior—The CVN behavior for the five carbon-steel rails investigated is shown in Fig. 13. The data show that the rail identified as

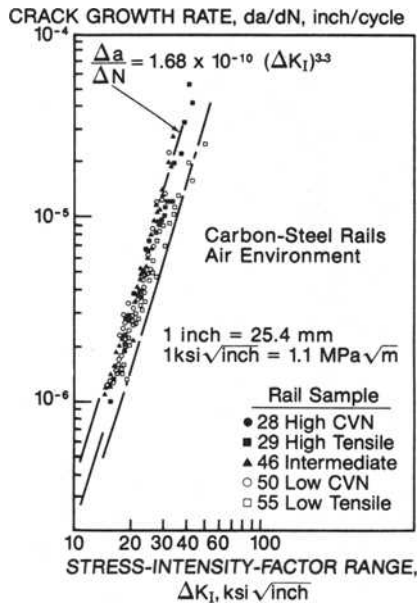


FIG. 12—Fatigue crack propagation for carbon-steel rails.

having the highest CVN value and the rail having the lowest tensile value had essentially identical CVN transition behavior; both had an upper-shelf energy absorption equal to 34 J (25 ft-lb). The upper shelf for these two rails occurred at about +175°C (+350°F). The rail having the highest tensile value and the rail having intermediate tensile and CVN values had similar CVN

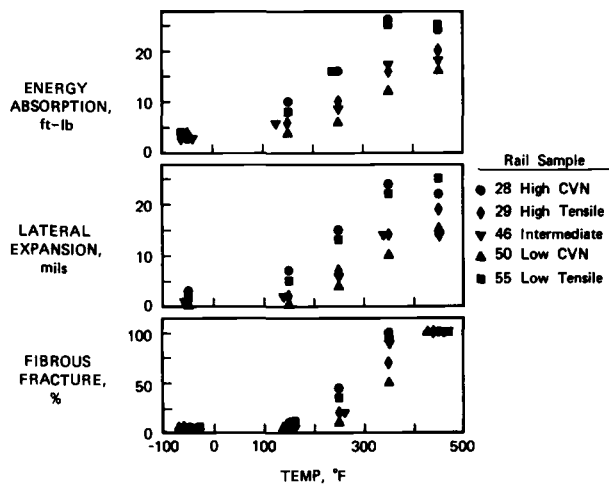


FIG. 13—Charpy V-notch properties of carbon-steel rails.

transition curves and an upper-shelf value between 24.5 and 27 J (18 and 20 ft-lb) occurring at about $+230^{\circ}\text{C}$ ($+450^{\circ}\text{F}$). The rail having the lowest room-temperature CVN value had the highest CVN transition temperature, with an upper-shelf, energy absorption value of 21.8 J (16 ft-lb) that occurred at $+230^{\circ}\text{C}$ ($+450^{\circ}\text{F}$). Despite these differences between the upper-shelf behavior, all five rails investigated had CVN energy absorption values between 4.1 and 6.1 J (3 and 4.5 ft-lb) at the minimum operating temperature of about -35°C (-30°F) expected for rails in the continental United States. Furthermore, the fracture appearance at temperatures below $+65^{\circ}\text{C}$ ($+150^{\circ}\text{F}$) was essentially 100 percent cleavage.

K_{Ic} Behavior—The stress intensity factor value for a given stress increases with increased crack length until it reaches a critical value, K_{Ic} at which the crack propagates unstably and the life of the component is terminated. For Mode I deformation (Fig. 14) and for small crack-tip plastic deformation (plane-strain conditions), the critical stress intensity factor for fracture instability, K_{Ic} , represents the inherent ability of a material to resist progressive tensile crack extension. However, this fracture toughness property varies with constraint, and, like other material properties such as yield strength, it varies with temperature and loading rate [2]. The fracture toughness K_{Ic} , obtained at a given loading rate increases with increased test

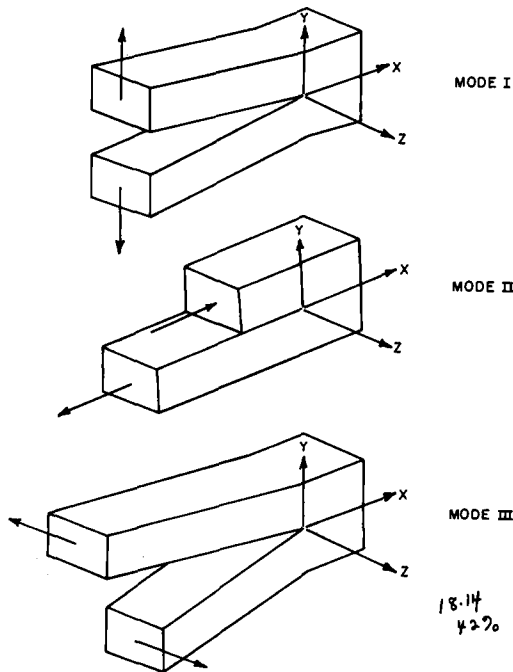


FIG. 14—Three basic modes of crack surface displacements.

temperature through the transition temperature region, and, at a given test temperature, it decreases with increased loading rate.

Because the K_{Ic} specimens tested had a nominal thickness of 12.7 mm (0.5 in.), valid K_{Ic} data were not obtained for most of the tests because of insufficient constraint. Consequently, the invalid K_{Ic} test records were analyzed by calculating K_q (ASTM Method E 399-74) values and by using J -integral procedures [1]. Moreover, static K_{Ic} values were estimated from the impact CVN data by first calculating the fracture toughness under impact loading, K_{Id} , using the empirical relationship [2,5]

$$\frac{K_{Id}^2}{E} = 5 \text{ (CVN ft-lb)} \quad (9)$$

where E is Young's modulus and then shifting these K_{Id} values to lower temperatures by using the following temperature shift equation between static and impact loading [2,5,6]

$$T_{\text{shift}} = 215 - 1.5\sigma_r \text{ for } 250 \text{ MPa} \leq \sigma < 965 \text{ MPa} \quad (10)$$

where T_{shift} is in degrees Fahrenheit.⁴

The fracture toughness data under slow loading conditions for the five rails investigated are presented in Fig. 15 for the rail with the highest CVN value and the rail with the lowest tensile value, and in Fig. 16 for the three remaining rails. The fracture mechanics toughness data show, like the CVN data, that the rail with highest room-temperature CVN value and the one with the lowest room-temperature tensile value had essentially identical fracture toughness values in the temperature range -45 to $+40^\circ\text{C}$ (-50 to $+100^\circ\text{F}$). The data show also that the fracture toughnesses for the three remaining rails were essentially identical in the temperature range -40 to $+65^\circ\text{C}$ (-50 to $+150^\circ\text{F}$). This observation confirms predictions based on temperature shift procedures between static and impact loading and shows that differences in CVN behavior for these steels that occur at temperatures above $+120^\circ\text{C}$ ($+250^\circ\text{F}$) have negligible effects on the fracture behavior in the temperature range -40 to $+65^\circ\text{C}$ (-50 to $+100^\circ\text{F}$). The data in Figs. 15 and 16 show that in this temperature range the static toughness for the rail with highest room-temperature CVN value and for the one with lowest room-temperature tensile value (Fig. 13) was higher than the static toughness for the rails with highest tensile value, intermediate tensile and CVN values, and lowest CVN value (Fig. 13). However, based on the static K_{Ic} data presented in Figs. 15 and 16 and the shift of this data to higher temperatures using Eq 10, and based on the CVN data and the corresponding K_{Id} values calculated by using Eq 9, the plane-strain, dynamic fracture toughness, K_{Id} , at the minimum operating temperature of about -35°C

⁴250 MPa = 36 ksi. 965 MPa = 140 ksi.

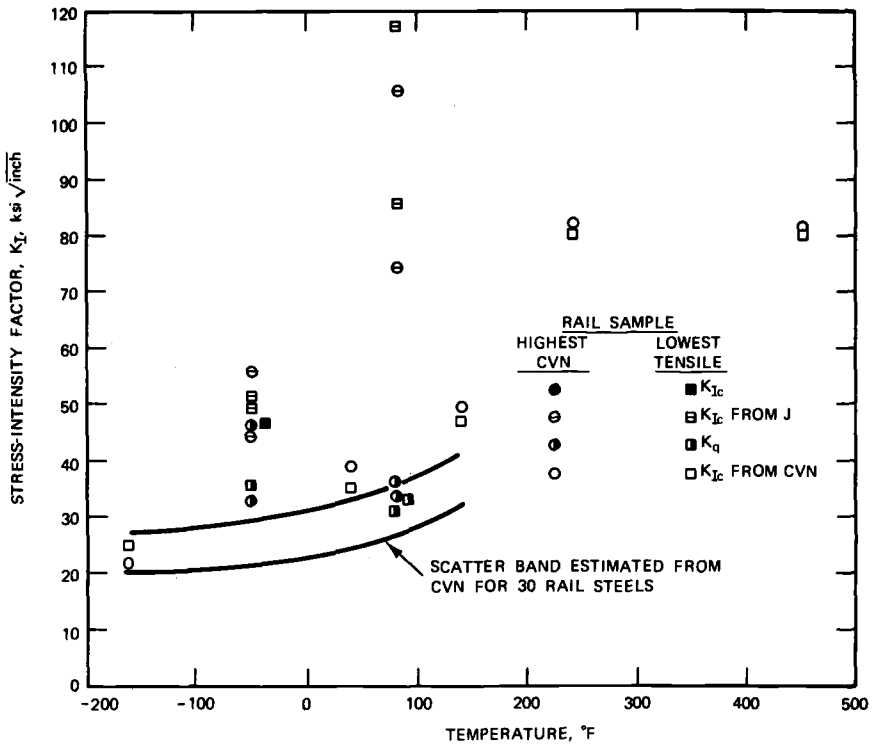


FIG. 15—Fracture toughness of carbon-steel rails.

(-30°F) for the rails investigated would be essentially identical and equal to about $27.5 \text{ MPa} \sqrt{\text{m}}$ ($25 \text{ ksi} \sqrt{\text{in.}}$).

Analysis of In-Service Behavior for Rails

The increased wheel loads that stress the rail above the yield point have increased damage to the track structure such that, in many instances, rail life is dictated by fatigue rather than wear. To improve the safety and reliability of the track structure requires a further understanding and possible modifications in present-day practices. The identification of the specific modifications needed requires a thorough study of material properties, design, fabrication, inspection, installation, and service conditions. Changes in these parameters affect the useful fatigue life of rails. Consequently, crack initiation, subcritical crack propagation, and fracture behavior of rail steels are primary considerations in the analysis of the safety and reliability of rails. Potential exists for increasing the fatigue life of rails by minimizing or eliminating the crack initiation sites such as inclusions in the rail steel, by decreasing the magnitude and fluctuation of the in-service stresses, and by increasing the toughness of the steel. The relative contribution of each of

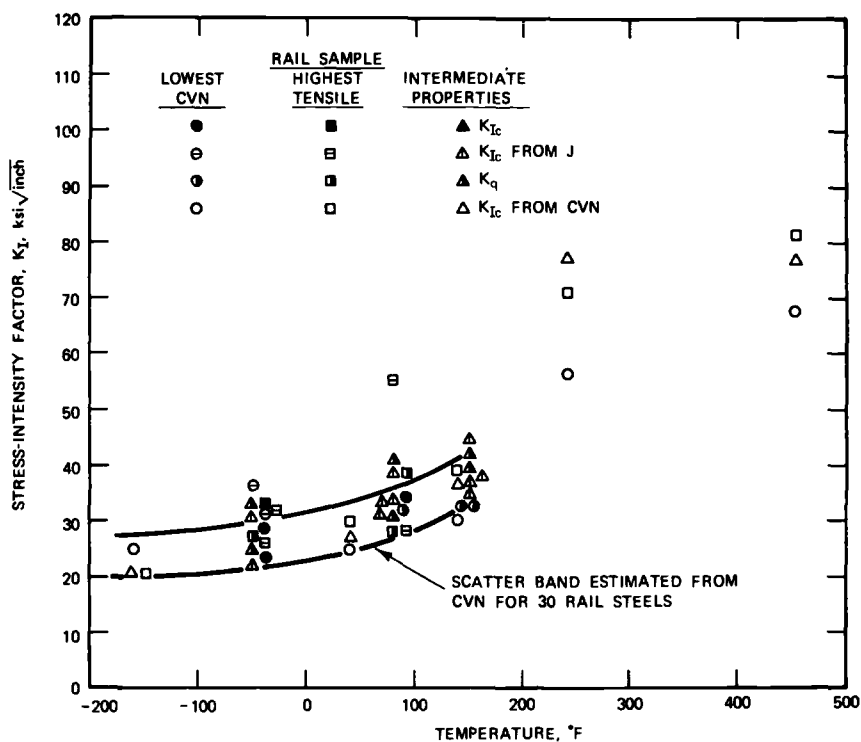


FIG. 16—Fracture toughness of carbon-steel rails.

these changes with respect to the fatigue life for rails are presented in the following discussion.

The discussion presented in the preceding sections showed that the fatigue crack initiation life for a given steel can be increased significantly by decreasing the applied stress range or the magnitude of the stress concentration factor, or by both. Furthermore, the fatigue crack initiation life for a component containing a given stress raiser (discontinuity, inclusion, or change in geometry) can be increased by selecting a higher strength steel. However, this difference between steels having different tensile strengths decreases significantly as the magnitude of the stress concentration factor increases. Thus, although the endurance limit for rail steels obtained in the laboratory by testing smooth specimens increases with increased strength, the in-service fatigue crack initiation life for heavily loaded rails may be negligible because in-service fracture of most rails is caused by fatigue cracks which nucleate at regions of relatively high stress concentration such as inclusions in the material.

In-service fracture of most rails is caused by the initiation of fatigue cracks and their propagation to critical dimensions. The fractographic analysis which is summarized in the companion paper in this symposium (Footnote 2) showed that these cracks initiate from stringer-type discontinuities (for

example, calcium aluminate inclusion stringers) that are located in the vicinity of the elastic-plastic boundary between the plastically deformed layer of the railhead and the remainder of the railhead. The depth of the plastically deformed layer was about 9.5 mm (3/8 in.).

Further investigation of these initiation sites showed that the length-to-width ratio of these stringers was very large and that their width varied from about 0.025 to 0.06 mm (1.0 to 2.5 mils). These discontinuities are subjected to Mode I, Mode II, and Mode III in-service deformations. Although the resulting in-service residual and applied stresses are very complex and are yet to be defined, the magnitude of the equivalent Mode I stress fluctuations applied to these discontinuities may be estimated by using Eq 6. Thus, assuming that these discontinuities behave as imbedded fatigue cracks having a crack width, $2a$, equal to 0.025 mm (1.0 mils), and substituting $\Delta K_{th} = 6 \text{ MPa } \sqrt{\text{m}}$ (5.5 ksi $\sqrt{\text{in.}}$) because $R < 0$, and $K_I = \sigma\sqrt{\pi a}$ for an imbedded tunnel crack, Eq 6 suggests that these discontinuities are subjected to an equivalent nominal tensile stress fluctuation equal to or greater than the tensile strength of steel.

Because fatigue crack initiation from notches is governed by the sum of the tensile and compressive stress range, and because of the high compressive stresses experienced by the discontinuities with the passage of each wheel, Eq 5 indicates that the fatigue cracks will initiate from these discontinuities even when the tensile stress component is a small fraction of the tensile strength of the steel.

Although the magnitude of residual stresses and stress fluctuations in a railhead cannot be predicted accurately at the present time, the fact still remains that in-service fatigue cracks initiate and propagate from inclusions that are 0.025 mm (1.0 mil) wide.

Consequently, to prevent in-service fatigue crack initiation and propagation in rail steels subjected to heavy wheel loads, stringer discontinuities having a width less than about 0.025 mm (1 mil) would have to be detected and eliminated. The cost of steelmaking practices required to eliminate such small discontinuities is believed to be economically prohibitive. Moreover, the detection of such discontinuities is beyond the capabilities of presently available nondestructive inspection procedures. The difficulties in using nondestructive testing are compounded by the fact that the severity of these discontinuities depends on their shape and their location and distribution in the rail.

The probability of the existence of a small discontinuity that could cause the initiation of a fatigue crack in rail service increases significantly with increased load. Once a fatigue crack is initiated, propagation occurs under the influence of the applied cyclic stress fluctuations that are caused by the passage of each wheel. The fatigue crack propagation data for carbon-steel rails (Fig. 12) has been shown to be independent of the chemical composition or the mechanical properties of the steel and is governed primarily by the magnitude of the applied stress intensity factor range.

The rails investigated in the present study were removed from service prior

to terminal fracture. The data presented in Table 1 show that these rails had been in service between 15 and 18 years and had carried between 436 and 505 MMT (481 and 557 MGT). The rails with the highest room-temperature tensile strength and with the lowest room-temperature CVN value were removed from service because of shell defects. The rails with highest room-temperature CVN value, intermediate room-temperature tensile and CVN values, and lowest room-temperature tensile strength were removed from service because they contained detail fractures from shelling. The room-temperature CVN values for these three rails ranged from 5.8 to 9.9 J (4.3 to 7.3 ft-lb), and the CVN values at about -35°C (-30°F) were between 4.1 and 5.4 J (3 and 4 ft-lb) (Fig. 13). When these rails were removed from service, they contained transverse fatigue cracks that had extended over an area representing between 25 and 65 percent of the railhead cross section (Fig. 17). One of the rails that was removed from service (AAR Rail No. 30) had a CVN value of 5.4 J (4 ft-lb) at room temperature and contained a transverse fatigue crack that extended over 82 percent of the railhead [7]. Such large transverse cracks can be tolerated in rails because the primary deformation of the transverse crack surfaces is in Mode II (Fig. 14) and because the tensile stresses perpendicular to this crack plane are small. However, these tensile stresses, as well as stresses caused by Mode III deformation (Fig. 14), will increase as the cracked area in the railhead increases.

The remaining useful fatigue life for rails containing large transverse cracks is very small, and a significant increase in the fracture toughness of the rail steel would result in a negligible increase in the fatigue life of the rail.

In summary, from the results of the present investigation, it is concluded that:

1. Fatigue cracks initiate in service from stringer inclusions having a width of about 0.025 mm (1.0 mils). The elimination of these discontinuities by changes in steelmaking or by nondestructive inspection is technologically and economically infeasible.
2. The fatigue crack propagation behavior was independent of the chemical composition and mechanical properties of carbon-steel rails.
3. A significant increase in the fracture toughness of the rails would result in a negligible increase in the useful fatigue life of the rail.
4. Fatigue crack initiation, fatigue crack propagation, and final fracture are strongly dependent on the magnitude and distribution of the residual stresses and the applied cyclic stresses.

Overall, it is reasonable to conclude that the service lives of the rails investigated would have been longer if the inclusions responsible for crack initiation had not been present. However, it should be noted that most of these rails had service lives lasting 16 years—454 MMT (500 MGT), with one sample lasting 22 years—685 MMT (755 MGT). Because fatigue cracks initiate in service from inclusions having a width of about 0.025 mm (1.0 mils), the cost of steelmaking practices required to eliminate such small discontinuities is believed to be economically prohibitive. Moreover, the

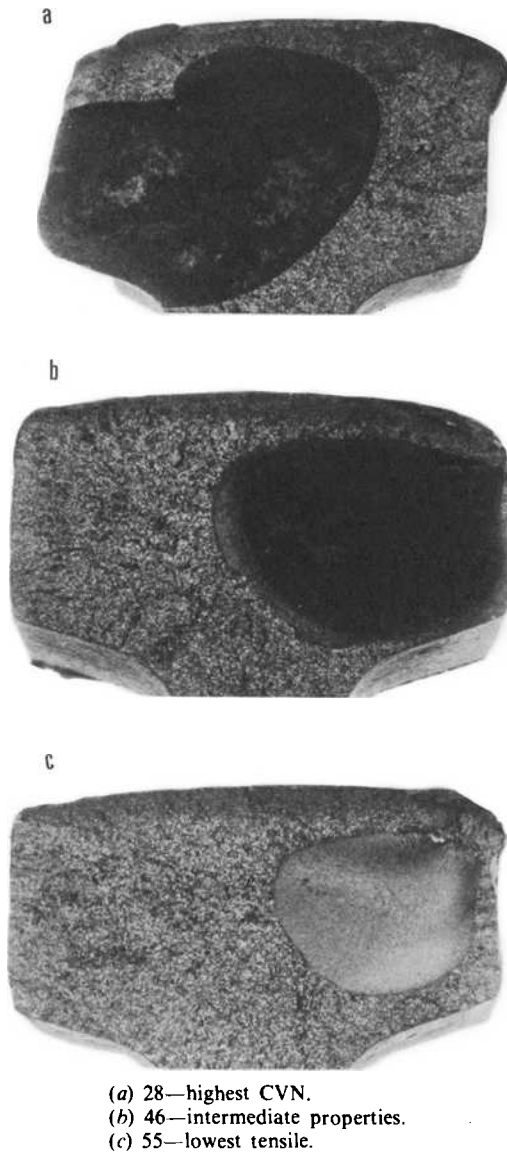


FIG. 17—*Transverse fatigue cracks in carbon-steel rails.*

detection of such discontinuities is beyond the capabilities of presently available nondestructive inspection procedures. The difficulties in using nondestructive testing are compounded by the fact that the severity of these discontinuities depends on their shape and their location and distribution in the rail. Consequently, it is believed that the safety and reliability of rails can

be ensured best by decreasing the magnitude and fluctuation of the stresses in the rail and by periodic nondestructive field inspection. Significant increase in the fatigue life of rails may be achieved by decreasing the wheel load, by maintaining the roadbed, by changes in the design of rails, and by establishing a residual compressive stress field in the upper portion of the railhead which can be accomplished, for example, by induction hardening.

References

- [1] *Fracture Toughness, ASTM STP 514*, American Society for Testing and Materials, 1976.
- [2] Rolfe, S. T. and Barsom, J. M., *Fracture and Fatigue Control in Structures—Applications of Fracture Mechanics*, Prentice-Hall, Inc., Englewood Cliffs, N.J., 1977.
- [3] Wilson, W. K. and Gabrielse, S. E., "Elasticity Analysis of Blunt Notched Compact Tension Specimens," Research Report 71-1E7, LOWFA-R1, Westinghouse Research Laboratory, Pittsburgh, Pa., 5 Feb. 1971.
- [4] Kapadia, B. M. and Imhof, E. J., Jr., in *Flaw Growth and Fracture, ASTM STP 631*, American Society for Testing and Materials, 1977, pp. 159–173.
- [5] Barsom, J. M., "The Development of AASHTO Fracture-Toughness Requirements for Bridge Steels," American Iron and Steel Institute, Washington, D.C., Feb. 1975.
- [6] Barsom, J. J., "Effect of Temperature and Rate of Loading on the Fracture Behavior of Various Steels," *Dynamic Fracture Toughness*, The Welding Institute, Abington, Cambridge, England, 1976.
- [7] Besuner, P. M., "Fracture Mechanics Analysis of Rails with Shell-Initiated Transverse Defects," Failure Analysis Associates Report, Contract FAA-75-1-1(B), Nov. 1975.

DISCUSSION

*F. B. Fletcher*¹ (*written discussion*)—The authors have concluded, apparently on the basis of ten specimens from five rails, that fatigue crack propagation rates are identical for all carbon rail steels. Such a sweeping assertion is unwarranted in the light of other fatigue crack propagation rate data on rail steels presented at this symposium and from their own reported data.

Feddersen and Broek² examined 66 rail samples and found a wide variation in fatigue crack propagation rates. While it is not yet possible to attribute the fatigue crack propagation rates to specific compositional or mechanical properties, the point is that different rail samples do exhibit different fatigue crack growth rates. Fowler and Tetelman³ have shown the strong effect of grain boundary ferrite on retarding the fatigue crack propagation rate of carbon rail steels. This is clearly an example of metallurgical structure affecting fatigue crack propagation. Similarly, Masumoto et al⁴ report that a quenched and tempered microstructure and a fine

¹Climax Molybdenum, Ann Arbor, Mich.

²Feddersen, C. E. and Broek, David, this publication, pp. 414–429.

³Fowler, G. J. and Tetelman, A. S., this publication, pp. 363–386.

⁴Masumoto, H., Sugino, K., Nisida, S., Kurihara, R., and Matsuyama, S., this publication, pp. 233–255.

pearlite microstructure exhibit slower fatigue crack propagation rates than a coarse pearlite microstructure.

The authors' own data indicate statistically significant ($\alpha = 0.05$) differences in fatigue crack propagation among the rails they examined. Assuming a log normal distribution of fatigue crack propagation rate measurements at a stress intensity range of 19 to 21 ksi $\sqrt{\text{in.}}$, the following average da/dN values were determined from the data in Fig. 12:

Rail No.	Rail Sample	da/dN at $\Delta K_I \cong 20$ ksi $\sqrt{\text{in.}}$, in./cycle
1	high CVN	1.63×10^{-6}
2	low tensile	2.05×10^{-6}
3	intermediate	2.74×10^{-6}
4	low CVN	2.91×10^{-6}
5	high tensile	3.12×10^{-6}

Applying student's t tests to the data show that the following rates are significantly ($\alpha = 0.05$) different: Rails 1, 3; 1, 4; 1, 5; 2, 5; and 4, 5. Note that the apparent crack propagation rate of Rail 5 is nearly twice that of Rail 1. To conclude, as the authors have, that these fatigue crack propagation rates are identical is incorrect.

The importance of differences in fatigue crack propagation rates between various rail steels cannot be overemphasized; a transverse defect in a rail with a slow fatigue crack propagation rate is more likely to be successfully detected before the critical defect size is reached than if the rail has a fast fatigue crack propagation rate. Further experimental work is required before a rail steel can be designed specifically for reduced fatigue crack propagation rate. However, refining the pearlite interlamellar spacing and providing ferrite envelopes around pearlite colonies are two potential approaches which may lead to rail steels with greater resistance to fatigue crack propagation—rails which will be both safer and more economical.

J. M. Barsom and E. J. Imhof, Jr. (authors' closure)—The authors believe that F. B. Fletcher's conclusions concerning the effects of chemical composition and microstructure on the rate of fatigue crack propagation and on the statistical significance of the differences between the carbon-steel rails investigated are erroneous for the following reasons.

Extensive data on ferrite-pearlite steels indicate that variations in fatigue crack propagation rates caused by differences in material properties, if they exist, are well within experimental scatter for a given material.⁵ The most comprehensive statistical analysis for fatigue crack propagation data was conducted by Task Group E24.04.01 on Fatigue Crack Growth Rate Testing

⁵Rolfe, S. T. and Barsom, J. M., *Fracture and Fatigue Control in Structures—Applications of Fracture Mechanics*, Prentice-Hall, Inc., Englewood, Cliffs, N.J., 1977.

of ASTM Committee E-24 on Fracture Testing of Materials.⁶ The task group undertook an extensive interlaboratory (round-robin) testing program to identify and characterize the sources of variability and bias inherent in fatigue crack growth rate testing. The results of this investigation showed, among other things, that "the overall interlaboratory variability was found to be approximately 3 to 1 (on crack growth rate at a given stress intensity range). The intralaboratory variability was typically 2 to 1. . . The results of this study show that the primary source of variability associated with fatigue crack growth rate testing is the experimental procedure used to obtain the raw test data (crack length versus elapsed cycles)." Because the variability in growth rate at $\Delta K_I = 20 \text{ ksi } \sqrt{\text{in.}}$ is within the 2-to-1 intralaboratory variability, the differences emphasized by Mr. Fletcher using student's t tests are not significant, contrary to his claims. Moreover, the decrease in growth rate by a factor of two that Fowler and Tetelman (Footnote 3) attributed to grain boundary ferrite is also within the intralaboratory variability.

The variability in growth rate observed by Feddersen and Broek (Footnote 2) and by Masumoto et al (Footnote 4) cannot be analyzed without full knowledge of testing procedures because "the primary source of variability associated with fatigue crack growth rate testing was found to be the experimental procedure used to obtain the raw test data (crack length versus elapsed cycles)" (Footnote 6). For example, the variability in the data for each specimen presented by Feddersen and Broek shows that they had experimental difficulties in obtaining the raw data.

Similarly, the data presented by Masumoto et al raise many questions about their experimental procedure. These include the magnitude of crack tunneling (cracks that are longer in the center of the specimen than on the surface) that they state to have occurred, and the variability in crack tunneling with the strength of the material; the reasons why the tests were conducted at different initial ΔK values, despite the fact that the specimen geometries were identical; as well as other questions.

It should be pointed up that microstructure can result in differences in the rate of fatigue crack growth. For example, one of the authors has published information to show that microstructure results in slower growth rate in ferrite-pearlite steels than in martensitic steels.⁷ However, differences in microstructure for carbon-steel rails resulted in variations in the rate of growth that are well within experimental error. Data scatter for fatigue crack-growth rates in the absence of microstructural differences is approximately 3 to 1 (Footnote 6). Thus, whether observed effects of microstructure on the rate of fatigue crack growth are significant should be judged on the basis of this experimental limitation. Because microstructural effects and

⁶Clark, W. G., Jr., and Hudak, S. J., Jr., "Variability in Fatigue Crack Growth Rate Testing," *Journal of Testing and Evaluation*, Vol. 3, No. 6, 1975.

⁷Barsom, J. M., "Fatigue-Crack Propagation in Steels of Various Yield Strengths," *Transactions of the ASME, American Society of Mechanical Engineers*, Vol. 93, Series B, No. 4, Nov. 1971.

heat-to-heat variations are within the limitations of present experimental procedures, the safety and reliability of carbon-steel rails can be ensured by the use of an equation that represents the lower bound for data scatter.

Fatigue Crack Propagation in Rail Steels*

REFERENCE: Feddersen, C. E. and Broek, David, "Fatigue Crack Propagation in Rail Steels," *Rail Steels—Developments, Processing, and Use*, ASTM STP 644, D. H. Stone and G. G. Knupp, Eds., American Society for Testing and Materials, 1978, pp. 414–429.

ABSTRACT: Baseline fatigue crack growth data at $R = 0$ and mechanical property data have been generated on 66 different rail materials which are in service on U.S. railroads. These data are evaluated, along with metallurgical variables such as chemical composition and microstructure, in an attempt to develop a correlation of mechanical and metallurgical factors affecting crack behavior in rail steels. The ultimate objective of this effort is the development of a rail failure model to enable the determination of safe inspection intervals, through prediction of fatigue crack growth in rail under service loading.

KEY WORDS: steels, railroad tracks, fatigue (materials), cracks

The evaluation and quantification of fatigue crack propagation behavior in rail steels is necessary to establish safe inspection intervals and useful service lifetimes for railroad track systems. Since fatigue cracks in rails can be the source of failures and subsequent train derailments, the prevention of such failures requires the timely detection of fatigue cracks and an assessment of their severity.

One portion of the Federal Railroad Administration's (FRA) Track Performance Improvement Program is the development of a predictive rail failure model which will enable a determination of optimal inspection periods based on a calculation of fatigue crack propagation behavior. Designation of the safe inspection interval must reflect variances in crack growth behavior and initial detection accuracy as well as the time increment necessary for subsequent rail repair or replacement.

The research reported here concerns the first phase of the program to develop this rail failure model. It consists of the generation and analysis of fatigue crack growth data on 66 rail samples of various ages, producers, and weights. The samples were taken from existing track from various sections of the United States. In order to predict fatigue crack growth and failures under

*Original experimental data were measured in U.S. customary units.

¹Research scientist and research leader, Structural Materials Section, respectively, Battelle Columbus Laboratories, Columbus, Ohio 43201.

a service load environment, fatigue crack rate data from a sufficiently large sample of rails presently in service are required to properly evaluate the statistical variability of fatigue crack growth properties. In the second phase of the program, fatigue crack propagation under simulated service loading will be evaluated. Subsequently, the rail failure model will be developed.

Experimental Program

Materials

Since the general objective of this phase of the program was to characterize crack growth in rail materials which are presently, and will continue to be, in service on U.S. railroads, an effort was made to assemble a representative sampling of rail materials. Variations in rail size, rail producer, and year of production were the primary selection criteria. A total of 66 material samples was received, representing sizes from 85 to 140 lb/yd, produced during the period from 1911 to 1975 in both U.S. and Japanese mills.

Chemical Analyses

Specifications for the chemical composition of rail steels vary slightly with the rail size (expressed as the weight per yard). The ASTM Specification for Carbon Steel Tee Rails (A 1-76) cites the following chemical requirements:

Element, %	Nominal Weight, lb/yd			
	61 to 80	81 to 90	91 to 120	121 and Over
Carbon	0.55 to 0.68	0.64 to 0.77	0.67 to 0.80	0.69 to 0.82
Manganese	0.60 to 0.90	0.60 to 0.90	0.70 to 1.00	0.70 to 1.00
Phosphorus, max	0.04	0.04	0.04	0.04
Silicon	0.10 to 0.23	0.10 to 0.23	0.10 to 0.23	0.10 to 0.23

Chemical analyses of the 66 rail samples were made for total carbon, manganese, silicon, sulfur, hydrogen, and oxygen. Phosphorus content was not determined. The manganese content of four samples was within a range of 1.36 to 1.48 percent. All others were within the acceptable range. With the exception of one sample, the hydrogen content was between 0.2 and 1.1 ppm. The oxygen content was generally well below 100 ppm with two exceptions.

Specimens

From each material sample, one compact fatigue crack propagation and one 0.25-in.-diameter tensile specimen were machined. (Following the segregation of these data into three categories of low, medium, and high

crack growth rates, Charpy V-notched specimens were also prepared.) The orientation of these baseline specimens is shown in Fig. 1, with the dimensions of the compact crack-growth specimen shown in Fig. 2. The thickness of the specimens was selected as 0.5 in., which was the largest web thickness (after cleanup) common to all rail sections.

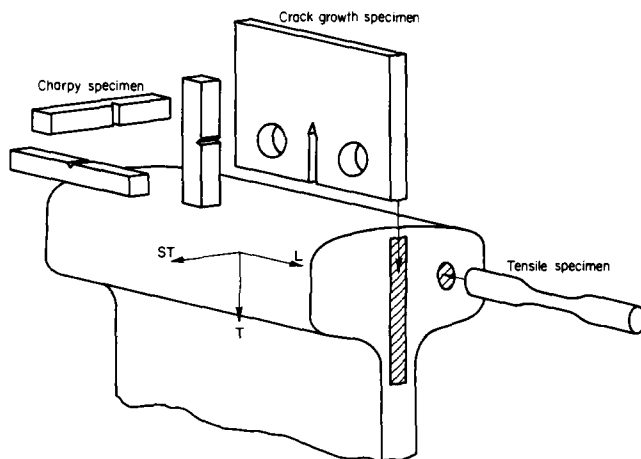


FIG. 1—Orientation of specimens for baseline data generation.

Experiments

Crack growth experiments were conducted in a 111 000-N (25-kip)-capacity servocontrolled hydraulic testing system. To expedite these tests, the chevron notch was precracked in a fatigue machine (Krouse).

The baseline crack growth tests with compact specimens were performed under constant-amplitude cyclic loading with a maximum load of 11 100 N (2500 lb) and a stress ratio of zero. The cyclic frequency was 40 Hz through most of the test; however, as the crack growth accelerated in approaching the terminal fracture condition, the frequency was reduced to 4 Hz to obtain a more accurate visual recording of the critical crack length. The laboratory air environment was maintained at $20 \pm 1^\circ\text{C}$ ($68 \pm 2^\circ\text{F}$) and 50 ± 5 percent relative humidity.

Crack growth was measured visually, using a $\times 30$ travelling microscope. Crack growth increments of 1.27 mm (0.050 in.) were allowed, after which the test was stopped for an accurate measurement of crack size. Crack size was then recorded as a function of the number of load cycles.

Results

Mechanical Properties

The rail materials used in this program typically had a tensile ultimate strength (TUS) of about 896 MPa (130 ksi) and a tensile yield strength (TYS)

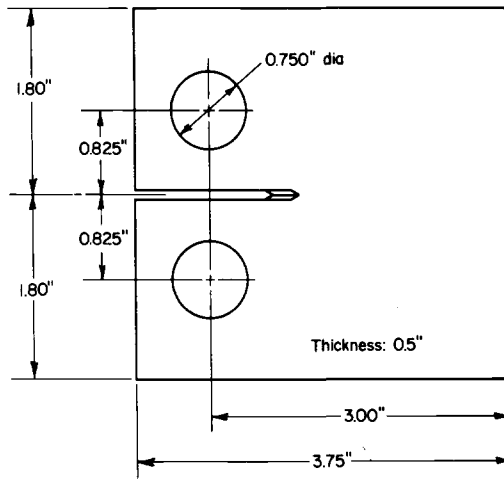


FIG. 2—Compact fatigue crack growth specimen.

of about 517 MPa (75 ksi). A detailed tabulation of the tensile test data is presented in the Appendix. One sample from a fully heat-treated rail exhibited values for TUS and TYS, respectively, of 1296 and 876 MPa (188 and 127 ksi). The low extreme values were associated with specimens containing longitudinal cracks.

The Charpy data are presented in Fig. 3. They show that, in the range of ambient temperatures, the Charpy energy is essentially the same for all these steels. Transition temperatures and upper-shelf behavior show some variation, but these are of limited interest under operational conditions.

Crack Growth Behavior

Typical fatigue crack growth curves derived for these materials samples are shown in Fig. 4. The curves show that the number of cycles to grow a 1-in. crack to failure varied widely for the different rail steel products. This will be reflected in the rate of growth, which is the basis on which the materials will be compared in the next section. Also, the final crack size at failure showed quite a wide variation which will be reflected in the toughness number.

The crack growth rate variation for these same specimens is illustrated in Fig. 5.

Data Analysis

In this program, the thrust of data analysis is twofold. On one hand, one must evaluate the basic experimental data in terms of conventional models of crack growth rate behavior for purposes of materials characterization. On the other hand, one must also be able to utilize these same data and their representation in various models in a predictive fashion for design and

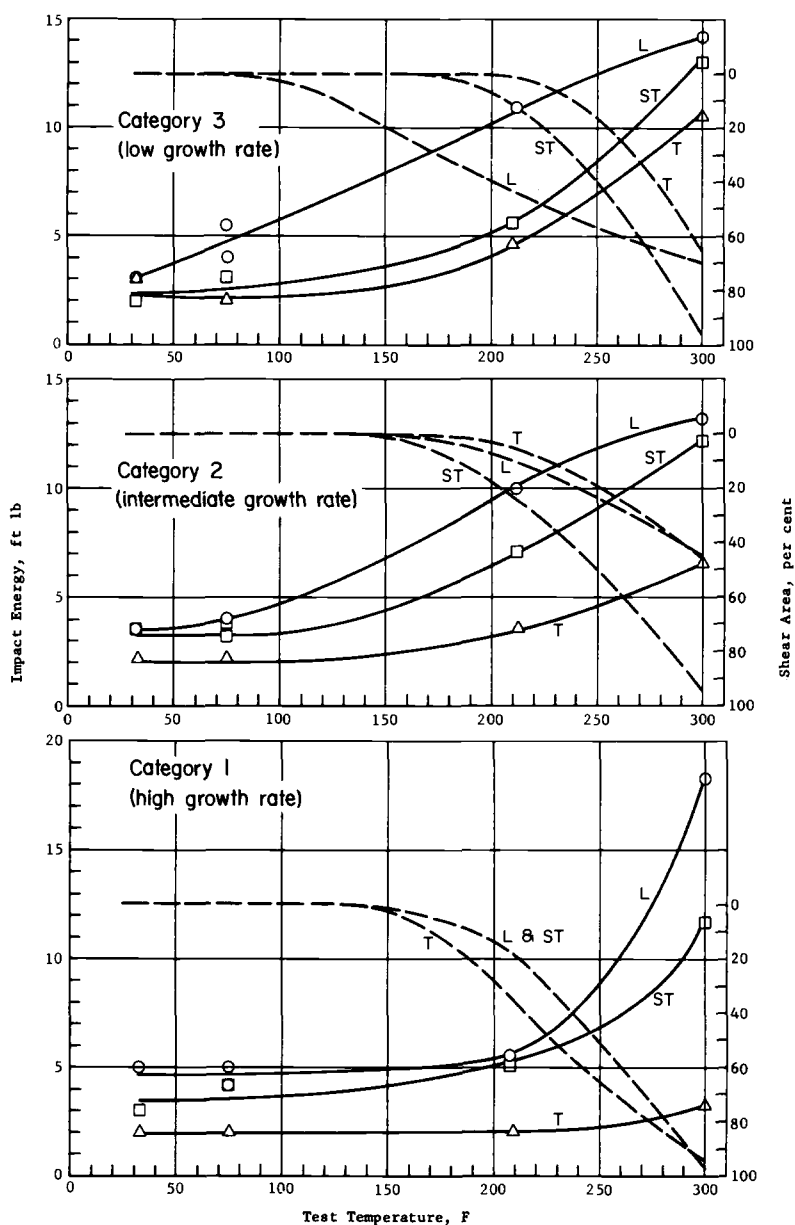


FIG. 3—Charpy impact data for three orientations (L, T, ST) of rail steels exhibiting low, medium, and high fatigue crack growth rates.

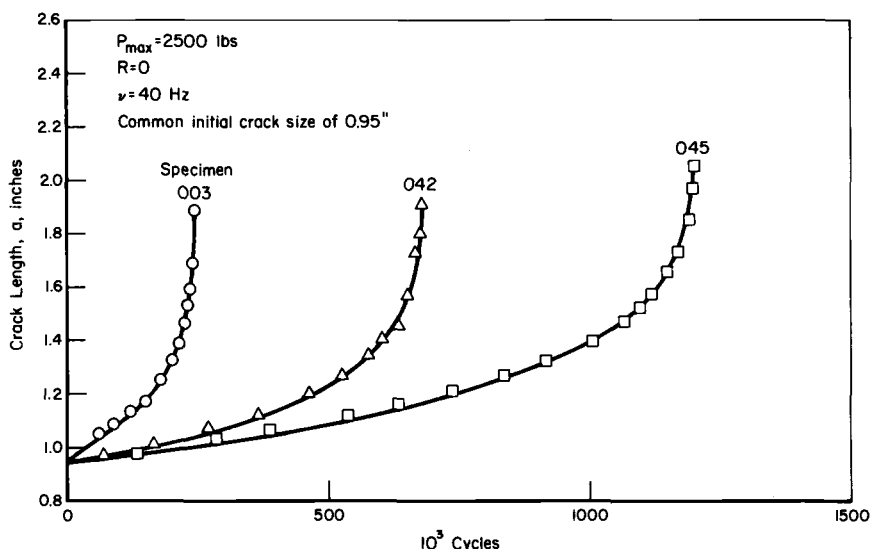


FIG. 4--Typical fatigue crack propagation curves.

damage tolerance applications. As a result, both the analysis of data as well as its synthesis (or resynthesis) must be considered.

Rate Analysis of Crack Growth Data

The rate of fatigue crack propagation can be expressed as a function of the stress intensity factor K . The stress-intensity factor is a measure of the stress singularity at the crack tip. If two planar cracks of the same orientation in the same material, but under different circumstances, are subjected to the same stress intensity, their behavior will be the same. For the compact tension (CT) specimen used in this investigation, the stress intensity can be given as

$$K = \frac{P}{2BW^{1/2}} (1 + a/W) (1 - a/W)^{-3/2} [7.000 - 7.050(a/W) + 4.275(a/W)^2] \quad (1)$$

where

- P = applied load,
- B = specimen thickness, and
- W and a = specimen width and crack size, respectively, measured from the load line.

The rate of crack growth is related to K through

$$\frac{da}{dN} = f(\Delta K, R) \quad (2)$$

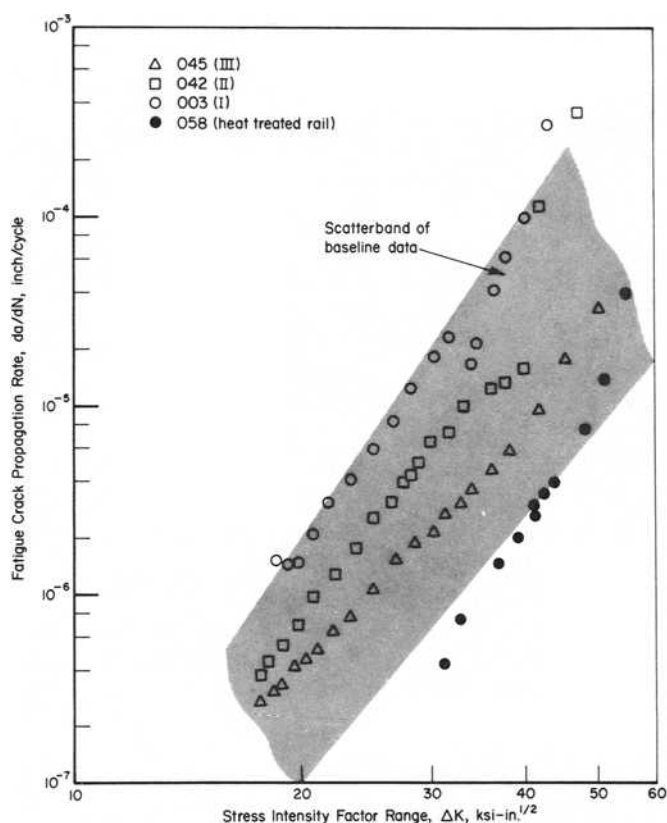


FIG. 5—Variability of fatigue crack propagation rate behavior.

where

N = cycle number,

R = ratio between minimum and maximum load in a cycle, and

ΔK = the range through which K varies during the cycle.

Thus, ΔK is found by substituting the load range ΔP into Eq 1. In the present tests, the load varied between 0 and 11 100 N (2500 lb) so that $\Delta P = 11\ 100$ N (2500 lb) and $R = 0$.

Over a wide range of growth rates in steels and for fixed R , Eq 2 can be approximated by

$$\frac{da}{dN} = C(\Delta K)^n \quad (3)$$

where C and n are constants for a given material. Hence, the various rail steels can be compared on the basis of their C and n values.

Equation 3 implies that a plot of da/dN versus ΔK on double-log paper is

a straight line. In reality, there will be an upswing in the rate of crack growth towards the end of the test because the final fracture conditions are being approached. This is reflected in the following equation

$$\frac{da}{dN} = C' \frac{(\Delta K)^{n'}}{(1-R) K_{Ic} - \Delta K} \quad (4)$$

Not only does this equation take into account the effect of the stress ratio R , it also shows that the crack growth rate becomes infinite if the stress intensity at maximum load becomes equal to K_{Ic} . The quantity K_{Ic} is the fracture toughness of the material, which is the value of K at which fracture occurs. For the special case of $R = 0$, the equation reduces to

$$\frac{da}{dN} = C \frac{\Delta K^{n'}}{K_{Ic} - \Delta K} \quad (5)$$

Both Eqs 3 and 5 were evaluated for their applicability to the present data base. For this purpose, da/dN was calculated from the measured crack growth data through the weighted average incremental slope approximation

$$\frac{da}{dN} \approx \left(\frac{\Delta a}{\Delta N} \right)_i + \frac{\Delta N_i}{(N_{i+1} - N_{i+1})} \left[\left(\frac{\Delta a}{\Delta N} \right)_{i+1} - \left(\frac{\Delta a}{\Delta N} \right)_i \right] \quad (6)$$

In essence, this is an average rate obtained from three successive crack size measurements. The measurement of crack size is difficult and introduces a certain error. Although the absolute crack size may be measured with reasonable accuracy, the differentiation procedure magnifies the error considerably. If an absolute crack size of 25.4 mm (1 in.) can be measured to an accuracy of 1 percent (error 0.25 mm (0.01 in.)), the error in a crack increment of 1.25 mm (0.05 in.) (differentiation) would be of the order of 40 percent. Thus, the calculated crack growth rate would be 40 percent in error. This would cause an apparent scatter in growth rates, which is not real and which was artificially introduced by the differentiation procedure. By taking the weighted average over two increments, that is $a_i - a_{i-1}$ and $a_{i+1} - a_i$, to determine the growth rate at a_i , this artificial scatter is reduced, if there is a random error in the crack size measurements. The calculated growth rate more nearly reflects the actual scatter in material behavior.

The resulting growth rates were plotted as a function of ΔK . Subsequently, curves were fitted through the data to give values for C and n . A special computer program was used to find the best fit.

The variability of crack growth rates in the 66 samples can be appreciated from Fig. 5. All the curve fitting data, in terms of C , n , and the correlation parameter, R^2 , are presented in Table 1. The correlation parameter is generally close to unity which is an indication of the goodness of the fits. Also presented in this table are the apparent toughness, defined as the stress

TABLE 1—Summary of crack behavior parameters for baseline rail material specimens.

Rail Sample Number	Linear Model			Modified Linear Model			Apparent Toughness, K_{Ic} , ^{1/2} ksi-in.	Crack Growth Life From 1 in. to Failure, kilocycles
	Coefficient, C	Exponent, n	Correlation Coefficient, R^2	Computed Life Margin	Coefficient, C'	Exponent, n'		
001	0.279×10^{-15}	7.09	0.785	-0.321	0.127×10^{-11}	5.63	69.4	736
002	0.256×10^{-10}	3.70	0.978	+0.020	0.459×10^{-8}	1.63	50.8	270
003	0.580×10^{-14}	5.73	0.954	-0.111	0.489×10^{-8}	3.08	44.0	211
004	0.340×10^{-11}	4.27	0.986	+0.012	0.913×10^{-7}	2.14	54.7	348
005	0.927×10^{-12}	4.77	0.983	-0.074	0.138×10^{-7}	2.72	48.6	271
006	0.654×10^{-14}	5.44	0.966	-0.056	0.130×10^{-8}	3.32	49.5	490
007	0.911×10^{-14}	5.23	0.976	-0.019	0.389×10^{-8}	2.89	52.5	796
008	0.487×10^{-14}	4.21	0.984	-0.040	0.177×10^{-10}	2.66	52.7	294
009	0.154×10^{-14}	6.76	0.951	-0.128	0.148×10^{-10}	4.73	41.1	381
010	0.183×10^{-10}	3.78	0.987	-0.057	0.150×10^{-10}	2.08	62.3	277
011	0.158×10^{-14}	6.08	0.922	-0.145	0.938×10^{-10}	4.41	55.4	262
012	0.463×10^{-11}	4.39	0.993	-0.046	0.965×10^{-7}	2.18	43.7	172
013	0.148×10^{-13}	3.21	0.985	-0.058	0.415×10^{-6}	1.84	62.4	216
014	0.266×10^{-11}	4.43	0.976	-0.052	0.218×10^{-7}	2.58	49.4	269
015	0.112×10^{-11}	4.58	0.870	-0.125	0.385×10^{-8}	3.05	52.2	395
016	0.425×10^{-10}	3.69	0.907	-0.083	0.143×10^{-8}	0.58	42.3	150
017	0.386×10^{-14}	5.81	0.857	-0.106	0.422×10^{-9}	3.84	47.8	288
018	0.105×10^{-14}	6.10	0.949	-0.070	0.106×10^{-9}	4.12	46.8	384
019	0.293×10^{-12}	4.99	0.920	-0.144	0.628×10^{-6}	2.80	46.9	435
020	0.373×10^{-15}	6.83	0.971	+0.041	0.138×10^{-11}	5.29	53.8	1302
021	0.218×10^{-11}	4.33	0.926	-0.059	0.414×10^{-7}	2.29	54.2	419
022	0.682×10^{-11}	5.23	0.864	-0.246	0.768×10^{-6}	3.38	56.8	803
023	0.846×10^{-10}	3.48	0.911	-0.084	0.768×10^{-6}	0.856	47.0	155
024	0.211×10^{-14}	6.58	0.915	-0.071	0.435×10^{-11}	5.11	46.8	495
025	0.804×10^{-14}	4.23	0.838	-0.144	0.313×10^{-6}	1.97	55.0	153
026	0.144×10^{-11}	4.63	0.978	+0.100	0.172×10^{-7}	2.48	39.1	233
027 ^a	0.319×10^{-13}	5.76	0.993	-0.045	0.274×10^{-9}	3.68	46.7	890
027A	0.204×10^{-14}	5.65	0.973	-0.087	0.159×10^{-9}	3.78	46.7	890
028	0.131×10^{-14}	4.47	0.991	+0.196	0.979×10^{-9}	3.55	65.3	536
029A	0.111×10^{-14}	6.50	0.987	-0.085	0.298×10^{-10}	4.26	49.6	1256
030	0.168×10^{-10}	3.91	0.927	+0.045	0.361×10^{-7}	3.53	53.7	197
031	0.214×10^{-12}	5.02	0.895	-0.088	0.208×10^{-8}	3.15	52.4	596
032	0.732×10^{-13}	5.45	0.957	-0.021	0.108×10^{-6}	4.12	48.3	404
033	0.113×10^{-13}	4.67	0.956	-0.236	0.233×10^{-6}	1.81	47.7	261
034	0.166×10^{-11}	4.61	0.976	-0.098	0.747×10^{-7}	2.14	42.6	221
035	0.380×10^{-14}	5.32	0.962	-0.131	0.254×10^{-9}	3.61	54.3	1218
036	0.138×10^{-14}	6.37	0.933	-0.164	0.678×10^{-11}	4.72	52.0	1269
037	0.812×10^{-12}	4.54	0.933	-0.136	0.104×10^{-8}	3.42	63.0	617
038	0.345×10^{-11}	3.90	0.838	-0.132	0.381×10^{-8}	2.86	66.2	1047

039	0.161×10^{12}	4.90	0.874	-0.243	0.173×10^8	3.06	0.967	-0.127	55.7	910
040	0.387×10^{11}	4.20	0.909	-0.137	0.287×10^8	1.67	0.978	-0.047	49.1	323
041	0.805×10^{12}	4.45	0.993	-0.058	0.211×10^8	3.19	0.969	+0.062	72.1	867
042	0.125×10^{11}	5.92	0.926	-0.086	0.172×10^8	3.91	0.969	+0.053	48.9	546
043	0.218×10^{10}	3.64	0.941	-0.058	0.692×10^7	2.19	0.981	-0.004	56.9	380
044	0.789×10^{12}	6.11	0.985	-0.114	0.108×10^8	4.10	0.961	+0.035	48.6	525
045	0.441×10^{12}	4.57	0.988	-0.045	0.106×10^8	3.26	0.996	+0.032	62.7	1019
046 ^b	0.335×10^{11}	11.4	0.942	+0.313	0.103×10^{17}	8.17	0.934	+0.334	61.4	...
047	0.294×10^{11}	5.39	0.984	-0.018	0.169×10^8	3.66	0.973	+0.056	51.0	1424
048	0.127×10^{10}	3.91	0.941	-0.061	0.916×10^7	2.21	0.956	+0.053	58.9	254
049	0.168×10^{11}	4.43	0.989	-0.077	0.701×10^8	2.86	0.977	-0.004	54.6	440
050	0.369×10^{11}	5.46	0.986	+0.021	0.132×10^8	3.91	0.989	+0.118	51.3	820
051	0.180×10^{15}	7.12	0.951	+0.033	0.187×10^{12}	5.95	0.958	+0.064	51.4	1047
052	0.508×10^{11}	5.49	0.957	-0.189	0.412×10^9	3.73	0.991	-0.059	57.2	540
053	0.881×10^{14}	5.99	0.951	+0.008	0.588×10^9	3.40	0.901	+0.145	44.7	788
054	0.317×10^{12}	6.05	0.855	-0.198	0.109×10^{10}	4.74	0.917	-0.129	58.7	881
055	0.560×10^{12}	4.78	0.861	-0.142	0.919×10^9	3.27	0.938	-0.072	55.2	923
056	0.288×10^{11}	5.45	0.995	-0.010	0.763×10^{10}	4.01	0.986	+0.070	52.6	1150
057	0.854×10^{11}	5.25	0.963	-0.009	0.229×10^9	3.80	0.979	+0.041	53.3	712
058 ^c	0.801×10^{17}	7.23	0.948	+0.085	0.792×10^{10}	3.58	0.963	+0.233	56.3	...
059	0.291×10^{11}	5.27	0.872	-0.037	0.116×10^9	3.74	0.925	+0.077	56.5	2317
060	0.144×10^{11}	4.64	0.971	-0.069	0.673×10^8	2.95	0.993	-0.006	46.9	247
061	0.154×10^{11}	4.67	0.937	-0.097	0.455×10^8	3.19	0.985	-0.032	52.8	211
062	0.327×10^{12}	5.14	0.935	-0.135	0.175×10^8	3.40	0.982	-0.053	46.7	217
063	0.243×10^{11}	4.50	0.933	-0.152	0.656×10^8	3.10	0.960	-0.085	56.1	217
064	0.862×10^{14}	5.89	0.986	-0.114	0.554×10^{10}	4.16	0.977	+0.010	52.3	1005
065	0.578×10^{15}	6.76	0.991	+0.092	0.336×10^{11}	5.01	0.986	+0.203	48.9	1118
066	0.105×10^{13}	5.72	0.986	+0.104	0.134×10^{10}	4.56	0.981	+0.158	59.1	1661

Conversion factors

1 ksi-in.^{1/2} = 1.1 MPa-m^{1/2}a₂ kip CT.h₂kip CT.a₄ 5 kip CT.

intensity factor, determined by Eq 1, for the last recorded crack measurement.

Very few crack growth data on rail steels have been reported in the literature. The data reported in the sources cited in Footnotes 2 and 3 are useful for a comparison with the present results. The British rail steel tested contained 0.56 percent carbon, 1.02 percent manganese, 0.13 percent silicon, and less than 0.05 of phosphorus and sulfur each. The steel had a 0.1 percent yield strength of 426 MPa (67 ksi) and an ultimate tensile strength of 834 MPa (121 ksi). Test results for center cracked panels showed a value of 4 for the exponent n in Eq 3 and $C \cong 0.9 \times 10^{-11}$ if K is given in $\text{ksi}\sqrt{\text{in.}}$ for the case of $R=0$ (Footnote 2). Experiments at various R ratios indicated that $n' = 2.69$ in Eq 4 gave the best fit. It appears that this material compares with those showing the higher growth rates in the present investigation.

Synthesis of Crack Growth Curves

Fatigue crack growth data have practical use only if they permit prediction of the growth of service cracks. For this purpose, crack growth data are presented as a function of the stress intensity factor. This provides a generalization through which the data are applicable to other geometries than the specimen for which they were derived. In the application of the data to other geometries, an integration of the rates is necessary to arrive at the crack length versus time information required for safety analysis. This raises the problem of how to integrate the data for the case of a crack in a complex structural geometry under variable-amplitude service loading. The first step in solving this problem is to investigate which integration procedure is best capable of reproducing the crack growth curves for the original specimen. (In the second phase of the program, the integration procedure for the general case will be developed, which is the rail failure model mentioned before.)

The crack growth curves were reconstructed by integrating the rate data according to both the linear and the modified linear fatigue crack propagation models. In simple terms, the integration can be expressed as

$$a = \int \frac{da}{dN} dN \quad (7)$$

$$N = \int \frac{da^{-1}}{dN} da \quad (8)$$

Since the crack growth model generally cannot be integrated in closed

²Evans, P. R. V., Owen, N. B., and Hopkins, B. E., *Journal of the Iron and Steel Institute*, 1970, pp. 560-567.

³Evans, P. R. V., Owen, N. B., and McCartney, L. N., *Engineering Fracture Mechanics*, Vol. 6, 1974, pp. 183-193.

form, the solution of these expressions was accomplished by a numerical integration in 100 steps.

If the basic rate data and the fitted rate model were in perfect correlation, the results of the summation, would, of course, agree perfectly with the experiment. In reality, however, perfect correlation is not achieved due to experimental error, material variation, and mere oversimplicity (that is, inadequacy) of the analysis. The measure of the effectiveness of the overall analysis and synthesis is expressed in the "cyclic life margin of safety (MS)" which is expressed as

$$MS_{\text{life}} = \frac{N_{\text{actual}}}{N_{\text{computed}}} - 1 \quad (9)$$

Positive values of this margin infer that the computed value is less than the actual and, hence, conservative. The degree of conservatism (+) or unconservatism (−) is reflected in the variation of the margin from zero.

The crack growth synthesis was applied to the 66 baseline data sets to obtain a set of life margins which, in turn, were analyzed statistically. These results, presented in Table 2, indicate that the linear model tends to be unconservative in that it predicts, on the average, a larger crack lifetime than was encountered in the test. This is evidenced by the negative value of the mean life margin. In contrast, the modified linear model provides a conservative estimate of life and for that reason may be a more preferable model to use. Second, since the variance and standard deviation are nearly equivalent for each model, it is judged that lifetime scatter about the mean is not particularly affected by the model.

Correlation of Rate Data with Other Properties

Approach

An attempt was made to correlate crack growth properties with mechanical properties and metallurgical variables. The detection and isolation of primary variables affecting crack growth would be a straightforward procedure if all variables were truly independent. However, the mechanical, metallurgical, and processing variables are not mutually independent and do

TABLE 2—Results of crack growth synthesis.

Model	Predicted Mean Life	Predicted Life Margin Statistics		
		Mean Life Margin	Variance	Standard Deviation
Linear	0.936	−0.064	0.010	0.100
Modified linear	1.035	+0.035	0.011	0.104

interact in a very complex manner. As a result, the discrimination of the dominant factors requires considerable trial-and-error data scanning.

The mechanical property, metallurgical, and crack growth variables were examined by a statistical procedure known as the automatic interaction detector (AID) program. The AID computer program is a tool for assessing the influence of a set of independent variables (termed predictors) on the behavior of a dependent variable.

For each predictor, the set of values of the dependent variable are ordered by either the order of the predictor (if a monotonic predictor) or the order of the dependent variable (if a free predictor). The set of values of the dependent variable is then divided (or split) successively into two subsets along the domain of the predictor. At each split, the within-subset variance (WSV) and between-subset variance (BSV) is computed. The split which produces the largest ratio of BSV to WSV (that is, F ratio or signal-to-noise ratio) is considered the optimum split for that predictor. The predictor which exhibits the largest ratio of BSV to total variance (TV) is the dominant or primary predictor for the dependent variable. Once the optimum split of the primary variable has been defined, the procedure is repeated for the two groups at each side of the split and so on.

The computational scheme is semiquantitative in that the independent variables are linearly scaled and coded to integral values from 0 to 63. However, since known correlations do not exist, a method that compares data on such a normalized basis can provide a clearer discrimination of the dominance (if such exists) of the primary independent variables.

Results of Analysis

The dominance of a particular independent variable may be expressed as the percentage contribution of its BSV to the TV of the dependent variable. The results of the AID analysis of independent variables for leading contenders are summarized as in Table 3.

TABLE 3—Result of AID analysis.

Category	Variable	Percent Contribution to Variance	
		On Crack Growth Rate	On Apparent Fracture Toughness
Mechanical property	tensile ultimate strength	13	32
	hardness	14	18
	elongation	7	18
Metallurgical	pearlite, %	19	32
	carbon, percent by weight	8	11
	oxygen, percent by weight	8	20
	sulfur, percent by weight	5	9
	manganese, percent by weight	4	16

For the mechanical property category, the nearly equivalent dominance of strength and hardness is not surprising because of their well-documented interrelationship. However, the statistical impact is lessened when one then views the graphical relationship of strength and life as shown in Fig. 6. A similar disillusionment is encountered when one displays the other parameters versus life.

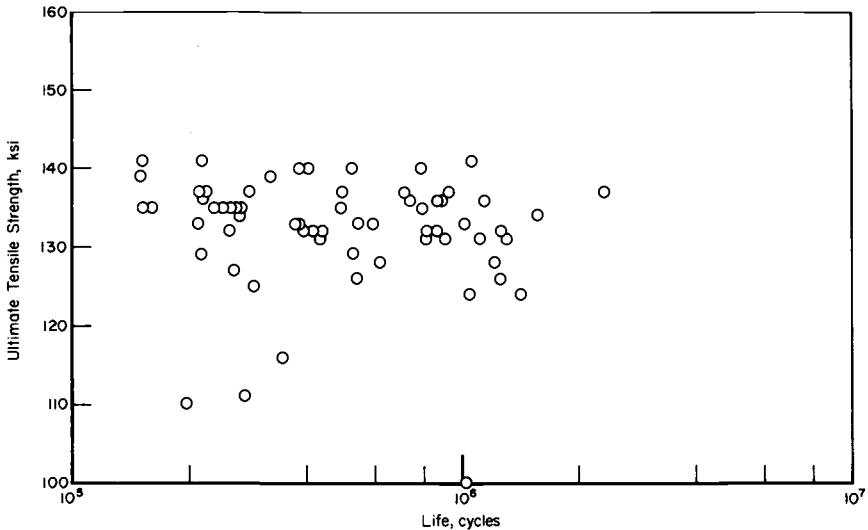


FIG. 6—Variation of crack growth life with tensile strength.

Since the toughness of the rail materials is of significance in a rail failure model, the apparent toughness (K_{app}) values were also analyzed with the AID program (Table 3). The leading predictors appeared to be hardness and carbon equivalent, but a graphical display showed similar shotgun patterns as in Fig. 6.

The contrast between the AID analysis and the weak evidence of the graphical displays suggests that any numerical correlation may be a coincidence of "noise" in the data. At the present time, a positive conclusion is not tendered. The analysis will be advanced as additional results are generated.

Acknowledgment

This investigation was performed under the sponsorship of the Transportation Systems Center (TSC) of the Department of Transportation under Contract DOT-TSC-1076. The work was conducted under the technical direction of Roger Steele of TSC.

APPENDIX

The tensile mechanical property results derived for the 66 rail samples are presented in Table 4.

TABLE 4—Tension test results for 66 rail samples.

Rail Number	T.U.S. ksi	T.Y.S. ksi	Elongation in 1 in., %	Reduction in Area, %	E, 10 ³ ksi	True Fracture Stress, ksi	True Fracture Strain, ϵ_t	Ramberg-Osgood Exponent, n	Work Hardening Exponent, $1/n$
001	136.4	76.5	13.5	28.0	34.0	171.2	0.1266	7.8	0.128
002	134.4	74.7	12.0	20.6	30.8	159.4	0.1133	7.7	0.130
003	137.4	73.6	12.0	17.7	30.3	160.1	0.1133	13.1	0.076
004	116.0	59.9	15.0	24.0	28.6	144.6	0.1397	10.4	0.096
005	134.8	76.4	13.5	26.0	31.8	154.9	0.1266	11.5	0.081
006	135.0	71.2	11.0	21.2	30.2	161.9	0.1043	11.5	0.087
007	135.8	70.0	12.0	17.6	30.3	156.9	0.1133	12.5	0.080
008	125.1	67.0	14.0	25.0	30.1	155.9	0.1310	10.8	0.093
009	139.8	81.8	14.0	29.4	32.0	180.0	0.1310	12.0	0.083
010	111.5	58.7	17.0	27.2	29.3	143.1	0.1570	9.8	0.102
011	126.9	73.2	12.5	20.8	33.8	144.3	0.1177	10.3	0.097
012	134.7	78.3	10.5	17.0	32.4	153.1	0.0998	8.4	0.119
013	129.3	72.8	12.5	29.1	29.1	160.8	0.1177	7.9	0.126
014	135.4	75.9	12.0	18.0	33.1	158.7	0.1133	7.5	0.133
015	131.6	71.5	11.0	16.5	30.6	150.0	0.1043	6.0	0.167
016	138.6	75.6	9.5	15.0	28.8	154.4	0.0907	6.3	0.159
017	137.1	74.4	10.0	19.5	28.2	163.6	0.0953	6.4	0.156
018	133.2	70.6	11.0	19.9	27.5		0.1043		
019	131.2	73.4	12.0	19.2	34.5	152.8	0.1133	8.5	0.118
020	131.4	72.0	11.0	18.4	30.4	152.6	0.1043	6.5	0.154
021	132.3	77.2	12.0	18.4	32.6	153.9	0.1133	9.8	0.102
022	130.7	76.0	13.0	22.7	31.7	157.9	0.1222	8.2	0.122
023	135.1	77.3	10.5	17.9	32.2	155.7	0.0998	7.7	0.130
024	136.7	74.6	10.0	16.2	32.4	158.7	0.953	6.3	0.159
025	141.1	75.7	9.5	18.8	26.5	164.9	0.0907	6.3	0.159
026	135.0	74.4	11.0	17.5	29.9	153.1	0.1043	8.2	0.122
027	136.4	69.4	10.0	13.6	29.0	150.1	0.0953	6.2	0.161
028	129.1	70.5	11.5	18.9	31.8	119.8	0.1088	7.5	0.133
029	125.5	61.7	12.0	19.9	29.4	146.6	0.1133	6.8	0.147
030	110.0 ^a	76.8			28.2			7.1	0.140
031	133.4	75.6	11.0	17.6	31.6	149.4	0.1043	8.6	0.116
032	139.5	80.0	12.0	19.5	34.8	165.3	0.1133	8.0	0.125
033	135.0	73.3	10.0	13.9	28.6		0.0953		
034	137.3	77.3	10.5	20.7	30.2	164.3	0.0998	6.0	0.167
035	128.1	69.3	12.5	19.6	33.6	154.1	0.1177	7.2	0.139
036	132.1	74.6	12.0	21.4	31.1	155.3	0.1133	10.0	0.100
037	127.7	68.6	16.0	25.9	32.6	156.8	0.1484	9.4	0.106
038	124.2	74.9	17.0	42.3	33.7	185.3	0.1570	11.5	0.087
039	130.7	75.0	14.5	21.6	30.9	155.9	0.1354	7.5	0.133
040	138.8	83.3	9.5	15.0	26.9	156.5	0.0907	7.7	0.130
041	132.0	73.6	11.5	22.0	28.6	156.1	0.1088	7.7	0.130
042	133.0	74.7	10.5	15.9	29.6	151.1	0.0998	6.8	0.147
043	133.2	75.6	13.0	20.5	32.8	156.9	0.1222	6.9	0.145
044	139.7	80.0	10.0	15.3	29.3	158.7	0.0953	11.5	0.087
045	96.8 ^a	66.0	8.0	16.3	33.8	98.0	0.0769	10.2	0.098
046	130.6	75.9	14.5	20.6	28.9	160.5	0.1354	25.0	0.040
047	123.8	60.4	14.0	21.0	29.2	150.1	0.1310	24.0	0.041
048	132.4	75.5	11.5	17.5	29.9	152.9	0.1088	10.5	0.095
049	132.0	72.4	11.5	20.1	30.5	157.8	0.1088	7.2	0.139
050	132.4	73.8	12.0	21.0	29.9	157.5	0.1133	7.8	0.128
051	141.5	81.2	9.5	13.3	31.2	159.1	0.0907	11.8	0.085
052	126.0	64.0	13.5	21.3	29.7	151.0	0.1266	14.0	0.071
053	140.2	75.8	9.5	13.3	30.3	159.4	0.0907	8.9	0.112
054	135.9	76.5	12.0	18.8	30.9	159.5	0.1133	9.2	0.109
055	137.4	77.9	9.0	14.2	29.5	156.1	0.0861	7.7	0.130
056	136.0	72.6	9.5	13.2	29.6	149.6	0.0907	9.2	0.109
057	136.6	72.9	10.5	18.2	27.1	158.9	0.0998	8.2	0.122
058	188.7 ^b	127.3	11.5	31.7	29.6	239.4	0.1088	30.0	0.033

TABLE 4—*Continued.*

Rail Number	TUS, ksi	TYS, ksi	Elongation in 1 in., %	Reduction in Area, %	<i>E</i> , 10 ³ ksi	True Fracture Stress, ksi	True Fracture Strain, ϵ_f	Ramberg- Osgood Exponent, <i>n</i>	Work Hardening Exponent, $1/n$
059	137.2	79.1	11.0	15.4	28.3		0.1043		
060	135.3	74.2	12.0	16.5	30.9	153.4	0.1133	13.0	0.077
061	132.5	70.7	11.5	17.1	31.2	154.4	0.1088	17.5	0.057
062	141.3	76.9	11.0	19.3	32.0	167.5	0.1043	13.5	0.074
063	135.6	73.5	11.0	18.8	29.6	155.3	0.1043	14.0	0.071
064	133.1	69.1	13.0	21.1	30.5	159.4	0.1222	14.8	0.067
065	131.3	73.3	11.0	17.7	31.0	157.5	0.1043	4.4	0.227
066	134.2	70.0	12.0	20.7	30.5	159.9	0.1133	13.0	0.077

^aLongitudinal cracks in specimen.^bHeat-treated rail.

Conversion factors—

1 ksi = 6.9 MPa

1 in. = 25.4 mm

An Evaluation of the Fatigue Performance of Conventional British Rail Steels

REFERENCE: Dabell, B. J., Hill, S. J., and Watson, P., "An Evaluation of the Fatigue Performance of Conventional British Rail Steels," *Rail Steels—Development, Processing, and Use*, ASTM STP 644, D. H. Stone and G. G. Knupp, Eds., American Society for Testing and Materials, 1978, pp. 430–448.

ABSTRACT: A comprehensive evaluation of the fatigue behavior of eight conventional pearlitic rail steels is presented. The materials examined are UIC Grades A, B, and C, 1 percent chromium, BS11 Cast 1879, BS11 Cast 500, BS11 Cargo Fleet and BS11 Concast 2971. Of these, the UIC and 1 percent chromium steels are all specifically designed for wear resistance, whereas the BS11 steels are representative of the rail steels in general usage by British Rail. The investigations ranged from the endurance limit to the low cycle region, and both smooth and notched specimens were employed to provide data indicating cyclic strength and ductility, notch sensitivity, and resistance to crack initiation and early growth. In constant-amplitude, strain-controlled, smooth specimen fatigue tests, the conventional BS11 steels proved superior in the low cycle region, whereas the more highly alloyed steels were generally stronger at long lives. Where a tensile mean stress is present, the superiority of the BS11 rail steels in the short life region is reduced, and the 1 percent chromium steel exhibits a high resistance to fatigue over a large range of endurance. In the notched plate tests, the 1 percent chromium and UIC Grade B steels proved most resistant in general to fatigue crack initiation and early growth. Overall, the superior performance of the 1 percent chromium steel on the basis of both fatigue characteristics and static properties is demonstrated.

KEY WORDS: steels, railroad tracks, fatigue (materials), fatigue limit, ductility, notch sensitivity, crack initiation, crack propagation, strains, notch tests

The correct selection of a material for a service application rests on a thorough understanding of its mechanical properties. If fatigue is the major concern, a knowledge of the performance of rail steels under cyclic loading is particularly vital as a premature fatigue failure will lead to an unacceptable reduction in the standard of safety, together with an expensive and disruptive replacement operation. Furthermore, steels selected for a particular attribute, for example, wear resistance, fracture toughness, or weldability, may possess poor fatigue properties, thereby nullifying any theoretical advantages.

¹Project leaders and manager, respectively, Materials Engineering Group, GKN Group Technological Centre, Wolverhampton, England; formerly, Strength of Materials Section, British Rail Research and Development Division, Railway Technical Center, Derby, England.

The parameters used to quantify the cyclic properties depend on the method of assessing the service endurance of the component. Either an empirical approach, by full-scale testing, or analytical techniques, such as those based on critical locations concepts, may be adopted. Objections to the former approach are that it is frequently extremely difficult to simulate the operating conditions adequately, and it is always very expensive. Moreover, analytical methods allow the ready adjustment necessary to accommodate changes in loading, design, or material in order to ascertain readily and cheaply the sensitivity of the endurance to these variables.

The failure criterion must be clearly defined to ensure that the appropriate method of analyzing fatigue is adopted. As rail steels are essentially brittle in nature, material selection on the basis of resistance to crack initiation and early growth is advocated. In this context, the critical location approach [1-3]² is the most suitable method for assessing the fatigue performance of a component. This method relates the stress-strain behavior which dictates crack initiation and fatigue failure at critical locations to that of small smooth laboratory specimens.

Hence, British Rail is adopting this technique as the basis for comparing the fatigue behavior of different rail steels. This paper presents and discusses the implications of results derived from smooth and notched specimens. The latter are relevant in that failures do occur at the bolt-holes utilized for fishplated joints. Cyclic strength and ductility, notch sensitivity, and resistance to crack initiation and early growth are all quantified, with endurances ranging from the fatigue limit to the low cycle region.

Materials and Specimens

The materials under study were UIC Grades A, B, and C, 1 percent chromium and four samples of BS11, identified as Cast 1879, Cast 500, Cargo Fleet, and Concast 2971. Of these, the UIC and 1 percent chromium steels are principally designed for application where wear is a problem, whereas the BS11 steels are used in more general applications by British Rail. The Cast 1879 and Cast 500 were produced by the acid Bessemer process and represent the extreme carbon contents in the range of permissible compositions. BS11 Cargo Fleet is manufactured by the open hearth process, whereas Concast 2971 is produced by means of a converter (Linz-Donawitz) and subsequently continuously cast. All the materials under study are conventional rail steels with a substantially pearlitic microstructure. The chemical compositions are listed in Table 1.

Two types of specimen were used. The smooth axial specimens were 7 mm in diameter with a uniform parallel gage length of 10 mm. These specimens were cut from the rail webs at 45 deg to the direction of running on the rail. This specimen orientation was selected because of its relevance to the star-cracking phenomenon associated with bolt-holes. The notched plate specimens 39 mm wide and 4 mm thick were machined with an 8-mm central hole

²The italic numbers in brackets refer to the list of references appended to this paper.

TABLE 1—*Chemical composition of steels.*

Material	Percent by Weight						
	Carbon	Silicon	Manga- nese	Sulfur	Phos- phorus	Nickel	Chro- mium
BS 11 Cast 1879	0.54	0.11	1.15	0.028	0.051	0.01	0.01
BS 11 Cast 500	0.44	0.12	1.60	0.030	. . .	0.01	0.02
BS 11 Cargo Fleet	0.54	0.22	1.05	0.040	0.043	0.03	0.03
BS 11 Concast 2971	0.55	0.35	1.43	0.026	0.048	0.01	0.01
UIC Grade A	0.72	0.22	0.95	0.019	0.025	0.03	0.02
UIC Grade B	0.63	0.20	1.54	0.021	0.035	0.01	0.01
UIC Grade C	0.53	0.18	1.74	0.023	0.025	0.03	0.14
1% Chromium	0.71	0.19	1.13	0.024	0.033	0.03	1.20

to give a K_t (theoretical stress concentration factor) of 2.5. The blanks for these plates were cut vertically from the rail webs and, as in the case of the axial specimens, stress relieved for 1 h at 650°C (1200°F) after machining and polishing. This treatment was found to have no significant effect on either the microstructure or hardness of the steels. A shortage of material precluded the manufacture of notched plates from UIC Grade C material.

Apparatus and Procedure

The testing program was carried out using two closed-loop servohydraulic testing systems with 250 and 100-kN actuators, the load on each specimen being measured by means of a load cell in series. In each case, a liquid metal gripping arrangement was used to ensure axial alignment of the specimens and to eliminate any stresses being induced during the setting-up operation.

Longitudinal strain measurements were made on the smooth specimens using a clip-on extensometer. The strains and the loads were monitored continuously on both a strip-chart recorder and a small digital computer programmed to provide on-line data reduction. In the notched plate tests, only the loads were recorded. Failure of both types of specimen was defined as complete separation into two pieces.

The four parts of the testing program were as follows:

1. Monotonic tension tests were carried out on smooth specimens at a constant strain rate of approximately 0.005/s. The true stress-strain data were calculated from the measured engineering stress-strain relationships. The value of the true fracture strength was corrected to allow for triaxiality induced during necking [4,5].
2. Strain-controlled incremental step tests (IST) were performed on smooth specimens to establish cyclic stress-strain curves. Specimens were subjected to blocks of gradually decreasing and then increasing strain amplitudes (from 1.5 to 0.1 percent) in 15 equal steps. Most materials cyclically stabilize after a few such blocks, whereupon parameters of the stable hysteresis loop are given at each strain level. At this

stage, initial effects due to asymmetrical behavior (for example, Bauschinger) will have been eliminated. A locus of the loop tips gives the cyclic stress-strain curve.

3. Constant-amplitude, fully reversed fatigue tests were carried out on smooth axial specimens, generally using strain control. Load control was utilized for the very long-life tests, after a stable material condition had been obtained, to allow the equipment to be operated at higher frequencies.
4. Notched plate specimens were tested under conditions of fully reversed nominal stress, once again using load control. The growth of cracks so induced was measured by means of travelling microscopes located on both sides of the specimen. Cracks were measured to an accuracy of 0.001 mm, and the average crack length was determined from the four readings (two on each side of the specimen). These tests were extended to specimen failure to determine the overall effect of specimen geometry on life, thus obtaining a measure of the material notch sensitivity.

Experimental Results

Table 2 summarizes the results of the monotonic tests. These results, together with those from the incremental step tests, are presented for strains up to about 0.02 in Figs. 1 to 8 to demonstrate any tendency to cyclic softening or hardening. Significant parameters (see Appendix) derived from the incremental step tests and constant-amplitude fatigue tests are listed in Table 3.

The results of the strain-controlled fatigue life tests are depicted graphically in Figs. 9 and 10. A combination of this information with the cyclic stress-strain data yields values of (maximum stress \times strain amplitude \times Young's modulus). This parameter $(\sigma_{\max} \epsilon_a E)^{1/2}$, identical to $(\sigma_a \epsilon_a E)^{1/2}$ for fully reversed tests, has been shown to be useful in assessing the effect of mean stress on fatigue life [6]. Combining these data with the results of the

TABLE 2—*Static mechanical properties.*

Material	Tensile Yield Point (MPa), S_{Ty}	Ultimate Tensile Strength (MPa), S_u	Percentage Reduction in Area (%), % RA	True Fracture Strength (MPa), σ_f	True Fracture Ductility, ϵ_f
BS 11 Cast 1879	350	612	40.4	890	0.52
BS 11 Cast 500	425	652	44.3	932	0.59
BS 11 Cargo Fleet	480	808	28.0	1010	0.33
BS 11 Concast 2971	510	760	38.0	1034	0.48
UIC Grade A	466	894	19.7	1070	0.22
UIC Grade B	434	787	37.7	1084	0.47
UIC Grade C	480	824	37.0	1070	0.46
1 percent chromium	523	985	24.8	1214	0.29

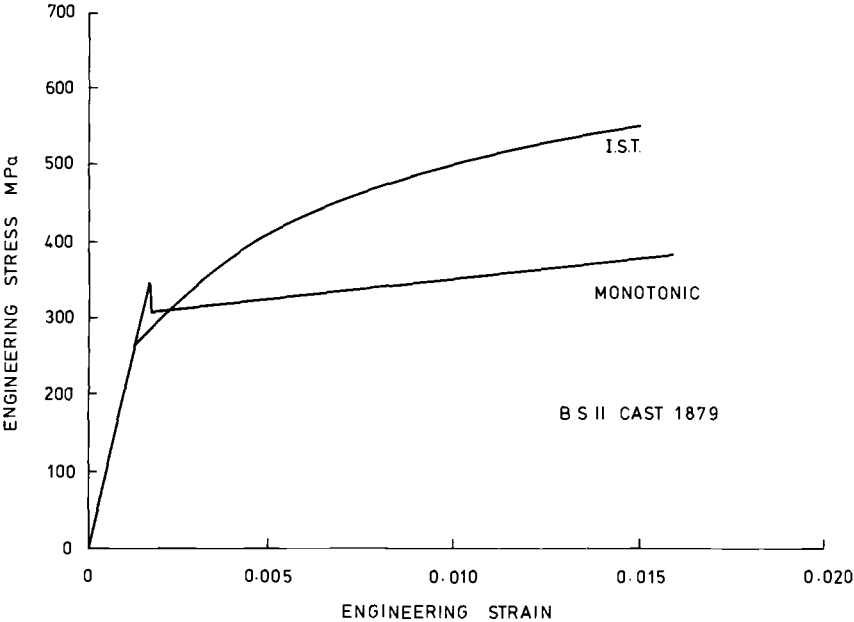


FIG. 1—Monotonic and cyclic stress-strain curves.

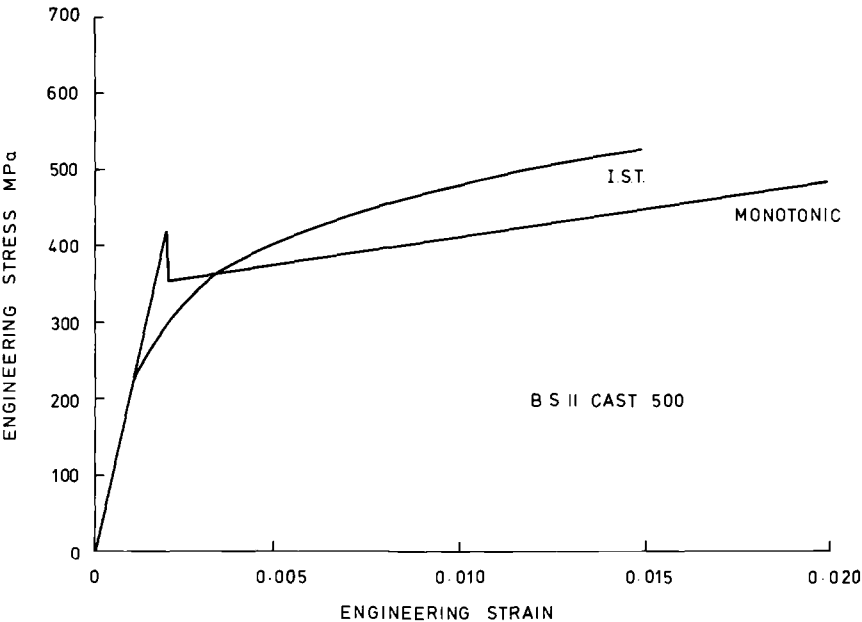


FIG. 2—Monotonic and cyclic stress-strain curves.

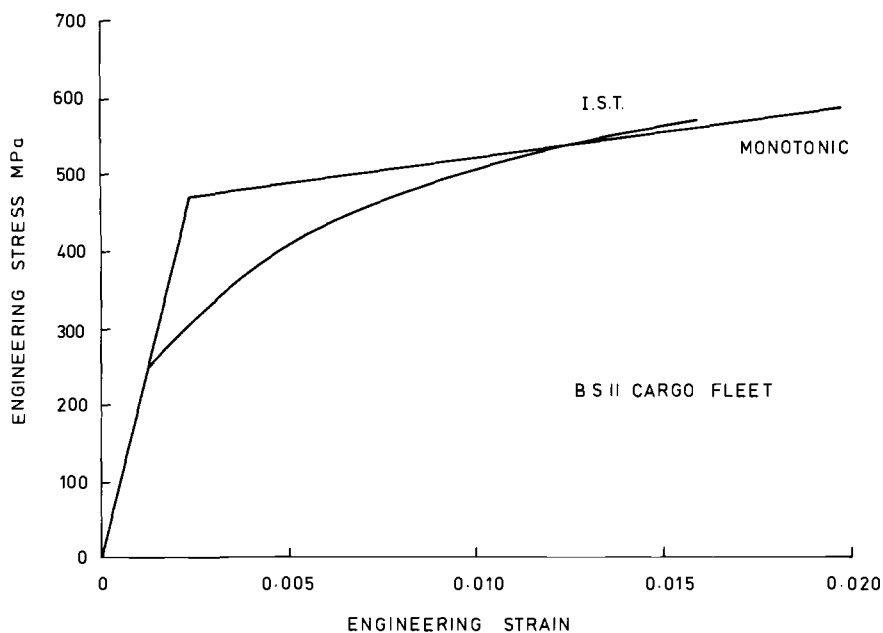


FIG. 3—Monotonic and cyclic stress-strain curves.

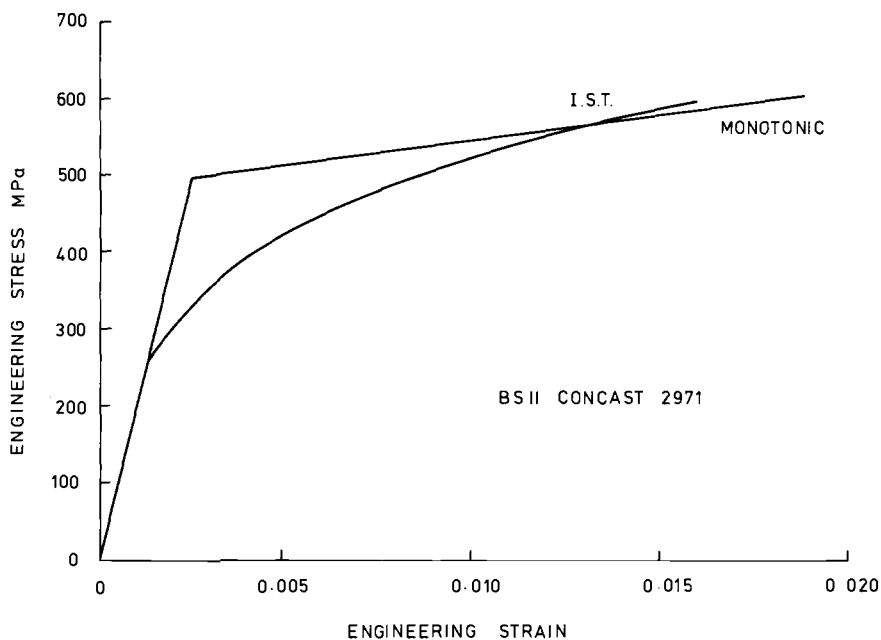


FIG. 4—Monotonic and cyclic stress-strain curves.

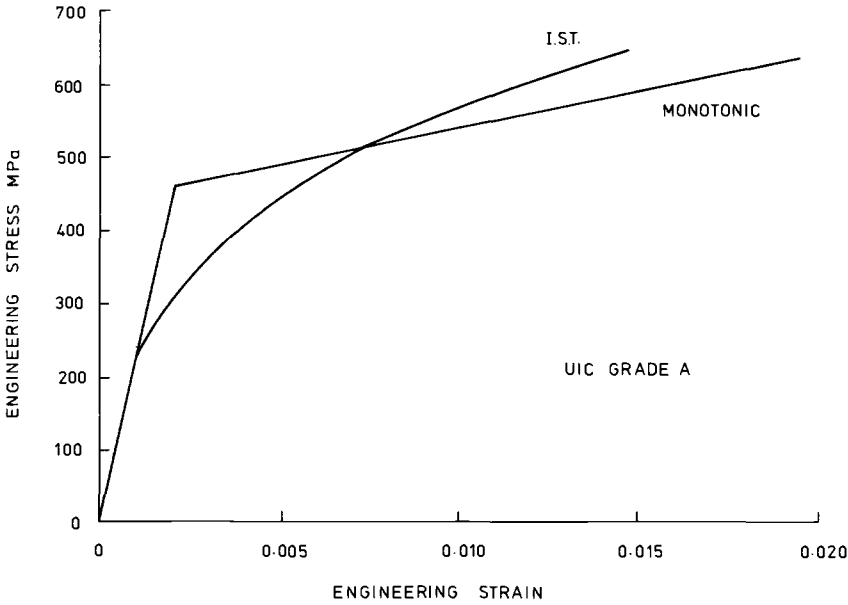


FIG. 5—Monotonic and cyclic stress-strain curves.

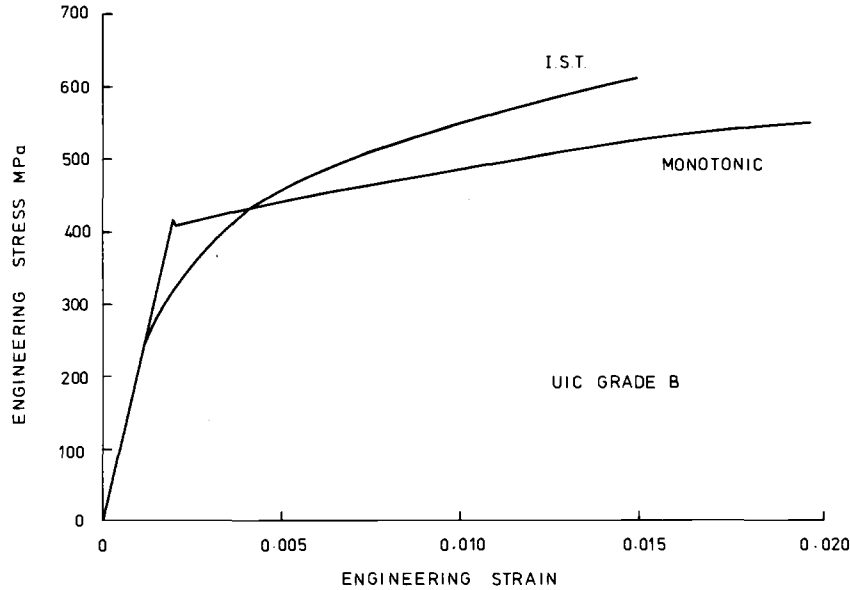


FIG. 6—Monotonic and cyclic stress-strain curves.

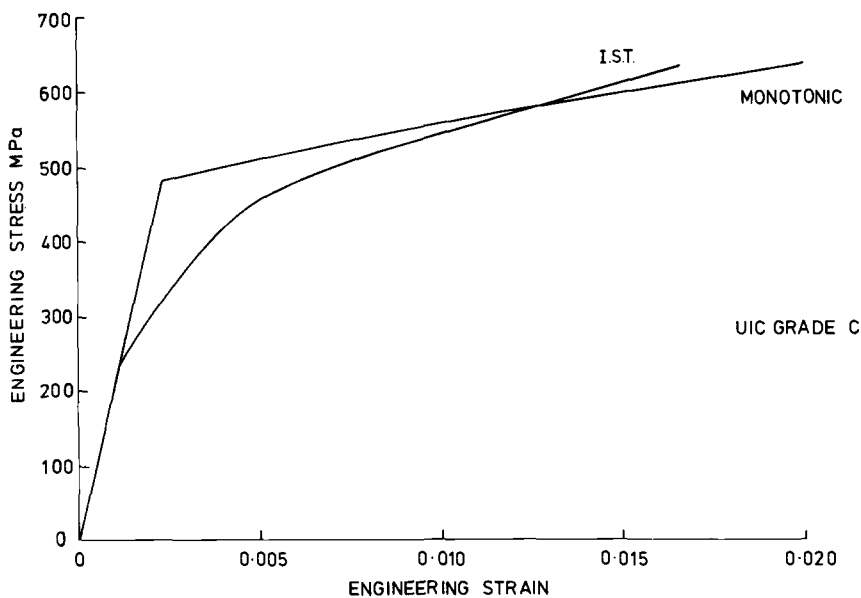


FIG. 7—Monotonic and cyclic stress-strain curves.

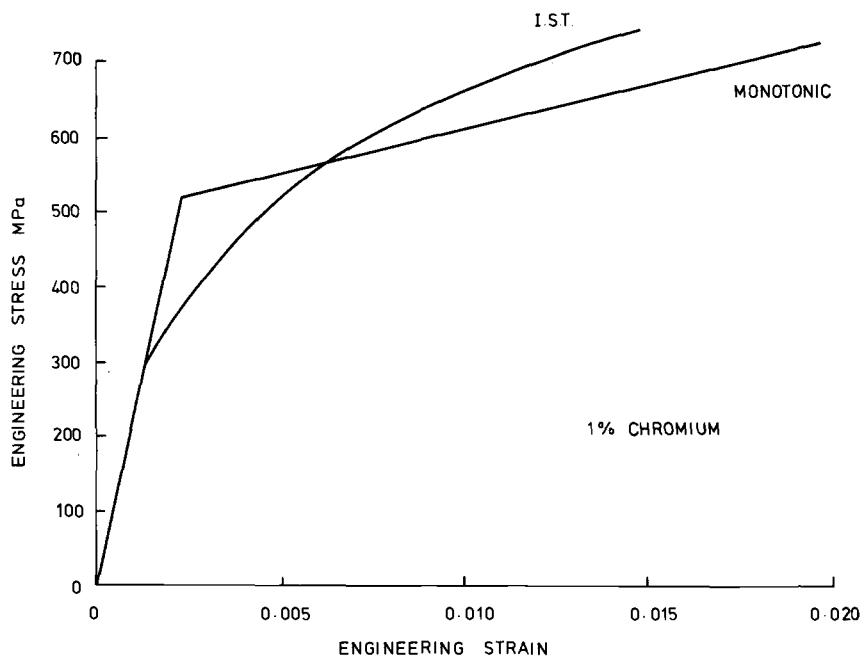


FIG. 8—Monotonic and cyclic stress-strain curves.

TABLE 3—Cyclic material properties.

Material	Strain Hardening Exponent, n'	Strength Coefficient (MPa), K'	Fatigue Strength (MPa), σ'_f	Fatigue Strength Exponent, b	Fatigue Ductility Coefficient, ϵ'_f	Fatigue Ductility Exponent c	Strain Level at Fatigue Limit
BS 11 Cast 1879	0.21	1442	945	-0.074	0.51	-0.61	0.0014
BS 11 Cast 500	0.19	1242	962	-0.094	0.55	-0.52	0.0011
BS 11 Cargo Fleet	0.23	1540	1150	-0.116	0.40	-0.49	0.0012
BS 11 Concast 2971	0.22	1490	1081	-0.100	0.31	-0.48	0.0014
UIC Grade A	0.26	2120	1179	-0.100	0.24	-0.45	0.0016
UIC Grade B	0.21	1566	1100	-0.093	0.47	-0.53	0.0012
UIC Grade C	0.21	1503	1098	-0.095	0.68	-0.56	0.0014
1 percent chromium	0.25	2240	1192	-0.087	0.33	-0.53	0.0019

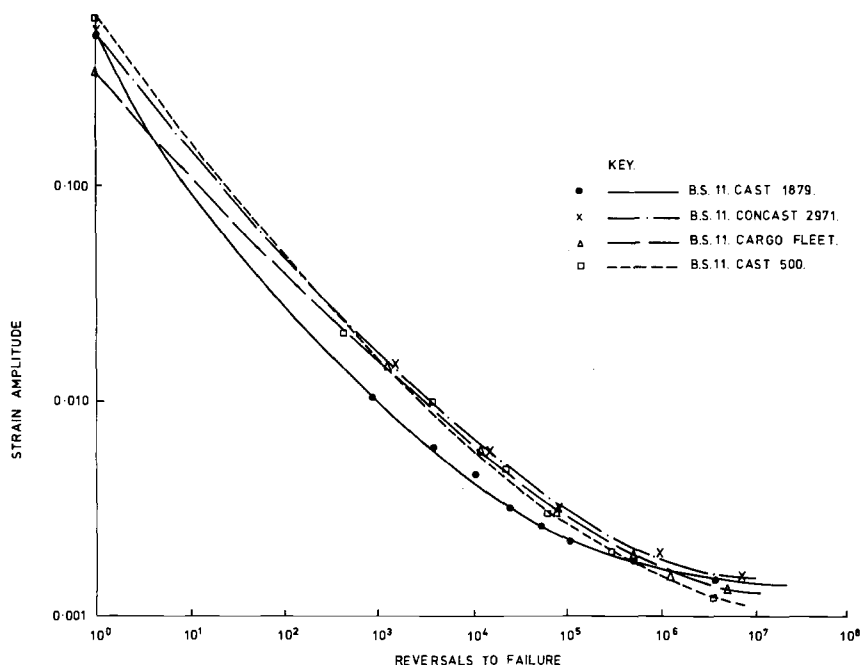


FIG. 9—Total strain-fatigue life relationship.

notched plate life tests (Table 4) gives Figs. 11 and 12, which are Neuber plots [7]. From these, the values of K_f , the fatigue notch factor, are calculated and tabulated in Table 5. The number of cycles required to initiate a 0.5-mm crack (N_i) and the cycles to failure (N_f) in the notched plate tests are compared in Table 6.

Discussion of Results

Cyclic Deformation

The fallacy of assessing the fatigue resistance of materials on the basis of static properties, particularly yield or proof stresses, is apparent when the cyclic stress-strain curves are compared with the monotonic test results (Figs. 1 to 8). In all the materials tested, strain cycling induced a considerable drop in yield point with this softening giving way to hardening at higher strains. Furthermore, any ranking of the materials based on the static results is not necessarily conformed to under cyclic conditions.

The slightly superior results obtained from cyclic studies of Cast 1879 compared with Cast 500 are in complete contrast to the static test results (Table 2). Indeed, the considerable differences evident in the monotonic

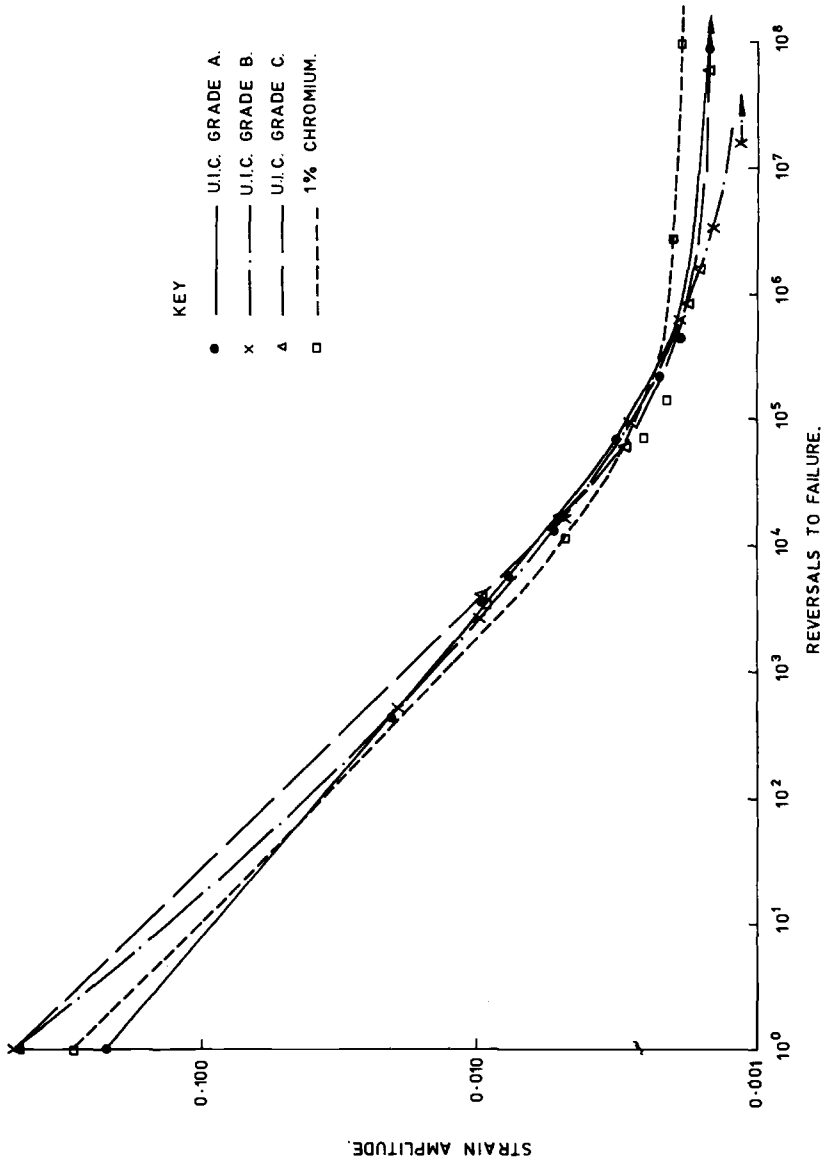


FIG. 10—Total strain-fatigue life relationship.

TABLE 4—Fatigue test results.

Notched Plates			
Nominal Stress Amplitude, $\Delta S/2$ (MPa)	$\frac{(\Delta S \cdot \Delta \epsilon \cdot E)^{1/2}}{2}$ (MPa)	Cycles to 0.5 mm Crack, N_i	Cycles to Failure, N_f
1. BS 11 Cast 1879			
325	421	3 486	4 200
220	220	20 250	33 450
160	160	125 858	174 810
138	138	...	463 720
108.5	108.5	1 905 870	...
2. BS 11 Cast 500			
405	652	240	252
219	219	13 496	23 850
181	181	35 776	67 500
140	140	324 846	415 750
3. BS 11 Cargo Fleet			
210	210	15 011	23 730
147	147	105 157	153 810
117	117	415 200	661 060
105	105	8 740 953	9 143 120
4. BS 11 Concast 2971			
210	210	20 585	34 500
151	151	226 912	329 956
123.5	123.5	881 605	1 202 020
114.5	114.5	943 067	1 170 870
107	107	4 262 167	4 804 980
5. UIC Grade A			
257	285	9 883	17 914
211	211	23 485	48 020
152	152	118 632	243 490
116.8	116.8	408 726	656 380
116.6	116.6	564 364	786 620
6. UIC Grade B			
349.5	428	2 016	2 255
300	332	6 304	9 487
200	200	48 495	81 250
140	140	762 287	975 000
128	128	346 275	470 705
7. 1 percent chromium			
250	250	13 713	24 553
214	214	27 684	64 030
152	152	373 200	474 370
123.5	123.5	2 506 285	2 754 120

curves of the four BS11 steels are greatly reduced (Figs. 1 to 4). This may be expected from the similar microstructures which were predominantly (90 to 95 percent) pearlitic with free ferrite at grain boundaries.

The results for the more highly alloyed UIC and 1 percent chromium steels (Figs. 5 to 8) display some superiority over those for the BS11 steels. In general, there is a greater degree of strain hardening, and the 1 percent chromium rail steel (Fig. 8) has a particularly high cyclic yield point, indicating a high fatigue limit.

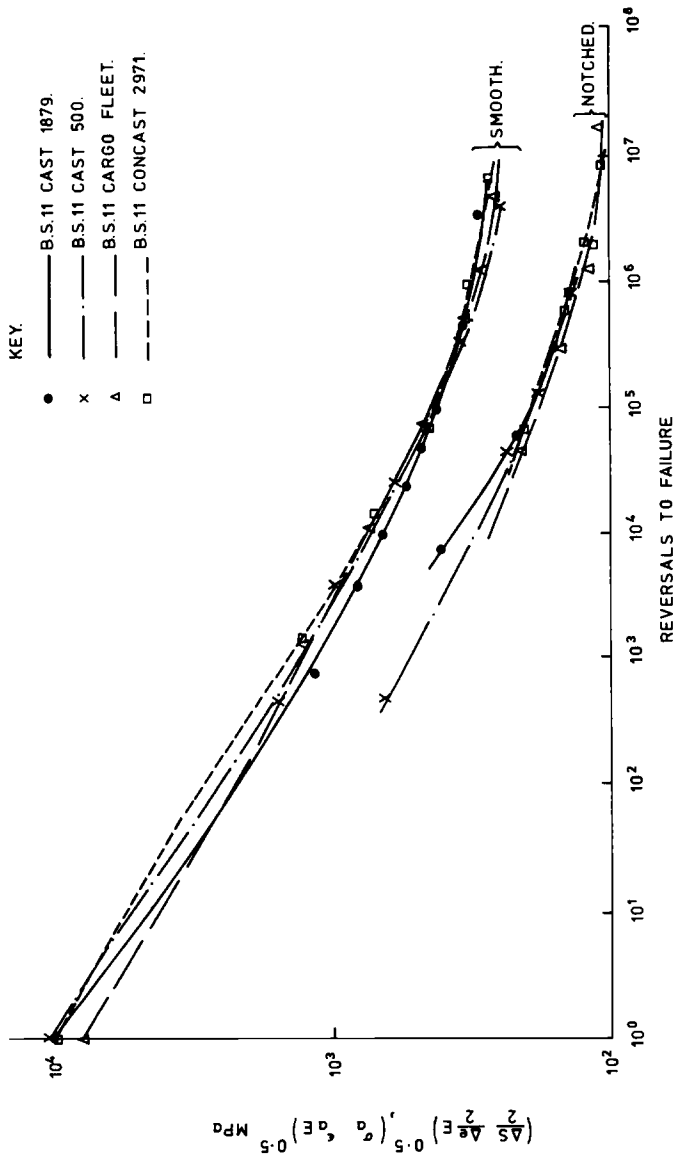


FIG. 11—Smooth and notched specimen life curves.

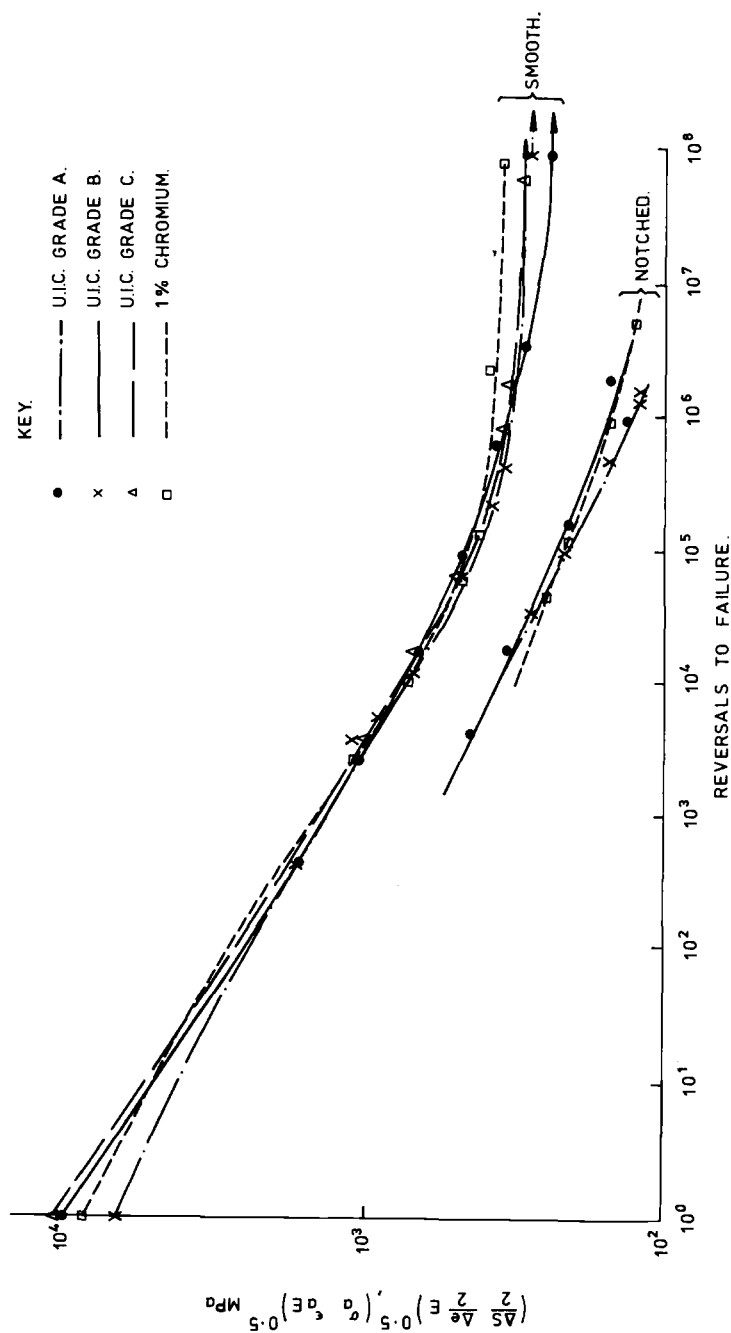


FIG. 12—Smooth and notched specimen life curves.

TABLE 5—Fatigue notch factors, K_f .

Material	K_f at 10^4 reversals	K_f at 10^5 reversals	K_f at 10^6 reversals
BS 11 Cast 1879	1.75	2.05	2.35
BS 11 Cast 500	2.30	2.20	2.30
BS 11 Cargo Fleet	. . .	2.35	2.40
BS 11 Concast 2971	. . .	2.20	2.40
UIC A	2.00	2.10	2.45
UIC B	2.05	2.05	2.30
1 percent chromium	2.05	2.05	2.45

Fatigue Life

The strain life results for all the materials follow the anticipated pattern with a smooth curve from the true fracture ductility (ϵ_f) to the fatigue limit. Of the BS11 steels, the initial superiority of the Cast 500 with a high ϵ_f is only maintained to about 10^6 reversals, where a low fatigue limit has a significant effect (Fig. 9). Cargo Fleet has a somewhat lower ϵ_f and is only marginally better than Cast 500 at long lives (Figs. 9 and 10). Any doubts concerning the ability of the continuously cast Concast 2971 to withstand fatigue, compared with the more conventionally produced rail steels, are not substantiated. In comparison, the remaining BS11 steel (Cast 1879) demonstrated a lower resistance to fatigue over a large range of endurances (Fig. 9). An apparent slight inferiority in the ability to resist low cycle fatigue ($<10^3$ reversals) is evinced by the UIC and 1 percent chromium steels: only beyond 2×10^5 reversals is there any superiority. However, as expected from the cyclic stress-strain relationship, the fatigue limit of the 1 percent chromium steel is especially high (Table 3).

Somewhat similar trends are evident in the $(\sigma_a \epsilon_a E)^{1/2}$ life relationships (Figs. 11 and 12). However, the former slight superiority of the BS11 steels in the short life region is reduced, due to the lower cyclic stresses necessary for a given strain in these materials. Thus, only the 1 percent chromium steel with its high fatigue limit displays any clear superiority and then only at lives greater than 10^4 reversals. With this one notable exception, the fatigue performances of all the steels were surprisingly similar considering the varying compositions and manufacturing processes employed.

Notch Sensitivity

The variations in K_f , the fatigue notch factor, with fatigue life show the trend that, as life increases, the values of K_f approach the theoretical value of 2.5. The apparent decrease in the effectiveness of the notch as fatigue life is reduced is not a material characteristic but is related to the increasing significance of the crack growth stage in the life of the plates.

TABLE 6—Stress levels in notched plates.

Material	$\Delta S/2$ at 10^6 reversals, (MPa)		$\Delta S/2$ at 10^7 reversals, (MPa)		$\Delta S/2$ at 10^8 reversals (MPa)	
	N_i	N_f	N_i	N_f	N_i	N_f
BS 11 Cast 1879	300	310	190	205	135	140
BS 11 Cast 500	260	275	175	195	135	140
BS 11 Cargo Fleet	165	180	115	120
BS 11 Concast 2971	180	200	130	140
UIC A	180	210	115	130
UIC B	310	320	205	220	140	145
1 percent chromium	195	225	145	150

Three of the BS11 steels have notched specimen stress-life curves which, in the limited region explored, can be considered parallel to the smooth specimen $(\sigma_a \epsilon_a E)^{1/2} - 2 N_f$ curves. This is a characteristic which was once thought to be common to all materials [3], but several exceptions have been found [8]. The use of a curve parallel to the smooth specimen data and displaced a vertical distance equal to K_t , or the value of K_f at the fatigue limit, in predicting the endurance of notched components should give a satisfactory conservative solution at all lives for the vast majority of metals.

If the materials are ranked in terms of stress ranges required to give various lives (Table 6), it can be seen that the 1 percent chromium and UIC Grade B steels are somewhat superior to UIC Grade A and the BS11 steels at all lives. In particular, the BS11 Cargo Fleet performed poorly over the limited range of results available. There is some variation between the BS11 steels; surprisingly the Cast 500 results are not inferior to the remainder of the BS11 rail steels, particularly at long lives.

Crack Initiation Resistance

The notch sensitivity results were obtained by taking the specimens to failure, and hence include the growth of relatively long cracks. In addition, the crack initiation resistance, as determined by the number of cycles required to produce a 0.5-mm crack, of the rail steels was measured (Table 4). This arbitrary length includes both the initiation phase and an element of early growth, where the crack is still strongly influenced by the presence of the hole and possibly subjected to some overall plasticity.

Once again, the UIC B and 1 percent chromium steels demonstrate the greatest resistance, with the former being superior at high stresses (Table 6). The BS11 steels are somewhat less resistant, with the Concast 2971 and Cast 1879 generally giving somewhat better performances.

Concluding Remarks

The tests have shown that the monotonic test can be an unreliable guide to the cyclic performance of a material, particularly when a notch is present. Thus, the apparent superiorities of Cast 500 over Cast 1879 and UIC A over UIC B are not always sustained in a cyclic environment. However, the evidence of cross-overs in the strain life curves from the smooth specimens tests precludes the choice of an overall best material. At long lives, the 1 percent chromium steel is clearly superior, but in the low cycle region only the BS11 Cast 1879 demonstrated any discernible evidence of a lower resistance to fatigue. Where a considerable mean stress is present, the 1 percent chromium rail steel maintains its superiority down to 10^4 reversals, and the resistance of the BS11 steels in the short life region is only marginally greater than that of the more sophisticated materials. Thus, in the majority

of practical situations, the replacement of BS11 steels by UIC Grades A, B, and C, or 1 percent chromium rail steels would not be a retrograde step from the point of view of fatigue resistance.

Notwithstanding the considerable differences in manufacturing methods and chemical compositions, the fatigue behaviors of the BS11 steels examined were remarkably similar when compared on the basis of $(\sigma_{\max} \epsilon_a E)^{1/2}$ curves. The BS11 Concast 2971 steel proved generally equal to the other BS11 steels manufactured by more conventional methods. Indeed, the notched plate and smooth specimen data indicate a relatively good performance in the high cycle region. However, the 1 percent chromium and UIC Grade B rail steels were clearly superior in the notched plate tests to all the other materials examined. The UIC Grade B steel demonstrated the greatest resistance to high strains, whereas the 1 percent chromium rail steel was better at long lives. A conservative method of obtaining data for notched components, based on Neuber plots where the smooth specimen $(\sigma_{\max} \epsilon_a E)^{1/2}$ curves are displaced by K_f , was noted. This is useful where a rapid assessment of the fatigue properties of a material is required, since tests have been devised to establish a satisfactory prediction of the material's fatigue performance from only two tests [9,10].

This last technique, together with those detailed in the paper, is currently being applied in the evaluation of the fatigue behavior of a wide range of railway materials. Less conventional rail steels, developed for high fracture toughness or extreme wear resistance, structural steels, wheel steels, and fishplate steels have been investigated, together with several nonferrous alloys.

Acknowledgments

The authors are indebted to A. J. Chelu for his outstanding experimental work. The difficult task of accurately measuring crack lengths was carried out by L. Shepherd to whom we are grateful. Valuable discussions have been held with K. Morton, R. G. Rebbeck, and R. McLester throughout this work.

APPENDIX

Cyclic Properties

The two relationships commonly used to describe the cyclic properties of most metals [9-11] are:

1. The cyclic stress-strain relationship, which may be described mathematically as

$$\sigma_a = K' (\epsilon_p/2)^{n'}$$

where

σ_a	=	stress amplitude,
ϵ_p	=	plastic strain amplitude,
K'	=	cyclic strength coefficient, and
n'	=	cyclic strain hardening exponent.

This information is established from the IST.

2. The relationship between applied strain and fatigue life, given by

$$(\epsilon_i/2) = \epsilon'_f (2N_f)^c + (\sigma'_f/E) (2N_f)^b$$

where

ϵ_i	=	total strain range,
ϵ'_f	=	fatigue ductility coefficient,
$2N_f$	=	number of reversals to failure,
c	=	fatigue ductility exponent—(the slope of the log (plastic strain)—log (life) line),
σ'_f	=	fatigue strength coefficient,
b	=	fatigue strength exponent—(the slope of the log (elastic strain)—log (life) line), and
E	=	Young's modulus.

This information is determined from constant-amplitude fatigue tests.

References

- [1] Endo, T. and Morrow, J., "Cyclic Stress-Strain and Fatigue Behaviour of Representative Aircraft Metals," *Journal of Materials*, JMLSA, Vol. 4, No. 1, March 1969.
- [2] Topper, T. H. and Gowda, C. V. Byre, "Local Stress-Strain Approach to Fatigue Analysis and Design," American Society of Mechanical Engineers Conference, Chicago, May 1970, "Design Engineering."
- [3] Morrow, J., Wetzel, R. M., and Topper, T. H., in *Effects of Environment and Complex Load History on Fatigue Life*, ASTM STP 462, American Society for Testing and Materials, 1970, pp. 74-91.
- [4] Yamashita, N., "The Stress and Strain Distribution in the Neck of a Tensile Specimen," *Bulletin of JSME*, Vol. 9, No. 36, 1966.
- [5] Morton, K., Rebbeck, R. G., Dabell, B. J., and Watson, P., "Cyclic Material Properties and Resistance to Fatigue—Part 1," British Railways Board Research and Development Division, Technical Note FM 26, Feb. 1974.
- [6] Smith, K. N., Watson, P., and Topper, T. H., "Stress-Strain Function for the Fatigue of Metals," *Journal of Materials*, JMLSA, Vol. 5, No. 4, Dec. 1970.
- [7] Gowda, C. V. Byre, "Fatigue Behaviour of Notched Mild Steel Plates in Plane Stress," Ph.D Thesis, University of Waterloo, Waterloo, Ontario, Canada, March 1969.
- [8] Watson, P. and Topper, T. H., "An Evaluation of the Fatigue Performance of Automotive Steels," SAE Paper No. 710597, Society of Automotive Engineers, New York, June 1971.
- [9] Morrow, J., "Fatigue Properties of Metals," Manual SAE ISTC, Div. 4, Society of Automotive Engineers, April 1964.
- [10] Morton, K., Dabell, B. J., and Watson, P., "Techniques for Predicting the Fatigue Performance of Materials," *Proceedings*, the Conference on Fatigue Testing and Design, Society of Environmental Engineers, London, April 1976.
- [11] Raske, D. T. and Morrow, J., in *Manual on Low Cycle Fatigue Testing*, ASTM STP 465, American Society for Testing and Materials, 1970, pp. 1-26.

Cyclic Inelastic Deformation and Fatigue Resistance Characteristics of a Rail Steel*

REFERENCE: Leis, B. N., "Cyclic Inelastic Deformation and Fatigue Resistance Characteristics of a Rail Steel," *Rail Steels—Developments, Processing, and Use, ASTM STP 644*, D. H. Stone and G. G. Knupp, Eds., American Society for Testing and Materials, 1978, pp. 449–468.

ABSTRACT: The cyclic inelastic deformation and fatigue resistance characteristics of a typical rail steel in use by American railroads have been determined. Uniaxial smooth specimens were obtained from the head of an unused section of rail and subjected to a variety of test conditions—static tension, static compression, and fully reversed constant-amplitude strain cycling. Additionally, a study of "history effects" was made. Included in this study were tests to examine the influence of orientation, mean stress, initial prestrain, and periodic overstrain, both the cyclic deformation response and the fatigue resistance being reported for each condition. Results obtained from these tests are discussed in light of predictive models for rail failure, particular attention being paid to the influence of stress state on deformation response and fatigue resistance.

KEY WORDS: steels, railroad tracks, deformation, fatigue (materials), stresses, strains

In order to determine both the fatigue resistance of new railroad rail and the remaining life of in-service rail, use is made of fatigue damage assessment and accumulation models. When the life to crack initiation of rail is defined as that life after which the progression of a crack can be adequately modeled as a rate process, crack initiation and propagation are both observed to occupy significant fractions of the rail's useful life. For the present paper, this useful life (design life) is considered to be that portion of the life until some minimum residual strength level is reached. This level is a function of the material, geometry, and loading and should be chosen with a view for the variable nature of both the loading and the fatigue process. In the context of these two definitions, damage assessment and accumulation models for each of crack initiation and propagation should be integrated into a single "continuing" damage model to make accurate fatigue life assessments for rail.

¹Research scientist, Structural Materials and Tribology Section, Battelle Columbus Laboratories, Columbus, Ohio 43201.

*Original experimental data were measured in U.S. customary units.

The purpose of the present paper is to report the results of an experimental program to develop both cyclic plasticity and fatigue life data for a rail steel which may be useful in performing both the initiation and the propagation analyses just noted. Specifically, results are reported from experiments designed to generate baseline fully reversed strain-controlled fatigue life and cyclic deformation response data for longitudinal and transverse samples cut from an as-rolled, unused section of steel rail (ASTM Specification for Carbon Steel Tee Rails A 1-76). Additionally, both cyclic deformation and fatigue life data developed during studies of mean stress effects and mechanical history effects are reported. Test conditions included in these studies designed to simulate certain events encountered in rail service loading are both compression and tension strain-controlled mean stress, initial compression overstraining and periodic overstraining. In addition to the just-noted use of cyclic deformation and fatigue life data in making rail fatigue life predictions, data reported in this paper are of value in analytical studies of cycle-dependent redistribution of stresses and strains due to railhead plastic flow. Of particular interest in this context are the inferences of transient material response on the shakedown phenomenon in rail [1].² The paper considers, in turn, the just-noted data in sections entitled Experimental Details, Experimental Results and Discussion, and Commentary and Conclusions. The results reported herein are taken from a current program [2] which is examining the phenomenon of cyclic plasticity in rail steels in greater depth.

Experimental Details

Materials and Specimens

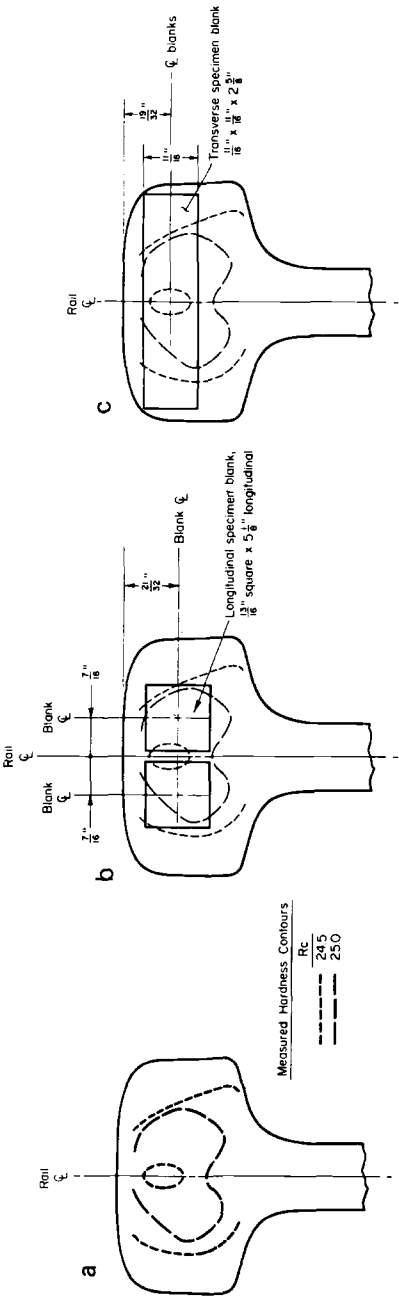
The rail from which specimen blanks were taken for this program was furnished by the Association of American Railways (AAR), Chicago. Three pieces, each about 2 m (6 ft) long, cut from a single section of 59.3 kg/m (119 lb/yd) rail were provided. The chemistry of samples of this rail showed its alloy composition in weight percent as: 0.82 percent carbon, 0.87 percent manganese, 0.035 percent phosphorus, 0.032 percent sulfur, 0.21 percent silicon, and the balance iron, a composition within ASTM Specification A 1-76 for rail steels in that weight range except that the carbon content was 0.02 weight percent too high. The microstructure of this nominally eutectoid steel was observed to be pearlite throughout the rail cross section. Figure 1 presents a micrograph typical of this structure. Hardness contours obtained from traverses on a grid in the head and web of the rail were, as expected, symmetric about the longitudinal plane of the rail, as shown in Fig. 2a. The Rockwell C hardness was in the range from 24 to 25.5 in the central region of the railhead.

²The italic numbers in brackets refer to the list of references appended to this paper.



FIG. 1—Photomicrograph of the pearlitic structure typical of the railhead, web, and flange microstructure (from the head); picral etchant, $\times 500$.

Uniaxial cylindrical test specimens with a 0.64 cm (0.250 in.) diameter by 1.28-cm (0.500-in.)-long gage section, as detailed in Fig. 3, were machined from 2.06-cm (13/16-in.)-square by 13.02 cm (5 $\frac{1}{8}$ in.)-long specimen blanks cut from the railhead symmetrically about the longitudinal plane of the rail, as shown in Fig. 2*b*. As evident from Fig. 2*a*, the Rockwell C hardness in the reduced section of these longitudinal specimens was about R_c 24 and varied less than one point. Transverse uniaxial test specimens having a reduced section identical to that of the longitudinal test samples were machined from specimen blanks 1.75 cm (11/16 in.) square by 6.67-cm (2 $\frac{5}{8}$ in.) long cut across the railhead, as shown in Fig. 2*c*. This location was chosen to best match the hardness in the reduced section of this transverse specimen with that of the longitudinal specimen. The reduced section of all test specimens was final machined in 20 passes of not more than 0.0254 mm (0.001 in.) per pass. Samples were subsequently longitudinally polished to yield a finish of about 380 mm (15 μ) root mean square (rms) and then degreased and stored. All specimens were provided with threaded ends. Longitudinal specimen grip ends were of sufficient length to preload the specimen grip connection through a locking nut. Transverse samples, however, had insufficient thread length for use of such a preload technique. These samples were preloaded



(a) Hardness contours.
(b) Longitudinal blank location.
(c) Transverse blank location.

FIG. 2—Hardness contours and locations of specimen blanks in the railhead.

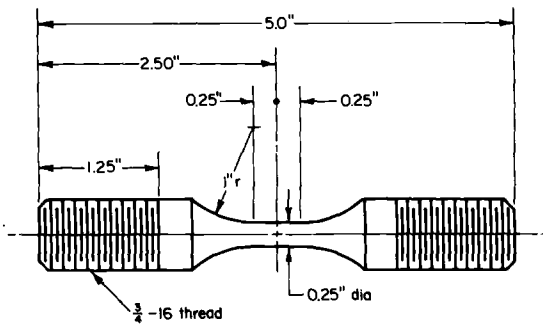


FIG. 3—Longitudinal uniaxial fatigue test specimen.

through bearing on a buttonhead during gripping, with care being taken to ensure that alignment was maintained.

Apparatus and Procedure

Data reported in this paper were derived from axially loaded specimens tested in similar closed-loop servocontrolled electrohydraulic test systems. All testing was performed in strain control.

Strain was controlled over a 1.28-cm (0.500-in.) gage length using a clip-on extensometer calibrated to ASTM Class B₁. Strain was programmed to follow a sinusoidal waveform at frequencies ranging from 0.1 to 30 Hz, depending on the amplitude of the control strain. The ability of the extensometer to operate over this range of frequencies was independently verified as a function of the strain amplitude prior to beginning the test program. To ensure that the temperature of the reduced section remained ambient in tests with either large strain amplitudes or higher frequencies, the frequency was chosen so that the indicated temperature (monitored via a thermocouple looped about and in contact with the test section) remained constant within 3°C (5°F) during testing. Strain was controlled to within 1 percent of the programmed signal. The extensometer calibration was performed and verified several times during the test program.

Load was monitored in all tests using a commercially available load cell mounted in series with the specimen. Calibration of the load cell was performed prior to and verified once during the test program. The load cell was observed to be accurate and linear within 0.1 percent of the operating range used in the present program.

All specimens were gripped in a fixture arrangement similar to that detailed in Ref 3. It is noteworthy that such an arrangement features a liquid-solid Woods metal grip which serves to minimize specimen mounting stresses. Prior to commencing the test program, the alignment was adjusted

to minimize bending strains, the adopted standard being bending strains less than 1 percent of the imposed axial strain.

Monotonic and cyclic deformation response was recorded continuously during the first ten cycles and at logarithmic intervals thereafter on an x - y recorder, while both load and strain were continuously recorded on a time-based, high-speed strip chart recorder. Specimens were examined after separation to determine if the failure was representative of the bulk of the metal or if it initiated at some rail processing flaw or inclusion. No detailed metallography of the fractures was performed. All data reported herein were derived from test records in accordance with the ASTM Committee E9.08 draft of a tentative standard for fatigue testing practice.

Experimental Results and Discussion

Deformation Response

Consider first the deformation response of the rail steel under each of static and cyclic straining. Pertinent results obtained from static tension, static compression, incremental step and constant-amplitude cyclic strain-controlled tests which characterize metal static and cyclic deformation and fatigue life properties after Morrow [4] are reported in Table 1 for both longitudinal and transverse orientations. Data used to establish the values of these mechanical properties are shown on coordinates of stress and strain in Fig. 4, which presents in Part *a* typical deformation response obtained from static tension and static compression testing along with that for the first and thirtieth blocks of incremental step cycling, whereas Part *b* presents that obtained from stable stress-strain loops developed under constant-amplitude strain cycling. For this paper, a stress-strain loop is said to be stable if the cyclic rate of change in stress was less than 6.89×10^{-6} MPa/cycle (10^{-6} ksi/cycle). Also shown in Fig. 4*b* is the metal's deformation response plotted as isocycle lines at cycle numbers of 1 (static tension), 10, 10^2 , 10^3 , and 10^6 . Note that, at higher strain amplitudes ($\Delta\epsilon/2 > 0.15$ percent), the deformation response for the longitudinal samples at cycle numbers greater than 10^4 is virtually coincident.

Upon examining Fig. 4*a*, it is apparent that the static response in tension and compression is virtually coincident at strain levels less than 1.5 percent. Results obtained for transverse specimens tested in static tension but not shown in this figure differ from the corresponding longitudinal data by less than 1 percent. Also, from Fig. 4*a*, it can be observed that the stable cyclic deformation response as developed from incremental step testing differs significantly from the static tension data, particularly at strain amplitudes between 0.15 and 0.35 percent and beyond 0.6 percent. In the range of amplitudes bracketed by 0.15 and 0.35 percent, the cyclic stress response lies below that for the corresponding static value—in which case, the metal is

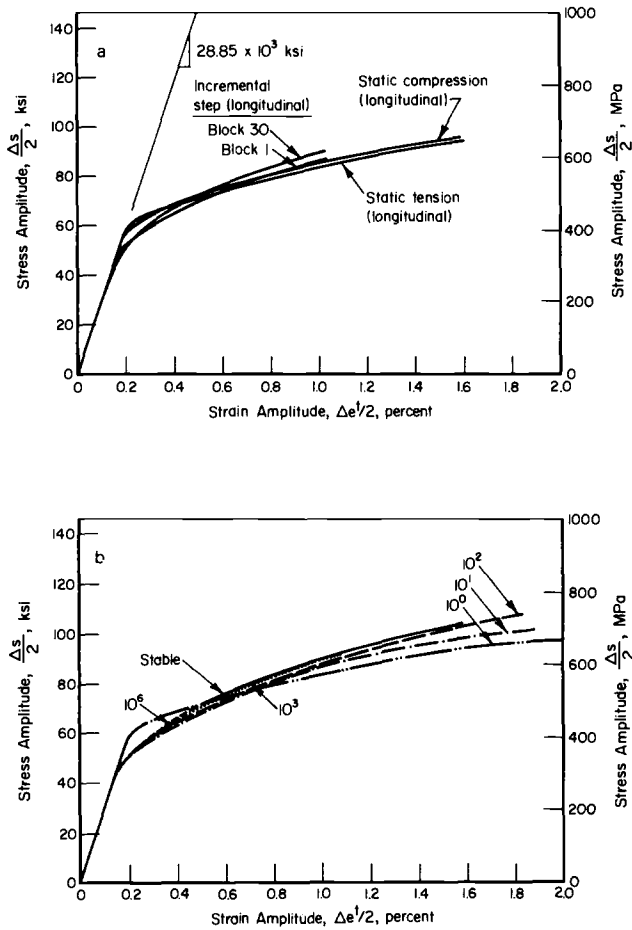
TABLE 1—*Deformation and fatigue of the rail steel; longitudinal orientation except as noted.*

Monotonic Properties ^a	Cyclic Properties ^d
Modulus of elasticity, E , 28.85 (28.25) ^b $\times 10^3$ ksi	proportional stress, 42.10 ksi
Yield strength, 0.2%, 70.08 (71.7) ksi	strain hardening exponent, n' , 0.239 ^{c,e}
Ultimate strength, 134.6 ksi	strength coefficient, K' , 88.63 ^{c,e} ksi
Reduction in area, 14.70%	fatigue strength coefficient, S'_f , 187.5 ^c ksi
True fracture strength, 151.6 ksi	fatigue ductility coefficient, e'_f , 0.22 ^f
True fracture ductility, 0.159	fatigue strength exponent, b , -0.096 ^f
Strain hardening exponent, 0.163 ^c	fatigue ductility exponent, c , -0.493 ^f
	transition life, $2N_t$, 7125 ^g reversals

Conversion factors—

1 ksi = 6.895 MPa

^a Average of four tests.^b Values in parenthesis are for transverse specimens; average of two tests.^c Also characteristic of the transverse orientation.^d Data derived from a total of ten tests.^e Parameters in the stress-strain equation $S = K' \epsilon_p^{n'}$; where S and ϵ_p are stress and plastic strain amplitudes, respectively.^f Parameters in the strain life equation $(\Delta \epsilon^h)/2 = (S'_f/E) (2N_f)^b + e'_f/(2N_f)^c$; where $\Delta \epsilon^h/2$ is the total strain amplitude corresponding to a life to failure of N_f cycles or $2N_f$ reversals.^g The life at which the quantities $(S'_f/E) (2N_f)^b$ and $e'_f/(2N_f)^c$ are equal.



(a) Static tension, static compression, and incremental step test stress-strain curves.
(b) Transient cyclic stress-strain curves.

FIG. 4—Material static and cyclic stress-strain response.

said to have cyclically softened. Conversely, beyond a strain of 0.6 percent, the cyclic stress response lies above the static curve, indicating the metal has cyclically hardened.

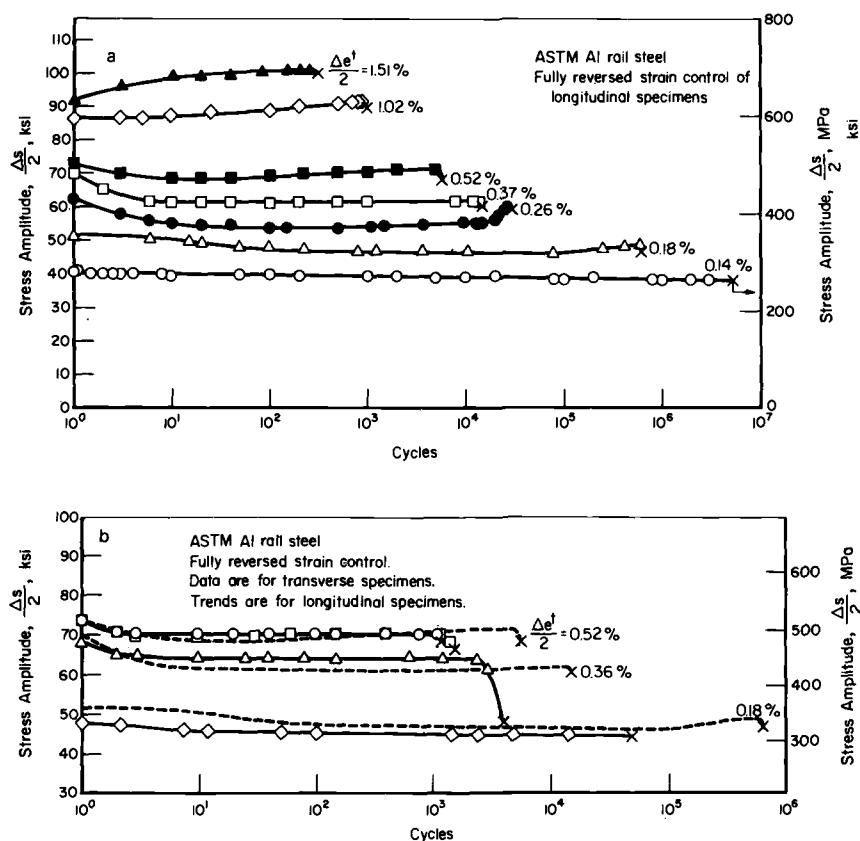
Note that a major fraction of the cyclic softening occurred in the first block of loading. This observation is significant since it indicates only a small amount of cumulative plastic strain causes virtually all of the softening evident after a total of 38 blocks of incremental step history. This behavior suggests that, very early in life, the deformation response of the metal in a rail may change radically. Also of interest in this context is the cyclic hardening observed at strains beyond 0.6 percent. Under incremental step loading, the rate of hardening cannot be similarly established by comparing

data from the first and thirtieth blocks shown in Fig. 4a. To study the rate of hardening, use must be made of transient stress-strain curves such as those shown in Fig. 4b. It is clear that several large amplitude cycles accumulating a significant amount of plastic strain must occur before the deformation response saturates. The hardening rate is, therefore, less as compared to the softening rate. As a consequence, many applications of higher loads would be required to achieve a comparable increase in the deformation response of the material in the railhead in this high strain regime.

A mathematical model of the transient stress-strain response shown in Fig. 4b has been constructed, the basis for and the results of which are detailed in Ref 2. Essentially, this model utilizes forcing functions which cause actual stress response to be simulated by varying each of the strength coefficients and strain hardening exponents reported in Table 1 as a function of accumulated plastic strain in the manner of Martin et al [5]. Because the details of such a model are beyond the scope of the present and the results of such modeling well documented in the literature, further discussion of this subject will not be pursued. The reader should consult Ref 2 for additional information.

Note that the deformation response presented in Fig. 4a for incremental step cycling was obtained from an incremental straining about a mean tension strain equal to 1.10 times the static proportional strain. This condition was imposed so as to relax any residual stress induced during the rails' manufacture. Stress response developed during this test virtually matched that obtained during a similar test without the mean strain. Such a result indicates that the manufacture of rail does not induce significant residual stresses in the region from which the longitudinal samples were obtained.

The dependence of the stress response on the number of strain cycles shown in Fig. 4b is more easily studied when these same data are replotted on coordinates of stress amplitude and cycles as in Fig. 5a. A significant feature of the rail steel's cyclic deformation response evident in this figure is that, even at endurance strain levels, the material softens continuously with cycles, as shown by the data for the 0.14 percent amplitude test. Because the driving force for this softening is the presence of inelastic strain and because, with softening, the magnitude of this inelastic component increases, this softening will continue with cycles. As a consequence of this softening at strains below the endurance strain, the use of elasticity analyses in fatigue life prediction models for rails may lead to significantly inaccurate estimates of the stress-strain fields about inclusions, rail bolt-holes, and the like. Stress response obtained as a function of cycles from transverse samples as a function of applied cycles is comparable to that obtained from longitudinal samples, as evident in the comparison data shown in Fig. 5b. The transverse data indicate that the stable stress response corresponds more closely to the static value, indicating less softening as compared to the data for longitudinal samples. Note also that the life of these transverse samples is signifi-



(a) Longitudinal stress response.

(b) Comparison of stress response for longitudinal and transverse orientations.

FIG. 5—Dependence of the stress response on the number of strain cycles.

cantly less than the corresponding longitudinal samples, this aspect being examined later in the paper. Consider now the deformation response obtained under nonfully reversed strain-controlled conditions.

In addition to determining material monotonic and cyclic deformation response under baseline fully reversed strain-controlled conditions, a study was also made of the deformation response under nonfully reversed strain control. The purpose of these tests was to develop data representative of both tensile and compressive mean and residual stress states in rails.

Typical results obtained from the mean stress studies are presented in Fig. 6 on coordinates of the ratio of the mean stress in the N^{th} cycle to that in the initial cycle and $(\text{reversals} + 1)/2$. The choice of these coordinates is based on convenience and ease in data interpretation. There are two important features of the cyclic mean stress relaxation behavior of this rail steel evident in the data presented in this figure. The first is that the rate of relaxation—

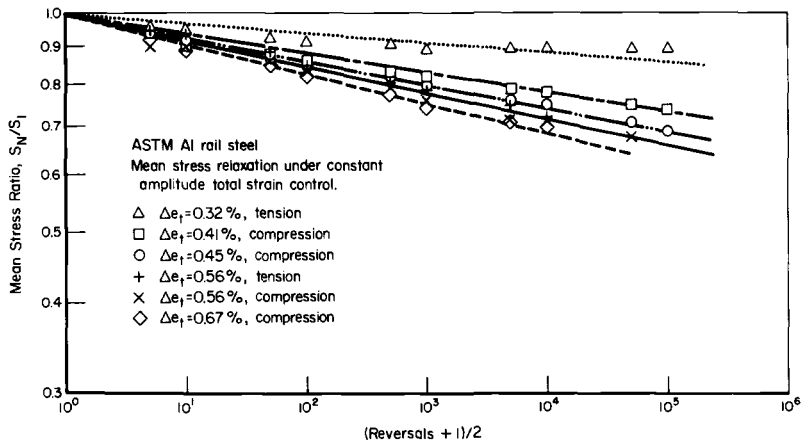


FIG. 6—Dependence of the mean stress ratio on the number of strain cycles.

manifest in the negative slope, more negative slopes indicating higher rates—is essentially identical for both tensile and compressive mean stress under comparable control conditions. Such a response is apparent in this figure in the data presented for a controlled cyclic strain range of 0.56 percent. Although not shown in this figure for reasons of clarity, this same behavior is also observed in comparable tests at a controlled strain range of 0.45 percent. The second important feature evident in this figure is that the data, as would be expected, show increasing relaxation rates as the range of total strain increases.

While more extensive testing could be performed to examine cycle-dependent mean stress relaxation, the span of controlled strain ranges which could be investigated would not significantly extend that of this investigation. This is because for smaller strain ranges the driving force for relaxation, plastic strain, is so small that the phenomenon does not occur, while at larger ranges the stress response becomes fully reversed, even if the metal is initially hardened by significant static straining. But, even with the results of additional testing, the rationale for relating these test data, which in this investigation show the relaxation rate to depend on the mean strain (or mean stress) and the range of controlled strain, is lacking when Fig. 6 is used as a format for data interpretation. Because plastic strain provides the driving force for this transient phenomenon, the data of Fig. 6 should be rationalized by plotting the relaxation rate as a function of plastic strain.

Figure 7 replots the relaxation data on coordinates of relaxation rate and plastic strain range. Additionally, data are included for tests which shared a common range but had differing mean strains. The close correspondence of all relaxation rates with the unique trend shown in this figure indicates plastic strain satisfactorily accounts for the observed dependence of relaxation rate on mean strain and total strain range for this rail steel. As with the fully reversed strain-controlled deformation response data, this cyclic mean

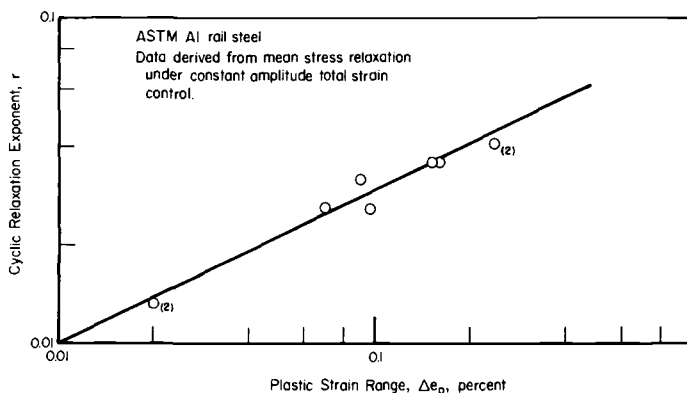


FIG. 7—Cyclic relaxation exponent as a function of the plastic strain range.

stress relaxation behavior has been mathematically modeled, details and results of which are reported in Ref 2. Like the model for fully reversed deformation response, relaxation is achieved by the use of a forcing function which causes the value of the strength exponent (Table 1) to vary so as to duplicate observed stress response. Details of this model are beyond the scope of the present; for further information, the reader may consult Ref 2. Let us now examine the fatigue resistance of this rail steel under baseline fully reversed strain control conditions and a variety of other strain histories.

Fatigue Resistance

As noted in the introduction, the fatigue life of a metal, be it in use in a structure or in a test in the laboratory, is spent first initiating, then propagating fatigue cracks until unstable growth leads to specimen separation. When examining the fatigue resistance of the rail steel using uniaxial test specimens as is done in this paper, the relative fraction of the total life spent in initiation and propagation strongly depends on three major factors in addition to the bulk character of the material. These are (a) the use of small-diameter specimens which preclude significant propagation periods, (b) the definition of crack initiation, and (c) the presence of inhomogeneities, such as inclusions and flaws which are induced during rail fabrication, whose size represents the tails of the inclusion and flaw size distribution.

Of these factors, the artificial restraint on the propagation period introduced by the use of small-diameter specimens precludes the direct comparison of the fatigue resistance of these rail steel samples with that for actual rail. These data are, however, useful in making assessments of the life to initiate cracks whose length is on the order of 2.54 mm (0.1 in.) long and whose surface occupies an area of about 6.5 square millimeter (0.01 square inch), the size and area typically observed for this test specimen configuration. In all cases for data reported in this paper, the number of cycles to

separation of the specimen differed from that at which the tensile component of the cyclic stress response first began decreasing as compared to the often stable compressive component by less than 13 percent of the total life. For longer life tests ($N > 10\,000$ cycles), this asymmetric decrease in tensile stress indicating the presence of a crack occurs, on the average, in the last 5 percent of the total life. Thus, separation is a fair measure of crack initiation life and, therefore, is adopted as a definition of crack initiation for this paper. In this context, the fatigue life data to be discussed in the ensuing paragraphs of this section are useful only in predicting the formation of cracks on the order of 0.1 in. long or smaller. It is noteworthy that such an initial crack length is convenient for use in fracture mechanics predictions of flaw growth which, in the past, typically utilized initial flaw sizes of the order of 0.254 to 2.54 mm (0.010 to 0.10 in.) [6].

Finally, the last of these factors—the presence of inhomogeneities and flaws—will be addressed. The influence of this factor is often manifest in a reduction in the number of cycles spent in crack initiation. Additionally, depending on the relative size and character of inclusions, their presence may likewise reduce the crack propagation period. The action of this factor, however, does not adversely affect the usefulness of the data reported here because similar inclusions and flaws exist in the actual rail. But care must be exercised to ensure that differences in the probability distributions of the sizes and locations of inclusions and flaws between test specimens and rails are accounted for, perhaps by the use of available probabilistic models. With these considerations in mind, the fatigue life characteristics of uniaxial, small-diameter rail steel samples will now be examined.

Fatigue resistance of the rail steel is reported in this section for a variety of strain-controlled conditions. Included are results obtained from extensive testing under constant-amplitude fully reversed and nonfully reversed (mean stress) conditions, along with those from systematic testing that interspersed initial cyclic compression prestrain and periodic overstrain histories in otherwise constant-amplitude fully reversed histories. Data obtained from the fully reversed baseline condition have been reduced and plotted in Fig. 8 on coordinates of strain and life in the manner detailed in Ref 4. Results developed using the nonfully reversed control condition are presented in Fig. 9 on coordinates of the product of stable maximum stress and the strain amplitude and life. The use of this product as a basis for consolidating mean stress effects in fatigue has been suggested by Smith et al [7]. It has recently been derived as a special case of a more general energy-based damage parameter [8]. Since too few data are available for the nonconstant amplitude histories to warrant graphical presentation, results of these tests will be reported later when the results are compared with the baseline data.

The constant-amplitude fully reversed data shown in Fig. 8 represent results of tests performed on longitudinal samples of the rail steel. Examination of the fracture surfaces of these specimens indicated the initiation/propagation process began at the free surface, the crack propagating in an

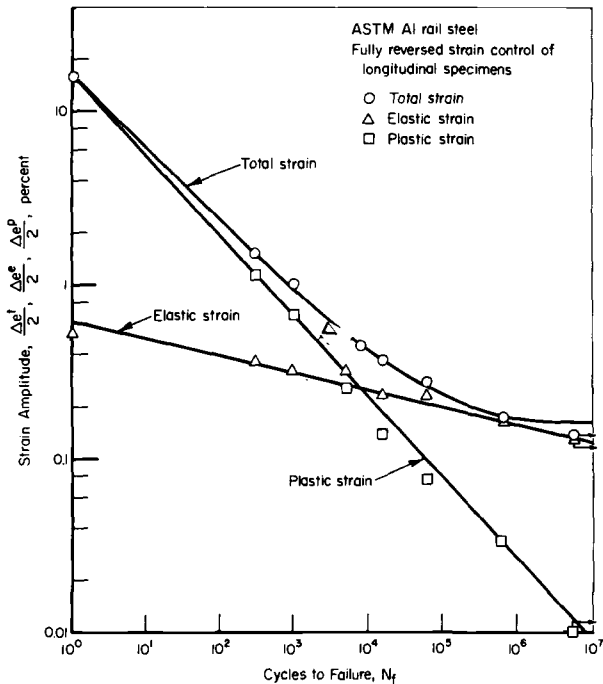


FIG. 8—Fatigue resistance of the rail steel as a function of applied strain.

intragranular manner terminating in unstable cleavage mode without shear lip formation as typified by the macrograph shown in Fig. 10a. In many cases, the fracture surface showed evidence of multiple initiation: as many as three sites in some instances. However, in no case were these initiation sites observed to be related to metallurgical inhomogeneities or flaws discernable at a magnification factor of 10. Furthermore, no “inside out” failures, typically encountered in dealing with metals whose fatigue resistance is controlled by void/inclusion initiation sites, were noted in this cursory metallographic study. These two facts suggest that the data of Fig. 8 should be tempered by the results of probabilistic flaw/inclusion distribution models before being used in predictive models of the fatigue resistance of actual rail.

Comparison of the data shown in Fig. 8 with that in the literature for intermediate carbon and alloy steels measured in terms of fatigue strength-based parameters as reported in Table 1 shows the fatigue resistance of this steel to lie slightly below the trend for steels of comparable hardness [9]. However, its resistance as assessed in terms of fatigue ductility-based parameters listed in Table 1 lies above the corresponding trend [9]. In contrast to observed differences in these measures of fatigue resistance between this rail steel and trends established for other steels, the transition

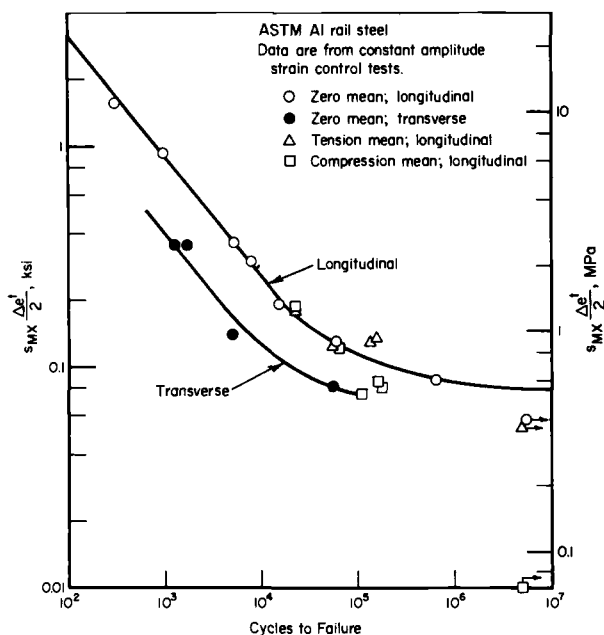
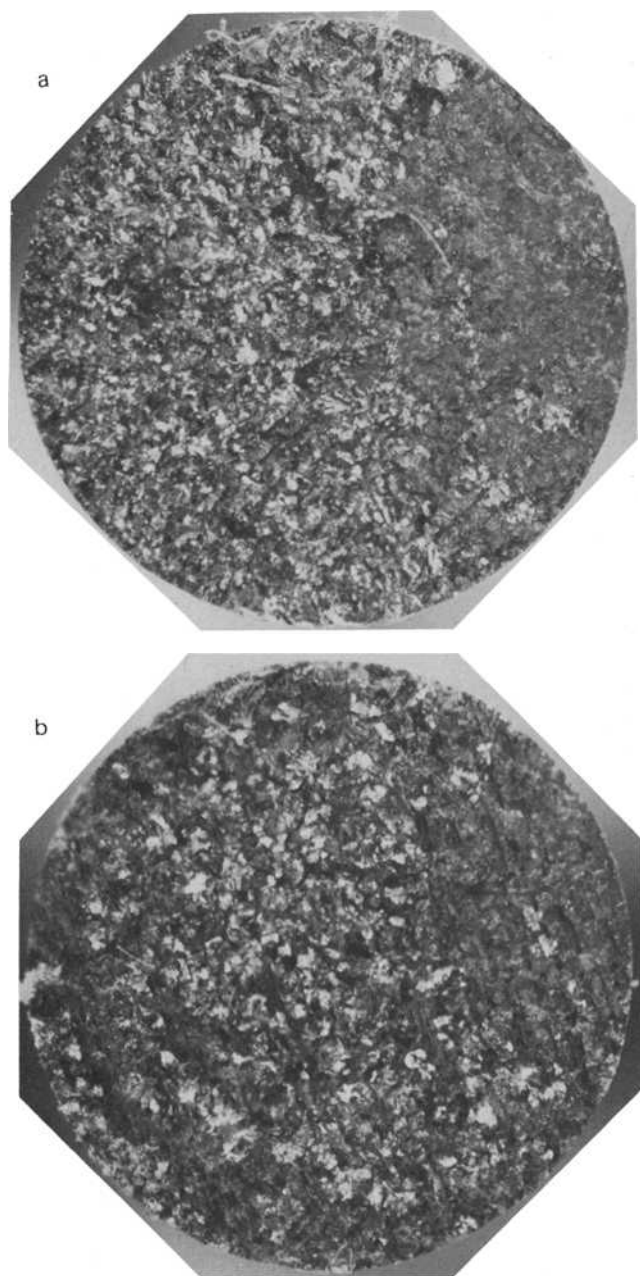


FIG. 9—Fatigue resistance of the rail steel as a function of the parameter $s_{mx}\Delta\epsilon^I/2$.

fatigue life corresponds closely with the trend value for steels of comparable hardness. As expected in view of the previously noted trend in stress-based resistance, the fatigue limit for the steel lies below that observed for steels of comparable hardness by about 18 percent. Finally, it should be noted that the total strain life behavior shown in Fig. 8 can be analytically characterized using the empirical strain life equation suggested by Morrow [4], the constants as well as the equation being reported in Table 1.

Consider now the effects of mean stress and transverse specimen orientation on the fatigue resistance of the rail steel. In order to establish the extent to which these effects alter the fatigue resistance as compared to that for longitudinal samples tested under fully reversed control conditions, use must be made of a fatigue damage parameter which provides an equivalence condition between differing control conditions for equal fatigue damage. The present paper utilizes the previously introduced parameter $s_{mx}\Delta\epsilon^I/2$ [7] for this purpose, a form parameter which has been shown to achieve high consolidation for a variety of steels and other metals [7,10]. Fatigue life data shown in Fig. 8 have been replotted in terms of the damage parameter $s_{mx}\Delta\epsilon^I/2$ in Fig. 9, the data being shown as open circular symbols. Also shown on this figure are data from tests of transverse samples, shown as solid circles, and from tensile and compressive mean stress tests, shown as open triangles and open squares, respectively.

It is clear from the data shown in Fig. 9 that transverse samples have



(a) Longitudinal orientation.
(b) Transverse orientation.

FIG. 10—*Typical fracture surfaces.*

significantly less fatigue resistance as compared to the corresponding longitudinal data. Some insight as to the cause of this reduced resistance is gained from a macroscopic examination of the fracture surface. It is apparent from such studies that the fracture surfaces of all transverse samples included an apparent delamination flaw region such as that shown in Fig. 10b. Such a flaw lying in a plane perpendicular to the loading axis would be expected to initiate fatigue cracks almost immediately after strain cycling commences. Assuming that such initiation occurred with the first cycle, the total life of the transverse specimens would be spent in propagation, a seemingly realistic circumstance as evident in the close correspondence between propagation periods in longitudinal samples and the total life of transverse samples, especially at the lower strain level. Given that such a circumstance prevails, predictive models for the initiation and growth of longitudinal vertical and horizontal flaws would best be based on fracture mechanics principles.

Consider now the role of mean stress in altering the rail steels fatigue resistance as compared to fully reversed conditions. Fatigue life data for a range of mean strains and strain amplitudes are shown in Fig. 9, along with the corresponding zero mean strain case. Mean stress data are available for only a small range of lives because, as noted earlier, at higher strains (and shorter lives), mean stress relaxes quickly to the fully reversed state while, at smaller strains, negligible fatigue damage is accumulated so that failure does not occur. It is apparent from Fig. 9 that values of $s_{mx}\Delta e'/2$ from about 1.38 to 0.48 MPa (0.20 to 0.07 ksi) bracket these limiting conditions. Between these values, the parameter achieves a very high data consolidation at shorter lives ($N_f < 100\,000$ cycles) of both the tensile and compressive mean stress data. But at longer lives, the scatter is somewhat greater: a factor in life of about 2.5 for tensile mean stress data and 10 for compressive mean stress data. It might be noted that fracture surfaces of all mean stress test samples are similar to that for the fully reversed case, an example for which is shown in Fig. 10a.

Finally, let us examine the role of initial compressive prestrain and periodic overstrain interspersed with constant-amplitude cycles in altering the fatigue resistance as compared to the constant-amplitude resistance. The initial compression cyclic prestrain history consisted of 50 cycles of zero-compression cycling at a strain range of 0.50 percent. Such compression precycling is said to cause crack initiation fatigue damage in the form of surface roughing which serves to reduce the total life substantially more than indicated by linear cumulative damage theory. After the application of the cyclic prestrain, linear damage theory would indicate 99 percent of the life remains. For the cases examined (0.165, 0.18, and 0.36 percent strain amplitude after initial compression cycling), the results obtained for the higher amplitudes show that significantly more damage occurred than was indicated by linear damage since only 88 and 69 percent of the life remained. (Note that no failure occurred at the lower level.) These results indicate that

large compression cycles early in the life of a rail steel can significantly reduce its fatigue resistance. In the context of predictive models for rail fatigue resistance, they suggest that events in the service loading which cause compression overstrains early in life do more extensive damage than would be expected based on linear damage theory. Such a history dependence of the damage rate can be conservatively accounted for by using initial compression precycled life data as a basis for damage assessment in predictive models. Consider now the influence of periodic overstrains in reducing the fatigue resistance as compared to baseline constant-amplitude data. To date, the results obtained from only one periodic overstrain condition followed by constant-amplitude cycling are available. That condition is overstrain cycles of 0.36 percent amplitude interspersed every 10^5 cycles in a fashion which does not induce a mean stress. Although the damage computed for the overstrain cycles using a linear theory is less than two hundredths of a percent of that considered to cause failure, the fatigue resistance of the rail steel is observed to decrease some 50 percent. Tests in which the periodic overstrain induces each of a tensile mean stress and a compressive mean stress are presently under way, the results to be presented in Ref 2. It is expected that, although differing amounts of mean stress damage will result in these tests, the life will be dominated by the periodic overstrain effect. Like the results for the compression precycling history, that obtained for the periodic overstrain history shows the fatigue resistance of the rail steel to be very sensitive to history effects, a dependence which must be accounted for in predictive models for rail failure. Again, the use of the appropriate overstrain life data would provide a conservative basis damage assessment in such a predictive model.

Commentary and Conclusions

Throughout the paper, the static and cyclic deformation response and fatigue resistance of a rail steel determined using small-diameter uniaxial test specimens have been reported and discussed in the context of predictive models for rails. One of the more vexing problems encountered in using these data in such predictive models resides in the use of uniaxial stress data developed under constant-amplitude control conditions in situations where the stress state is multiaxial and the service loading significantly different from that used to develop the data.

The extension of data developed under uniaxial constant-amplitude conditions to deal with multiaxial variable-amplitude loading requires (a) an equivalence condition between stress states for both deformation and fatigue and (b) a means of resolving variable-amplitude cycles into equivalent constant-amplitude cycles which cause equal fatigue damage. Under conditions of proportional stressing (that is, stresses in an element of material increase or decrease in direct proportion to each other), the available data indicate that deformation equivalence can be provided by criteria of the form of Von Mises [11] with care being taken to ensure that equivalence

criteria for stress and total, elastic, and plastic strain satisfy the stress-strain equation. Likewise, under proportional stressing, criteria of the form of Von Mises seem to provide adequate consolidation of fatigue life data [8,12], while complex stress-strain histories seem to be suitably resolved into equivalent constant-amplitude cycles using procedures like rain flow counting [13]. However, the deformation response in situations where the multiaxial principal stress field rotates (under nonproportional stressing) is not easy to characterize analytically; suitable theories being complex and few in number [14]. Likewise, difficulty is encountered in resolving complex histories into equivalent constant-amplitude cycles since techniques such as rain flow counting are invalid [15]. The task of formulating models for fatigue failure in the contact stress field of a rail in which the principal stress field rotates will, therefore, not be simple and straightforward. Further research, both analytical and experimental, is needed to understand adequately the physical processes which lead to rail flaw initiation and propagation. Without an understanding of these physical processes, it is doubtful that accurate mathematical models for rail life prediction can be developed.

In summary, this paper has examined the monotonic and cyclic deformation response and fatigue life characteristics of a rail steel. Results were presented for a variety of strain-controlled test conditions. The experimental results were discussed in light of predictive models for rail fatigue resistance, with particular attention being paid to the influence of stress multiaxiality.

Conclusions which can be drawn from this work studying the deformation and fatigue character of a rail steel follow:

1. The ASTM specification A 1-76 rail steel undergoes significant cyclic softening at lower inelastic strains, while, at larger strain levels, the metal cyclically hardens.
2. Stable deformation response for this rail steel is similarly characterized by single specimen and incremental step test data.
3. Relaxation rates for this rail steel are similar under comparable control conditions for each of tensile and compressive mean stresses.
4. Relaxation rates under differing combinations of the control mean strain and cyclic range can be rationalized on the basis of the plastic strain range.
5. The fatigue resistance of longitudinal samples of this rail steel falls slightly below that for a variety of intermediate carbon and alloy steels.
6. The fatigue resistance of transverse samples falls significantly below that for longitudinal samples.
7. Compression precycling and period overstrains significantly reduce the life of the rail steel as compared to that anticipated on the basis of a linear damage theory.

Acknowledgments

This work was funded by the Transportation Systems Center as an extension to the contract "Rail Material Failure Characteristics," Number

DOT-TSC-1076. The experimental work was performed in the Fatigue Laboratories of Battelle's Columbus Laboratories by Norman Frey, whose work, care, and diligence are gratefully acknowledged.

References

- [1] Johns, T. G. and Davies, K. B., "Preliminary Description of Stresses in a Railroad Rail," Report Number FRA-ORD-71-35, Battelle's Columbus Laboratories, Nov. 1976.
- [2] Leis, B. N. and Laflen, J. H., "Cyclic Inelastic Deformation and Fatigue Resistance of a Rail Steel: Experimental Results and Mathematical Models," Topical Report to the Transportation Systems Center, Contract No. DOT-TSC-1076, Battelle's Columbus Laboratories, June 1977.
- [3] Feltner, C. E. and Mitchell, M. R., in *Manual on Low-Cycle Fatigue Testing*, ASTM STP 465, American Society for Testing and Materials, 1969, pp. 100-128.
- [4] Morrow, J., in *Internal Friction, Damping, and Cyclic Plasticity*, ASTM STP 378, American Society for Testing and Materials, 1965, pp. 45-84.
- [5] Martin, J. F., Topper, T. H., and Sinclair, B. F., "Computer Based Simulation of Cyclic Stress-Strain Behavior," T&AM Report No. 326, University of Illinois, July 1969; see also *Materials Research and Standards*, Vol. 11, No. 2, Feb. 1971.
- [6] "Airplane Damage Tolerance Design Requirements," Military Specification, U.S. Air Force, MIL-A-83444 (tentative), May 1974.
- [7] Smith, K. N., Watson, P., and Topper, T. H., *Journal of Materials*, Vol. 5, No. 4, Dec. 1970, pp. 767-778.
- [8] Leis, B. N., *Journal of Pressure Vessels and Piping*, American Society of Mechanical Engineers, Vol. 99, No. 4, Nov. 1977, pp. 524-533.
- [9] Landgraf, R. W., in *Achievement of High Fatigue Resistance in Metals and Alloys*, ASTM STP 467, American Society for Testing and Materials, 1970, pp. 3-36.
- [10] Jaske, C. E., Feddersen, C. E., Davies, K. B., and Rice, R. C., "Analyses of Fatigue, Fatigue Crack Propagation, and Fracture Data," NASA CR-132332, National Aeronautics and Space Administration, Nov. 1973.
- [11] Havard, D. G., Williams, D. P., and Topper, T. H., "Biaxial Fatigue of Mild Steel: Data Compilation and Analysis," *Proceedings, 3rd International Conference on Structural Mechanics in Reactor Technology*, Vol. L, Sept. 1975.
- [12] Havard, D. G., "Fatigue and Deformation of Normalized Mild Steel Subjected to Cyclic Biaxial Loading," Ph.D. Thesis, University of Waterloo, 1970.
- [13] Endo, T., Mitsunaga, K., Takahashi, K., Kobayashi, K., and Matsuishi, M., "Damage Evaluation of Metals for Random or Varying Load," paper presented at 1974 Symposium on Mechanical Behavior of Materials, Kyoto, August 1974; see also, Dowling, N. E., *Journal of Testing and Evaluation*, Vol. 1, No. 4, July 1973, pp. 271-287.
- [14] Hunsaker, B., Vaughan, D. K., and Stricklin, J. A., "A Comparison of the Capability of Four Hardening Rules to Predict a Materials Plastic Behavior," American Society of Mechanical Engineers, ASME Paper No. 75-PVP-43.
- [15] Leis, B. N. and Laflen, J. H., "A General Energy Based Postulate for Fatigue and Creep Fatigue Damage Assessment," Contractor Report to Association of American Railroads, Battelle's Columbus Laboratories, Sept. 1977.

Summary

Summary

The conference published in this volume represents the first meeting held in the United States on rail steels, but much of the information presented contributes to the general knowledge of the behavior of high-carbon steels; for example, the unique fracture behavior of eutectoid steels was revealed as being dependent on ferrite crystallographic orientation and not on cementite cracking as was previously believed.

By direct correlation of fracture surface and microstructure, it was shown that a crack could often be obstructed at a prior austenite grain boundary. This phenomenon is believed to be due to the discontinuous nature of ferrite orientations across the boundary. Since the pearlite colonies usually nucleate at prior austenite grain boundaries, the constituents of pearlite bear specific orientation relationships with the parent austenite grain, pearlite colonies across an austenite grain boundary can thus often have different orientations. It was further observed that, while a crack could change direction at pearlite colony boundaries, more often it continued as a single cleavage facet across several pearlite colonies. Since a crack propagates along (100) cleavage planes of ferrite in pearlitic steels, the latter observation suggests that the cleavage planes in these colonies must be continuous. In support of this, (100) cleavage planes of ferrites were found to be closely aligned across a number of pearlite colonies, using thin foil transmission electron microscopy, and to some extent were compatible with the facet size. These colonies are expected to lead to a single cleavage facet. The cleavage facet size can therefore be considered as an effective parameter to describe the toughness of materials with similar microstructures. Since the average facet size is a strong function of the prior austenite grain size, these considerations support the results of a previous study which show that the fracture toughness in fully pearlitic rail steel is primarily dependent on the prior austenite grain size.

The results of this study also suggest that, if there is any preferred orientation in the microstructure, this could lead to large cleavage facets and a loss of toughness. Therefore, in designing rail steels with better toughness, alloying elements and processing schedules should be selected carefully to minimize the formation of a strong texture.

This work explains the unique ability of eutectoid steels to increase their strength and toughness independently and explains the effect of some alloying elements (for example, vanadium) on toughness, which was presented in another of the papers.

The area of fatigue in rail steels produced two differing views. Two papers showed a wide band of fatigue crack growth rates. One of these papers reported that the presence of grain boundary ferrite could reduce the growth rate by a factor of two at low and intermediate growth rates. In addition, the phenomenon of stable cleavage bursts during fatigue crack growth was shown to be a function of the stress intensity.

The opposite view presented was that crack propagation was independent of chemical composition and mechanical properties. It was contended that fatigue life would be extended more effectively by controlling the load environment.

A third view on the fatigue behavior of rails was presented in two papers on the cyclic inelastic deformation behavior of rail steels. These papers reported that rail steels undergo significant cyclic softening at lower inelastic strains while, at larger strain levels, the metal hardens cyclically. It is to be expected that work based on this methodology can eventually produce a predictive model for rail fatigue resistance.

A further major contribution of the conference was that the role of nonmetallic inclusions in the initiation of transverse cracks (detail fractures) was isolated. Heretofore, detail fractures were thought to have been initiated from rail shells turning into the transverse plane. However, two of the papers presented show clearly that transverse fatigue defects are initiated from nonmetallic inclusions, especially complexes of calcium, silicon, and aluminum oxides.

With respect to the contribution of stress on crack growth and nucleation, two differing views were proposed. One view held that the reversal of shear stress as the wheel passed over the crack was responsible for crack growth. The other view held that vertical bending of the railhead imposes tensile stresses on the crack tip. Both papers agreed that, whichever stress was dominant in promoting crack growth, the crack growth was occurring in a mixed stress intensity. It is interesting to note that these two papers represent the first attempt at a complete stress analysis of rail since that of Timoshenko and Langer in 1934.

In view of the problems associated with the increasing wheel loads in the United States, several papers discussed the development of higher strength alloy-steel rails. The principal alloying elements whose effects were investigated were chromium, molybdenum, and vanadium. Two of the authors demonstrated that yield and tensile strengths similar to those produced in heat-treated rails could be obtained in alloy rails.

A list of the accomplishments of this symposium and publication would therefore consist of the following:

- Presentation of the mechanism of fracture in pearlitic steels.
- Clarification of some unusual fatigue phenomena in pearlitic steels.
- Isolation of nonmetallic inclusions as the origin of detail fractures.

- Two stress analyses of rails using finite element and boundary integration techniques.
- The development of several types of high-strength alloy rails to meet increasing service demands.

D. H. Stone

Director-Metallurgy, Association
of American Railroads, Chicago,
Ill.; coeditor.

Index

- | | |
|--|---|
| <p>A</p> <p>Abrasion (<i>see</i> Wear)</p> <p>Alloy steels</p> <p> Chromium, 67, 199, 215, 221</p> <p> Chromium-columbium-vanadium, 175-177</p> <p> Chromium-molybdenum, 175, 182-186, 217</p> <p> Chromium-vanadium, 175, 181-182</p> <p> Columbium, 225-227</p> <p> Manganese, manganese-vanadium, 17, 36</p> <p> Molybdenum, 215-218</p> <p> Silicon, 17, 36</p> <p> Vanadium, 222-224</p> <p>B</p> <p>Bearings, 10</p> <p>C</p> <p>Continuous casting process, 15, 17, 257-267</p> <p>Continuous-welded rail, 119</p> <p>Controlled cooling, 10, 274, 275</p> <p>D</p> <p>Design, 8</p> | <p>E</p> <p>Economics, 13</p> <p>F</p> <p>Fatigue, 26, 29, 30, 33, 81, 82, 195, 244-248, 251, 324-327, 363-385, 397-401, 414-427, 430-468</p> <p>Flakes (<i>see</i> Shatter cracks)</p> <p>Fracture toughness, 31, 36-39, 85-88, 157, 158, 195, 268, 284, 307-327, 391-396, 401-405</p> <p>H</p> <p>Heat treating, 17</p> <p>Hydrogen, 38, 53, 56-61</p> <p>I</p> <p>Ingot practice, 15</p> <p>L</p> <p>Lubrication, 66, 74</p> <p>M</p> <p>Microstructure, 36, 101-104, 150-154, 163, 215, 222-231, 246-</p> |
|--|---|

248, 251, 260–262, 291–297,
365–384

U

Ultrasonic testing, 48–54, 262, 283

R

RALUS process (*see* Ultrasonic
testing)

Residual stresses, 25–28, 73

S

Shatter cracks, 10, 18, 39, 40, 56–60,
64

Shelling, 10, 66, 110

Steelmaking, 14, 15, 18

Straightening, 18, 19

Stress analysis, 330–340, 343–367

V

Vacuum degassing, 57–62

W

Wear, 32–35, 59, 67–78, 88–96, 168,
187–195, 284

Welding

Arc, 134

Electric flash, 12, 120, 127–132

Electroslag, 135

Gas pressure butt, 12, 132, 133

Shielded metal arc, 136

Submerged arc, 135

